The Effects of Early-Age Stress on the Elastic and Viscoelastic Behavior of Cement Paste

Christopher L. Galitz

Dissertation submitted to the faculty of the Virginia Polytechnic Institute and State University in partial fulfillment of the requirements for the degree of

Doctor of Philosophy

In

Civil and Environmental Engineering

Zachary Grasley, Committee Co-Chair

Carin Roberts-Wollmann, Committee Co-Chair

David Mokarem

Finley Charney

Johan Foster

September 25, 2015

Blacksburg, VA

Keywords: cement paste, relaxation, early age cement, viscoelasticity, aging, Young's modulus, beam bending, micro-CT, X-ray diffraction, thermogravimetric analysis

The Effects of Early-Age Stress on the Elastic and Viscoelastic Behavior of Cement Paste

Christopher L. Galitz

Abstract

The viscoelastic behavior of concrete, nearly completely attributable to changes in properties in the cement paste, is an ongoing area of research with the objective of avoiding unpredictable response and potentially failure of concrete structures. This research explores the elastic and viscoelastic response in cement paste beams using relaxation testing, with and without strain reversals in the load history. It was seen that strain reversal imparts significant changes in mechanical response, retarding load relaxation. Companion beams were tested for chemical composition at varying depths in the beam section and the results were compared to those of control specimens not subject to stress. Results indicate significant variations in composition implying that stress accelerates the hydration process. The reasons behind the acceleration are discussed and incorporated into a preliminary solidification-dissolution model for beam relaxation. The model, though in need of improvement through further research, shows promise in potentially predicting relaxation in cement paste and by extension, in concrete structures.

Dedication

For my kids in hopes they will one day understand its content and its *raison d'être.*

Acknowledgements

I wish to acknowledge, with gratitude, the guidance and support of my committee, each offering a unique perspective toward the work presented here. I especially give thanks to my Co-Chairs, Dr. Carin Roberts-Wollmann for always having an open door to discuss anything from cement hydration to the joys of living in Blacksburg and Dr. Zachary Grasley for pushing me far beyond the limits of my past experiences into a whole new world of knowledge to be gained, explored, and shared.

This material is based upon work supported by the National Science Foundation under Grant No. 1327314. Any opinions, findings, and conclusions or recommendations expressed in this material are those of the author and do not necessarily reflect the views of the National Science Foundation.

Table of Contents

List of Figures

List of Tables

1. Introduction

Characterization of the early age properties of concrete is an ongoing area of research particularly important in understanding longer-term behavior of prestressed and conventional concrete members subjected to varying load histories. Despite the research and resulting behavioral models in widespread use, long-term performance is still unable to be accurately predicted. In some cases, this may lead to serviceability issues, relatively minor in scope. However, in the extreme, a lack of predictive ability can lead to structural failures, as seen recently with the Koror-Babeldaob Bridge in Palau (Bazant et al. 2012a; Bazant et al. 2012b). Study of that failure using models produced by several international engineering societies is unable to explain the excessive deflections leading to the bridge failure. This indicates that the models, as conceived, are incomplete to describe material behavior.

The viscoelastic behavior of concrete is a complex subject. Ongoing hydration of cement, combined with accumulating cracking and dissolution of hydration products leads to an evolution of properties that is dependent on mix design, time, stress, temperature, and humidity, at the least. Current models attempt to account for individual effects, as they can be identified through the study of past performance at the macro and global scales. These models generally do not investigate the actual mechanisms responsible, at the micro-scale, for viscoelastic behavior. A better understanding of this micro-scale behavior is imperative if a more accurate predictive model is to be produced.

It is generally accepted that viscoelastic behavior of concrete is controlled by the behavior of the cement paste with aggregate showing little if any change in behavior over time. Thus, a study of cement paste, without aggregate and its inherent variability in geometry and properties, may be sufficient to more accurately describe concrete's long-term behavior. Because the rate of change of cement paste is most pronounced at early ages (less than 28 days), a study of this period of the paste's evolution should provide the greatest insight into mechanisms responsible for behavior.

When studying quasi-static viscoelastic response, there are two potential categories of test most commonly conducted: creep and relaxation. A creep test applies a constant

load and measures resulting displacements or strains over time. Because the cement paste is hydrating throughout, each increment of time results in a differing volume of hydration products and cement grains subject to the applied load. In relaxation testing, the specimen is subjected to a displacement that is held constant with the force required to hold that displacement measured over time. In some modeling approaches, it is assumed that hydration products formed after the initial displacement do not carry any load, thus keeping the volume of hydration products under load constant throughout the test. This simplifies the analysis of results, eliminating the change in volume with time as a variable and thus should provide a clearer picture of material behavior.

Over the past several decades, viscoelastic behavior of concrete has been considered from several different viewpoints. The preponderance of recent research considers the influence of viscoelastic properties on the performance of prestressed members. In a typical prestressed beam, the creep of the concrete leads to an induced loss of stress in prestressing strands, which in turn alters the stress state in the concrete. Because the stress state in the steel and concrete determines the beam behavior in terms of serviceability issues, estimating this continuous viscoelastic effect before and after the member has been put in service is topic of great importance in ongoing research. Thus, any relaxation testing conducted should simulate, to the extent possible, the anticipated stress states in a typical prestressed beam. Specifically, a beam relaxation test can more appropriately address stress gradients than would uniaxial or ring tests.

1.1 Background and Review of Literature

1.1.1 Viscoelastic Behavior

It has long been understood that concrete, and more specifically, the cement paste within concrete, evolves over time. Cement is a mixture of varying proportions of compounds including alite (Ca_3SiO_5), belite (Ca_2SiO_4), aluminate ($Ca_3Al_2O_6$), and ferrite (Ca_2AlFeO_5) based chemical compounds, typically referred to as “phases” (Taylor 1990). Each of these phases reacts with added water to form hydrates. Because the rate of reaction of each phase is different and the distribution of cement particle sizes is highly variable, it is difficult to predict the exact makeup

of the resulting structure. However, it is generally assumed that at the macro scale (specimens > 1mm in every dimension), structural properties, both elastic and viscoelastic, are generally isotropic and homogenous and can be studied and potentially predicted.

The study of the viscoelastic nature of cement paste is a growing field with research spanning from the nanoscale to the macro scale. See, for example: (Bazant et al. 1973; Fischer et al. 2014; Grasley and Lange 2007a; Grasley and Lange 2007b; Jones and Grasley 2011; Milauer 2010; Parrott 1973). As technology improves the ability to focus on smaller and smaller regions in the paste, the study of individual phases has become possible (Alizadeh et al. 2010; Allen et al. 2007; Aono et al. 2009; Huang et al. 2013). However, these various studies rarely bridge the gap between small-scale observation or modeling and global scale concrete performance.

In concrete, the majority of research on viscoelastic properties has been focused on macro or global-scale specimens with results of hundreds of tests collected into a large database for creep and shrinkage data (H. Hubler et al. 2015). Thus far, consideration of this database has resulted in the formulation of four different design methods included within applicable design practices (ACI 2008). The approach typically used within these methods is to fit equations to data while the fundamental factors causing the observed behavior are often overlooked. Recent studies examining the efficacy of these four models, and others, have concluded that the quality of the models varies widely when compared to observed behaviors (Al-Manaseer and Prado 2015; Bazant and Li 2008; Goel et al. 2007). Thus, research continues in an effort to improve the available prediction models (Duan 2013; Hilaire et al. 2014; TC-242 2015; Wendner et al. 2013).

Of interest in the current study is that the ACI document specifically excludes use of the included methods when strain reversals, such as a situation where a beam experiences a change from a negative moment to a positive moment, are present. Though relaxation after strain reversal has been studied in several polymer

materials (Drozdov 2010; Gramespacher and Meissner 1995; Jansons et al. 2012), including the development of complex mathematical models (Drozdov 1998), the behavior has not to date been adequately characterized for cementitious materials.

1.1.2 Relaxation Testing

There has been very little relaxation testing of cement paste beams as reported in the literature. There has been limited research working with saturated beams focused on relaxation due to hydraulic movement of fluid through the pore structure (Valenza and Thomas 2012; Vichit-Vadakan and Scherer 2003). However, this research focused on the near-immediate response (less than 2 hours of load) and not on longer-term early-age behavior and therefore did not examine viscoelastic relaxation in great detail. The testing is relevant even for later behavior because in a typical early age cement paste, even under sealed conditions, the material is not completely saturated. This allows capillary flow at the local level due to applied pressures (Acker 2004; Grasley and Leung 2011b), a process analogous to flow to a surrounding medium.

Other relaxation testing, of rings (material placed in a donut-shaped mold around a steel ring and strain in the ring monitored) and uniaxial specimens, has been conducted by several authors, e.g. (Beushausen et al. 2012; Choi and Oh 2010; Hossain and Weiss 2004; Li et al. 2014), but using concrete and mortar specimens rather than cement paste. The testing protocols vary from author to author and typically include influences of multiple factors including mix design, temperature history, and drying shrinkage. Though the authors present the results of these variations, they do not focus on the physical mechanisms responsible for stress relaxation. Relaxation in beam bending has been studied in other materials, showing similar trends as those seen in cementitious materials (Evans et al. 2011; Taiy-In et al. 2015; Zhang and Kitching 1987).

1.1.3 Viscoelastic Modeling

Cement paste viscoelastic properties as a function of time, both with the actual age of the cement paste and with the time under particular conditions, have been

addressed in several ways in the literature, one of which is the solidification theory (Bazant 1977). The theory considers aging as a solidification process such that during any change in time, additional hydration products form, with each new segment created in a stress-free state and with age-independent physical properties. Though other authors have provided additional modeling techniques (Lothenbach and Winnefeld 2005; Mounanga et al. 2004; Yang et al. 2011), the solidification theory is still in widespread use as a basis for modified methods. These modifications have taken the form of "time shifts" to address additional viscoelastic aging of the cement paste (Bazant et al. 1997; Grasley and Lange 2007a), and slight changes to the rheologic model (Mabrouk et al. 2004). All of these methods rely on fitting techniques to provide equations for creep and/or relaxation curves. In each, the fit terms themselves have no real physical meaning but overall trends in the terms can provide insight.

1.1.4 Cement Paste Properties and Evolution

The properties of hardened cement paste have long been studied with perhaps the definitive work presented in a series of articles in the mid-20th century, e.g., (Powers and Brownyard 1946). Since this early work, there have been numerous studies presented looking at the influence of various chemical compositions, cement properties, and environmental factors on these hardened properties, e.g., (Bentz et al. 2001; Dias et al. 1990; Igarashi 2011; Maia et al. 2011; Valenza and Thomas 2012). However, as the current research is intended to look at ongoing effects during early age loadings, it is more relevant to consider the evolution of properties during this early age.

The development of cement paste properties can be broken into several different categories. The first relates to the development of stiffness, as measured by the elastic Young's modulus. This modulus is generally considered to be a function of the degree of hydration that is seen to accelerate due to load (Galitz and Grasley 2015; Harsh et al. 1990; Inozemtsev 1995; Tamtsia et al. 2004; Zhou and Beaudoin 2003).

The second category is that of microstructure evolution, both during formation and as a result of imparted stresses. Though the microstructure likely has a direct effect on macro and global scale behavior, it is typically considered separately from work involving determination of Young's modulus (Chen et al. 2004; Li et al. 2012; Plassais et al. 2005; Venkiteela et al. 2010). Of particular note is work conducted on cement paste beams (Sun et al. 2013). In this testing, the authors considered the resulting microstructure and chemical composition of regions of a beam subjected to bending. However, the results were limited to a single point in time (28 days).

The third category to consider as an evolution of the cement paste is somewhat the inverse of the previous category. It has been hypothesized that when subjected to stresses, the microstructures of hydration products can dissolve into the solution within adjoining spaces (Grasley et al. 2014; Li et al. 2015; Suter and Benipal 2006). This behavior is consistent with the governing thermodynamic equilibrium but has not been verified experimentally. A similar mechanism involving damage to the microstructure, typically known as submicrocracking, has been observed by several researchers (Bazant and Zubelewicz 1988; Bernard et al. 2003). Though these changes in microstructure may help explain relaxation behavior, until now it has been difficult to verify the mechanisms at the sub-micro scale.

1.1.5 Chemical Composition

Along with the evolution of the microstructure is the change in chemical composition as cement grains hydrate to form hydrations products. Numerous papers have been written studying the chemical composition of pastes throughout hydration (Bergold et al. 2013; Fagerlund 2009; Stepkowska et al. 2005). Of specific importance are those that additionally explain in depth the methods used to determine the composition. Two methods are used most commonly to track both chemical composition and, by inference, degree of hydration. The first is X-ray diffraction ("XRD"), typically performed on crushed or powdered cement paste specimens, and consists of using an X-ray beam to reflect off crystalline

structures at varying angles of incidence corresponding to known chemical compounds (Hong et al. 2003; Scrivener et al. 2004; Vidican et al. 2008). The second method, thermo gravimetric analysis ("TGA"), uses mass loss during high temperature heating to determine the actual quantity of particular hydration products present in the sample (Kar et al. 2012; Pane and Hansen 2005; Zeng et al. 2012). Taken together, as is the case for most of the cited work, the test methods identify individual phases of hydration products, their proportions, and the overall degree of hydration of the sample.

1.1.6 Microstructure Visualization

In recent years, technology has advanced to the point where micro and sub-micro scale evaluation of materials is relatively commonplace. Several methods are available with each varying in pixel resolution, i.e., the smallest scale at which a material can be observed. In cementitious materials, to obtain the highest resolution images, often helpful in identifying phases of hydration products, a scanning electron microscope ("SEM") is often used (Aichele et al. 2015; Chen et al. 2010; Ylmén et al. 2009). However, as with any microscopy, information is limited to a two-dimensional image at a single location. The alternative method being increasingly used in the field of concrete research is X-ray computed microtomography ("micro-CT") (Artioli et al. 2010; Halleck et al. 2006; Stock 2008; Stock et al. 2002). Through algorithms compiling the results of numerous X-ray images, a three-dimensional model of X-ray absorption of the material can be constructed (Bentz et al. 1995; Chotard et al. 2001; Hu et al. 2014; Landis and Keane 2010; Promentilla et al. 2008).

Through analysis of gray scale slices of the 3D model, unhydrated cement grains and hydration products may be identified. This analysis has traditionally used methods seeking boundaries or gradients within the gray scale images (Otsu 1979; Weszka 1979). In micro-CT studies, it has been seen that this approach can have limitations, given that histograms of gray scale reconstructions often show overlapping distributions corresponding to the paste constituents (Huang et al. 2013; Landis and Keane 2010). With higher definition micro-CT imaging,

individual phases of hydration products may also be delineated (Promentilla et al. 2009).

1.1.7 Relationship between Cement Paste and Concrete Properties

The intent of the current research is to characterize properties and behaviors of cement paste under the assumption that the information derived can be extrapolated to macro- and global-scale behaviors of concrete. This extrapolation has been studied for various properties including elastic (Endo 2009) and viscoelastic (Neville 1964) properties. However, as much of the viscoelastic behavior of concrete is dictated by drying shrinkage and creep (Grasley and Leung 2011a; Ling 2012; Rajagopal and Wineman 2004; Wittmann 2009), mechanisms not being considered in this study, a true correlation of derived cement paste behavior to concrete in general, would require incorporation of additional work.

1.2 Research Objectives

In the large field of viscoelastic behavior of concrete, one goal of additional research should be to better understand long-term behavior with an eye to explaining anomalies and inconsistencies with current models and prediction methods. However, achieving this goal would involve dozens if not hundreds of research projects and related analysis. For the current project, the goal was to focus on a small piece of this larger field, specifically, to examine how long-term behavior of concrete members might be affected by changes in cement paste brought about by early-age stresses. Considering past work performed in this area, as summarized above, the following objectives were determined such that results, if achieved, would dovetail into the existing knowledge base and help to more fully explain the viscoelastic behavior of concrete.

1. Characterize relaxation in cement paste specimens subject to early-age stresses of varying magnitude, duration, and direction
2. Investigate the effect of past stress history on the evolution of elastic properties of cement paste specimens

3. Identify differences, if any, between relaxation in tensile and compressive regions of cement paste beams subject to three-point loading
4. Compare beam relaxation to uniaxial compressive stress relaxation
5. Identify changes in hydration rate in regions of varying stress in beam specimens using multiple test methods
6. Identify changes in chemical composition in regions of varying stress in beam specimens using multiple test methods
7. Identify areas of possible improvement in commonly used design and prediction models

1.3 Scope

To achieve the listed objectives, the project was broken into several parts. Some of the later parts were designed based on preliminary results of earlier parts. The cement paste used for each test was a 0.4 w:c ratio using Type I/II Portland cement. Mixing and casting were done using ASTM standard methods, where such standards exist and were deemed appropriate, with consolidation of specimens of particular importance to reduce or eliminate the effect of entrapped air.

1.3.1 Beam Relaxation with Strain Reversal

Small-scale (15 mm x 15 mm x 300 mm) cement paste beams were fabricated, sealed, and loaded in three-point bending within the assumed elastic range. Application of initial load occurred at one and four days of age with additional loading applied at four and ten days of age. For the additional loads, some were applied in the same direction as the original orientation while some were applied in reverse, imparting a stress reversal within the beam section. After each load application, displacement was held constant and the load required to maintain the displaced position captured using automated data acquisition equipment. During load application, measurement of displacement was made within the assumed elastic range to determine the quasi-instantaneous Young's modulus of elasticity at the given age. Comparison specimens, not previously loaded, were tested for Young's modulus throughout the approximately 21-day protocol.

Results of the relaxation tests were used to fit relaxation function curves consistent with models used in the literature. Comparison of different ages and loading histories were made with specific consideration of the effects of stress reversal. Young's modulus was fit using models available in the literature, comparing previously loaded specimens to those not previously loaded.

1.3.2 Comparing Beam Behavior to Cylinder Behavior

In addition to beams, several small (3 mm diameter) cylinders were cast, sealed, and subject to relaxation testing in compression. Loads were applied once within the testing protocol and displacement kept constant throughout. Results were fit to the same models used for beam testing. The resulting relaxation curves were compared to those of beam tests to determine whether viscoelastic behavior within beam sections can be considered using a series of uniaxial fibers, as is typically done in non-viscoelastic materials.

1.3.3 Degree of Hydration and Chemical Composition of Specimens

Some of the beam specimens subject to single direction loading were cut up into individual samples throughout five regions of beam height at several ages within the testing protocol. These samples, each representing an average stress condition ranging from "high" tension to "high" compression, were crushed to powder and tested using both XRD and TGA analyses. Results were used to determine the degree of hydration and chemical composition at the various age / load duration points. Comparison was made to samples not previously loaded.

Additionally, throughout beam and cylinder testing, cylindrical companion specimens were imaged using micro-CT. Samples included cylinders in a loaded condition, cylinders not loaded, and "cores" from beam specimens, oriented vertically. These images were used to determine the degree of hydration with specific emphasis on any variation in the measurement along the height of the beam.

1.3.4 Consideration of Fluid Effects within Specimens

Because there is the possibility that the stress gradient present in the beams may provide significant relaxation due to fluid migration within the pore structure, an effect not present in uniaxial tests, additional beam specimens were tested at varying temperature, changing the viscosity of the pore fluid, thereby increasing the flow rate of the fluid through the pore structure. The resulting relaxation curves were compared to the sealed specimens previously tested to identify the relative effect.

1.3.5 Research components not in scope

Preliminary consideration of the project objectives leads to several possible research components that are not part of the project. The first is a consideration of the similarities or differences between relaxation and creep behavior. Though creep testing may provide similar insight into physical mechanisms responsible for viscoelastic behavior, the level of complexity added was deemed not warranted. The second possible task for future work is uniaxial tensile relaxation testing. The test configuration necessary to provide relaxation data, with specimens at a similar physical scale to those used for compression is not feasible within the larger scope of the project. An additional protocol looking at slightly larger scale specimens could potentially include the tensile testing. Thirdly, all considerations of stress are limited to the assumption that effects of stress on properties and behavior are linear; the exact relationship of varying stress levels beyond the loads applied was not considered. Lastly, note that there was no SEM visualization work conducted. The coordination of the use of the equipment, with sufficient data points to effectively compare not only variations in age but stress, was deemed to be impractical and likely cost ineffective.

2. Framework for Analysis

Before results of various mechanical and chemical tests can be analyzed, it is necessary to create the underlying framework for the analyses that will be used to describe chemical compositions and mechanical response. For cement pastes, both are linked to the hydration process but as will be seen in subsequent sections, assumptions often made in the literature, and those made for purposes of this work, are subject to opinion and approximation. The hydration relationships chosen and used for this research are described below.

2.1 Volumetrics of Cement Hydration

At the initial time of cement paste creation, $t=0$, the mixture exists as a mass of cement grains and a mass of water. Each of these masses has volume, determined or assumed by dividing by the specific gravity of the two materials. Because cement paste is typically proportioned using masses, it is most often described by the water:cement ratio ("w:c") expressed as the ratio of the mass of water to the mass of cement. So for a batch that uses 400g of water and 1000g of cement, the w:c would be 0.4. The initial mass fraction of the cement grains as compared to the total would be 1000g/(400g + 1000g) or 0.714. If the cement grains have a specific gravity of 3.15 and the water has a specific gravity of 1.0, the initial volume fraction of cement grains would be (1000g/3.15) / (1000g/3.15 + 400g/1.0) or 0.442. As later verified with micro-CT visualization, the initial volume of air was negligible and therefore ignored in this calculation.

In each time increment after the cement and water are mixed, a portion of the cement grains is dissolved into solution and, depending on the chemical composition of the cement, reactions within the solution form various hydration products including calcium hydroxide and a series of calcium and silica hydrates. As this process is tracked through time, the grains continue to dissolve and react with the water and hydration products are formed. In a cement paste mix with excessive water, such as a mix with a w:c of 0.5, at some time after the initial mixing, all grains have dissolved and reacted giving a final composition of the paste as being mostly hydration products

with some excess water remaining. In a mix with a very low w:c ratio, such as 0.2, at some time, all available water is consumed by the chemical reaction with the cement grains and the paste composition is mostly hydration products with some unhydrated cement remaining. The degree of hydration, $\alpha(t)$, is defined as the ratio of the initial cement mass that has been dissolved at any time, t. Thus for high w:c ratios, α increases from 0 to 1 and for low w:c ratios, α increases from 0 to 1 minus the mass fraction of cement remaining when all water has been consumed in the reaction. Because α relies only on the cement content and the specific gravity of the cement grains is constant throughout the reaction, the degree of hydration can also be written in terms of the volume of cement,

$$\alpha(t) = 1 - \frac{m_c(t)}{m_{ci}} = 1 - \frac{V_c(t)}{V_{ci}}, \tag{2.1}$$

where m and V represent mass and volume of cement grains and the subscript i represents the initial content at time $t=0$.

The consideration of the hydration products is slightly more complex. It has been seen that generally, 1g of cement will form 1.42g of hydration products (Powers and Brownyard 1946). However, these hydration products are composed of chemical compounds that include the original 1g of cement, chemically bound water (0.24g) and evaporable water trapped within the matrix of the hydration products (0.18g). Therefore, for testing involving measurements of mass or mass loss, such as in thermogravimetric analysis, the mass of hydration products actually being measured must be carefully considered. Expressing the relationships in terms of degree of hydration,

$$m_{htot}(t) = \alpha(t) m_{ci} * (1 + 0.24 + 0.18) = m_{hc}(t) + m_n(t) + m_g(t), \tag{2.2}$$

where m_{htot} is the total mass of hydration products, m_{hc} is the mass of cement that has reacted into the solid hydration products, m_n is the mass of non-evaporable, chemically bound water, and m_g is the mass of evaporable gel water trapped within the hydration products. For TGA testing, if the sample is dried, the free water (that not yet used for

hydration) and gel water are evaporated before the test. Thus any mass loss recorded in a particular temperature range would be divided by the dry mass,

$$m_{dry}(t) = m_c(t) + m_{hc}(t) + m_n(t) = m_{ci}(1 + 0.24\alpha(t)). \tag{2.3}$$

Using the equations and relationships above, similar relationships for volume can be derived. For the volume of cement, the mass is divided by the specific gravity of cement, γ_c. Thus,

$$V_c(t) = (1-\alpha(t))V_{ci} = (1-\alpha(t))\frac{m_{ci}}{\gamma_c}, \tag{2.4}$$

where V_{ci} is the initial volume of cement and the other variables are as previously defined.

Conversion of the mass equations for hydration products to volume equations requires knowledge of the various components in Equation (2.2). As previously, the mass of the cement is divided by its specific gravity. Though the same approach could be used for each of the water terms, it is more common to use specific density as a multiplier. Values for specific density of chemically-bound water and evaporable water in the hydration products were originally presented by Powers and Brownyard but later verified by others (Brouwers 2004; Copeland 1956). Using the presented values, the volume equation becomes

$$V_{htot}(t) = \alpha(t)m_{ci} * \left(\frac{1}{\gamma_c} + 0.82 * 0.24 + 0.90 * 0.18\right) = \alpha(t)m_{ci} * \left(\frac{1}{\gamma_c} + 0.359\right), \tag{2.5}$$

where V_{htot} represents the total volume of hydration products, including chemically bound and gel water. Were the above equations used with a cement paste containing 1g of cement with a γ_c of 3.15 and a w:c ratio of 0.42, it would be found that as t approaches ∞ and therefore $\alpha(t)$ approaches 1, m_c approaches 0 as expected and V_{htot} approaches 0.676 cm^3. However, the initial volume of cement plus water is found to be 0.737 cm^3. Therefore, the hydration process causes approximately 8.3 per cent shrinkage of the paste assuming no moisture gain or loss other than self-desiccation. The majority of this chemical shrinkage is accommodated by the formation of air

voids (pores) within the hydration products while a small portion corresponds to macro scale changes in dimension, known as autogenous shrinkage (Tazawa et al. 1995).

In testing that considers the volume of solids in a material, such as XRD analysis, the results are in terms of the volume percentage of each component with respect to the total volume of solids examined. Assuming that X-rays do not reflect from water, it may be appropriate to use the total volume of solids, similar to the mass of dry solids presented in Equation (2.3), as the normalizing quantity, such as

$$V_{sol}(t) = (1-\alpha(t))\frac{m_{ci}}{\gamma_c} + \alpha(t)m_{ci} * \left(\frac{1}{\gamma_c} + 0.82 * 0.24\right) = m_{ci} * \left(\frac{1}{\gamma_c} + 0.197\alpha(t)\right). \qquad (2.6)$$

However, because a number of solid phases of hydration products, specifically, forms of C-S-H, are amorphous and also do not reflect X-rays, Equation (2.6) doe not truly represent the solids examined by X-ray. Because the volume proportion of C-S-H is unknown, there is not a way to define the volume of solids examined in terms of the equations above. Thus, though comparisons can be made from sample to sample to examine effects of stress, XRD analysis alone will not yield exact volume percentages of the initial volume.

All cement paste used for the current research was mixed with a w:c value of 0.4. Using this value in the above equations with an assumed cement mass of 1g gives a slightly different result. The degree of hydration, α(t) cannot approach 1.0 as there is insufficient water present in a sealed specimen to supply the demand of the cement. Thus, $\alpha(\infty)$ = 0.4/0.42 = 0.952 and $m_c(\infty)$ = 1 - 0.952 = 0.0476g. The volume of hydration products approaches 0.644 cm^3 and the shrinkage is approximately 6.2 per cent. Assuming that the dissolution of cement grains and the formation of hydration products is linear between the end points, Figure 2.1 and Figure 2.2 present the graphs of both mass and volume ratios of cement and hydration products with respect to the initial total mass and volume as a function of the degree of hydration.

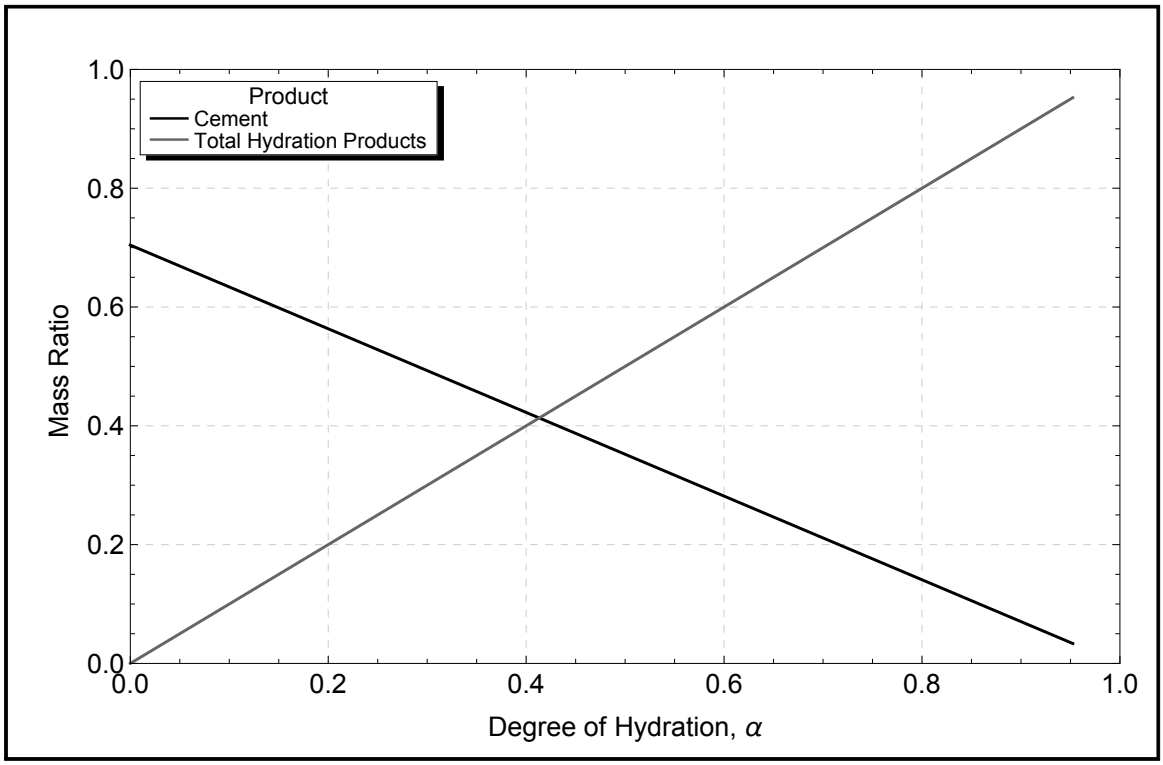

Figure 2.1 - Mass ratios of cement and hydrations products with respect to total initial mass. Due to water in the initial mix being less than that needed to fully hydrated the cement content, both curves end at an α value of 0.952.

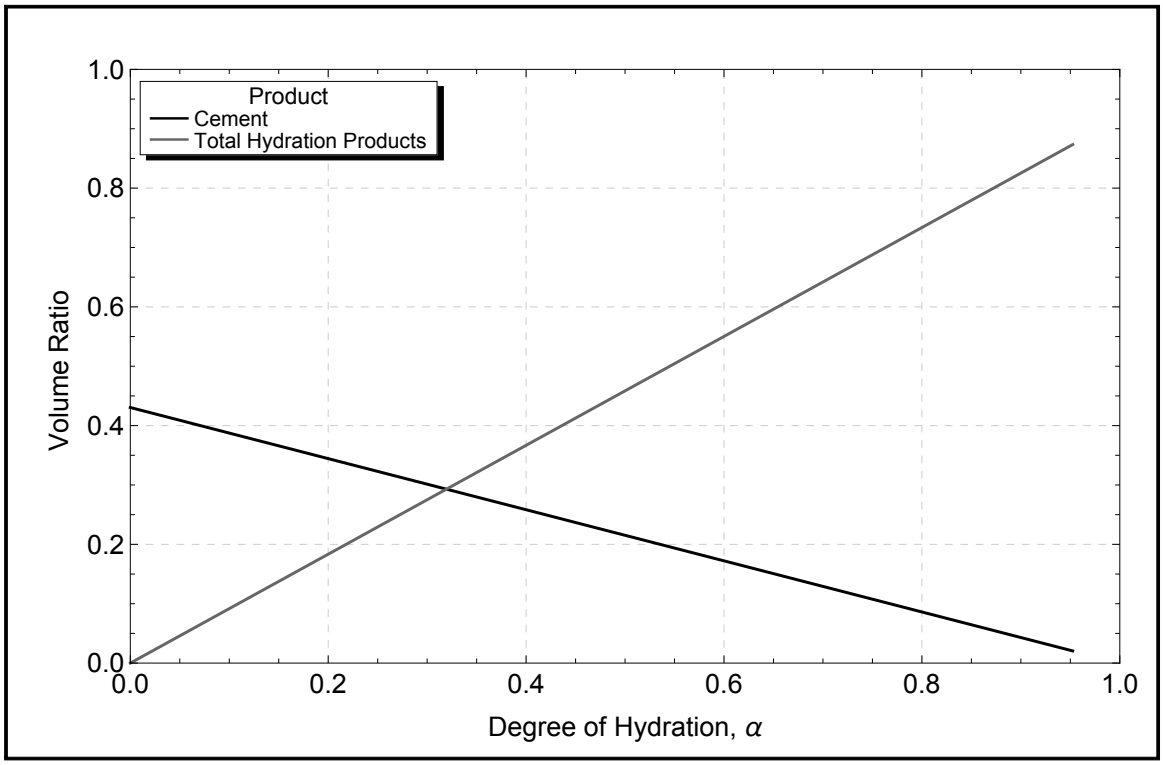

Figure 2.2 - Volume ratios of cement and hydrations products with respect to total initial volume. Due to water in the initial mix being less than that needed to fully hydrated the cement content, both curves end at an α value of 0.952. The sum of the end points gives a volume ratio of 0.938 of initial indicating shrinkage due to self-desiccation.

2.2 Solidification Model

One of the significant complications in considering the viscoelastic properties of cementitious materials is the fact that as time passes; the cement hydrates, changing its physical properties and therefore, its response to future loading. This process, called aging, has been handled in several ways in the literature, one of which is the solidification theory (Bazant 1977). Though not necessarily as precise as other methods, its relative simplicity makes it a logical choice as a foundation for comparisons and curve fitting, such as is performed here. The theory considers aging as a solidification process such that during any change in time, additional hydration products form, with each new segment created in a stress-free state and with age-independent physical properties. Because the model completely ignores the presence of water, cement grains, pore solution, and non-solidified constituents, the application of load causes stress only in the hydration products. At a later point in time, additional load application would result in additional strain in the original hydration products and

strain in the material solidified since the previous load application. This evolution is depicted in Figure 2.3.

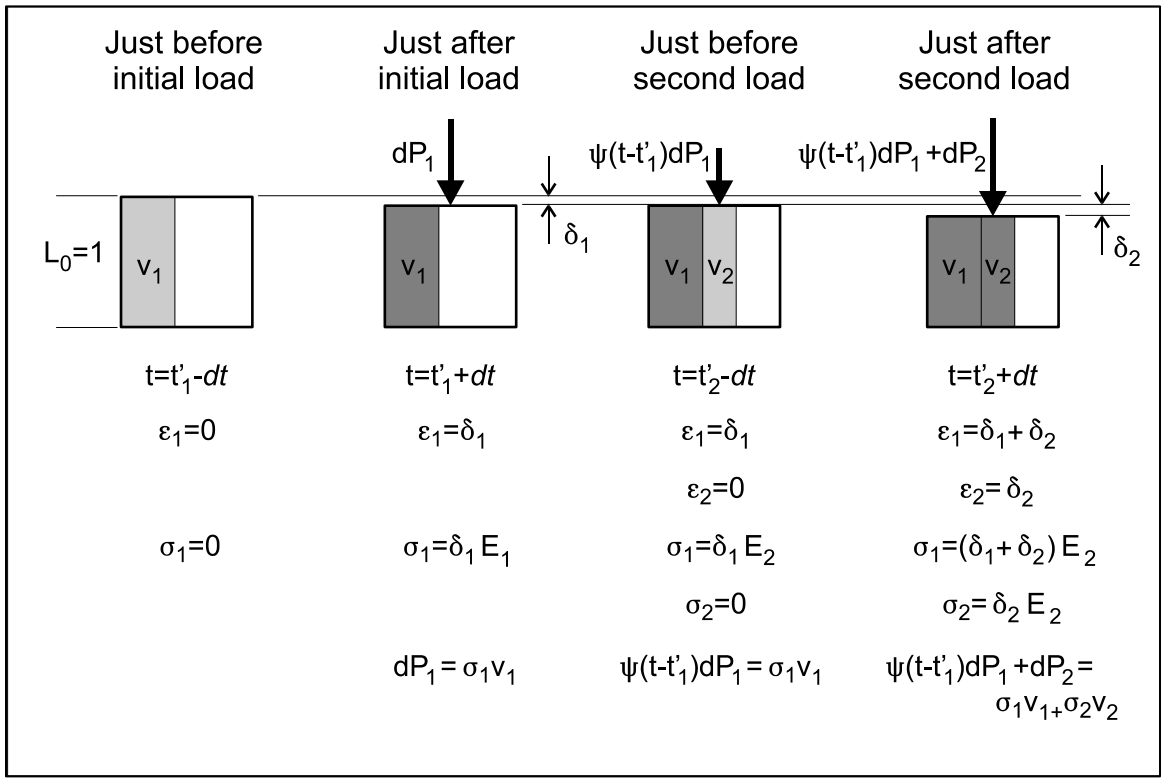

Figure 2.3 – Illustration of the solidification model used for relaxation showing stressed and un-stressed regions of hydrated products before and after load applications. Applied loads are carried by the volume of hydration products at the time of application (darker gray regions) with all new products formed in a stress-free state (lighter gray regions). The Young's modulus of elasticity is a function of time; E_2 is E at time t_2.

As later explained (Bazant and Prasannan 1989; Carol and Bazant 1993), the response to a flexural or uniaxial relaxation test such as considered currently, can be characterized by the constitutive relation

$$\sigma(t) = \int_{t'=0}^{t} \Psi(t-t')v(t')d\varepsilon(t'), \tag{2.7}$$

where $\sigma(t)$ is the axial stress at time t, v is the volume fraction of solidified material, $d\varepsilon$ is the change in axial strain, and Ψ is the uniaxial relaxation function. Bazant defines v as an effective volume of solidified matter with some relationship to porosity of the material. However, he does not define whether the volume fraction includes of

excludes areas of trapped water. Thus, $v(t)$ as used here should be considered independent of the volume fractions defined in Section 2.1.

For a beam relaxation test where displacement, and therefore strain, is induced only at discrete times, t', the incremental strain term, $d\varepsilon(t)$, is zero at all t not equal to t'. Replacing Ψ with $E_\infty\Psi^*$ and converting to a summation of discrete steps in strain, yields

$$\sigma(t) = \sum_{i=1}^{n} E_\infty \Psi^*(t - t_i) v_i d\varepsilon_i, \tag{2.8}$$

where n is the total number of displacements, each at time t_i, and E_∞ is the Young's elastic modulus of a non-relaxing cement paste once all hydration has occurred.

In a simply-supported, three-point loading, prismatic beam test, assuming that the beam behaves as an Euler-Bernoulli beam, σ and ε can be replaced by functions of the applied load P and displacement δ, such that

$$\frac{3L}{2h^3} P(t) = \sum_{i=1}^{n} E_\infty \Psi^*(t - t_i) v_i \frac{6h}{L^2} d\delta_i, \tag{2.9}$$

where L is the length of the beam and h is the height and width of a square cross-section beam. Collecting constants and moving the modulus outside the summation yields

$$P(t) = \frac{4E_\infty h^4}{L^3} \sum_{i=1}^{n} \Psi^*(t - t_i) v_i d\delta_i. \tag{2.10}$$

Consider the case where n=1 (a single displacement at time t_1 with a corresponding load increase dP_1) . Knowing that at $t=t_1$, Ψ^* must be equal to 1, it can be seen that,

$$dP_1 = \frac{4h^4 E_\infty d\delta_1 v_1}{L^3}, \tag{2.11}$$

and therefore for $t>t_1$,

$$P(t) = dP_1 \Psi^*(t - t_1). \tag{2.12}$$

Now consider the case where n=2. The load, P, just before the second displacement, is simply $dP_1\Psi^*(t_2-t_1)$. Just after the displacement, with $t=t_2$,

$$\begin{aligned} P(t_2) &= dP_1 \Psi^*(t_2 - t_1) + dP_2 \\ &= \frac{4E_\infty h^4}{L^3} \Psi^*(t_2 - t_1) v_1 d\delta_1 + E_\infty v_2 d\delta_2 . \end{aligned} \tag{2.13}$$

Recognizing that the first term on the right-hand side of Equation (2.13) is the load response to the first displacement and the second term is that to the second, it can be generalized for any number of induced displacements,

$$P(t) = \sum_{i=1}^{n} dP_i \Psi^*(t - t_i). \tag{2.14}$$

The function, $P(t)$ in Equation (2.14) implies that the relaxation function can be determined, independent of aging, and without consideration of the magnitudes of displacements or E values. For a single load cycle, the Ψ^* function can be determined by normalizing the current load by the initial load, as will be presented in Section 3. Because the solidification theory relies on the assumption that cement paste solidifies in a zero-stress condition, when displacement is held constant, the increased volume of solidified products has no influence on material response to previously applied loads. Thus, for a particular load step, the volume fraction is a constant and normalizing by the initial load removes this variable. Likewise, as the Young's modulus of elasticity of a particular volume fraction is a function only of time, the normalization also

removes this variable, leaving only the relaxation function, Ψ^*. This same function can then be used throughout all load cycles.

3. Relaxation Testing

As discussed above, one can study viscoelastic behavior of cement paste or concrete using creep or relaxation tests. Because the objectives of the current research are focused more on comparisons of behaviors than to characterizing behavior of a particular load case, and to broaden the knowledge base in the field, the mathematically simpler relaxation testing was chosen. Beam bending was chosen as the test method so that stress variations could be studied and to provide results that could be compared to the published work of others. However, as preliminary consideration of the problem revealed the potential for differences between bending behavior and uniaxial behavior, relaxation of cement paste cylinders was included in the protocol. The methodology, results, analysis and preliminary discussion of the testing appear hereafter.

3.1 Beam Testing

3.1.1 Methodology

Beams were cast using a cement paste mixture of ASTM C150 Type I/II Portland cement and a w:c of 0.40. Batches were mixed using a paddle mixer and of sufficient size to cast six to eight beams in general accordance with ASTM C305-14. Exceptions to the standard were: the paddle blade used was plastic rather than stainless steel, the bowl scraper was integrated onto the outer edges of the paddle for continuous scraping, and the mixing times at slow and high speed were 1 minute and 5 minutes, respectively, with no break in between to scrape down the bowl. Beams were cast by inducing suction at one end of a square cross-section acrylic tube, nominally 15 mm on a side and 300 mm long. Ends were sealed immediately after filling and the beams cured at 21 °C +/- 2 °C, placed horizontally on a series of rotating rods (a hot dog roller without heat applied) to limit segregation due to bleed water migration. After approximately 24 hours, the molds were removed and the paste beams sealed using foil-backed tape, similar to previous research (Grasley et al. 2006a; Grasley et al. 2006b), with seams sealed with wax. Beams were stored at the same curing temperature until and throughout loading.

A review of ASTM beam testing standards revealed that for cementitious materials, beams are typically of dimensions dictated by aggregate size and loaded using third-point loading. Third-point loading is typically used to facilitate the measurement of strains in regions of constant moment. In the current research, however, aggregate was not included in the mix and therefore beam sizes could be small than that used in ASTM methods. Further, because strain was not of primary concern, a simpler three-point loading method was chosen for relaxation testing. The designed testing frame, as shown in Figure 3.1, was constructed of steel angles and plate, bolted together rigidly to provide moment connections between members, and steel rod supports placed to give a span length of approximately 250 mm. Displacements were applied at midspan through a 12 mm square bearing plate attached to a spherical bearing resting on the load cell below. The load cell was displaced from beneath using a steel lever attached to the reaction frame. The capacity of the load cell was approximately 444 N with data collected in increasing time intervals at a resolution of approximately 0.01 N.

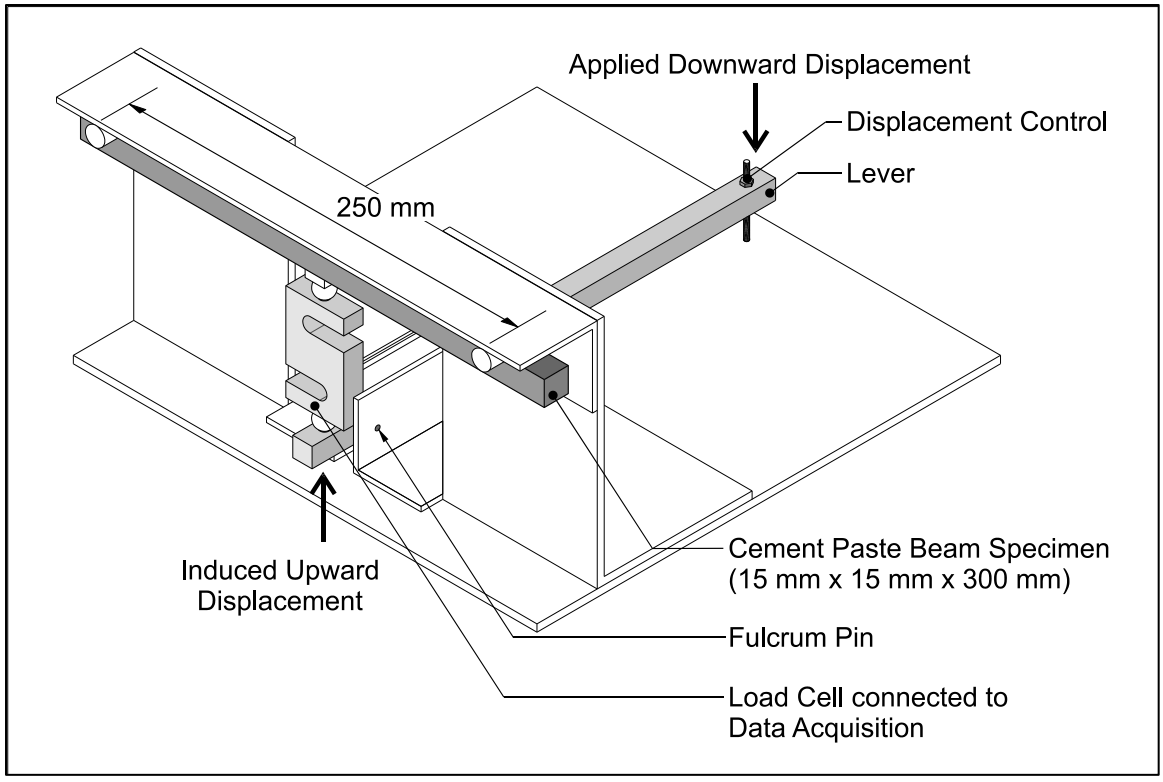

Figure 3.1 - Three-point beam bending test set up that was used for relaxation testing. Tightening the nut at the rear of the frame displaces the lever downwards, pivoting at the fulcrum to apply an upward displacement at the beam midspan. The ratio of displacements is approximately 10:1.

Displacements were induced by manually tightening a screw at the opposite end of the lever, holding the position in place between loadings. Where strain reversal was necessary, the beam was first unloaded and then flipped upside down for the next cycle. Midspan displacements, relative to the steel angle above, were measured at the top surface of the beam using a digital dial gage during the first 70 per cent of load application to give sufficient data to compute the (quasi) instantaneous Young's modulus of elasticity, and the dial gage removed for the duration of the cycle. The rate at which the screw was tightened was kept relatively constant and, assuming linear elastic beam behavior, corresponded to a loading rate for each application of approximately 20 N/min corresponding to an average strain rate of approximately 0.018 per cent per minute. The peak strain rate varied from sample to sample but was generally less than approximately 0.04 per cent per minute. The approximate displacement history for the different combinations of load cycles can be seen in Figure 3.2. For reference, a

displacement of 0.25 mm equates to a strain of approximately 0.011 per cent. The duration of each load cycle for each beam, including the initial load application, appears in Table 3.1. Note that although displacement was typically not measured throughout a load cycle, the assumption that the beam midpoint does not change displacement after initial loading was verified by measurements of select beams. Further note that the testing frame and lever rigidity, along with the use of a relative measurement between beam and frame, limited the influence of frame or lever deflection on recorded displacements to that caused by the force of the dial gage itself, estimated to be less than 0.005 per cent of the beam deflection.

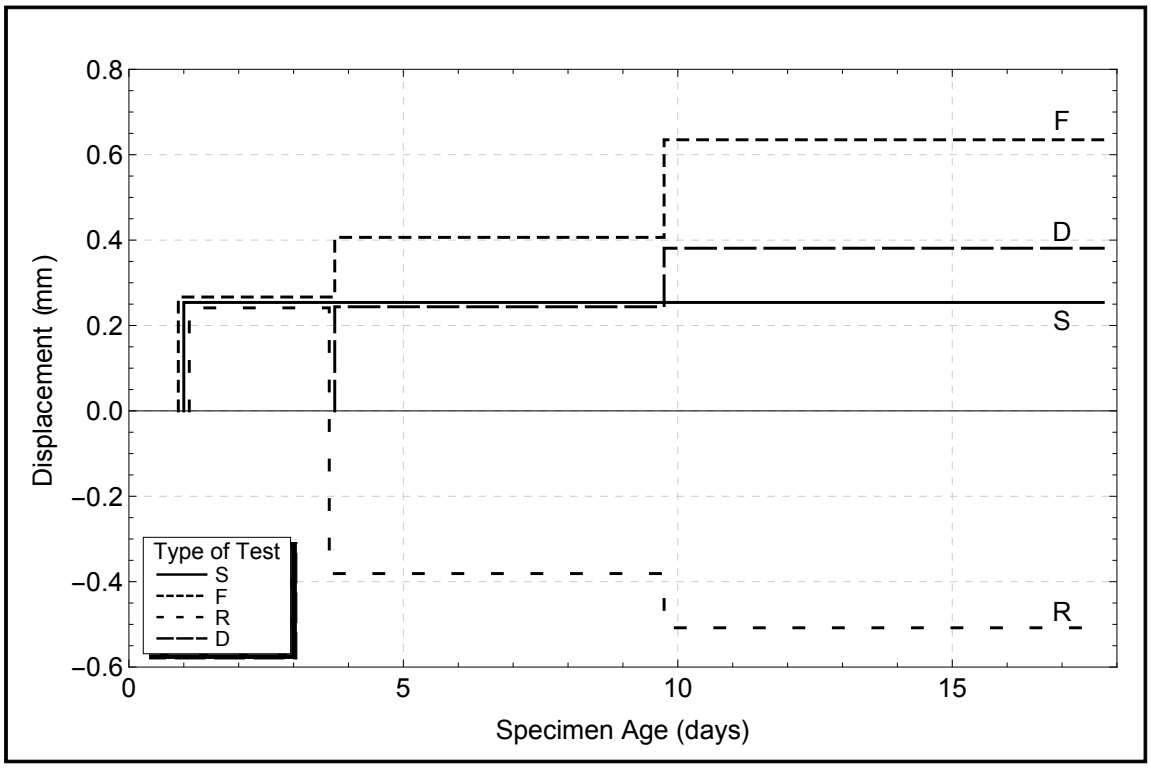

Figure 3.2 – Approximate stepped displacement histories defining four cement paste beam loading profiles. "S" samples are subjected to a single load increment at an age of approximately 1 day. "F" samples have multiple load increments in the same, forward, direction at 1, 4, and 10 days. "R" samples are loading in the forward direction at 1 day but in the reverse direction at 4 and 10 days. "D" samples are loaded in the forward direction at 4 and 10 days.

Table 3.1 - Incremental load values, *dP*, and cement paste age at application, *t'*

Beam[1]	Cycle 1		Cycle 2		Cycle 3		End
	t'	dP	t'	dP^2	t'	dP^2	t
	days	N	days	N	days	N	days
C1S	1.16	29.9					17.00
C2S	0.96	41.0					3.70
C2F	0.94	38.7	3.72	34.1	9.75	23.4	17.77
C2R	0.95	41.3	3.72	-61.8	9.75	-28.0	17.76
C3F	0.98	38.5	3.72	28.8	9.76	20.7	17.71
C3R	0.97	39.8	3.75	-53.6	9.75	-31.7	17.72
C3D1			3.75	44.2	9.75	35.6	17.73
C3D2			3.76	53.3	9.75	24.5	17.73
C4F	1.04	41.8	3.73	31.1	9.84	25.6	17.76
C4R	1.05	39.8	3.74	-60.8	9.84	-34.0	17.77
C4D			3.76	43.9	9.84	27.4	17.76
C8S1	1.02	45.1					54.91
C8S2	1.02	44.7					54.91
C8S3	1.02	45.8					54.92
C10S1	1.06	39.1					1.88
C10S2	1.07	50.5					6.91
C10S3	1.07	40.5					10.87
C10S4	1.07	51.1					16.89
C11S1	0.97	43.9					6.89
C11S2	0.98	44.7					12.93
C11S3	0.98	44.7					15.93

[1]Beam designations C*mXn* indicate cement paste batch m subject to displacement history X and specimen number n within each batch and history combination. Histories are as depicted in Figure 3.2 and can be termed "Single sustained load", "Forward loading in all cycles", "Reverse loading in 2nd cycle" and "Delayed first loading".
[2]Negative load values indicate load direction opposite from original beam configuration (1st loading cycle).

3.1.2 Results – Elastic Behavior

During load application for the long-term tests, displacement and load history was collected and the Young's modulus of elasticity during that loading calculated. Additionally, companion beams were cast and tested to failure for comparison purposes. A typical load to failure curve appears in Figure 3.3. Note the early variations in the load-displacement relationship are likely due to initial setting of the test frame. These data were generally discarded. The superimposed line is fit to a selected portion of the data, approximated to be linear. The slight variations from the line, seen most significantly at a displacement of approximately 0.06 mm, correspond to either slight movement of the loading screw within its seat in

the lever or slight hesitations in the movement of the lever within its brackets due to friction. Both of these effects were only present when the screw was being turned and no similar variations were noticed in relaxation data. Note that the very good linearity (the coefficient of determination, R^2 = 0.951) of the lower portion of the curve (<85 per cent ultimate) implies that both the tensile and compressive load-displacement relationships are likely linear over the test range. It should be further noted that all beam relaxation testing described above was conducted within this lower, linear region.

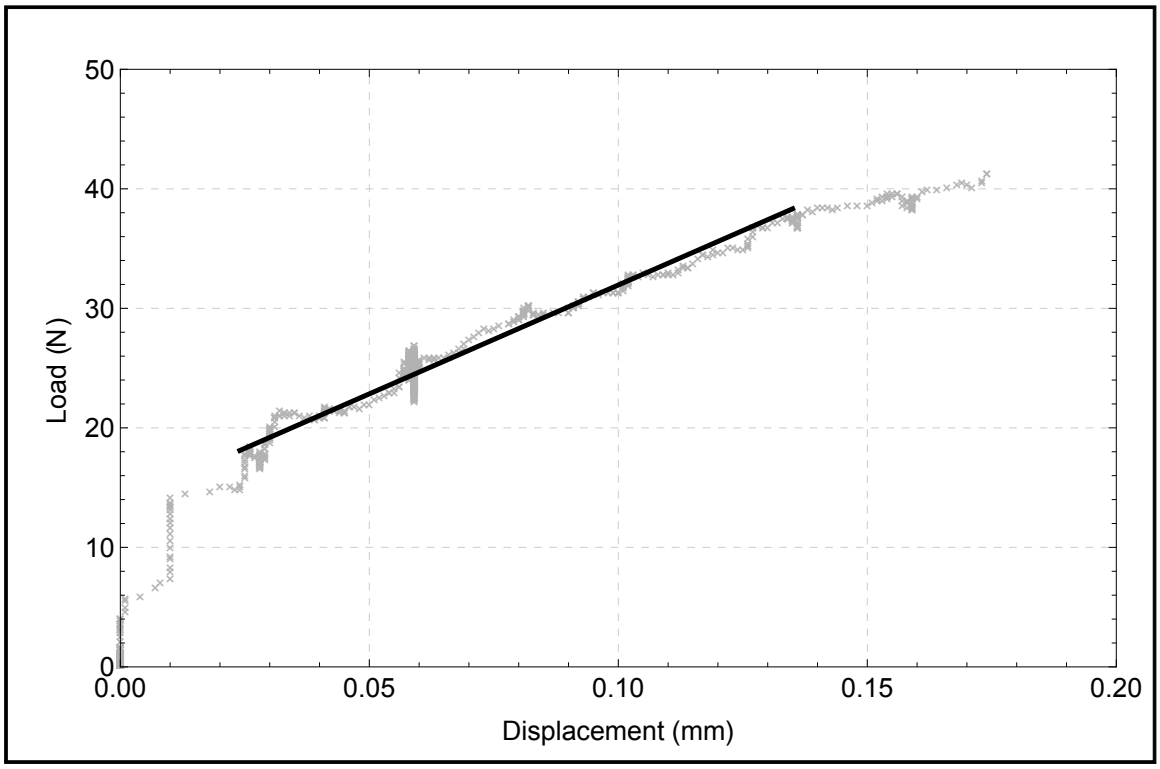

Figure 3.3 – Typical load-displacement to failure for cement paste beams with linear portion, after initial seating, used to determine Young's modulus of elasticity. The slope of the load-displacement curve is converted to *E* using the three-point moment and gross-section moment of inertia. All loads for relaxation testing were designed to be within the linear section of the load-displacement curve.

By taking the slope of the load-displacement curve and assuming that the beam response may be approximated as an Euler-Bernoulli beam response, the Young's modulus of elasticity at the time of loading was determined. The results are presented in Figure 3.4 with curves fit to the relationship (Jiang et al. 2012)

$$E = 0.938E_{\infty}\left\{1-\exp\left\{-\left[a(t-b)^{c}\right]\right\}\right\}, \tag{3.1}$$

where 0.938 corresponds to the maximum ratio of solids to total volume at time $t=\infty$, based on the calculations presented in Section 2.1, E_{∞} is the Young's modulus of hardened material at infinite time, b represents a time delay before stiffening of the paste occurs, and a and c are fit parameters. The R^2 values for the first loadings and previously loaded curves are both 0.985. Note that the data for previously loaded specimens includes those in both the forward and reverse load direction. Close examination of individual results reveals no trend indicating that reversal of load affects the value of Young's modulus.

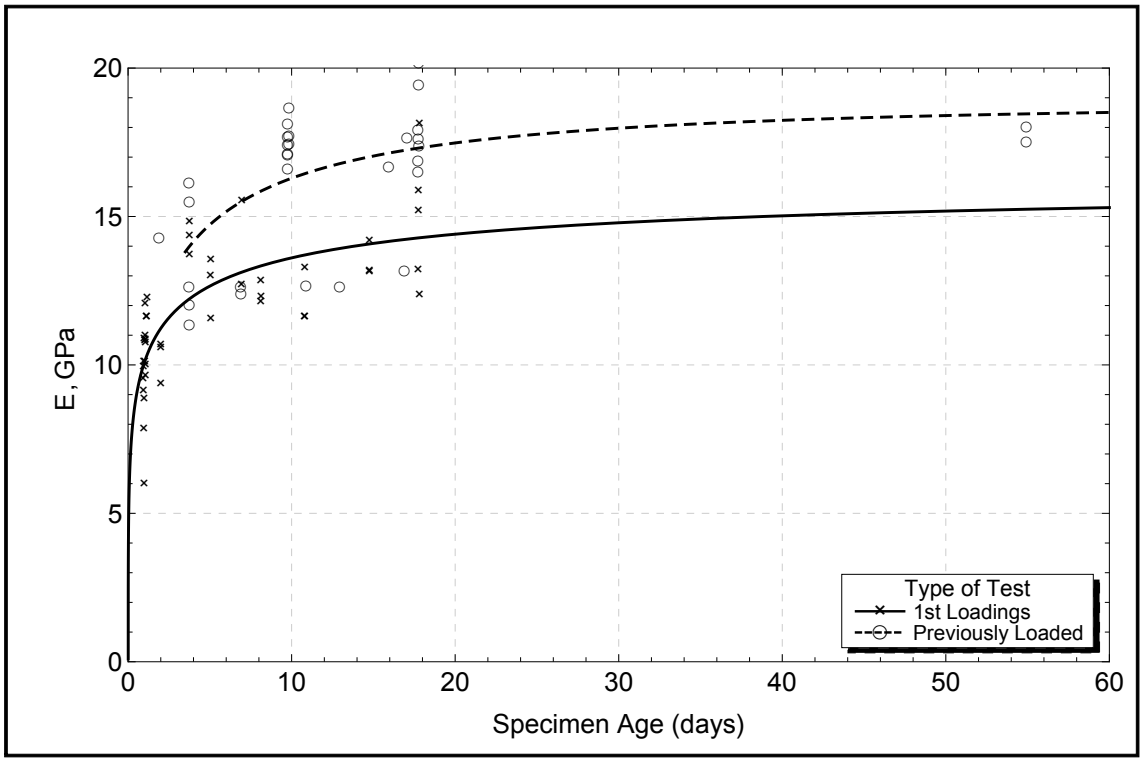

Figure 3.4 – Young's modulus of elasticity versus age indicating a significantly higher stiffness in cement paste beams previously loaded. Superimposed fit curves are in accordance with an assumed exponential relationship as presented in Equation (3.1). The difference between the two curves is approximately 11 to 18 per cent.

Based on the curve fits shown in Figure 3.4, the eventual extrapolated Young's modulus of elasticity, E_{∞}, is approximately 17.0 GPa for virgin specimens and approximately 20.1 GPa for specimens previously loaded. Note that these values

are based on the assumption of the full beam section carrying stress and use the total section for the calculation of the moment of inertia. However, as the solidification theory assumes that only a portion of the area is being stressed, and this portion is a function of the degree of hydration at the time of load application as shown in Figure 2.3, the resulting *E* value for the beams should be divided by the degree of hydration at the time of loading to determine an *E* value for the hydration products. This issue will be addressed more thoroughly in Section 6.3.

3.1.3 Results – Relaxation

Throughout each loading cycle, the load necessary to maintain displacement was captured using an automated data acquisition system. For the first loading cycles of each specimen the data for the first 12 days are plotted in Figure 3.5. Note that captured load is normalized by the initial load increment to assist in later analysis. The series of data depicted in Figure 3.5 are seen to be overlapping and consistent within each group of load initiation (approximately 1 day and 3.75 days). Because these are the first loadings and the specimens are replicates of the same mix design, it should be expected that the only trend between specimens would relate to specimen age at the beginning of the first loading cycle.

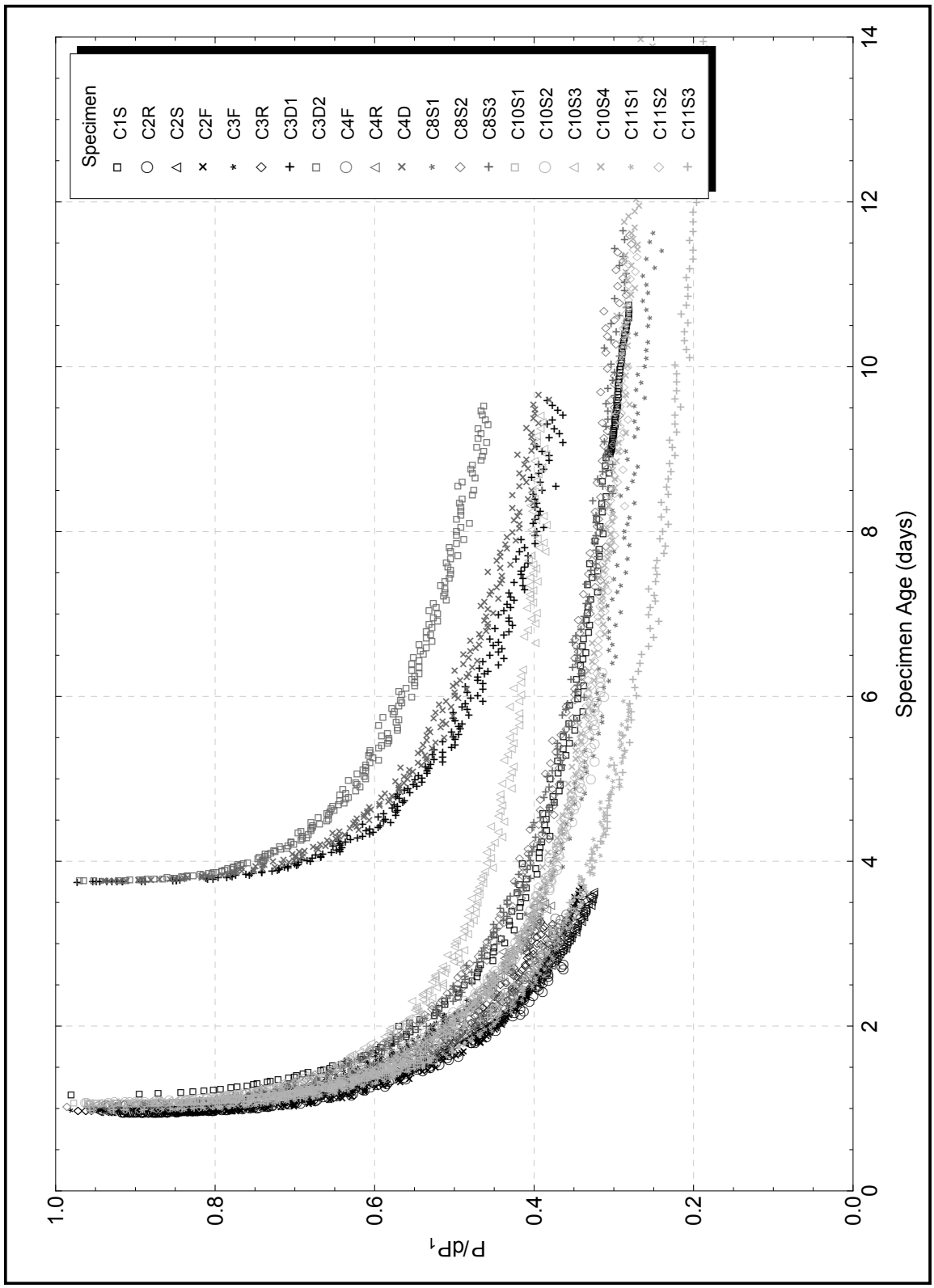

Figure 3.5 – Relaxation, P/dP, during first loadings initiated at different ages where P is the load measured throughout the testing period and dP is the magnitude of the load when first applied. The data series for "S", "F", and "R" specimens are subject to the same loads during this first load increment. For clarity, only a portion of the data points is presented.

For the second and third loading cycles, it is first approximated that relaxation, in general accordance with the Boltzmann superposition principle, can be determined as the summation of the influence of individual load applications. Thus, during subsequent load cycles, the influence of the first load increment can be subtracted from the overall data to give the net load from the second load application. For this research, this was accomplished by projecting the curve fit to the initial loading data past the point of second and third load applications and then subtracting this curve from the collected data during those later loadings. The results of this subtraction are presented in Figure 3.6. Note that in the second load cycle, immediately after reversal, beams loaded in the opposite direction retain a significantly higher percentage of the applied load than those loaded in the same direction as the previous cycle. This trend is not as apparent in the third loading cycle. Further note the similarity in curves between the third cycle of both forward and reverse loaded specimens and the second cycle of the delayed loading specimens, all initiated at approximately 10 days.

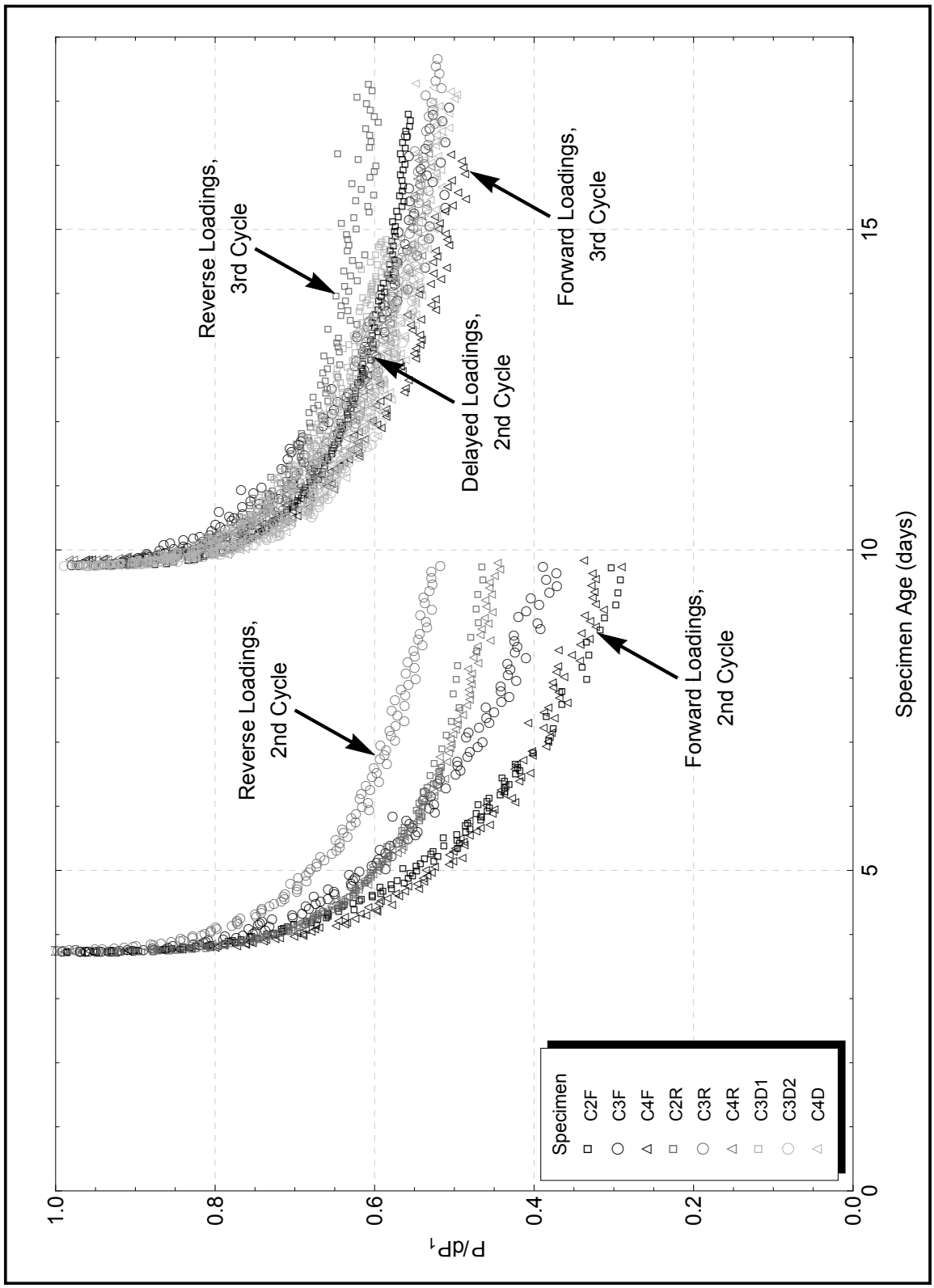

Figure 3.6 – Relaxation, P_{net}/dP, during second and third loadings after the effect(s) of the previous load step(s) has been removed from the raw data, indicating significant difference in relaxation during time interval immediately following strain reversal. For clarity, only a portion of the data points is presented.

3.1.4 Analysis

The first step in considering relaxation in the beams was to examine each portion of the data for trends and anomalies. One behavior of interest was seen in most data sets, and was most pronounced during the first application of load. As can be seen in Figure 3.7, there is a small but steep decline in retained load, typically between 1 and 10 seconds, before relaxation settles out to its long-term behavior. This phenomenon is similar to that seen in saturated beams tested by others (Valenza and Thomas 2012; Vichit-Vadakan and Scherer 2003). In the cited work, the early relaxation was attributed to hydraulic movement of fluid through the pore structure of the specimen and into the surrounding fluid. In the current research, with sealed boundaries, the mechanism of this relaxation is not precisely the same. In a typical early age cement paste, even under sealed conditions, the material is not completely saturated. This allows capillary flow at the local level due to applied pressures (Acker 2004; Grasley and Leung 2011b; Wyrzykowski and Lura 2014), a process analogous to flow to a surrounding medium. However, as this early relaxation mechanism is not of primary interest in the current work, the first 100 seconds of data was truncated from all specimens and the associated load loss modeled as a constant, R_0, similar to the method presented by Vichit-Vadakan and Scherer.

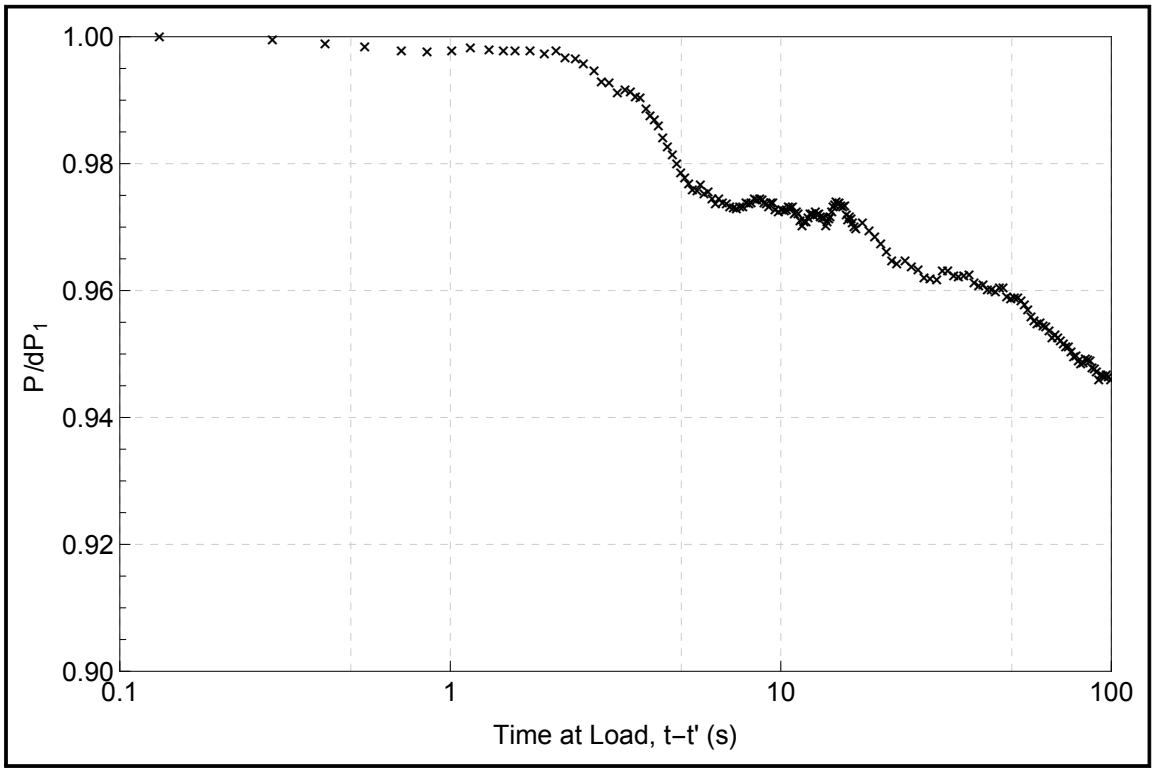

Figure 3.7 – Very early relaxation behavior indicating marked drop in load during first 10 sec. This drop was accounted for in curve fits by incorporating a scaling constant, less than 1, to the fitted curves and removing the first 100 seconds of raw data.

The second trend observed in most data sets was the tendency of the load to approach a non-zero asymptotic value. As seen in Figure 3.5, the longer a particular load cycle lasted, the more pronounced the trend. This tendency was incorporated into the fit model as explained below.

With the preliminary observations, it was then possible to characterize the viscoelastic relaxation and compare to functions published elsewhere. Though several theories for modeling exist, for simplicity and ease of comparison, the solidification theory was selected for comparison to the experimental data due to its connection to actual mechanisms.

As noted above, there were two trends apparent in the data sets, an early offset and an eventual lower threshold. The first trend can be simulated by fitting the data to a function $R_0\Psi^*$ where R_0 represents the constant associated with hydraulic relaxation after some short time duration, consistent with the work of Vichit-

Vadakan and Scherer (Vichit-Vadakan and Scherer 2003). For the second trend, the fit model for Ψ^* must include a constant term. This leaves the span in between the upper and lower limits to be fit. Though several models have been used to characterize relaxation curves, the most common corresponds to a series of dashpots and spring combinations (e.g., Maxwell model). For the current case, and incorporating the modifications mentioned above, the resulting Maxwell chain fit model for a particular load cycle can be written as

$$\frac{P(t)}{dP} = R_0 \Psi^*(t - t') = R_0 \left[\sum_{i=1}^{n} a_i \exp\left(-\frac{t - t'}{\tau_i} \right) + b \right], \tag{3.2}$$

where τ_i are relaxation times typically chosen as regular intervals during the span of interest, b is the asymptotic value, and a_i are weighting factors used as fit parameters (summed to 1). The value of n, the number of terms needed to obtain a good fit, is somewhat arbitrary. However, for purposes of this paper, seven terms were found to be sufficient, corresponding to the rheologic model of a Maxwell chain of seven parallel elements with each element consisting of a spring and dashpot in series.

Using a nonlinear fitting routine within *Mathematica* (Wolfram 2012), and assigning τ_i at equal intervals of log time from 0.0001 to 100 days, a method in use for many years (Bazant and Asghari 1974), fit parameters were determined for the results of each specimen, with the coefficients a_i and b shown in Table 3.2. The value of R_0, the initial reduction attributed to very early hydraulic relaxation varied between 0.94 and 1.00, corresponding to a maximum value of load loss of 6 per cent and indicating a relatively minor effect compared to long-term relaxation. The R^2 value exceeded 0.9994 for all Ψ^* curves. An example fit for the first loading cycle is included as Figure 3.8. Curve fits for all samples are included in Appendix A.1.

Table 3.2 - Fit results for relaxation functions

Cycle 1 at 1 day								
	a_1[1]	a_2	a_3	a_4	a_5	a_6	a_7	b
τ (days)[2]	0.0001	0.001	0.01	0.1	1	10	100	
C1S[3]	0.000	0.089	0.048	0.157	0.304	0.224	0.178	0.036
C2S	0.066	0.055	0.079	0.147	0.369	0.224	0.060	0.078
C2F	0.348	0.023	0.087	0.147	0.395	0.000	0.000	0.340
C2R	0.215	0.039	0.092	0.141	0.396	0.029	0.089	0.212
C3F	0.156	0.061	0.076	0.104	0.419	0.031	0.153	0.205
C3R	0.093	0.173	0.069	0.148	0.352	0.034	0.131	0.205
C4F	0.085	0.081	0.098	0.132	0.373	0.119	0.110	0.128
C4R	0.159	0.047	0.082	0.135	0.378	0.041	0.158	0.184
C8S1	0.064	0.060	0.072	0.136	0.327	0.243	0.097	0.088
C8S2	0.028	0.081	0.066	0.116	0.343	0.234	0.132	0.090
C8S3	0.075	0.040	0.068	0.125	0.328	0.250	0.114	0.104
C10S1	0.000	0.032	0.125	0.127	0.366	0.351	0.000	0.000
C10S2	0.000	0.035	0.073	0.150	0.331	0.211	0.201	0.001
C10S3	0.000	0.045	0.057	0.140	0.278	0.114	0.366	0.000
C10S4	0.172	0.076	0.106	0.122	0.306	0.219	0.000	0.212
C11S1	0.000	0.084	0.071	0.165	0.331	0.188	0.160	0.016
C11S2	0.147	0.073	0.066	0.154	0.337	0.223	0.000	0.212
C11S3	0.104	0.007	0.122	0.134	0.355	0.278	0.000	0.117
Cycle 2 at 4 days								
	a_1	a_2	a_3	a_4	a_5	a_6	a_7	b
τ (days)	0.0001	0.001	0.01	0.1	1	10	100	
C2F	0.002	0.015	0.055	0.122	0.265	0.541	0.000	0.000
C2R	0.131	0.026	0.077	0.126	0.205	0.231	0.204	0.155
C3F	0.007	0.016	0.049	0.105	0.196	0.549	0.078	0.000
C3R	0.153	0.000	0.038	0.119	0.215	0.253	0.222	0.196
C3D1	0.081	0.037	0.100	0.144	0.205	0.363	0.071	0.111
C3D2	0.085	0.040	0.078	0.108	0.175	0.325	0.188	0.111
C4F	0.019	0.000	0.096	0.152	0.252	0.419	0.061	0.031
C4R	0.093	0.033	0.069	0.134	0.206	0.247	0.218	0.113
C4D	0.075	0.069	0.081	0.139	0.215	0.338	0.083	0.137
Cycle 3 at 10 days								
	a_1	a_2	a_3	a_4	a_5	a_6	a_7	b
τ (days)	0.0001	0.001	0.01	0.1	1	10	100	
C2F	0.177	0.340	0.021	0.075	0.163	0.224	0.000	0.472
C2R	0.531	0.007	0.022	0.086	0.162	0.166	0.026	0.500
C3F	0.324	0.000	0.044	0.053	0.200	0.379	0.000	0.355
C3R	0.376	0.000	0.041	0.089	0.186	0.308	0.000	0.401
C3D1	0.428	0.000	0.036	0.087	0.189	0.260	0.000	0.468
C3D2	0.223	0.014	0.036	0.123	0.197	0.181	0.226	0.258
C4F	0.292	0.028	0.039	0.101	0.228	0.311	0.000	0.349
C4R	0.356	0.023	0.040	0.093	0.202	0.285	0.000	0.412
C4D	0.479	0.013	0.032	0.063	0.169	0.244	0.000	0.418

[1] a and b are fit parameters for the curves with b representing the asymptotic ratio of the applied load.
[2] τ values were chosen to allow relative influence of mechanisms or processes at all decades of time.
[3] Beam designations C*mXn* indicate cement paste batch *m* subject to displacement history *X* and specimen number *n* within each batch and history combination. Histories are as depicted in Figure 3.2.

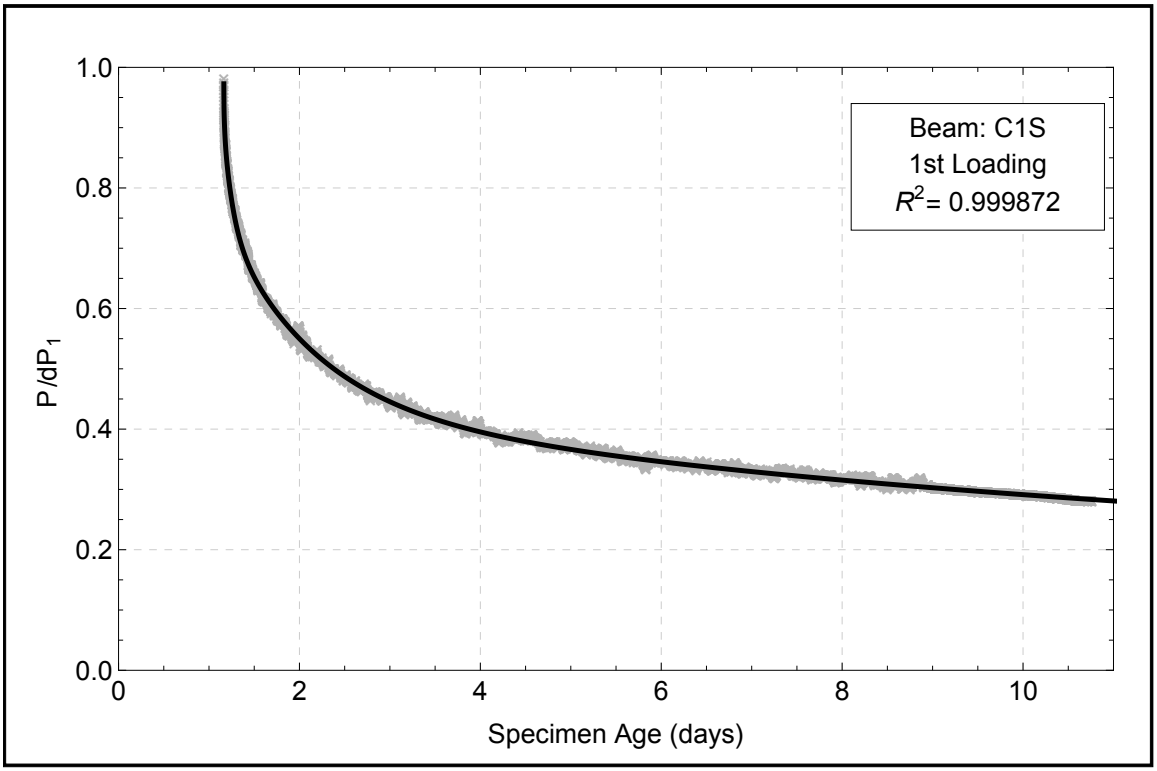

Figure 3.8 – Example of curve fit to raw relaxation data for first loading cycle of specimen. The parameters of the fit curve indicate a load loss of approximately 70 per cent in the first 10 days and a loss of over 96 per cent at infinite time.

Consideration of data in Table 3.2 reveals several key points. First, the highest weighting factors are typically within the region of the age of the specimen at time of load, $\tau = 1$ for the first cycle and τ=10 for later cycles. Though the values of τ do not correspond directly to physical processes, the shift in relative weighting factors to later time intervals implies that aging of the cement has an observable effect on material response beyond that predicted by solidification. Second, the eventual value of the relaxation function, signified by b, varies significantly. For the load cycles of longest duration, specifically batch C8, the values are similar and non-zero, verifying the suspected asymptote of the fit curve. Considering that each term of the fit is reduced to essentially zero within an order of magnitude of time after τ, this asymptote would be reached at a cement paste age less than 1000 days. Lastly, the high variability in the weighting coefficients from specimen to specimen and batch to batch, even within the same loading cycle and load directions, indicates that as a general rule, a simpler model

may be more appropriate. The extra terms used here can more accurately capture small variations in the data where a simpler model may more readily be modified for additional parameters such as temperature or w:c ratio while retaining sufficient accuracy of the fit.

To better illustrate the consistency of the data for the first load cycle, results for all specimens loaded for the first time at approximately 1 day and those at 4 days were combined into two single data sets and fits generated. Figure 3.9 shows the fit curve with the probability density distribution of the data represented as shaded regions on each side of the curve where gray level represents probability. Note that the age at first loading has a significant influence on the relaxation function throughout early age but the curves tend to converge as the time at load exceeds 10 days. Though there are anomalies in the fit for certain portions of the curve, the density of the data depicted in the figure shows that use of a single fit curve to represent multiple specimens loaded at similar ages is appropriate.

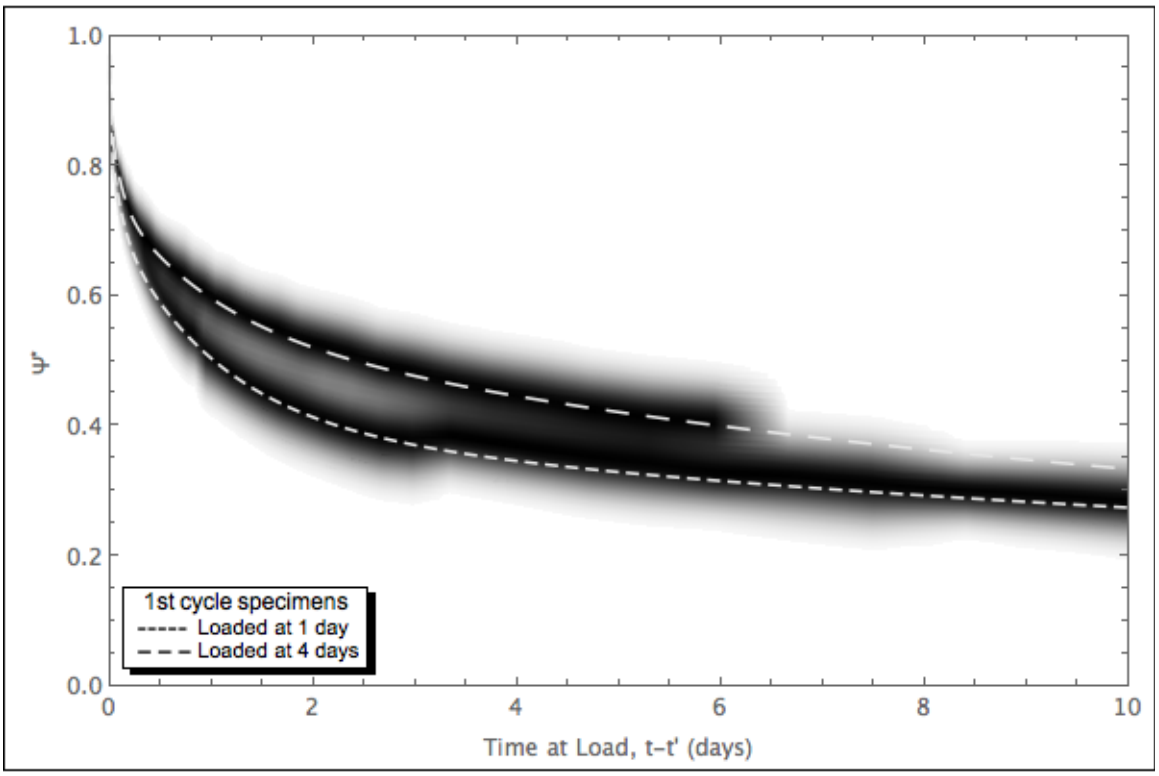

Figure 3.9 – Probability density of first loading cycle data compared to derived fit curves showing a significant difference in relaxation between samples first loaded at 1 day and those first loaded at 4 days. The gray scale values indicate the relative density of data within a particular region with black corresponding to 100 per cent of the data and white indicating no data. The white dashed lines correspond to the fit curves for the entire data sets in the two categories presented. Note that for loads initiated at 4 days, loads were typically increased at an age of 10 days, thus ending the load cycle and causing an absence of data density for the upper curve at a *t-t'* value of approximately 6 days.

3.1.5 Effect of Strain Reversal

Given the results of fits described in the previous section, data presented in Figure 3.6 was similarly grouped for comparison purposes. For each second loading cycle, the projected effects of the first loading on the same specimen, using curve fits previously generated, were subtracted from the data. The results, after dividing out the R_0 term for the second cycle, are presented in Figure 3.10. Note that data is limited to specimens with a first loading cycle at 1 day.

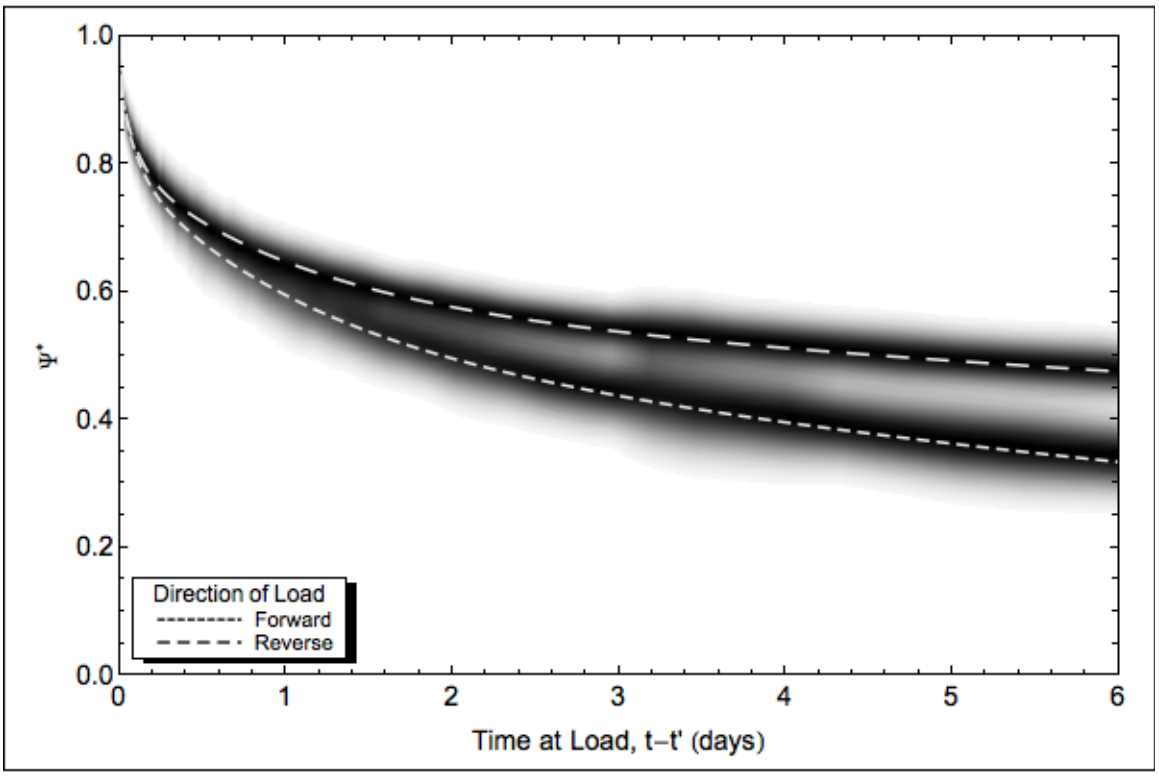

Figure 3.10 – Probability density of second loading cycle data with derived fit curves comparing relaxation in beams subject to strain reversal to those with same direction load steps. The gray scale values indicate the relative density of data within a particular region with black corresponding to 100 per cent of the data and white indicating no data. The white dashed lines correspond to the fit curves for the entire data sets in the two categories presented.

As seen in the figure, at later ages (time at load > 5 days), there is virtually no overlap of probability density of the two curves and thus, virtually no statistical likelihood that the relaxation function for specimens subject to strain reversal is the same as that for forward-loaded specimens. The load eventually relaxes to approximately 0.35 per cent of original for forward-loaded specimens, (i.e., the second step load was of the same sign as the first) while for reverse specimens, (i.e., the second step load was opposite in sign to the first) the eventual relaxed load is 14.8 per cent of the initial. This gap between the curves develops over the first few days, reaching 14 per cent at the end of 6 days of the second loading cycle (10 days of total aging).

Considering the variability inherent in comparing specimens from different batches, and to compare stress effects directly, the relaxation data was analyzed in an additional manner. For three batches, there were companion specimens loaded

in the forward and reverse directions in loading cycles 2 and 3. By reducing the data to the Ψ^* fit curves only and dividing the reverse curves by the forward curves for each cycle, Figure 3.11 was generated, taking the average for each grouping of three specimens (three different batches). This ratio compares curves of equal age during each cycle, eliminating the viscoelastic aging effects seen in previous figures. Note that the relaxation function for later cycles is based on the net load for that individual load step, meaning the effect of earlier cycles has been subtracted out using the Boltzmann superposition theory. Further note that in the first cycle, the load direction for companion specimens is the same and the ratio is theoretically 1.0.

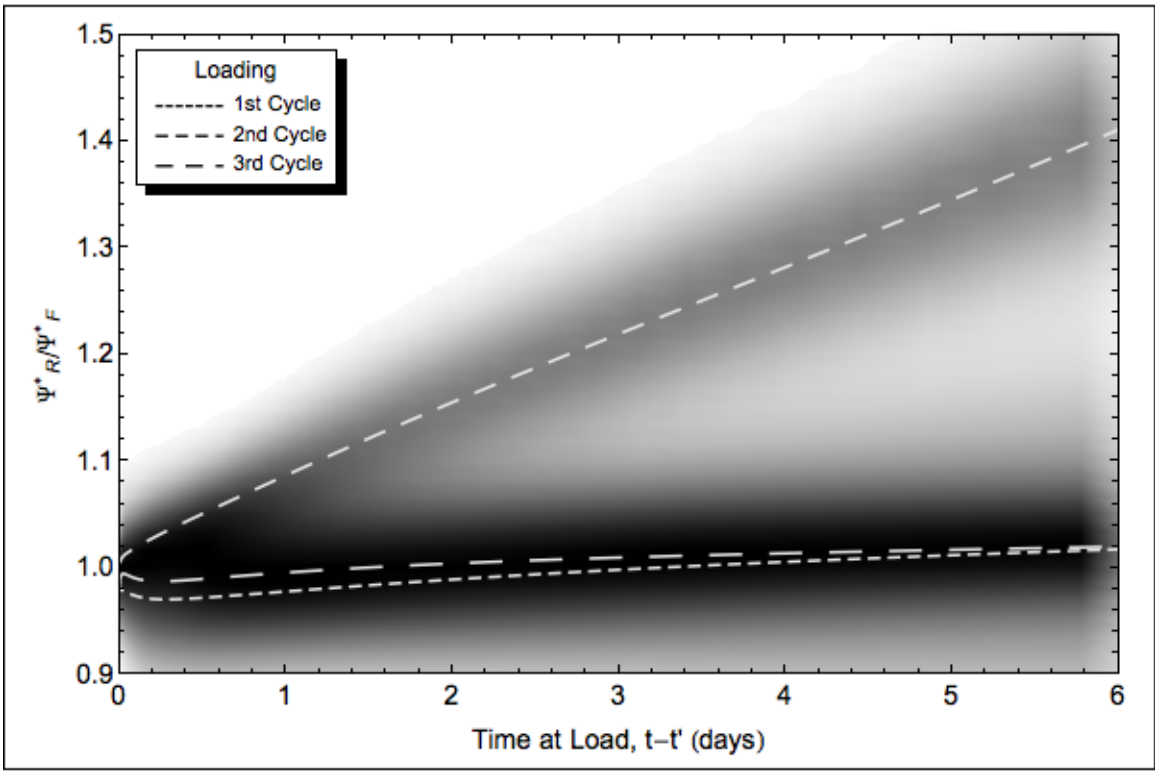

Figure 3.11 – Ratio of relaxation, reverse to forwarded loaded specimens during each of three loading cycles indicating significant influence of strain reversal on relaxation behavior. The gray scale values indicate the relative density of the ratio of reverse specimen data to the forward specimen fit curve within a particular region with black corresponding to 100 per cent of the data and white indicating no data. The white dashed lines correspond to the ratios of fit curves for the data sets in the three loading cycles.

Examination of Figure 3.11 reveals clearly that load and strain reversal have a significant effect throughout the life of the specimen whereas relaxation due to

forward loading at later cycles is virtually indistinguishable from the relaxation during the very first load cycle. It is also interesting to note the curvature of the first and third load cycles. If there were no aging effects present other than those accounted for by the solidification theory, the curves would be flat lines at Ψ^*=1.0.

3.1.6 Temperature Variation

To offer additional insight into the relative influence of fluid flow within the beams' pore structure on beam relaxation, a series of six additional beams were cast and tested in general accordance with the methodology presented in Section 3.1.1. The first series of three beams was tested within an oven maintained at 40 °C and the second series of three beams was tested at 60 °C. Due to size limitations of the oven, displacements of the beams were not measured during load application as had been done previously. Relaxation data for the two series are presented in Figure 3.12 and Figure 3.13.

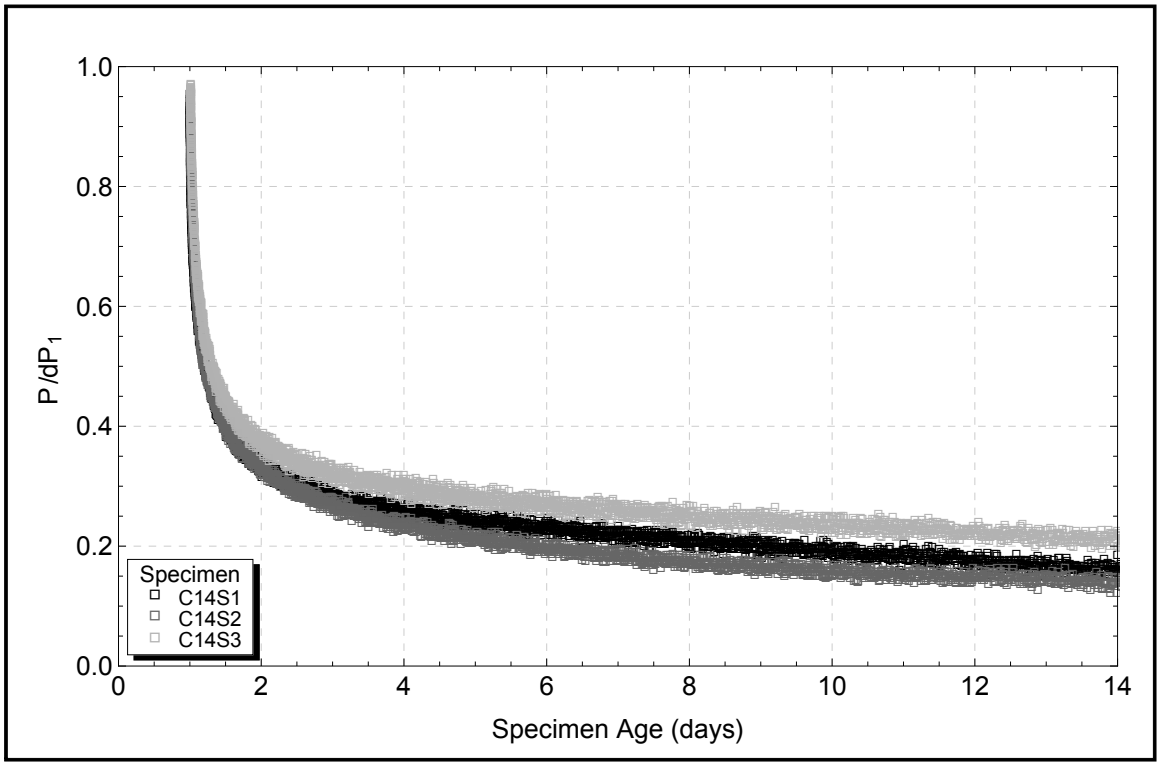

Figure 3.12 – Relaxation data for beam specimens tested at 40 °C. The three specimens show very similar relaxation rates at very early ages (less than 4 days) with a slight divergence at later ages.

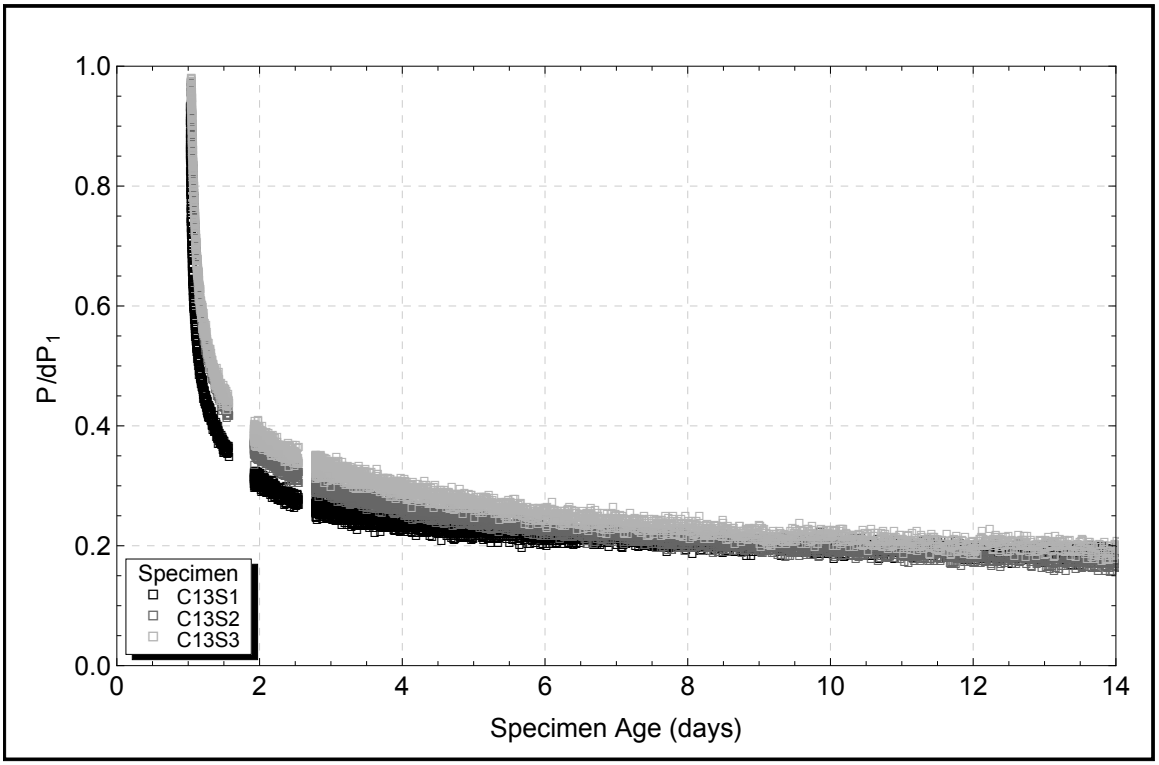

Figure 3.13 – Relaxation data for beam specimens tested at 60 °C. Relaxation rates of the three specimens are similar throughout testing and nearly indistinguishable from one another at later ages. Gaps in the data in the first 3 days indicate times of power loss in the data acquisition system.

As was previously done for the series of room temperature beams, as explained in Section 3.1.4, the relaxation data was used to generate curve fits based on a seven-element Maxwell chain. The curves for the three specimens in each elevated temperature grouping were averaged. The resulting two curves are shown in Figure 3.14 along with the average relaxation curve of room temperature beams as previously presented in Figure 3.9.

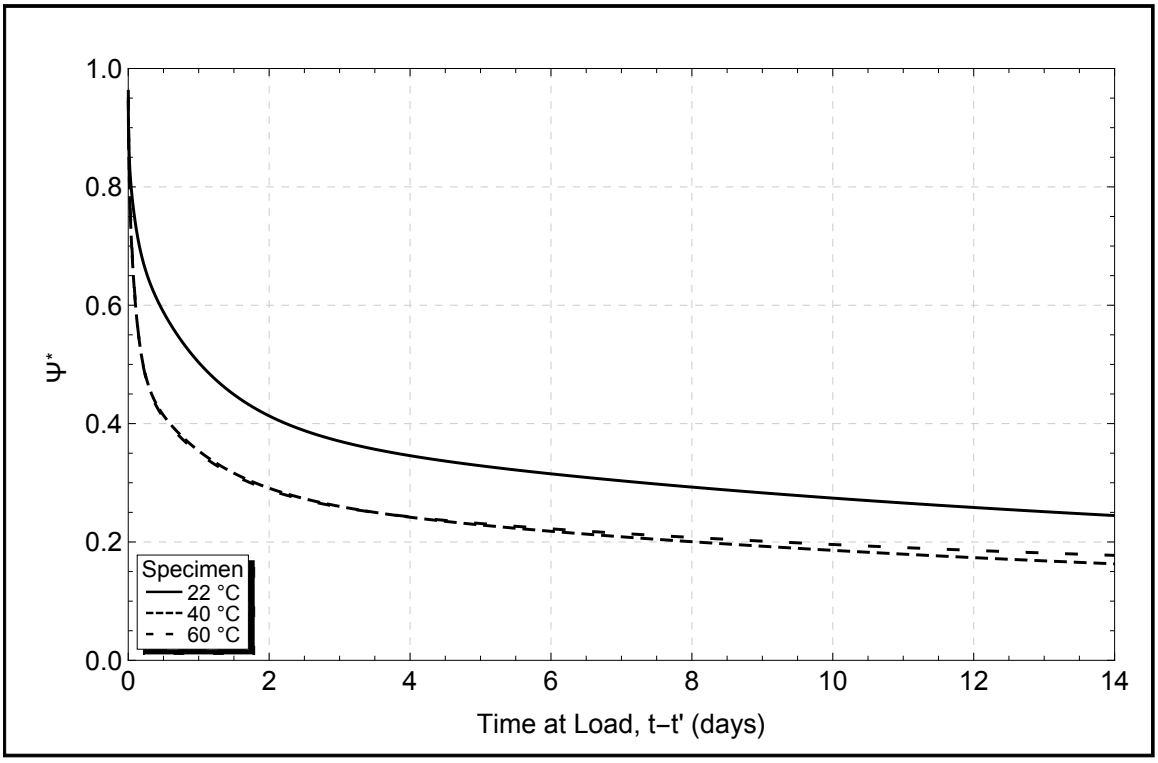

Figure 3.14 – Comparison of beam relaxation fit curves from beams tested at 22, 40, and 60 °C showing significant acceleration of relaxation at higher temperatures. The solid fit curve, corresponding to room temperature testing, is taken from previously presented results. The two dashed fit curves, corresponding to testing at two different elevated temperatures, are nearly indistinguishable at early ages (less than 7 days) with a slight difference at later ages.

As can be seen in Figure 3.14, by raising the temperature of the beam, thus increasing the flow rate of fluid within, relaxation is significantly accelerated. Theoretically, the higher temperature should also accelerate cement hydration, potentially retarding relaxation, but the overall relaxation acceleration indicates this effect is insignificant compared to other mechanisms. It is also worthy of note that the acceleration of relaxation for specimens tested at 40 °C is approximately the same as that for those tested at 60 °C. The reason for this similarity is unclear, as flow rate of a fluid through a porous medium is typically consistent with Darcy's law (Darcy 1856) and should be inversely proportional to viscosity:

$$Q = \frac{-\kappa A(p_b - p_a)}{\mu L}, \tag{3.3}$$

where Q is the volumetric flow rate, κ is the permeability of the cement paste pore structure, A and L are the cross-sectional area and length of the flow, p_b and p_a are the pressures on each end of the flow, and μ is the viscosity of the fluid. With load carried by the fluid being proportional to its pressure, the load loss due to flow should vary throughout the range of viscosities.

To better understand the potential influence of fluid flow on overall beam relaxation, the curves from the higher temperature tests were normalized to the viscosity of the fluid by dividing time by the ratio of the dynamic viscosity of water at the various temperatures and the dynamic viscosity at room temperature. The values used were 0.961, 0.653, and 0.466 Pa•s for 22, 40, and 60 °C, respectively (Lindeburg 2013). The results of the normalization are shown in Figure 3.15. Because the entire relaxation curve uses a modified time axis, the figure is based on the assumption that all the relaxation is a function of fluid flow. Further, the results only consider one-dimensional flow, assumed to be from the compression face to the tension face of the beam. These assumptions, taken together, limit the usefulness of the results. However, the results do show that the relaxation curves for higher temperature specimens converge to approximately that of room temperature specimens within 21 days; as there is less fluid available for flow due to ongoing hydration, the relative influence of that flow diminishes.

The preceding consideration of the elevated temperature testing assumes that the higher temperatures only affect the viscosity of pore fluids, potentially accelerating relaxation. However, as will be discussed in Sections 6.2.3 and 6.2.4, the higher temperatures also have a potential effect on dissolution of cement grains (increasing the rate of hydration) and dissolution of hydration products (accelerating the rate of relaxation). The combination of these effects appears to result in a net increase in relaxation, as shown in Figure 3.14 but consideration of each effect individually is beyond the scope of the current research.

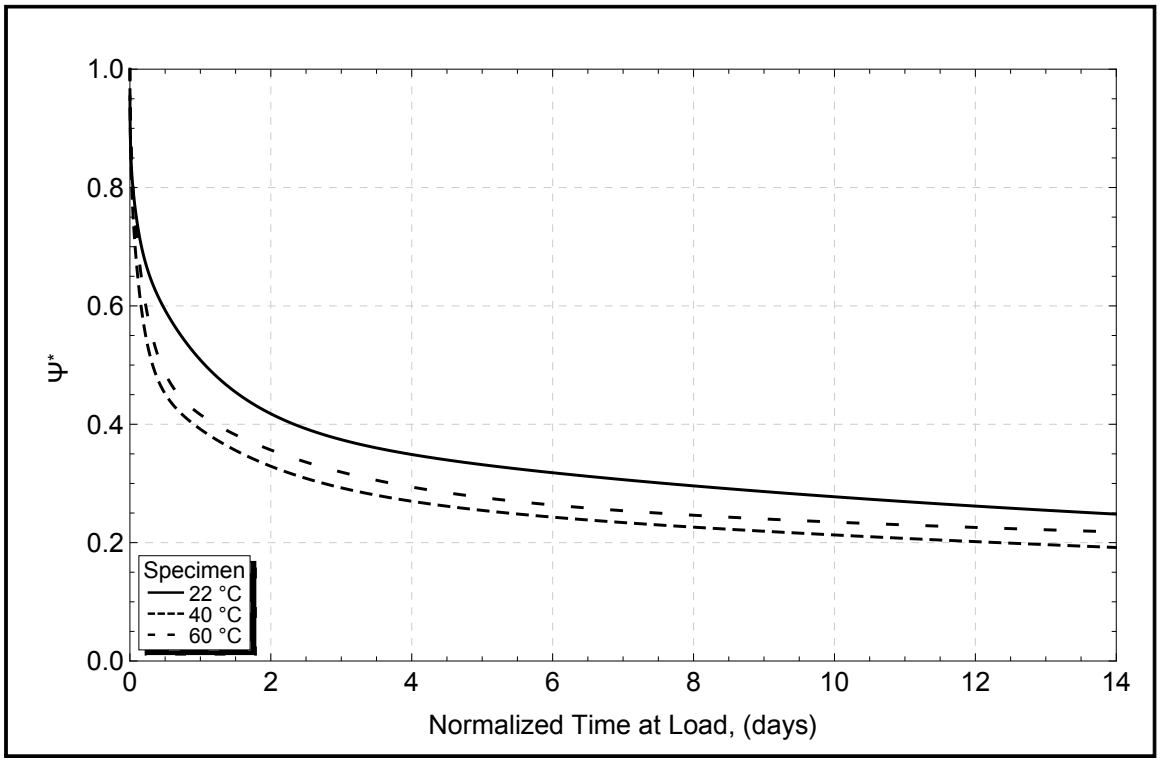

Figure 3.15 – Comparison of beam relaxation fit curves from beams tested at 22, 40, and 60 °C with time axis normalized by viscosity of water. The normalization would yield three identical curves if the only mechanism responsible for load relaxation were the flow of fluid within the cement paste. The differences in the curves indicate that the effects of this flow are likely small compared to the effects of other relaxation mechanisms.

3.2 Cylinder Testing

3.2.1 Methodology

Several batches of the cement paste used to cast beams, as discussed above, were also used to cast small-scale cement paste cylinders. Once the beams were cast, portions of the remaining mix were placed into Teflon tubing using suction. The inside diameter of the tubing was 3 mm and the length of each mold was approximately 50 mm. The tubes of paste were sealed at the ends using wax and cured using the same methods as beam specimens.

After the initial 24-hour curing period, the tubes, still containing the paste, were cut into segments approximately 6 mm long using a utility knife and the end segments were discarded. The remaining paste cylinders were carefully pushed from the tubing lengths and visually examined to determine whether a complete

filling of the tube had occurred. Incomplete samples were discarded. A total of three of the resulting test specimens were used to measure relaxation.

To facilitate X-ray computed tomography, described in Section 5, a testing frame was designed that would be sufficiently small to be mounted in the micro-CT scanner. Figure 3.16 is a schematic of the testing frame used. The total height of the acrylic cylinder used as the reaction frame is approximately 63 mm. The load cell had a capacity of approximately 111 N and data was acquired at a precision of approximately 0.0025 N.

At the beginning of each test cycle, the screw at the top of the frame was tightened to apply compressive load to the specimen. The rate of loading was similar to that for the beams, approximately 20 N/min. The magnitude of the compressive load and the age of specimen at time of loading are presented in Table 3.3. Assuming the Young's modulus for the cylinders to be approximately the same as that measured in the beams, the loads resulted in a strain within the range of the "high compression" region in the beams. No adjustments to the screw were made during the duration of testing. Initially, the load cell within the frame was connected to an automated data acquisition system. At each planned scanning time, the frame was disconnected from the data acquisition system and transported to the micro-CT lab. After completion of the scan (typically within 24 hours) the frame was re-connected to the system and load data captured until the next micro-CT scan. Tests were discontinued at end times listed in Table 3.3.

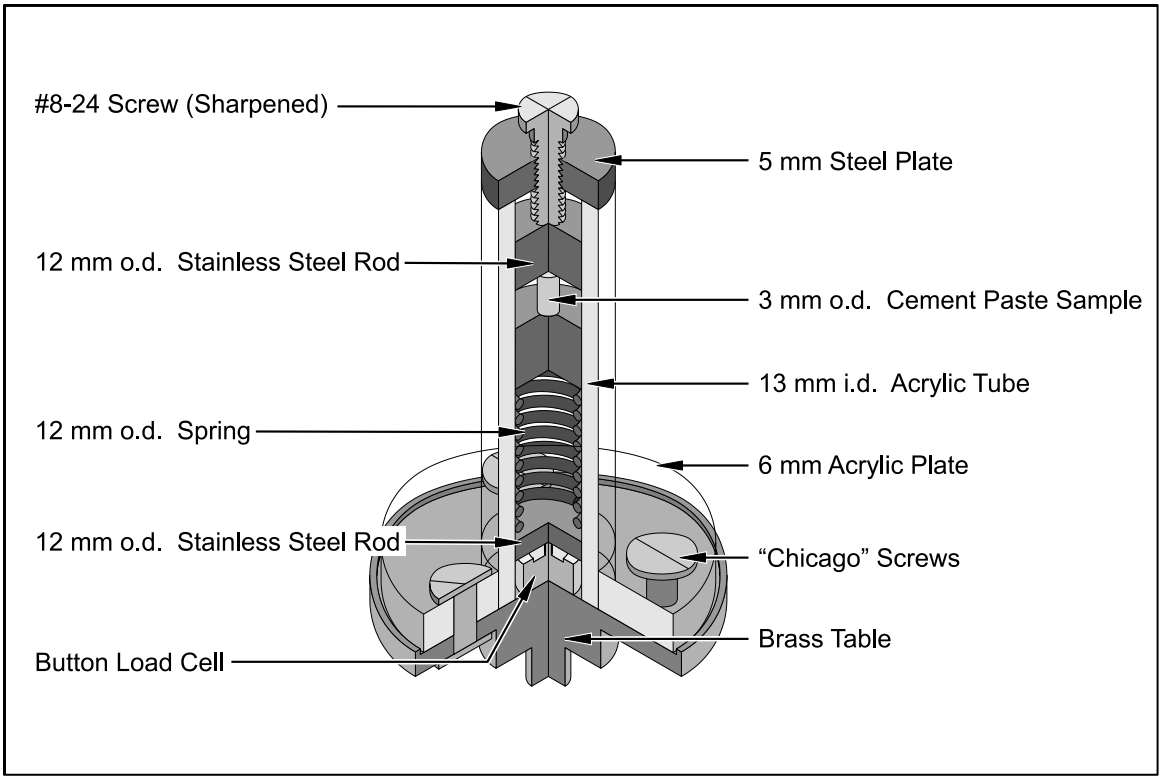

Figure 3.16 – Testing frame used for compression of cement paste cylinders. Loads were applied to the cement paste specimen by tightening the screw at the top of the frame. The spring used below the specimen increased the necessary displacement of the top of the specimen to achieve a given load, increasing the usability of the frame. The brass table was used to facilitate mounting of the frame into the micro CT scanner.

Table 3.3 – Testing parameters for cylinder relaxation

Sample ID	Age at loading (days)	Applied Load (N)	Length of Test (days)
C9c1[1]	1.19	80.47	19.94
C10c1	1.22	67.79	35.70
C11c1	0.97	67.48	82.16
[1]Beam designations C*mcn* indicate cylinder number *n* within cement paste batch *m*			

3.2.2 Results

Using the same logic and model as was used for beams, the raw data for cylinder relaxation was reduced to the P/P_0 values presented in Figure 3.17. Discontinuities in the chart were the result of the disconnection from the data acquisition system during micro-CT scans. The changes in magnitude seen when comparing values before and after scanning, most significant in sample C10c1 at day 13, were attributed to inadvertent jostling of the loading screw during transport and handling. Though this adjustment could likely be deemed an

additional load cycle, as was done intentionally with the beam testing, the magnitude of the load increase or decrease is unknown and therefore the data was not corrected for the change.

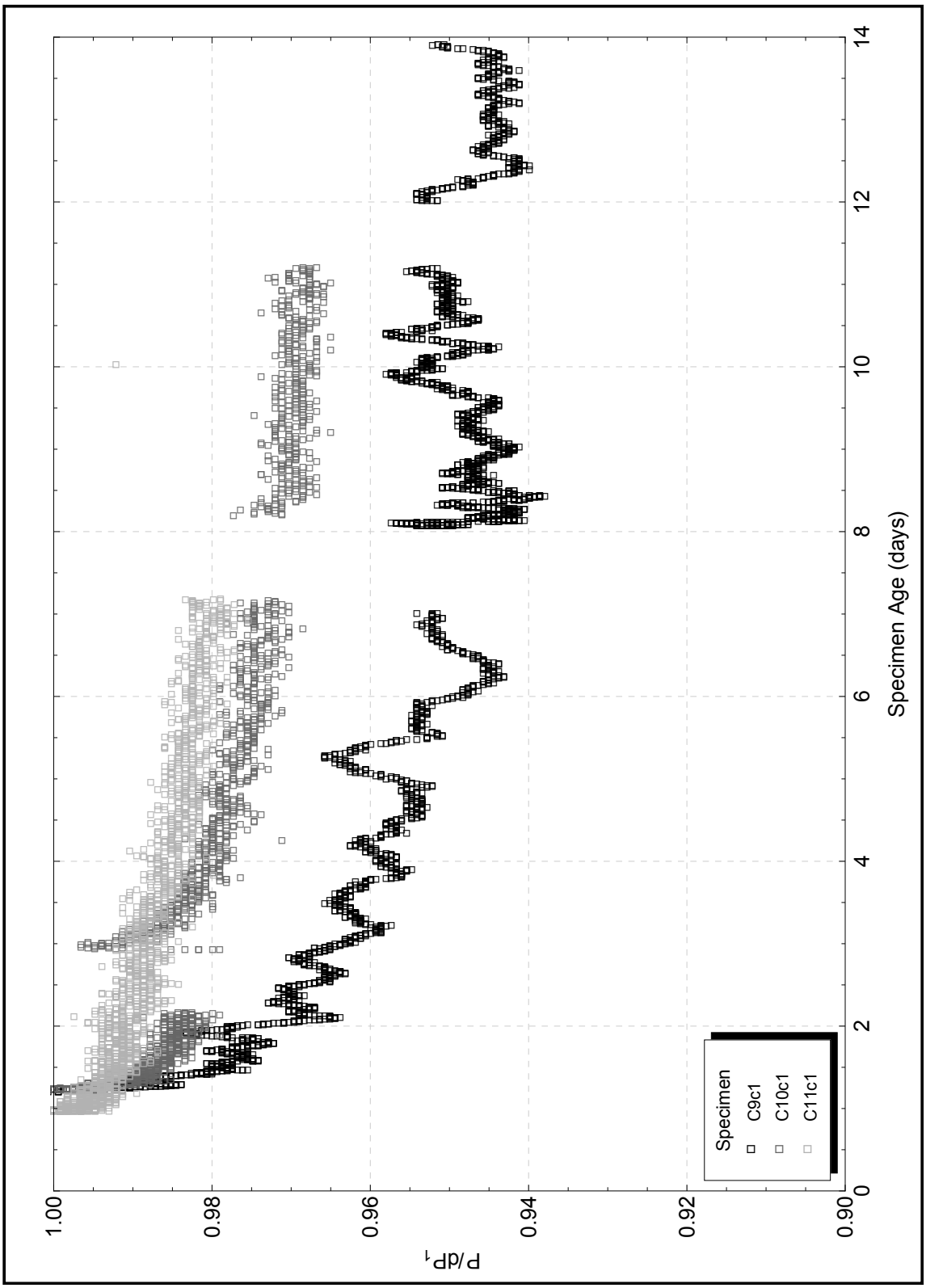

Figure 3.17 – Relaxation data for cement paste cylinders placed in compression. Gaps in the presented data correspond to times when the testing frame was disconnected from data acquisition to allow micro CT scanning. Offsets in measured load before and after these gaps likely indicate inadvertent jostling of the frame resulting in changes to applied load.

3.2.3 Analysis

Consideration of the results presented in Figure 3.17 reveals several important characteristics of cylinder relaxation. The first trend evident is that the overall shape of the relaxation curves is the same as that for the beam specimens, though the time needed to fully relax to the asymptotic value appears to be longer; the slope of the right end of the curves is steeper than seen previously. The second feature of the curves of note is instability of the load seen in sample C9c1 between approximately 8 days and 14 days. The sample was connected and stationary during this span of time and the variations are not easily explained. It is possible that the variations were due to temperature and/or humidity fluctuations in the lab environment. Though the lab used had some coarse control of environmental factors, fluctuations were expected. Due to the small scale and mix of materials used for the testing frames, it is likely that small fluctuations in environmental conditions would cause more significant changes in measured load within the testing frame. It is also possible, because the cylinders were being tested along side the beams using the same data acquisition system, the connection or disconnection of load cells used for beam testing, due to initiation or completion of testing, caused voltage variations in the data acquisition itself and led to the observed behavior. Regardless of cause, the instability in readings suggests that the precise values reported cannot be taken as definitive and the results should be used more to indicate trends than to define properties.

The final and, for purposes of this research, most significant feature of Figure 3.17 is the magnitude of the relaxation value seen on the y-axis. The maximum load loss seen, after nearly 7 weeks of testing, is less than 10 per cent of the original load. This value is in sharp contrast to that of beam relaxation where a load loss of over 60 per cent was typically seen in the first 4 days of testing. To better illustrate this difference, the curve for 1-day beam loading was superimposed on the cylinder results as presented in Figure 3.18. Additionally, beam relaxation data from (Vichit-Vadakan and Scherer 2003) and tensile

relaxation in mortar from (Beushausen et al. 2012) are shown for comparison purposes.

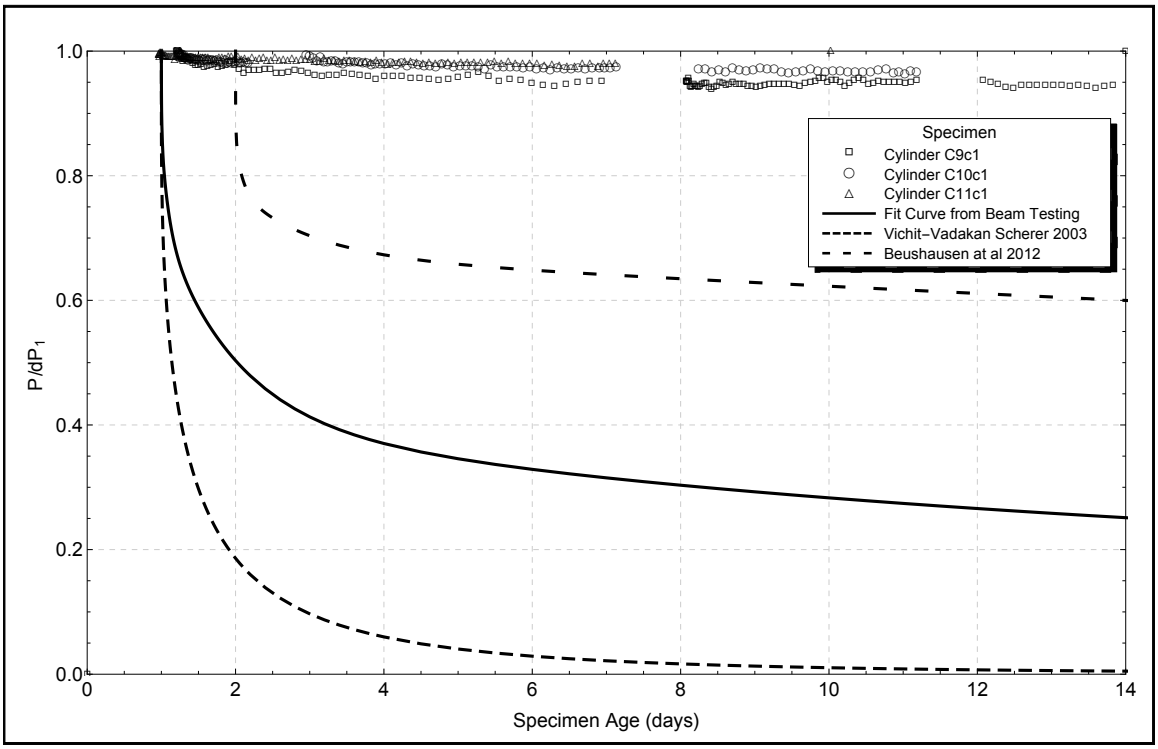

Figure 3.18 – Comparison of cylinder relaxation data to beam relaxation fit curve indicating significantly different magnitudes of relaxation throughout. Beam relaxation data from (Vichit-Vadakan and Scherer 2003) and tensile relaxation in mortar from (Beushausen et al. 2012) shown for comparison.

Consideration of the relaxation data in Figure 3.18 reveals significant differences in the magnitudes and trends, some of which are explainable. The curve fit from Vichit-Vadakan and Scherer is based on short duration (<1 day) testing of cylindrical beams with a w:c of 0.45 that are placed under water and kept saturated throughout testing. The variation of the cement content, beam shape, and exposure conditions from the parameters used in the current research should lead to differences in observed behavior. However, as can be seen, the overall trend of the relaxation is similar to that presented in Section 3.1.3. The data from Beushausen et al. is based on tensile relaxation testing of mortar samples with a w:c of 0.45. The mortar mix used contains aggregate, water reducers, and other components that would cause variations in viscoelastic response versus testing of solely cement paste. However, as can be seen, the general shape of the

curve is similar to that of the current research with less load relaxation likely due to the later age at which the specimens were loaded and the presence of aggregate in the mix.

When comparing the cylinder relaxation data to the other sets, a significant difference in magnitude of relaxation is seen. Theoretically, the cylinder relaxation should be similar to that seen in beams. It is likely that beams would experience a slightly higher relaxation rate throughout testing due to submicrocracking in tensile regions, but that difference does not explain the contrasting data presented in Figure 3.18. It is far more likely that the cylinder relaxation data is not a true depiction of material behavior but instead represents errors in the testing protocol.

The cylinder testing frame depicted in Figure 3.16 relies on precise alignment of all parts such that no friction develops between the testing platens and the surrounding acrylic cylinder. Though during initial loading, this friction would likely have been overcome during adjustment of the loading screw, slight misalignments in the surface of the cement paste cylinders could cause a rotation of the platens, wedging them into the acrylic cylinder. The friction between the platen and the cylinder would interfere with the slight movements and spring elongation needed to keep up with load losses and/or shrinkage of the cement paste cylinder. The load cell would read a load that is partially from the paste cylinder and partially from this friction, giving falsely high readings. Though it is possible the effect of friction is negligible and therefore the cylinder relaxation results are accurate, this would represent a dramatic difference between assumed and observed relaxation behavior. Additional testing, using a protocol less susceptible to error, should be performed to confirm the behavior.

4. Chemical Analyses

As discussed in Section 3, the relaxation testing of cement paste beams and cylinders revealed results not easily explained by traditional models of behavior. Based on those results, it was hypothesized that properties of cement paste under tensile load may vary from those in specimens being loaded in compression. Assuming that cement paste properties are derived mainly from the chemical composition of the paste, a series of specimens with varying load histories were produced, to be tested using two proven methods for determination of chemical composition.

4.1 Thermogravimetric Analysis

Thermogravimetric analysis ("TGA") is a process whereby a small sample of material is slowly heated to high temperature while continuously being weighed. Results throughout the temperature history show directly the mass loss of the specimen and, given knowledge of the overall chemical components of the material, can be used to determine the mass fractions of the individual components.

In the case of cement or cement paste, a number of constituents of the raw cement as well as hydration products have predictable mass loss behavior when subjected to high temperatures. As an example, when heated in the temperature range between approximately 400 and 500 °C, calcium hydroxide ($Ca(OH)_2$), decomposes into calcium oxide (lime or CaO), and water (Ukrainczyk et al. 2006). Therefore, knowing the mass loss in this temperature range can be attributed to the evaporation of the water, the approximate percentage of calcium hydroxide in the original sample can be computed.

4.1.1 Methodology

During the casting of cement paste beams described in Section 3.1.1, additional samples were placed in sealed plastic bags and allowed to cure in the same conditions as the beam specimens, though without sample rotation. These specimens comprised the reference groups used for comparison and were subjected to no loadings beyond those imparted by sample preparation.

At the designed testing age/time of loading, a total of six specimens were prepared. The first specimen was taken from the sealed container and crushed manually using a mortar and pestle to a fineness approximating that of a well-graded fine sand. The other five specimens in a particular series were collected by dissecting an approximate 25 mm long section adjacent to the failure point of a tested beam (typically at midspan, the point of load application) into five slices spaced evenly along the height of the beam. These five slices, corresponding to stress conditions of "high tension (HT)", "low tension (LT)", "neutral axis (NA)", "low compression (LC)", and "high compression (HC)" were also pulverized manually to yield specimens able to be tested.

For a given test specimen, a portion of the sample, ranging from approximately 30 mg to 50 mg, was removed from the bulk powder, placed into a platinum crucible, and weighed. The specimen was then placed into a Netzsch model STA 449C Simultaneous Thermal Analyzer and subjected to the temperature-time profile presented in Figure 4.1 using an 80/20 mix of nitrogen and oxygen as the makeup air during burning. The plateau corresponding to 110 °C was used to insure complete drying of the specimen before higher-temperature heating and degradation. Data for temperature and mass loss were captured by the control software and later downloaded for analysis.

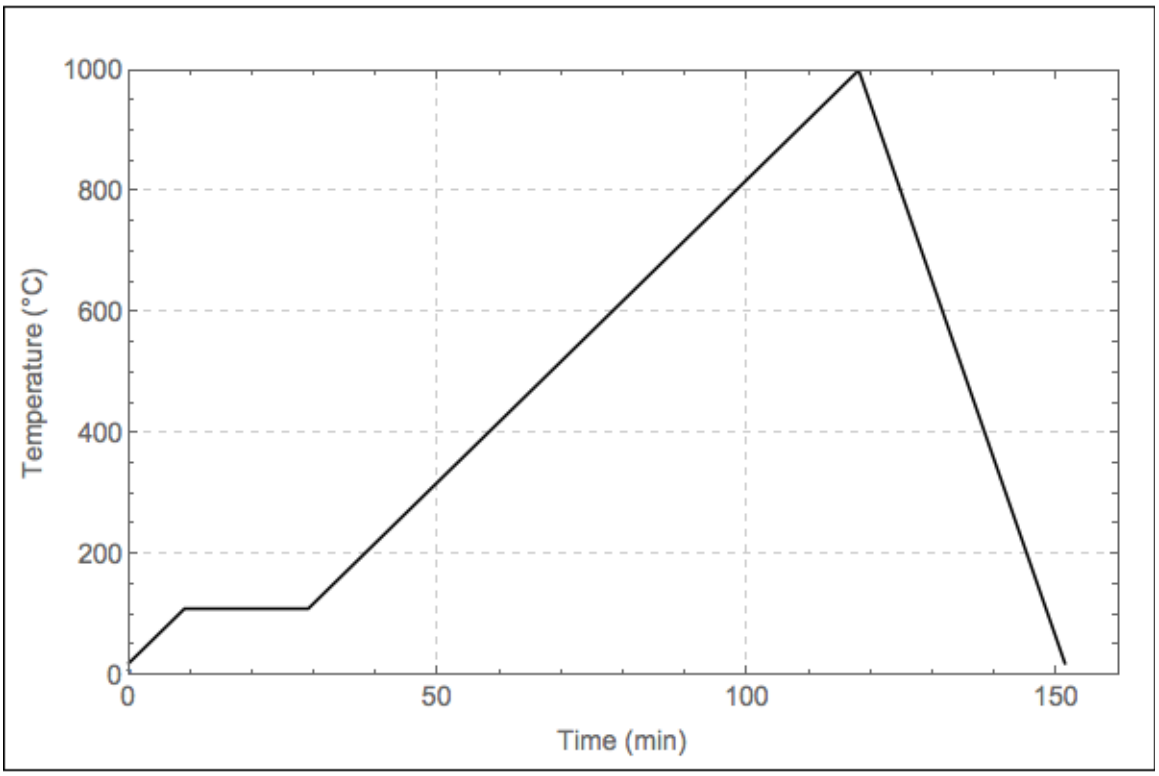

Figure 4.1 – Temperature-Time profile applied for TGA testing. The plateau at 110 °C insured complete drying of the specimen before additional heating.

4.1.2 Results

For each specimen, the mass and temperature as functions of time were converted to graphs showing mass loss as a function of temperature. Figure 4.2 shows an example of the raw data generated. Graphs of the raw data for all specimens tested appear in Appendix C.1. The distinct drops in mass at approximately 450 °C and 700 °C represent expected mass losses due to degradation of hydration products with the associated release of attached water. Note the results presented and used in subsequent calculations were computed using the assumed dry weight of the specimen, the mass just after the 20-minute hold at 110 °C. As noted in Section 2.1, this mass fraction could be related back to the total mass of the specimen before drying. However, as the analysis presented here is mainly comparing losses from one range to another or one stress condition to another, the conversion to a percentage of the total mass, including evaporated water, is not performed.

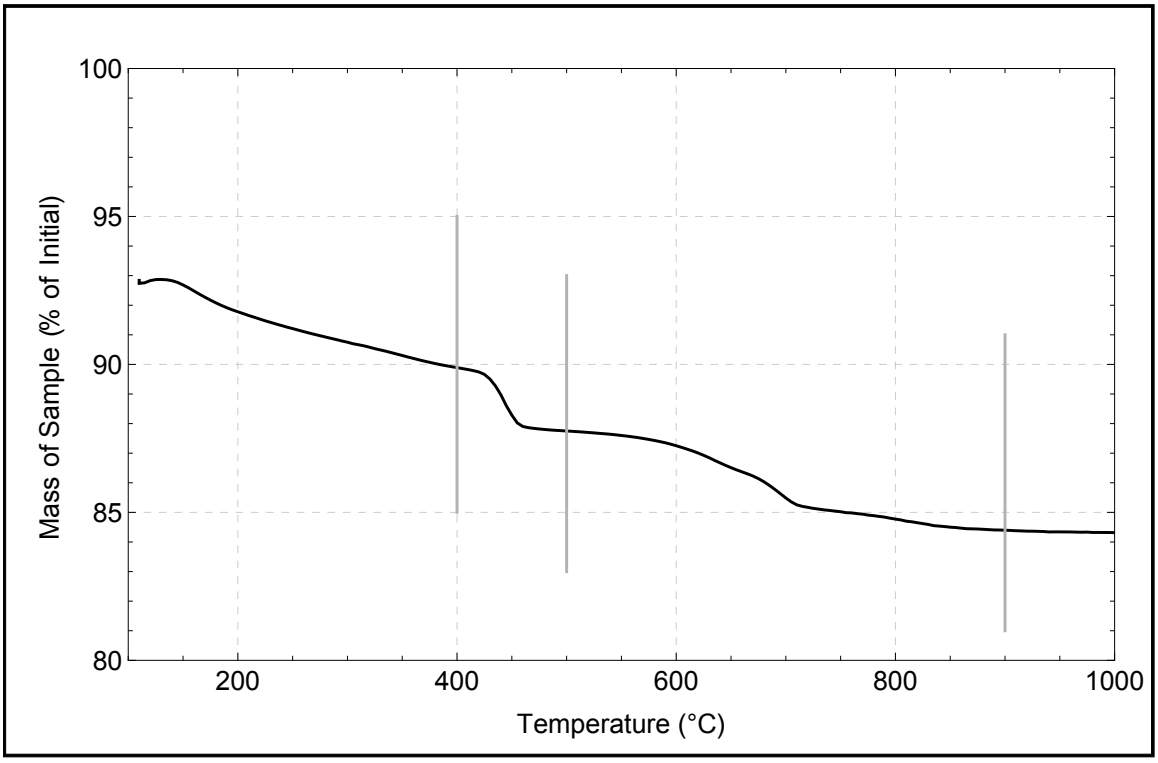

Figure 4.2 – Sample raw data of mass vs. temperature with distinct mass losses corresponding to loss of evaporable water at 110 °C and loss of attached water from hydration. Vertical lines at 400, 500, and 900 °C are boundaries of regions of data used for later analysis. Noticeable mass losses at approximately 450 and 700 °C were attributed to losses due to degradation of calcium hydroxide and calcium carbonate, respectively.

Using temperature ranges taken from the aggregate of past publications of TGA data for various cements (Kar et al. 2012; Pane and Hansen 2005; Taylor 1990; Ukrainczyk et al. 2006), the results of the current analysis were broken into four pieces. Mass losses, as a percentage of dry weight, were calculated for each of the four temperature ranges with results of all samples appearing in Table 4.1.

Table 4.1- Percentage mass loss within four temperature ranges for all specimens

Age of Specimen (days)	Stress[1] Condition	% Loss 110 to 400 °C	% Loss 400 to 500 °C	% Loss 500 to 900 °C	% Loss 900 to 1000 °C
0[2]	All	0.380	0.072	1.400	0.017
0	All	0.522	0.101	1.504	0.006
0	All	0.013	0.051	1.466	0.050
0	All	0.029	0.071	1.508	0.041
0	All	-0.004	0.045	1.470	0.072
1	X	2.535	2.668	2.596	0.085
2	X	2.926	2.254	3.518	0.104
2	X	3.020	2.950	2.389	0.198
2	X	3.497	3.261	3.088	0.163
2	X	3.369	3.031	2.469	0.117
3	X	3.617	2.466	2.434	0.147
3	X	3.337	2.895	2.715	0.142
3	X	3.668	3.124	2.524	0.148
3	X	3.694	3.136	2.443	0.132
4	X	3.127	2.364	3.291	0.146
7	X	4.361	3.165	2.556	0.156
7	X	3.973	3.246	2.467	0.163
7	X	3.993	3.253	2.588	0.150
7	X	4.145	3.209	2.616	0.145
8	X	3.355	2.383	2.423	0.135
8	X	5.071	3.959	2.491	0.155
10	X	4.115	3.272	2.769	0.162
10	X	3.938	3.283	2.689	0.159
10	X	4.154	3.266	2.938	0.150
11	X	4.438	2.974	2.547	0.153
14	X	3.544	2.519	2.757	0.159
14	X	4.180	3.354	2.778	0.198
14	X	4.266	3.345	2.795	0.175
14	X	4.480	3.441	2.796	0.159
16	X	5.607	3.915	2.908	0.168
17	X	4.2265	2.922	2.816	0.156
17	X	4.662	3.501	2.960	0.160
17	X	4.633	3.464	2.924	0.158
17	X	4.455	3.407	2.961	0.167
2	HT	4.030	3.588	2.890	0.114
7	HT	4.455	3.767	3.223	0.159
7	HT	4.527	3.658	2.757	0.135
7	HT	5.120	3.865	3.073	0.145
10	HT	4.761	3.617	2.467	0.144
11	HT	5.151	3.961	2.656	0.140
13	HT	5.803	4.150	3.018	0.175
14	HT	5.308	3.973	3.385	0.165
16	HT	6.982	4.819		
17	HT	5.507	3.976	2.975	0.091

Age of Specimen (days)	Stress[1] Condition	% Loss 110 to 400 °C	% Loss 400 to 500 °C	% Loss 500 to 900 °C	% Loss 900 to 1000 °C
2	LT	4.227	3.697	2.595	0.127
7	LT	4.398	3.587	3.201	0.164
7	LT	4.809	3.850	2.811	0.165
7	LT	4.637	3.761	2.904	0.171
10	LT	4.777	3.503	2.621	0.150
14	LT	5.858	3.937	2.893	0.174
17	LT	5.722	4.074	3.004	0.195
2	NA	5.992	5.065	3.884	0.193
7	NA	4.496	3.671	2.448	0.170
7	NA	5.477	4.135	2.503	0.142
7	NA	4.984	3.945	2.480	0.163
10	NA	5.101	3.740	2.697	0.179
11	NA	5.547	3.994	2.570	0.166
14	NA	5.533	3.804	2.636	0.175
16	NA	6.146	4.198	2.737	0.171
17	NA	5.713	4.090	2.706	0.177
2	LC	4.340	3.707	2.556	0.132
7	LC	4.562	3.471	3.313	0.157
7	LC	4.911	3.865	2.679	0.161
7	LC	5.094	4.010	2.759	0.171
10	LC	5.130	3.712	2.730	0.169
14	LC	5.505	4.005	2.877	0.184
17	LC	6.111	4.236	2.670	0.178
2	HC	3.655	3.104	2.497	0.135
7	HC	4.520	3.653	3.199	0.175
7	HC	4.849	3.604	2.762	0.155
7	HC	5.038	3.806	3.238	0.162
10	HC	5.194	3.847		
11	HC	5.493	3.983	2.809	0.165
13	HC	5.363	3.980	2.693	0.158
14	HC	4.925	3.715	3.169	0.217
16	HC	5.612	4.025	2.989	0.169
17	HC	5.764	3.874	2.859	0.176

[1]Stress conditions are: X – control specimens, HT and HC – high tension and high compression, LT and LC – low tension and compression, NA – neutral axis
[2]Specimen age of "0" indicates test on cement powder without addition of water

The results for each temperature range, plotted as curves of mass loss in percentage of dry weight versus specimen age appear in Figure 4.3 through Figure 4.6. Note that all beams used for chemical analysis were originally loaded at approximately 1 day and subject to only a single displacement ("S" specimens from the beam testing protocol).

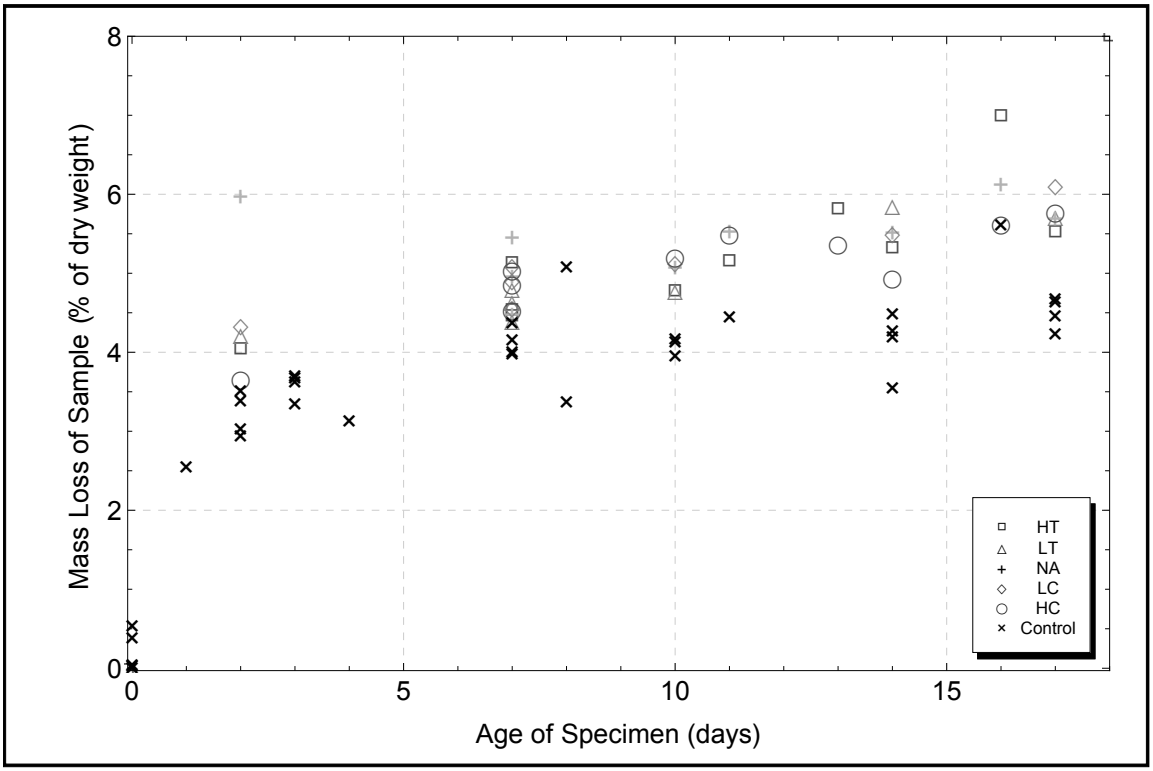

Figure 4.3 – Mass loss as percentage of dry weight between 110 and 400 °C for samples tested at various ages and subject to varying stress histories. Stress conditions, as shown in the legend, correspond to "High Tension", "Low Tension", "Neutral Axis", "Low Compression", and "High Compression". Results generally indicate that all stress conditions result in higher mass losses than the loss seen in unstressed control specimens.

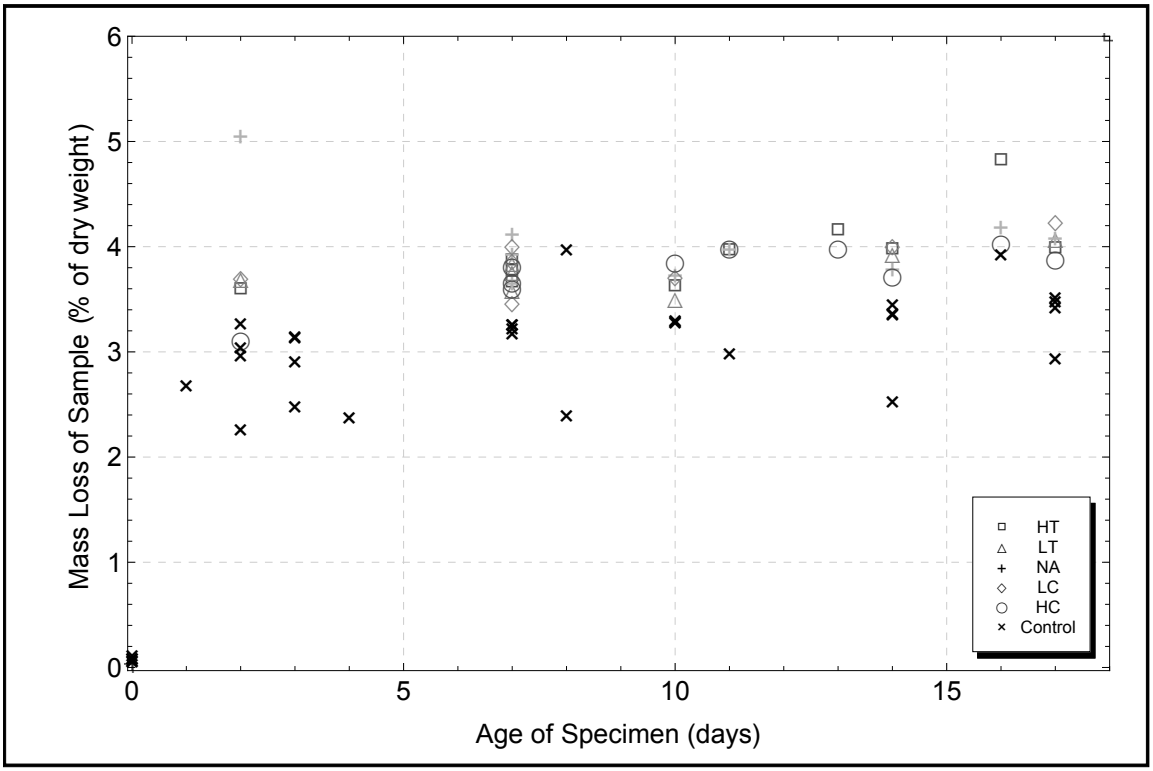

Figure 4.4 – Mass loss as percentage of dry weight between 400 and 500 °C for samples tested at various ages and subject to varying stress histories. Stress conditions, as shown in the legend, correspond to "High Tension", "Low Tension", "Neutral Axis", "Low Compression", and "High Compression". Results generally indicate that all stress conditions result in higher mass losses than the loss seen in unstressed control specimens.

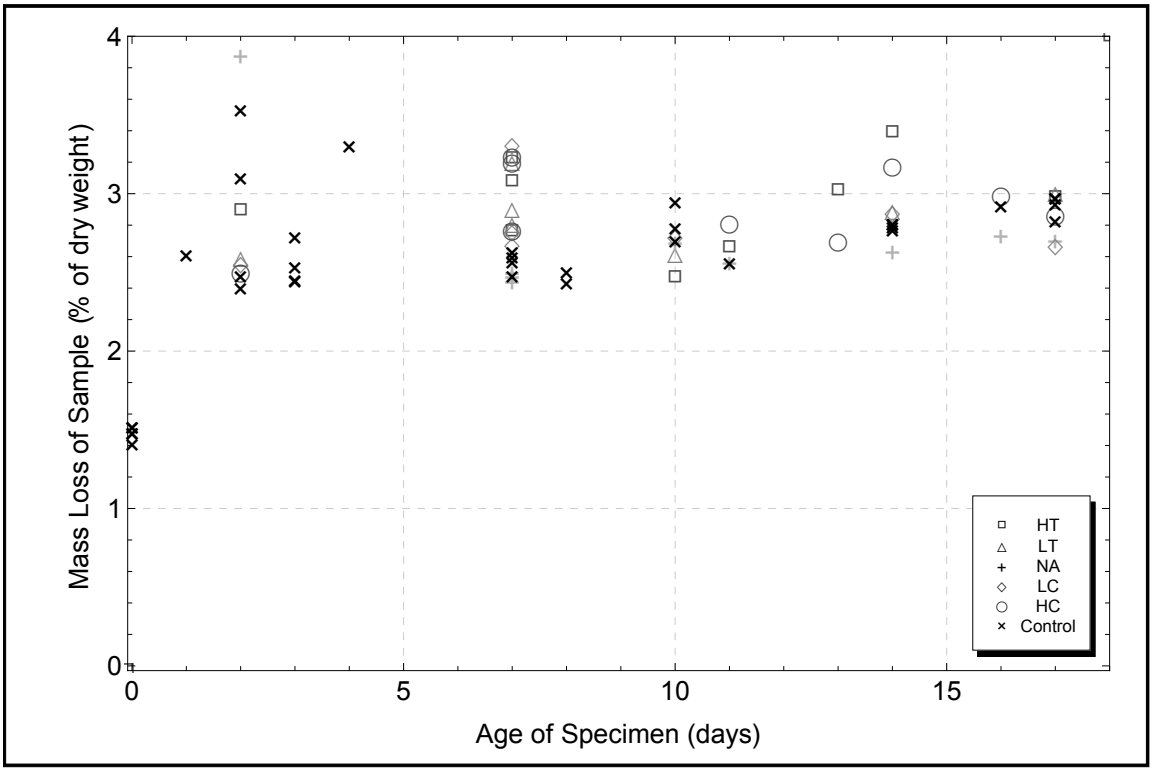

Figure 4.5 – Mass loss as percentage of dry weight between 500 and 900 °C for samples tested at various ages and subject to varying stress histories. Stress conditions, as shown in the legend, correspond to "High Tension", "Low Tension", "Neutral Axis", "Low Compression", and "High Compression". Results generally indicate that stress conditions result in higher mass losses than the loss seen in unstressed control specimens.

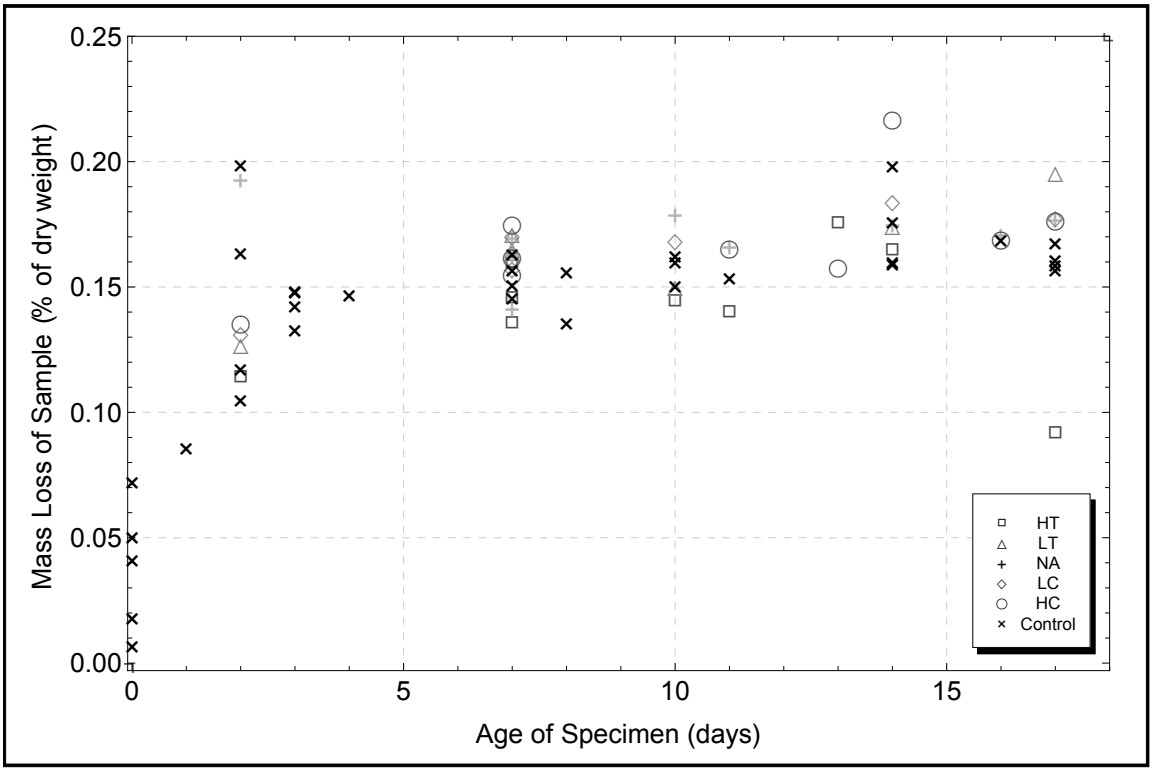

Figure 4.6 – Mass loss as percentage of dry weight between 900 and 1000 °C for samples tested at various ages and subject to varying stress histories. Stress conditions, as shown in the legend, correspond to "High Tension", "Low Tension", "Neutral Axis", "Low Compression", and "High Compression". Results generally indicate that stress conditions result in approximately the same mass losses than the loss seen in unstressed control specimens.

4.1.3 Analysis

The TGA results presented in the previous figures indicate a high likelihood that mass loss within at least some temperature ranges is dependent on both the age of the specimen and the region of the beam from which the specimen was taken. The latter dependency is most apparent in Figure 4.3 at later ages where there is nearly no overlap of data from previously unstressed specimens with those taken from the beam. The same figure also shows the time-dependence of the results with an increasing mass loss ratio with time. The first step in the analysis of these results was to attempt to separate the two dependencies for further consideration.

In a hydrating cement paste, at any given time, the dry weight of the paste represents a mix of unhydrated cement grains and hydration products. If it is assumed that within a given temperature range, a certain fraction, r_c, of cement

grains are ignited and their mass lost and a certain fraction, r_h, of hydration products are similarly lost, then the total mass loss can be written as a combination of r_c, r_h, and the mass percentage of each constituent present. These losses are in addition to the initial loss of evaporable water during the first stage of the test. Using the calculations presented in Section 2.1, the relationship for the total mass loss, as a proportion of the dry weight of the specimen, within a particular temperature range becomes

$$\Delta mr = \frac{r_c m_{ci}\left[1-\alpha(t)\right]+r_h\left[1.24 m_{ci}\alpha(t)\right]}{m_{ci}\left[1+0.24\alpha(t)\right]}, \tag{4.1}$$

where r_c and r_h are as defined above, m_{ci} is the initial mass percentage of cement grains (determined by the w:c ratio), and $\alpha(t)$ is the degree of hydration.

Assuming the hydration curve, $\alpha(t)$, takes the same exponential form as was used for the curve fitting for Young's modulus of elasticity and presented in Equation (3.1), the results for all unstressed samples were fit to curves using Mathematica. Values for mass loss for stressed specimens were then divided by this resulting baseline. The results of this calculation are presented for each temperature range in subsequent sections.

110 to 400° C Range

Between approximately 110° C and 400° C, mass losses in a dry cement paste sample can be attributed to a combination of dehydration of C-S-H, ettringite, and calcium aluminate hydrate (Ukrainczyk et al. 2006). The precise mix of these hydration products, based solely on mass loss in this temperature range, would require information about the cement chemistry beyond that obtained as part of this research. As can be seen in Figure 4.2, the loss is generally a steady slope between the temperature limits with no obvious spikes attributable to a single product. However, as all the products listed are hydration products, mass losses can give an indication of the degree of hydration of the sample tested. Figure 4.7 presents the results of the curve fit discussed above as applied to the mass loss in this temperature range for unstressed specimens. The fit parameters for the degree

of hydration were a=0.6204, b=0.01, and c=0.4105. The ratio of cement grain mass loss in this temperature range was calculated to be 0.001874 and the ratio of hydration products lost was 0.05065. The R^2 for the fit curve was 0.9894.

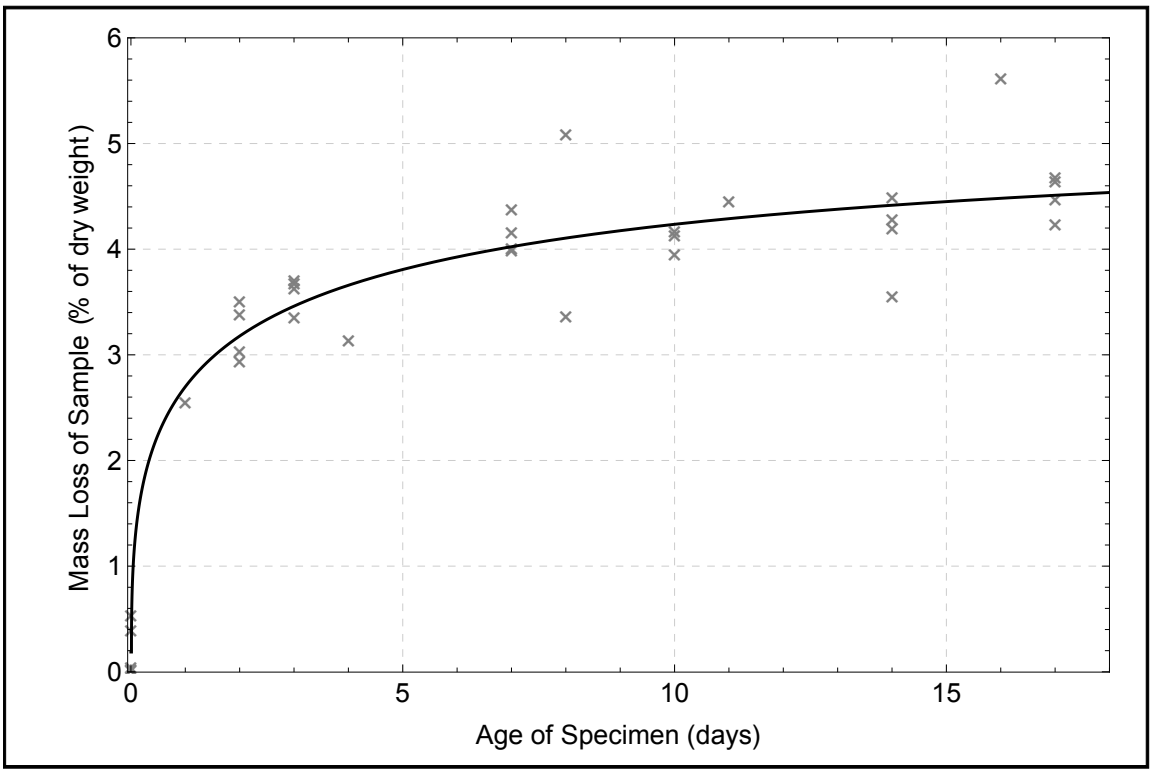

Figure 4.7 – Curve fit of percentage mass loss vs. time for the 110 to 400 °C range for samples not previously loaded. The form of the curve equation is based on an unknown mass fraction of hydration products and a different fraction of cement grains being lost during the heating with both fractions remaining constant throughout the age of the specimens. Thus, the only time-dependency is that of the underlying hydration curve.

Using the unstressed sample curve fit as a baseline, the results for stressed samples presented in Figure 4.3 were normalized to the unstressed condition, removing the time dependency of the results so that stress effects, if any, could be seen. To better understand the trends in the data, a cubic polynomial curve was fit to the data, as a function of applied stress. Though the trend curve does not necessarily yield numerical importance, it does give insight into possible variations in behavior between the various stress conditions. Figure 4.8 presents the results of the normalization with the superimposed trend curve. Note that the x-axis is a measure of relative stress in the cross-section with "HT" corresponding to a value of +1 and "HC" corresponding to -1.

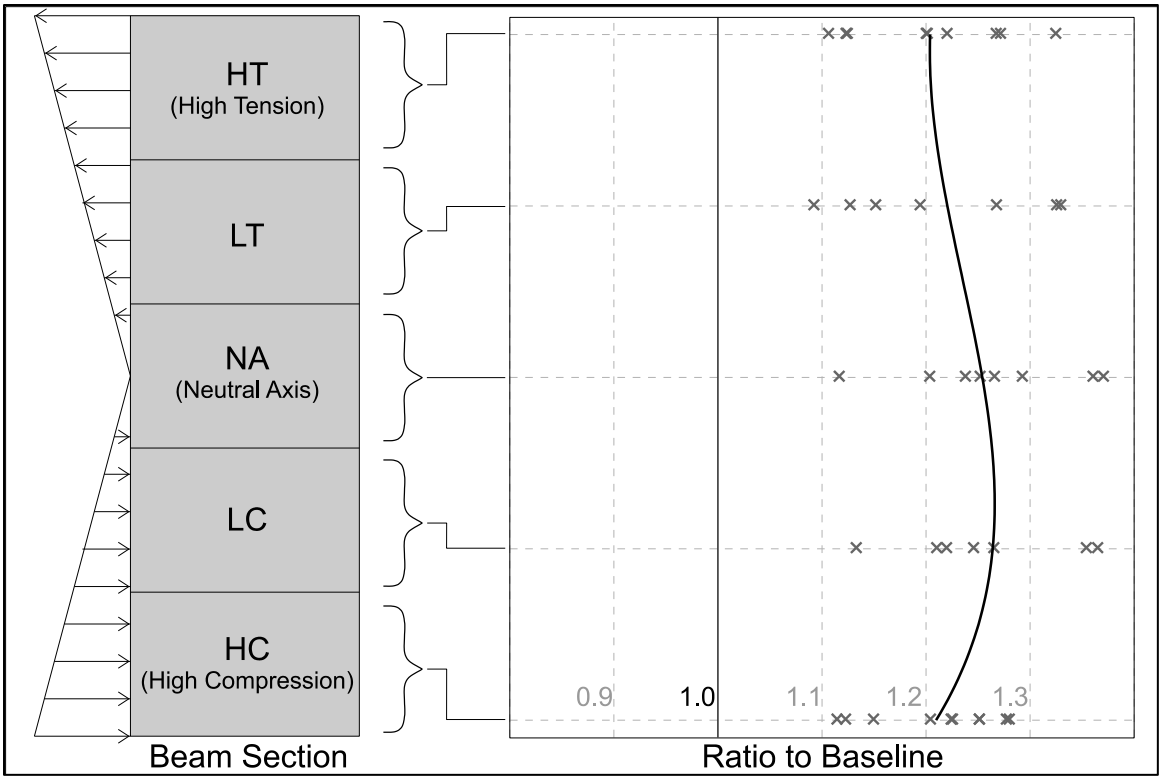

Figure 4.8 –Ratio of percentage mass loss for stressed samples to the fit curve of those not previously loaded for the 110 to 400°C range. Using the resulting ratios for each of the five stress conditions, a cubic trend curve was fit to the data indicating that not only does stress increase the mass loss, but also there is a potential difference in loss between samples taken from compressive regions and those from tensile regions.

There are two important trends evident in the results presented in Figure 4.8. The first is that regardless of stress condition, the ratio of mass loss is significantly higher than that for the baseline obtained from stress-free data. Given that products responsible for the mass loss in this temperature range are assumed to be all hydration products, this implies that stress accelerates the formation of these products. The second trend seen is the shape of the fitted trend curve. Using typical beam assumptions, the material within the region of the neutral axis would have little to no stress applied. Thus, if the acceleration of hydration is a function of the magnitude of stress, the neutral axis samples should have the lowest relative ratio of mass loss. Further, if the acceleration is due to a physical phenomenon, such as stress dissolution of cement grains, the distribution of the degree of hydration should be symmetric relative to the neutral axis. Neither of these expected relationships is true of the data presented.

Given the spread of the data points and the relatively small sample sizes, additional statistical analysis was performed to examine the trends. Each of the five stress conditions was compared to the other four using a two-sample t-test with both means and variances unknown (a Welch's t-test) (Snedecor and Cochran 1989). The test was conducted in two directions, the first applying a 0.05 level of significance to the null hypothesis that the two sets of results being compared had the same mean. The second direction determined the level of significance at which the two samples were different, with a value of 1 indicating the two samples were identical. This second calculation can be taken as the probability that the two samples being compared have the same mean. An explanation of the Welch's t-test, as used for this research, is given in Appendix B.2. The results of the statistical tests are given in Table 4.2 with "Same" indicating that there is insufficient reason to reject the null hypothesis that the sample means are the same and "Different" indicating that at a 0.05 level of significance, the two means are different. Note that because the baseline fit forces a value of 0 for hydration products at an age of 0, the five data points for cement powder, which could give a ratio of ∞, were removed from consideration for t-tests.

Table 4.2 – Results of t-tests for the 100 to 400 °C TGA results

Stress	HC[1]	LC	NA	LT	HT	X
Sample mean	1.211	1.257	1.263	1.213	1.205	1.000
Sample std. dev.	0.0612	0.0819	0.0825	0.0960	0.0757	0.0991
n	10	7	8	7	9	29
HC		0.235[2]	0.160	0.952	0.861	0.000
LC	Same[3]		0.885	0.381	0.219	0.000
NA	Same	Same		0.307	0.155	0.000
LT	Same	Same	Same		0.856	0.001
HT	Same	Same	Same	Same		0.000
X	Different	Different	Different	Different	Different	

[1]Stress conditions are: X – control specimens, HT and HC – high tension and high compression, LT and LC – low tension and compression, NA – neutral axis
[2]Values in the upper right portion of the table indicate the level of significance at which the two sample means can be considered different, corresponding to a probability that the two means are the same.
[3]Text in the lower left portion of the table indicates the results at a 0.05 level of significance.

The results in Table 4.2 confirm the trends seen in Figure 4.8 and discussed previously. The 0.000 values when comparing X data to any other data set indicates a greater than 99.9 per cent chance that the mean mass loss (and by extension, degree of hydration) is different in stressed samples than in unstressed controls. The beam specimen sets of data most likely to be different are the NA data compared to HT data, with an approximate 16 per cent chance the neutral axis data is the same as that at either of the stressed faces. This further implies that there is an 84 per cent probability that the degree of hydration within the neutral axis region is higher (based on the figure) than that of the high tension and high compression regions.

Further consideration of the table also reveals that the two data sets most likely to be the same are the LT and HC data with a greater than 95 per cent likelihood. If the effects of stress were independent of stress direction, it would be expected that the HT and HC data sets would be most similar. The actual results may indicate that there is a difference between hydration rates in tensile regions than in compressive regions.

400 to 500 °C Range

Between approximately 400 °C and 500 °C, mass losses in a dry cement paste sample can be attributed to a degradation of calcium hydroxide and the release of water vapor (Pane and Hansen 2005; Ukrainczyk et al. 2006). Though other TGA studies of cements have used correction factors applied to this mass loss to compute calcium hydroxide content (Marsh and Day 1988), Pane and Hansen as well as Midgley show that the factors have an insignificant effect (Midgley 1979). As can be seen in Figure 4.2, the loss is generally a steep slope approximately halfway between the temperature limits. Because the losses are all attributed to a single product, the percentage of calcium hydroxide in the paste can be estimated directly by multiplying the ratio of mass loss by the difference in molecular weights of the calcium hydroxide and water, 74.09/18.01 (Kar et al. 2012). It should be noted that in the literature, the temperature limits for CH degradation vary and the 400 to 500 °C range was chosen based on consideration of the literature and examination of the data in the current research. The resulting calculation of percentage calcium hydroxide is presented in Figure 4.9. The mass percentage shown in the figure is generally consistent with that seen in the referenced studies by others.

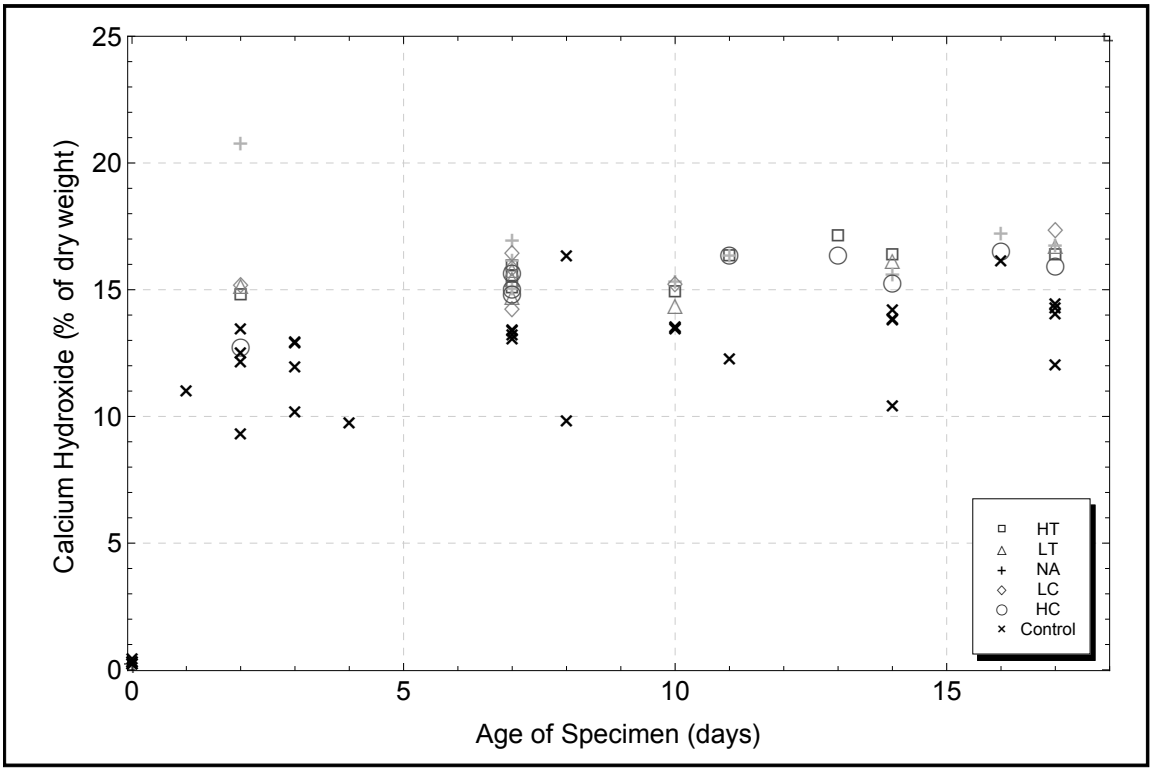

Figure 4.9 – Percentage calcium hydroxide in cement paste samples determined from TGA analysis. Stress conditions, as shown in the legend, correspond to "High Tension", "Low Tension", "Neutral Axis", "Low Compression", and "High Compression". Results generally indicate that stress conditions result in higher mass percentage of calcium hydroxide than that seen in unstressed control specimens.

Figure 4.10 presents the results of the curve fit discussed above as applied to the mass loss in this temperature range for unstressed specimens. The fit parameters for the degree of hydration were a=0.3714, b=0, and c=0.1152. The ratio of cement grain mass loss in this temperature range was calculated to be 0.000683 and the ratio of hydration products lost was 0.0727. The R^2 for the fit curve was 0.9866. The curve is similar to that seen for the previous temperature range, though the development of the hydration products appears to occur much more quickly at earlier ages and slow down with time more quickly than did the products considered in the lower temperature range. Figure 4.11 presents the results for stressed samples normalized to the unstressed baseline.

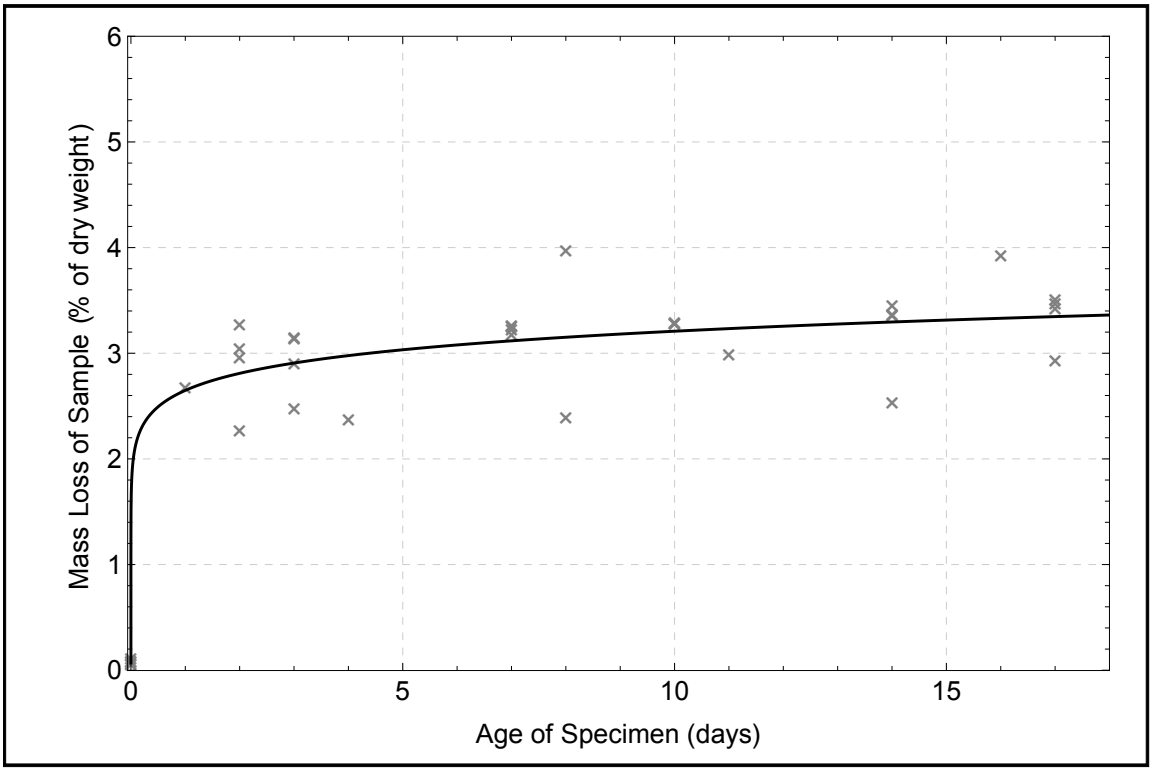

Figure 4.10 – Curve fit of percentage mass loss vs. time for the 400 to 500 °C range for samples not previously loaded. The form of the curve equation is based on an unknown mass fraction of hydration products and a different fraction of cement grains being lost during the heating with both fractions remaining constant throughout the age of the specimens. Thus, the only time-dependency is that of the underlying hydration curve.

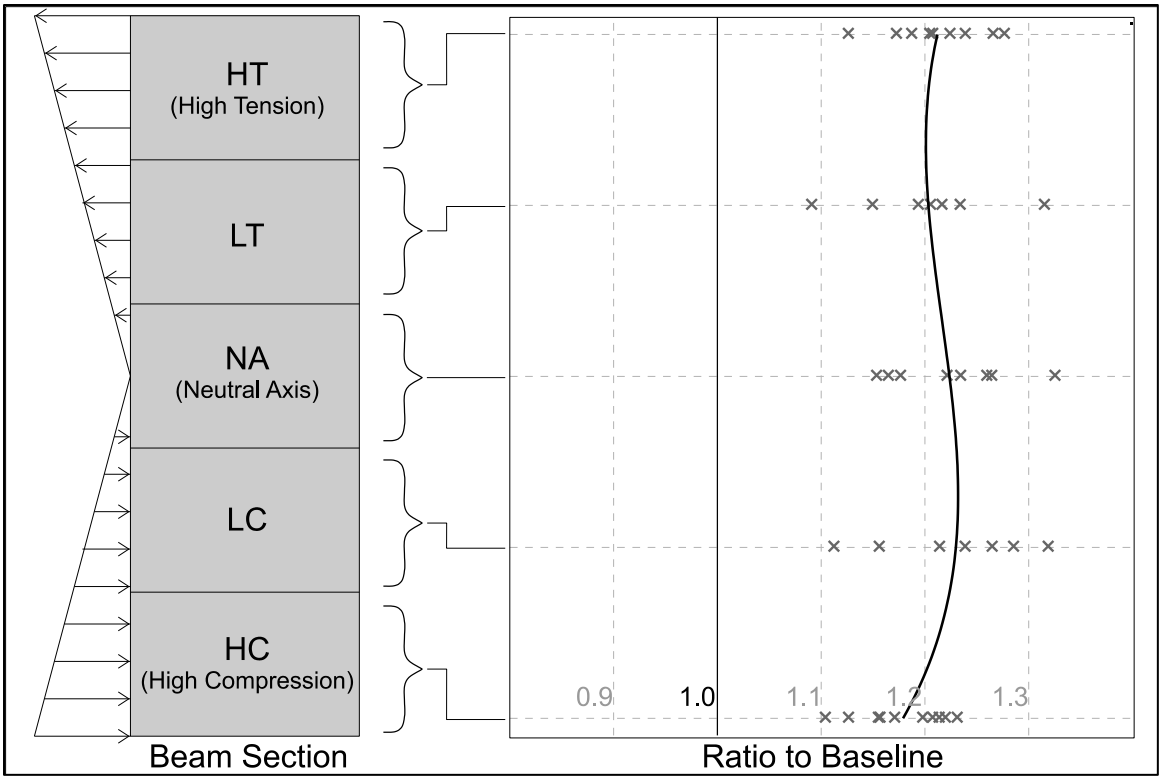

Figure 4.11 – Ratio of percentage mass loss for stressed samples to the fit curve of those not previously loaded for the 400 to 500 °C range. Using the resulting ratios for each of the five stress conditions, a cubic trend curve was fit to the data indicating that not only does stress increase the mass loss, but also there is a potential difference in loss between samples taken from the compressive face and those from other stress regions.

As was done with the results in the 110 to 400 °C range, the data for this temperature range were subjected to two-sample t-tests. The results are presented in Table 4.3.

Table 4.3 – Results of t-tests for the 400 to 500 °C TGA results

Stress	HC[1]	LC	NA	LT	HT	X
Sample mean	1.179	1.228	1.226	1.202	1.212	1.000
Sample std. dev.	0.0425	0.0728	0.0586	0.0698	0.0468	0.1191
n	10	7	8	7	9	29
HC		0.149[2]	0.083	0.468	0.127	0.000
LC	Same[3]		0.952	0.501	0.632	0.000
NA	Same	Same		0.483	0.611	0.000
LT	Same	Same	Same		0.732	0.000
HT	Same	Same	Same	Same		0.000
X	Different	Different	Different	Different	Different	

[1]Stress conditions are: X – control specimens, HT and HC – high tension and high compression, LT and LC – low tension and compression, NA – neutral axis
[2]Values in the upper right portion of the table indicate the level of significance at which the two sample means can be considered different, corresponding to a probability that the two means are the same.
[3]Text in the lower left portion of the table indicates the results at a 0.05 level of significance.

The results in Table 4.3 show similar trends as those presented previously. There is a nearly 100 per cent likelihood that the content of hydration products is different in beam specimens than in unstressed control samples. The sets of data most likely to be different are the NA data compared to the HC data, with an approximate 8 per cent chance the neutral axis data is the same as that at the compressive face. And, as seen in the previous temperature range, the data sets most likely to be the same are NA and LC with a 95 per cent chance.

Where the results differ from the previous temperature range is interesting. The left portion of the trend curve in Figure 4.11 shows a downward trend at the HC data, confirmed through the t-tests to indicate a high likelihood (greater than 85 per cent) that the HC data is different than HT and LC data sets. This further reinforces the possibility that hydration rates and/or the rates at which hydration products are dissolved due to stress are different in compressive regions than they are in tensile regions.

500 to 900 °C Range

Between approximately 500 and 900 °C, mass losses in a dry cement paste sample can be attributed to a degradation of calcium carbonate and the release of carbon dioxide. As can be seen in Figure 4.2, the loss is generally a steep slope at

approximately 700 °C, preceded by a slowly increasing slope. As with the previous temperature interval, because the losses are all attributed to a single product, the percentage of calcium carbonate in the paste can be estimated directly by multiplying the ratio of mass loss by the difference in molecular weights of the calcium carbonate and carbon dioxide, 100.09/44. The resulting calculation of percentage calcium carbonate is presented in Figure 4.12. It should be noted that although the mass loss is generally attributed to calcium carbonate, for the current testing protocol, using sealed specimens, it is unlikely that the material could form to the mass percentages presented. It is therefore likely that other hydration products are also losing mass in this temperature range.

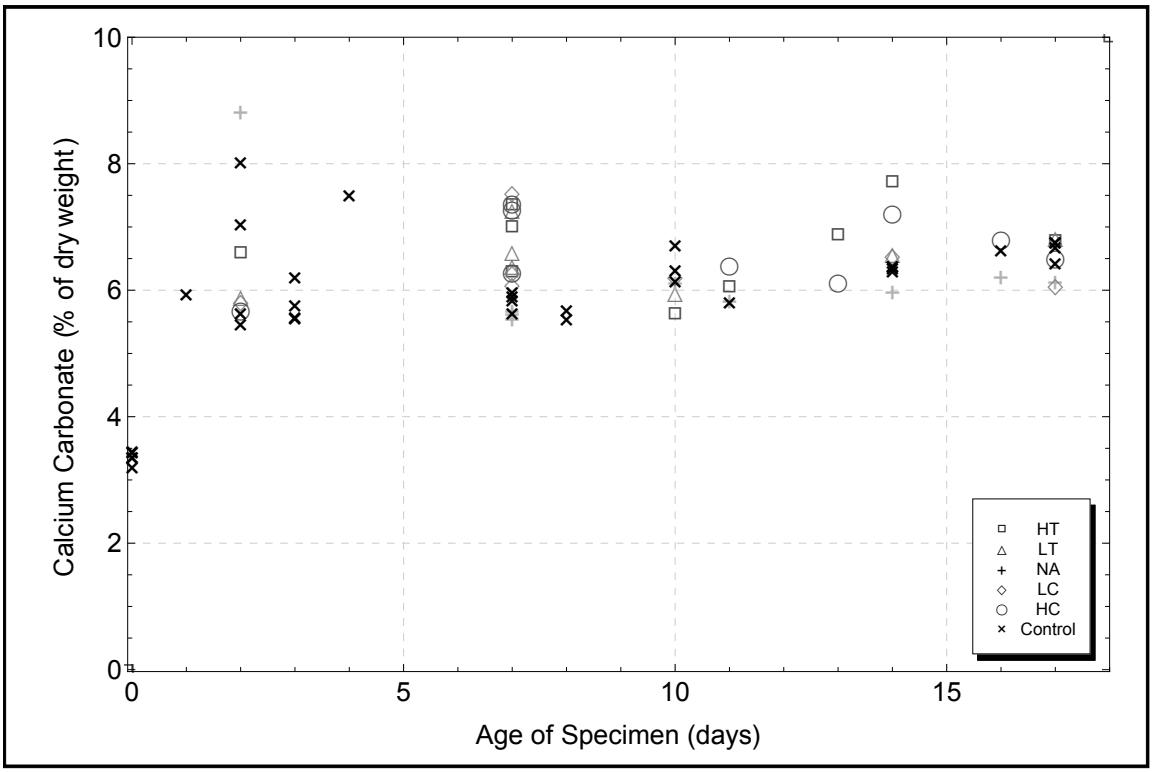

Figure 4.12 – Percentage calcium carbonate in cement paste samples determined from TGA analysis. Stress conditions, as shown in the legend, correspond to "High Tension", "Low Tension", "Neutral Axis", "Low Compression", and "High Compression". Results generally indicate that stress conditions result in a slightly higher mass percentage of calcium carbonate than that seen in unstressed control specimens.

Figure 4.13 presents the results of the curve fit discussed above as applied to the mass loss in this temperature range for unstressed specimens. The fit parameters for the degree of hydration were a=0.5163, b=0, and c=0.0506. The ratio of

cement grain mass loss in this temperature range was calculated to be 0.01470 and the ratio of hydration products lost was 0.04065. The R^2 for the fit curve was 0.9912. The curve is similar to that seen for the previous temperature range, though the development of the hydration products appears to occur even more quickly at earlier ages and slow down with time to an almost constant value within 14 days. In fact, the calculated degree of hydration is approximately 36.8 per cent after 0.1 days and approximately 44.6 per cent after 14 days. Because the curve is based on the assumed formation and degradation of calcium carbonate, it is likely that it does not represent a true hydration curve. Rather, the shape of the curve suggests early carbonation due to reactions with entrapped air with no further reaction due to the samples being sealed throughout curing and aging. Though the curve is not a typical shape, it does accurately represent the data and can therefore be used as a baseline. Figure 4.14 presents the results for stressed samples normalized to the unstressed baseline. Results of the t-tests are given in Table 4.4.

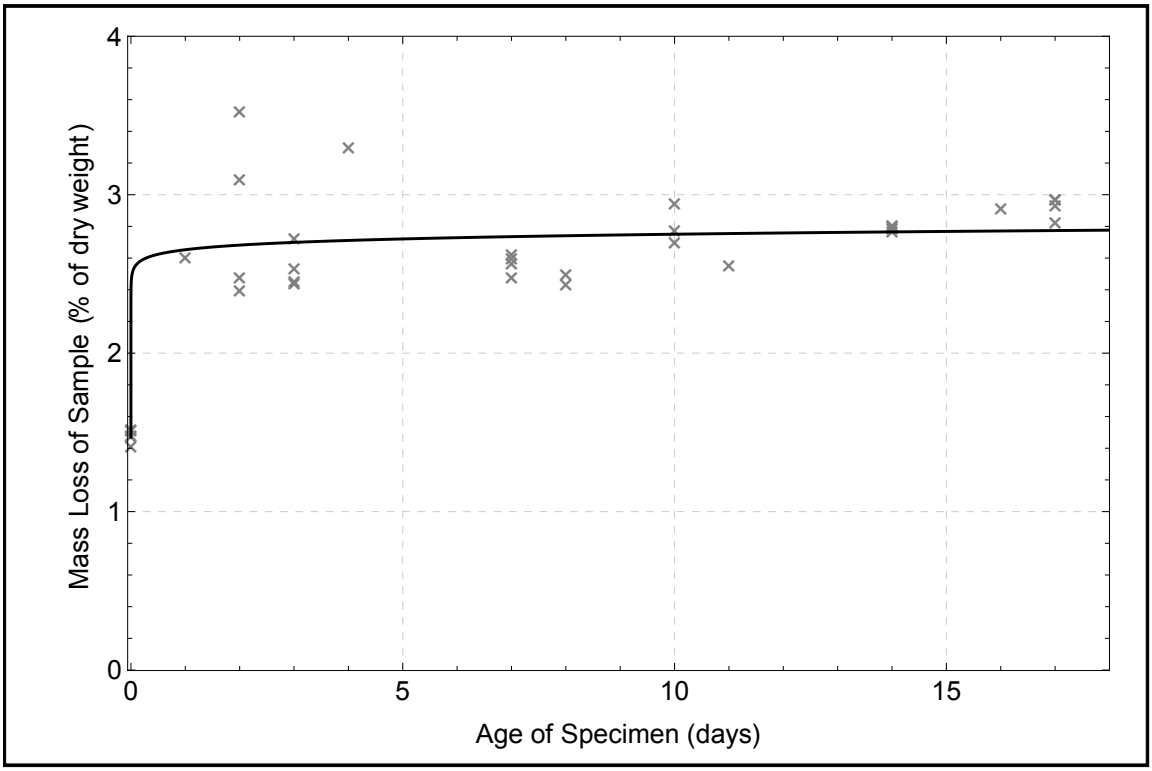

Figure 4.13 – Curve fit of percentage mass loss vs. time for the 500 to 900 °C range for samples not previously loaded. The form of the curve equation is based on an unknown mass fraction of hydration products and a different fraction of cement grains being lost during the heating with both fractions remaining constant throughout the age of the specimens. Thus, the only time-dependency is that of the underlying hydration curve.

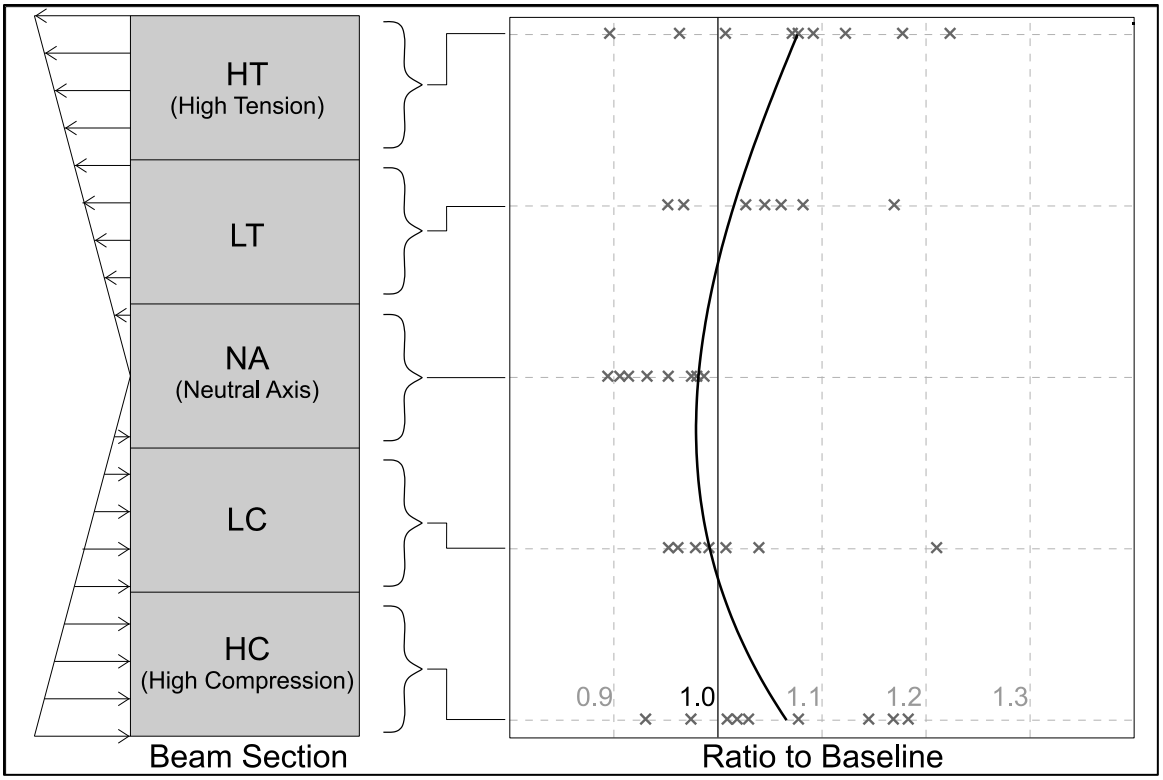

Figure 4.14 – Ratio of percentage mass loss for stressed samples to the fit curve of those not previously loaded for the 500 to 900 °C range. Using the resulting ratios for each of the five stress conditions, a cubic trend curve was fit to the data indicating that stress tends to increase the mass loss at the highest stressed regions while samples taken at or near the neutral axis show similar mass loss as that of control specimens.

Table 4.4 – Results of t-tests for the 500 to 900 °C TGA results

Stress	HC[1]	LC	NA	LT	HT	X
Sample mean	1.060	1.021	0.943	1.044	1.071	1.000
Sample std. dev.	0.0893	0.0887	0.0360	0.0732	0.1024	0.0989
n	10	7	8	7	9	29
HC		0.396[2]	0.005	0.695	0.820	0.106
LC	Same[3]		0.067	0.607	0.317	0.595
NA	Different	Same		0.011	0.006	0.017
LT	Same	Same	Different		0.553	0.211
HT	Same	Same	Different	Same		0.093
X	Same	Same	Different	Same	Same	

[1]Stress conditions are: X – control specimens, HT and HC – high tension and high compression, LT and LC – low tension and compression, NA – neutral axis
[2]Values in the upper right portion of the table indicate the level of significance at which the two sample means can be considered different, corresponding to a probability that the two means are the same.
[3]Text in the lower left portion of the table indicates the results at a 0.05 level of significance.

The trends for mass loss ratio seen within the 500 to 900 °C range are significantly different than those seen in lower temperature bands. The trend curve in Figure 4.14 indicates what might normally be expected if it is assumed that stresses accelerate hydration but cause no other changes in behavior, the neutral axis values are nearly equal to those of unstressed samples and the mass loss increases with stress in both directions. Further, in looking at the values in Table 4.4, the NA data cannot be considered the same as any data set other than LC at the 0.05 level of significance. When compared to the X data, it is seen that the neutral axis has a slightly lower mean than the unstressed samples.

When considering all three temperature ranges and the hydration products assumed to be present based on mass loss data, it seems that though stresses cause acceleration of hydration, other mechanisms are likely occurring for some, but not all, of the hydration products. Specifically, the differences in trend curves may indicate that calcium hydroxide is more readily dissolved by stress than is calcium carbonate, resulting in the opposite signs in the concavity of the two trend curves.

900 to 1000 °C Range

Between approximately 900 and 1000 °C, mass losses in a dry cement paste sample can be attributed to crystallization of the C-S-H gel, primarily to alite and belite (Stepkowska et al. 2005). As can be seen in Figure 4.2, the loss is generally very small with a nearly flat slope once the carbon dioxide release is complete in the previous temperature range. As seen in Figure 4.6, the loss does appear to be a function of time and therefore, though small, the loss ratio in this uppermost temperature range was subjected to the same curve fitting and analysis as were the previous ranges. Results are presented in Figure 4.15, Figure 4.16, and Table 4.5. The fit parameters for the degree of hydration were a=0.4813, b=0.00131, and c=0.4474. The ratio of cement grain mass loss in this temperature range was calculated to be 0.000426 and the ratio of hydration products lost was 0.00194. The R^2 for the fit curve was 0.9780.

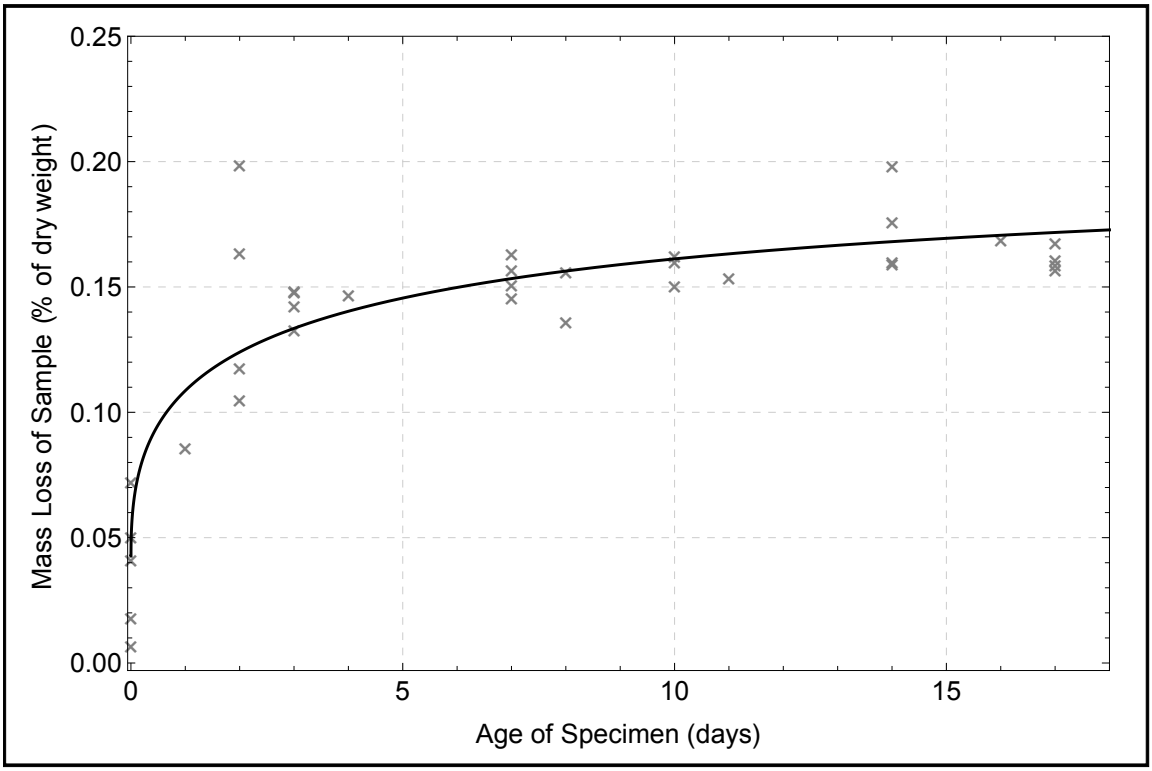

Figure 4.15 – Curve fit of percentage mass loss vs. time for the 900 to 1000 °C range for samples not previously loaded. The form of the curve equation is based on an unknown mass fraction of hydration products and a different fraction of cement grains being lost during the heating with both fractions remaining constant throughout the age of the specimens. Thus, the only time-dependency is that of the underlying hydration curve.

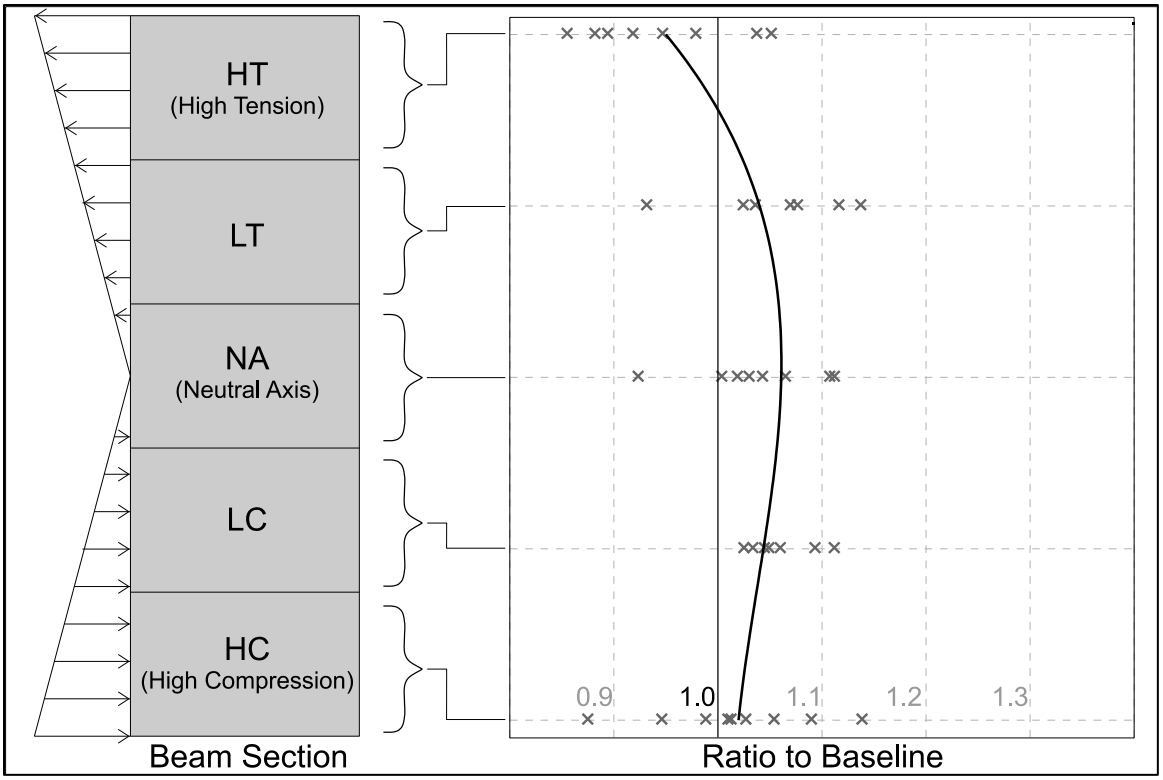

Figure 4.16 – Ratio of percentage mass loss for stressed samples to the fit curve of those not previously loaded for the 900 to 1000 °C range. Using the resulting ratios for each of the five stress conditions, a cubic trend curve was fit to the data indicating that not only does stress tend to increase the mass loss, but also there is a potential difference in loss between samples taken from the tensile face and those from all other stress regions.

Table 4.5 – Results of t-tests for the 900 to 1000 °C TGA results

Stress	HC[1]	LC	NA	LT	HT	X
Sample mean	1.034	1.061	1.039	1.057	0.946	1.011
Sample std. dev.	0.0602	0.0318	0.0607	0.0680	0.0720	0.1523
n	8	7	8	7	8	29
HC		0.306[2]	0.881	0.509	0.020	0.522
LC	Same[3]		0.397	0.900	0.003	0.118
NA	Same	Same		0.599	0.016	0.444
LT	Same	Same	Same		0.010	0.245
HT	Different	Different	Different	Different		0.101
X	Same	Same	Same	Same	Same	

[1]Stress conditions are: X – control specimens, HT and HC – high tension and high compression, LT and LC – low tension and compression, NA – neutral axis
[2]Values in the upper right portion of the table indicate the level of significance at which the two sample means can be considered different, corresponding to a probability that the two means are the same.
[3]Text in the lower left portion of the table indicates the results at a 0.05 level of significance.

Based on the t-test results and the shape of the trend curve, stress condition generally has very little effect on the mass loss in the 900 to 1000 °C range. The

one exception is in the high tension region. The trend curve has a sharp downward dip at the HT end of the data with the data set having a significantly lower mean than for any other region. The reasons for the difference seen between the HT data and all other data sets are unknown but the results do imply that chemical composition in the tensile region is significantly different than in the compression region.

4.2 X-Ray Diffraction

X-ray diffraction ("XRD") is a method of identifying the chemical composition of a material, or mix of materials, by measuring the crystallinity of the sample. As shown in Figure 4.17, for a particular crystalline structure with atomic spacing, d, a predictable portion of an incoming X-ray beam is reflected toward a collector, depending upon the angle of incidence, θ. For a powder sample where it is assumed that the crystalline structure is randomly oriented in all three directions, if the angle of incidence is varied, the intensity of the X-ray beam received at the collector will have maxima at various discrete angles which are functions of the three-dimensional structure of the crystal. For a mixed sample, such as a crushed cement paste sample, the locations and intensities of the various spikes can be compared to known patterns of individual components to determine the relative proportions of the crystalline components of the sample.

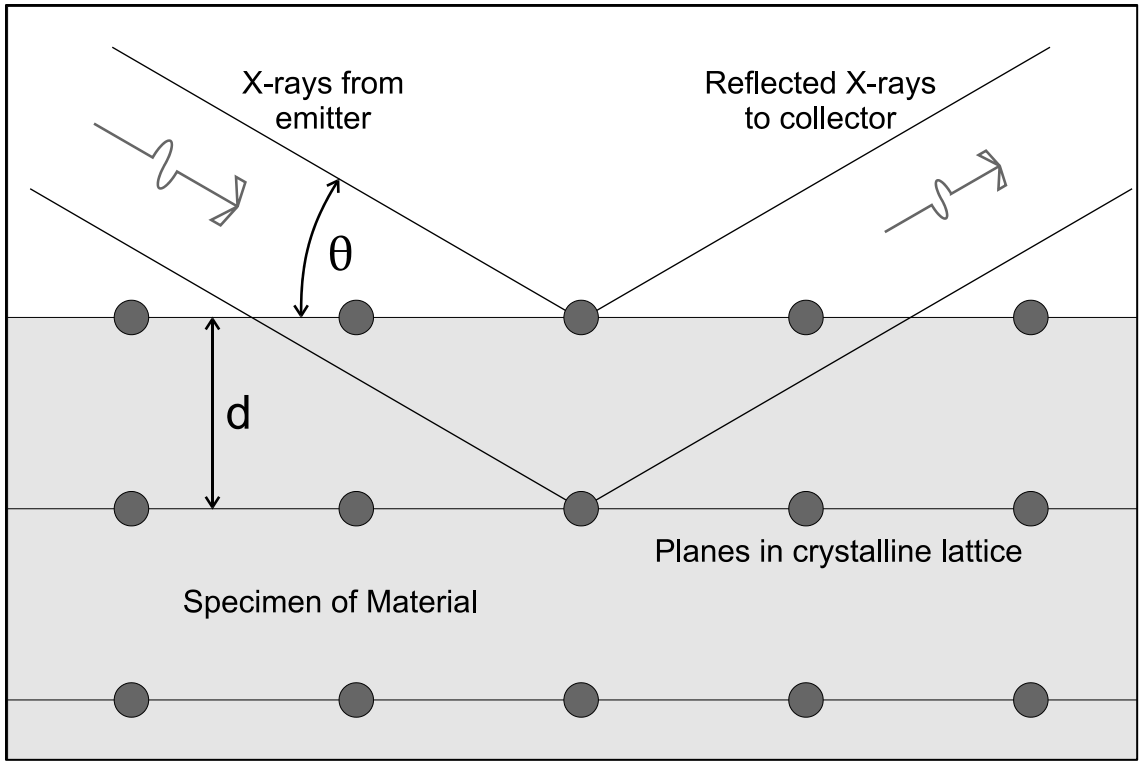

Figure 4.17 – Principles of X-ray diffraction showing the reflection of incident X-rays as a function of crystalline plane orientation and spacing. Knowing the intensity of the incoming X-ray beam and measuring the intensity collected after diffraction, the crystalline plane spacing can be determined. Using reference data, the obtained spacing can be identified as belonging to a particular element or compound.

4.2.1 Methodology

Crushed samples prepared for TGA analysis, as described in Section 4.1.1, were used to create XRD specimens. The powder was compacted into a stainless steel specimen holder and mounted into the PANalytical X'Pert Powder cabinet diffractometer. Using an angle range, 2θ, of 20 to 70°, a step size of 0.1°, and a time at each angle of 5 s, each sample was analyzed and data collected to a file for later analysis.

4.2.2 Results

A sample of the raw data collected from the XRD system is presented in Figure 4.18 with raw data for all samples presented in Appendix C.1.

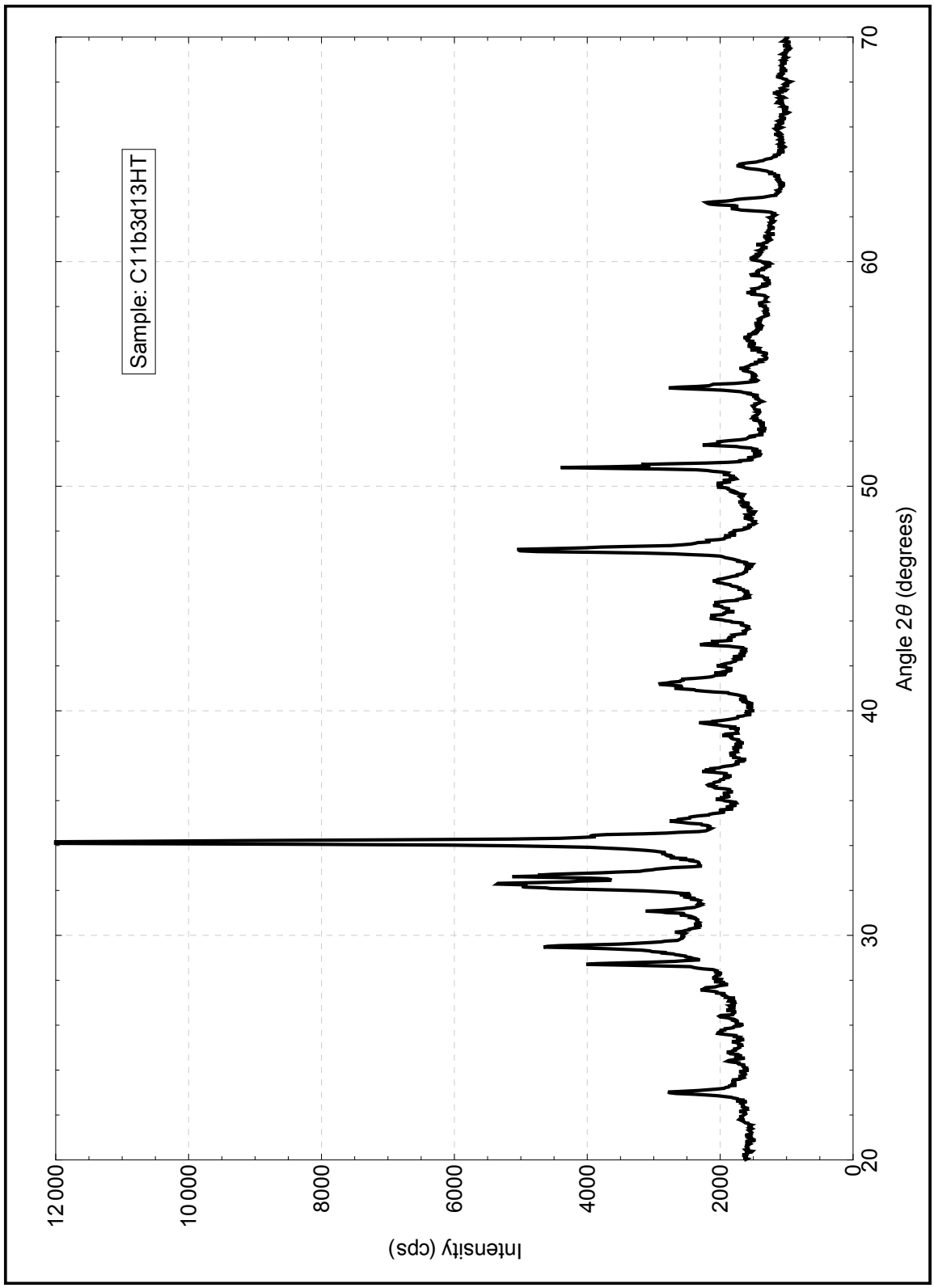

Figure 4.18 – Sample raw data XRD curve showing intensity of reflected X-rays for angle rotations, 2θ, between 20 and 70°. Intensity peak locations indicate angles at which X-rays are reflected with relatively high intensity and can be correlated to known crystalline structures.

As can be seen in Figure 4.18, there are a number of peaks in the collected signal, corresponding to angles at which the X-rays were most efficiently reflected to the collector based on the various crystalline structures present in the sample. Though the consideration of peak locations for an unknown sample can be helpful, e.g., the pattern of locations of peaks for calcium hydroxide is different than the pattern for calcium carbonate, working solely with the raw data is tedious and imprecise. Therefore, the various results were used as input for PANalytical's HighScore Plus software (PANalytical 2006). The software relies on a library of expected signals taken from past testing of single-component samples. For purposes of the current research, the library used was limited to fifteen potentially expected components, as listed in Table 4.6 with the crystalline geometry for each obtained from the Crystallography Open Database (Downs and Hall-Wallace 2003; Grazulis et al. 2009; Grazulis et al. 2012). After inserting the geometry of each of the fifteen components, a semi-automatic Rietveld analysis was used to determine relative proportions of each component. The refinement was performed in steps with each step limited to refining the geometry of the one component most present but not yet refined in previous steps. As part of the analysis, the background, attributable in part to non-crystalline structures present in the sample, was removed automatically. The results for the obtained proportions of the six un-hydrated products are presented in Table 4.7 and for the nine hydration products in Table 4.8.

Table 4.6 – List of cementitious components used for analysis of XRD data

Name	CCN[1]	Variation	Formula
Alite	C_3S	T-1	Ca_3SiO_5
Belite	C_2S	β	Ca_2SiO_4
		γ	
Aluminate	C_3A		$Ca_3(AlO_3)_2$
Ferrite	C_4AF	0.285	$4CaO•Al_2O_3•Fe_2O_3$
		0.36	
Calcium hydroxide	CH		$Ca(OH)_2$
Calcite	$C\overline{C}$		$CaCO_3$
Aragonite	$C\overline{C}$		
Gypsum	$C\overline{S}H_2$	Hydrous	$CaSO_4•2H_2O$
	$C\overline{S}H_{0.5}$	Hemi-hydrate	$CaSO_4•0.5H_2O$
	AFm		$3CaO•Al_2O_3•CaCO_3•11H_2O$
Ettringite	AFt		$Ca_6Al_2(SO_4)_3(OH)_{12}•26H_2O$
Thaumasite	AFt		$Ca_3Si(OH)_6(CO_3)(SO_4)•12H_2O$
Hydrogarnet	C_3AH_6		$3CaO•Al_2O_3•6H_2O$

[1]Cement chemistry notation

Table 4.7 – Volume percentage of un-hydrated products using XRD

Age of Specimen (days)	Stress[1] Condition	C_3S[2]	$C_2S\beta$	$C_2S\gamma$	C_3A	$C_4AF_{0.285}$	$C_4AF_{0.36}$
0	All	62.05	0.00	11.97	1.86	0.00	12.61
0	All	53.04	4.32	1.18	6.53	8.56	7.47
0	All	50.99	8.29	0.00	10.85	8.59	7.41
0	All	56.55	7.06	0.00	2.37	11.15	8.44
0	All	47.97	3.72	5.80	12.94	1.73	11.53
0	All	53.49	4.25	3.65	11.06	12.44	2.14
1	X	24.66	5.70	16.72	2.43	17.77	11.15
2	X	30.75	0.02	9.17	6.13	15.79	8.01
2	X	29.72	0.00	19.37	11.29	24.43	0.00
2	X	26.32	0.00	21.25	10.90	24.57	0.00
2	X	22.79	1.09	12.79	3.57	11.89	11.09
2	X	23.64	4.83	6.64	4.19	12.60	7.32
2	X	21.12	4.67	7.72	10.19	17.43	0.40
3	X	25.92	12.17	0.00	9.92	9.74	11.54
3	X	25.10	16.49	4.32	15.08	17.60	2.33
3	X	22.58	13.69	4.83	12.66	15.85	8.32
4	X	29.31	7.73	0.50	8.01	12.44	9.97
7	X	26.14	7.20	10.47	7.22	19.47	0.25
7	X	23.83	23.45	0.00	0.47	28.38	0.00
7	X	29.73	28.59	0.00	0.30	31.87	0.95
7	X	19.92	1.62	17.58	5.70	10.84	7.43
7	X	26.52	12.39	4.49	0.00	10.88	7.08
8	X	26.02	2.66	5.30	2.31	12.62	7.49
10	X	29.39	9.97	0.00	5.68	6.21	14.03
10	X	21.78	15.47	0.37	10.84	8.40	8.44
10	X	18.85	3.70	5.11	7.89	6.77	8.33
10	X	20.10	4.42	13.58	11.98	7.79	7.66
11	X	24.59	4.87	5.26	2.55	12.58	8.52
14	X	28.48	2.11	11.67	2.66	11.32	8.18
14	X	18.87	10.26	0.48	0.04	10.20	8.56
14	X	17.80	6.34	3.86	0.05	10.54	7.18
14	X	17.35	2.04	7.26	0.00	9.84	6.17
17	X	28.70	7.29	1.43	2.56	11.32	8.98
17	X	14.97	2.88	11.68	11.78	9.63	6.91
17	X	15.48	6.76	8.20	0.00	12.34	7.48
17	X	21.45	1.40	19.31	1.55	6.80	5.80
2	HT	21.78	2.92	10.83	15.39	10.63	8.84
7	HT	24.88	6.98	10.59	0.09	10.08	6.65
7	HT	23.62	9.37	10.77	3.74	8.08	8.76
7	HT	23.67	7.98	13.61	10.48	5.30	8.93
10	HT	17.70	4.42	9.44	4.68	8.65	8.90
11	HT	19.45	8.19	0.28	6.86	10.37	6.80

Age of Specimen (days)	Stress[1] Condition	C_3S[2]	$C_2S\beta$	$C_2S\gamma$	C_3A	$C_4AF_{0.285}$	$C_4AF_{0.36}$
13	HT	19.46	6.80	0.20	6.20	9.79	6.54
14	HT	20.39	0.00	16.55	0.00	10.00	6.18
16	HT	19.14	2.83	10.33	0.46	10.60	6.59
17	HT	18.50	5.18	5.80	3.63	9.23	6.41
2	LT	20.57	6.56	11.45	9.97	8.41	7.73
7	LT	19.94	8.96	7.24	11.38	6.04	7.45
7	LT	23.29	10.24	14.22	1.52	5.83	9.48
7	LT	23.53	6.50	17.47	9.64	12.48	6.95
10	LT	19.81	4.50	11.14	0.51	8.33	9.14
11	LT	16.39	4.40	7.97	11.82	9.78	7.60
14	LT	18.99	2.01	11.91	0.00	10.39	6.71
17	LT	18.76	6.89	5.33	4.66	7.78	6.10
2	NA	25.21	20.13	5.02	2.32	11.68	7.18
7	NA	20.70	8.47	11.81	3.27	4.32	8.88
7	NA	23.80	8.86	10.42	0.79	4.33	9.15
7	NA	25.24	7.43	16.90	1.84	6.06	8.88
10	NA	19.46	0.00	17.05	0.65	10.74	7.56
11	NA	17.65	7.37	0.55	11.95	9.95	6.97
14	NA	17.52	5.86	8.74	0.75	10.23	3.13
17	NA	18.75	3.48	10.71	0.33	10.59	7.22
2	LC	21.30	6.00	6.93	13.92	11.24	7.74
7	LC	20.84	6.91	11.97	5.08	2.07	10.67
7	LC	22.34	5.69	13.48	11.12	15.51	1.37
7	LC	22.84	1.99	18.20	1.39	8.77	9.12
10	LC	18.15	7.13	0.75	0.00	10.70	5.80
11	LC	16.79	6.37	3.61	6.52	9.10	9.43
14	LC	14.66	6.01	10.18	0.18	9.43	8.76
17	LC	16.61	9.74	0.85	13.52	7.71	6.86
2	HC	20.89	4.80	12.37	5.80	10.23	8.62
7	HC	17.89	3.62	5.42	0.61	9.84	7.91
7	HC	23.02	10.10	13.95	2.42	6.00	10.47
7	HC	21.15	5.86	14.93	4.65	12.34	7.44
10	HC	19.59	6.51	6.25	0.25	9.88	8.14
11	HC	20.69	4.19	0.52	0.54	12.54	9.69
14	HC	17.64	4.77	7.01	0.00	9.69	7.34
16	HC	15.58	7.13	3.10	17.35	9.14	5.88
17	HC	18.86	2.76	11.39	0.00	10.34	6.31

[1]Stress conditions are: X – control specimens, HT and HC – high tension and high compression, LT and LC – low tension and compression, NA – neutral axis

[2]Abbreviations given are CCN as defined in Table 4.6.

Table 4.8 – Volume percentage of hydration products using XRD

Age of Specimen (days)	Stress[1] Condition	CH[2]	$C\overline{C}_C$	$C\overline{C}_A$	$C\overline{S}H_2$	$C\overline{S}H_{0.5}$	AFm	AFt_E	AFt_T	C_3AH_6
0	All	0.00	3.26	0.00	1.10	4.01	0.30	1.23	1.36	0.24
0	All	0.57	0.00	0.00	4.06	0.93	10.21	2.51	0.07	0.55
0	All	2.36	4.18	0.00	1.11	1.18	1.75	1.59	1.15	0.54
0	All	1.54	5.36	0.00	1.48	2.78	0.00	2.61	0.00	0.66
0	All	1.10	2.12	0.00	3.92	4.11	0.00	3.28	1.32	0.46
0	All	1.61	4.56	0.00	1.54	2.57	0.12	1.29	0.20	1.07
1	X	2.39	7.89	0.00	10.29	0.00	0.00	1.01	0.00	0.00
2	X	7.73	3.23	0.00	7.50	7.85	1.24	2.51	0.00	0.08
2	X	1.68	3.33	0.00	6.92	0.13	0.00	2.38	0.00	0.76
2	X	1.64	3.39	0.00	8.48	0.20	0.24	2.93	0.00	0.10
2	X	12.20	2.51	0.00	11.75	9.67	0.00	0.66	0.00	0.00
2	X	11.98	3.65	0.00	12.67	9.26	0.00	2.46	0.00	0.77
2	X	11.93	3.49	0.00	11.28	8.30	0.00	2.72	0.00	0.75
3	X	9.61	3.40	0.00	6.57	7.79	0.00	2.40	0.81	0.14
3	X	1.40	4.48	0.00	11.56	0.00	0.06	1.21	0.00	0.37
3	X	2.93	3.65	0.00	12.10	0.00	0.44	2.77	0.00	0.18
4	X	6.53	3.47	0.00	9.55	0.30	7.86	2.87	0.00	1.45
7	X	9.88	4.28	0.15	4.46	7.74	0.00	2.11	0.00	0.64
7	X	3.75	5.59	0.37	10.42	0.00	0.00	2.91	0.00	0.83
7	X	4.72	0.86	0.48	0.00	0.00	0.00	2.19	0.00	0.31
7	X	10.87	4.14	0.00	10.36	6.08	0.00	2.25	2.24	0.96
7	X	9.92	3.75	0.00	10.05	9.13	0.00	2.38	2.51	0.90
8	X	6.38	3.10	0.00	10.61	6.38	12.46	2.80	0.00	1.90
10	X	10.57	2.55	0.00	4.61	0.30	13.29	3.02	0.00	0.38
10	X	11.19	2.97	0.00	9.80	5.92	0.00	2.97	0.77	1.07
10	X	11.96	4.57	0.22	13.59	10.56	0.00	1.14	6.04	1.28
10	X	12.99	4.87	0.00	12.47	0.46	0.98	1.71	0.00	0.98
11	X	8.67	2.76	0.00	9.85	7.29	9.65	2.14	0.00	1.26
14	X	8.44	4.35	0.00	11.70	7.15	0.41	1.54	0.00	1.99
14	X	13.22	3.39	0.03	13.54	9.63	7.78	2.03	0.00	1.98
14	X	13.57	4.41	0.00	13.26	9.62	8.67	2.92	0.00	1.77
14	X	11.93	3.15	0.00	12.08	9.63	46.30	2.13	0.00	2.13
17	X	10.24	4.16	0.00	12.24	8.76	0.96	1.46	0.00	1.90
17	X	13.03	2.54	0.00	11.53	0.00	11.46	2.34	0.00	1.26
17	X	13.10	4.41	0.00	4.79	8.10	14.69	2.92	0.00	1.73
17	X	12.51	3.94	0.12	17.57	0.70	1.03	4.00	3.43	0.40
2	HT	10.75	4.78	0.00	12.15	0.32	0.01	1.24	0.00	0.36
7	HT	14.63	4.59	0.00	5.94	7.60	0.00	1.74	2.78	3.47
7	HT	14.38	4.99	0.00	11.38	0.74	1.28	2.41	0.00	0.49
7	HT	10.50	5.96	0.00	9.41	0.00	0.00	2.13	0.02	2.03

Age of Specimen (days)	Stress[1] Condition	CH[2]	$C\overline{C}_C$	$C\overline{C}_A$	$C\overline{S}H_2$	$C\overline{S}H_{0.5}$	AFm	AFt_E	AFt_T	C_3AH_6
10	HT	15.00	3.20	0.00	12.07	0.19	11.97	2.08	0.00	1.69
11	HT	14.94	2.08	0.00	11.73	0.43	14.63	2.52	0.00	1.71
13	HT	15.29	2.78	0.00	12.45	6.86	9.66	2.03	0.00	1.95
14	HT	14.45	3.82	0.00	13.80	10.46	0.30	2.01	0.00	2.03
16	HT	14.24	3.36	0.00	13.40	7.56	8.11	1.84	0.00	1.55
17	HT	14.98	3.42	0.05	12.45	6.95	8.91	2.63	0.00	1.85
2	LT	8.02	4.44	0.00	5.01	0.42	11.86	3.52	0.00	2.04
7	LT	12.31	2.87	0.00	9.19	0.11	10.95	1.90	0.00	1.66
7	LT	14.15	3.37	0.00	13.32	0.74	0.00	2.65	0.48	0.70
7	LT	13.32	3.43	0.00	3.41	0.23	0.00	2.15	0.66	0.22
10	LT	15.10	2.60	0.00	11.79	0.00	13.11	2.40	0.00	1.58
11	LT	15.01	2.70	0.00	10.51	0.00	10.86	1.67	0.00	1.27
14	LT	15.24	3.89	0.00	10.10	9.04	7.93	2.01	0.00	1.77
17	LT	15.15	3.38	0.00	10.50	6.61	10.59	2.19	0.00	2.06
2	NA	0.00	9.38	0.00	13.15	0.16	0.00	1.17	4.10	0.50
7	NA	12.80	2.86	0.00	10.97	0.05	11.09	2.76	0.00	2.01
7	NA	14.06	4.09	0.00	9.87	8.96	0.00	2.80	0.30	2.58
7	NA	13.69	4.78	0.00	11.52	0.23	0.00	2.43	0.19	0.81
10	NA	16.08	2.04	0.00	11.45	0.00	12.22	2.11	0.00	0.65
11	NA	14.43	3.21	0.13	10.81	7.68	5.44	2.10	0.00	1.76
14	NA	12.36	2.03	0.00	14.46	10.82	10.33	2.74	0.00	1.04
17	NA	15.96	2.92	0.00	12.94	0.28	12.78	2.27	0.00	1.76
2	LC	9.91	8.95	0.00	9.15	0.11	0.00	3.19	0.66	0.90
7	LC	14.49	2.83	0.22	10.45	0.00	9.84	2.88	0.00	1.77
7	LC	13.46	3.26	0.00	10.47	0.37	0.00	2.24	0.00	0.68
7	LC	12.77	4.69	0.00	13.12	0.46	0.40	3.12	0.45	2.67
10	LC	13.68	2.66	0.00	10.60	9.25	16.92	2.16	0.00	2.19
11	LC	13.84	1.57	0.00	11.57	0.32	17.69	2.45	0.00	0.73
14	LC	16.40	4.31	0.00	15.73	9.76	0.44	2.21	0.00	1.92
17	LC	15.15	2.31	0.00	11.14	0.00	12.09	2.39	0.00	1.63
2	HC	9.35	6.25	0.00	9.21	8.33	0.00	2.41	0.01	1.73
7	HC	13.33	1.84	0.00	11.67	7.48	16.29	2.09	0.00	2.02
7	HC	13.60	4.96	0.00	11.16	0.00	0.14	2.35	0.00	1.83
7	HC	12.68	3.71	0.00	12.51	0.30	0.20	2.89	0.39	0.95
10	HC	16.41	1.01	0.00	12.64	0.21	14.74	2.42	0.00	1.95
11	HC	11.80	4.37	0.42	13.00	9.06	10.04	1.48	0.00	1.64
14	HC	13.16	3.54	0.03	11.81	8.16	12.54	2.37	0.00	1.93
16	HC	10.84	2.31	0.00	7.42	8.50	9.65	1.46	0.00	1.64
17	HC	14.55	2.24	0.00	11.52	9.07	8.51	2.49	0.00	1.95

[1]Stress conditions are: X – control specimens, HT and HC – high tension and high compression, LT and LC – low tension and compression, NA – neutral axis

[2]Abbreviations given are CCN as defined in Table 4.6.

A cursory examination of the data presented in the tables above reveals significant variation in several of the constituents considered. However, for several others, data is relatively consistent and may indicate trends of importance. Two of the latter categories of constituents were subject to additional analysis: alite and calcium hydroxide. The mass percentages of these two components, as a function of age and stress condition, are presented in Figure 4.19 and Figure 4.20. Additionally, the total mass percentage of hydration products (the sum of values in the rows of Table 4.8) was computed with results, as a function of specimen age and stress condition, shown in Figure 4.21.

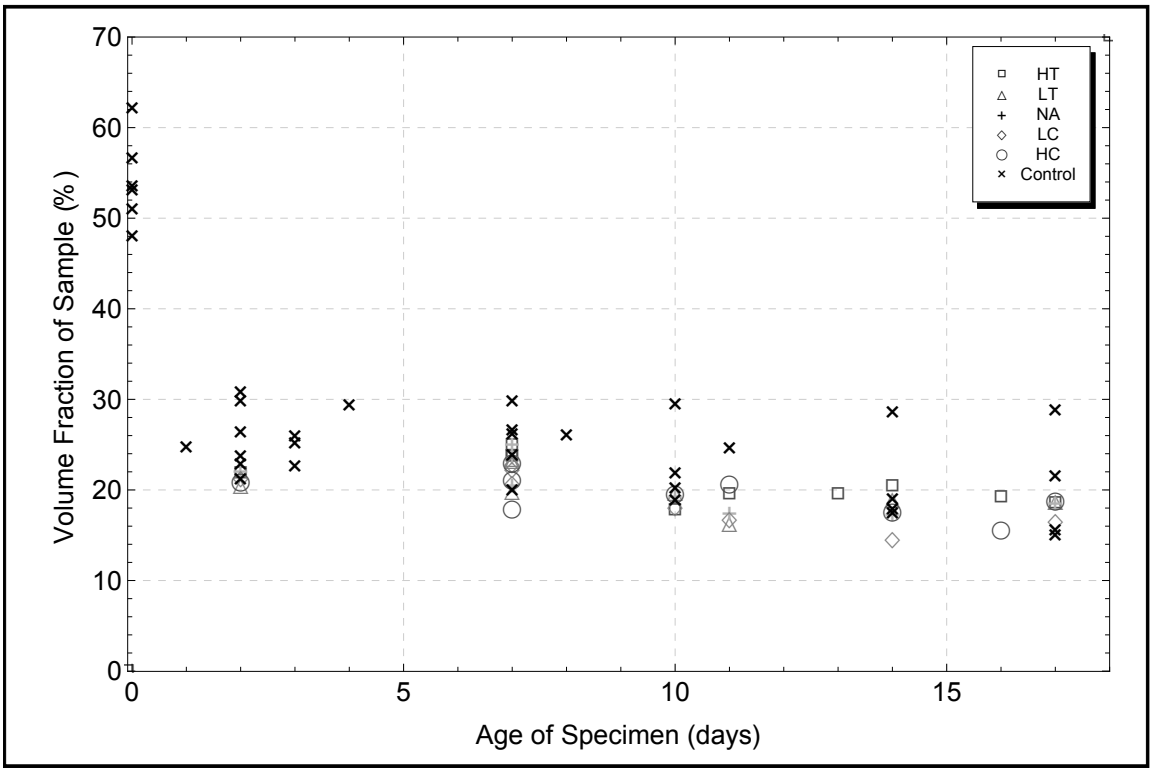

Figure 4.19 – Volume percentage of alite versus specimen age for powder specimens from tested beams and specimens not previously loaded. Stress conditions, as listed in the legend, are "High Tension", "Low Tension", "Neutral Axis", "Low Compression", and "High Compression". Results generally indicate that stress results in a lower volume fraction of alite as compared to the fraction in unstressed control specimens.

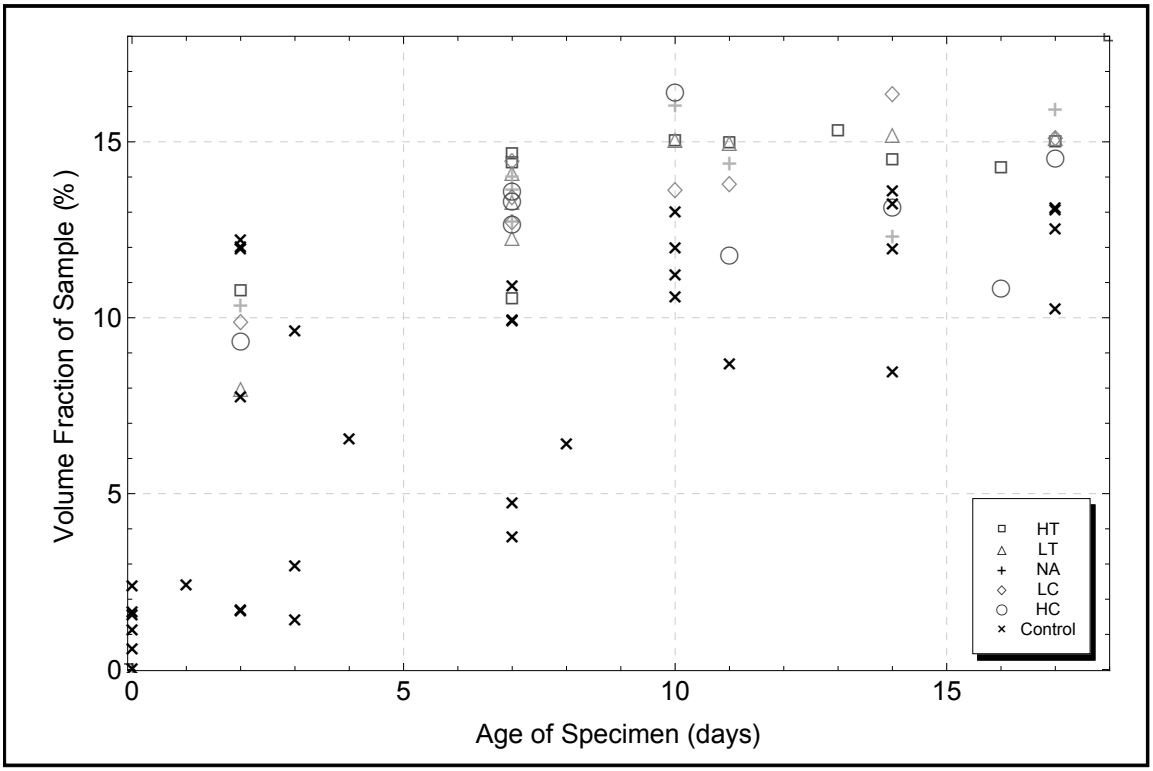

Figure 4.20 – Volume percentage of calcium hydroxide versus specimen age for powder specimens from tested beams and specimens not previously loaded. Stress conditions, as listed in the legend, are "High Tension", "Low Tension", "Neutral Axis", "Low Compression", and "High Compression". Results generally indicate that stress results in a higher volume fraction of calcium hydroxide as compared to the fraction in unstressed control specimens.

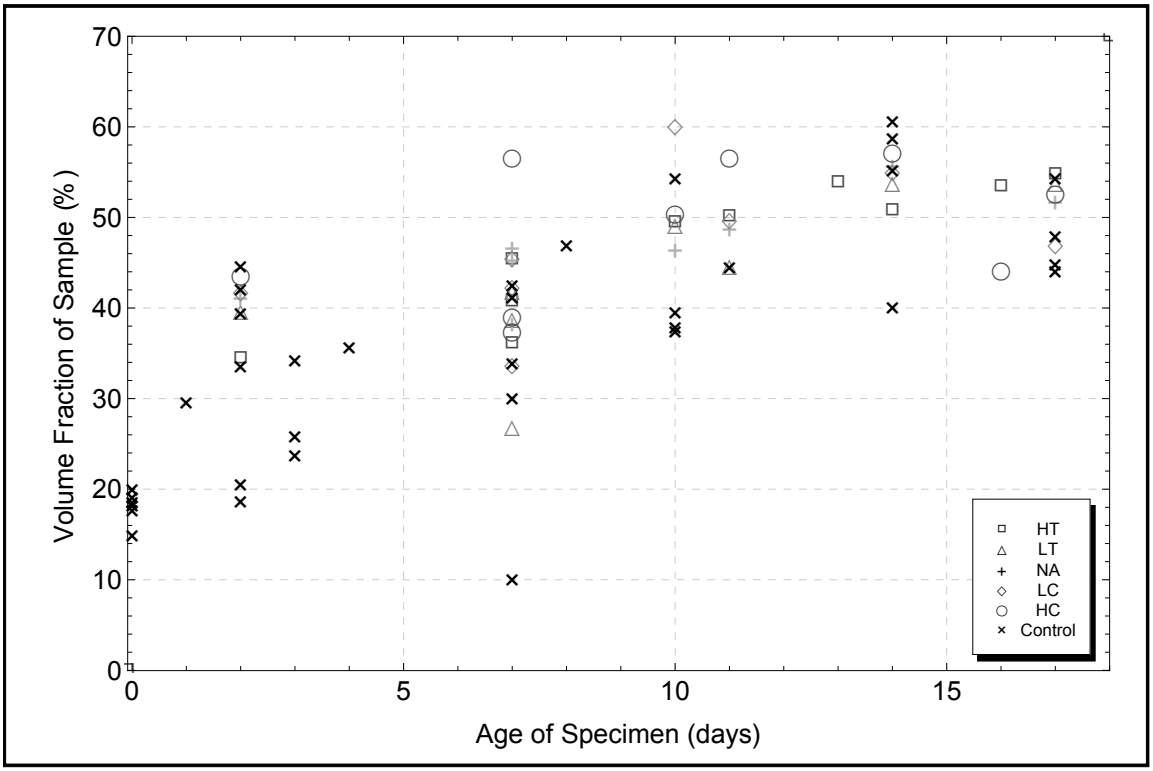

Figure 4.21 – Total volume percentage of hydration products versus specimen age for powder specimens from tested beams and specimens not previously loaded. Stress conditions, as listed in the legend, are "High Tension", "Low Tension", "Neutral Axis", "Low Compression", and "High Compression". Results generally indicate that stress results in a higher volume fraction of hydration products as compared to the fraction in unstressed control specimens.

4.2.3 Analysis

The results for alite, calcium hydroxide, and total hydration products were subject to an analysis similar to that used with TGA results as presented in Section 4.1.3. Because XRD calculates volume ratios rather than mass ratios, Equations (2.4) and (2.6) were used. As noted in Section 2.1, because XRD does not calculate the portion of amorphous solids, such as C-S-H, the volume ratio will be somewhat over-predicted by the method. If it is assumed that alite is a constant fraction of the total cement grain volume, the equation of the volume ratio of alite becomes

$$vr_{alite} = \frac{r_c \frac{m_{ci}}{\gamma_c}[1-\alpha(t)]}{m_{ci}\left(\frac{1}{\gamma_c}+0.197\alpha(t)\right)}, \tag{4.2}$$

where r_c is the fraction of cement grains that is alite, m_{ci} is the initial mass percentage of cement grains, γ_c is the assumed specific gravity of cement, and $\alpha(t)$ is the degree of hydration. The results are presented in Figure 4.22. As with the results of TGA, results from stress samples were divided by the unstressed baseline with the result of this calculation presented in Figure 4.23. Similar figures showing the ratio comparisons for all products considered as part of XRD testing appear in Appendix C.3. The results of t-tests comparing the data sets of each stress condition for the alite samples are given in Table 4.9.

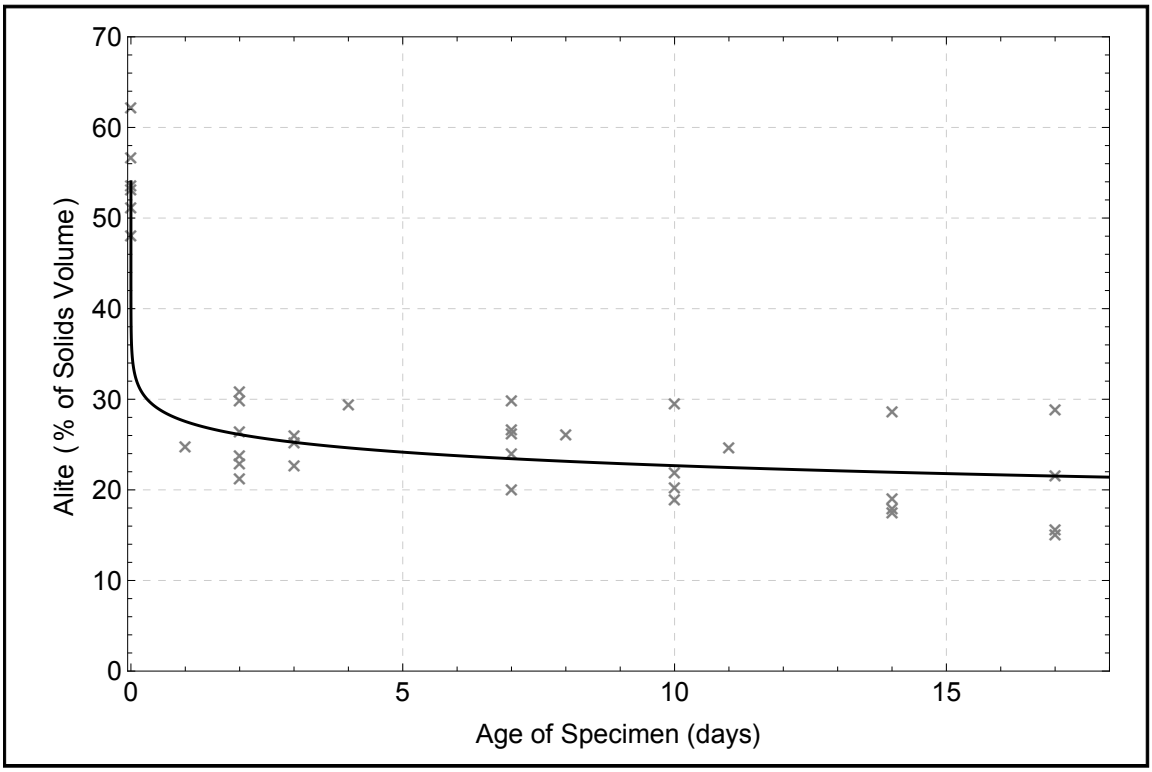

Figure 4.22 – Curve fit of percentage alite vs. time for samples not previously loaded. The form of the curve equation is based on an unknown volume fraction of cement grains being alite and only components of cement grains being lost during hydration in accordance with the hydration curve.

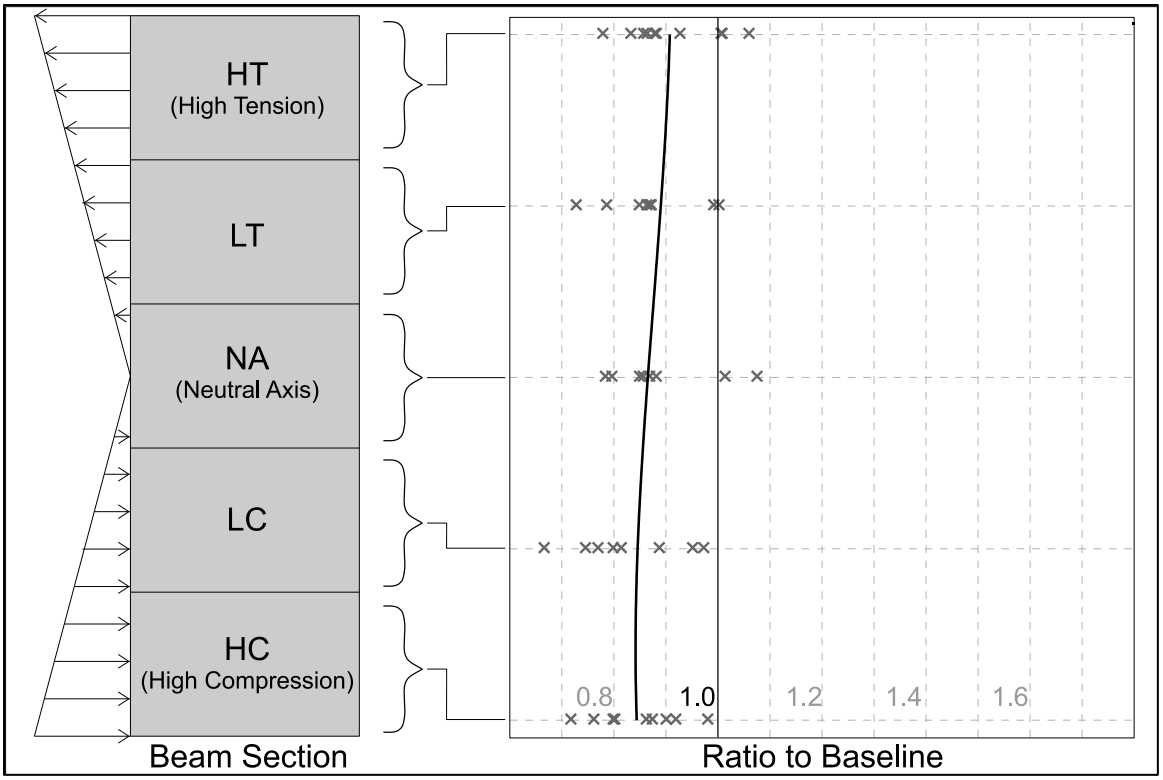

Figure 4.23 – Ratio of percentage alite for stressed samples to the fit curve of those not previously loaded, as determined by XRD. Using the resulting ratios for each of the five stress conditions, a cubic trend curve was fit to the data indicating that stress tends to cause lower volume percentages of alite versus that of unstressed control specimens.

Table 4.9 – Results of t-tests for alite percentage using XRD results

Stress	HC[1]	LC	NA	LT	HT	X
Sample mean	0.848	0.827	0.892	0.872	0.911	1.000
Sample std. dev.	0.0831	0.1049	0.1020	0.0926	0.0890	0.1658
n	9	8	8	8	10	36
HC		0.665[2]	0.346	0.585	0.129	0.001
LC	Same[3]		0.231	0.384	0.095	0.002
NA	Same	Same		0.682	0.688	0.031
LT	Same	Same	Same		0.379	0.008
HT	Same	Same	Same	Same		0.033
X	Different	Different	Different	Different	Different	

[1]Stress conditions are: X – control specimens, HT and HC – high tension and high compression, LT and LC – low tension and compression, NA – neutral axis

[2]Values in the upper right portion of the table indicate the level of significance at which the two sample means can be considered different, corresponding to a probability that the two means are the same.

[3]Text in the lower left portion of the table indicates the results at a 0.05 level of significance.

Given the trends seen in the TGA results presented previously, the trends in the alite percentage are consistent with what would be expected. The most obvious is that the majority of the data points for beams specimens are significantly below a value of 1.0, indicating that there is less alite in stressed specimens than in the unstressed controls. At the neutral axis, the level of significance at which the data sets are different from the baseline is only approximately 3.1 per cent, meaning there is over a 96 per cent likelihood that they are different.

It is also interesting to note the slope of the trend in the data and t-tests. The percentage alite is lower in the compression regions than in the tensile regions, with the highest likelihood of a difference, approximately 90.5 per cent, being between the LC and HT datasets. Because alite is a component of the unhydrated cement grains, the potential difference may indicate that dissolution of the grains is accelerated more in compression regions than in tension regions, though with the significant difference from the baseline results, both regions indicate that stress likely accelerates hydration.

Using the same logic for hydration products, the equation characterizing volume ratios becomes

$$vr_{hyd} = \frac{r_h \alpha(t) m_{ci} \left(\frac{1}{\gamma_c} + 0.197 \right)}{m_{ci} \left(\frac{1}{\gamma_c} + 0.197 \alpha(t) \right)}, \tag{4.3}$$

where r_h is the fraction of hydration products that is the component being considered and other variables are as previously defined. Similar to Equation 3.2, r_c has been assumed to be zero such that a fully hydrated sample contains no cement grains. The ratios of stressed samples to the unstressed baseline were computed with the results presented for calcium hydroxide in Figure 4.24 and for total hydration products in Figure 4.25. The results of t-tests for the two groupings of data are given in Table 4.10 and Table 4.11. Note that because the baseline fit forces a value of 0 at an age of 0, the six data points for cement

powder, which would give a ratio of ∞, were removed from consideration for t-tests.

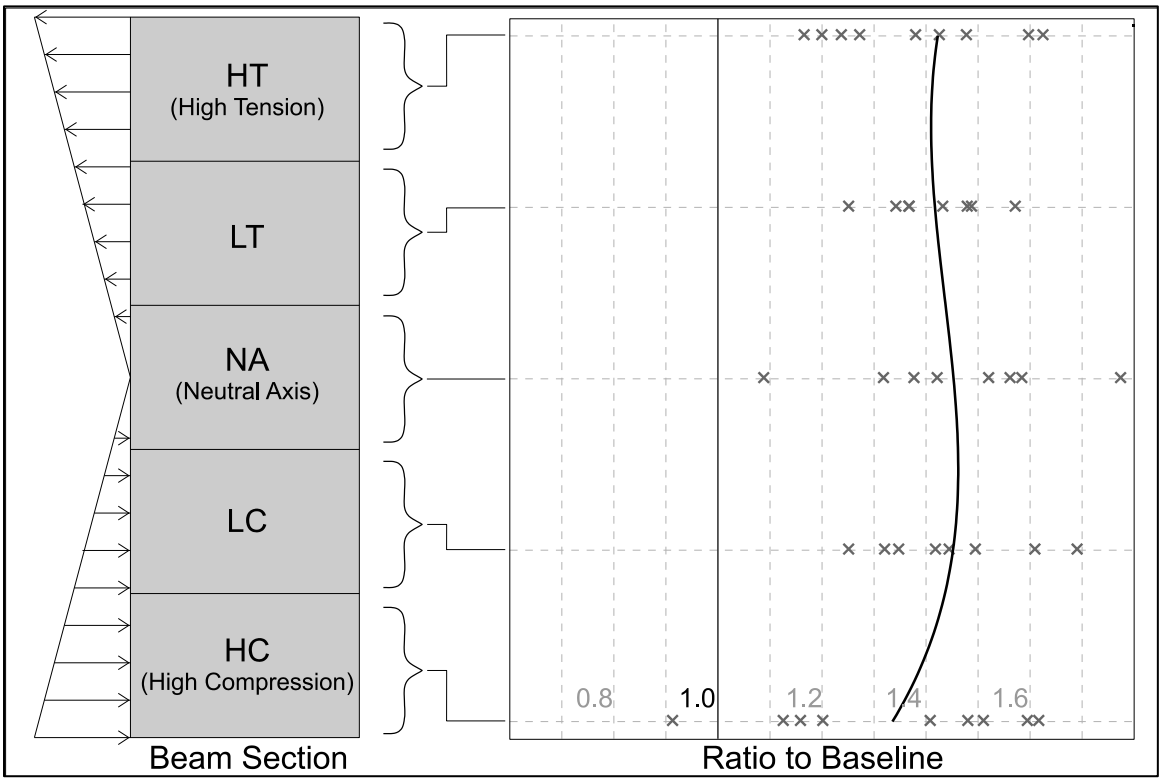

Figure 4.24 – Ratio of percentage calcium hydroxide for stressed samples to the fit curve of those not previously loaded, as determined by XRD. Using the resulting ratios for each of the five stress conditions, a cubic trend curve was fit to the data indicating that not only does stress increase the volume ratio of calcium hydroxide, but also there is a potential difference in this ratio between samples taken from compressive regions and those from tensile regions. It is also seen that samples taken from the region surrounding the neutral axis have significantly higher amounts of calcium hydroxide than seen in unstressed control samples.

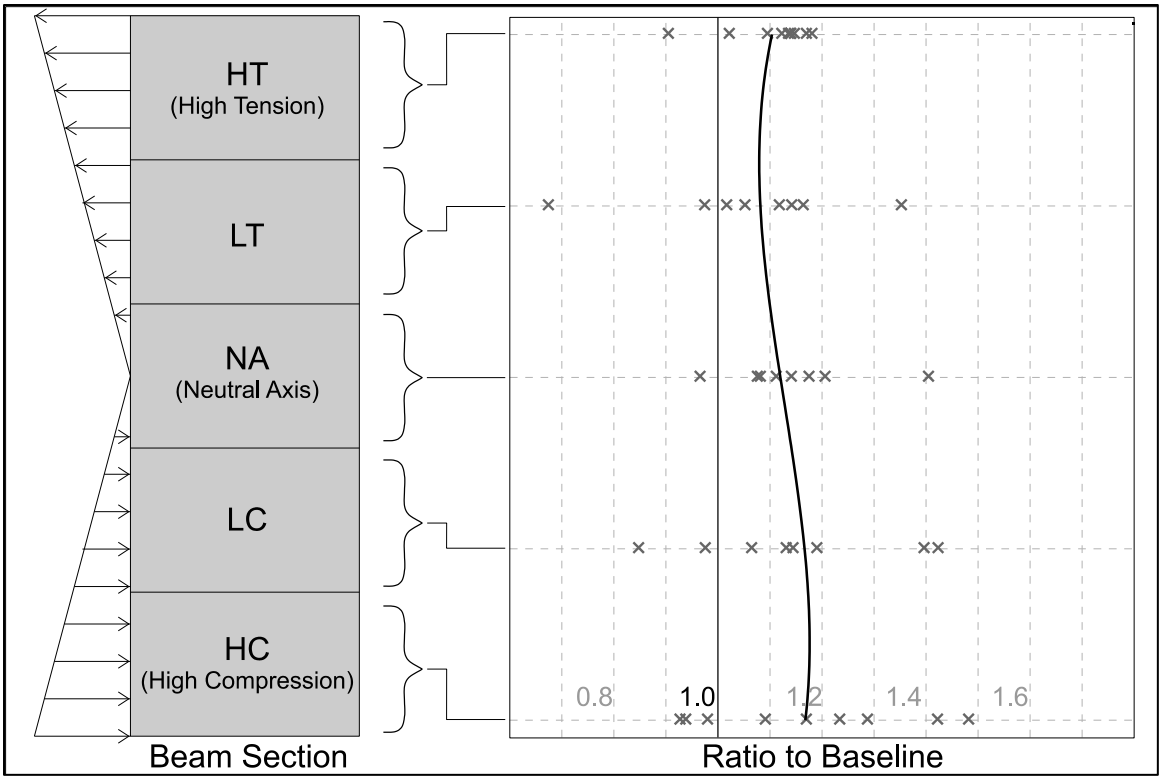

Figure 4.25 – Ratio of percentage hydration products for stressed samples to the fit curve of those not previously loaded, as determined by XRD. Using the resulting ratios for each of the five stress conditions, a cubic trend curve was fit to the data indicating that not only does stress increase the volume ratio of hydration products, but also there is a potential difference in the ratio between samples taken from compressive regions and those from tensile regions.

Table 4.10 – Results of t-tests for calcium hydroxide percentage using XRD results

Stress	HC[1]	LC	NA	LT	HT	X
Sample mean	1.336	1.449	1.457	1.414	1.423	1.006
Sample std. dev.	0.2434	0.1473	0.2047	0.1007	0.2150	0.4874
n	9	8	8	8	10	30
HC		0.264[2]	0.284	0.399	0.423	0.011
LC	Same[3]		0.925	0.593	0.769	0.000
NA	Same	Same		0.604	0.736	0.001
LT	Same	Same	Same		0.908	0.000
HT	Same	Same	Same	Same		0.001
X	Different	Different	Different	Different	Different	

[1]Stress conditions are: X – control specimens, HT and HC – high tension and high compression, LT and LC – low tension and compression, NA – neutral axis
[2]Values in the upper right portion of the table indicate the level of significance at which the two sample means can be considered different, corresponding to a probability that the two means are the same.
[3]Text in the lower left portion of the table indicates the results at a 0.05 level of significance.

Table 4.11 – Results of t-tests for percentage of hydration products using XRD results

Stress	HC[1]	LC	NA	LT	HT	X
Sample mean	1.172	1.149	1.147	1.064	1.107	1.005
Sample std. dev.	0.2045	0.1950	0.1278	0.1943	0.0830	0.2631
n	9	8	8	8	10	30
HC		0.813[2]	0.766	0.281	0.397	0.062
LC	Same[3]		0.987	0.398	0.591	0.109
NA	Same	Same		0.329	0.463	0.041
LT	Same	Same	Same		0.566	0.495
HT	Same	Same	Same	Same		0.069
X	Same	Same	Different	Same	Same	

[1]Stress conditions are: X – control specimens, HT and HC – high tension and high compression, LT and LC – low tension and compression, NA – neutral axis
[2]Values in the upper right portion of the table indicate the level of significance at which the two sample means can be considered different, corresponding to a probability that the two means are the same.
[3]Text in the lower left portion of the table indicates the results at a 0.05 level of significance.

The trends seen in the calcium hydroxide data are similar to those of alite, though with a marked increase in the distance from the baseline. Multiple values of 0.000 in the t-tests indicate that the percentage of calcium hydroxide in the LC, NA, and LT data sets have a less than 0.05 per cent likelihood of being the same as for unstressed control specimens. Unlike in the alite results, there is not a significant likelihood that tension and compression regions differ in calcium hydroxide content. Note that the curve fit for calcium hydroxide resulted in a prediction that CH comprised 100 per cent of the hydration products, an unrealistic condition. Though the curve is the best fit to the data, and therefore can be appropriately used for comparison of stress conditions, the hydration curve is likely not realistic. This will be further examined in Section 6.3.

The trends and statistics for the total hydration products appear to differ significantly from what would be expected. Although the majority of data points in Figure 4.25 are above 1.0, the t-tests rate all the majority of the data sets to be the same as the baseline at a 0.05 level of significance. There are two characteristics of the data likely responsible for this discrepancy. The first is the variability of the control data. As seen in Table 4.8, data for individual hydration products varies significantly with the most unexpected result being that the cement powder samples contain approximately 18 per cent hydration products.

This variability results in a wide band for the likely mean values of the baseline, as supported by the relatively high sample standard deviation in Table 4.11. The second cause for the discrepancy is the spread of the stressed sample data, most notably in the LC and LT data sets. The combination of the two sources of variability increases the level of significance at which the data sets are different. However, even with the variability, it is seen that there is over a 93 per cent likelihood that the HT and HC data are different than the baseline. This indicates that there is a high probability that stressed regions have a higher content of hydration products, reinforcing the suggestion that stress accelerates hydration.

5. X-Ray Computed Microtomography

X-ray computed microtomography ("micro-CT") is a method of non-destructive evaluation that uses a series of X-ray radiographs to examine the internal structure of a sample. For a single image radiograph, the micro-CT scanner emits X-rays from a point source, through the object being examined, to a collector, as depicted in Figure 5.1. As a particular ray passes through the sample, its intensity is attenuated by the absorption characteristics of the material with denser materials generally absorbing more of the X-ray than lighter materials. Thus, a particular pixel at the collector represents the resulting intensity after the ray has passed through the thickness of the object. For samples that vary in X-ray absorption from location to location, the single-pixel intensity represents a cumulative loss due to all the types of material passed through between the source and the collector. The overall radiograph represents this combined attenuation over the entire field of view of the sample. If the sample is then rotated slightly, the X-rays pass through the same locations but in slightly different combinations, giving a potentially completely different radiograph. If the object is rotated again and again, the resulting series of radiographs gives a sufficient number of combinations of attenuations to characterize the sample completely. Through the use of reconstruction software, the series of radiographs can be examined to determine the X-ray absorption of any three-dimensional location within the sample. The results of the reconstruction are generally presented as a stack of reconstructed slices of the sample where denser areas are shown in lighter color and vice versa; air would result in black areas on the reconstruction.

Micro-CT has been in use for medical imaging for decades. However, as the technology has become more accessible, there has been a recent dramatic increase in the use of the method for examination of engineering materials. With appropriate resolution and distances between the emitter, sample, and collector, the method can detect differences in structure at or below a 1μm length scale.

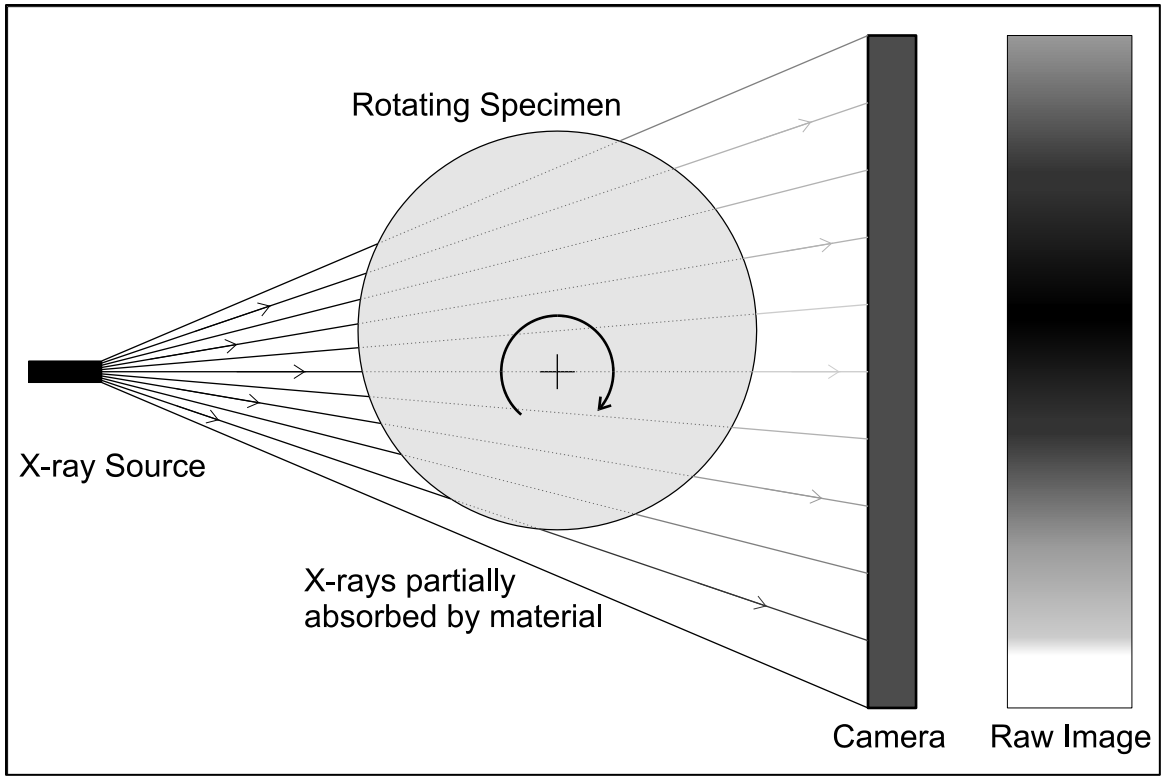

Figure 5.1 – Principles of X-ray computed tomography showing a single sample alignment subject to X-ray examination. As the sample is rotated through multiple alignments, examined regions are photographed in different combinations allowing identification of X-ray absorption of small regions throughout the scanned sample.

5.1 Methodology

Samples to be used for micro-CT evaluation were cast and prepared as described in Section 3.2.1. For cylinders to be scanned while under compression, the testing frame depicted in Figure 3.16 was used for the scans. For control specimens, a similar frame, but without the spring, load cell, and top plate with screw, was used for the scan. For both, the outside surfaces of the cylinders were sealed with cyanoacrylate.

Specimens were mounted into a Skyscan 1172 desktop micro-CT as produced by Bruker MicroCT. The mounting was typically slightly off-center such that an outer edge of the cylinder was visible in the radiographs to facilitate image alignment during reconstruction. Scans were conducted using no filter, a voltage of 100kV, and a current of 100 μA. The X-ray source was adjusted to the nearest distance possible within the limitations of the machine yielding radiograph resolutions of 1280x1024 pixels with each pixel corresponding to 2.09 microns. Scans were conducted using a

full 360° of rotation at 0.1° increments, averaging eight images at each angle increment, and allowing the equipment to perform random movement of the sample from increment to increment to avoid excessive repetition in the scans of the center-most portion of the sample. At the end of each scan, the 3600 raw images were converted to a stack of approximately 1000 reconstructed slices using the NRecon software packaged with the scanner.

In addition to control specimens and compressive cylinders, additional scans were performed on samples crafted from the approximate midspan of selected beams. After relaxation testing, at the breaking point of the beams, typically at or near midspan, rough samples approximately 6 mm x 6 mm x the full beam height were cut from the beam portion using a high-speed rotary cutting tool. Each prism was mounted to a stainless steel cylinder (approximately the same as the bottom platen used in compression testing) using cyanoacrylate and slowly shaved to a 3 mm cylindrical shape using a hobby knife. Once the final shape was achieved, the assembly was placed within the acrylic tube of the test mounting and a full height scan conducted. These full height scans typically yielded approximately 7800 reconstructed slices, representing the full range of stress conditions in the beam.

5.2 Results

The micro-CT scans yielded raw images of high quality, such as the radiograph presented in Figure 5.2. In the image, the edge of sample and thickness of sealant are easily seen. In the field of view corresponding to the cement paste, the slightly lighter gray toward the edge of the sample indicates less attenuation of the X-ray due to less of the sample lying along the line from the source to the detector. The gray to the outside of the sealant is the background associated with X-ray penetration through the surrounding acrylic tube.

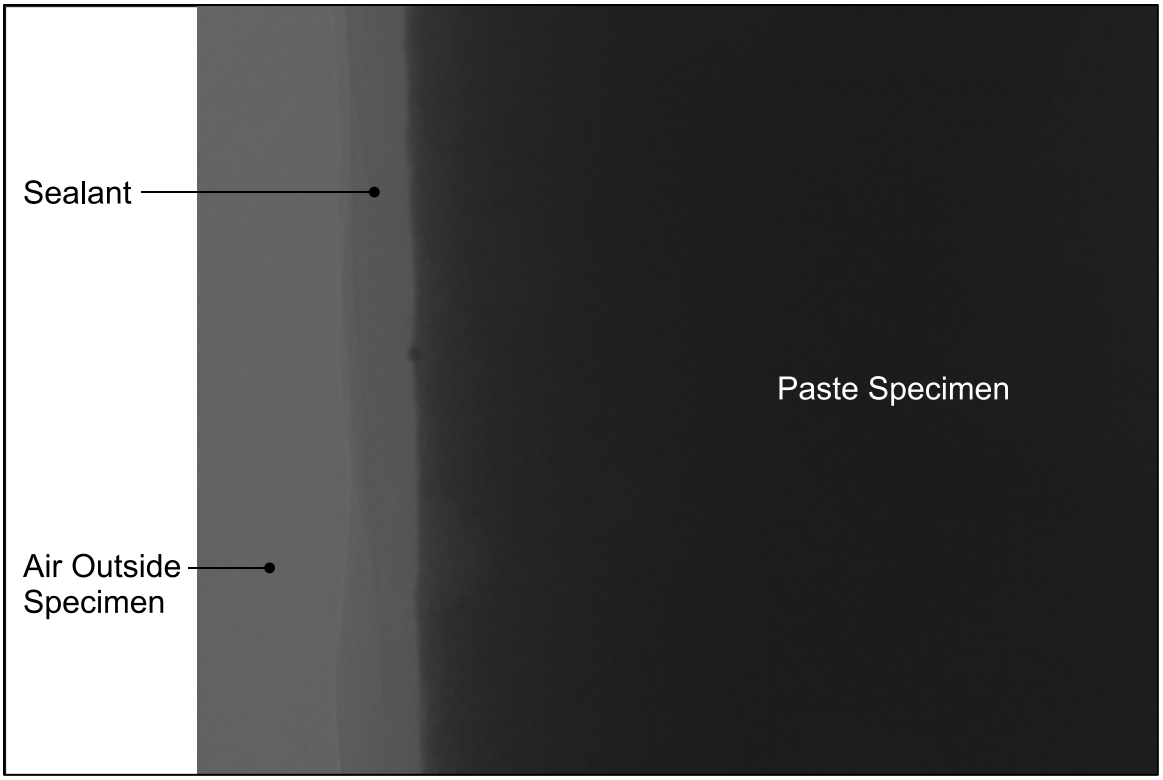

Figure 5.2 – Sample X-ray image showing sealed edge of sample from a single angle. Color variation within the field of the paste specimen gives an approximation of the total thickness of material penetrated by X-rays with thicker regions resulting in darker images.

Using the array of 3600 raw images, stacks of reconstructed slices for each scan were produced, such as the example slice presented in Figure 5.3. The cylinder depicted in the example was scanned at an age of 1 day. The light-colored shapes spread throughout the field of the sample are assumed to be cement grains and the few very dark, smaller shapes, are assumed to be air. The medium gray field of the sample is likely a combination of hydration products and unhydrated cement paste, though the color difference between the two, representing a difference in the X-ray density of the two products, is minimal. There are two interesting features of the image that should be noted. First, there appears to be a concentration of small cement grains along the outer edge of the sample. The exact reasons for this apparent concentration are unknown, but this characteristic was seen in most scans. The second item of note is the overall quality of the image. Although boundaries of the cement grans can be estimated from the image, they are indistinct. The blur is likely due to the fact that the scans took approximately 13

hours to complete with ongoing hydration during that time. Thus edges of cement grains were continuously evolving throughout the scan.

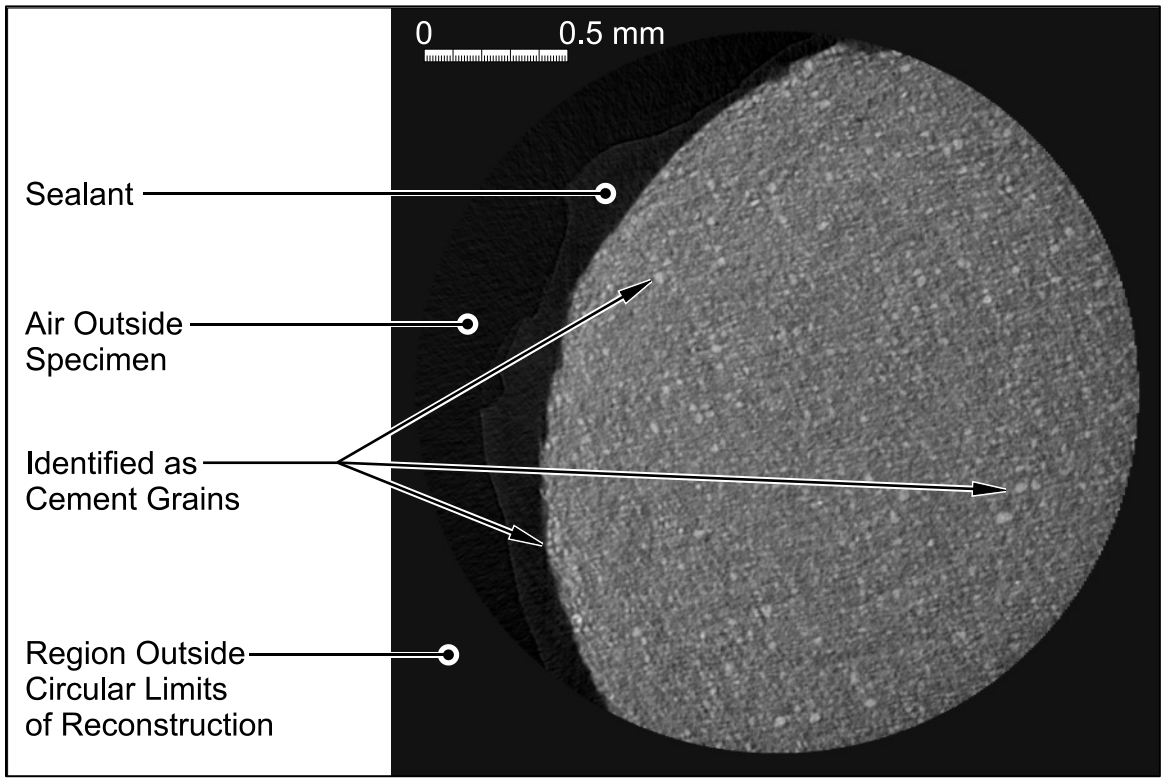

Figure 5.3 – Sample reconstructed "slice" indicating X-ray densities throughout cross-section of cement paste cylinder. The rough surface to the left of the image corresponds to the outside surface of the cylinder and the smoother surface to the right of the image is the circular limit of reconstruction.

Although traditional approaches may dictate that the individual reconstructed slices be examined visually to discern the volumetric ratio of cement grains, and thus the degree of hydration, examining the tens of thousands of images was not deemed feasible. Instead, a preliminary attempt at boundary definition was conducted using a gradient method within Mathematica. The results indicated that the method of boundary definition was highly dependent on the gradient settings chosen with results varying widely. Although there is likely a method by which gradients could be used in combination with traditional threshold methods, this method for grain boundary discernment was set aside for purposes of the current research.

Considering the goal of the image analysis was to determine the proportions of air, hydration products or gel, and cement grains, each stack of reconstructed slices was first

cropped to square images approximately 500 pixels on each side, and a histogram produced from the resulting matrix of gray scale values. If, for example, air was exactly black, cement grains exactly white, and hydration products halfway in between, the histogram would show three distinct spikes of three different heights at the three gray scale values. Because there was some X-ray scatter and color variation associated with each of the three components, it would be expected that the spikes on the histogram would appear as bell curves corresponding to some statistical distribution. However, the actual histograms were more like the example shown in Figure 5.4. The overall shape of the distribution has no discernible peaks except the main peak. Air content, if significant, would show as a peak at or near a gray scale value of 0. Cement grains, if white in the slices, would show as a peak at or near a gray scale value of 255.

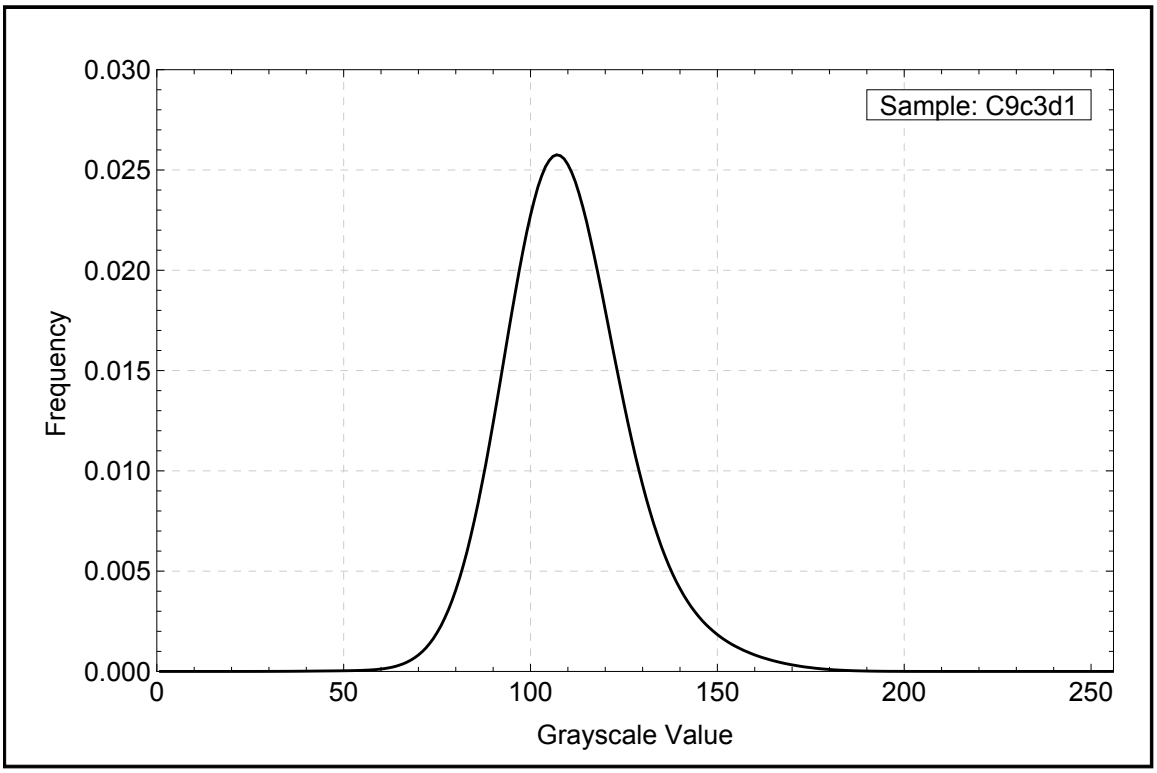

Figure 5.4 – Sample histogram of gray scale values of X-ray density taken from stack of 980 reconstructed slices. Lower gray scale values correspond to darker regions in the reconstructed slices with a gray scale of 0 assumed to be air. Higher gray scale values correspond to lighter regions in the reconstructed slices, assumed to be the denser areas of the specimen. Thus peaks corresponding to cement grains would have a slightly higher gray scale value than those of hydration products.

5.3 Analysis

Although the histograms derived from the micro-CT reconstruction do not show distinct peaks, careful examination of the shape of the histogram reveals an asymmetry with the right half of the distribution being slightly wider than the left. Thus it was assumed that the main peak was actually the addition of two separate Gaussian distributions. If the sample were a combination of only two materials, cement grains and hydration products, and if each of the materials had a variability in X-ray absorption corresponding to a Gaussian distribution, it would be expected that the overall distribution of gray scale values in the reconstructed slices would be the combination of the individual distributions, each multiplied by the proportion of the corresponding material. Thus, if these assumptions hold true, the overall histogram should provide sufficient information to determine the individual distributions and the proportion of each material.

Using this logic, data points for each histogram were used to create a fit within Mathematica. An example of the fit is given in Figure 5.5. Fits for all samples are given in Appendix D.1. The tall and relatively thin distribution is assumed to be that of the hydration products and the lower distribution, with a mean value at a gray scale closer to white, corresponds to that of cement grains. The mean and standard deviation for each distribution, and the proportions of each in the total model, were determined by the curve fitting program. The R^2 values of the resulting fits were typically greater than 0.9998, lending validation to the underlying assumptions. It is possible, and may be likely, that some other combination of distributions would characterize the collected data as well or better than the combination assumed herein. However, for purposes of this research, the combination presented Figure 5.5 appears to be sufficient. Note that as suspected, the weighting factor for the distribution corresponding to air is 0.0 indicating that the overall air content is insignificant compared to cement grains and hydration products.

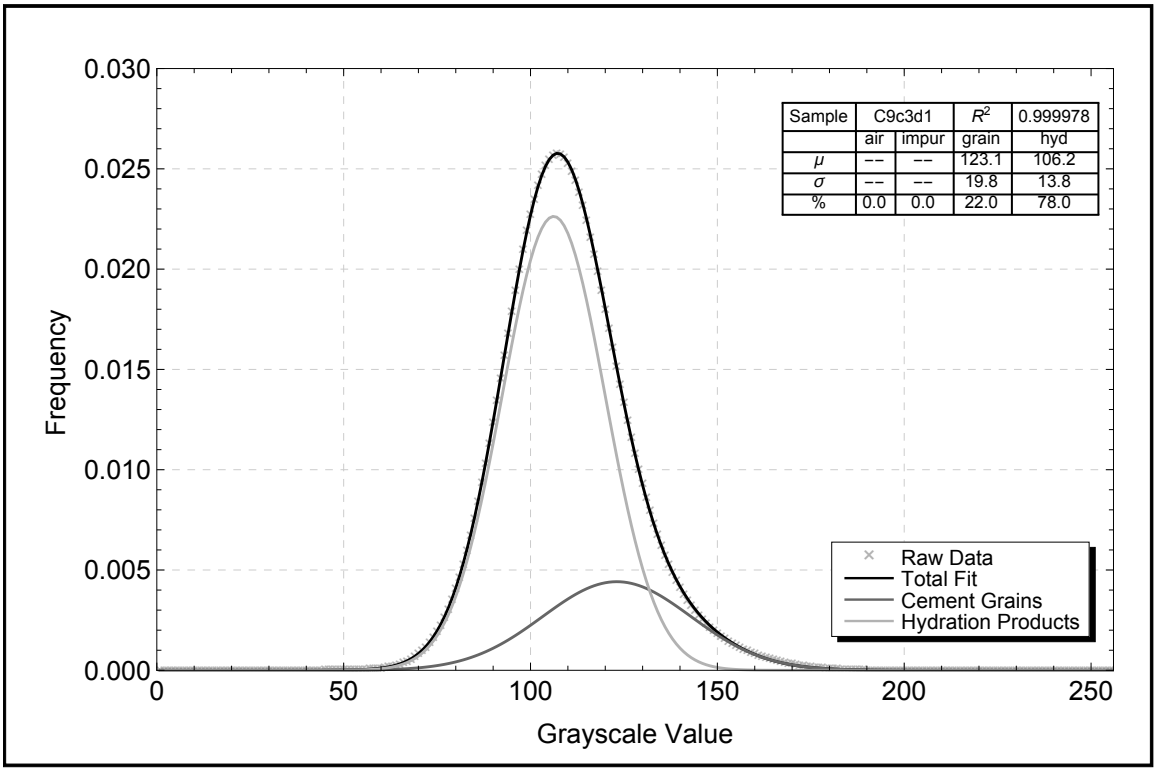

Figure 5.5 – Sample fit to reconstruction histogram using Gaussian mixture model of standard distributions for cement grains, hydration products, air, and impurities. For this sample, neither air nor impurities had any appreciable content. Grains show a wider, flatter distribution at a higher gray scale value as compared to hydration products. As shown in the annotation, the mixture model indicates a 22 per cent volume of cement grains.

As an additional check of the validity of the method, the fit distribution was used to determine thresholds for the gray scale value corresponding to cement grains and hydration products. Figure 5.6 presents the results using threshold values corresponding to a 90 per cent chance that a particular pixel is part of the cement grain distribution or hydration product distribution. With these thresholds, 3.87 per cent of the sample was determined to be cement grains and 32.3 per cent hydration products with the remaining pixels unknown. Figure 5.7 presents the same manipulation with thresholds set at a 50 per cent probability and resulting in 12.2 per cent cement grains and 87.8 per cent hydration products. Though the value for cement grain content is significantly lower than the 22.0 per cent determined with the mixture model, the locations of the lighter-colored pixels appear to correspond to what would be seen as cement grains in the raw image. It should be noted that because the mixture model

was derived using a full stack of images rather than a single slice, a difference in the two values for cement grain content is expected.

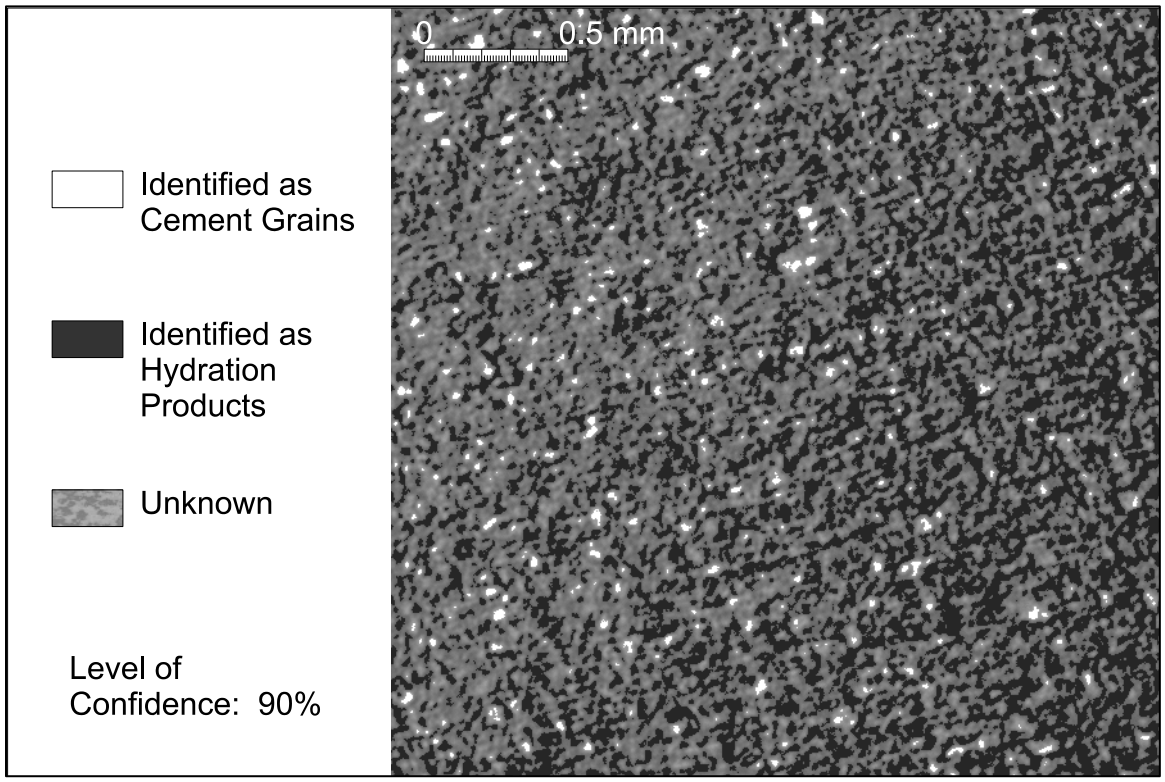

Figure 5.6 – Sample application of Gaussian mixture model to reconstructed slice showing regions of 90 per cent probability that a pixel is a cement grain or hydration product with unknown pixels appearing in their original gray scale.

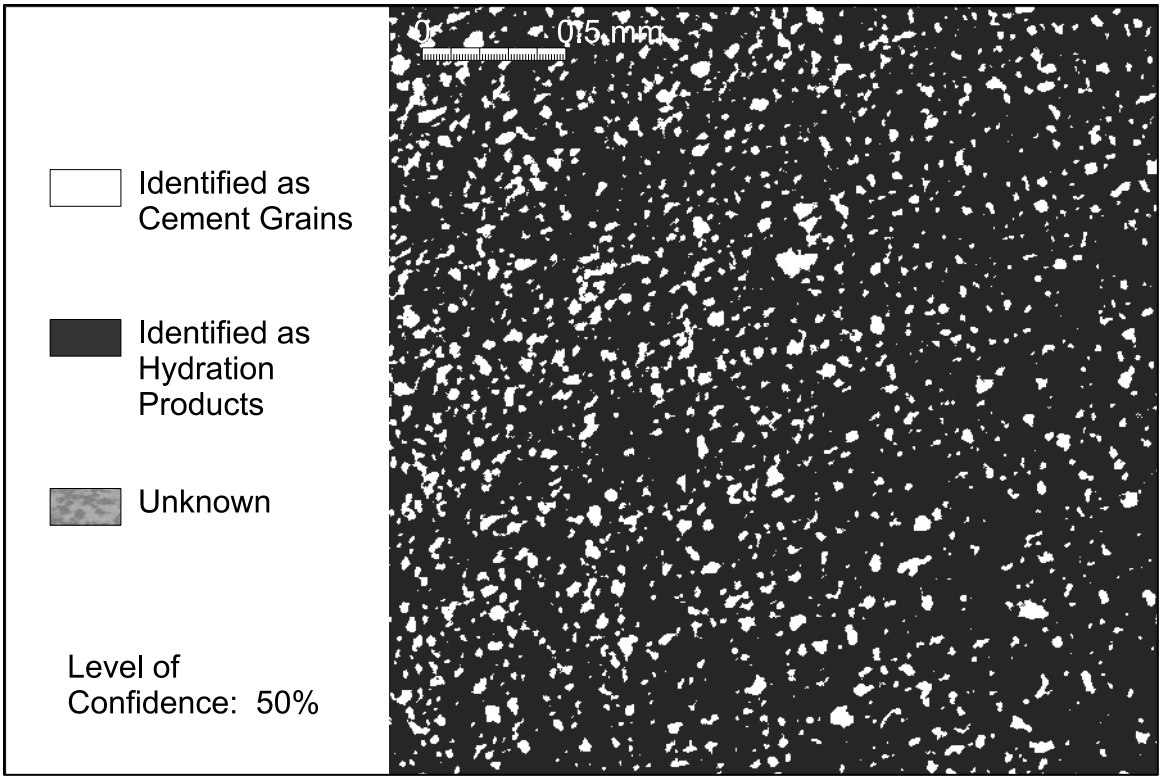

Figure 5.7 – Sample application of Gaussian mixture model to reconstructed slice showing regions of 50 per cent probability that a pixel is a cement grain or hydration product with unknown pixels appearing in their original gray scale. Based on size and shape, it is apparent that a number of pixels tentatively identified as cement grains most likely are not.

Based on the Gaussian mixture models determined, the volumetric proportion of cement grains was determined. Assuming a w:c ratio of 0.4 and a specific gravity of cement grains of 3.15, the initial volumetric ratio of cement grains in a cement paste sample should be 44.25 per cent. Subtracting the ratio of current grain percentage by the original from unity will therefore give the degree of hydration. Results of the analysis are presented in Table 5.1 and Figure 5.8.

Table 5.1 – Degree of hydration as determined by micro-CT analysis

Age of Specimen (days)	Stress Condition[1]	Volume Fraction of Cement Grains (%)	Degree of Hydration (%)
0[2]	All	38.74	12.44
1	X	44.34	-0.20
1	X	21.98	50.34
1	X	29.57	33.18
2	X	36.24	18.09
4	X	22.93	48.17
4	X	20.68	53.27
6	X	28.58	35.40
8	X	16.86	61.90
8	X	32.32	26.96
8	X	33.55	24.17
8	X	25.78	41.74
10	X	26.47	40.18
13	X	25.62	42.10
14	X	55.26	-24.89[3]
20	X	24.62	44.36
23	X	19.63	55.63
85	X	22.25	49.73
2	CC[4]	45.61	-3.09
3	CC	26.51	40.08
4	CC	24.27	45.14
7	CC	22.90	48.25
7	CC	30.55	30.96
7	CC	25.06	43.36
11	CC	22.69	48.72
11	CC	28.12	36.44
14	CC	29.74	32.78
21	CC	20.14	54.48
84	CC	24.98	43.54
5	HT	26.87	39.27
14	HT	33.96	23.25
16	HT	18.00	59.32
17	HT	33.64	23.97
17	HT	26.83	39.36
5	LT	28.72	35.09
14	LT	30.51	31.05
16	LT	21.33	51.80
17	LT	16.86	61.90
5	NA	31.68	28.41
14	NA	18.74	57.66
16	NA	19.48	55.98

Age of Specimen (days)	Stress Condition[1]	Volume Fraction of Cement Grains (%)	Degree of Hydration (%)
17	NA	31.86	28.00
17	NA	23.57	46.73
5	LC	33.90	23.39
14	LC	29.21	34.00
16	LC	21.65	51.07
17	LC	22.85	48.36
5	HC	27.18	38.58
14	HC	38.19	13.70
16	HC	37.33	15.63
17	HC	24.97	43.57
17	HC	19.00	57.06

[1]Stress conditions are: X – control specimens, HT and HC – high tension and high compression, LT and LC – low tension and compression, NA – neutral axis
[2]Specimen prepared using wax in place of water to avoid hydration.
[3]Significant negative value for hydration not physically possible. Data point removed from subsequent analysis.
[4]CC represents cylinders placed in compression corresponding to the same approximate strain as HC beam specimens.

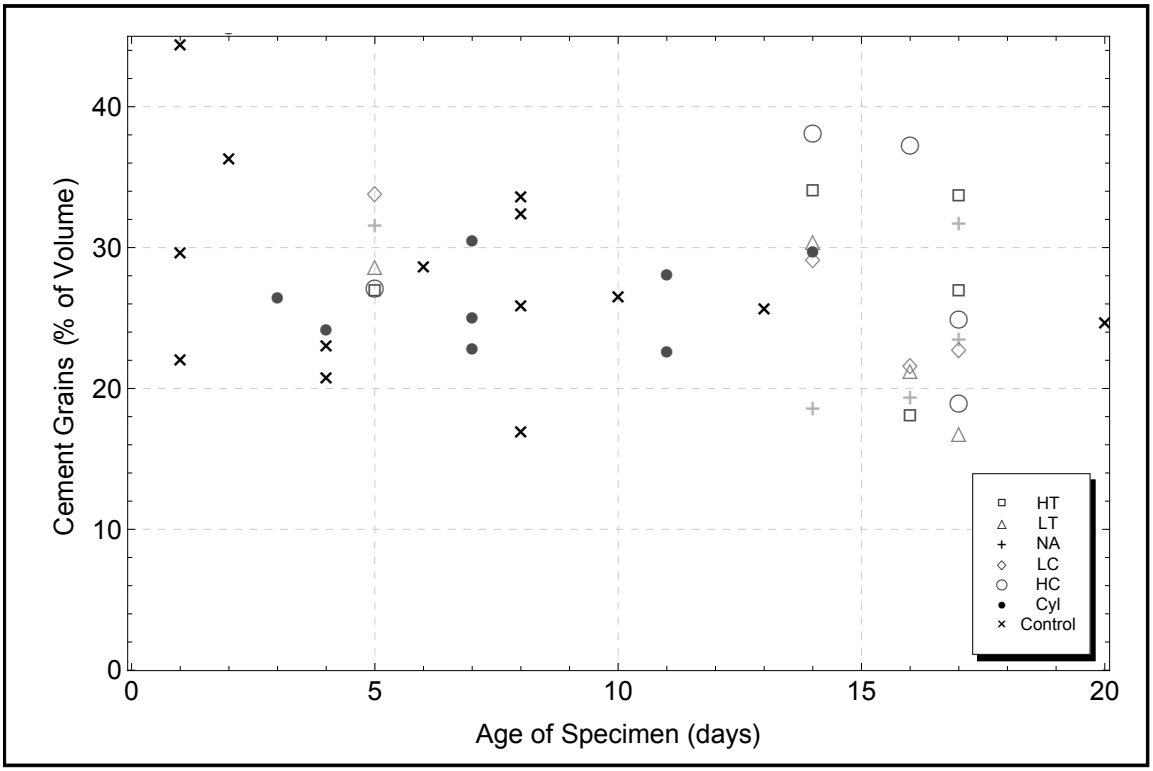

Figure 5.8 – Total percentage of cement grains versus specimen age for tested beams, tested cylinders, and specimens not previously loaded. Stress conditions from beam specimens, as listed in the legend, are "High Tension", "Low Tension", "Neutral Axis", "Low Compression", and "High Compression". Cylinder specimens had a stress approximately equal to that of the "High Compression" samples. Overall, any trends in the data appear to be overshadowed by the scatter of the data points.

Examining the data points in the above figure reveals a high degree of uncertainty in the results as evidenced by the wide spread of data points at all ages. This uncertainty is likely associated with the quality of the reconstruction images, which is highly variable from sample to sample. Nonetheless, the same analysis techniques were used with the micro-CT data as had been used previously with TGA and XRD results. Because micro-CT measures the volumetric ratios directly and considers the entire cross-section of the sample, Equation 3.3 can be used but the denominator is set to 1. Figure 5.9 presents the curve fit to the control data, showing the same basic shape as with previous test results. Figure 5.10 presents the ratio of stressed samples to the baseline with X's as used previously for beam samples and O's for stressed cylinders. Although t-tests were performed, the high variability of the data sets prevented any useful observations from the statistical data and thus, results are not included here.

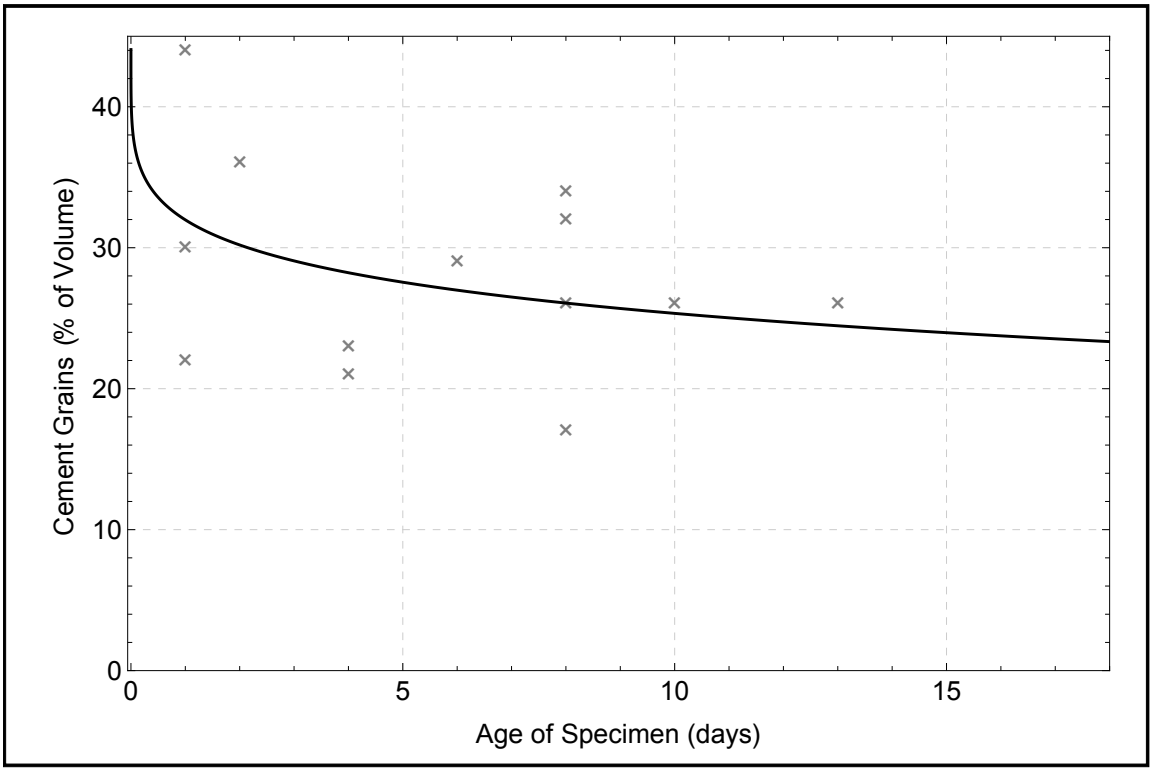

Figure 5.9 – Curve fit of percentage cement grains vs. time for samples not previously loaded. The form of the fit curve corresponds to an inverted hydration curve with the volume percentage equal to the theoretical volume ratio at time zero and equal to zero at infinite time.

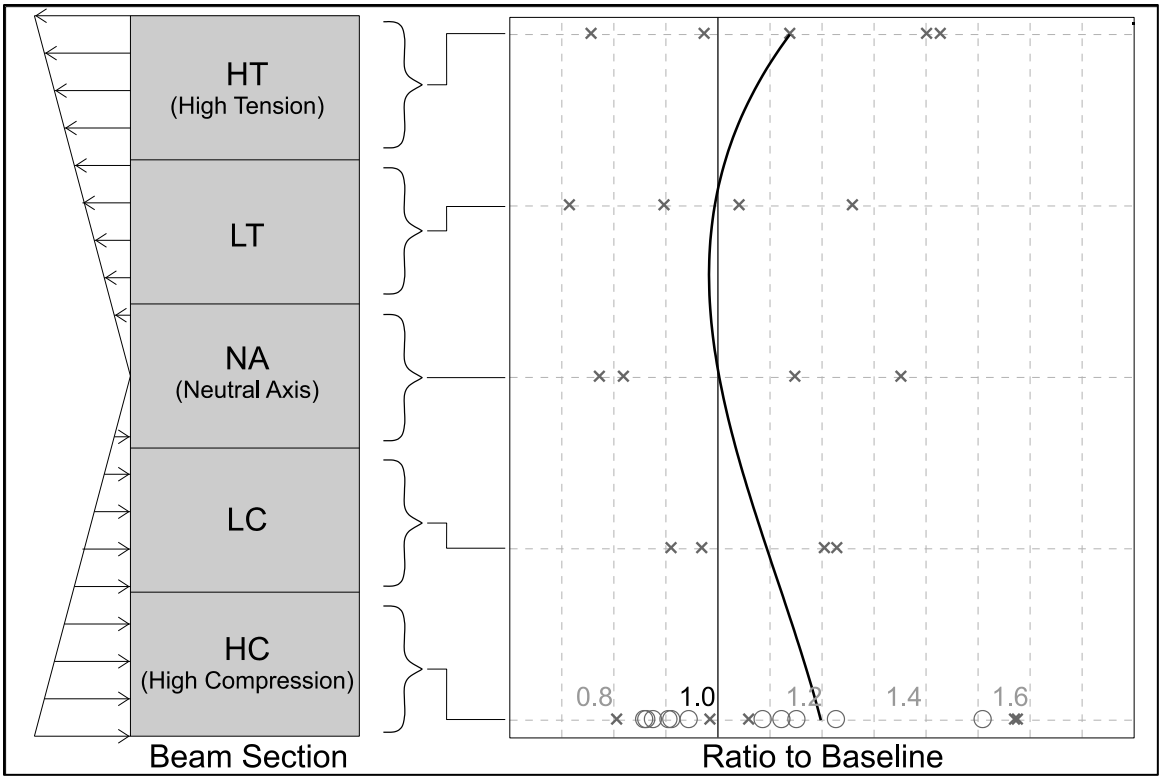

Figure 5.10 – Ratio of percentage cement grains for stressed samples to the fit curve of those not previously loaded. Using the resulting ratios for each of the five stress conditions, a cubic trend curve was fit to the data. The dispersion of data points make the trend somewhat unclear, though the shape of the trend curve indicates a higher cement grain volume percentage in high stress areas, a trend completely opposite of what would be expected from previous results. Data points marked by circles are those from cylinders placed in compression at a stress approximately equal to that in the "HC" region of the beams.

6. Analysis and Discussion

In Section 1, it was stated that the majority of research in the field of viscoelasticity starts with observations and then develops or applies a model to describe the observed behavior. This is in fact the same general approach applied in Sections 3 through 5 when fitting curves for relaxation and hydration to data obtained from testing. However, to truly understand the trends in the data, it is necessary to reverse the process, starting first with a realistic model of the material and applying scientific principles, track behavior of the model under various conditions to hopefully align results with experimental observation. Unfortunately, the full development of such a model is beyond the scope of this research. But by setting up the model and considering the general characteristics and behavior of its components, the trends seen in relaxation and chemical data can be more fully understood. Further, the model may help explain some of the apparent discrepancies and counter-intuitive trends seen in some of the testing data.

6.1 Anomalies in Elastic and Viscoelastic Behaviors

Taken individually, results presented above for elastic Young's modulus and relaxation might be explained by previously published theories. Starting with relaxation, it is apparent that intrinsic viscoelastic aging must be accounted for in order to produce higher precision models. However, by limiting comparisons to specimens of similar age, this issue can be set aside. That leaves the readily seen difference in relaxation behavior between specimens loaded at multiple steps in a single direction versus those with a strain reversal in the loading history.

At first glance, the reduction in relaxation rate (higher retention of load) in reversed specimens lines up with the theory of relaxation being a function, at least in part, of microcracking in the structure (Bazant and Zubelewicz 1988; Bernard et al. 2003). A forward load causes cracking primarily in the tension regions of the beam to grow under additional load. Essentially, relaxation is compounded when additional loads are applied in the same direction. This effect is somewhat offset by aging, as seen in comparing Figure 3.9 to Figure 3.10 where a higher load retention is present, even after multiple loads are applied. When a beam is reversed (or strain is reversed), the

tension face goes into compression, tending to close the pre-existing micro-cracks and starting new micro-crack patterns in the face previously under compression.

Similarly, the trends seen in the elastic Young's modulus of loaded specimens is consistent with existing theories and previously published research (Harsh et al. 1990; Inozemtsev 1995). The shapes of the two curves in Figure 3.4 suggest that loaded specimens develop stiffness more quickly than previously unloaded specimens. As stiffness is typically a direct function of the degree of hydration, this suggests that load applied to a specimen accelerates hydration, as has been reported previously (Tamtsia et al. 2004), possibly due to stress-induced dissolution of the cement grains (Grasley et al. 2014).

When taken together, however, trends are less intuitive. The microcracking that might explain the relaxation results would, in theory, also reduce stiffness during loading. As stated above, the results for Young's modulus of elasticity of forward versus reverse specimens are indistinguishable. This apparent contradiction implies that a mechanism other than or in addition to microcracking is responsible for relaxation behavior.

A full consideration of other mechanisms potentially responsible for observed behavior is beyond the scope of this work. However, there are certain aspects of the current testing that may provide some additional insight. In Section Analysis, it was noted that the early relaxation observed could be attributed to movement of pore fluid within the specimen. For later analysis, the presence and movement of this pore fluid was ignored, consistent with the assumptions of the solidification model that only hydrated cement paste carries load. If this limiting assumption is removed, and the pressure exerted on and by the pore fluid is considered, relaxation behavior may be more fully understood. In the quasi-instantaneous loading stage, if the loads are carried by both the pore fluid and the solid structure, the fluid would be pressurized in compressive regions of the specimen and tend to flow into adjoining empty cells within that structure. This flow would be hampered by the small size of the capillaries present in the material. After some time, the fluid would equalize at a local level,

relieving pressure and therefore, relieving load at the macro scale. The magnitude of load and the time required to reach equalization would be a function of both the initial proportion of water, as determined by the w:c ratio, and by the rate at which capillaries shrink, related to the degree of hydration. The general shape of the load relaxation curve due to this fluid movement would resemble that seen in Figure 3.5. Determining the magnitude and precise shape of such a relaxation curve would require testing and analysis beyond the scope of the current research.

6.2 Solidification-Dissolution Model

Based on results presented in Section 3, it is apparent that the solidification model is insufficient to fully predict beam relaxation behavior. As an illustration, consider the curves presented in Figure 3.6. If the solidification theory holds, and assuming that the influence of earlier load cycles has been appropriately subtracted (the first cycle fit curve accurately represents longer-term behavior), the resulting relaxation curves for second and third cycles should be the same, merely shifted in time (horizontally). As can be seen, relaxation of load is significantly over-predicted by the solidification theory for displacement increments after the first. This implies that relaxation is retarded by the aging of the hydration products, i.e., viscoelastic aging is not fully characterized by the solidification model. This same conclusion was drawn in previous research (Bazant et al. 1997; Grasley and Lange 2007a).

After considering the relaxation behavior in both uniaxial (cylinder) specimens and beam bending, it should be evident that a new model for material behavior, incorporating additional elements, is needed. The solidification model contains only two components, the load-bearing hydration products and the non-load-bearing gel. To more accurately capture actual behaviors, it is suggested that a model consisting of seven components, placed in parallel, be used, as depicted in Figure 6.1.

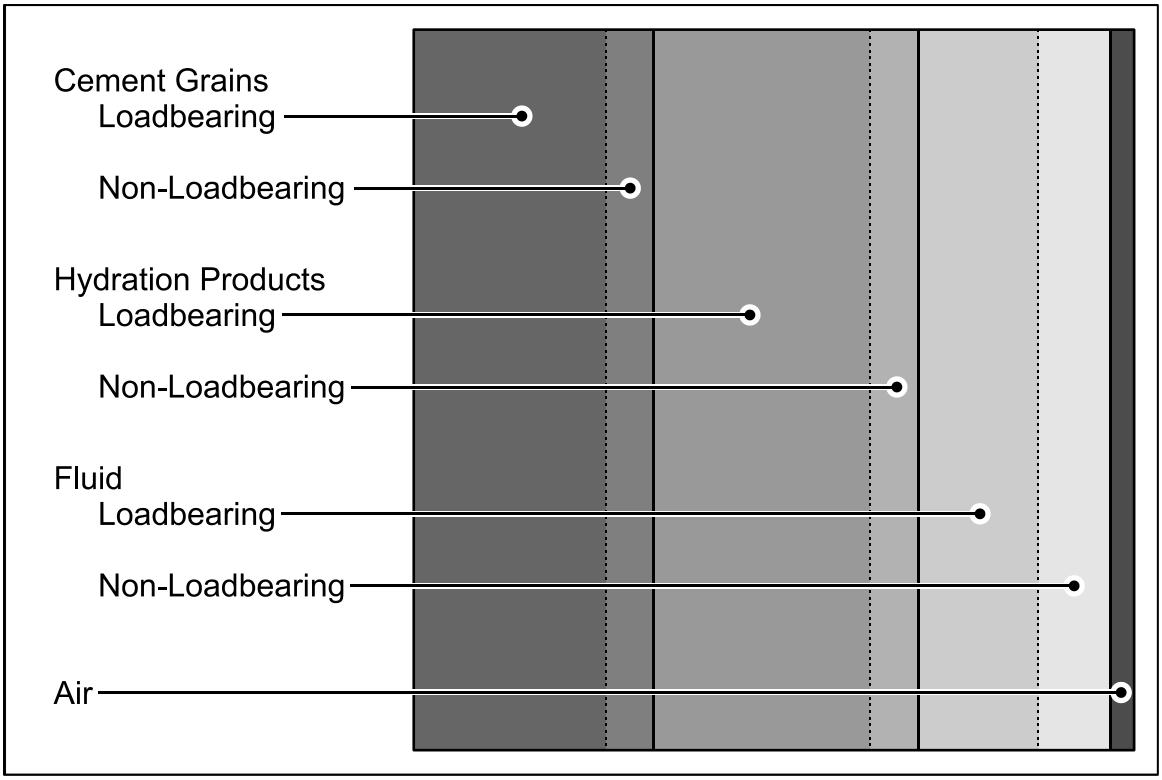

Figure 6.1 – Proposed mechanical model providing load-bearing and non-load-bearing cement grains, hydration products, and fluid. During the hydration process, volume percentages of cement grains and fluid decrease while those of hydration products and air increase.

6.2.1 Unstressed Hydration Process

To understand the need for the seven components included in the proposed model, it is necessary to briefly consider the typical hydration process. At the moment that water is mixed with cement grains, the resulting paste is a mixture of the various chemical compounds of the grains and clean water. Very quickly, the boundaries of the grains start to dissolve into the water and diffuse through the liquid, leaving a mixture of unhydrated cement and a solution. Based on the kinetics of the chemical reactions, species in solution begin to precipitate, generally starting at edges of unhydrated grains, and a microstructure of hydration products grows within the field of the solution. At very early times, typically less than 90 minutes, these hydration products are insufficiently connected to hold load. Likewise, remaining cement grains are also free to move within the surrounding fluid. As the microstructure grows at several nucleation sites, hydration products connect to one another, providing an intricate structural

pattern of both hydration products and connected cement grains that could carry load. Not all of each component is immediately connected to this structure and thus a sample of cement paste at any given time will contain load-bearing and non-load-bearing cement grains and hydration products. As hydration continues, a portion of the fluid is trapped within the growing structure, surrounded by permeable material. As with the solid components, there is a portion of the fluid that is free to flow to surfaces or pockets of air. Thus some of the fluid could be modeled as load-bearing and some as existing at zero pressure, regardless of applied loads or displacements.

Keeping this assumed structure in mind, the model of Figure 6.1 was produced with each component in parallel. Though the actual structure is far more complex, the conceptual parallel model should be sufficient to further consider relaxation behavior and potential chemical changes in the overall product. If it is assumed, for the sake of simplicity, that each solid component of the model is linearly elastic, it is a straightforward application of Hooke's law and compatibility constraints to determine stresses and strains in each component given an applied load or displacement at the macro scale. The Young's modulus of elasticity for the material would be dependent on the modulus of each of the two load-bearing solids, the bulk modulus of the fluid, and the cross-sectional areas of each of the three load-bearing components. This last, the geometry of the model, is dependent upon the degree of hydration, i.e., the percentage of cement grains that have been converted to hydration products.

Estimates for the E value of cement paste have been reported as 80 GPa, calcium hydroxide as 40 GPa, and cement grains as 118 GPa (Haecker et al. 2005; Jones et al. 2012). Therefore, it would be expected that at infinite time (100 per cent hydration) Young's elastic modulus would approach 80 GPa. At earlier ages, however, the modulus of just the solid components would be somewhere between 80 and 118 GPa. If at some point in time, a load is applied to the composite, stresses in the load-bearing cement grains would be higher than those in the hydration products. After an increment of time, if the load is maintained, a

portion of the load-bearing cement grains dissolve due to the hydration reaction, increasing the amount of load to be carried by hydration products. However, because hydration products are formed during this time increment, with a portion now bearing load, the stress distribution across the products is not uniform. The effects of this load re-distribution are the subject of ongoing research by others (Li et al. 2015; Rahman and Grasley 2014). Preliminary results of that research are focused on the effects of stress on dissolution of cement grains, as will be discussed below. However the basic concept that stress does re-distribute based on the dissolution of cement grains, whether or not induced by stress, is sufficient for the current discussion.

For cases of constant displacement, such as in uniaxial relaxation testing, the mechanics of the model are slightly different. If it is assumed that changes to the geometry of the model are limited to that caused by hydration reactions, during the referenced increment of time, the section of load-bearing cement grains tends to get smaller and the section of hydration products tends to get larger. Though the macro scale displacement of both materials remains constant, one must consider the micro scale and account for local displacements in the solid components.

As an example of the implementation of the model, consider the schematic presented in Figure 6.2 representing a sample subject to a uniaxial compressive load to a constant strain. Assuming that 100% of the grains and hydration products can bear load, at the time, t_1, that a load, P_1, is applied, the load is divided to the two layers based on stiffness and volume percentage of the layers. The volume percentage of cement grains at any time is dependent upon the degree of hydration with the percentage at time 0, v_{g0}, computed using the original w:c ratio. For purposes of the model, it is being approximated that hydration is fully achieved at infinite time and therefore the volume percentage of hydration products at any time is equivalent to the degree of hydration. To avoid confusion, this approximated degree of hydration is denoted as $h(t)$. Thus at the time of loading, t_1, $v_{g1}=v_{g0}(1-(h(t_1))$ and $v_{h1}=h(t_1)$ as presented in Figure 6.2. During the

next time interval, a series of three events is assumed. First, a portion of the loadbearing grains dissolves, corresponding to the amount of cement grains that hydrate. This dissolution leads to a load loss in the grains, ΔP_g, that is the previous load reduced by the ratio of the volume loss during the time increment and the volume at the previous time step, t_1. The next step is that this incremental load loss is re-distributed to the volume of loadbearing hydration products that were present at the previously load step, v_{h1}, causing a theoretical displacement, δ. However, because the test being simulated is a relaxation test, in the third step, this displacement is corrected by applying a fictitious tensile load to the entire width of hydration products that have formed by the end of the time increment, v_{h2}. This third step implies that newly formed hydration products do in fact carry load, representing a distinct difference in approach from the solidification model presented above. The tensile load applied to maintain a constant overall displacement of the specimen is the overall load loss associated with the time step.

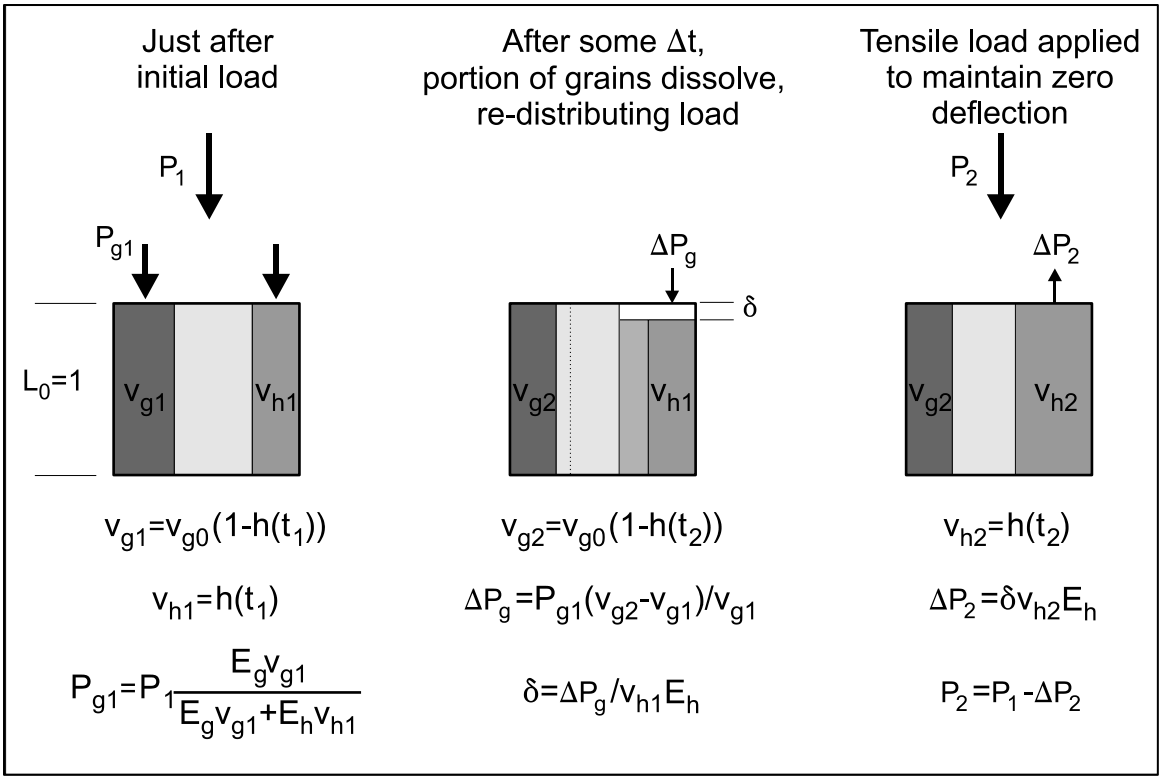

Figure 6.2 – Load re-distribution in a solidification-dissolution relaxation model. As the width of the loadbearing cement grain layer narrows due to hydration, the load loss, assuming no change in length of the cement, is re-distributed to the loadbearing hydration products causing compressive strain. This strain is then negating by the application of a tensile load to the total current volume of loadbearing hydration products. The total load carried after the redistribution is calculated and is slightly lower than at the previous time step.

Using the sequence of steps outlined above and assuming that a load, P_1, is applied at time, t_1, the initial load on the cement grains can be written as

$$P_{g1} = P_1 \frac{E_g v_{g1}}{E_g v_{g1} + E_h v_{h1}} = P_1 \frac{E_g (1 - h(t_1))}{E_g (1 - h(t_1)) + E_h h(t_1)}, \tag{6.1}$$

where E_g and E_h are the Young's moduli of elasticity for grains and hydration products, respectively, and $h(t)$ is the function defining the hydration curve. Recognizing that throughout the time history, the stress in the cement grains can be written as P_g/v_g, and remains constant, the load at any particular time step, t_i, with $i > 1$, can be written as

$$P(t_i) = P(t_{i-1}) - \Delta P_{hi} = P(t_{i-1}) - P_{g1} \frac{h(t_i) - h(t_{i-1})}{v_{g1}} \frac{h(t_i)}{h(t_{i-1})}, \tag{6.2}$$

where variables are as previously defined.

The relaxation model defined by Equations (6.1) and (6.2) was implemented using values obtained in the beam testing presented in Section 1.1. The Young's modulus of the cement paste, not determined by the current research, was assumed to be 118 GPa. For the paste, the Young's modulus was approximated based on the asymptotic value obtained from previously stressed beams as 20GPa. Though this value is significantly different than that seen in past research, it more closely matches the cement paste tested in the current research. For the model, the hydration curve corresponding to the curve fit to previously loaded samples in Figure 3.4 was chosen. The model assumed a load at 1 day when hydration was 32.5 per cent complete. Assuming that 100 per cent of solidified hydration products and 100 per cent of cement grains can bear load, the initial area of grains bearing load was 30 per cent and the initial area of hydration products bearing load was 18 per cent, both as proportions of the total sample area. Using time increments of 0.05 days, the total load carried by the specimen was tracked through time, as charted in Figure 6.3, with the load normalized to the initial application. For reference, the 1st cycle beam relaxation fit is superimposed in the figure.

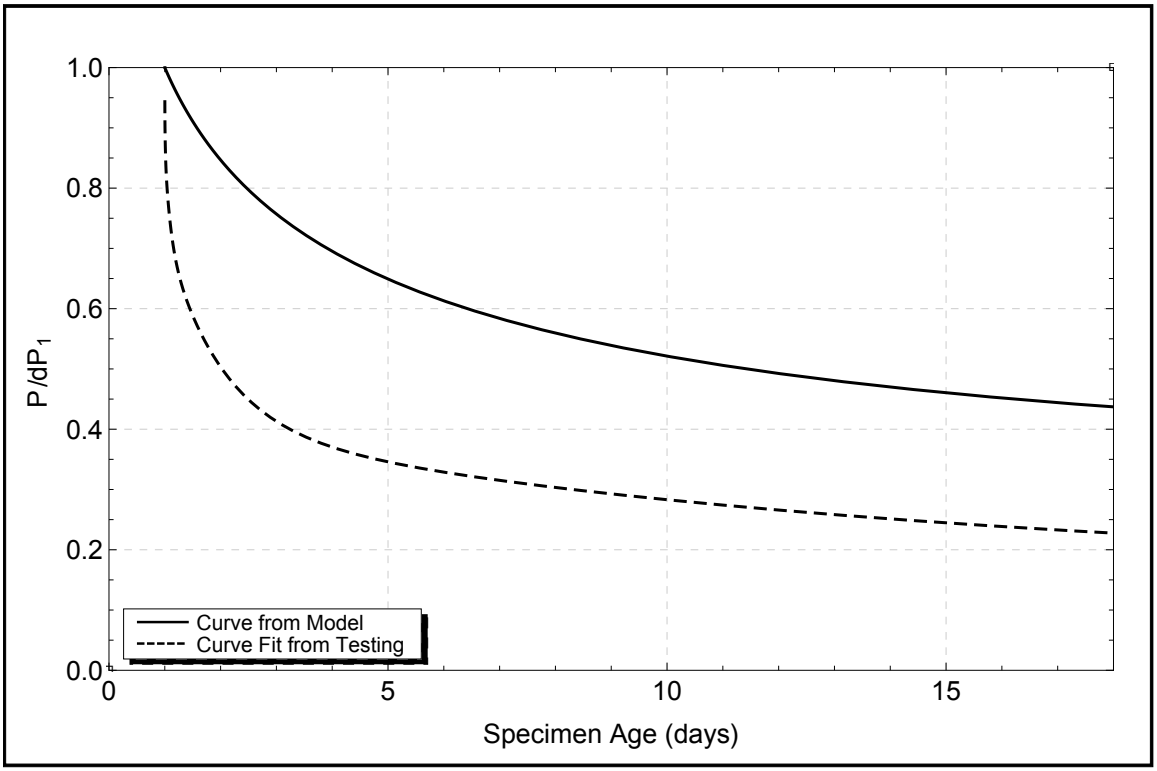

Figure 6.3 – Example load relaxation considering load redistribution due to cement grain dissolution. P is the load carried as a function of time and dP_1 is the load applied at time 1. The solid curve from the proposed model is of similar shape and trend as that derived from lab testing data. Refinement of the model or variation of parameters used for the model could likely close the gap between the two curves.

When considering that the model being presented is based solely on mechanics of the cementitious materials without the use of any fit parameters, the correlation between the predictive model and observed beam relaxation is surprisingly good. As should be expected, the model under-predicts relaxation behavior, indicating the likely need to consider additional mechanisms responsible for load relaxation. Some of these possible mechanisms are discussed in Sections 6.2.2 through 6.2.4 below. It should be noted that the relaxation curve produced by the model is highly dependent on the choice of hydration curve. As will be discussed in Section 6.3, there are a number of ways to derive this curve from testing performed within the current research.

Of further note is the marked difference between beam relaxation and cylinder relaxation, as first discussed in Section 3.1.4. Given the strong alignment of the beam relaxation and model curves, it is likely that beam testing gives a more

accurate representation of actual relaxation behavior than does the cylinder testing protocol used. It is possible that the cylinder testing method is inherently flawed, whether due to imperfections in the testing frame violating the conditions of a true relaxation test, or to operator error.

6.2.2 Stress-Induced Dissolution

Research conducted by Li et. al considers additional dissolution of cement grains due to applied stresses, as determined by finite element analysis of a complex structure of hydrating cement (Li et al. 2015). The research predicts a threshold of stored mechanical energy within the grains that, when reached, would result in dissolution of the grain. Given that this energy is the product of stress and strain, the stress-induced dissolution would be most likely to occur at the highest values for stress and strain, e.g., at the compressive and tensile faces of a beam. When applying this concept to the current model being considered, it should be expected that load relaxation would occur more quickly, closing the gap between the model and observed relaxation, as previously shown in Figure 6.3. Note that at least some of this acceleration was likely accounted for through the use of the previously-loaded hydration curve but without further investigation and expansion of the model, there is no way to determine exactly how much additional acceleration could be expected.

Not yet included in research by others is the potential for dissolution of hydration products due to applied stresses. Considering a beam cross-section in relaxation, any load no longer being carried by cement grains due to dissolution is re-distributed to adjacent hydration products. If these, too, have a threshold at which they are dissolved, additional micro-scale deflections would occur in the model and need to be corrected by the application of a load in the opposite direction. This mechanism would also tend to accelerate load relaxation. Because the dissolution is associated with a threshold value, the acceleration would be most pronounced at early time increments when stresses are at their highest values. Once a sufficient portion of the initial stresses is relieved, stress-induced dissolution should no longer occur. However, due to the non-constant distribution

of stresses in grains and hydration products, it is possible that dissolution will continue to occur, albeit much more slowly.

To this point, the discussion of dissolution has been limited to the effects on the mechanical behavior of the material. However, as should be evident from the discussion of the hydration process, the mechanical properties are directly linked to chemical reactions within the material. Thus, stress-induced dissolution should also affect the chemical composition of the material, as measured by various tests, including TGA and XRD. For purposes of discussion, it is assumed that the baseline composition, i.e., the composition of a cement paste sample not subjected to stress, is known. Therefore, the effects of dissolution can be considered relative to this baseline.

In a beam specimen, if the rate of hydration of the cement paste were independent of stress, the mass percentage of any particular species, whether hydrated or not, should be constant from the compressive face to the tension face. With the introduction of stress-induced dissolution of cement grains, the concentrations of unhydrated products should be lower at the tensile and compression regions (stress dissolution is independent of sign). And, the percentage of hydration products should be higher at the stressed faces. At the neutral axis, where applied stress is zero, there should be no difference between the baseline concentrations and the beam specimen concentrations. As dissolution is a function of the product of stress and strain and has a threshold value, it would be expected that the trend of species percentages would be at a flat line of 1 within the middle portion of the beam and following a quadratic curve at the faces, when normalized to the baseline concentrations. If the dissolution of hydration products is then considered, the distribution of concentration changes. At the stressed faces, these products would be dissolved, lowering the tails of the upward curve in the trend line and spreading the tails toward the middle as stresses re-distribute.

The trends described above do not correlate directly with the chemical results presented in Section 4. Considering first the alite content presented in Figure

4.23, cement grain content at stressed faces is less than 1, as would be expected, but the neutral axis also shows an increased rate of hydration. The trend curve, rather than having tails, is nearly linear with the highest rate of hydration at the compressive face and lowest at the tension face. This trend cannot be explained by dissolution alone. In comparing the two graphs for calcium hydroxide content, TGA results depicted in Figure 4.9 and XRD results in Figure 4.24, a similar discrepancy is observed. Although the concentration of the hydration product is greater than 1 at the stressed faces, it is also greater at the neutral axis. The trend is relatively flat in all five considered regions other than at the compressive face, which shows a decreased concentration of CH in both sets of results. The third comparison of prediction to actual can be made by examining Figure 4.14. The mass percentage lost in the 500 to 900°C range, attributable to calcium carbonate and/or other hydration products, generally shows the trend that would be expected, a ratio near 1 at the neutral axis and curved upward at the stressed faces.

When considering all the chemical compositions as a whole, there are three potential explanations for the behaviors observed. The first is the possibility that some hydration products, such as calcium hydroxide, are more susceptible to stress-induced dissolution than are others, such as calcium carbonate. Incorporation of various hydration products and their individual properties is beyond the scope of the rudimentary model presented above. However, if the properties and relative proportions of each product were known, the model could be expanded to account for dissolution and load re-distribution amongst the various products.

Secondly, the graphs discussed above indicate accelerated hydration at the neutral axis. This tendency cannot be explained by the dissolution and load re-distribution model presented. Rather, additional focus on the precipitation phase of the hydration process must be explored. Although there has been little to no work to date examining the formation of hydration products while under varying stress, precipitation in metals while subject to mechanical stresses has been extensively studied and published. One such characterization examines the

kinetics and thermodynamics of the dissolution-precipitation process in the general case of a two-phase crystalline solid (Johnson 1987). Johnson's research concludes that externally applied stresses affect both the growth rate and shape of precipitating crystals. The actual trends depend on the properties of the crystals considered. However, if it is assumed that a precipitate such as calcium hydroxide has a higher growth rate in zero stress conditions, this could explain concentration ratios higher than 1.0 at the neutral axis in the beams currently being considered. Confirmation of this assumption is beyond the scope of the current research.

The third item of note in the chemical composition trends is the slight asymmetry seen in calcium hydroxide and alite contents. The trends suggest that there is a difference in composition in tensile and compressive regions. As discussed in Section 6.1, it is possible that there is a difference between the structures of the two regions due to microcracking or other physical changes. These changes would likely also affect the deposition of hydration products. A second possible explanation for the asymmetry involves actual mass flow due to pressure differentials in trapped pore fluids, as discussed below.

6.2.3 Fluid Flow

The model presented above includes a region of fluid trapped within permeable boundaries, as might be expected in an evolving cement paste matrix. Upon application of an external load, the boundaries, comprised of cement grains and hydration products, would deform consistent with their elastic properties. This would therefore pressurize any trapped fluid in accordance with the bulk modulus of the fluid. If the boundaries are then held to a constant geometry, and adjacent cells contain a lower pressure fluid, such as air or cells subject to the stress gradient associated with beam bending, the trapped fluid will flow from the high pressure toward the lower pressure through capillaries in the paste. The poromechanics of this fluid flow is the topic of past and ongoing research by many and will not be repeated here (Grasley et al. 2006c; Leung and Grasley

2012; Rahman and Grasley 2014; Ulm et al. 2004). Rather, the concept of fluid flow will be considered as may relate to beam relaxation.

In considering one-dimensional flow, with fluid leaving the compressive face and flowing toward the tensile face, pressure in the cells in the compressive region are reduced and those in the tension region increased. Thus, the load carried by these cells, and their contribution to the overall moment capacity of the beam, are reduced. This flow is a function of the pressure differential between the cells, the permeability of the surrounding medium, and time. Eventually, all fluid would come to an equilibrium state where its pressure, and contribution to the beam capacity, is zero. For flow within larger pores or other gaps in microstructure toward pockets of air or outer surfaces, the flow is rapid and likely accounts for the sharp drop in load seen in the first 100 seconds of beam relaxation, as depicted in Figure 3.7. However, flow through smaller openings could cause much longer-term relaxation depending on the size of the capillaries. Given that the bulk modulus of water is an order of magnitude smaller than the Young's modulus of cement paste and grains, the magnitude of potential relaxation is likewise smaller than that possible due to dissolution. However, unlike the mechanisms discussed above, the relaxation associated with fluid flow could induce asymmetry in the load distribution through the section of the beam.

If the pore fluid trapped within a cement paste has the same bulk modulus in tension and compression, with no phase changes, relaxation caused by fluid flow should be symmetric across a beam section. However, because the pore fluid also contains dissolved species, the flow from compression to tension regions moves mass from one region to the other. The loss of mass in the compressive region would lead to a drop in concentration of the solution, slowing the rate of deposition of hydration products. Conversely, the influx of mass in the tensile region would increase the amount of hydration products. This mass flow could explain the general trend of the concentration of calcium hydroxide as discussed above. However, this trend, if present, is relatively minor and does not explain the dramatic difference seen in relaxation of beams subject to strain reversal. It is

likely that some combination of chemical differences and physical changes to the structure, such as microcracking, is responsible for the anomalous behavior.

6.2.4 Temperature Effects

In Figure 3.15, the effect of pore fluid viscosity of the trapped fluid on the relaxation of beam specimens was presented. It was seen that this viscosity change alone was insufficient to explain the difference in relaxation rates of beams tested at room temperature and those tested at elevated temperatures. Thus, other effects of the higher temperatures must be considered. As presented above, dissolution of cement grains, and potentially hydration products, is a function of stored energy. Though the work of Li et al., as discussed in Section 6.2.2, has focused on mechanical energy, the same principles apply to thermal energy applied to the hydration process. Past work has determined that the rate of hydration is significantly influenced by varying temperature (De Schutter and Taerwe 1995). Curves presented in that work indicate a non-linear relationship between temperature and the rate of hydration within the first several days. In terms of the current model being considered, cement grains would dissolve more quickly, loads would be re-distributed to hydration products more quickly, and overall loads would relax more quickly. This is in agreement with the trends in the relaxation curves seen in Figure 3.15. Though the intent of the higher temperature testing was to examine the possible influence of fluid viscosity, the additional influence of higher rates of dissolution make it difficult to discern which mechanism is which based on the data.

6.2.5 Viscoelastic Changes to Material Properties

In other research, there have been attempts to incorporate material property changes, due to viscoelasticity, into models for overall response (Li et al. 2015). For the model proposed herein, response is totally unaffected by changes to the modulus of elasticity of the hydration products. The model assumes that the initial load application is split to the two layers based on the stiffness of the two materials. However, after this initial application, the stress in the cement grain

layer is assumed to remain constant with volume losses only occurring in the width of the layer. Therefore, the load carried by the grains is no longer a function of the stiffness of the layers but only the degree of hydration. The stiffness of the hydration products affects the stress distributions within those products, but does not affect the overall load carried by the products.

Were the cement grains assumed to have viscoelastic properties, or if their volume loss was associated with shrinkage in the height of the model that would then need to be corrected by application of a tensile load, relaxation rates would likely accelerate, potentially coming closer to the curve generated from test results. However, this refinement would require assumptions for individual component behavior beyond information currently available.

6.2.6 Limitations of the Model

In addition to the shortcomings of the proposed model as discussed in paragraphs above, there are several observed phenomena that the model does not capture nor predict. The first is the effect of multi-dimensional stresses. For current purposes, beam loads have been considered as the sum of individual uniaxial elements placed along the height of the beam. However, due to the Poisson effect, it is likely that off-axis stresses would occur and could potentially influence the rate of beam relaxation. Second, the model as presented does not account for shrinkage, whether through drying or self-desiccation. Depending upon the magnitude of this shrinkage, a forced constant displacement could induce stresses, dissolution, and/or fluid flow not currently included in the model. Lastly, the model, as designed, does not explain viscoelastic responses in cement paste that has hydrated more fully. For example, were the same model run with a load applied at 4 days rather than 1 day, load relaxation would be dramatically under-predicted as compared to the "D" specimen relaxation presented in Figure 3.5. For these and other reasons, it is noted that though the model is conceptually valid and can offer the frameworks for future development, and despite its good correlations to most of the beam relaxation data collected, several deficiencies would need to be addressed before any widespread use.

6.3 Comparison of Degree of Hydration between Methods

In Section 3.1.2, the Young's modulus of elasticity for a cement paste beam was calculated as the eventual modulus of the paste multiplied by the degree to which the beam had hydrated. For purposes of comparing one beam to another or one loading on a beam to another, and when limited to the assumptions of the solidification model, Equation 2.9 is likely sufficient to produce appropriate fit curves to data. However, the equation does not consider that the calculation of E from a beam bending test has the implied assumption of a constant value for I, the moment of inertia. Due to volumetric changes during chemical shrinkage, a better assumption would be that I is also equivalent to some eventual value multiplied by the degree of hydration. Thus, for a beam test during the initial loading at some age, t, the equation for Young's modulus becomes

$$E = E_{\infty}\left[0.938\left\{1-\exp\left\{-\left[a(t-b)^{c}\right]\right\}\right\}\right]^{2}, \tag{6.3}$$

where variables are as previously defined. Using this equation as the fit to beam bending, a truer hydration curve can be generated and used to compare to that calculated from other test methods.

Using the same logic, it may seem appropriate to produce the accelerated hydration curve for beam samples previously loaded, such as the curve previously presented in Figure 3.4. However, that curve was based on the assumption that stresses started at time 0, which is not true. For comparison purposes, the fit was likely sufficient. However, if the effects of acceleration of the hydration process, as explained in Section 6.2.2, were to be incorporated, the fit curve would need to be conducted in two pieces. The first piece would be fit to data up to the time of load application and the second curve, showing an accelerated rate of hydration, would be fit to data after the time of load application. If the only effect of stress were to increase the rate of dissolution, the two fit curves to the E values would converge to E_{∞}. As seen with the data presented in Figure 3.4, this is not the case. Thus, stress likely induces other physical changes in the structure of the specimen, raising the effective stiffness of the

material, and any hydration curve fit to the data would not be directly comparable to other test methods.

With these modifications and provisions, the fit curve parameters for degree of hydration using the beam tests, TGA, XRD, and micro-CT were compared, as shown in Table 6.1. The predicted degree of hydration at 28 days is given for reference. Note that the fit parameter, *b*, was allowed to vary up to a value of 0.01 days, for all curves. The hydration curves using these parameters are presented in Figure 6.4.

Table 6.1 – Comparison of parameters for degree of hydration from all testing methods

Test Method	a[1,2]	b[3]	c	R^2	h(28)
Beam tests – gross section	1	0.01	0.280	0.985	92.1%
Beam tests – variable I	1	0.01	0.116	0.984	77.0%
TGA – 110 to 400 °C	0.738	0.01	0.397	0.989	93.8%
TGA – 400 to 500 °C	0.888	0.000	0.157	0.987	77.7%
TGA – 500 to 900 °C	0.734	0.000	0.053	0.991	58.3%
TGA – 900 to 1000 °C	0.399	0.004	0.188	0.981	52.6%
XRD – alite	0.354	0.000	0.130	0.983	42.0%
XRD – CH	0.021	0.000	0.363	0.887	6.8%
XRD – hyd prod	0.134	0.000	0.332	0.911	33.3%
Micro-CT	0.325	0.01	0.234	0.951	50.8%

[1]a, b, and c are fit parameters where b represents a time delay before the onset of hydration.
[2]Constrained to a maximum value of 1.
[3]Constrained to a maximum value of 0.01.

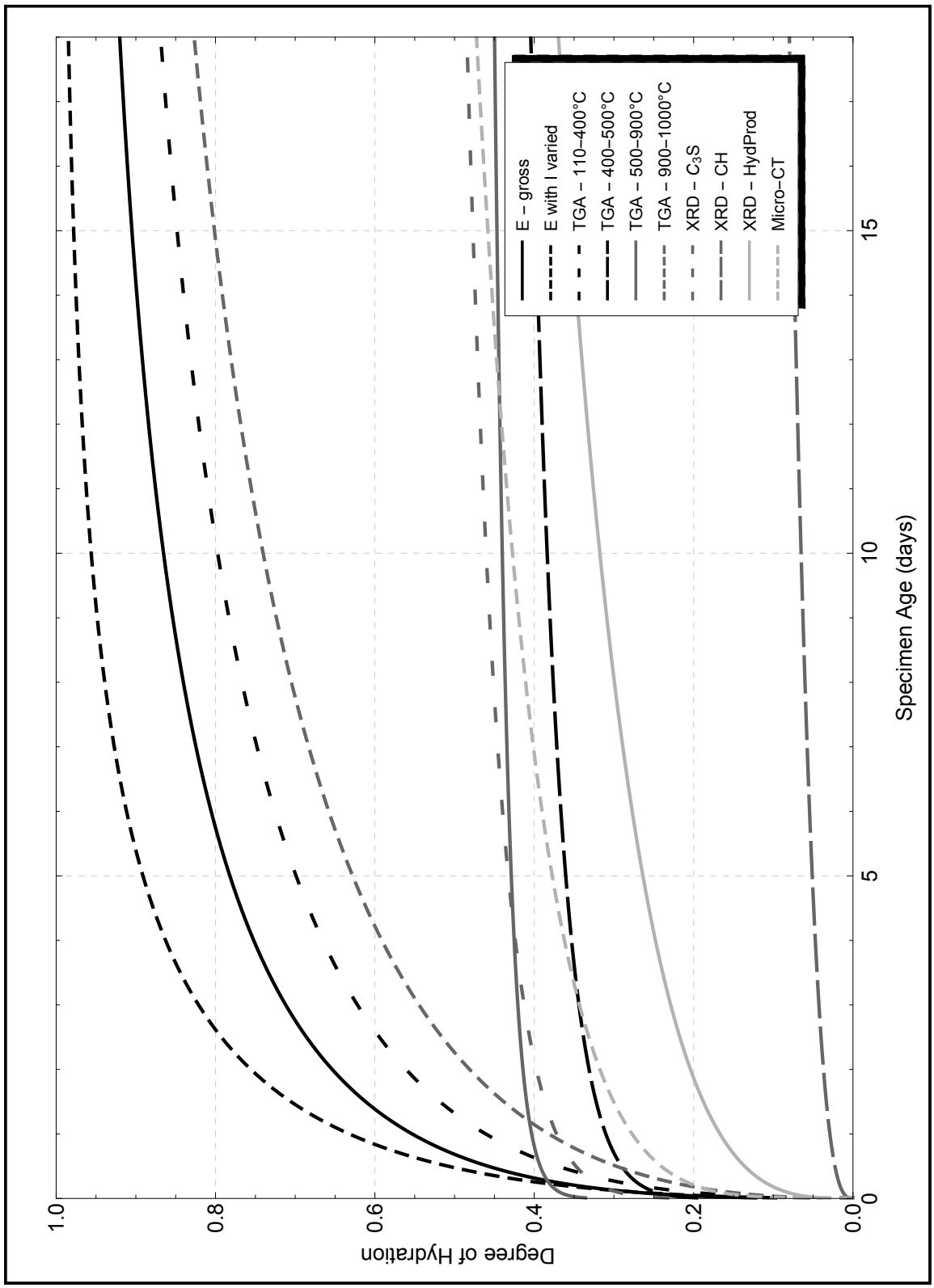

Figure 6.4 – Comparison of degree of hydration curves from all testing methods: Young's modulus of elasticity, TGA, XRD, and micro-CT. Each curve was derived based on equations presented in previous sections and in theory should all line up to a single curve.

Consideration of the hydration curves presented above reveals a high degree of variation, depending on the test method. The curve associated with the Young's modulus of elasticity using the gross section properties matches what might be expected based on typical strength development curves used for concrete (which are also based on gross section properties). When allowing the section properties to vary, the curve generated using *E* values shows a faster stiffness development with a long slow progression toward the asymptotic value. The results from TGA, in the 400 to 500 °C range – the range associated with calcium hydroxide degradation, are very nearly the same as that from beam bending. In contrast, the curve corresponding to calcium hydroxide content as determined by XRD, is dramatically different than most other curves, showing a nearly constant and low value of hydration starting almost immediately. Due to the differing rates of chemical reactions of individual components, a high degree of variability throughout the remaining curves should be expected. However, based on this variability, it is difficult to determine the best ways to estimate the overall degree of hydration using any method other than traditional strength / stiffness testing.

It is interesting to note the *b* values listed in Table 6.1. Best fit curves typically have a delay in development of hydration products, indicating that cement paste does have a dormant phase before hydration occurs. For purposes of the current research, this dormant phase was limited to 0.01 days, approximately 14 minutes. However, based on the number of calculated values being at this limit, the dormant phase may in fact last longer.

6.4 Extrapolation to Concrete Behavior

Within this research, the microstructure of cement paste has been simplified to a series of parallel elements subject to uniaxial stress. Were this same method used to analyze concrete samples, the model depicted in Figure 6.1 would comprise only approximately 10 per cent of the total model with additional layers for coarse and fine aggregate comprising the other 90 per cent. Assuming the Young's modulus of elasticity of the aggregates is on the order of that of cement grains, the initial load distribution to the cement grains would be only approximately 5 per cent of the total.

At the end of all grain dissolution, the load carried by the hydration products would also be only approximately 5 per cent of the total. Therefore, it is reasonable to approximate that in concrete, relaxation due to dissolution and load re-distribution would be approximately 5 per cent of that seen in cement paste. Likewise, in mortars, it would be expected that relaxation is significantly less than that in cement pastes, as briefly presented in Figure 3.18. However, due to the complexities of the geometry of any given concrete or mortar cross-section, in all likelihood, the parallel model is an over-simplification of the material and a more complex, two-dimensional analysis would be required to predict behavior.

To more accurately predict the effects of paste properties on concrete behavior, a model incorporating a combination of elements in parallel and in series could be developed based on the same principles presented here. Past work has defined the boundaries of composite behavior as the region formed between the assumption of all elements in series and the assumption of all elements in parallel (Christensen 1979). These boundaries can be narrowed using principles of variable stress and strain (Hashin and Shtrikman 1962; Hashin and Shtrikman 1963) and/or through the consideration of spatial three-point correlation functions (Beran 1965). Other refinements to the composite model might include the consideration of the composite as spherical rather than layered (Hashin 1962) or by consideration of the concrete as a 3-phase system (Christensen and Lo 1979). Regardless of the method, the work presented here can assist in the development of a more precise prediction of concrete behavior based on cement paste properties. Such development is beyond the current scope.

6.5 Recommendations for Future Research

As noted in various sections above, results of several of the test methods used show a high degree of variability. It is hoped that with additional replications of those methods, the variability in the results would decrease and a clearer indication of trends would be apparent. Specific areas of improvement include the use of a cement with known chemical composition such that TGA and XRD analysis techniques can be refined, the study of compressive relaxation at a slightly larger scale to eliminate

possible issues with the testing frame used, and a higher resolution micro-CT scanner that could more readily identify cement grain boundaries as well as potentially differentiate individual hydration products.

The results presented here represent only a limited set of testing parameters. Assuming that variations in applied load, temperature, and/or w:c ratio, parametric studies using some of the testing methods should be conducted to ascertain the relative influence of such variations. It is anticipated that all of the listed parameters would have significant effects on specific results but would lie within the general trends discussed above.

As the current research suggests a difference between tensile and compressive properties in relaxation, a new protocol using uniaxial specimens subject to each direction of stress could clarify the issue. Though there are challenges to setting up the testing protocol, the information gathered, including examining differences in chemical composition, could verify the reasons behind trends seen in the current research.

The beam testing conducted at varying temperatures was a minor part of this project, aimed specifically at identifying changes in relaxation rates brought about by changes in fluid viscosity. Given the lack of chemical testing of these specimens, and associated higher temperature, unstressed controls, the effects of fluid viscosity changes could not be readily separated from those due to higher dissolution rates due to thermal energy. Expanding this portion of the research to include the chemical analyses, and potentially more temperatures, would aid in this separation.

Given that the proposed solidification-dissolution model implies changes in stress at the micro scale, it could be insightful to conduct beam bending of larger specimens such that internal locations and exterior surfaces could be instrumented and monitored. Differences in properties in tensile and compressive regions should modify stress distributions in the cross-section, relocating the neutral axis to maintain equilibrium. Monitoring stresses and/or strains throughout the section may verify this evolution.

Beyond the elements of the scope of the current research, viscoelasticity of cement paste is still a largely unexplored topic. Additional testing, including both relaxation and creep, in uniaxial and bending specimens, should be conducted in hopes of refining models that can better predict long-term behaviors.

7. Conclusions

Based on the research and analysis presented herein, the following conclusions can be drawn regarding the effects of early age stress on the behavior of cement paste with a reasonable degree of engineering certainty:

1. *Stress accelerates the cement hydration process*. This trend was first inferred from the increased Young's modulus of elasticity when comparing previously stressed beams to those not previously loaded. In the chemical testing, the same characteristic would explain the decreased levels of alite and increased levels of hydration products in comparing beam specimens to control specimens. The level of hydration acceleration varied from test method to test method, ranging from approximately 10 to 40 per cent.
2. *Sustained load alters the manner in which cement paste, and therefore concrete, reacts to additional load*. This change is typically not accounted for in concrete design practice and may in some cases provide additional capacity while in others lead to unforeseen complications.
3. *Strain reversal in a loading history results in a significantly lower rate of relaxation than would otherwise be predicted*. This longer retention of applied loads could lead to unpredictable long-term performance. The reason for the difference remains unexplained.
4. *The solidification theory is insufficient to fully explain viscoelastic aging.* Significant differences in the relaxation rates between specimens loaded at 1 day and those loaded at 4 days show that aging functions in addition to or in lieu of solidification based aging should be incorporated into any prediction model. Such functions previously published may not be appropriate for use with cement paste analysis.
5. *Measuring the instantaneous Young's modulus of elasticity of virgin specimens may not be sufficient to predict global scale structural performance*. The presence of sustained load, regardless of sign or direction, leads to an apparent increase in stiffness of cement paste beams. This increase, as much as 17 per cent in the long

term, can have a significant effect on load distributions and deformations of large-scale structures

6. *In beam bending specimens, the chemical composition in tensile regions is likely different than that in compressive regions.* In the seven tests presented herein, the likelihood that the two regions were different varied from approximately 18 per cent to 99.7 per cent. The reason(s) for the differences is unknown without additional testing.
7. *The chemical composition at the assumed neutral axis of a beam bending specimen is different than in a control specimen not subjected to load.* If the hydration process in a beam is symmetric and stress sign independent, the two specimens should have the same chemical composition. In results of five of the seven test methods presented, the two were seen to be different at or below a 0.05 level of significance.
8. *Beam relaxation can likely be accurately, if not precisely, modeled using algorithms that account for the combination of dissolution of cement grains and solidification of hydration products with both assumed to be linear elastic*. The preliminary model presented here, using only mechanics of the materials and not using fit parameters, under-predicted observed relaxation with an error between approximately 20 and 30 per cent of load. As such, it could be used as a first approximation of anticipated behavior. However, with refinement of the assumptions and underlying equations of the model, better accuracy should be expected.
9. *The degree of hydration of a cement paste specimen can be determined using a number of methods but of the methods presented herein, mechanical testing appears to be the most accurate.* Certain portions of the TGA results showed good correlation with the degree of hydration as predicted by measurement of the Young's modulus of elasticity in a beam bending specimen. Curves derived using other methods, including the micro-CT and XRD results presented, varied widely.

7.1 Practical Implications

A typical pretensioned, prestressed beam or girder starts as pretensioned tendons in the lower portion of the cross-section surrounded by freshly placed concrete. After approximately 1 day, the tendons are released from their external anchorage and the beam is subject to a compressive force and negative moment (tension in the top and compression in the bottom), in addition to carrying its own weight once upward displacement occurs. After some period of time, the beam is placed on its permanent supports in the field and subject to additional dead and live loads, imparting positive moments. Though a beam in this configuration is rarely held to a constant displacement or subject to a constant load, the basic results of the current research do apply to its behavior.

With a post-tensioned member, the initial loading of a beam, floor, or girder would typically be a positive moment corresponding to self-weight and potentially other loads placed on the member prior to tensioning of embedded tendons. In the typical case, these tendons appear in the lower portions of the concrete cross-section and therefore, upon application of tension, the member is subjected to a negative moment. As with the pretensioned case, this causes a potential strain reversal in portions of the member and therefore, the results of the current research apply to its potential behavior.

Consider first that the relaxation testing conducted as part of this research predicts that nearly the entire applied load on the cement paste relaxes. This implies that the paste's ability to carry load degrades with time. If extrapolated to concrete behavior under an increasing displacement (creep), this implies that creep deformation is without bound. Though observed behavior shows this to not be true, currently used predictive models do tend to under-predict long-term creep deformation.

Second, consider that the evolution of cement paste under load is dependent upon stress magnitude and direction. In the design of pretensioned, prestressed beams, a single value for Young's modulus is used throughout the cross-section and determines the distribution of stresses and strains, which in turn dictates beam capacity. Though it

is likely that a 10 to 15 per cent increase in cement paste stiffness due to stress, as seen in this research, would only increase the capacity of the beam, other changes to the properties throughout the section likely lead to unpredictable distributions. Dependent upon the design, including tendon layouts and assumed losses, the variations in material properties could have positive or negative effects on the beam's serviceability.

Third consider the differing properties in tensile and compressive regions. Though some prestressed beams are designed to experience no tensile stresses at any point during their lifespan, with potentially increased creep or relaxation, actual stress conditions could lead to unexpected tensile regions. If these regions are more likely to relax and/or creep, whether due to changes in material properties or submicrocracking, cracking at the global scale is more likely. This cracking may be inconsequential in some designs but additional cracking in concrete tends to lead to corrosion of embedded items and eventual loss of capacity.

Finally, it should be expected that behavior of the beam after the strain reversal induced upon placement in service is not the same as that predicted based on single load-direction laboratory tests. A single model for creep and/or relaxation does not apply to all steps in the beam's actual load history and therefore, standard design practice, which tends to use a single model for loads before and after strain reversal, may not accurately predict actual beam behavior.

8. References

ACI (2008) ACI 209.2R-08 Guide for Modeling and Calculating Shrinkage and Creep in Hardened Concrete. American Concrete Institute, Farmington Hills, MI

Acker P (2004) Swelling, shrinkage and creep: A mechanical approach to cement hydration Materials and structures 37:237-243

Aichele CP et al. (2015) A comparison of automated scanning electron microscopy (ASEM) and acoustic attenuation spectroscopy (AAS) instruments for particle sizing Colloids and Surfaces A: Physicochemical and Engineering Aspects 479:46-51 doi:http://dx.doi.org/10.1016/j.colsurfa.2015.03.052

Al-Manaseer A, Prado A (2015) Statistical Comparisons of Creep and Shrinkage Prediction Models Using RILEM and NU-ITI Databases ACI Materials Journal 112:125-135 doi:http://dx.doi.org/10.14359/51686982

Alizadeh R, Beaudoin JJ, Raki L (2010) Viscoelastic nature of calcium silicate hydrate Cement & concrete composites 32:369-376

Allen AJ, Thomas JJ, Jennings HM (2007) Composition and density of nanoscale calcium-silicate-hydrate in cement Nature materials 6:311-316

Aono Y, Matsushita F, Shibata S (2009) Pore and nano-structural changes in C-S-H during drying at 50C vol 1. Taylor & Francis [Imprint],

Artioli G et al. (2010) X-ray diffraction microtomography (XRD-CT), a novel tool for non-invasive mapping of phase development in cement materials Analytical and bioanalytical chemistry 397:2131-2136

Bazant ZP (1977) Viscoelasticity of solidifying porous material - concrete J Eng Mech 103:1049-1067

Bazant ZP, Asghari A (1974) Computation of age-dependent relaxation spectra Cement and Concrete Research 4:567-579 doi:http://dx.doi.org/10.1016/0008-8846(74)90007-6

Bazant ZP, Hauggaard AB, Baweja S, Ulm F-J (1997) Microprestress-solidification theory for concrete creep. I:Aging and drying effects J Eng Mech 123:1188-1194

Bazant ZP, Hemann JH, Koller H, Najjar LJ (1973) Thin-wall cement paste cylinder for creep tests at variable humidity or temperature Materiaux et constructions 6:277

Bazant ZP, Li G-H (2008) Unbiased Statistical Comparison of Creep and Shrinkage Prediction Models ACI Materials Journal 105:610-621

Bazant ZP, Prasannan S (1989) Solidification theory for concrete creep I. Formulation J Eng Mech 115:1691-1703

Bazant ZP, Yu Q, Li G-H (2012a) Excessive Long-Time Deflections of Prestressed Box Girders. I: Record-Span Bridge in Palau and Other Paradigms Journal of structural engineering (New York, NY) 138:676-686

Bazant ZP, Yu Q, Li G-H (2012b) Excessive long-time deflections of prestressed box girders. II: Numerical analysis and lessons learned Journal of structural engineering (New York, NY) 138:687-696

Bazant ZP, Zubelewicz A (1988) Strain-softening bar and beam: Exact non-local solution International Journal of Solids and Structures 24:659-673 doi:http://dx.doi.org/10.1016/0020-7683(88)90015-7

Bentz DP, Jensen OM, Hansen KK, Olesen JF, Stang H, Haecker CJ (2001) Influence of Cement Particle-Size Distribution on Early Age Autogenous Strains and Stresses in Cement-Based Materials Journal of the American Ceramic Society 84:129-135

Bentz DP, Martys NS, Stutzman P, Levenson MS, Garboczi EJ, Dunsmuir J, Schwartz LM (1995) X-ray microtomography of an ASTM C109 mortar exposed to sulfate attack MRS proceedings 370:77-82

Beran M (1965) Use of vibrational approach to determine bounds for effective permittivity in random media Nuovo Cimento 38:772-782

Bergold ST, Goetz-Neunhoeffer F, Neubauer J (2013) Quantitative analysis of C-S-H in hydrating alite phases by in-situ XRD Cement and Concrete Research 53:119-126

Bernard O, Ulm F-J, Germaine JT (2003) Volume and deviator creep of calcium-leached cement-based materials Cement and Concrete Research 33:1127-1136

Beushausen H, Masuku C, Moyo P (2012) Relaxation characteristics of cement mortar subjected to tensile strain Materials and Structures 45:1181-1188 doi:http://dx.doi.org/10.1617/s11527-012-9825-2

Brouwers HJH (2004) The work of Powers and Brownyard revisited: Part 1 Cement and Concrete Research 34:1697-1716

Carol I, Bazant ZP (1993) Viscoelasticity with aging caused by solidification of nonaging constituent J Eng Mech 119:2252-2259

Chen JJ, Sorelli L, Vandamme M, Ulm F-J, Chanvillard G (2010) A Coupled Nanoindentation/SEM-EDS Study on Low Water/Cement Ratio Portland Cement Paste: Evidence for C–S–H/Ca(OH)2 Nanocomposites Journal of the American Ceramic Society 93:1484-1493 doi:10.1111/j.1551-2916.2009.03599.x

Chen JJ, Thomas JJ, Taylor HFW, Jennings HM (2004) Solubility and structure of calcium silicate hydrate Cement and concrete research 34:1499-1519

Choi SC, Oh BH (2010) New viscoelastic model for early-age concrete based on measured strains and stresses ACI materials journal 107:239-247

Chotard TJ, Boncoeur-Martel MP, Smith A, Dupuy JP, Gault C (2001) Application of X-ray computed Tomography for evaluating density-gradient formation during hydration of aluminous cement at the young age Key engineering materials 206:1863-1866

Christensen RM (1979) Mechanics of composite materials. Wiley,

Christensen RM, Lo KH (1979) Solutions for effective shear properties in three phase sphere and cylinder models Journal of the Mechanics and Physics of Solids 27:315-330 doi:http://dx.doi.org/10.1016/0022-5096(79)90032-2

Copeland LE (1956) Specific volume of evaporable water in hardened Portland cement pastes Journal of American Concrete Institute 52:633-640

Darcy H (1856) Les Fontaines Publiquies de la Ville de Dijon. Dalmont, Paris

De Schutter G, Taerwe L (1995) General hydration model for portland cement and blast furnace slag cement Cement and concrete research 25:593-604

Dias WPS, Khoury GA, Sullivan PJE (1990) Mechanical Properties of Hardened Cement Paste Exposed to Temperatures up to 700 C (1292 F) Materials Journal 87 doi:10.14359/1981

Downs RT, Hall-Wallace M (2003) The American mineralogist crystal structure database American Mineralogist 88:247-250

Drozdov AD (1998) Modelling an anomalous stress relaxation in glassy polymers (the Kitagawa effect) Mathematical and Computer Modelling 27:45-67 doi:http://dx.doi.org/10.1016/S0895-7177(98)00072-7

Drozdov AD (2010) Time-dependent response of polypropylene after strain reversal International Journal of Solids and Structures 47:3221-3233 doi:http://dx.doi.org/10.1016/j.ijsolstr.2010.08.001

Duan RF (2013) Concrete shrinkage and creep effect prediction model and the influence factors analysis Advanced Materials Research 756:2051-2054

Endo T (2009) Determination of the static elastic constant of concrete derived from the elastic constant of cement paste vol 1. Taylor & Francis [Imprint],

Evans M, Marchildon R, Hesp S (2011) Effects of Physical Hardening on Stress Relaxation in Asphalt Cements Transportation Research Record: Journal of the Transportation Research Board 2207:34-42 doi:doi:10.3141/2207-05

Fagerlund G (2009) Chemically bound water as measure of degree of hydration. Lund Institute of Technology,

Fischer I, Pichler B, Lach E, Terner C, Barraud E, Britz F (2014) Compressive strength of cement paste as a function of loading rate: Experiments and engineering mechanics analysis Cement and Concrete Research 58:186-200 doi:http://dx.doi.org/10.1016/j.cemconres.2014.01.013

Galitz CL, Grasley Z (2015) Effects of strain reversal on elastic and viscoelastic properties of early age cement paste beams Materials and structures Online open access

Goel R, Kumar R, Paul D (2007) Comparative Study of Various Creep and Shrinkage Prediction Models for Concrete Journal of Materials in Civil Engineering 19:249-260 doi:doi:10.1061/(ASCE)0899-1561(2007)19:3(249)

Gramespacher H, Meissner J (1995) Reversal of recovery direction during creep recovery of polymer blends Journal of Rheology (1978-present) 39:151-160 doi:doi:http://dx.doi.org/10.1122/1.550696

Grasley Z, Lange D, D'Ambrosia M (2006a) Internal relative humidity and drying stress gradients in concrete Materials and Structures 39:901-909 doi:10.1617/s11527-006-9090-3

Grasley ZC, Lange DA (2007a) Constitutive modeling of the aging viscoelastic properties of Portland cement paste Mechanics of time-dependent materials 11:175-198

Grasley ZC, Lange DA (2007b) The viscoelastic response of cement paste to three-dimensional loading Mechanics of time-dependent materials 11:27-46

Grasley ZC, Lange DA, D'Ambrosia MD, Villalobos-Chapa S (2006b) Relative Humidity in Concrete Concrete International 28:51-57

Grasley ZC, Leung CK (2011a) Desiccation shrinkage of cementitious materials as an aging, poroviscoelastic response Cement and concrete research 41:77-89

Grasley ZC, Leung CK (2011b) Quasi-static axial damping of poroviscoelastic cylinders J Eng Mech 137:561-570

Grasley ZC, Rajagopal K, Li X (2014) Theoretical basis for dissolution–induced viscoelastic and viscoplastic behavior of cementitious materials Cement & concrete composites In press

Grasley ZC, Scherer GW, Lange DA, Valenza JJ (2006c) Dynamic pressurization method for measuring permeability and modulus: II. cementitious materials Materials and structures 40:711-721

Grazulis S et al. (2009) Crystallography Open Database (COD) - an open-access collection of crystal structures Journal of applied crystallography 42:726-729

Grazulis S et al. (2012) Crystallography Open Database (COD): an open-access collection of crystal structures and platform for world-wide collaboration Nucleic Acids Research 40:D420-D427

H. Hubler MH, Wendner R, Bazant ZP (2015) Comprehensive Database for Concrete Creep and Shrinkage: Analysis and Recommendations for Testing and Recording Materials Journal 112 doi:10.14359/51687453

Haecker CJ, Garboczi EJ, Bullard JW, Bohn RB, Sun Z, Shah SP, Voigt T (2005) Modeling the linear elastic properties of Portland cement paste Cement and Concrete Research 35:1948-1960 doi:http://dx.doi.org/10.1016/j.cemconres.2005.05.001

Halleck PM, Grader AS, Roberts JW (2006) Four-Dimensional X-ray Microtomography Study of Water Movement During Internal Curing. United States

Harsh S, Shen Z, Darwin D (1990) Strain-rate sensitive behavior of cement paste and mortar in compression ACI materials journal 87:508-516

Hashin Z (1962) The elastic moduli of heterogeneous materials Journal of applied mechanics 29:143-150

Hashin Z, Shtrikman S (1962) On some variational principles in anisotropic and nonhomogeneous elasticity Journal of mechanics and physics of solids 10:335-342

Hashin Z, Shtrikman S (1963) Variational Approach to theory of elastic behaviour of multiphase materials Journal of mechanics and physics of solids 11:127-140

Hilaire A, Benboudjema F, Darquennes A, Berthaud Y, Nahas G (2014) Modeling basic creep in concrete at early-age under compressive and tensile loading Nuclear Engineering and Design 269:222-230 doi:http://dx.doi.org/10.1016/j.nucengdes.2013.08.034

Hong H-l, Fu Z-y, Min X-m (2003) Quantitative XRD analysis of cement clinker by the multiphase Reitveld method Journal of Wuhan University of Technology - Material Science Edition 18:56-59

Hossain AB, Weiss J (2004) Assessing residual stress development and stress relaxation in restrained concrete ring specimens Cement and Concrete Composites 26:531-540 doi:http://dx.doi.org/10.1016/S0958-9465(03)00069-6

Hu Q, Aboustait M, Ley MT, Hanan JC, Rose V, Winarski R (2014) Combined three-dimensional structure and chemistry imaging with nanoscale resolution Acta Materialia 77:173-182 doi:http://dx.doi.org/10.1016/j.actamat.2014.05.050

Huang J, Krabbenhoft K, Lyamin AV (2013) Statistical homogenization of elastic properties of cement paste based on X-ray microtomography images International journal of solids and structures 50:699-709

Igarashi G (2011) Relationships between mechanical properties and phase composition of hardened cement paste Nihon Kenchiku Gakkai kōzōkei ronbunshū 76:213-222

Inozemtsev UP (1995) Cement paste and concrete hardening under strain: I. Cement paste research Cement and concrete research 25:231-239

Jansons J, Aniskevich A, Pazhe L (2012) Analysis of reversible and irreversible strains in the creep of a nonlinear viscoelastic polymer Mech Compos Mater 48:209-216 doi:10.1007/s11029-012-9266-6

Jiang L, Zhang Y, Hu C, Li Z (2012) Calculation of elastic modulus of early-age cement paste Advances in cement research 24:193-201

Johnson WC (1987) Precipitate shape evolution under applied stress - thermodynamis and kinetics Metallurgical Transactions 18A:233-247

Jones CA, Grasley Z (2011) Short-term creep of cement paste during nanoindentation Cement & concrete composites 33:12-18

Jones CA, Grasley ZC, Ohlhausen JA (2012) Measurement of elastic properties of calcium silicate hydrate with atomic force microscopy Cement and Concrete Composites 34:468-477 doi:http://dx.doi.org/10.1016/j.cemconcomp.2011.11.008

Kar A, Ray I, Unnikrishnan A, Davalos JF (2012) Estimation of C-S-H and calcium hydroxide for cement pastes containign slag and silica fume Construction and Building Materials 30:505-515

Landis EN, Keane DT (2010) X-ray microtomography Materials characterization 61:1305-1316

Leung CK, Grasley Z (2012) Poromechanical dampling of cementitious materials Journal of materials in civil engineering 24:232-238

Li S, Yao T, Wang Y, Li H, Cheng J, Li L, Tian Q (2014) Determination of tensile creep and stress relaxation of concrete by ring test Applied mechanics and materials 584-586:1172-1175

Li X, Dong Y, Yang H (2012) Hydration performance and pore structure of fly ash-cement pastes Applied mechanics and materials 204-208:3867-3871

Li X, Grasley ZC, Garboczi EJ, Bullard JW (2015) Modeling the apparent and intrinsic viscoelastic relaxation of hydrating cement paste Cement and Concrete Composites 55:322-330 doi:http://dx.doi.org/10.1016/j.cemconcomp.2014.09.012

Lindeburg MR (2013) Mechanical Engineering Reference Manual for the PE Exam, Thirteenth Edition. Professional Publications, Inc., Belmont, CA

Ling Y (2012) Moisture Transport And Shrinkage In Concrete At Early Age Applied mechanics and materials 174:232-235

Lothenbach B, Winnefeld F (2005) Thermodynamic modelling of the hydration of Portland cement Cement and Concrete Research 36:209-226

Mabrouk R, Ishida T, Maekawa K (2004) A unified solidification model of hardening concrete composite for predicting the young age behavior of concrete Cement & concrete composites 26:453-461

Maia L, Azenha M, Faria R, Figueiras J (2011) Influence of the cementitious paste composition on the E-modulus and heat of hydration evolutions Cement and concrete research 41:799-807

Marsh BK, Day RL (1988) Pozzolanic and cementitious reactions of fly ash in blended cement pastes Cement and Concrete Research 18:301-310

Midgley HG (1979) The determination of calcium hydroxide in set portalnd cements Cement and concrete research 9:77-82

Milauer V (2010) Identification of viscoelastic C-S-H behavior in mature cement paste by FFT-based homogenization method Cement and concrete research 40:197-207

Mounanga P, Khelidj A, Loukili A, Baroghel-Bouny V (2004) Predicting Ca(OH)2 content and chemical shrinkage of hydrating cement pastes using analytical approach Cement and Concrete Research 34:255-265

Neville AM (1964) Creep of concrete as function of its cement paste content Magazine of concrete research 16:21-30

Otsu N (1979) A threshold selection method from gray-level histograms IEEE transactions on systems, man, and cybernetics 9:62-66

PANalytical (2006) HighScore Plus vol 2.2e. Almelo, The Netherlands

Pane I, Hansen W (2005) Investigation of blended cement hydration by isothermal calorimetry and thermal analysis Cement and Concrete Research 35:1155-1164

Parrott LJ (1973) Examination of the effects of age at loading upon the creep of hardened cement paste Magazine of concrete research 25:197-200

Plassais A, Pomies M-P, Lequeux N, Korb J-P, Petit D, Barberon F, Bresson B (2005) Microstructure evolution of hydrated cement pastes Physical Review 72:041401-041401 - 041401-041408

Powers TC, Brownyard TL (1946) Studies of physical properties of hardened Portland cement paste American Concrete Institute -- Journal 18

Promentilla MAB, Sugiyama T, Hitomi T, Takeda N (2008) Characterizing the 3D pore structure of hardened Cement paste with synchrotron microtomography Journal of advanced concrete technology 6:273-286

Promentilla MAB, Sugiyama T, Hitomi T, Takeda N (2009) Quantification of tortuosity in hardened cement pastes using synchrotron-based X-ray computed microtomography Cement and concrete research 39:548-557

Rahman S, Grasley Z (2014) A poromechanical model of freezing concrete to elucidate damage mechanisms associated with substandard aggregates Cement and Concrete Research 55:88-101 doi:http://dx.doi.org/10.1016/j.cemconres.2013.10.001

Rajagopal KR, Wineman AS (2004) A note on viscoelastic materials that can age International journal of non-linear mechanics 39:1547-1554

Scrivener KL, Fullmann T, Gallucci E, Walenta G, Bermejo E (2004) Quantitative study of Portland cement hydration by X-ray diffraction / Reitveld analysis and independent methods Cement and Concrete Research 34:1541-1547

Snedecor GW, Cochran WG (1989) Statistical Methods, Eighth Edition. Iowa State University Press,

Stepkowska ET, Blanes JM, Real C, Perez-Rodriguez JL (2005) Hydration products in two aged cement pastes Journal of Thermal Analysis and Calorimetry 82:731-739

Stock SR (2008) Recent advances in X-ray microtomography applied to materials International materials reviews 53:129-181

Stock SR, Naik NK, Wilkinson AP, Kurtis KE (2002) X-ray microtomography (microCT) of the progression of sulfate attack of cement paste Cement and concrete research 32:1673-1675

Sun T, Li X, Shui Z, Han W (2013) Effects of bending stress on the microstructure and properties of hydrated cement paste Electronic Journal of Geotechnical Engineering 18:5339-5352

Suter M, Benipal G (2006) Time-dependent behaviour of reacting concrete I: Mechanism and theory Mechanics of Time-Dependent Materials 10:51-62 doi:10.1007/s11043-006-9008-z

Taiy-In L, Chih-Yung H, Li IY, Jihperng L (2015) Stress and stress relaxation behaviors of multi-layered polarizer structures under a reliability test condition characterized by use of a bending beam technique Japanese Journal of Applied Physics 54:046601

Tamtsia BT, Beaudoin JJ, Marchand J (2004) The early age short-term creep of hardening cement paste: Load-induced hydration effects Cement & concrete composites 26:481-489

Taylor HFW (1990) Cement Chemistry. Academic Press, Ltd., San Diego, CA

Tazawa E-i, Miyazawa S, Kasai T (1995) Chemical shrinkage and autogenous shrinkage of hydrating cement paste Cement and Concrete Research 25:288-292 doi:http://dx.doi.org/10.1016/0008-8846(95)00011-9

TC-242 RTC (2015) RILEM draft recommendation: TC-242-MDC multi-decade creep and shrinkage of concrete: material model and structural analysis* Materials and Structures 48:753-770 doi:10.1617/s11527-014-0485-2

Ukrainczyk N, Ukrainczyk M, Sipusic J, Matusinovic T XRD and TGA investigation of hardened cement paste degradation. In: 11. International Conference on Materials, Processes, Friction, and Wear MATRIB'06, Vela Luke, Korcula, Zagreb, 2006. pp 243-249

Ulm FJ, Constantinides G, Heukamp FH (2004) Is concrete a poromechanics material - a multiscale investigation of poroelastic properties Materials and structures 37:43-58

Valenza JJ, Thomas JJ (2012) Permeability and elastic modulus of cement paste as a function of curing temperature Cement and concrete research 42:440-446

Venkiteela G, Sun Z, Shah S (2010) Observation of Cement Paste Microstructure Evolution Transportation Research Record: Journal of the Transportation Research Board 2141:75-81 doi:doi:10.3141/2141-13

Vichit-Vadakan W, Scherer GW (2003) Measuring permeability and stress relaxation of young cement paste by beam bending Cement and concrete research 33:1925-1932

Vidican I, Phan B, Farr J, Norton N (2008) XRF, XRD, and thermal analysis techniques for quantitative determination of portland cement and slag cement constituents Journal of ASTM International 5:1-10

Wendner R, Hubler MH, Bazant ZP The B4 model for multi-decade creep and shrinkage prediction. In: CONCREEP 2013, 2013. American Society of Civil Engineers, pp 429-436

Weszka JS (1979) Histogram modification for threshold selection IEEE transactions on systems, man, and cybernetics 9:38-52

Wittmann FH (2009) Heresies on shrinkage and creep mechanisms vol 1. Taylor & Francis [Imprint],

Wolfram (2012) Mathematica, 9.0 edn., Champaign, IL

Wyrzykowski M, Lura P (2014) The effect of external load on internal relative humidity in concrete Cement and Concrete Research 65:58-63 doi:http://dx.doi.org/10.1016/j.cemconres.2014.07.011

Yang W, Wang Y, Guo ZQ (2011) A Numerical Approach for the Simulation of Cementitious Materials Advanced materials research 284:11-18

Ylmén R, Jäglid U, Steenari B-M, Panas I (2009) Early hydration and setting of Portland cement monitored by IR, SEM and Vicat techniques Cement and Concrete Research 39:433-439 doi:http://dx.doi.org/10.1016/j.cemconres.2009.01.017

Zeng Q, Li K, Fen-chong T, Dangla P (2012) Determination of cement hydration and pozzolanic reactoin extents for fly-ash cement pastes Construction and Building Materials 27:560-569

Zhang SY, Kitching R (1987) Experimental relaxation behaviour of chopped-strand mat glass fibre reinforced polyester beams in three point bending Composite structures 7:59-76

Zhou Q, Beaudoin JJ (2003) Effect of applied hydrostatic stress on the hydration of Portland cement and C_3S Advances in cement research 15:9-16

Appendix A.1 – Beam Relaxation Data and Fit Curves

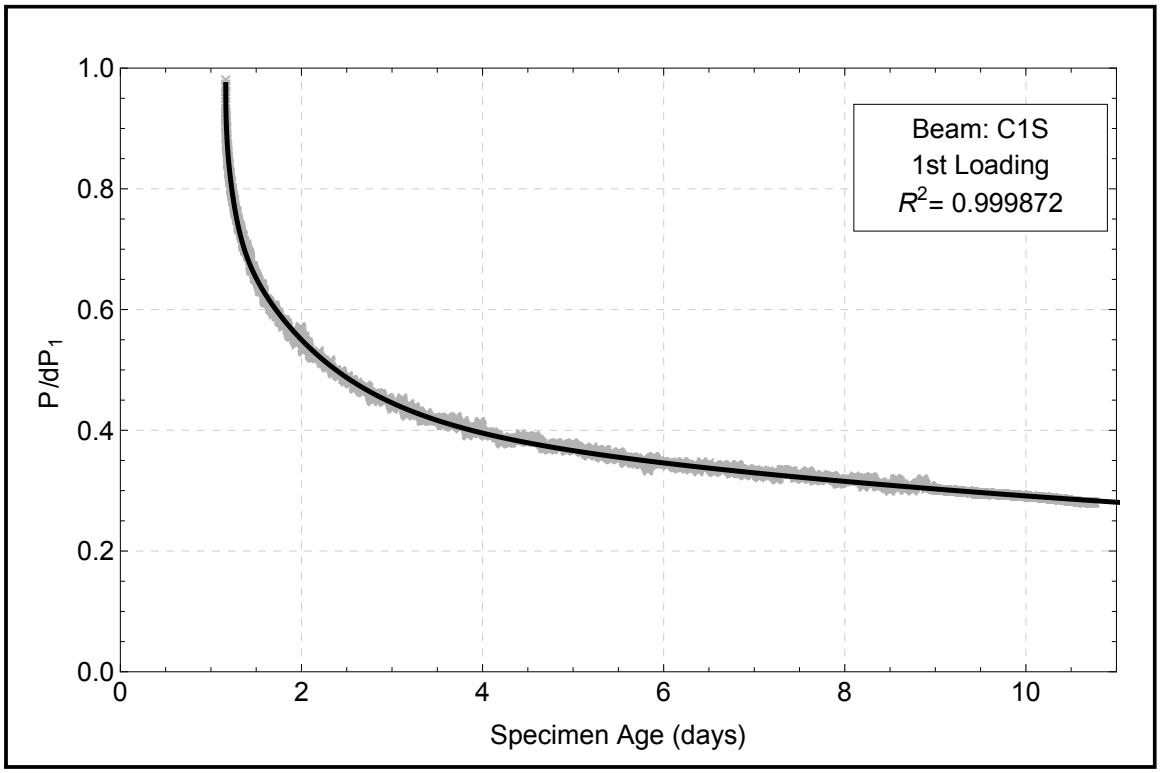
Beam: C1S
1st Loading
R^2= 0.999872
P /dP$_1$
Specimen Age (days)
0.0
0.2
0.4
0.6
0.8
1.0
0
2
4
6
8
10

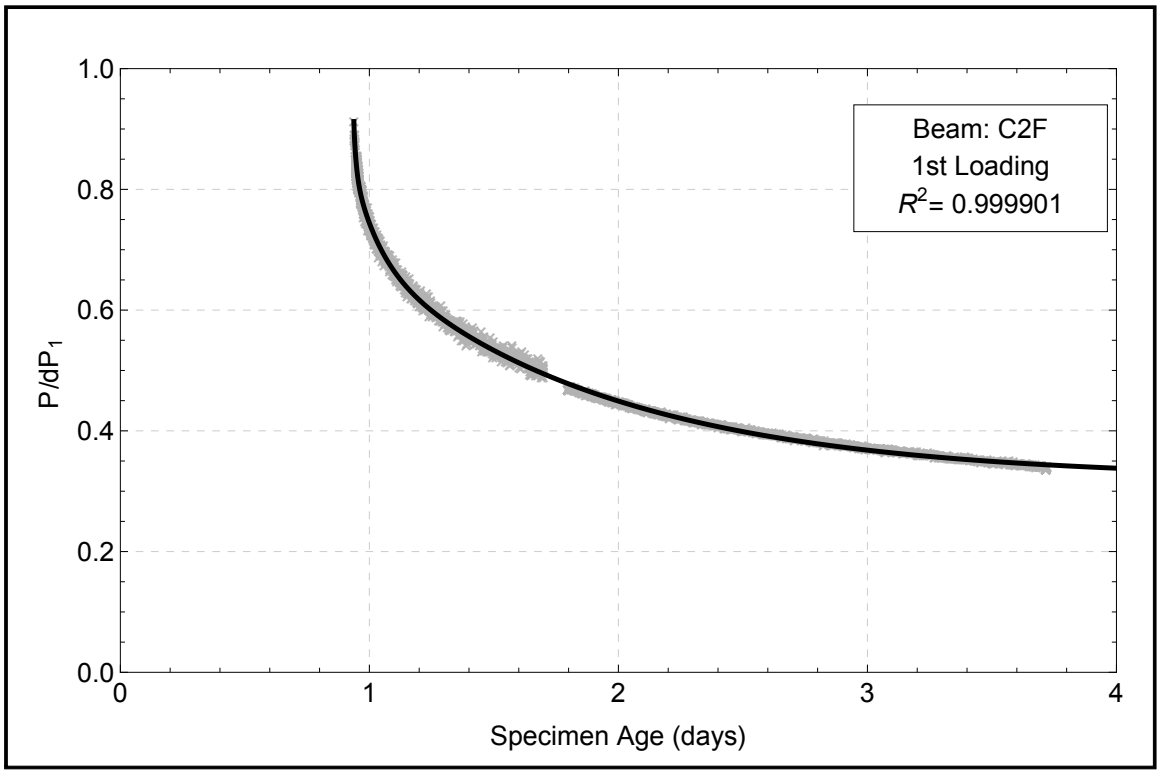
Beam: C2F
1st Loading
R^2= 0.999901
P /dP$_1$
Specimen Age (days)
0.0
0.2
0.4
0.6
0.8
1.0
0
1
2
3
4

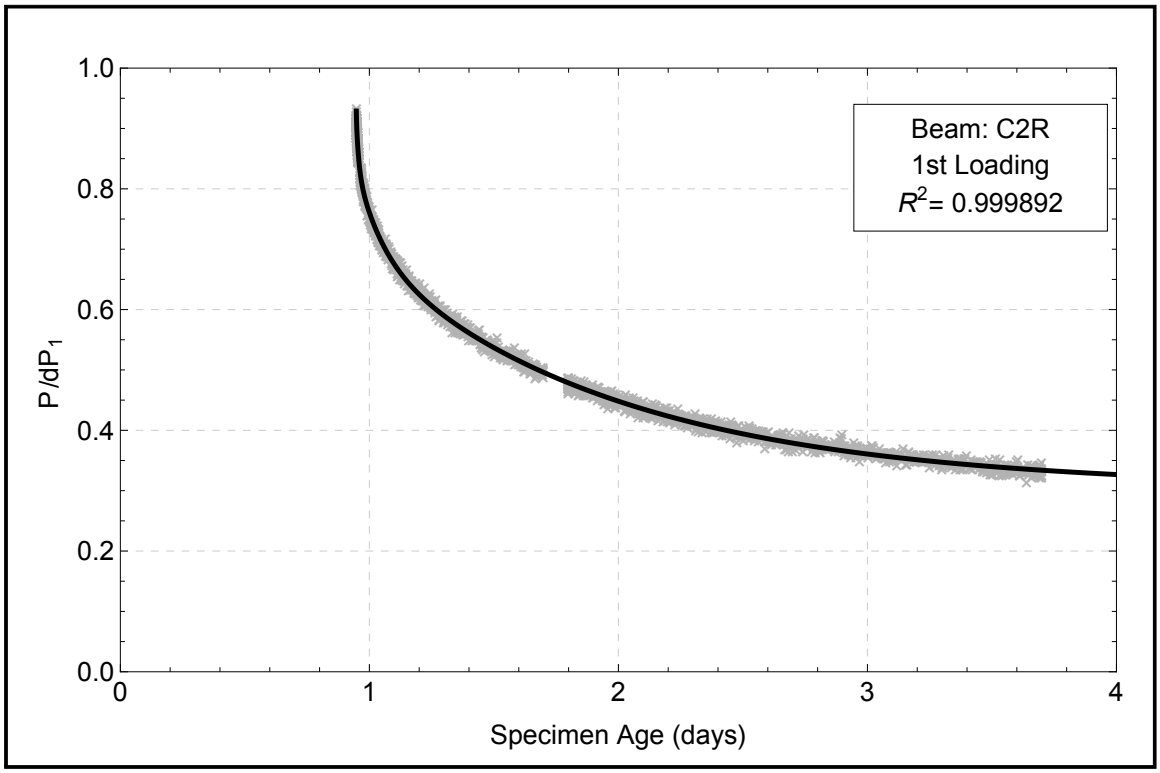
Beam: C2R
1st Loading
R^2= 0.999892
P /dP$_1$
Specimen Age (days)
0.0
0.2
0.4
0.6
0.8
1.0
0
1
2
3
4

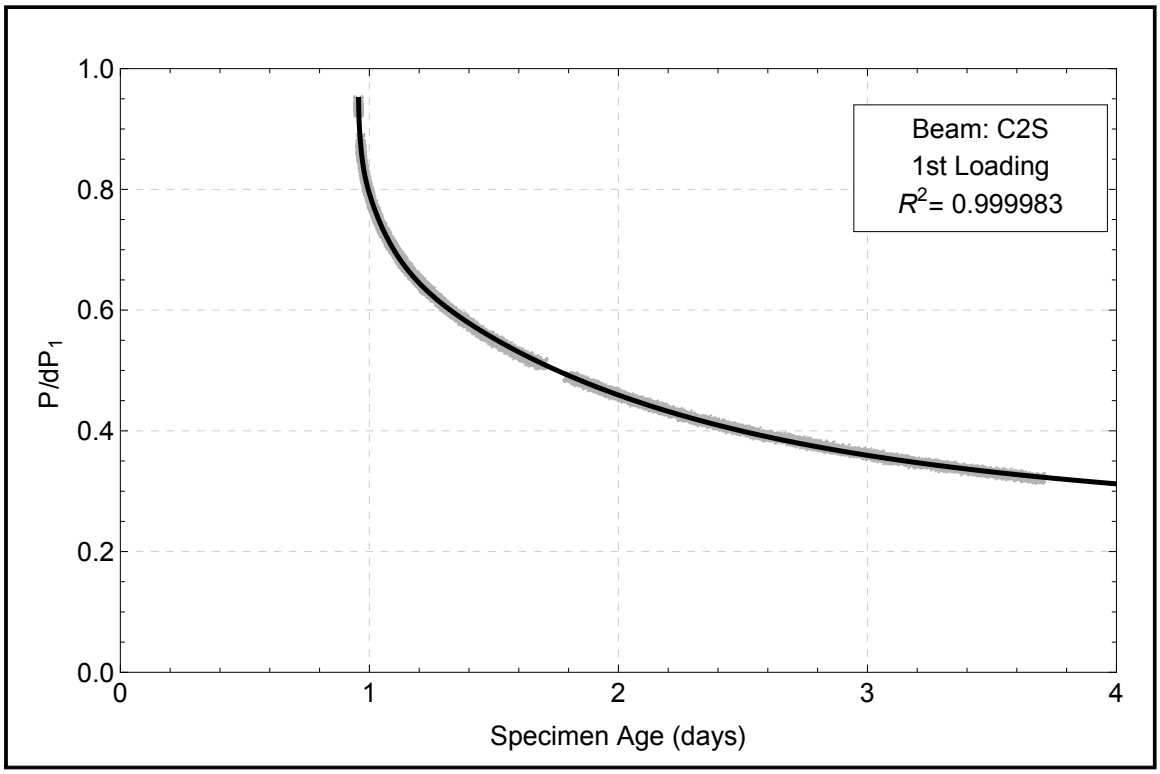
Beam: C2S
1st Loading
R^2= 0.999983
P /dP$_1$
Specimen Age (days)
0.0
0.2
0.4
0.6
0.8
1.0
0
1
2
3
4

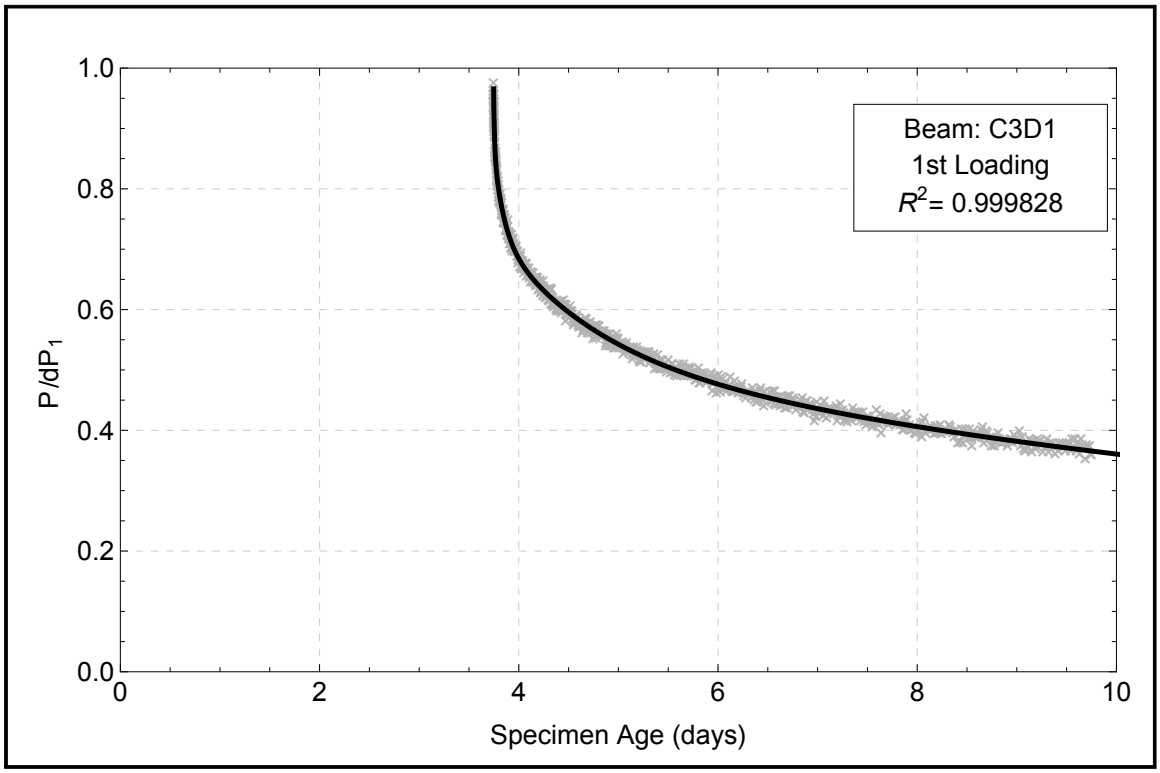
Beam: C3D1
1st Loading
R^2= 0.999828
P /dP$_1$
Specimen Age (days)
0.0
0.2
0.4
0.6
0.8
1.0
0
2
4
6
8
10

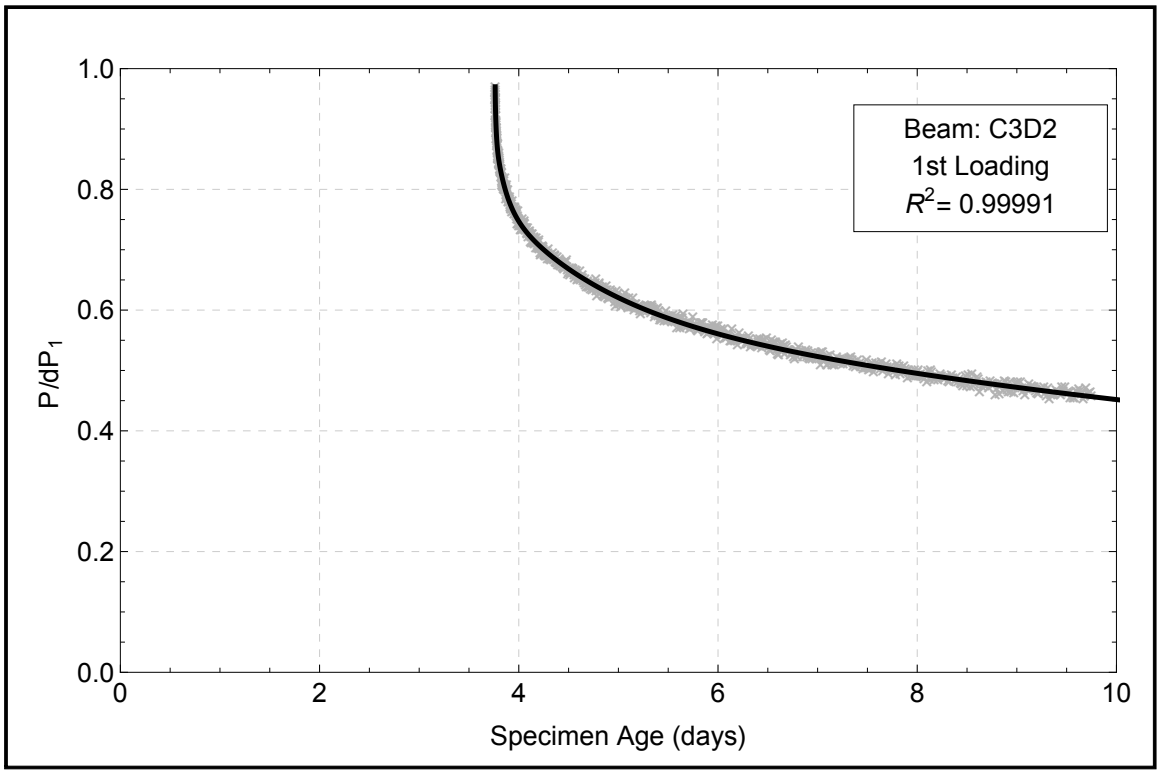
Beam: C3D2
1st Loading
R^2= 0.99991
P /dP$_1$
Specimen Age (days)
0.0
0.2
0.4
0.6
0.8
1.0
0
2
4
6
8
10

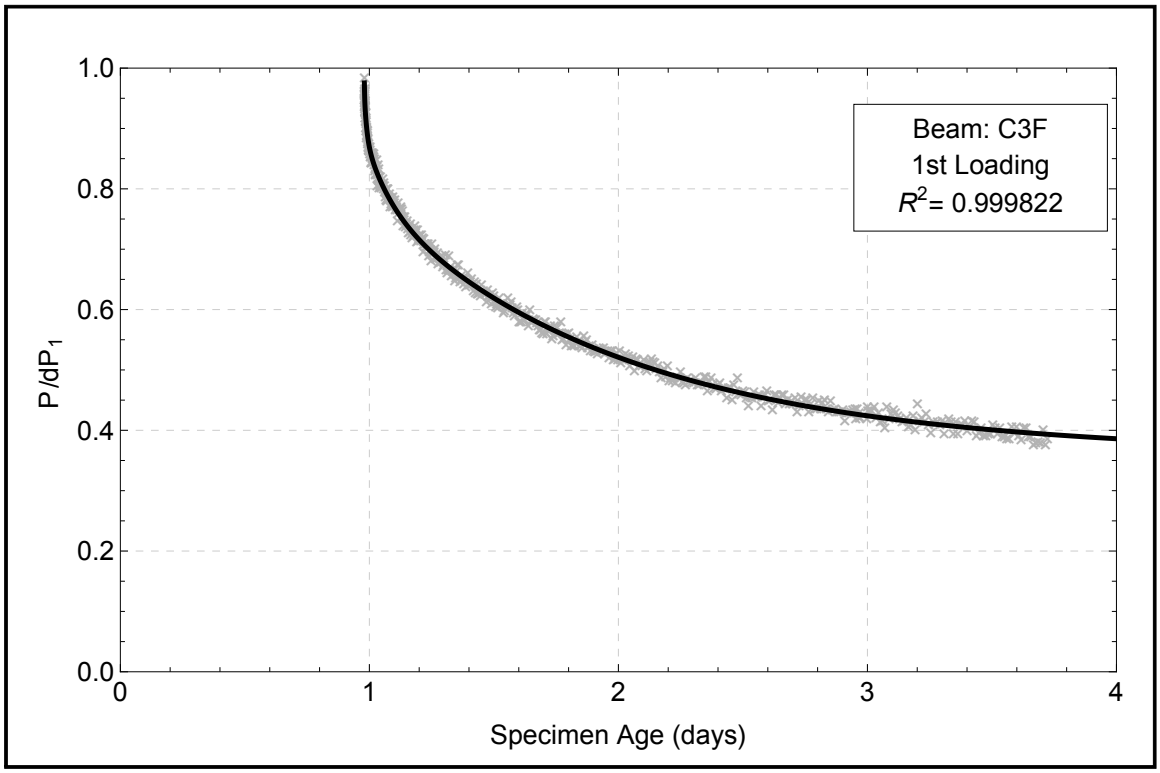
Beam: C3F
1st Loading
R^2= 0.999822
P/dP1
Specimen Age (days)
0.0
0.2
0.4
0.6
0.8
1.0
0
1
2
3
4

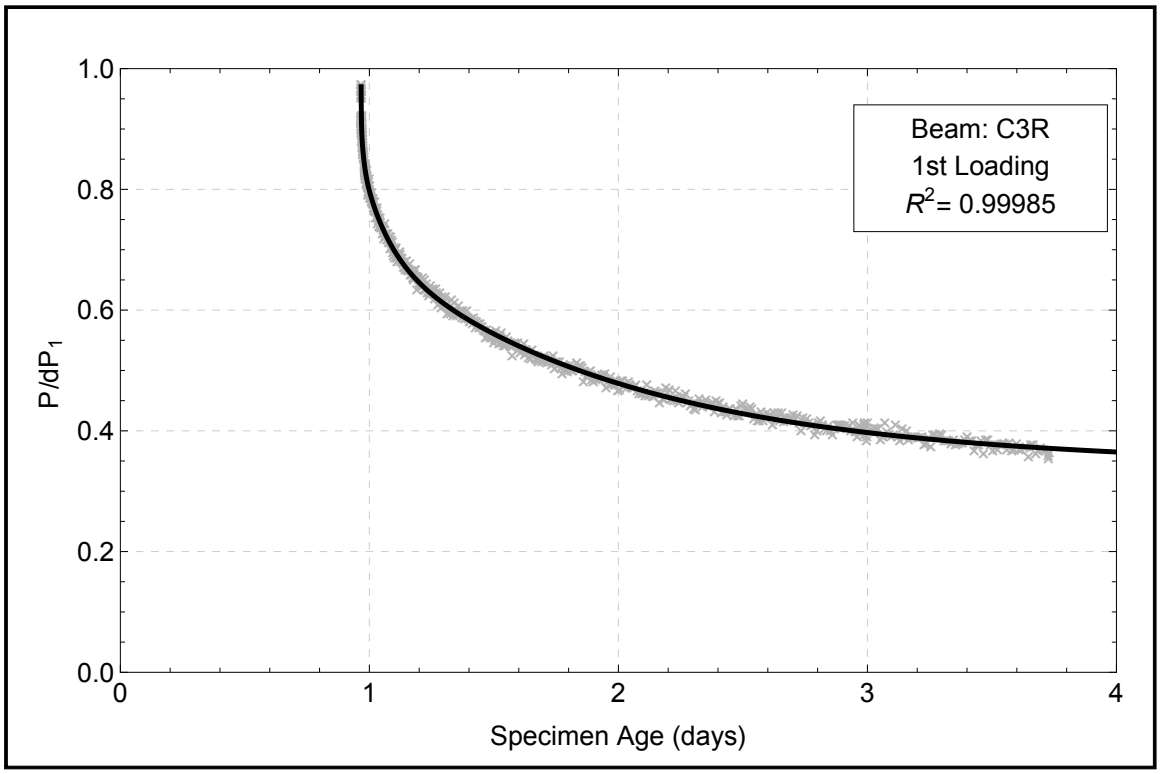
Beam: C3R
1st Loading
R^2= 0.99985
P/dP1
Specimen Age (days)
0.0
0.2
0.4
0.6
0.8
1.0
0
1
2
3
4

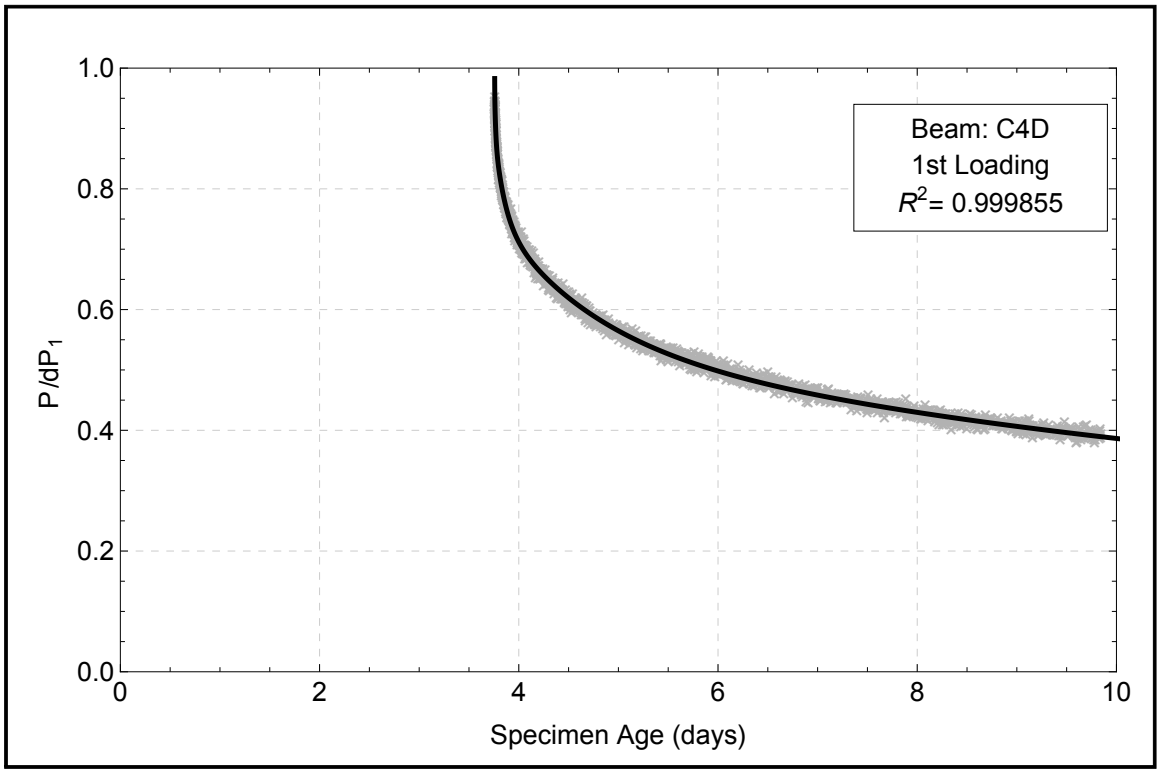
Beam: C4D
1st Loading
R^2= 0.999855
P/dP1
Specimen Age (days)
0.0
0.2
0.4
0.6
0.8
1.0
0
2
4
6
8
10

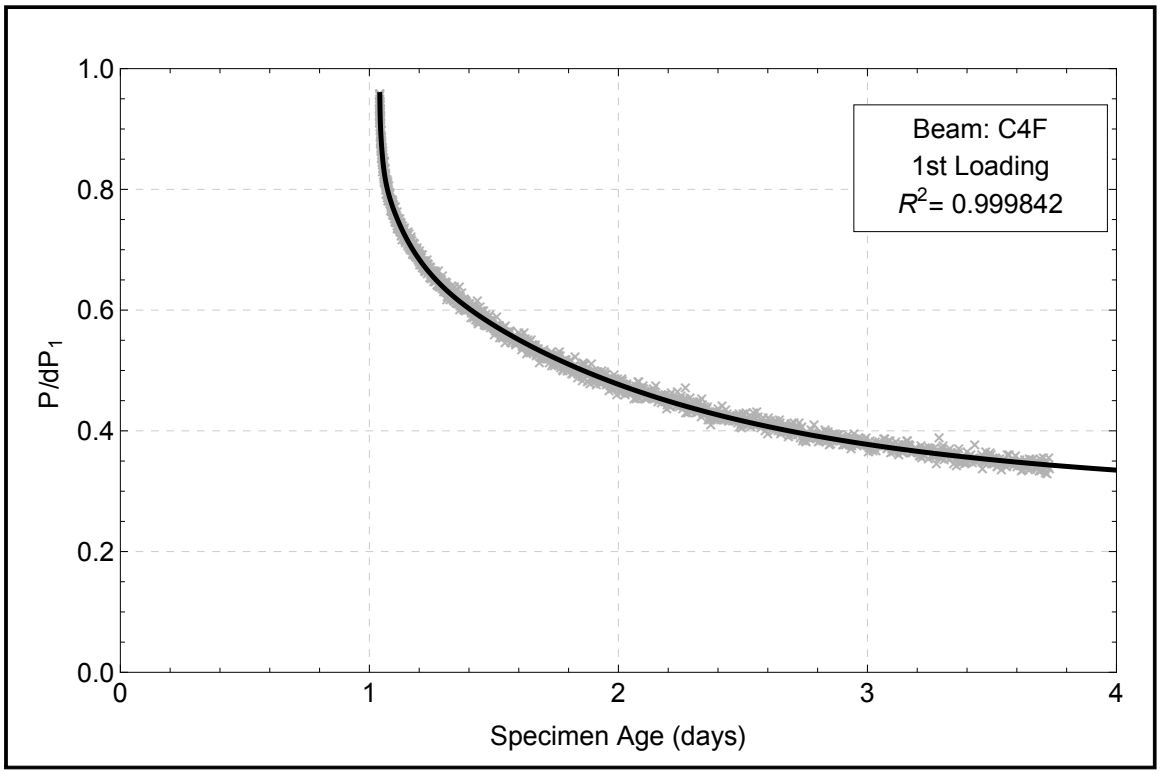
Beam: C4F
1st Loading
R^2= 0.999842
P/dP1
Specimen Age (days)
0.0
0.2
0.4
0.6
0.8
1.0
0
1
2
3
4

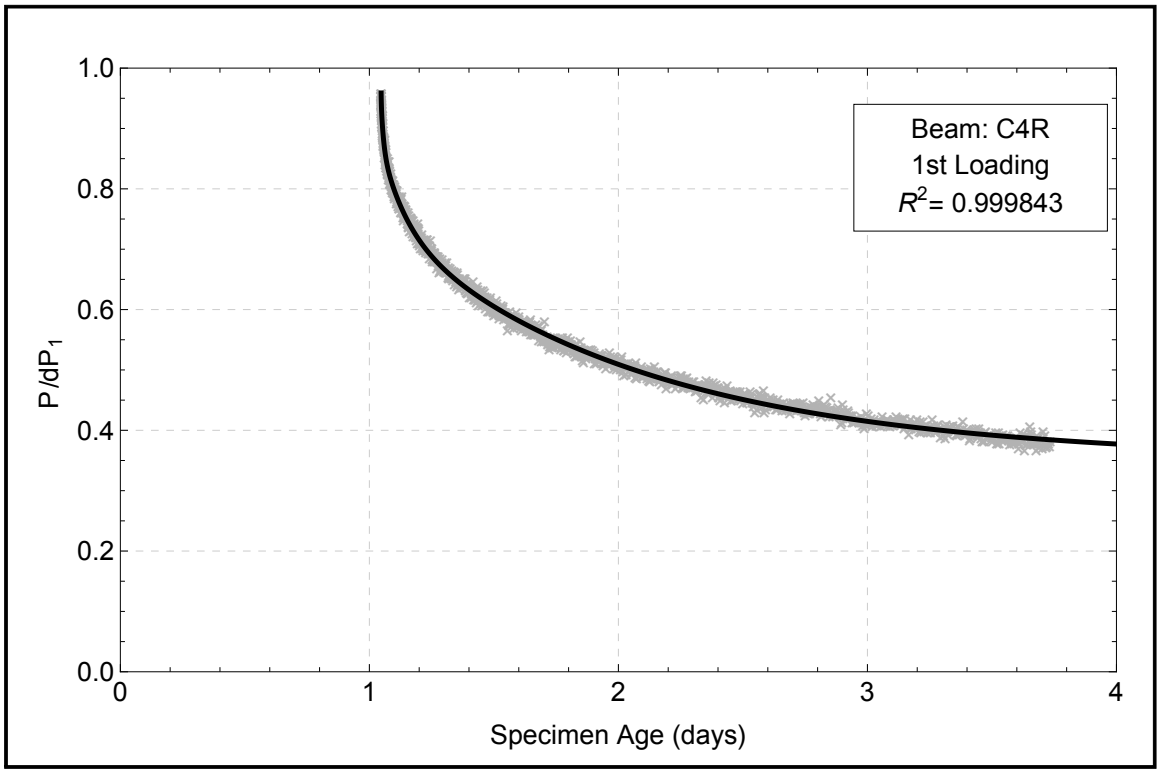
Beam: C4R
1st Loading
R^2= 0.999843
P /dP$_1$
Specimen Age (days)
0.0
0.2
0.4
0.6
0.8
1.0
0
1
2
3
4

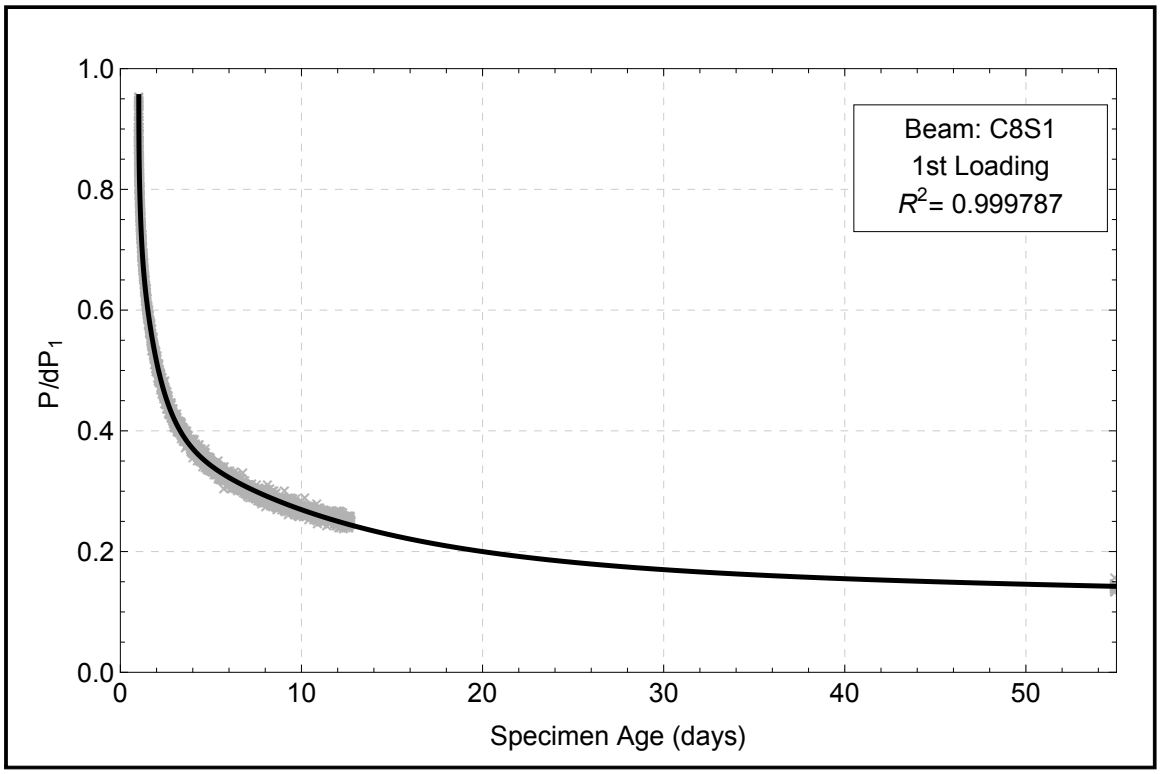
Beam: C8S1
1st Loading
R^2= 0.999787
P /dP$_1$
Specimen Age (days)
0.0
0.2
0.4
0.6
0.8
1.0
0
10
20
30
40
50

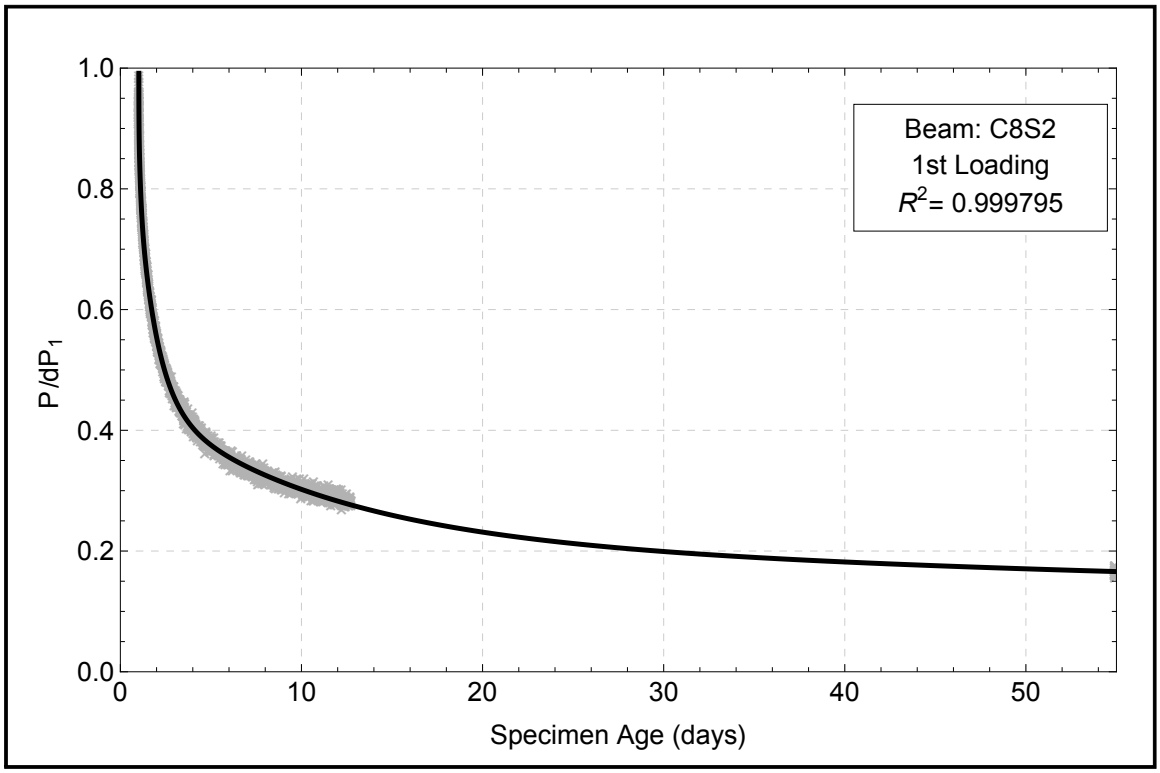
Beam: C8S2
1st Loading
R^2= 0.999795
P /dP$_1$
Specimen Age (days)
0.0
0.2
0.4
0.6
0.8
1.0
0
10
20
30
40
50

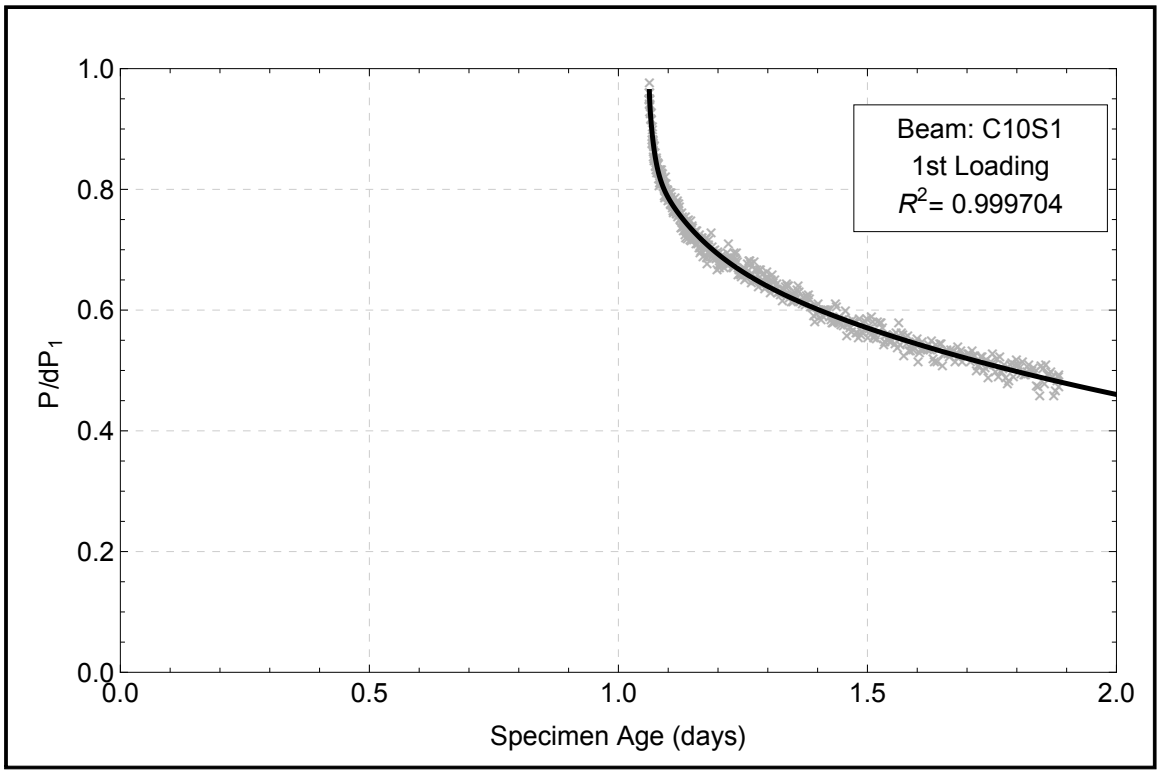
Beam: C10S1
1st Loading
R^2= 0.999704
P /dP$_1$
Specimen Age (days)
0.0
0.2
0.4
0.6
0.8
1.0
0.0
0.5
1.0
1.5
2.0

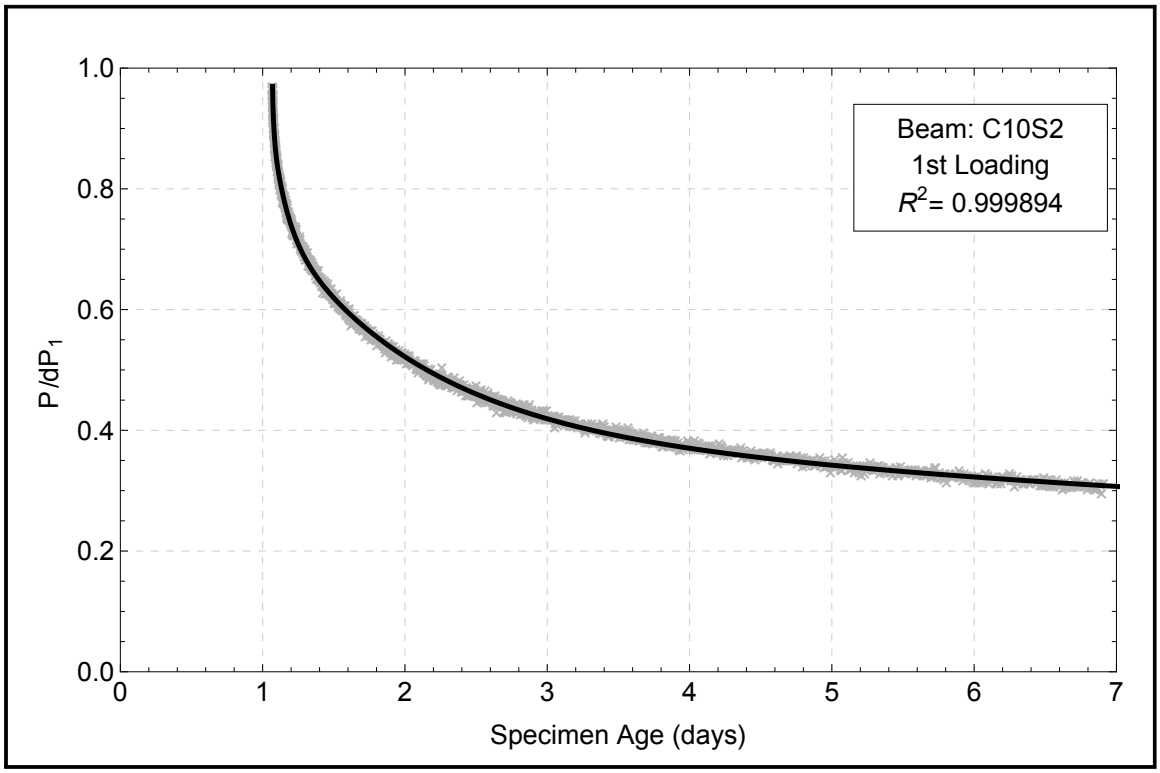
Beam: C10S2
1st Loading
R^2= 0.999894
P /dP$_1$
Specimen Age (days)
0.0
0.2
0.4
0.6
0.8
1.0
0
1
2
3
4
5
6
7

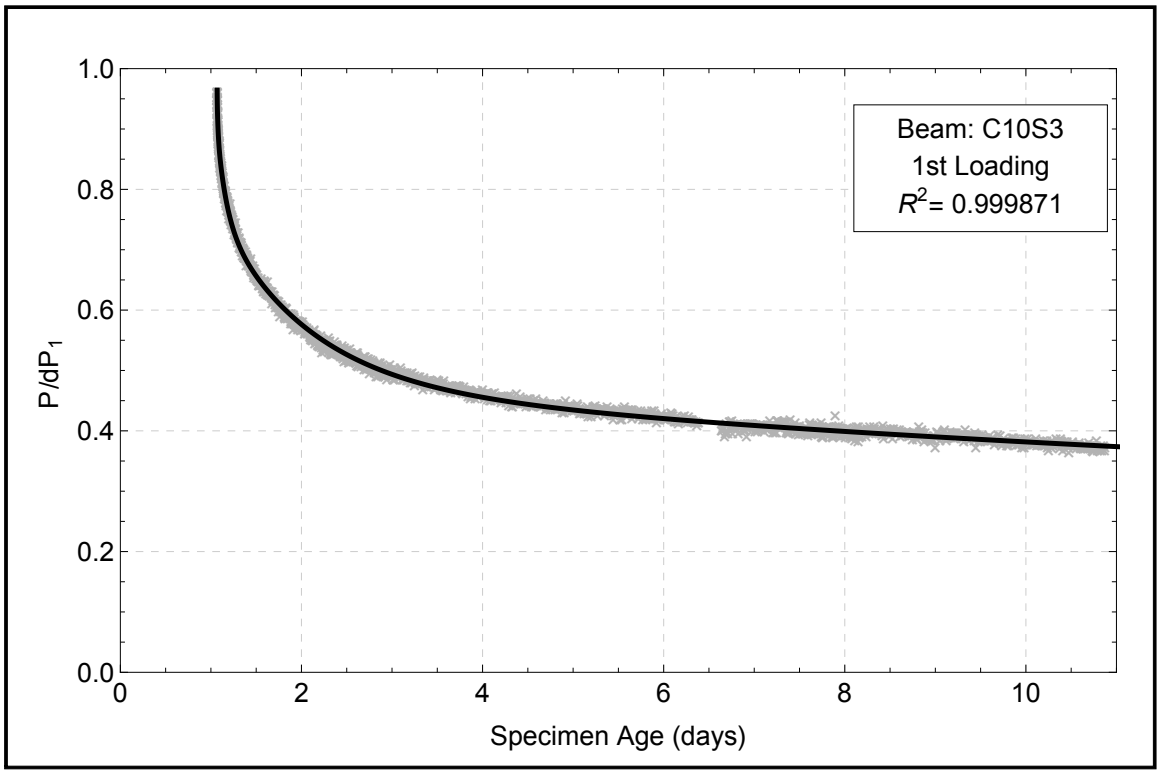
Beam: C10S3
1st Loading
R^2= 0.999871
P /dP$_1$
Specimen Age (days)
0.0
0.2
0.4
0.6
0.8
1.0
0
2
4
6
8
10

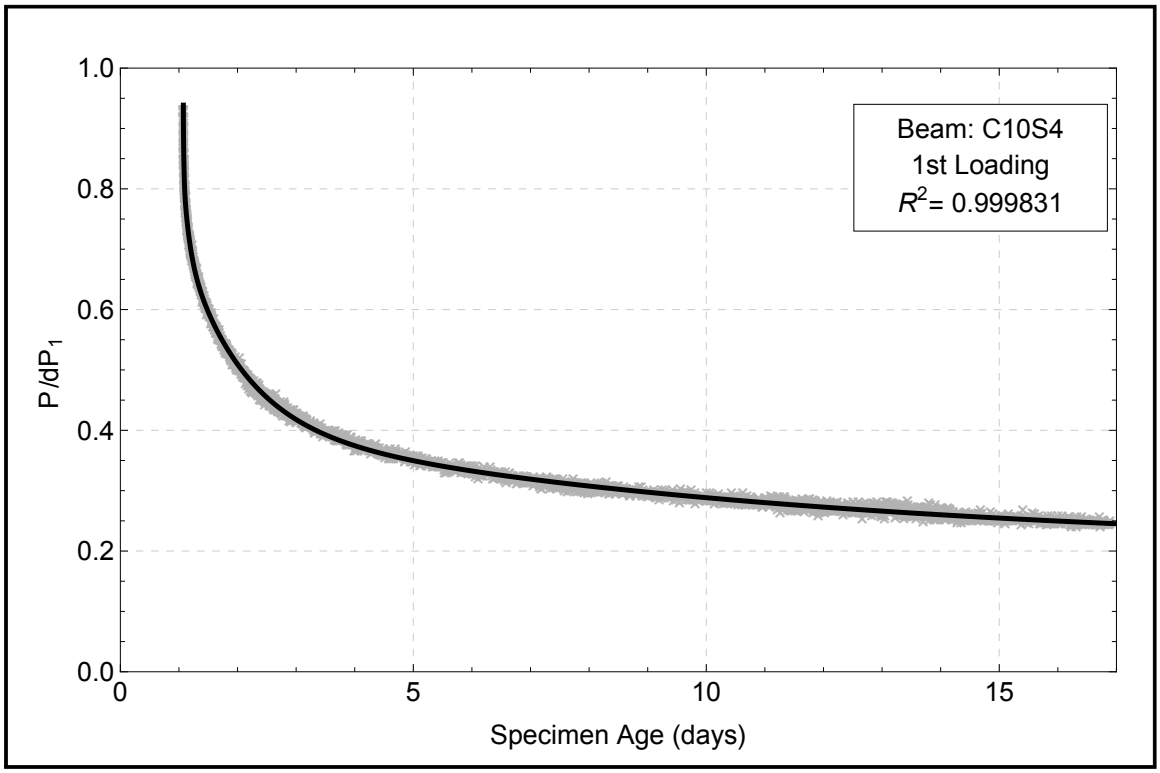
Beam: C10S4
1st Loading
R^2= 0.999831
P/dP$_1$
Specimen Age (days)
0.0
0.2
0.4
0.6
0.8
1.0
0
5
10
15

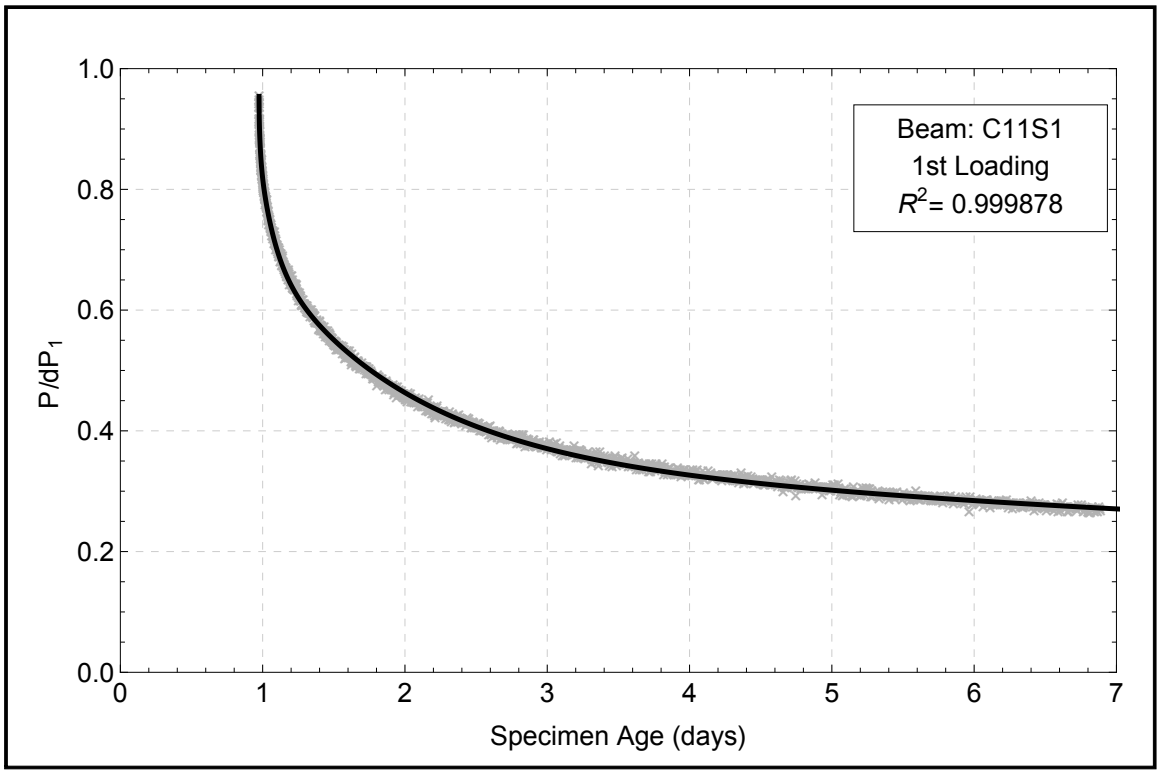
Beam: C11S1
1st Loading
R^2= 0.999878
P/dP$_1$
Specimen Age (days)
0.0
0.2
0.4
0.6
0.8
1.0
0
1
2
3
4
5
6
7

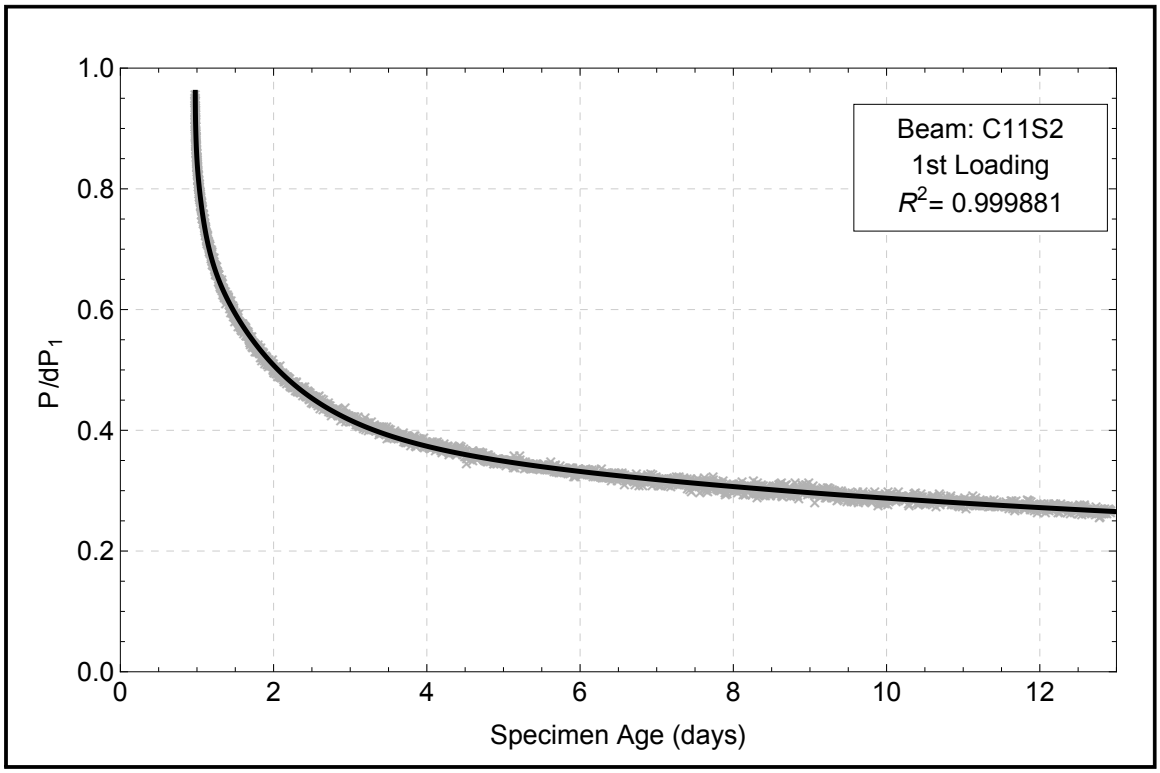
Beam: C11S2
1st Loading
R^2= 0.999881
P /dP$_1$
Specimen Age (days)
0.0
0.2
0.4
0.6
0.8
1.0
0
2
4
6
8
10
12

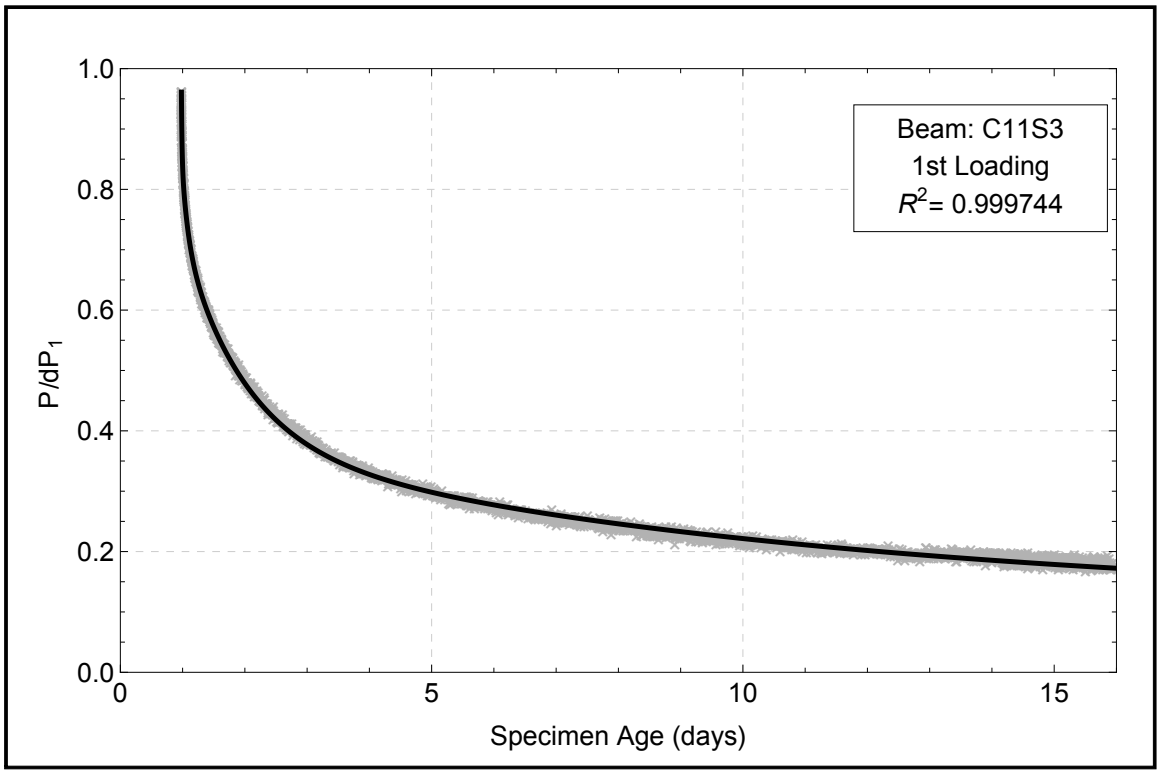
Beam: C11S3
1st Loading
R^2= 0.999744
P /dP$_1$
Specimen Age (days)
0.0
0.2
0.4
0.6
0.8
1.0
0
5
10
15

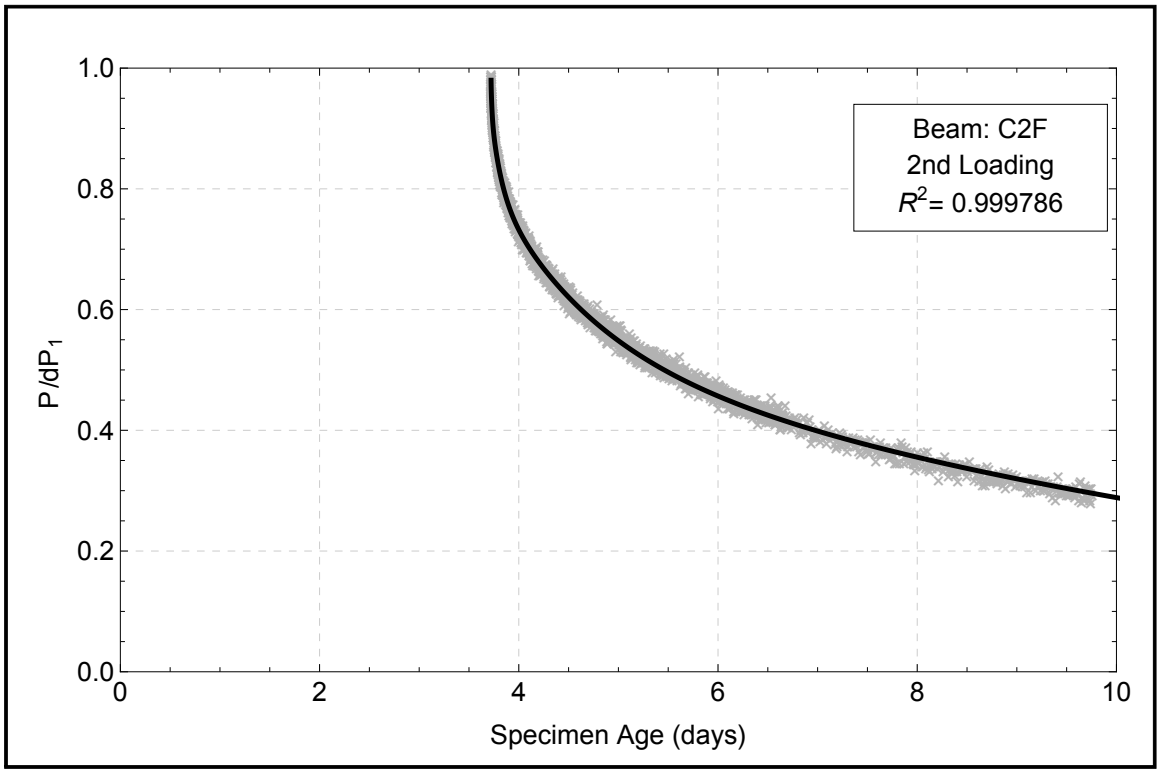
Beam: C2F
2nd Loading
R^2= 0.999786
P /dP$_1$
Specimen Age (days)
0.0
0.2
0.4
0.6
0.8
1.0
0
2
4
6
8
10

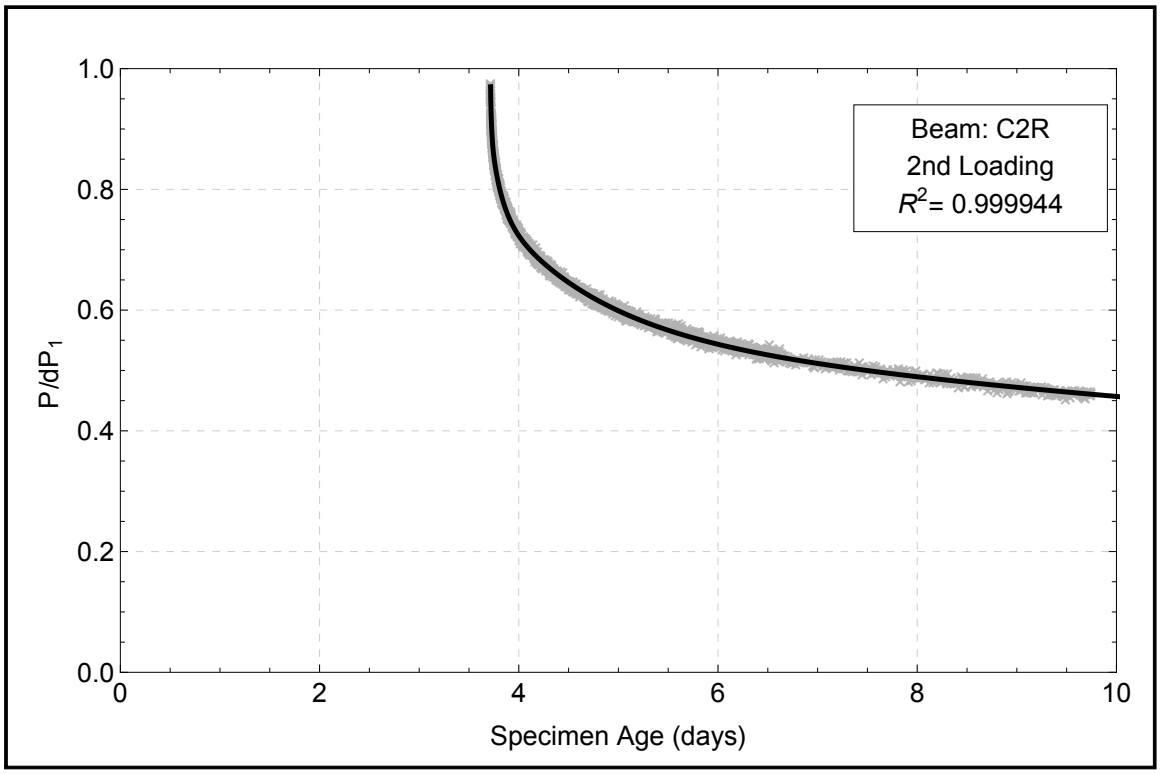
Beam: C2R
2nd Loading
R^2= 0.999944
P /dP$_1$
Specimen Age (days)
0.0
0.2
0.4
0.6
0.8
1.0
0
2
4
6
8
10

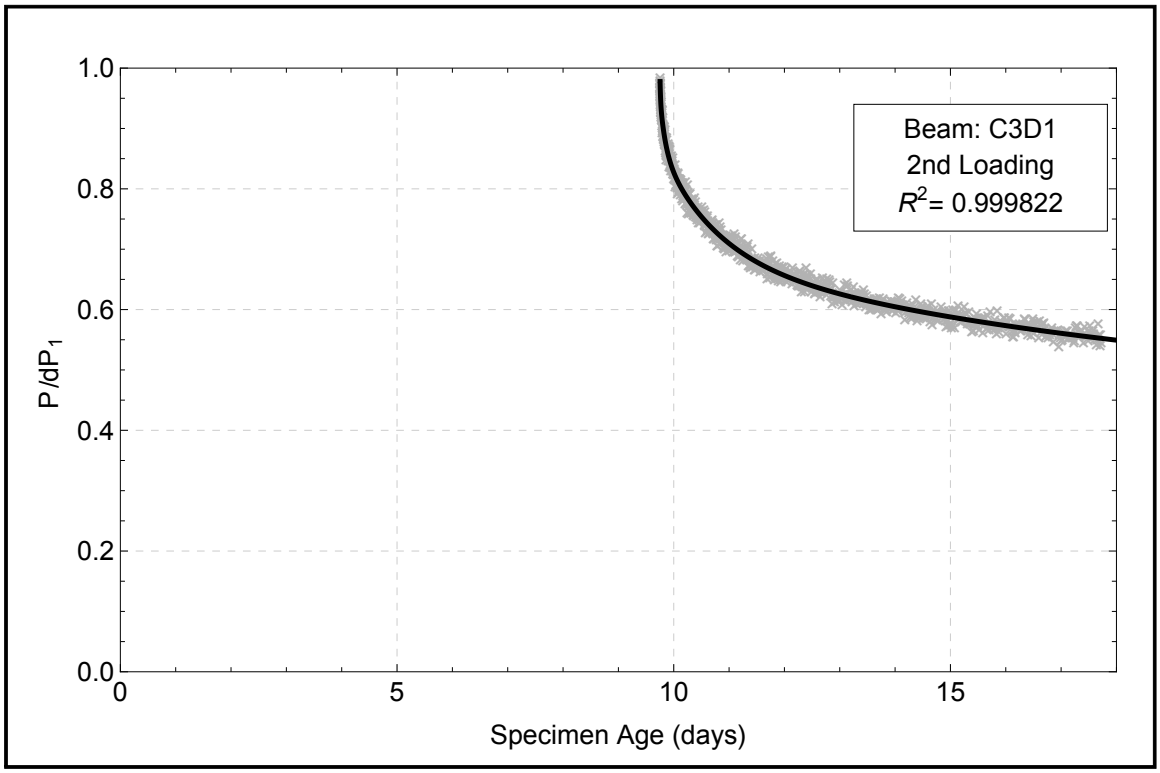
Beam: C3D1
2nd Loading
R^2= 0.999822
P/dP1
Specimen Age (days)
0.0
0.2
0.4
0.6
0.8
1.0
0
5
10
15

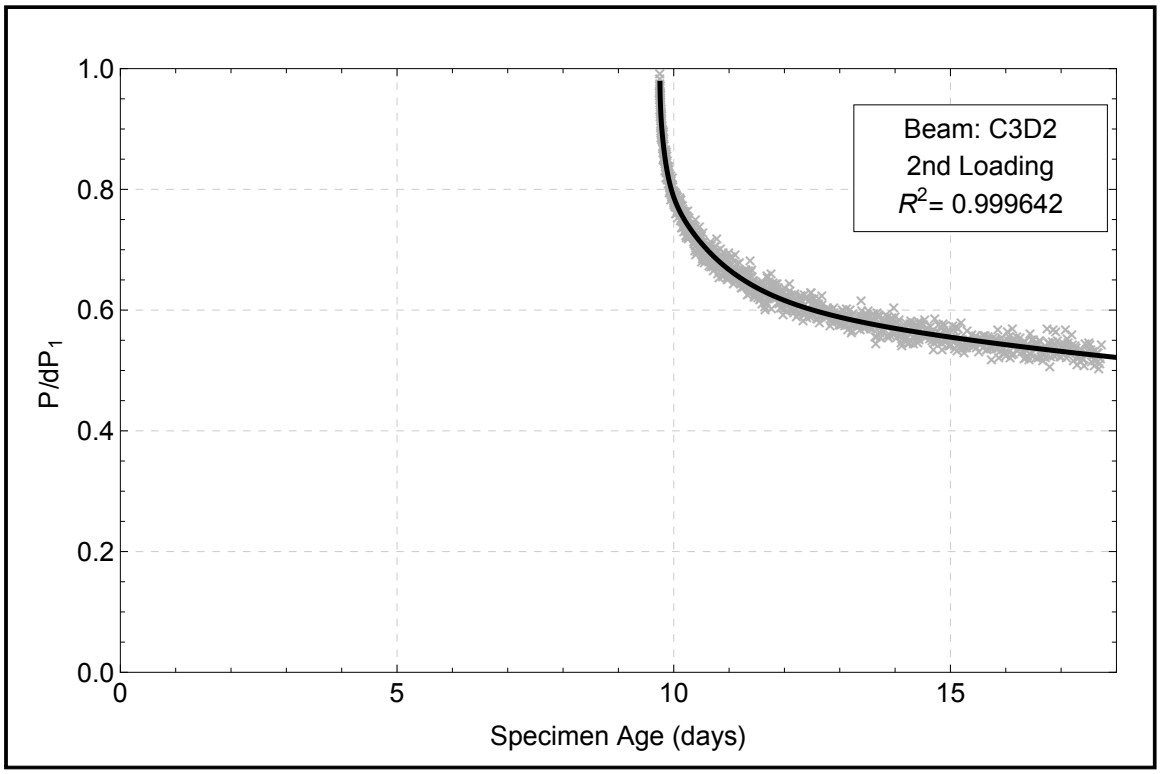
Beam: C3D2
2nd Loading
R^2= 0.999642
P/dP1
Specimen Age (days)
0.0
0.2
0.4
0.6
0.8
1.0
0
5
10
15

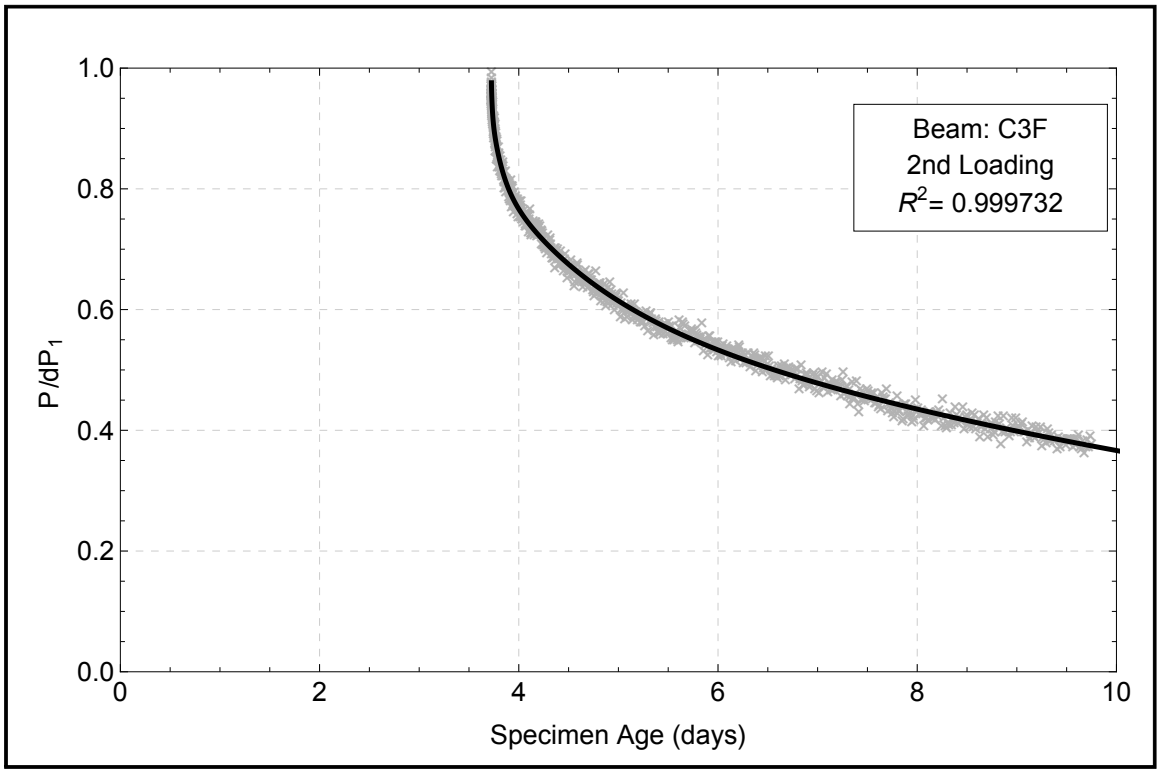
Beam: C3F
2nd Loading
R^2= 0.999732
P/dP$_1$
Specimen Age (days)
0.0
0.2
0.4
0.6
0.8
1.0
0
2
4
6
8
10

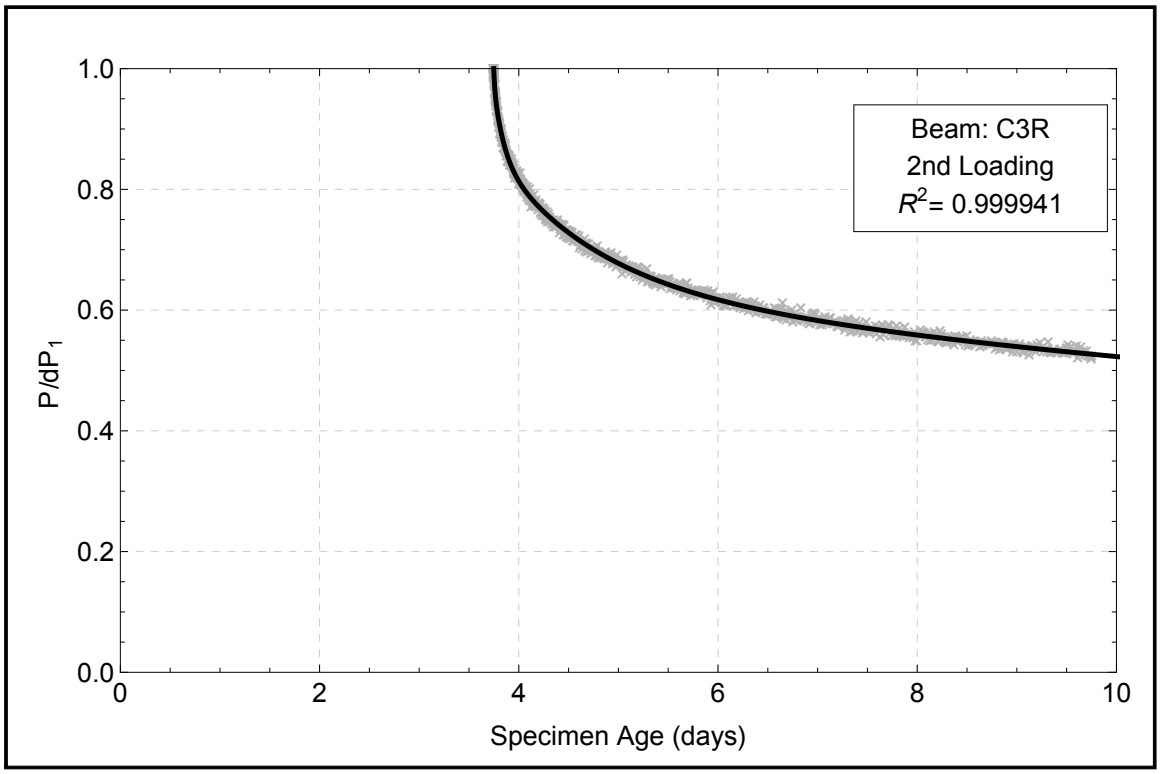
Beam: C3R
2nd Loading
R^2= 0.999941
P/dP$_1$
Specimen Age (days)
0.0
0.2
0.4
0.6
0.8
1.0
0
2
4
6
8
10

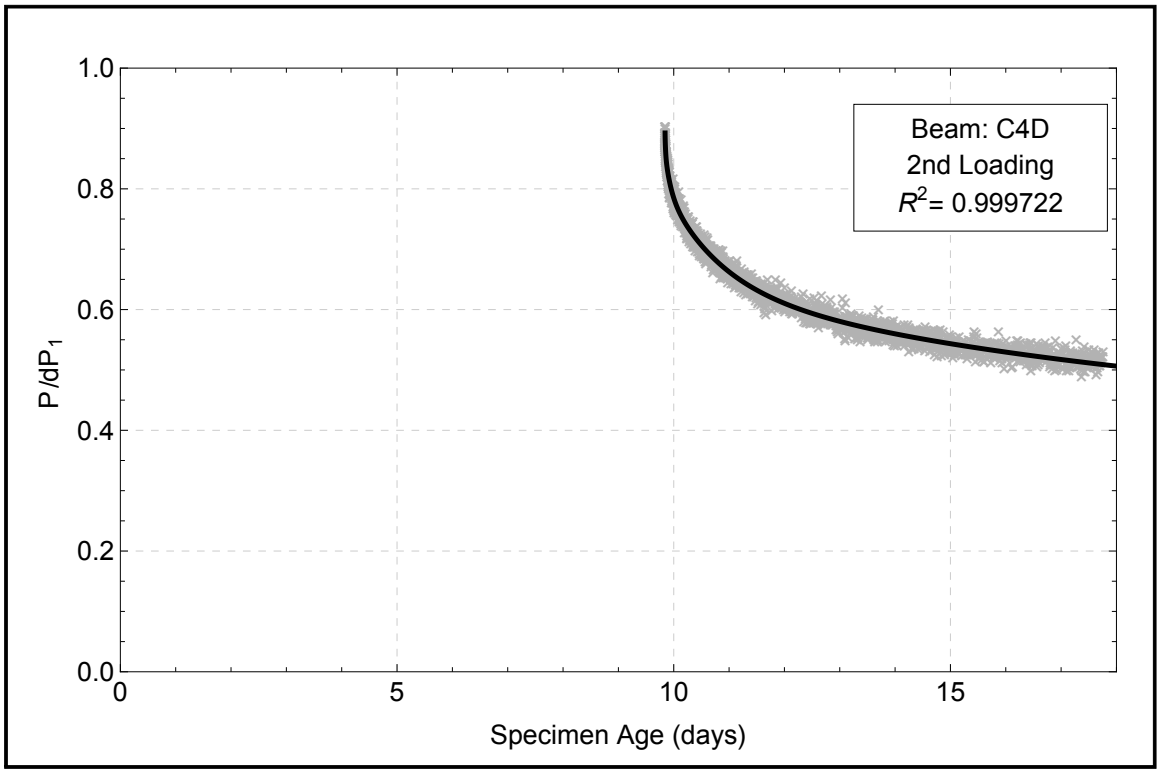
Beam: C4D
2nd Loading
R^2= 0.999722
P /dP$_1$
Specimen Age (days)
0.0
0.2
0.4
0.6
0.8
1.0
0
5
10
15

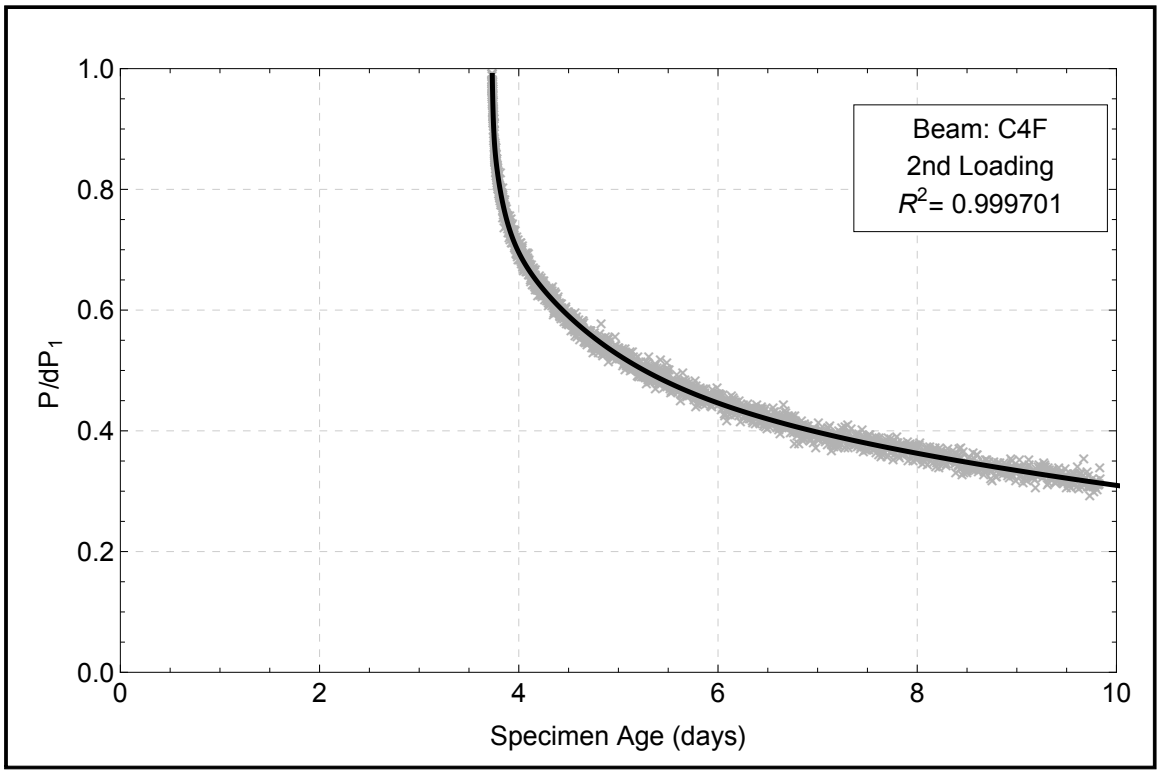
Beam: C4F
2nd Loading
R^2= 0.999701
P /dP$_1$
Specimen Age (days)
0.0
0.2
0.4
0.6
0.8
1.0
0
2
4
6
8
10

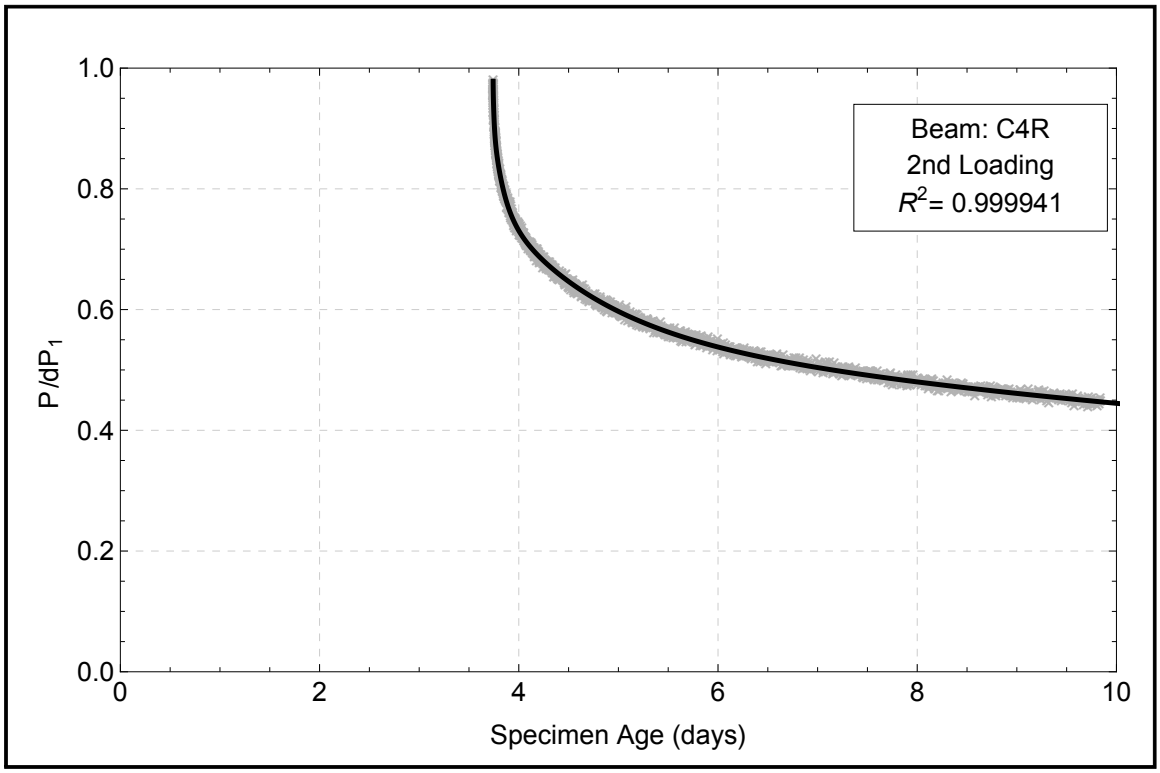
Beam: C4R
2nd Loading
R^2= 0.999941
P/dP1
Specimen Age (days)
0.0
0.2
0.4
0.6
0.8
1.0
0
2
4
6
8
10

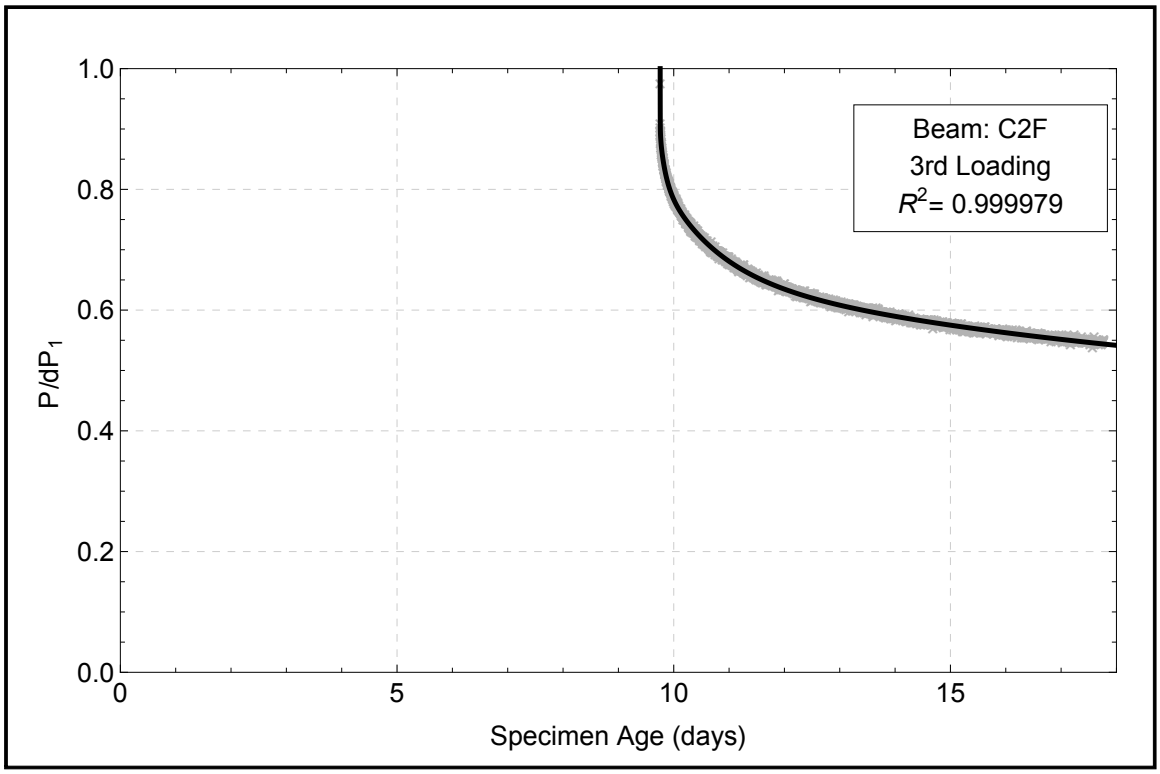
Beam: C2F
3rd Loading
R^2= 0.999979
P/dP1
Specimen Age (days)
0.0
0.2
0.4
0.6
0.8
1.0
0
5
10
15

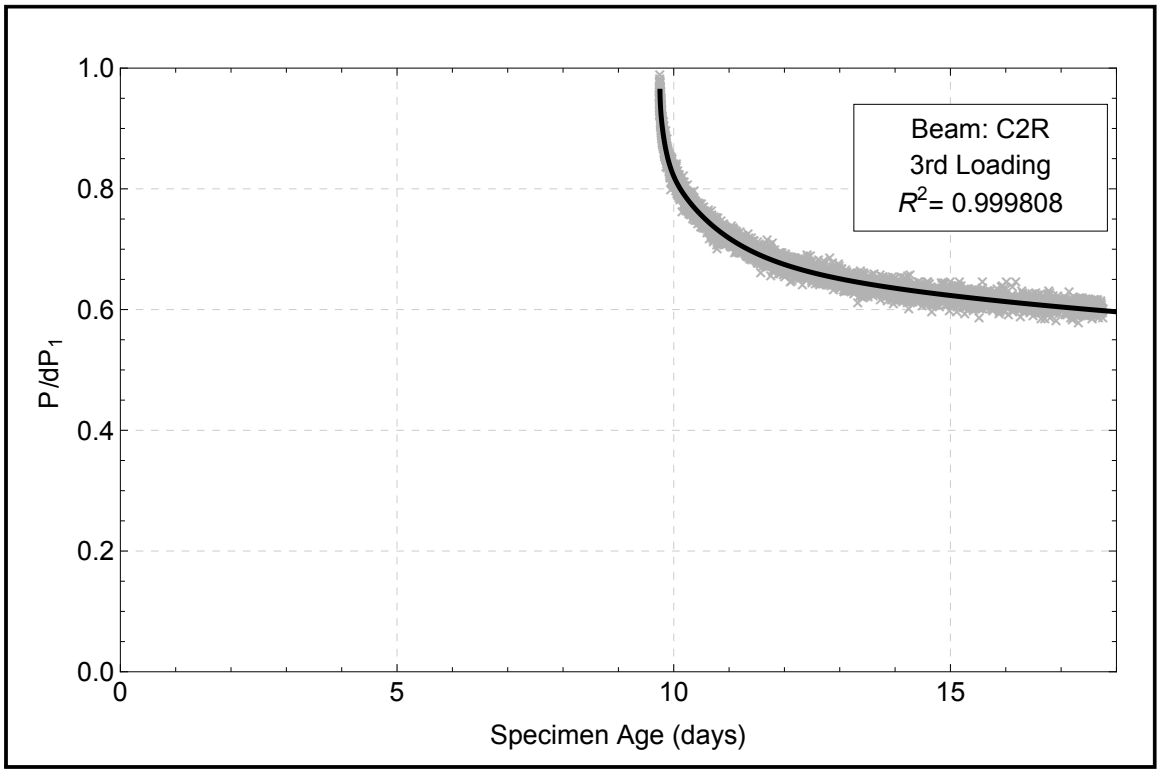
Beam: C2R
3rd Loading
R^2= 0.999808
P/dP1
Specimen Age (days)
0.0
0.2
0.4
0.6
0.8
1.0
0
5
10
15

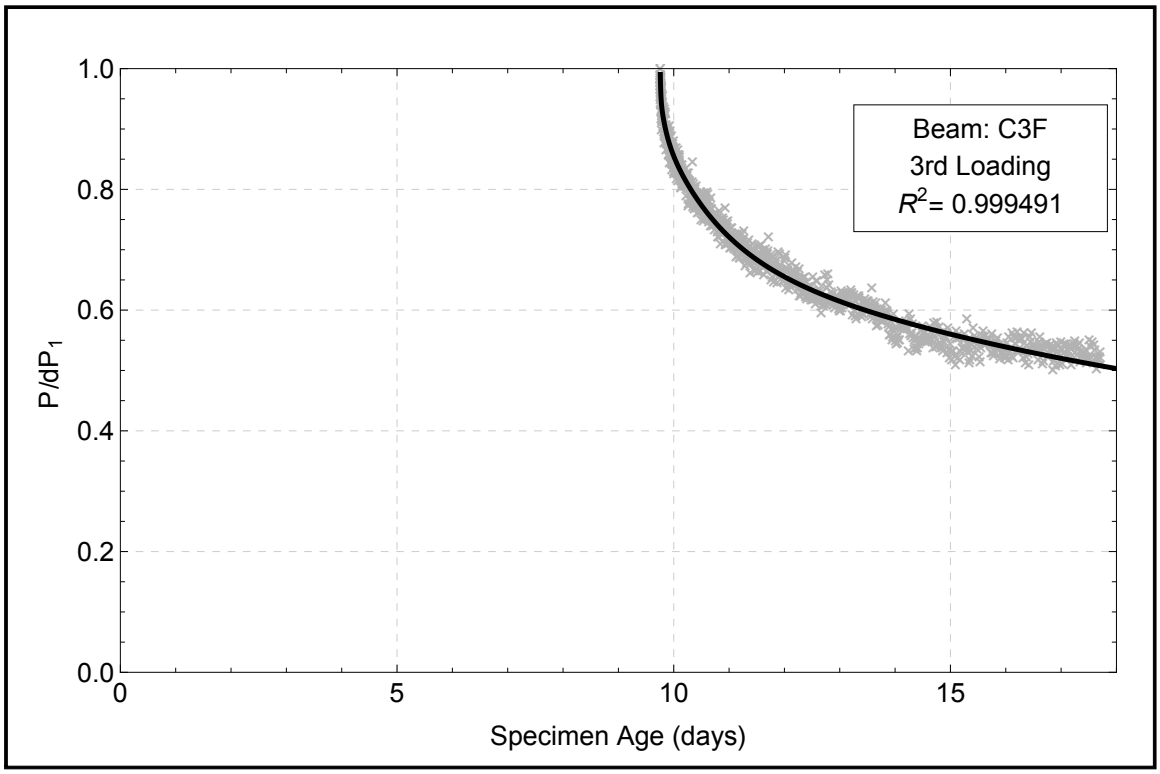
Beam: C3F
3rd Loading
R^2= 0.999491
P/dP1
Specimen Age (days)
0.0
0.2
0.4
0.6
0.8
1.0
0
5
10
15

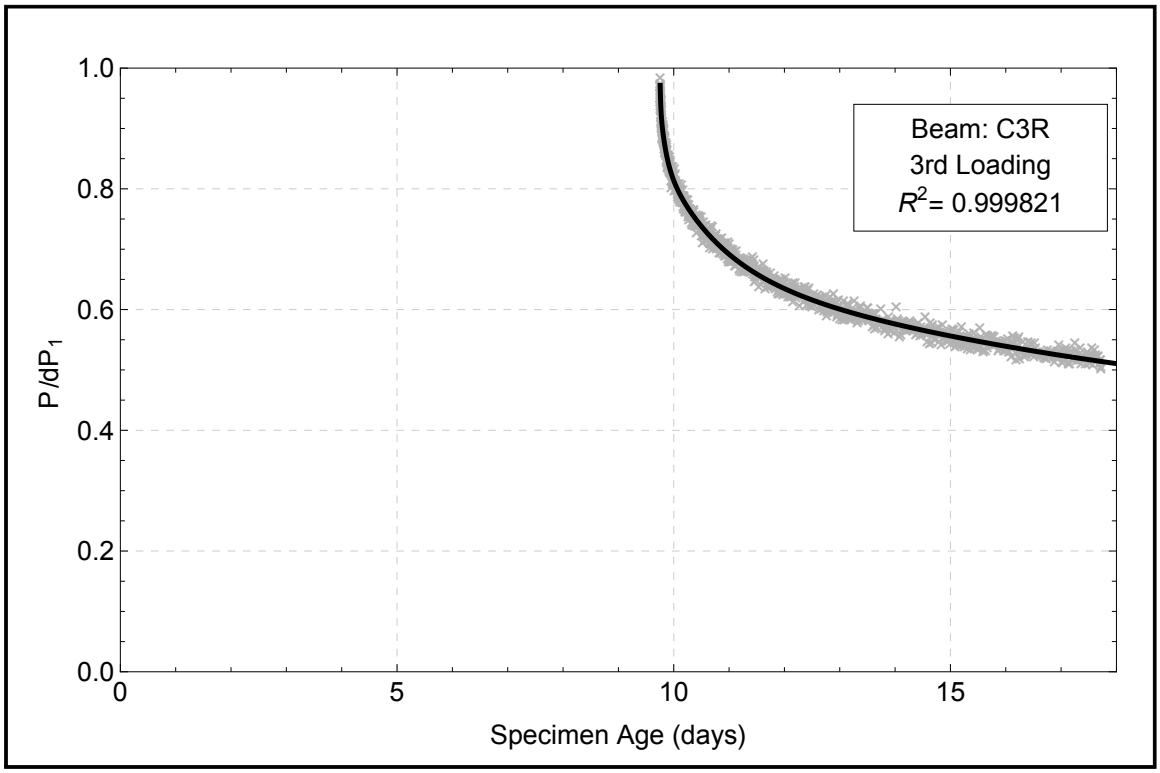
Beam: C3R
3rd Loading
R^2= 0.999821
P/dP$_1$
Specimen Age (days)
0.0
0.2
0.4
0.6
0.8
1.0
0
5
10
15

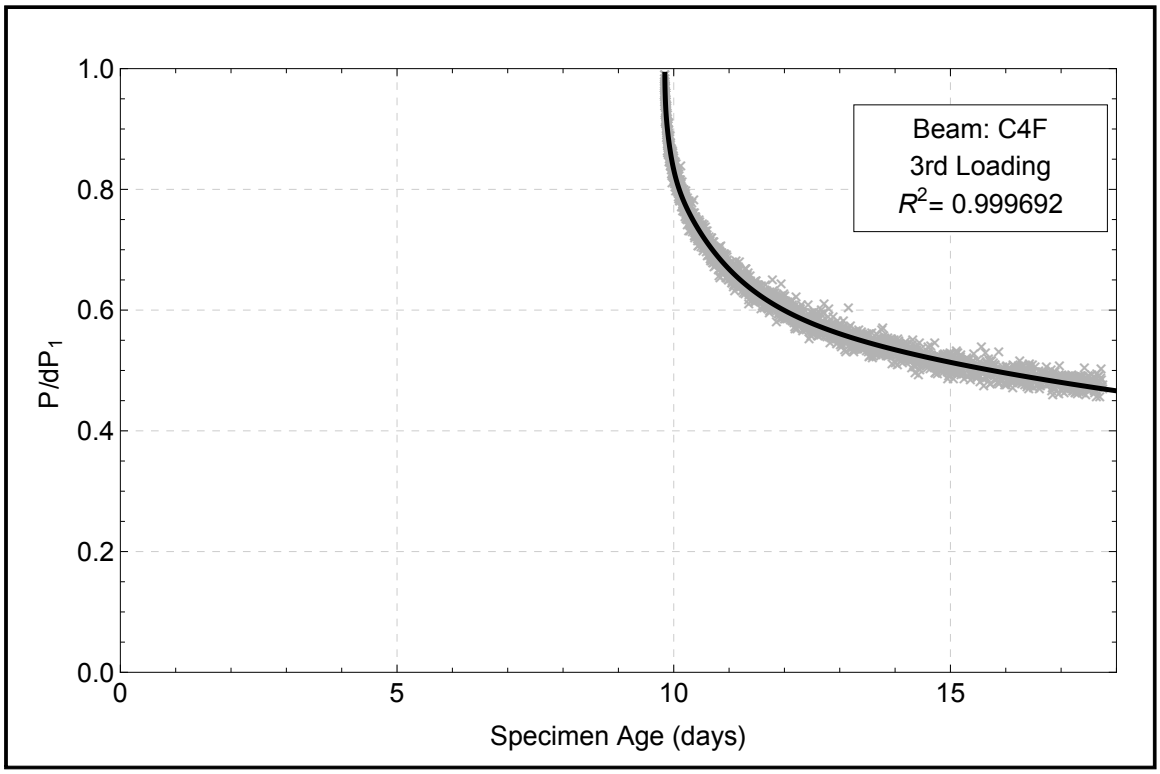
Beam: C4F
3rd Loading
R^2= 0.999692
P/dP$_1$
Specimen Age (days)
0.0
0.2
0.4
0.6
0.8
1.0
0
5
10
15

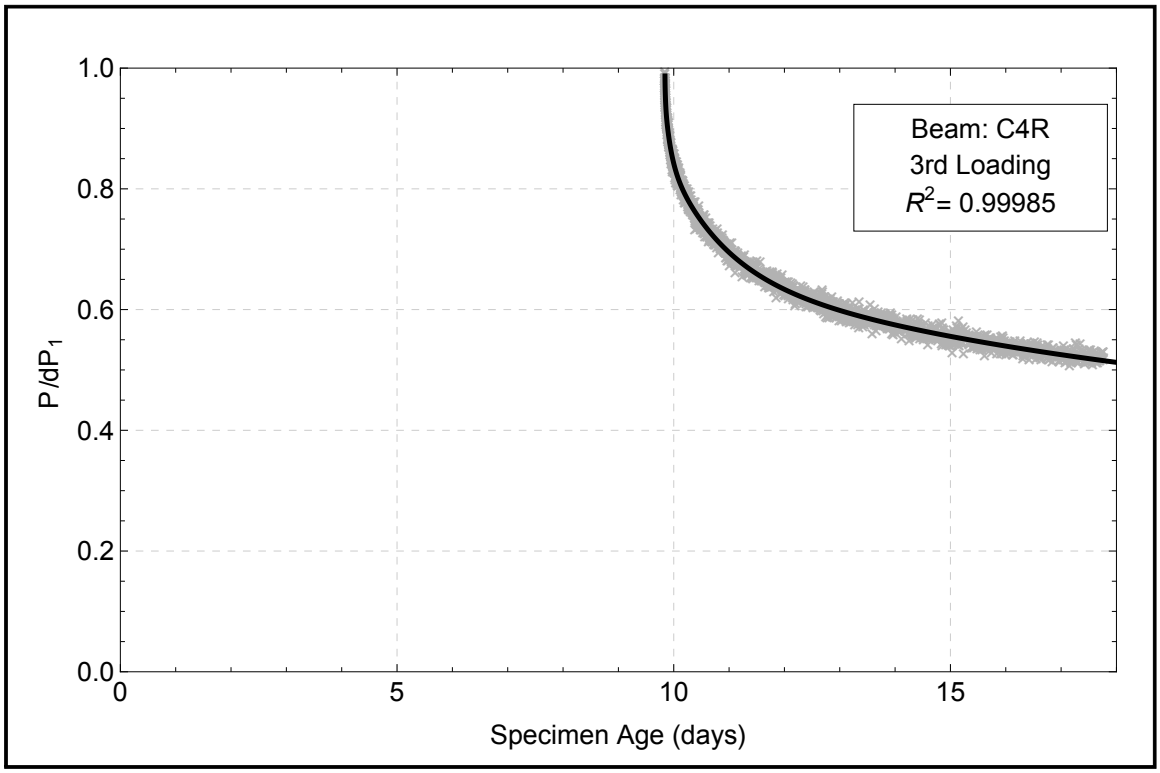
Beam: C4R
3rd Loading
R^2= 0.99985
P /dP$_1$
Specimen Age (days)
1.0
0.8
0.6
0.4
0.2
0.0
0
5
10
15

Appendix B.1 – TGA Raw Data

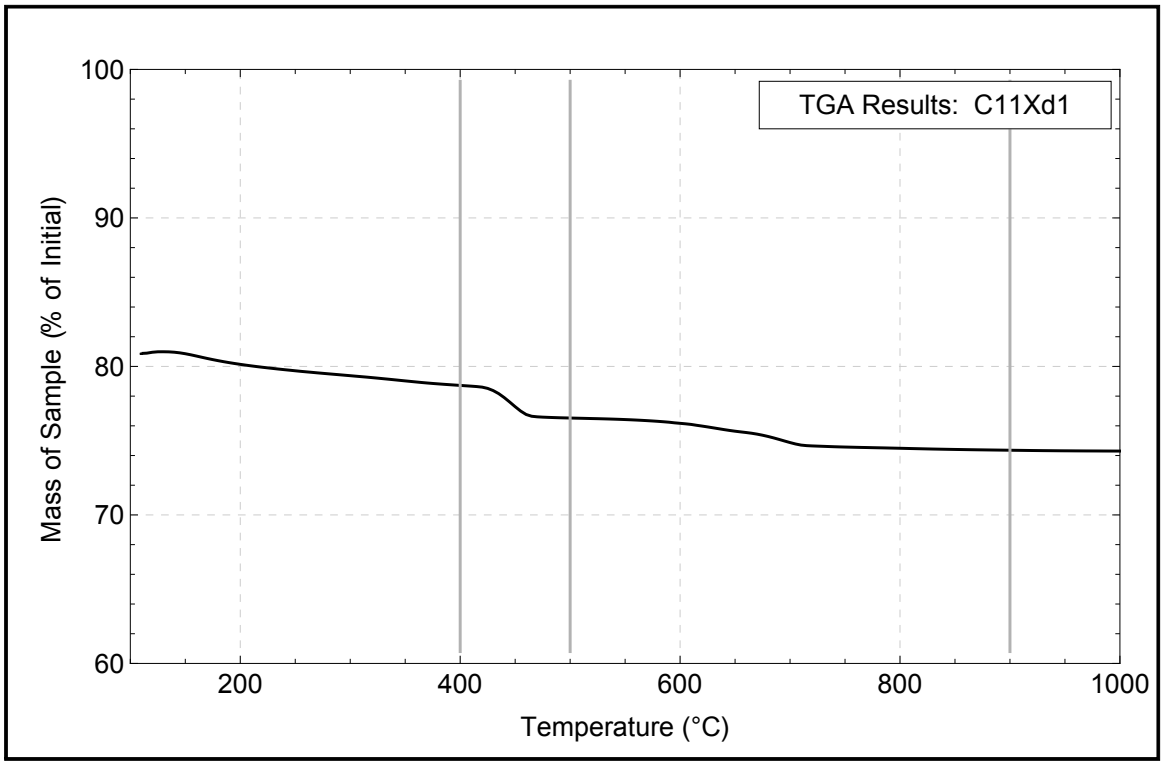
TGA Results: C11Xd1
Mass of Sample (% of Initial)
100
90
80
70
60
200
400
600
800
1000
Temperature (°C)

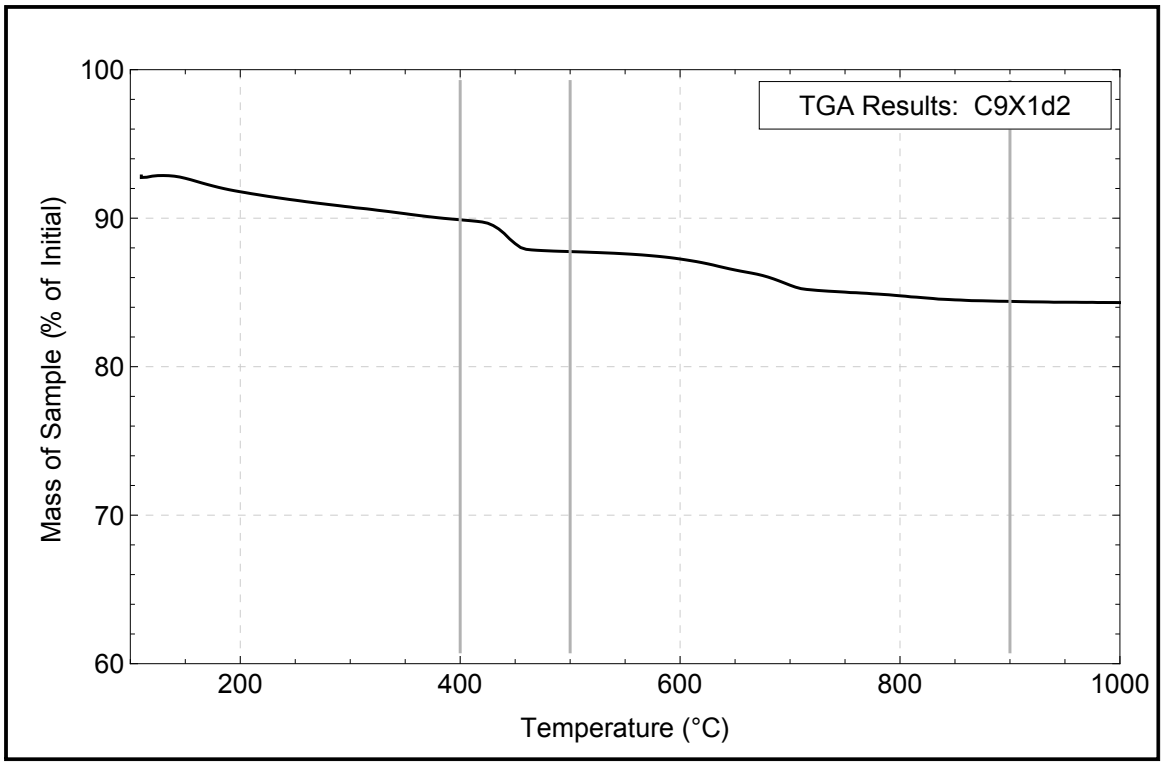
TGA Results: C9X1d2
Mass of Sample (% of Initial)
100
90
80
70
60
200
400
600
800
1000
Temperature (°C)

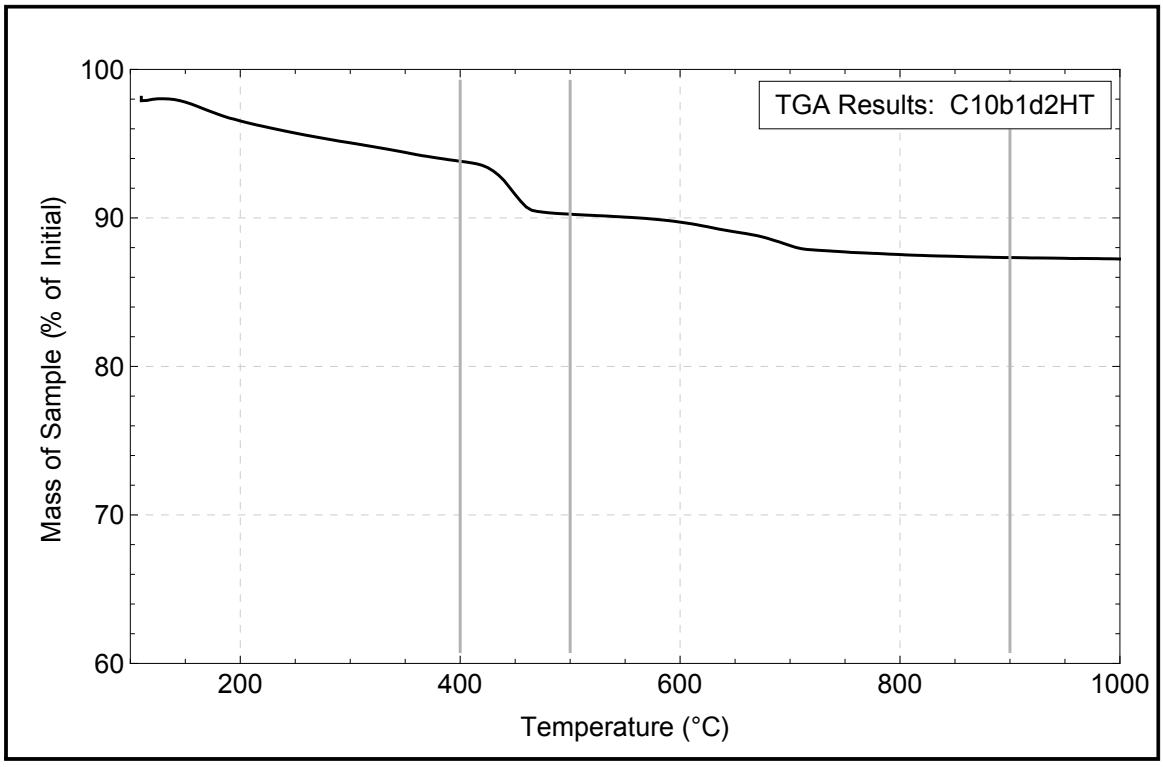
TGA Results: C10b1d2HT
Mass of Sample (% of Initial)
100
90
80
70
60
200
400
600
800
1000
Temperature (°C)

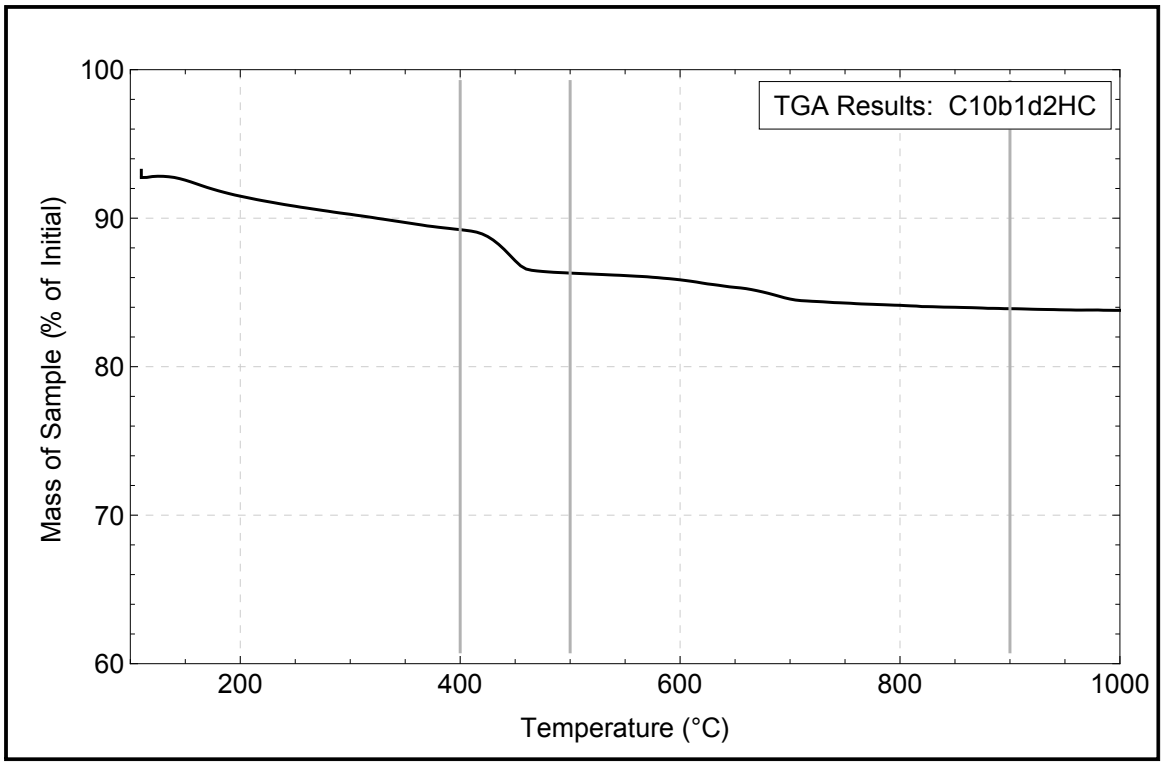
TGA Results: C10b1d2HC
Mass of Sample (% of Initial)
100
90
80
70
60
200
400
600
800
1000
Temperature (°C)

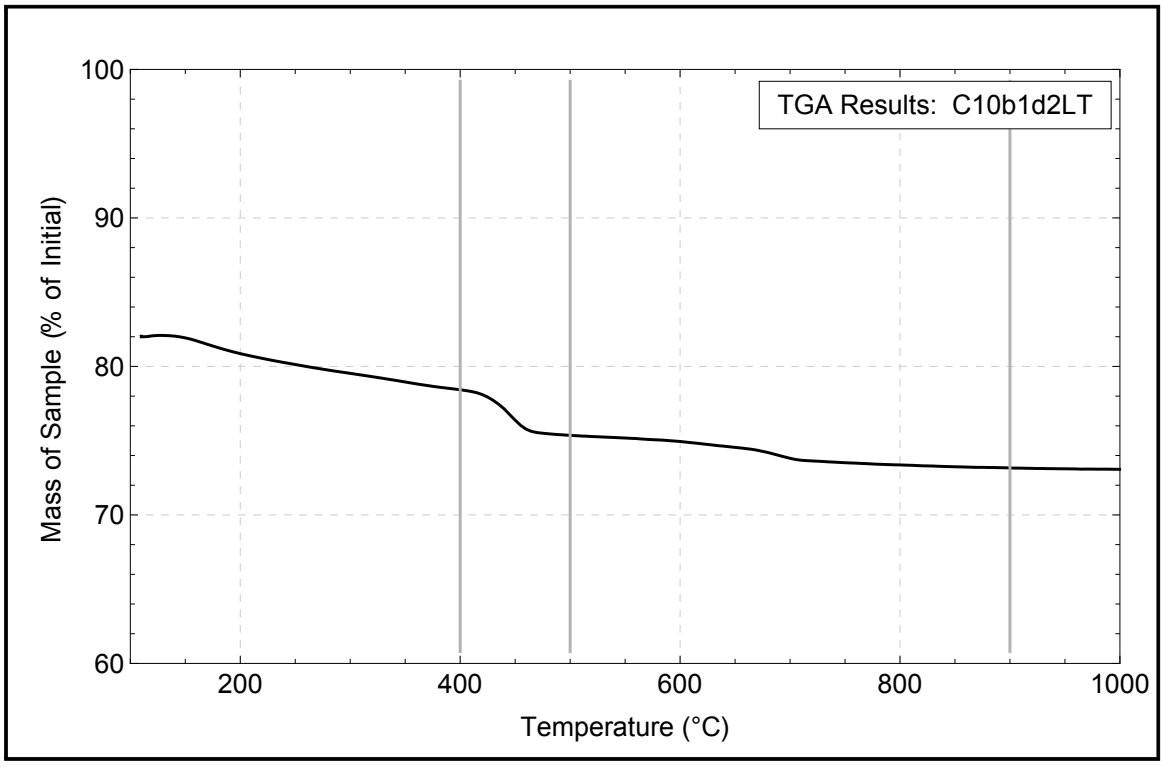
TGA Results: C10b1d2LT
Mass of Sample (% of Initial)
100
90
80
70
60
200
400
600
800
1000
Temperature (°C)

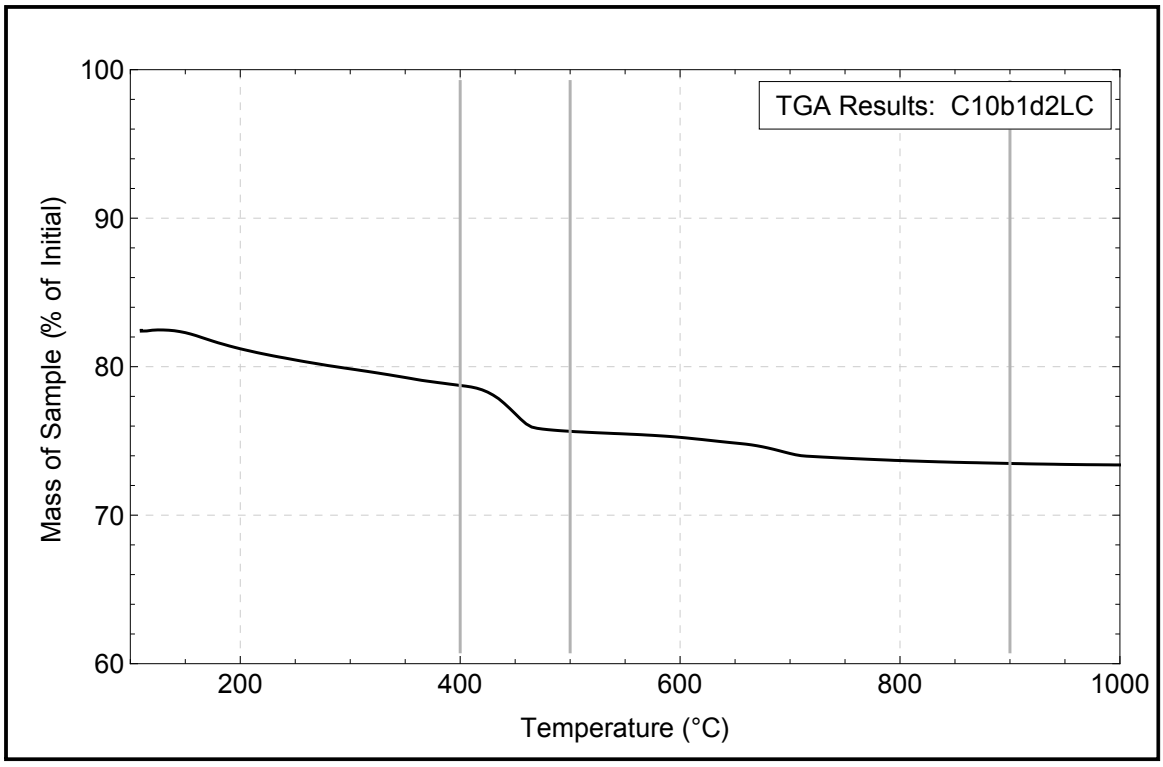
TGA Results: C10b1d2LC
Mass of Sample (% of Initial)
100
90
80
70
60
200
400
600
800
1000
Temperature (°C)

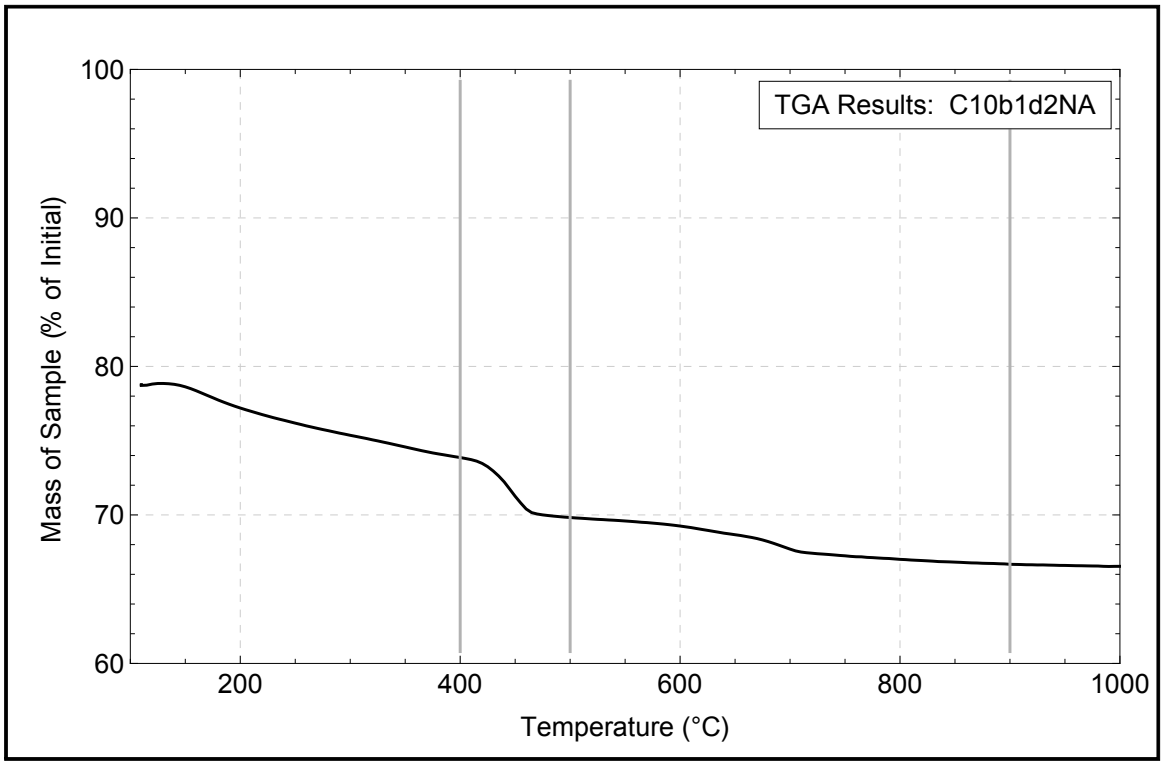
TGA Results: C10b1d2NA
Mass of Sample (% of Initial)
100
90
80
70
60
200
400
600
800
1000
Temperature (°C)

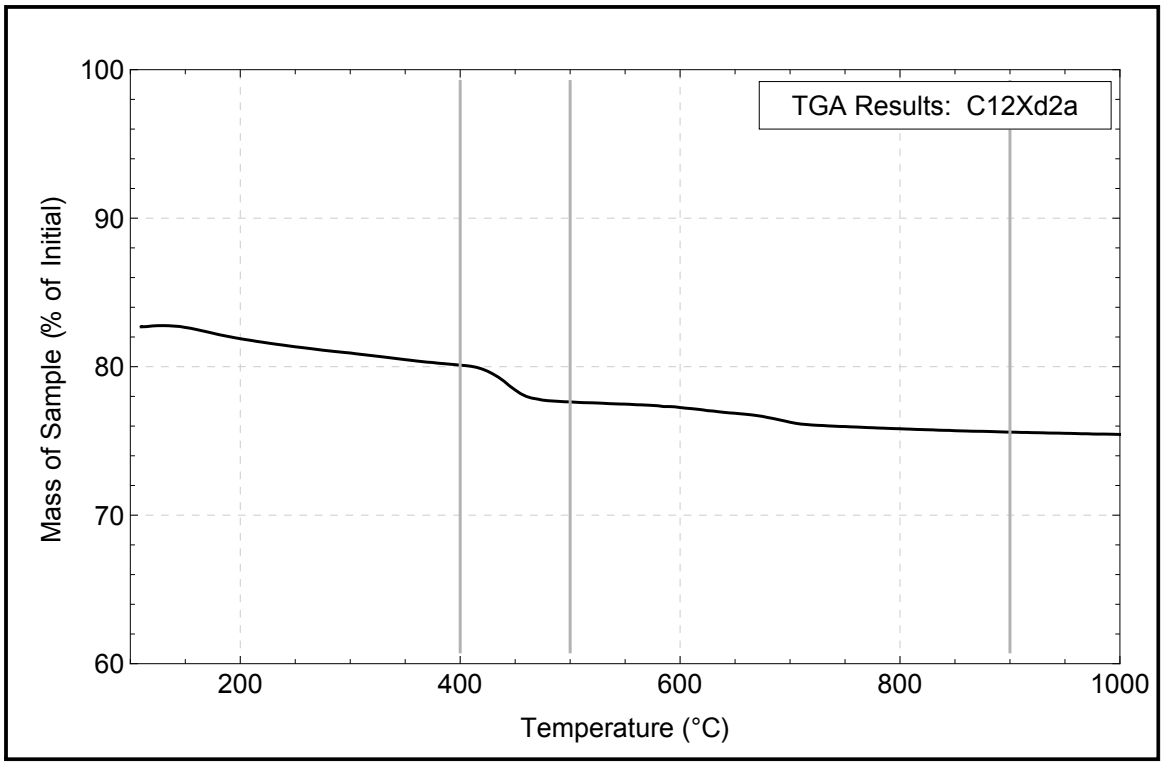
TGA Results: C12Xd2a
Mass of Sample (% of Initial)
100
90
80
70
60
200
400
600
800
1000
Temperature (°C)

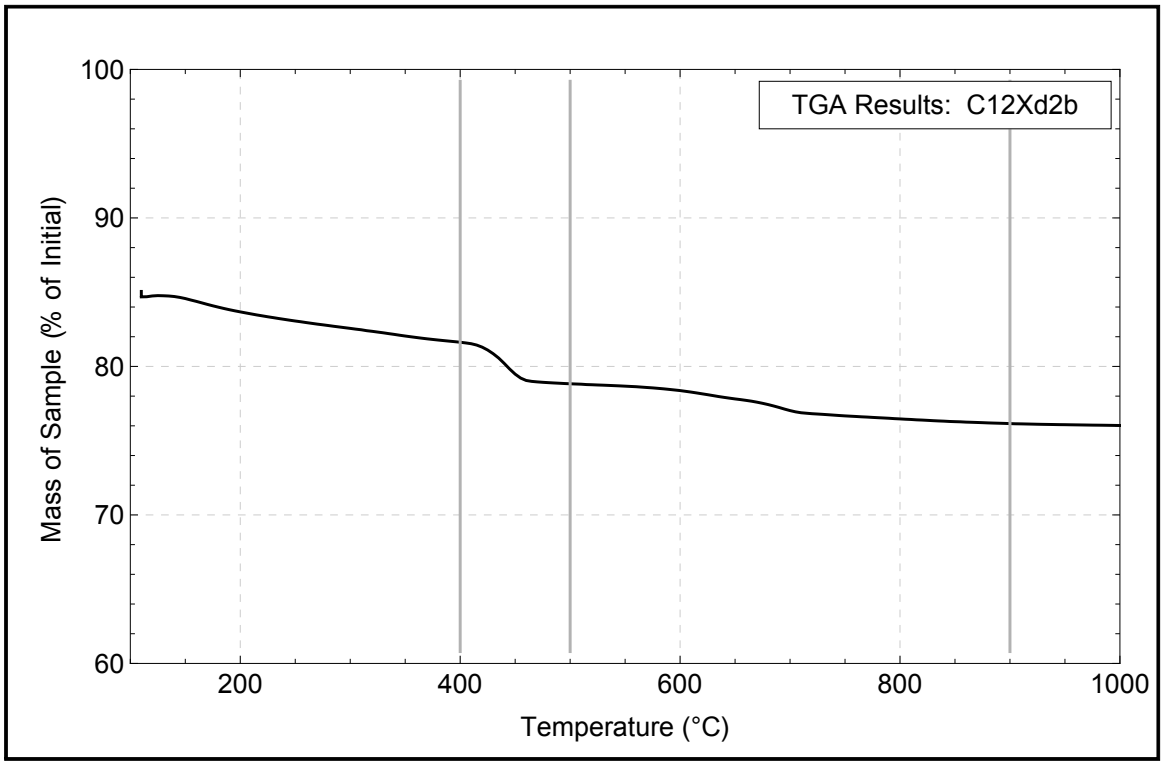
TGA Results: C12Xd2b
Mass of Sample (% of Initial)
100
90
80
70
60
200
400
600
800
1000
Temperature (°C)

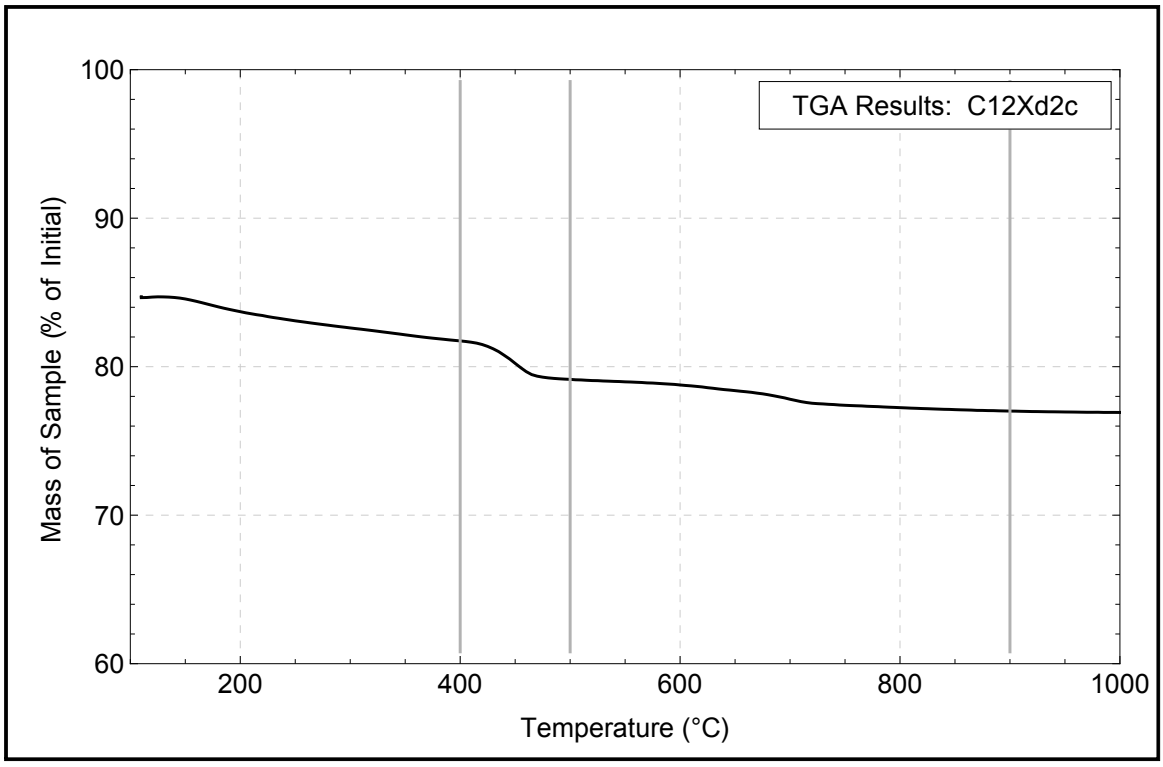
TGA Results: C12Xd2c
Mass of Sample (% of Initial)
100
90
80
70
60
200
400
600
800
1000
Temperature (°C)

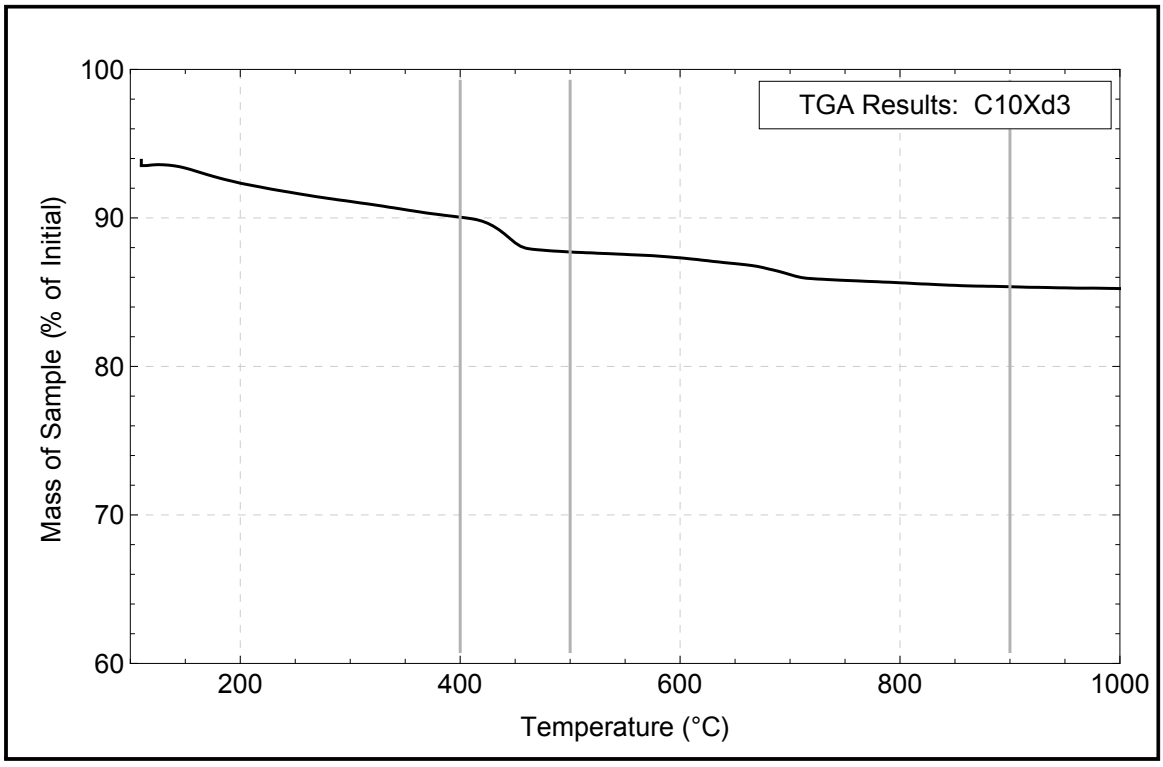
TGA Results: C10Xd3
Mass of Sample (% of Initial)
100
90
80
70
60
200
400
600
800
1000
Temperature (°C)

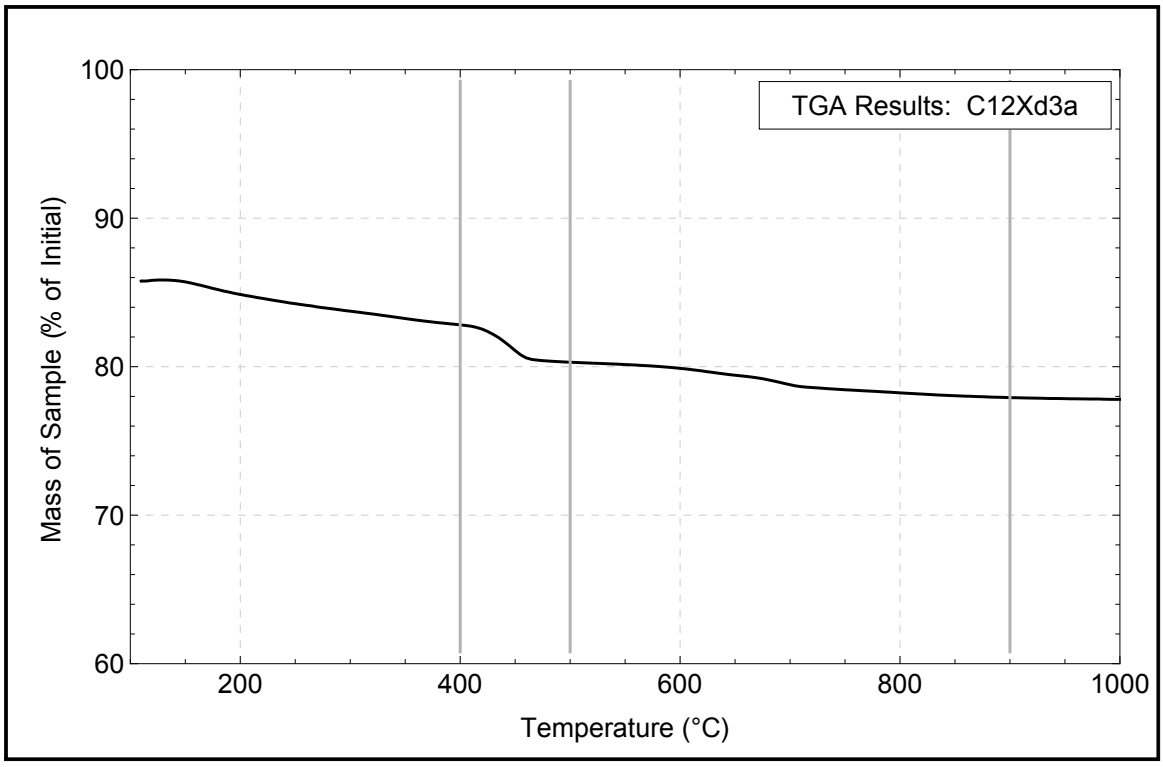
TGA Results: C12Xd3a
Mass of Sample (% of Initial)
100
90
80
70
60
200
400
600
800
1000
Temperature (°C)

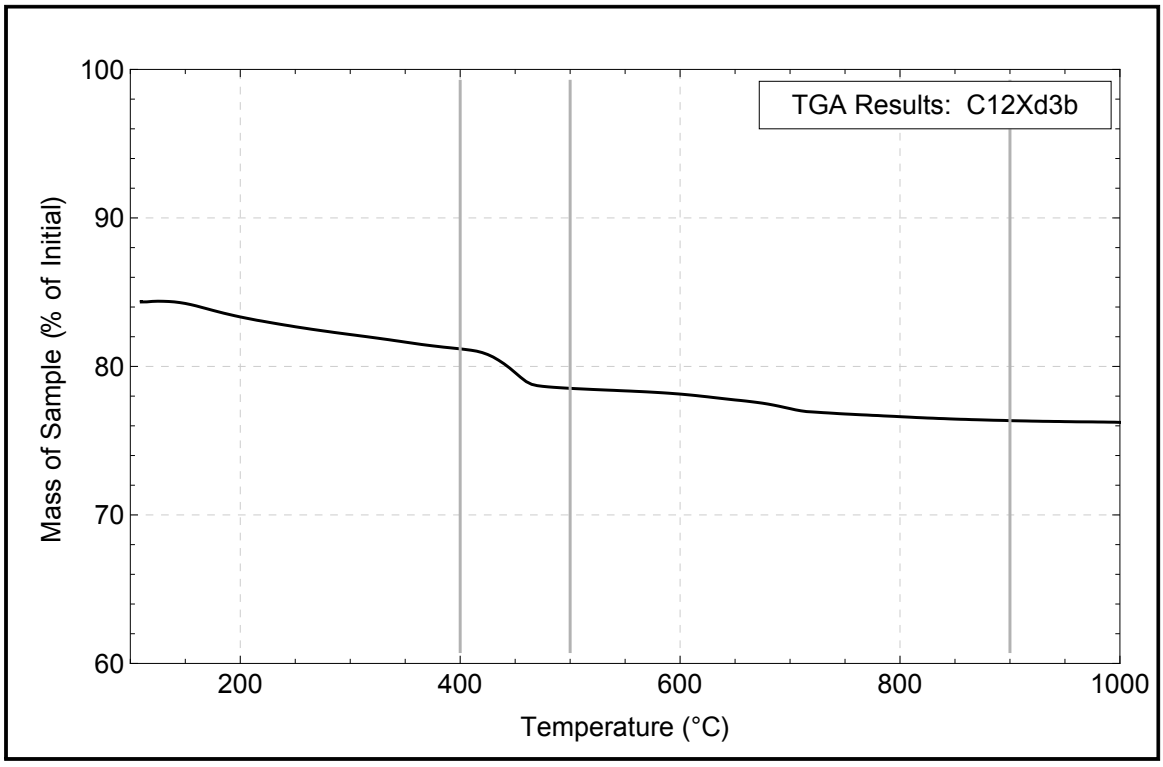
TGA Results: C12Xd3b
Mass of Sample (% of Initial)
100
90
80
70
60
200
400
600
800
1000
Temperature (°C)

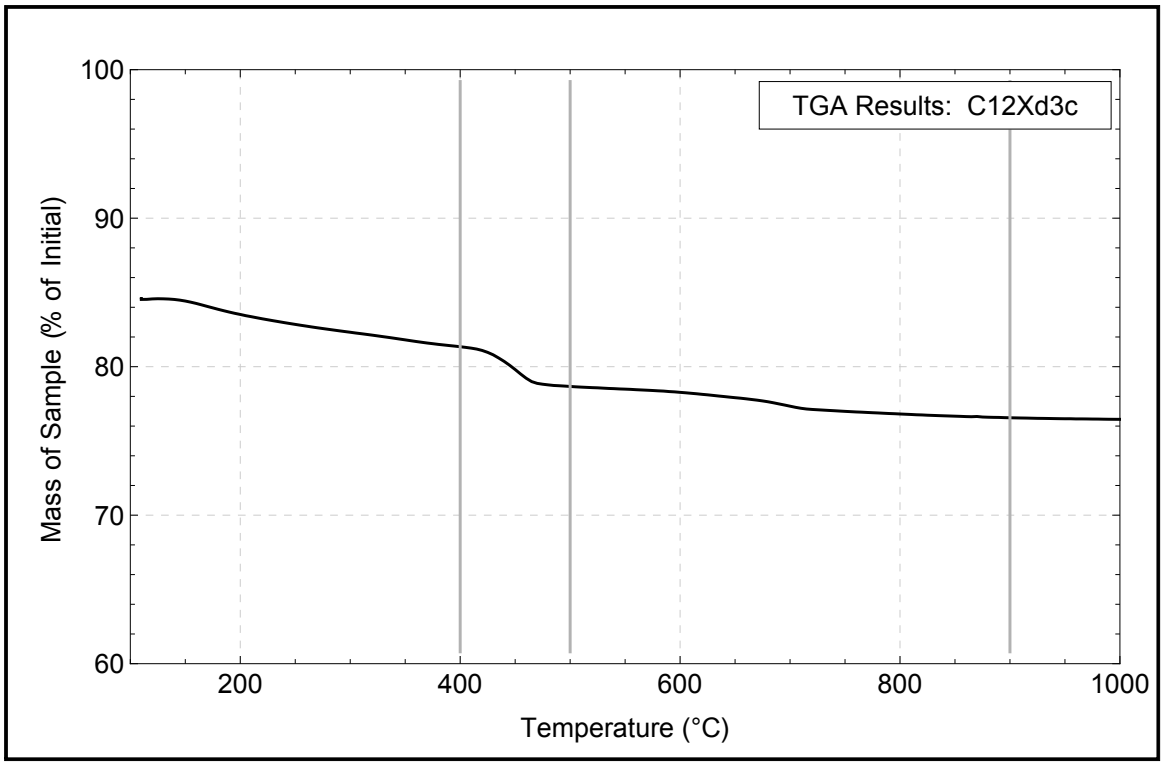
TGA Results: C12Xd3c
Mass of Sample (% of Initial)
100
90
80
70
60
200
400
600
800
1000
Temperature (°C)

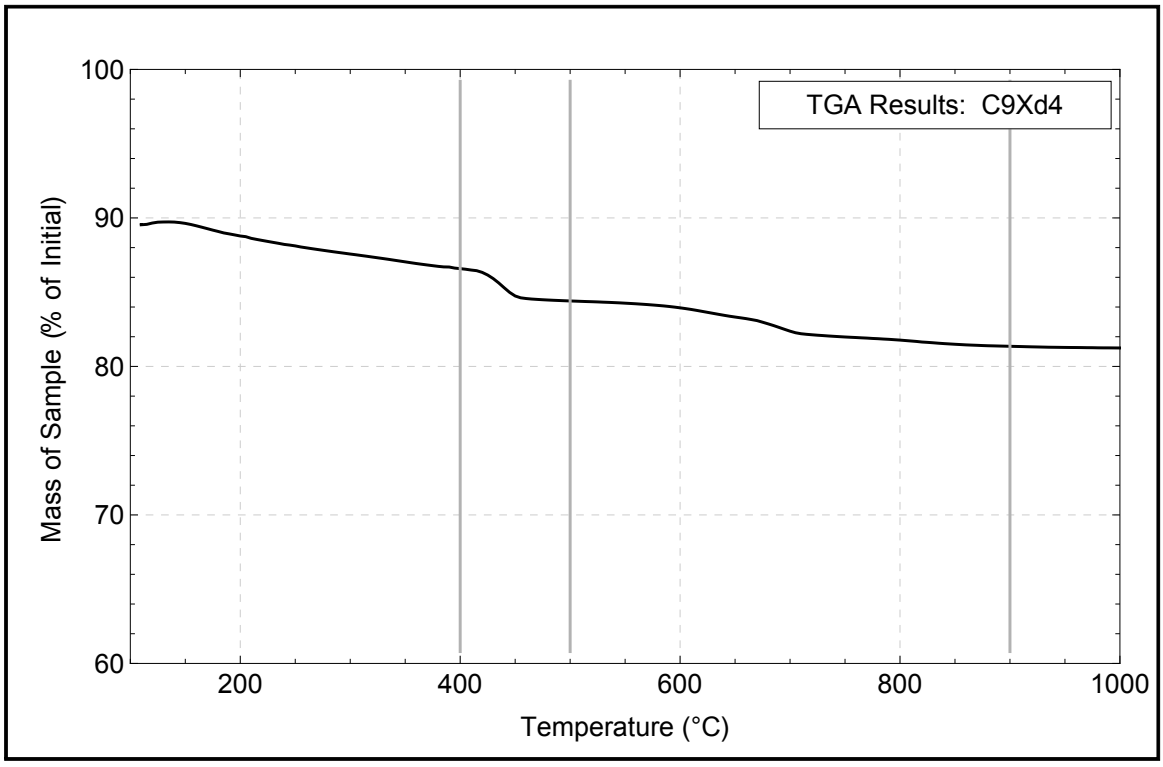
TGA Results: C9Xd4
Mass of Sample (% of Initial)
100
90
80
70
60
200
400
600
800
1000
Temperature (°C)

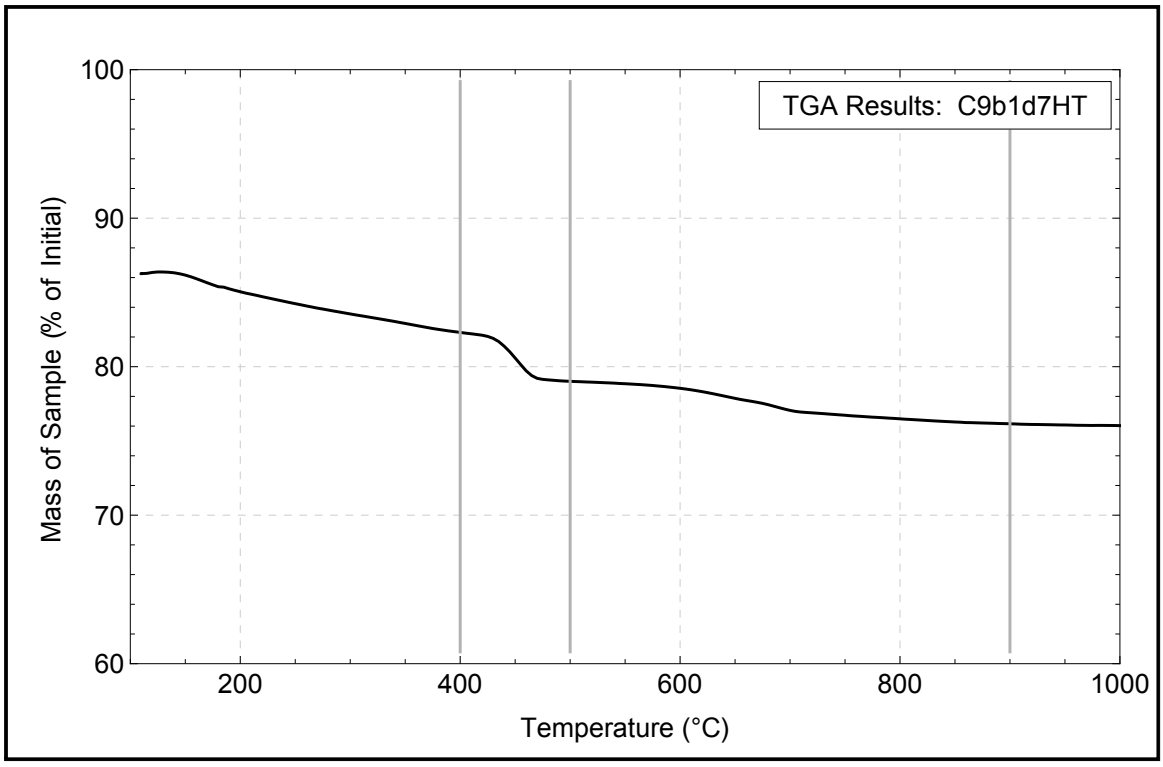
TGA Results: C9b1d7HT
Mass of Sample (% of Initial)
100
90
80
70
60
200
400
600
800
1000
Temperature (°C)

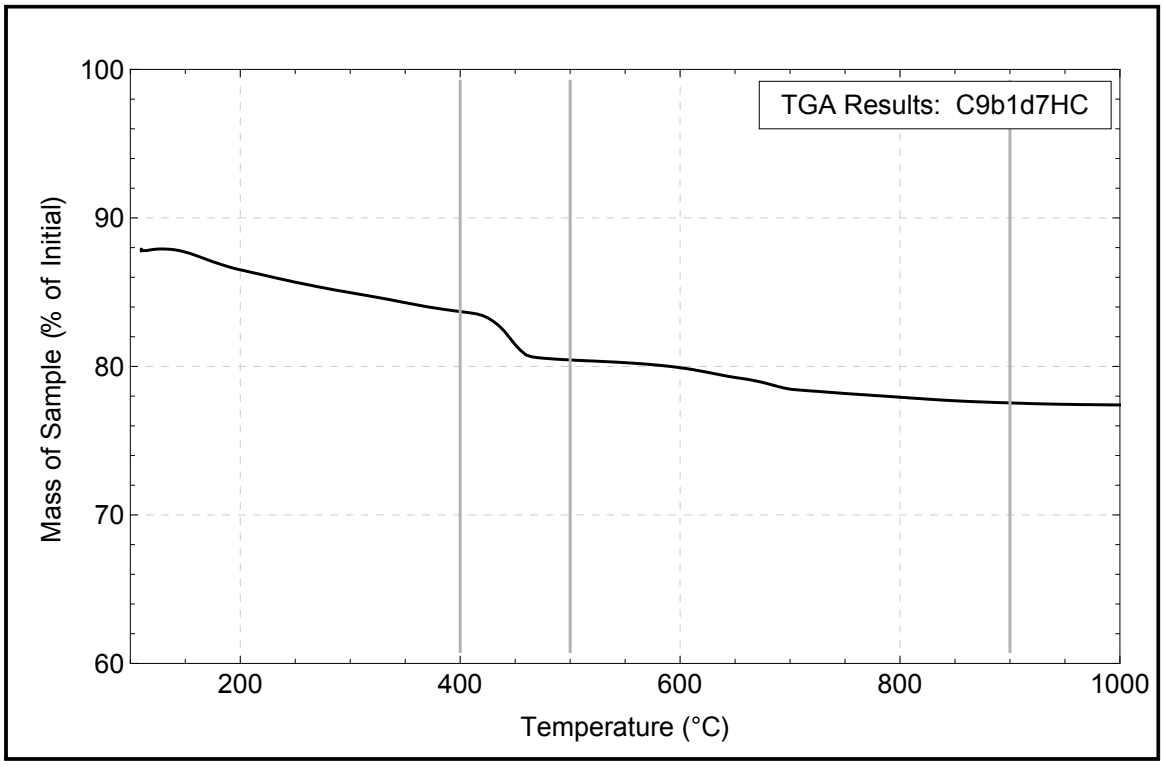
TGA Results: C9b1d7HC
Mass of Sample (% of Initial)
100
90
80
70
60
200
400
600
800
1000
Temperature (°C)

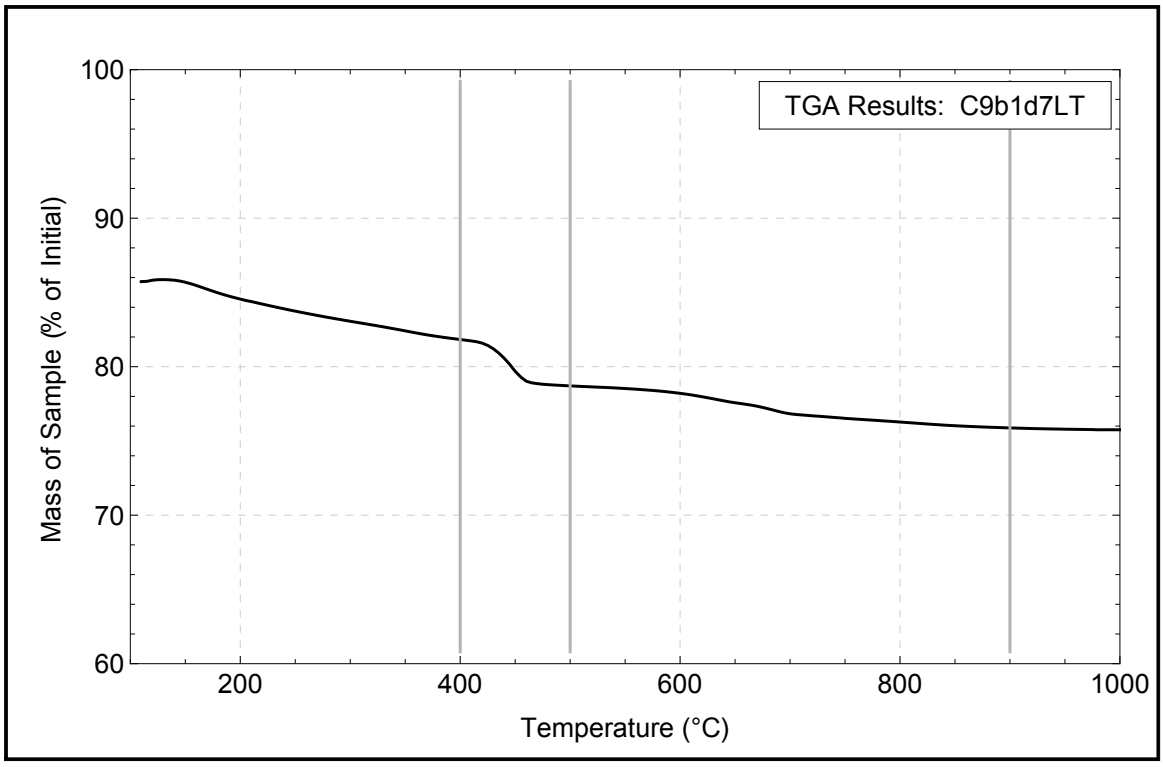
TGA Results: C9b1d7LT
Mass of Sample (% of Initial)
100
90
80
70
60
200
400
600
800
1000
Temperature (°C)

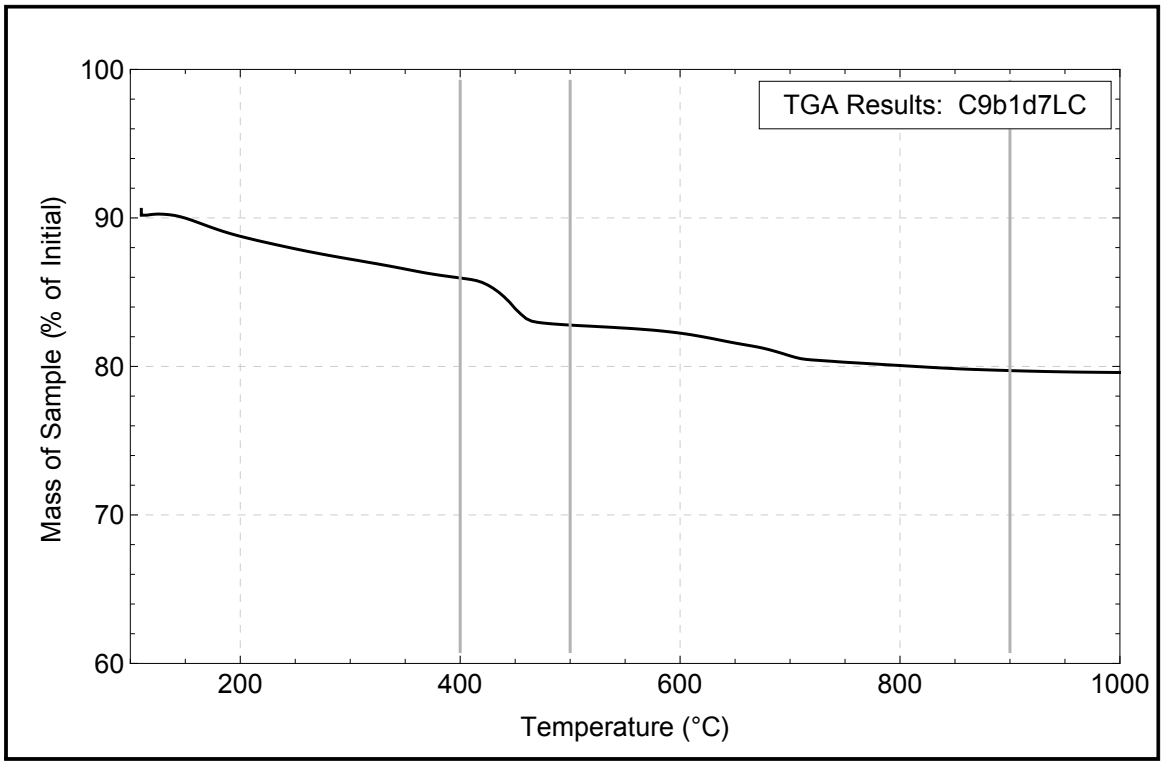
TGA Results: C9b1d7LC
Mass of Sample (% of Initial)
100
90
80
70
60
200
400
600
800
1000
Temperature (°C)

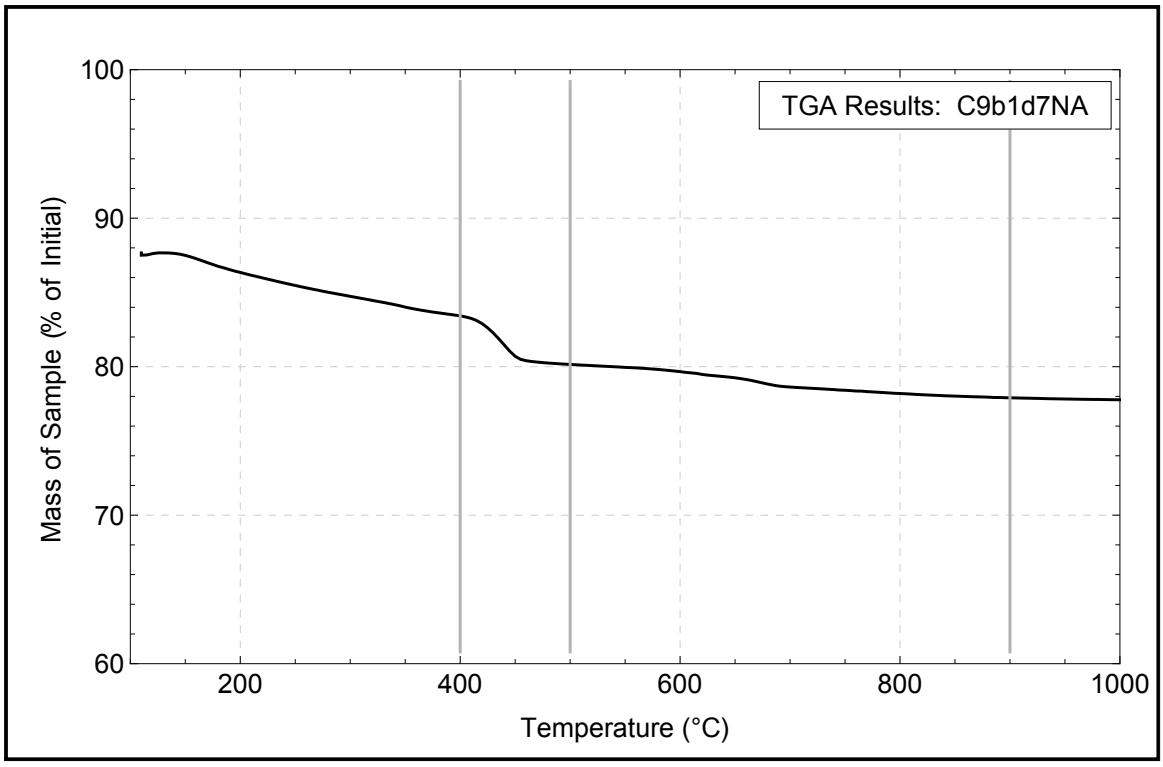
TGA Results: C9b1d7NA
Mass of Sample (% of Initial)
100
90
80
70
60
200
400
600
800
1000
Temperature (°C)

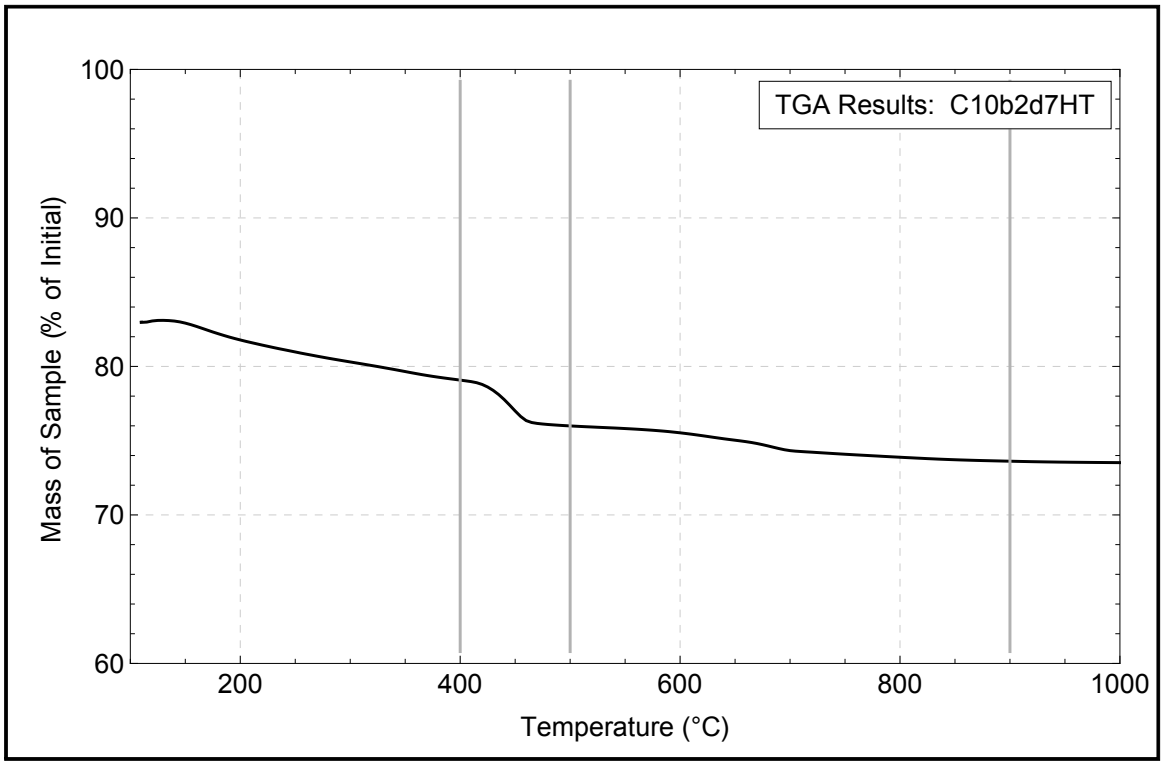
TGA Results: C10b2d7HT
Mass of Sample (% of Initial)
100
90
80
70
60
200
400
600
800
1000
Temperature (°C)

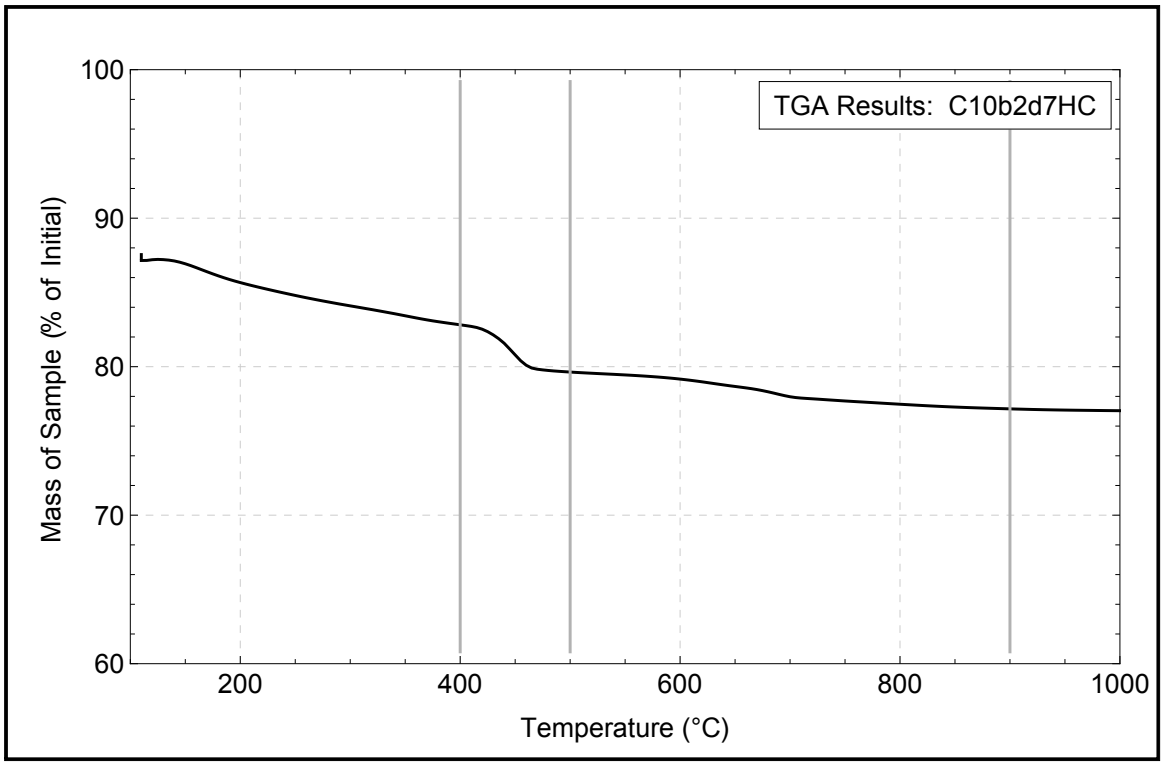
TGA Results: C10b2d7HC
Mass of Sample (% of Initial)
100
90
80
70
60
200
400
600
800
1000
Temperature (°C)

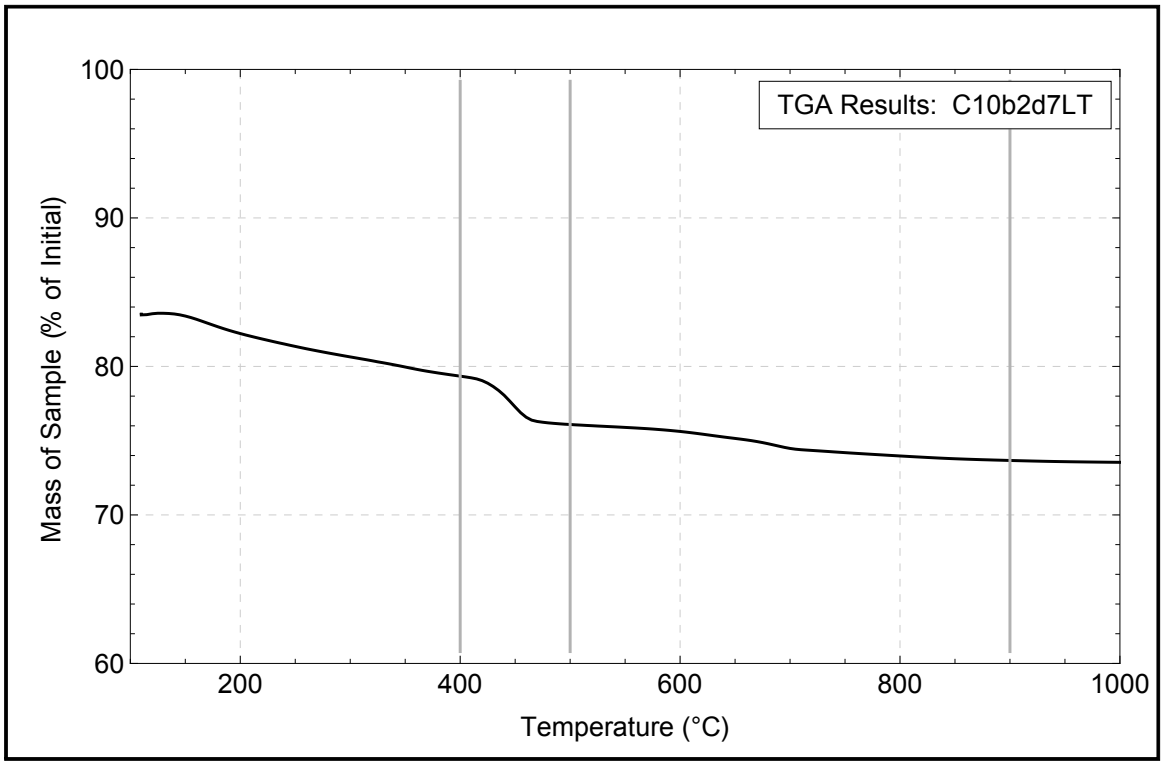
TGA Results: C10b2d7LT
Mass of Sample (% of Initial)
100
90
80
70
60
200
400
600
800
1000
Temperature (°C)

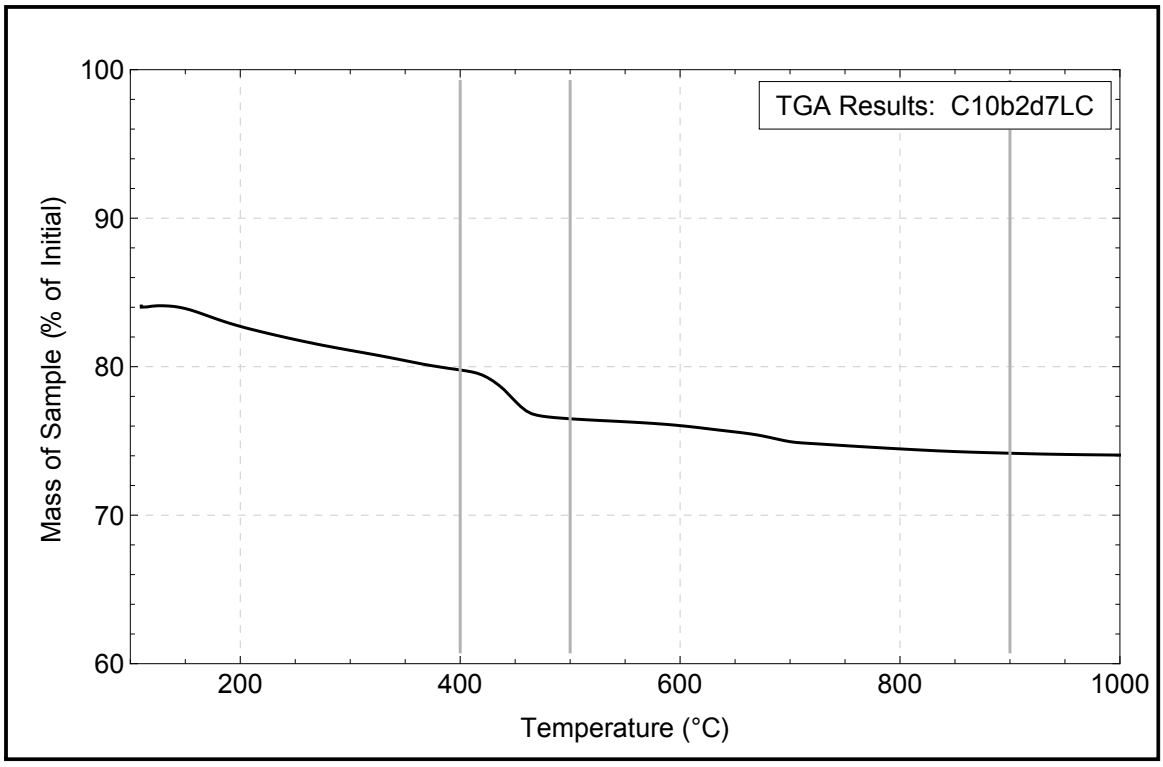
TGA Results: C10b2d7LC
Mass of Sample (% of Initial)
100
90
80
70
60
200
400
600
800
1000
Temperature (°C)

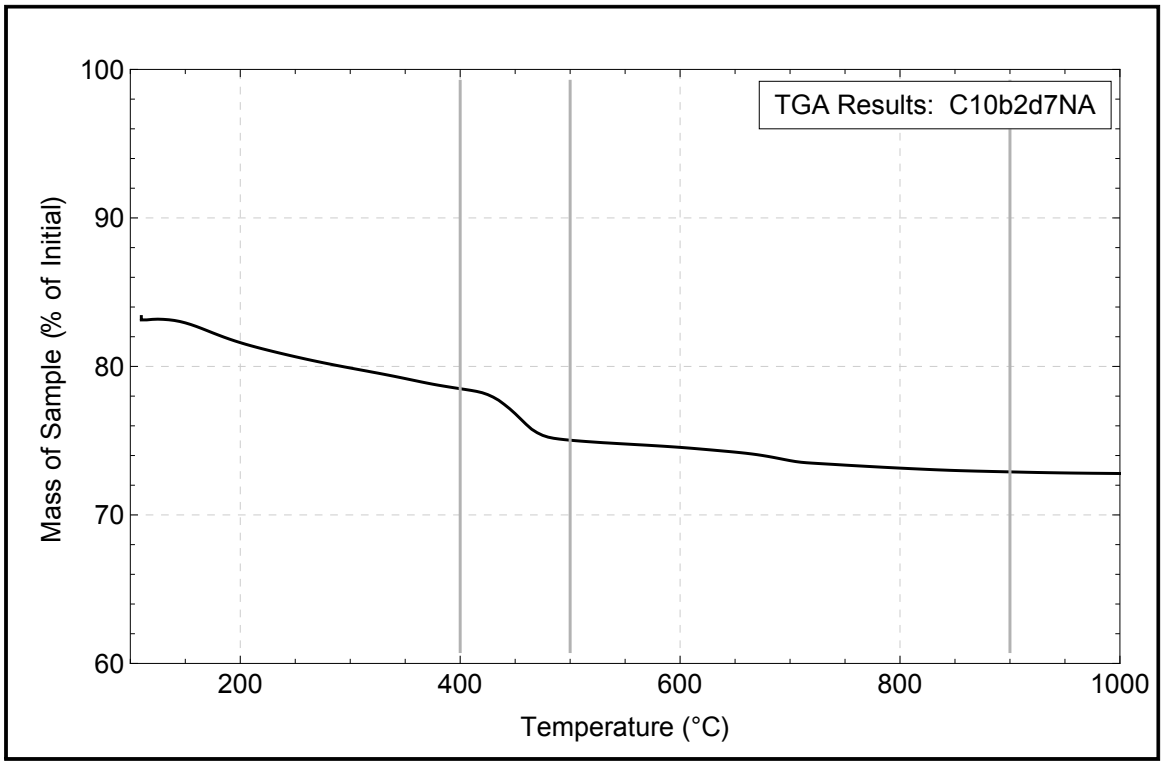
TGA Results: C10b2d7NA
Mass of Sample (% of Initial)
100
90
80
70
60
200
400
600
800
1000
Temperature (°C)

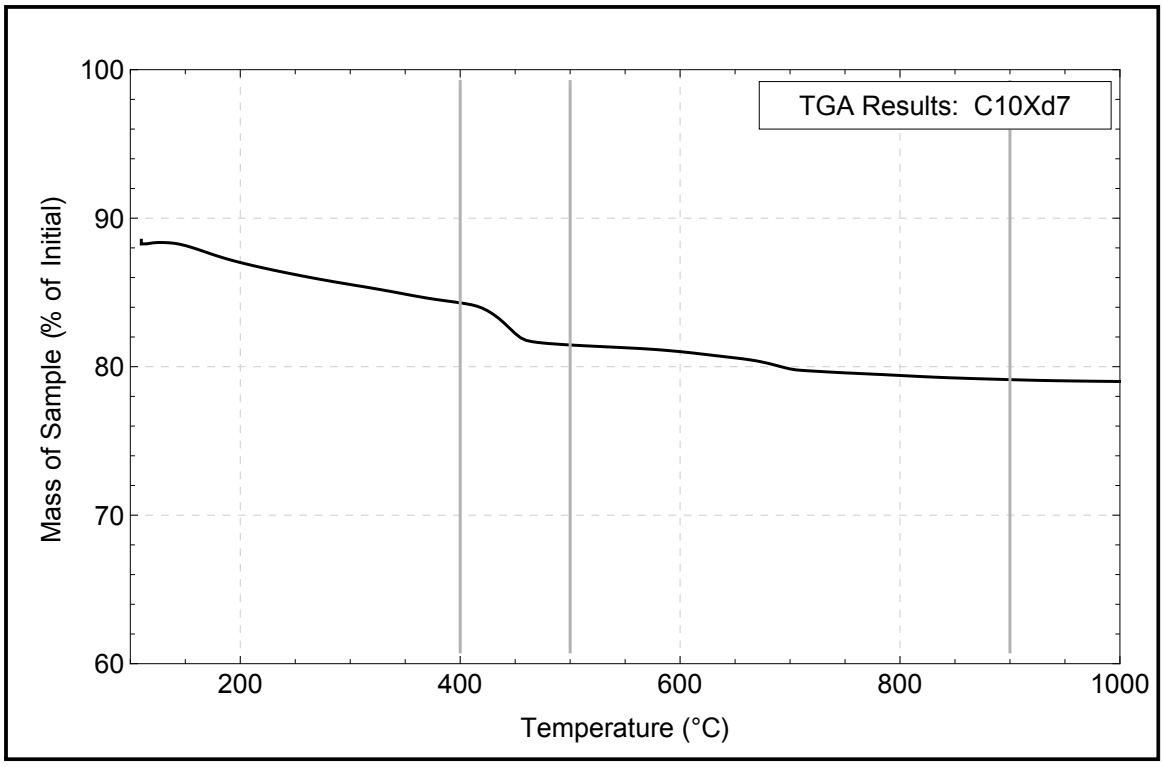
TGA Results: C10Xd7
Mass of Sample (% of Initial)
100
90
80
70
60
200
400
600
800
1000
Temperature (°C)

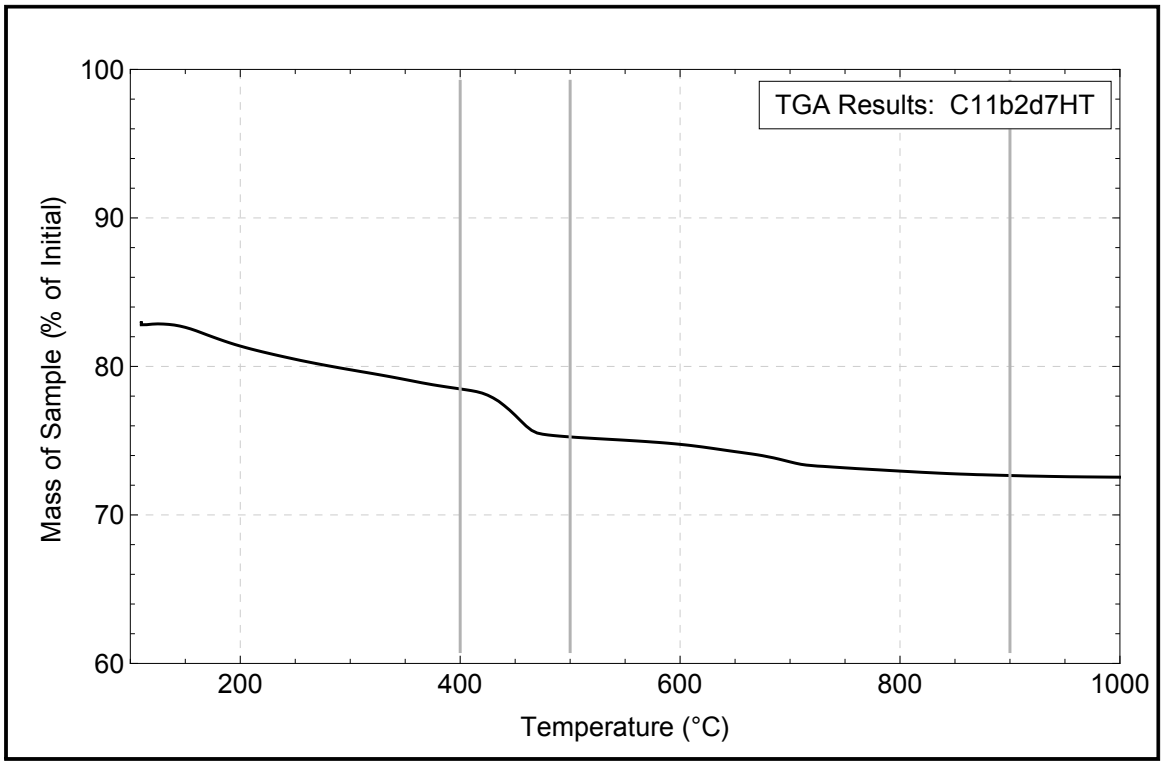
TGA Results: C11b2d7HT
Mass of Sample (% of Initial)
100
90
80
70
60
200
400
600
800
1000
Temperature (°C)

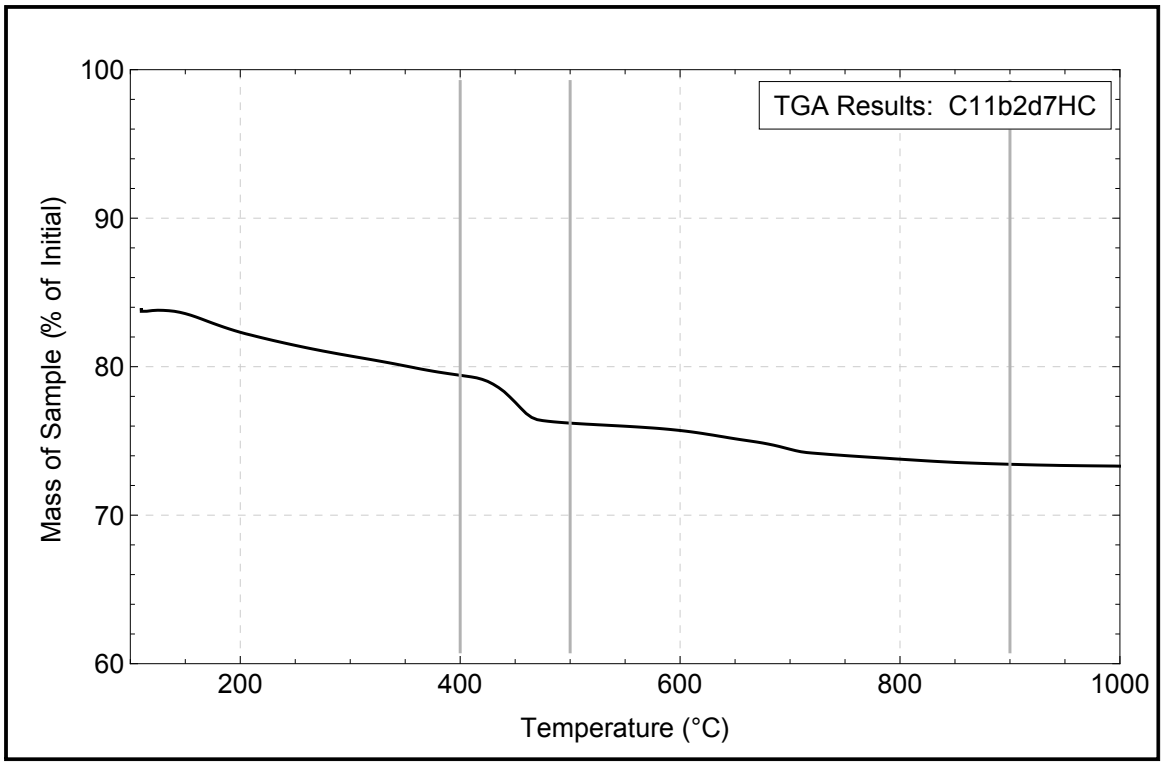
TGA Results: C11b2d7HC
Mass of Sample (% of Initial)
100
90
80
70
60
200
400
600
800
1000
Temperature (°C)

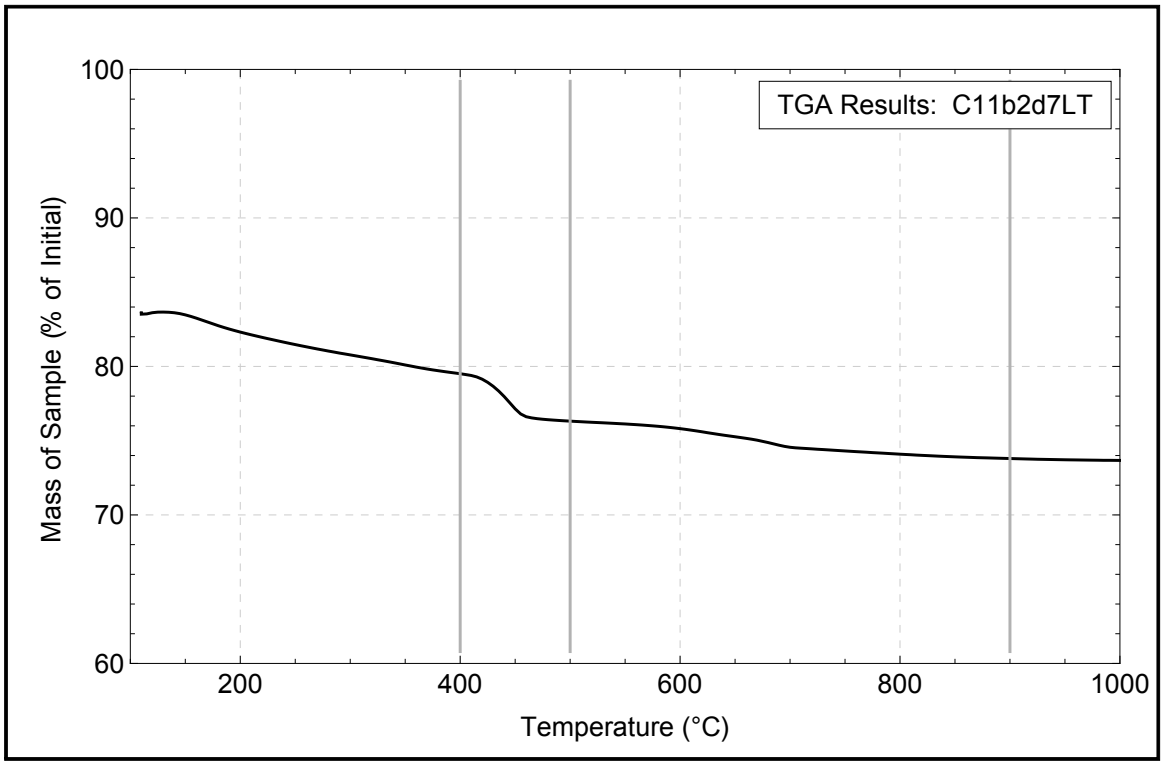
TGA Results: C11b2d7LT
Mass of Sample (% of Initial)
100
90
80
70
60
200
400
600
800
1000
Temperature (°C)

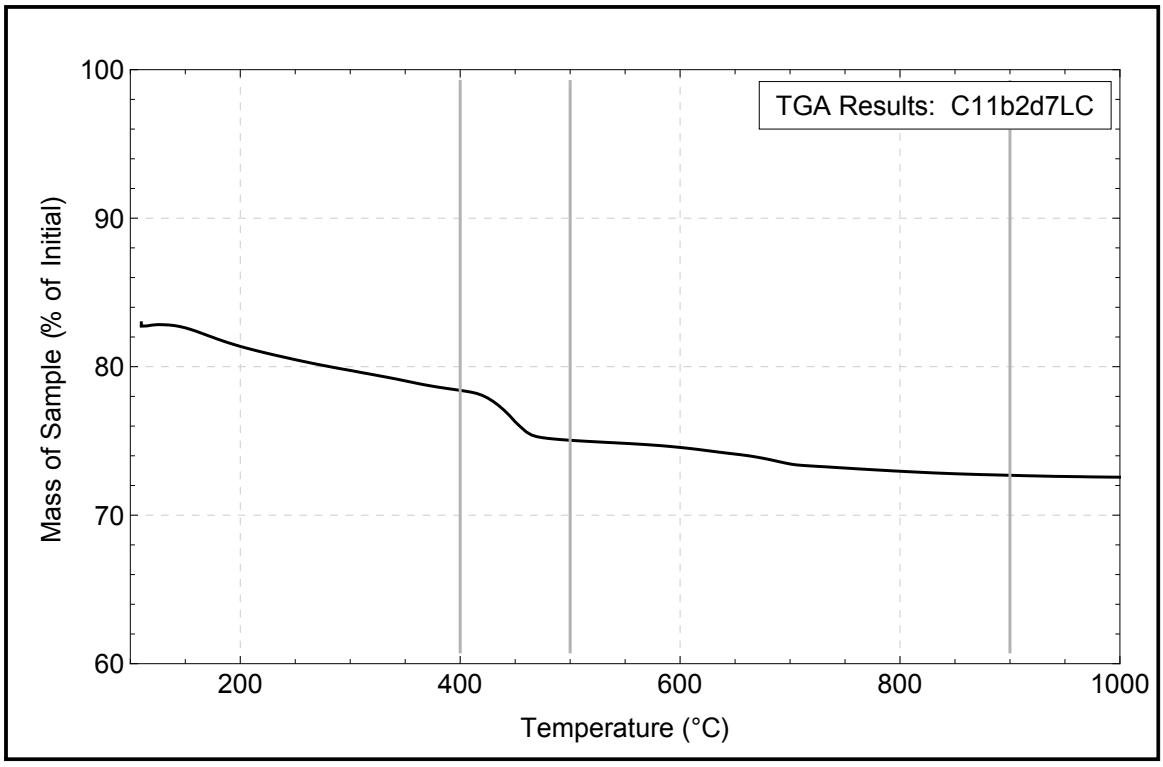
TGA Results: C11b2d7LC
Mass of Sample (% of Initial)
100
90
80
70
60
200
400
600
800
1000
Temperature (°C)

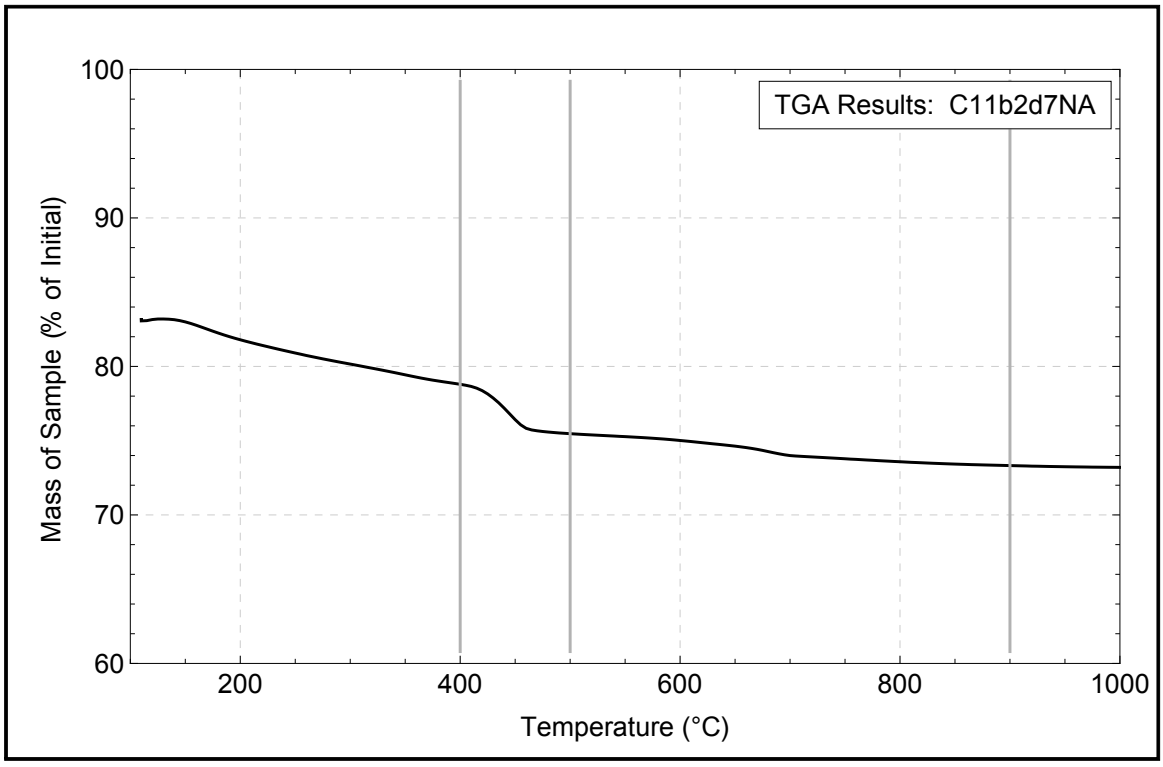
TGA Results: C11b2d7NA
Mass of Sample (% of Initial)
100
90
80
70
60
200
400
600
800
1000
Temperature (°C)

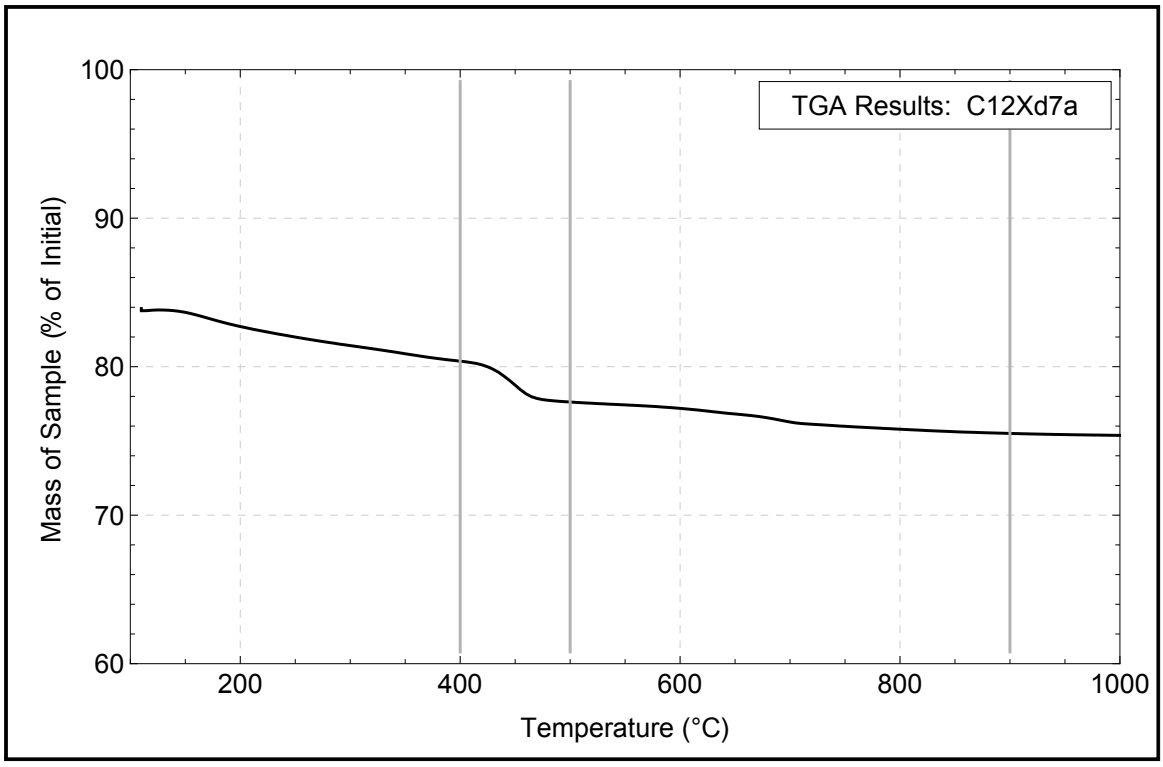
TGA Results: C12Xd7a
Mass of Sample (% of Initial)
100
90
80
70
60
200
400
600
800
1000
Temperature (°C)

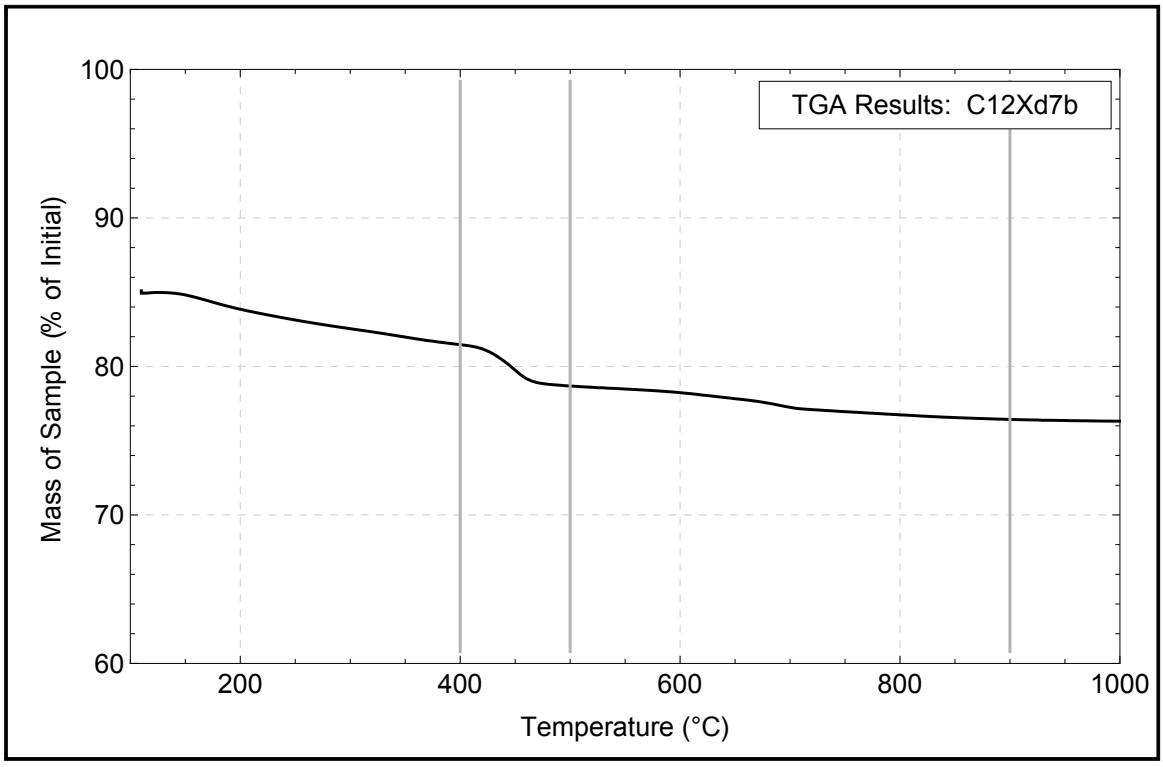
TGA Results: C12Xd7b
Mass of Sample (% of Initial)
100
90
80
70
60
200
400
600
800
1000
Temperature (°C)

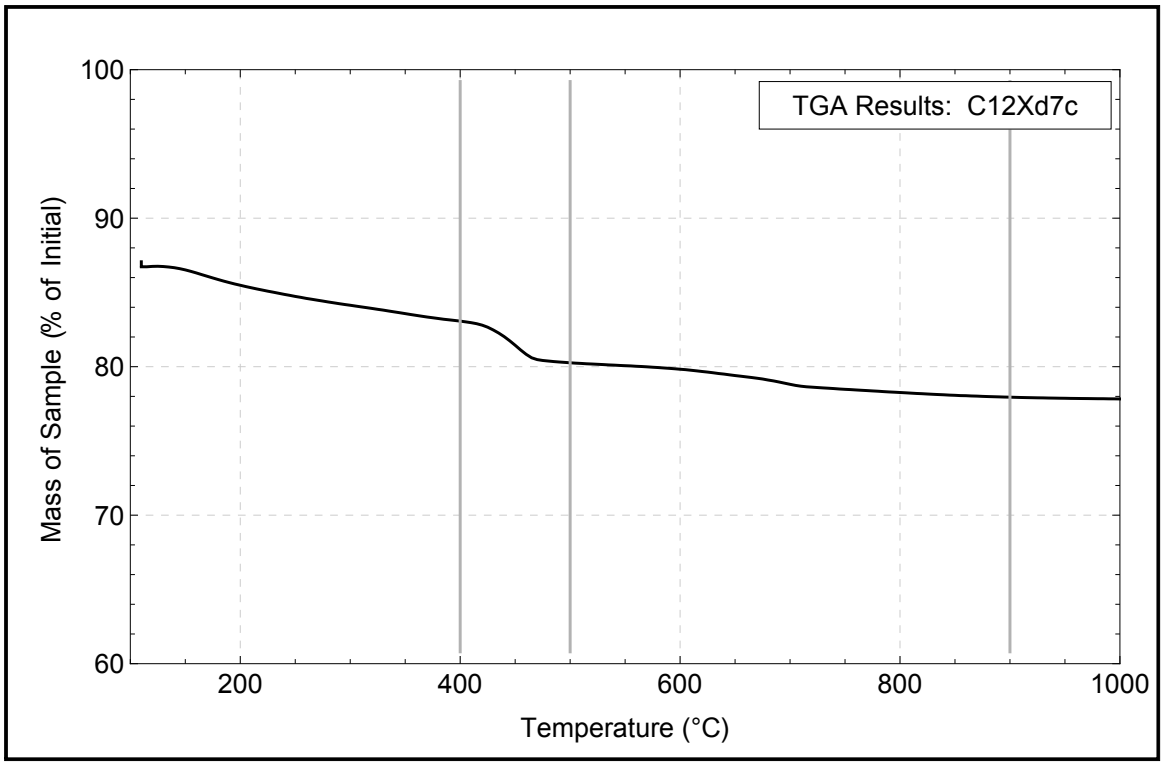
TGA Results: C12Xd7c
Mass of Sample (% of Initial)
100
90
80
70
60
200
400
600
800
1000
Temperature (°C)

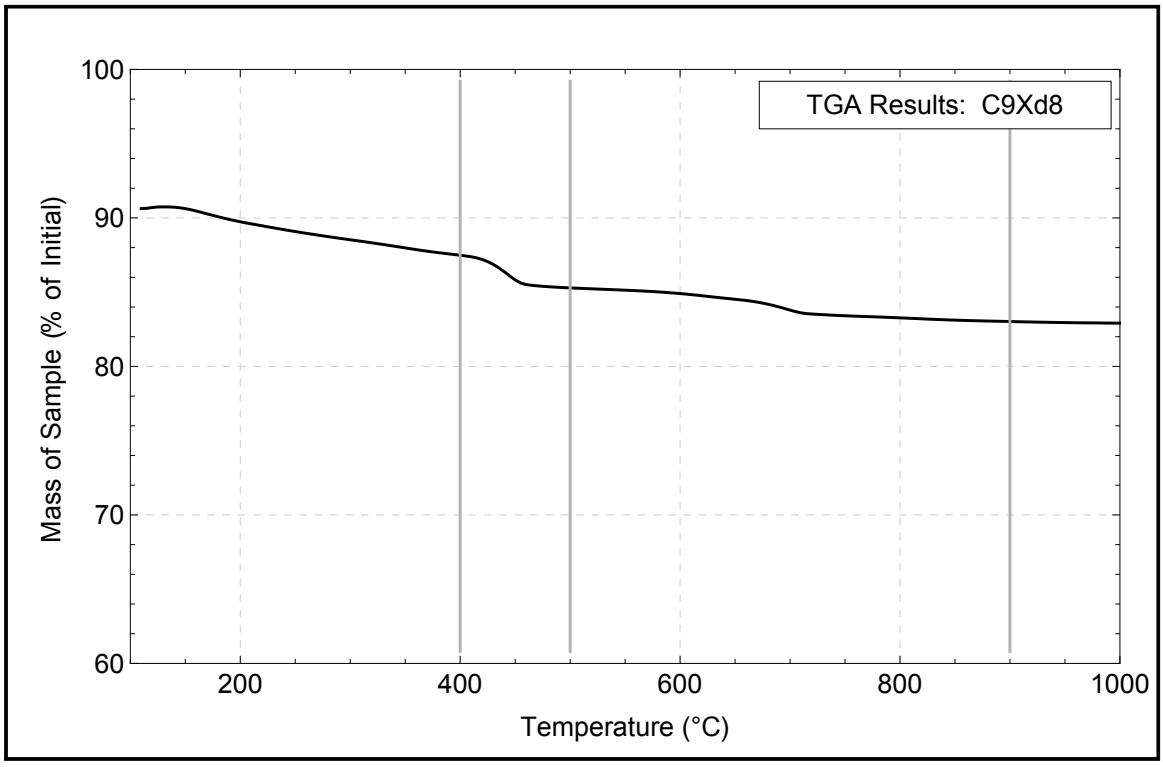
TGA Results: C9Xd8
Mass of Sample (% of Initial)
100
90
80
70
60
200
400
600
800
1000
Temperature (°C)

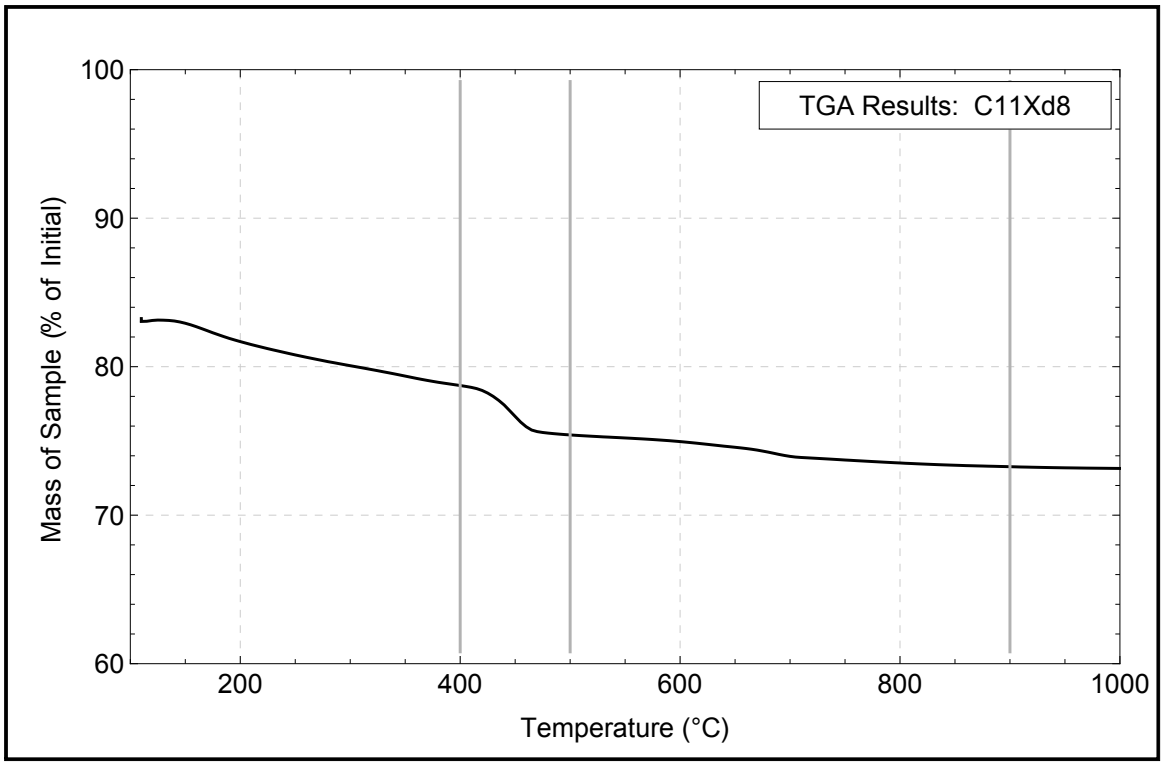
TGA Results: C11Xd8
Mass of Sample (% of Initial)
100
90
80
70
60
200
400
600
800
1000
Temperature (°C)

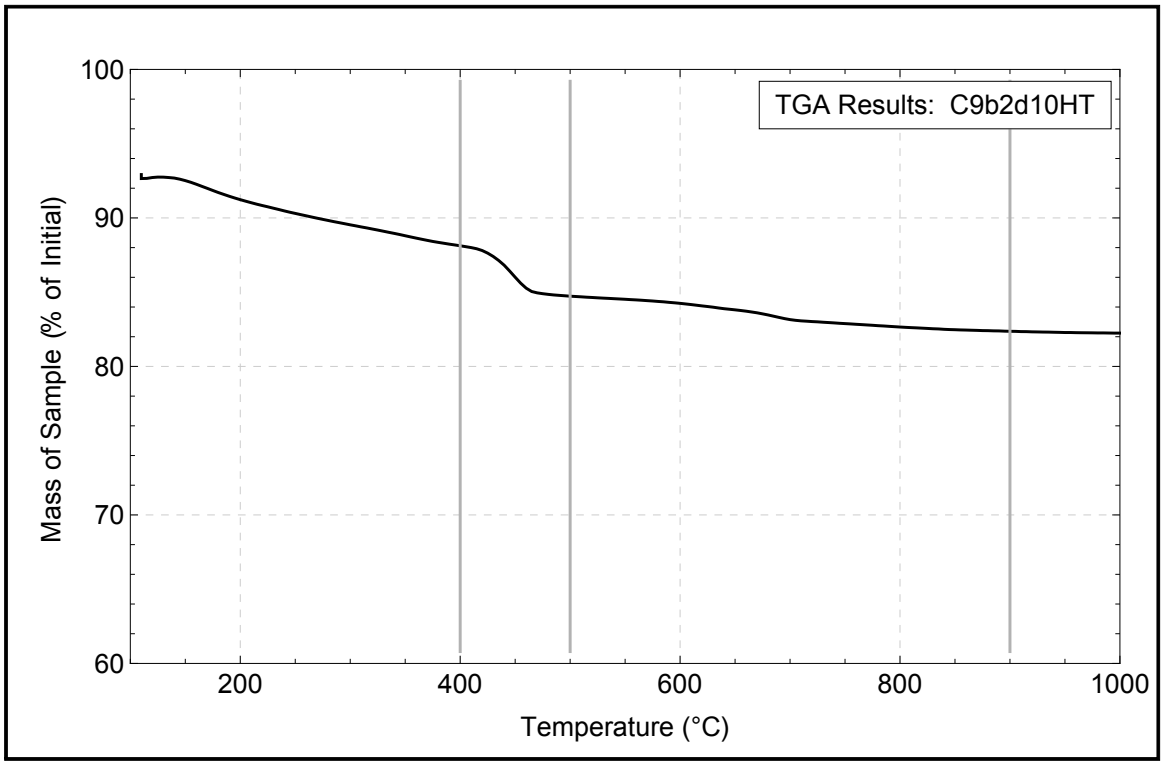
TGA Results: C9b2d10HT
Mass of Sample (% of Initial)
100
90
80
70
60
200
400
600
800
1000
Temperature (°C)

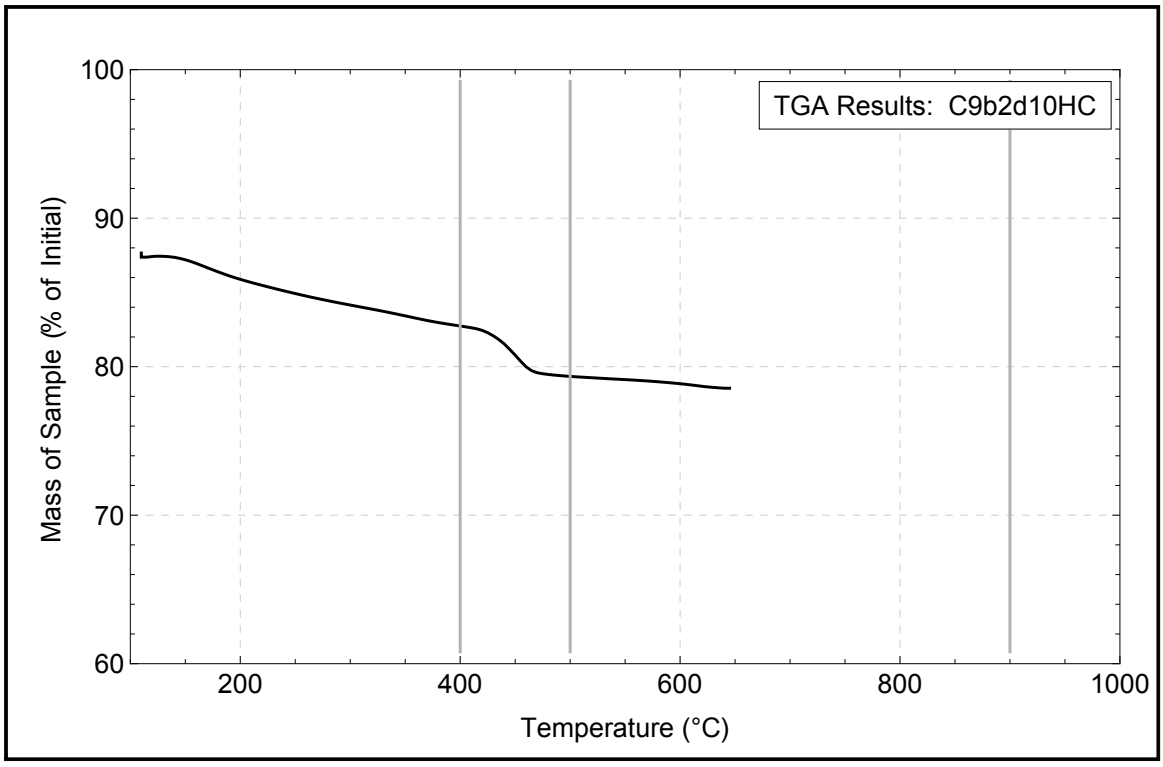
TGA Results: C9b2d10HC
Mass of Sample (% of Initial)
100
90
80
70
60
200
400
600
800
1000
Temperature (°C)

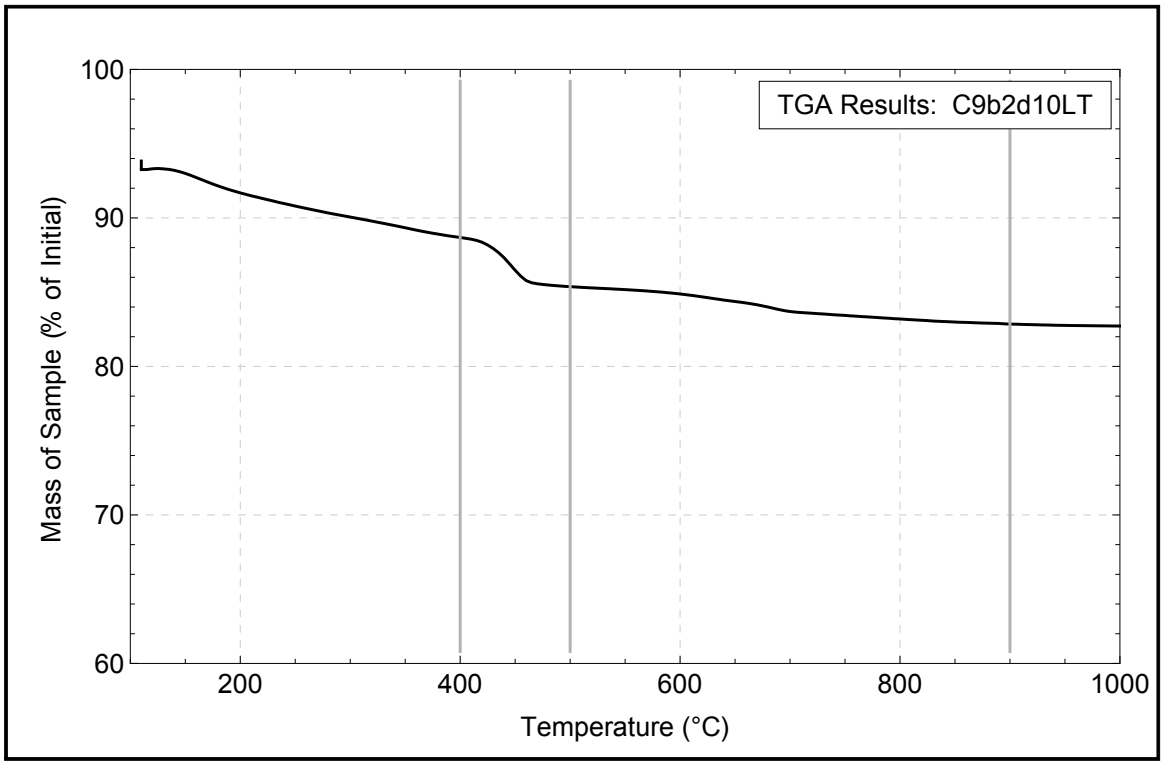
TGA Results: C9b2d10LT
Mass of Sample (% of Initial)
100
90
80
70
60
200
400
600
800
1000
Temperature (°C)

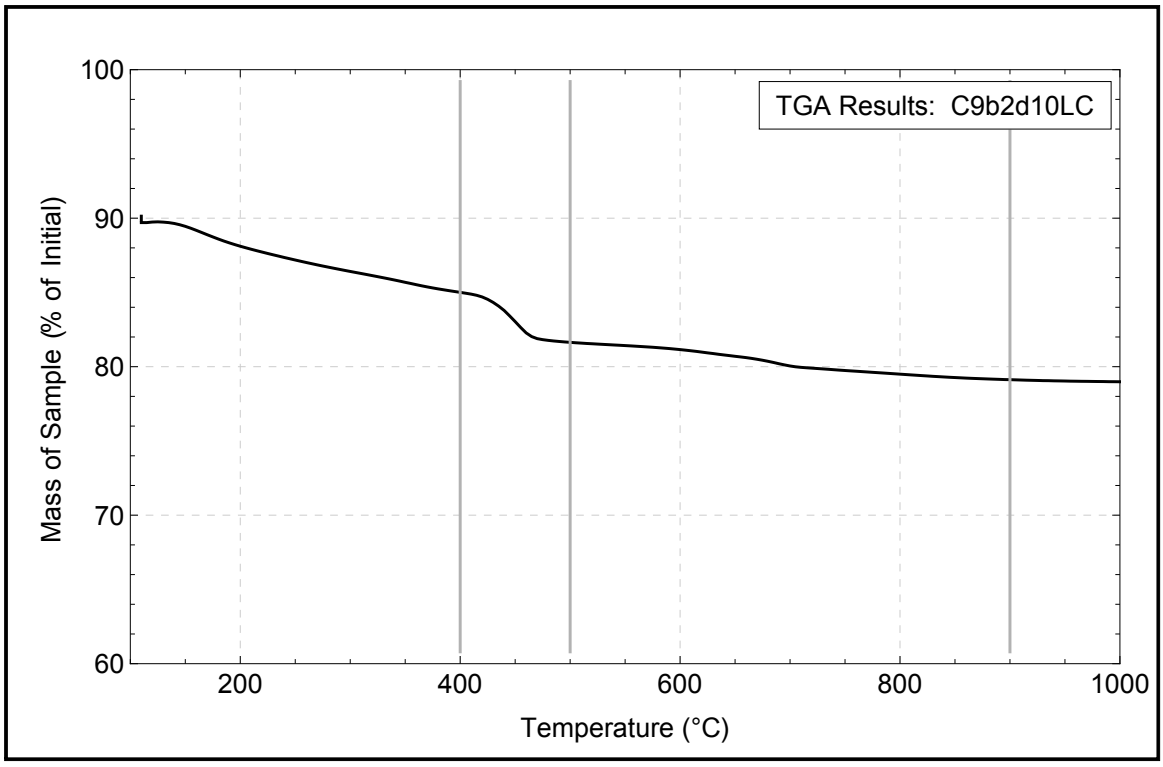
TGA Results: C9b2d10LC
Mass of Sample (% of Initial)
100
90
80
70
60
200
400
600
800
1000
Temperature (°C)

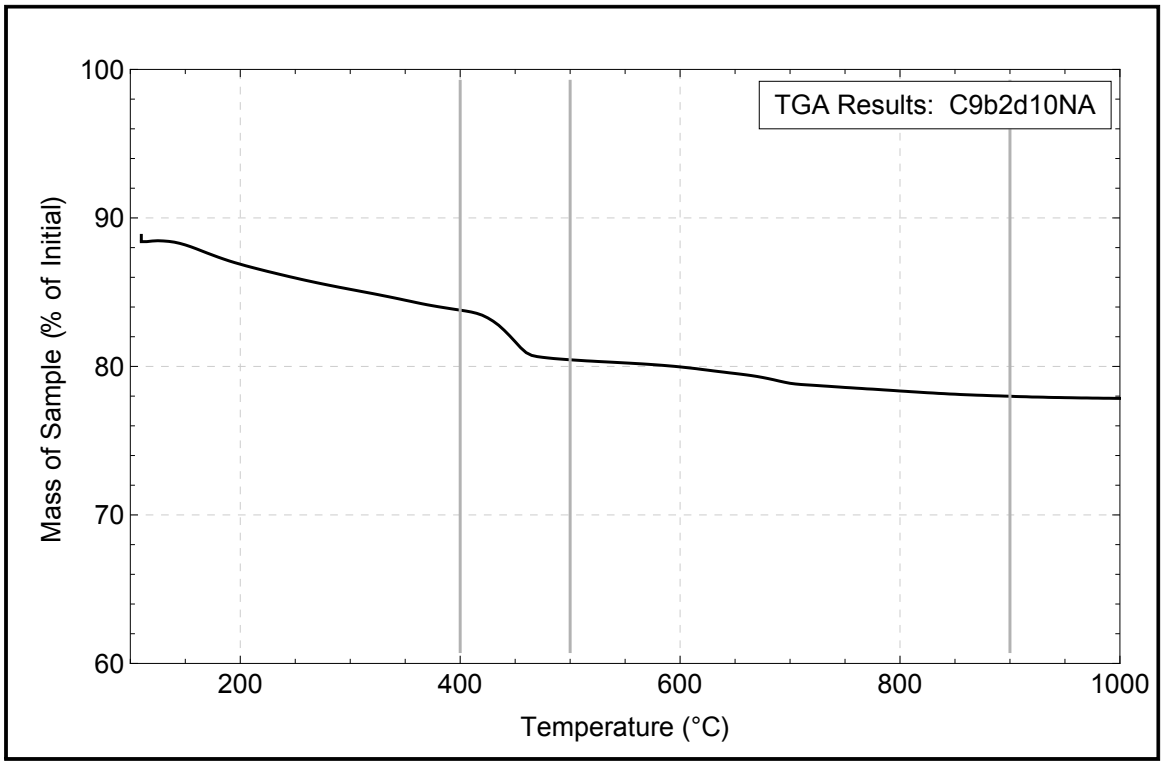
TGA Results: C9b2d10NA
Mass of Sample (% of Initial)
100
90
80
70
60
200
400
600
800
1000
Temperature (°C)

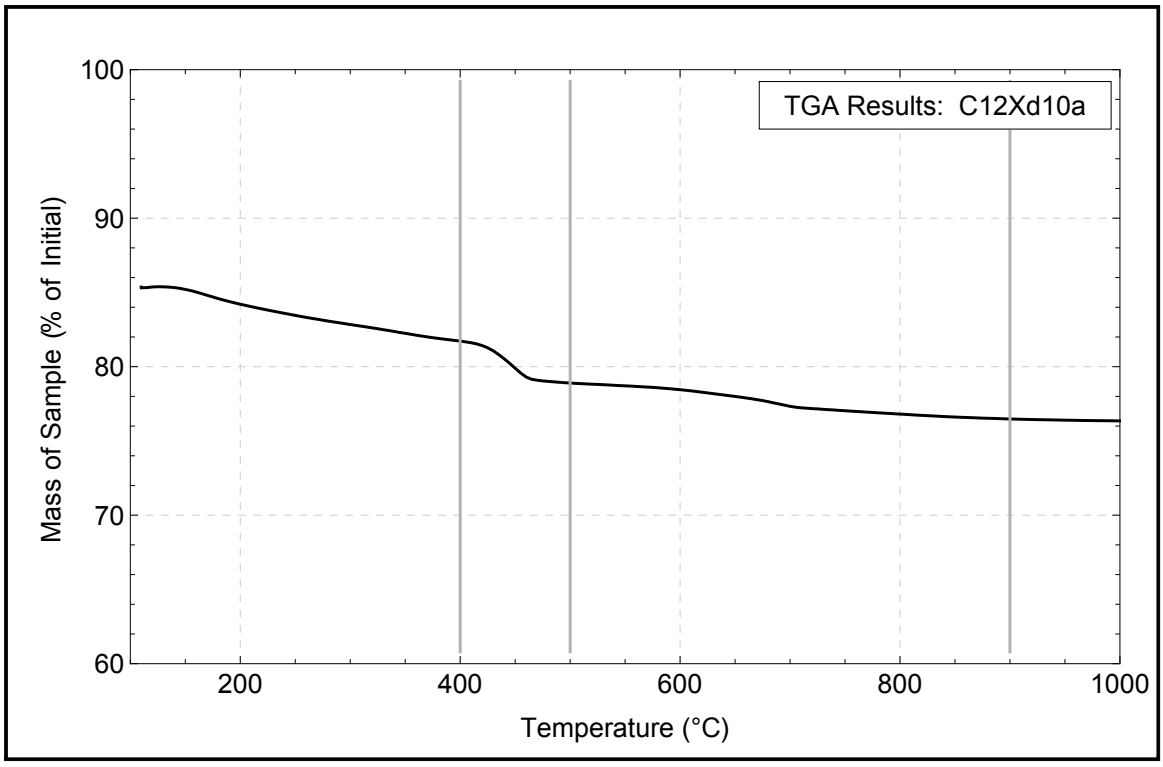
TGA Results: C12Xd10a
Mass of Sample (% of Initial)
100
90
80
70
60
200
400
600
800
1000
Temperature (°C)

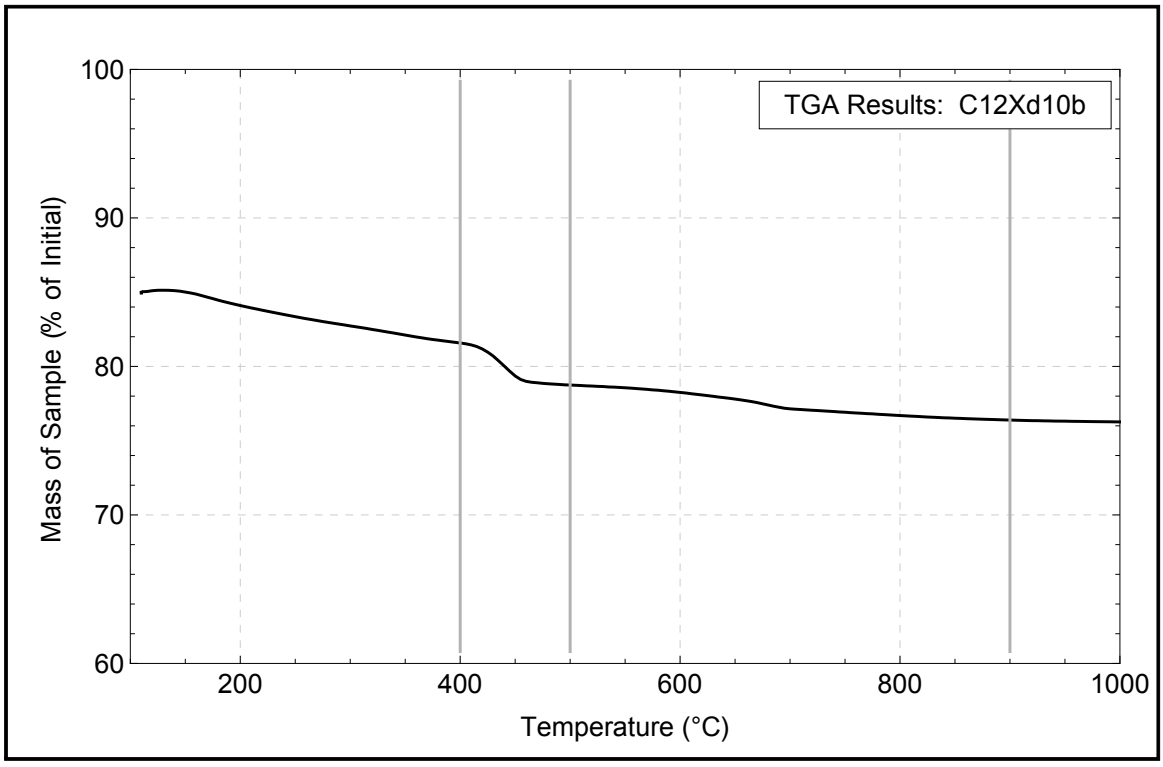
TGA Results: C12Xd10b
Mass of Sample (% of Initial)
100
90
80
70
60
200
400
600
800
1000
Temperature (°C)

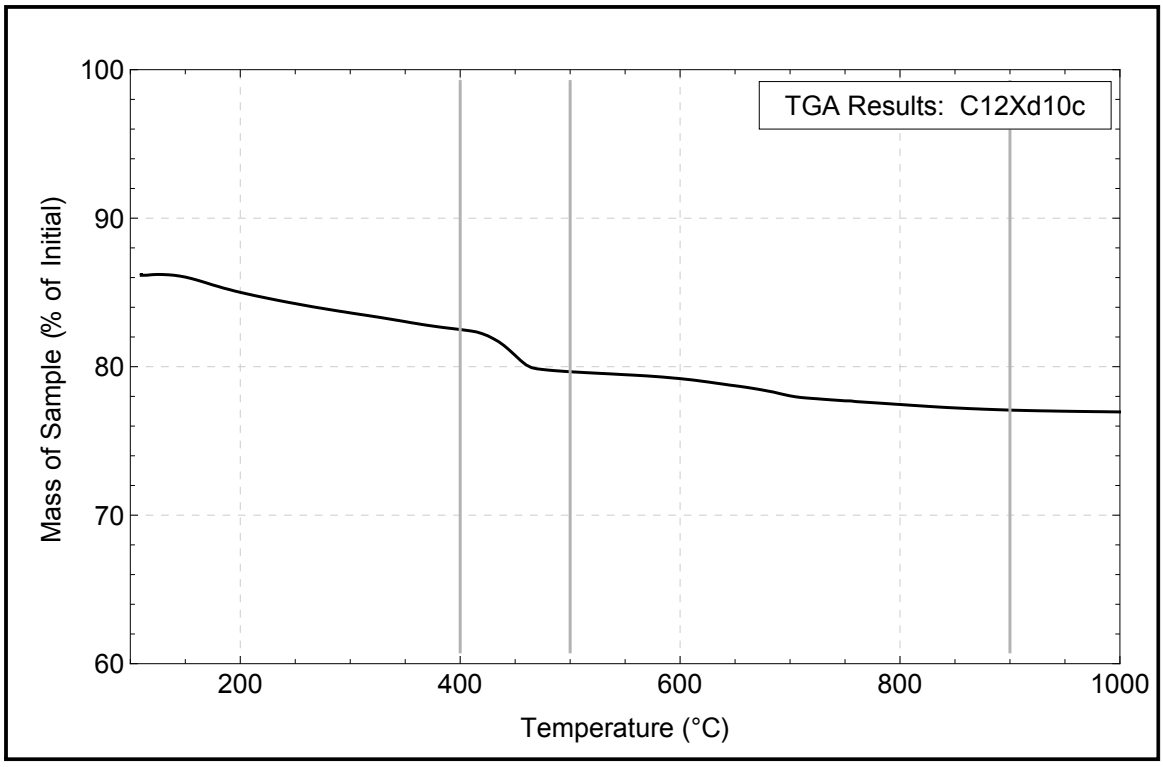
TGA Results: C12Xd10c
Mass of Sample (% of Initial)
100
90
80
70
60
200
400
600
800
1000
Temperature (°C)

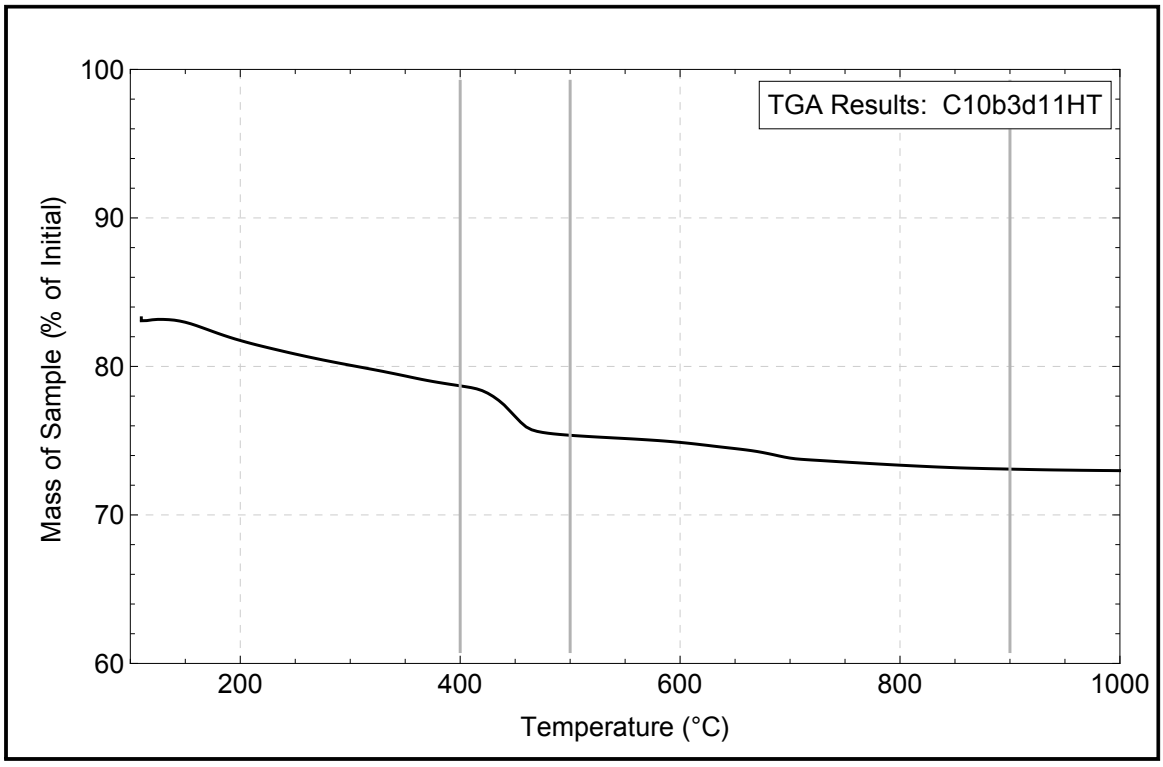
TGA Results: C10b3d11HT
Mass of Sample (% of Initial)
100
90
80
70
60
200
400
600
800
1000
Temperature (°C)

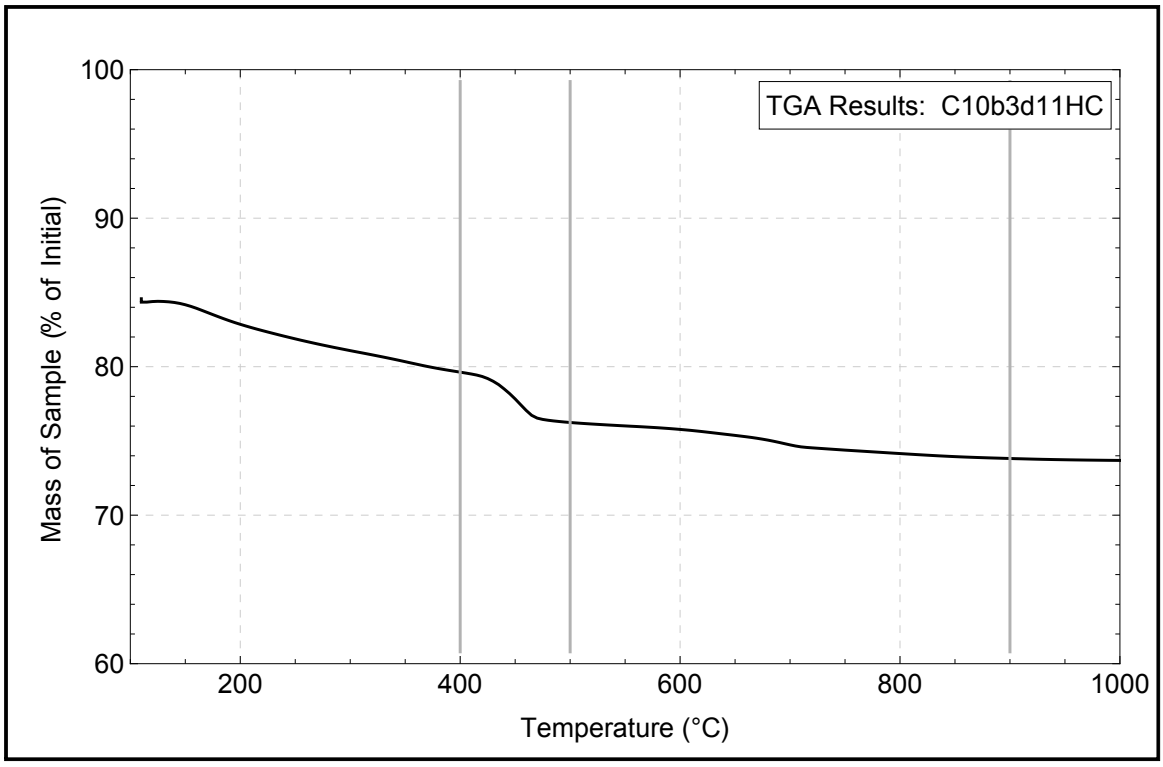
TGA Results: C10b3d11HC
Mass of Sample (% of Initial)
100
90
80
70
60
200
400
600
800
1000
Temperature (°C)

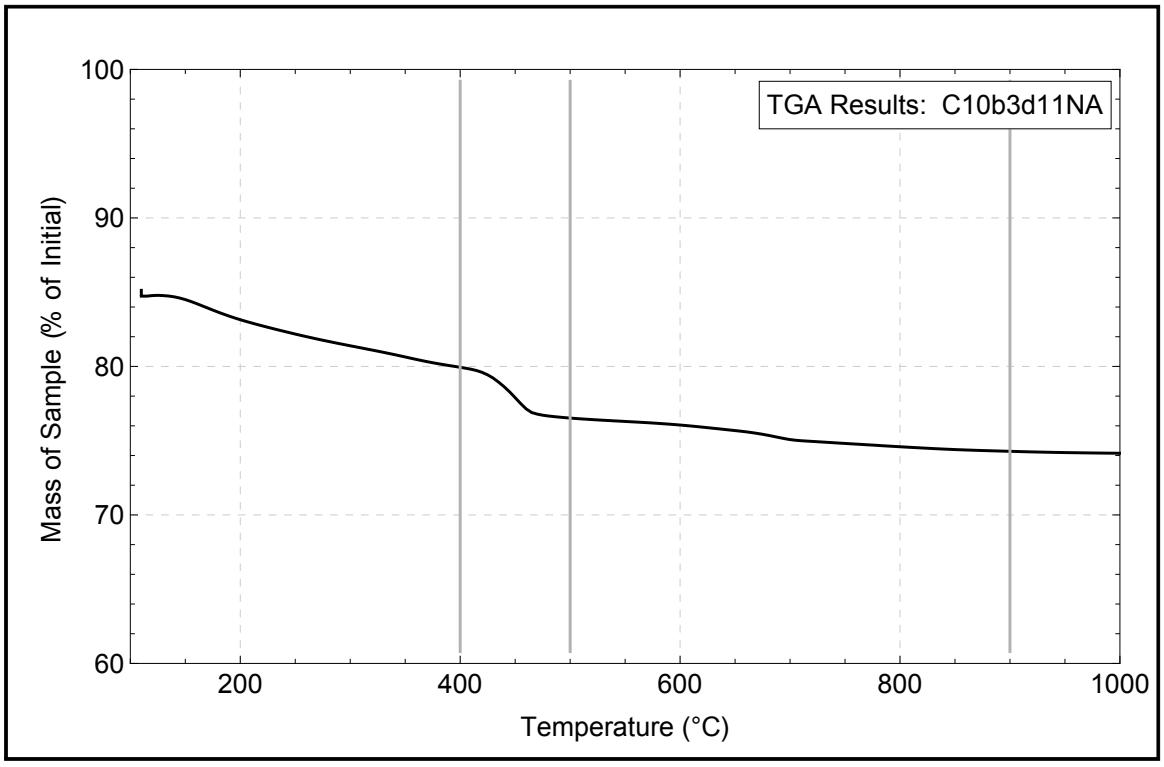
TGA Results: C10b3d11NA
Mass of Sample (% of Initial)
100
90
80
70
60
200
400
600
800
1000
Temperature (°C)

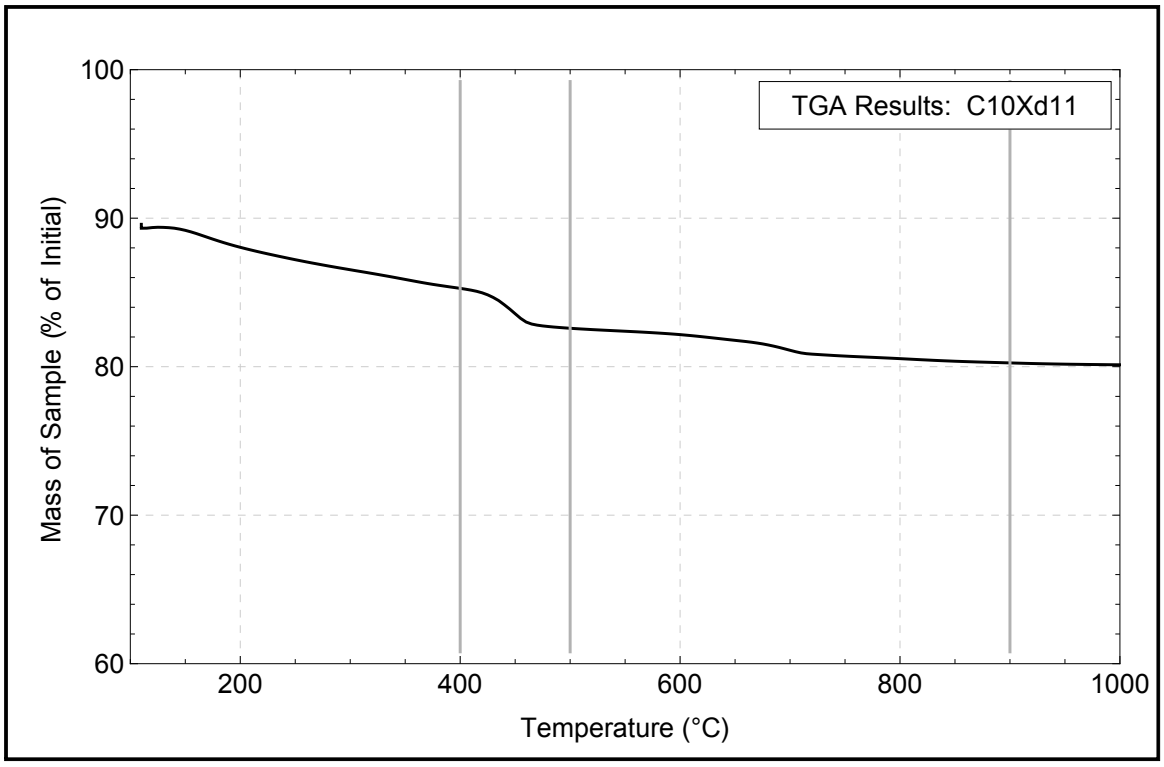
TGA Results: C10Xd11
Mass of Sample (% of Initial)
100
90
80
70
60
200
400
600
800
1000
Temperature (°C)

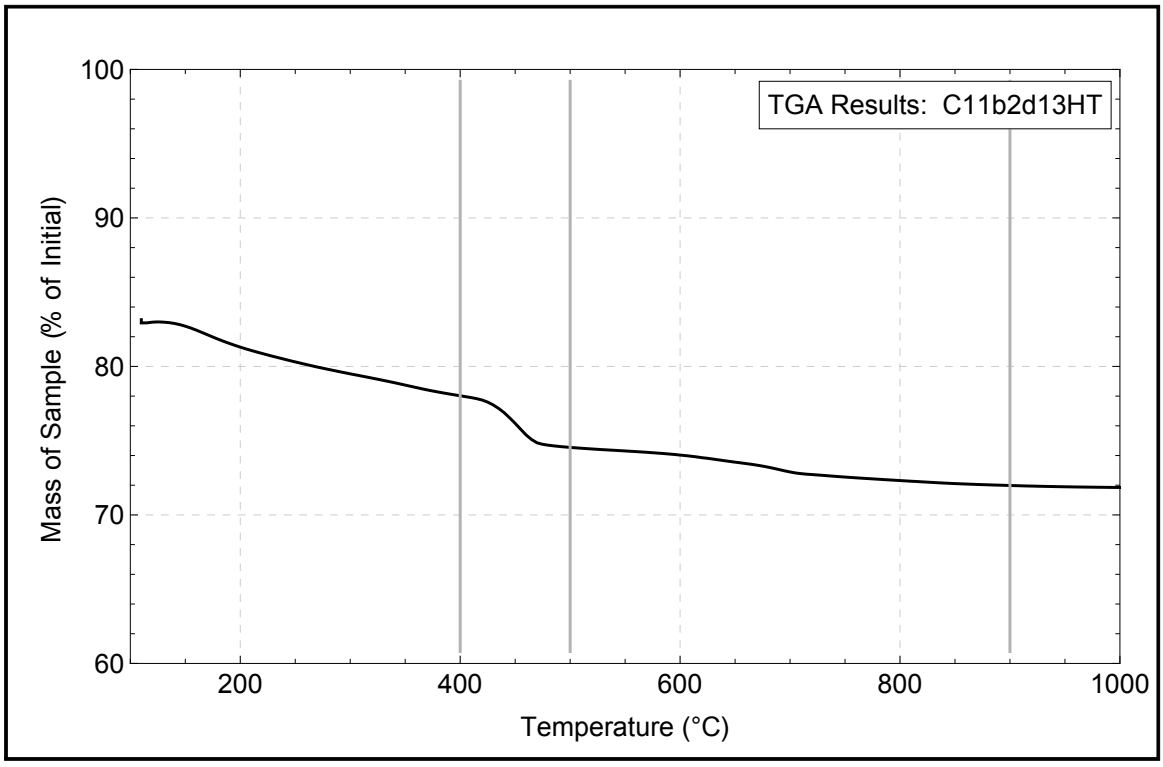
TGA Results: C11b2d13HT
Mass of Sample (% of Initial)
100
90
80
70
60
200
400
600
800
1000
Temperature (°C)

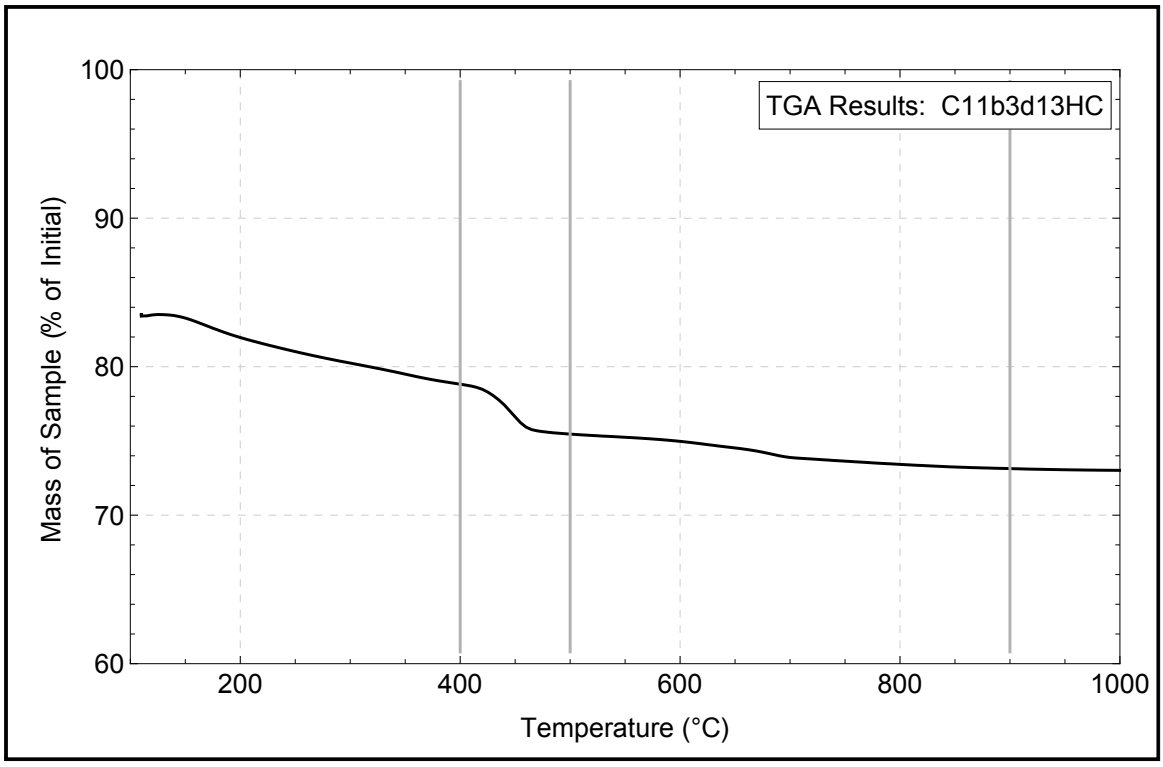
TGA Results: C11b3d13HC
Mass of Sample (% of Initial)
100
90
80
70
60
200
400
600
800
1000
Temperature (°C)

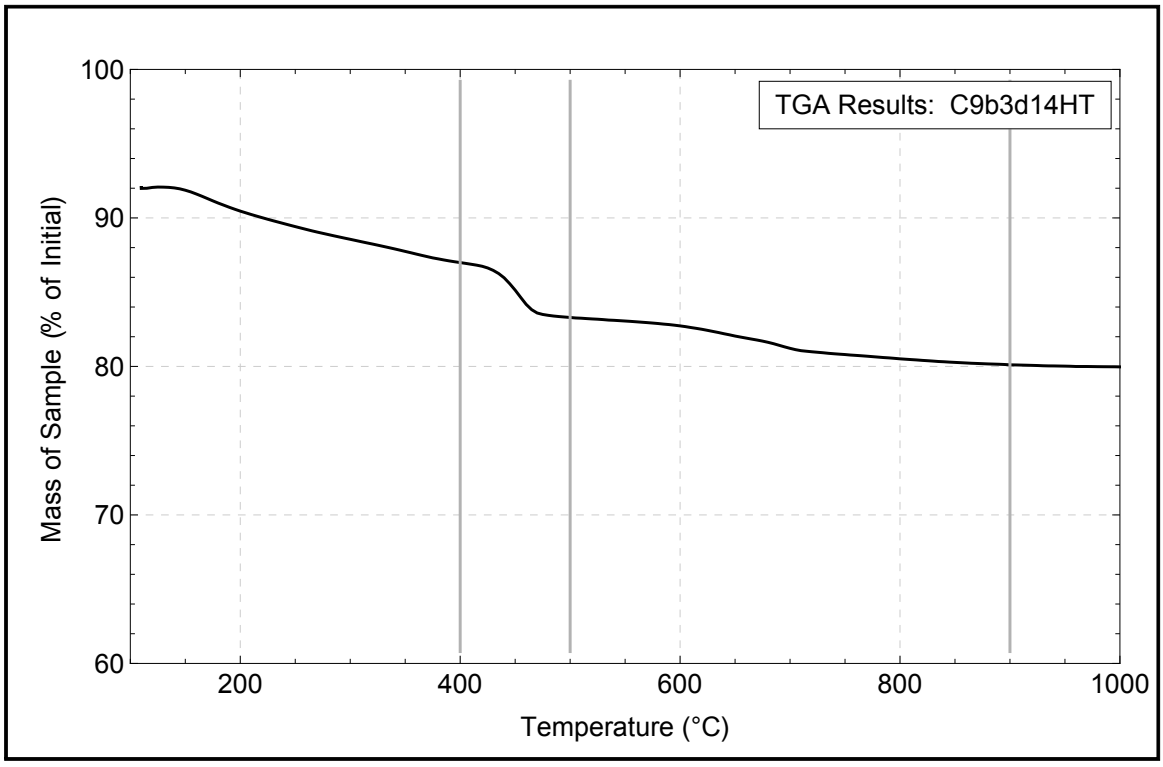
TGA Results: C9b3d14HT
Mass of Sample (% of Initial)
100
90
80
70
60
200
400
600
800
1000
Temperature (°C)

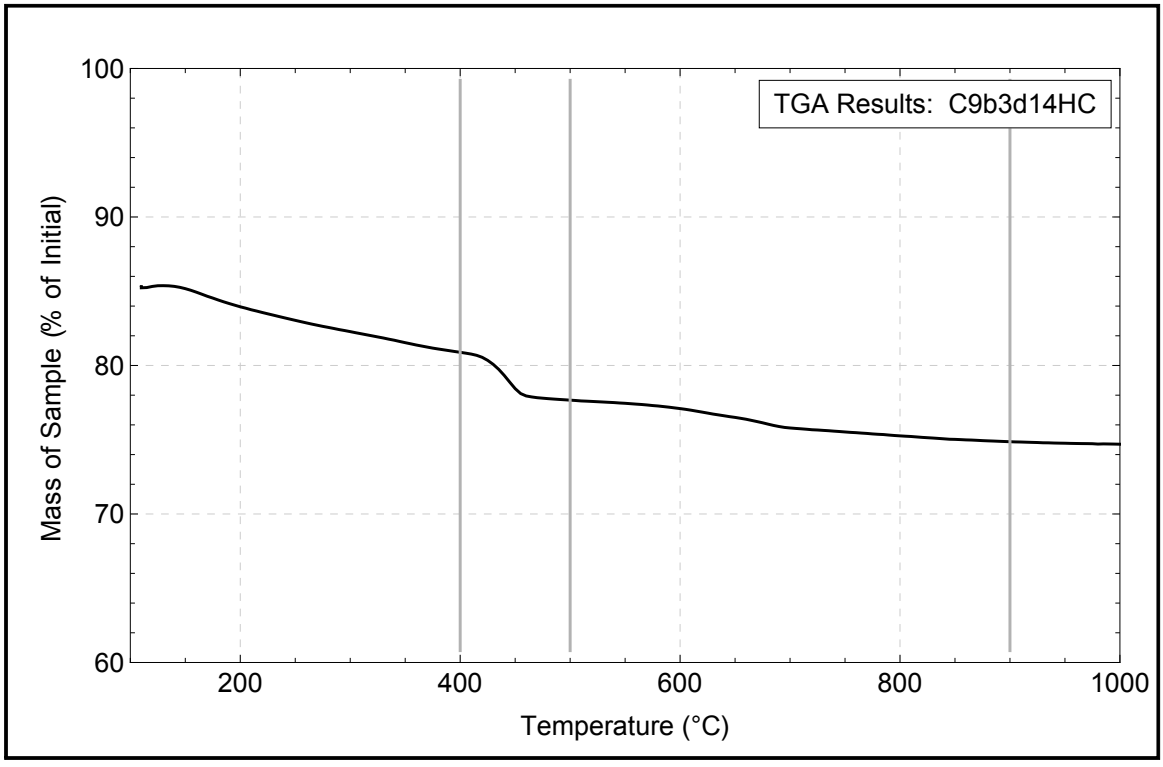
TGA Results: C9b3d14HC
Mass of Sample (% of Initial)
100
90
80
70
60
200
400
600
800
1000
Temperature (°C)

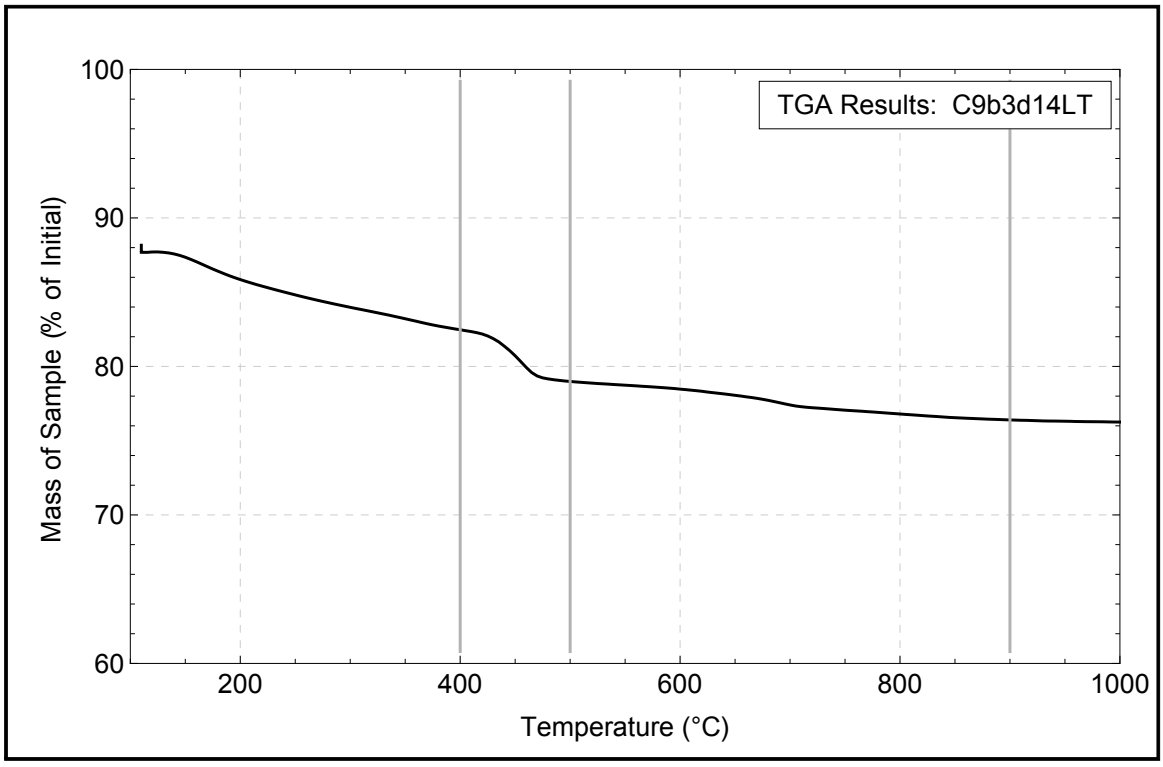
TGA Results: C9b3d14LT
Mass of Sample (% of Initial)
100
90
80
70
60
200
400
600
800
1000
Temperature (°C)

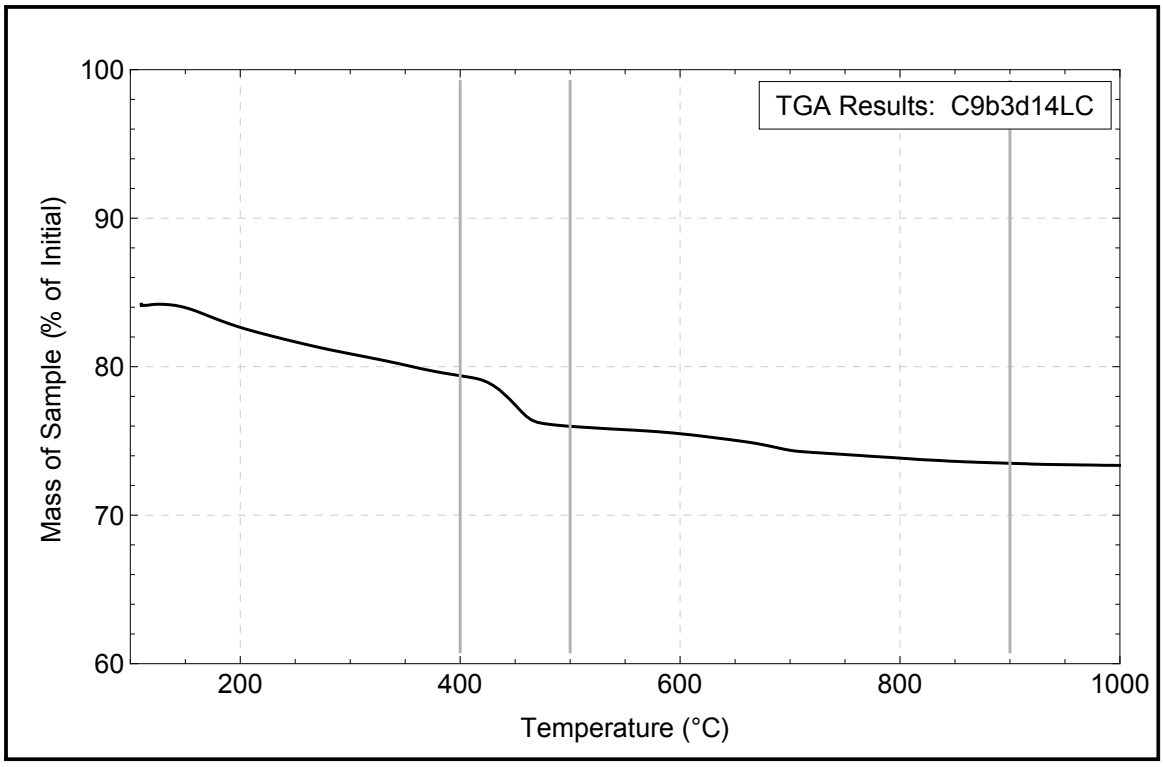
TGA Results: C9b3d14LC
Mass of Sample (% of Initial)
100
90
80
70
60
200
400
600
800
1000
Temperature (°C)

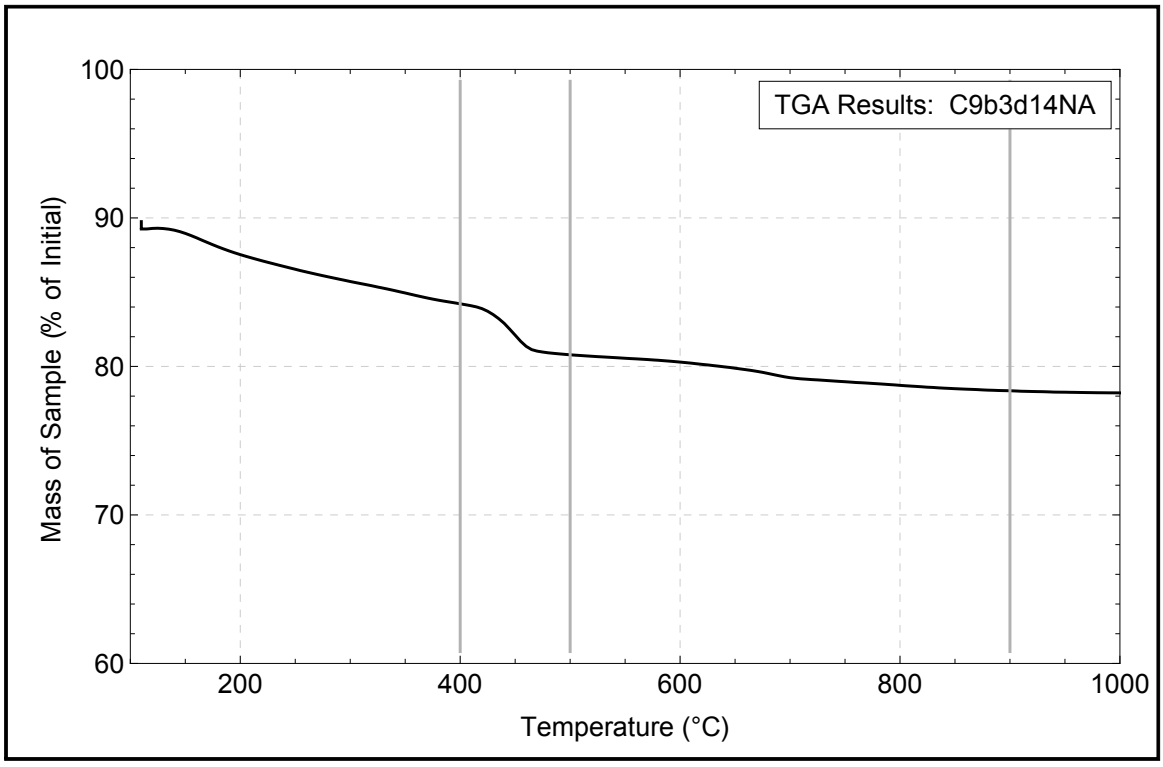
TGA Results: C9b3d14NA
Mass of Sample (% of Initial)
100
90
80
70
60
200
400
600
800
1000
Temperature (°C)

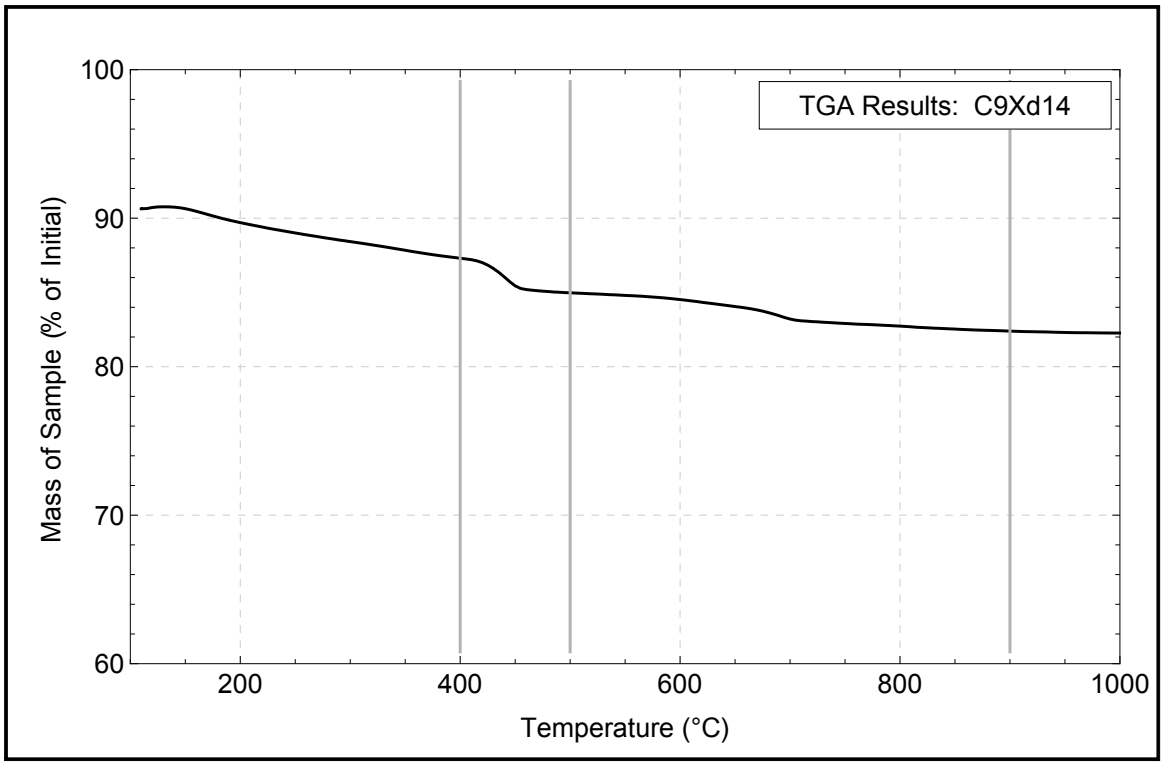
TGA Results: C9Xd14
Mass of Sample (% of Initial)
100
90
80
70
60
200
400
600
800
1000
Temperature (°C)

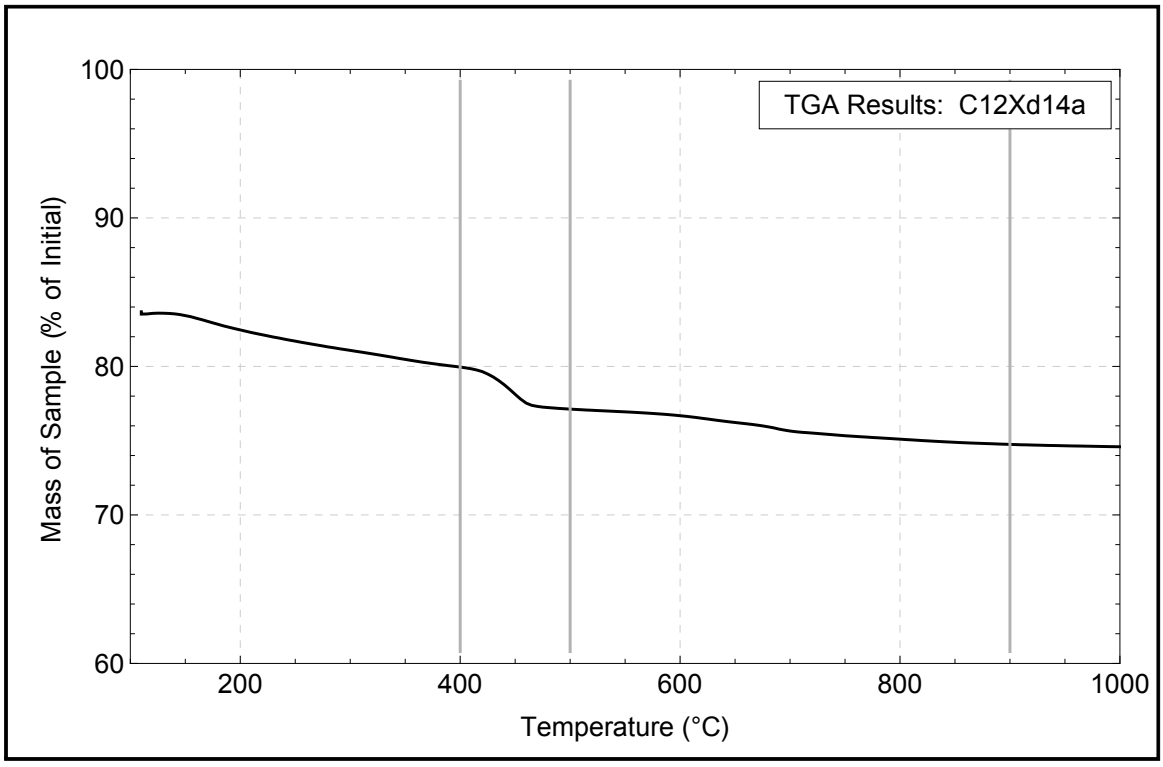
TGA Results: C12Xd14a
Mass of Sample (% of Initial)
100
90
80
70
60
200
400
600
800
1000
Temperature (°C)

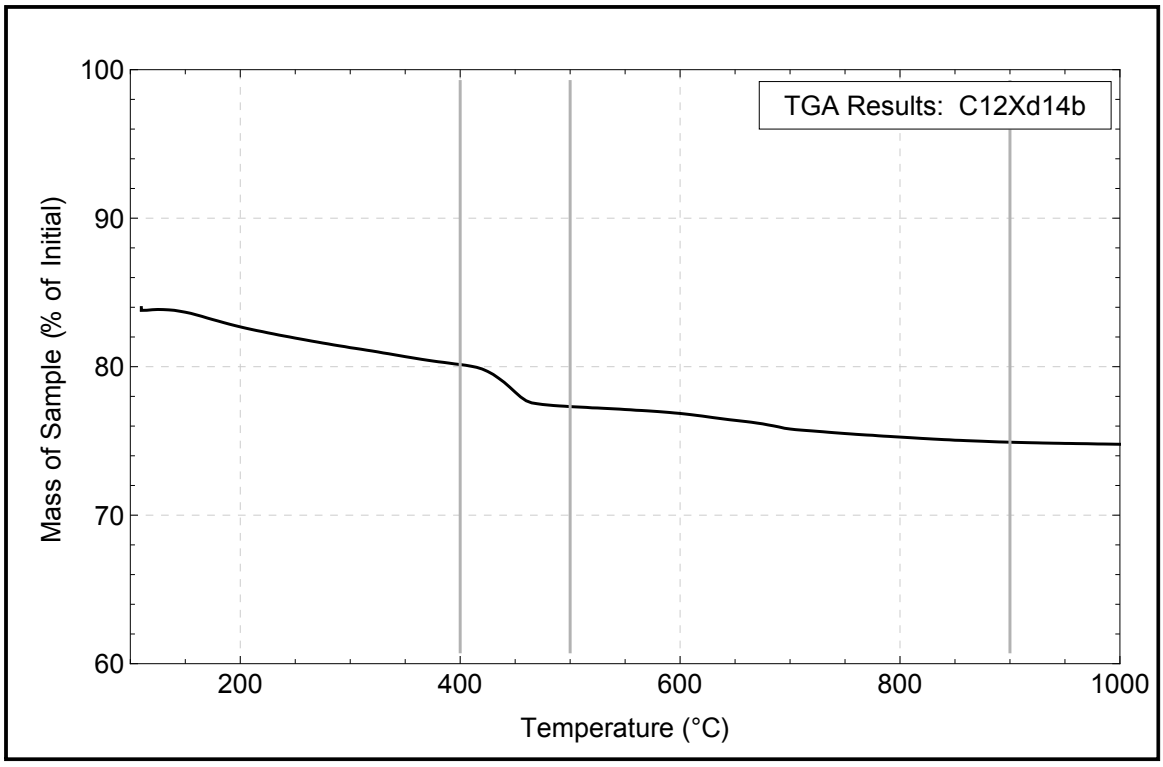
TGA Results: C12Xd14b
Mass of Sample (% of Initial)
100
90
80
70
60
200
400
600
800
1000
Temperature (°C)

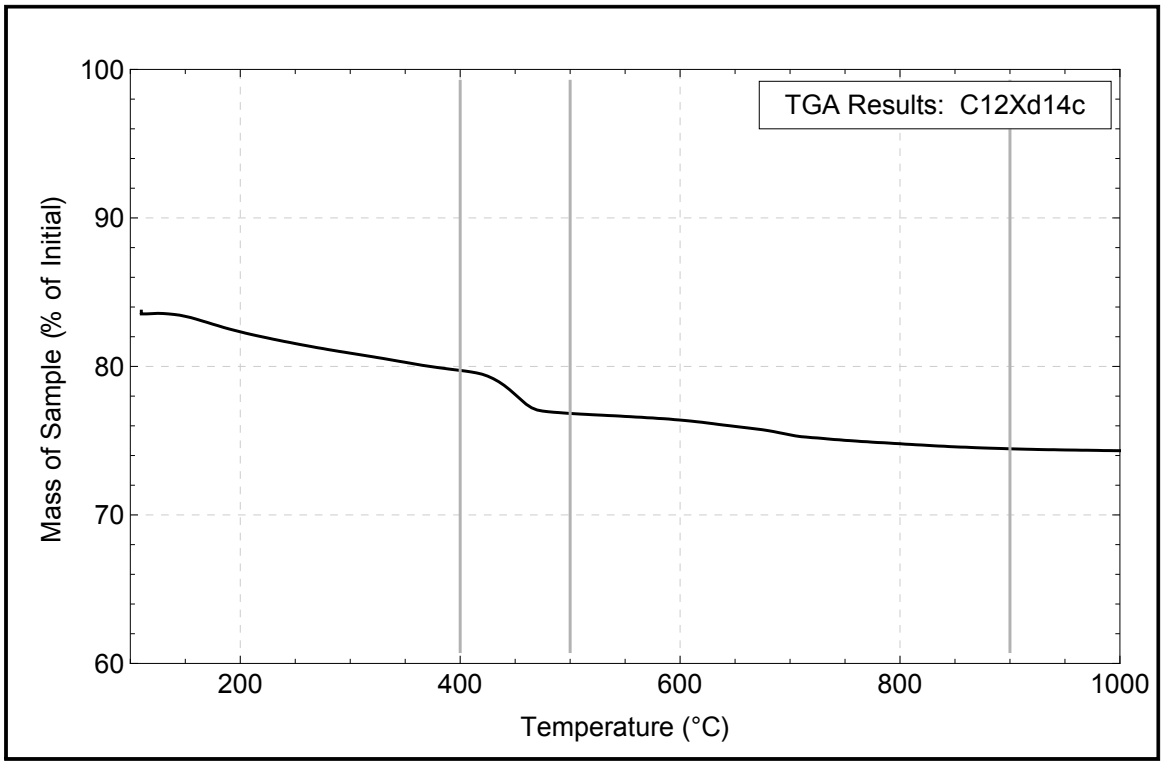
TGA Results: C12Xd14c
Mass of Sample (% of Initial)
100
90
80
70
60
200
400
600
800
1000
Temperature (°C)

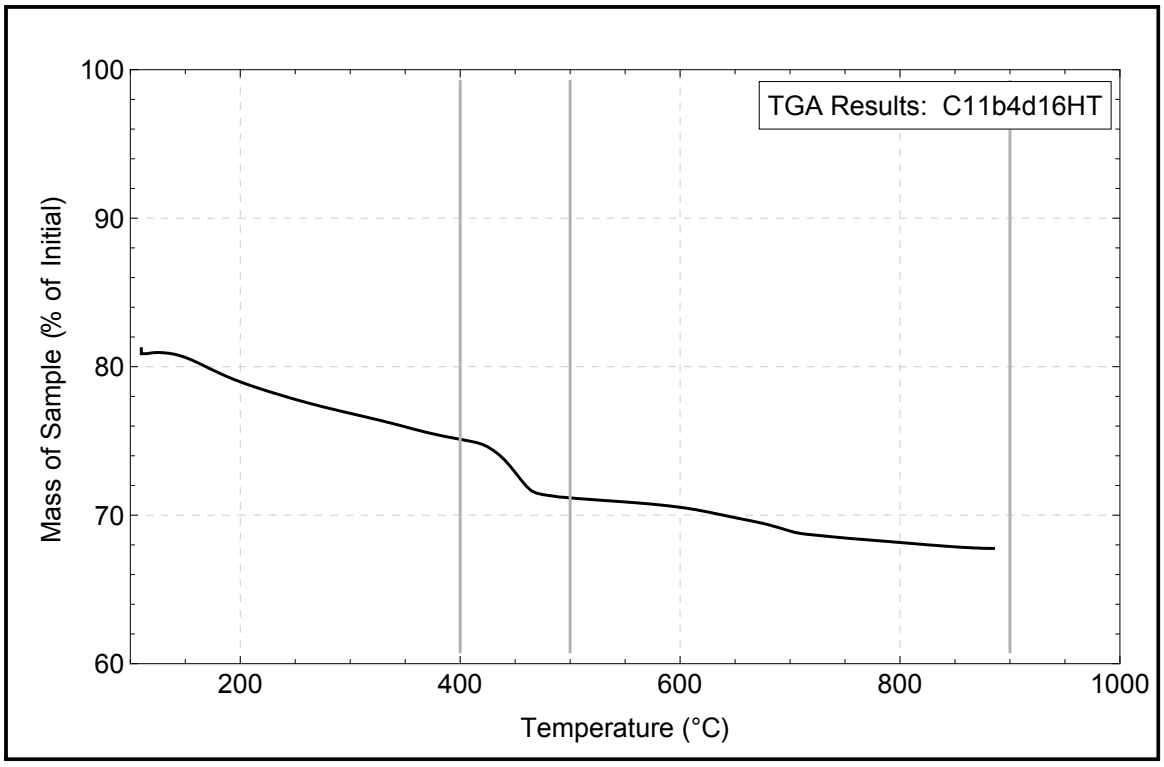
TGA Results: C11b4d16HT
Mass of Sample (% of Initial)
100
90
80
70
60
200
400
600
800
1000
Temperature (°C)

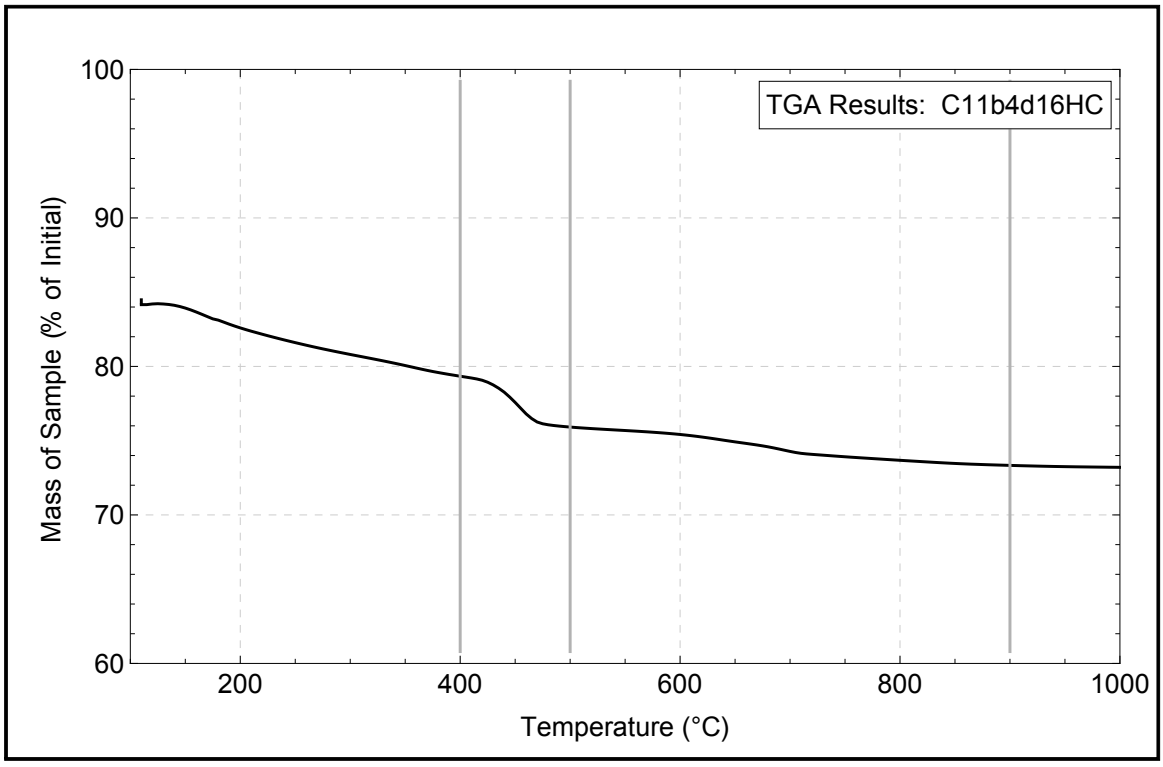
TGA Results: C11b4d16HC
Mass of Sample (% of Initial)
100
90
80
70
60
200
400
600
800
1000
Temperature (°C)

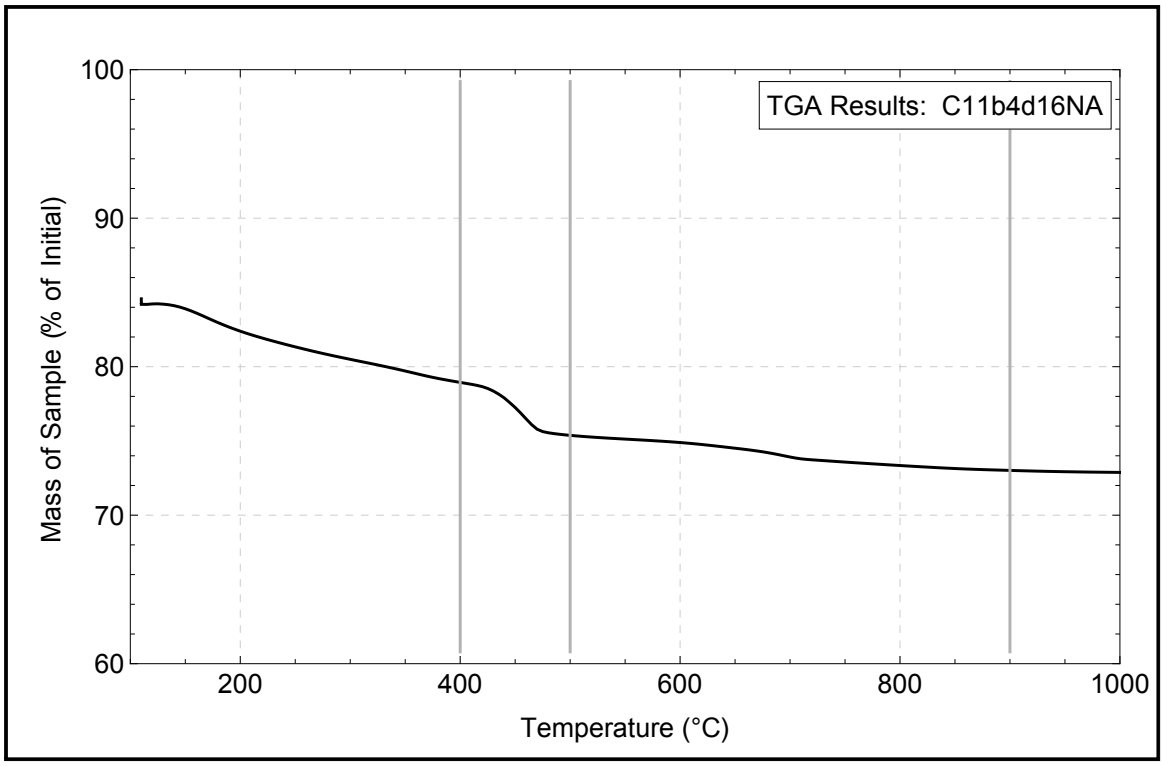
TGA Results: C11b4d16NA
Mass of Sample (% of Initial)
100
90
80
70
60
200
400
600
800
1000
Temperature (°C)

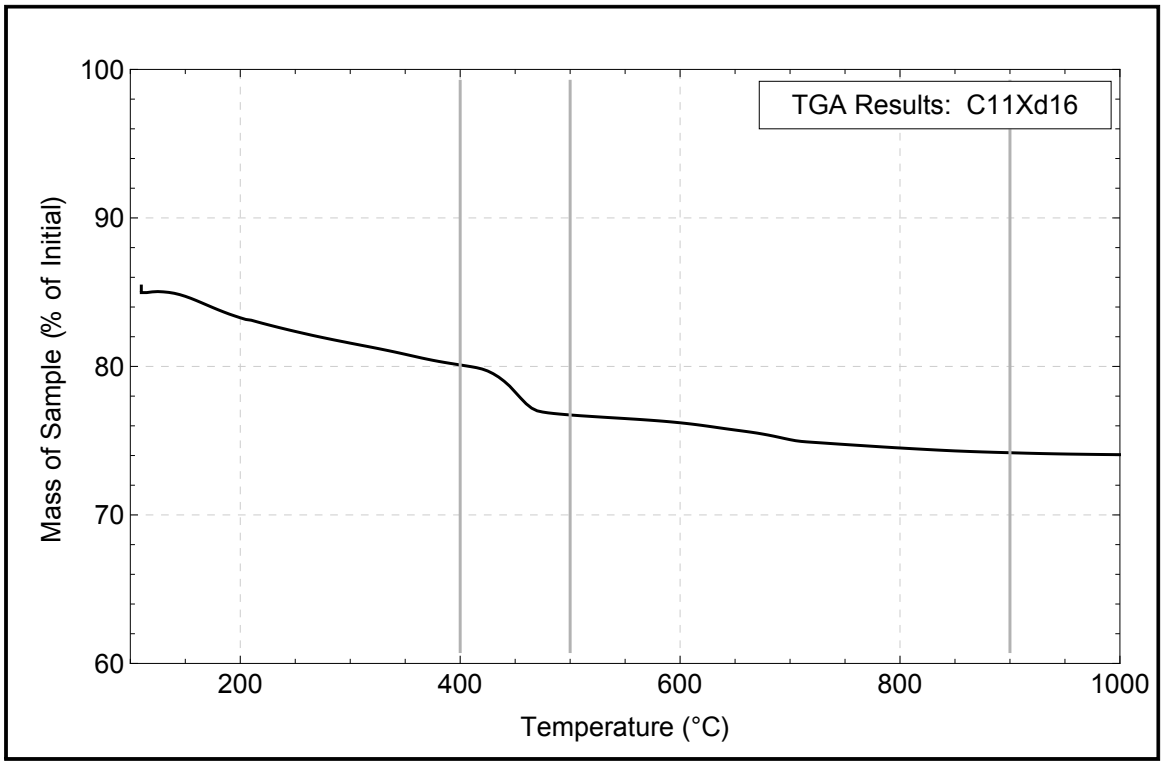
TGA Results: C11Xd16
Mass of Sample (% of Initial)
100
90
80
70
60
200
400
600
800
1000
Temperature (°C)

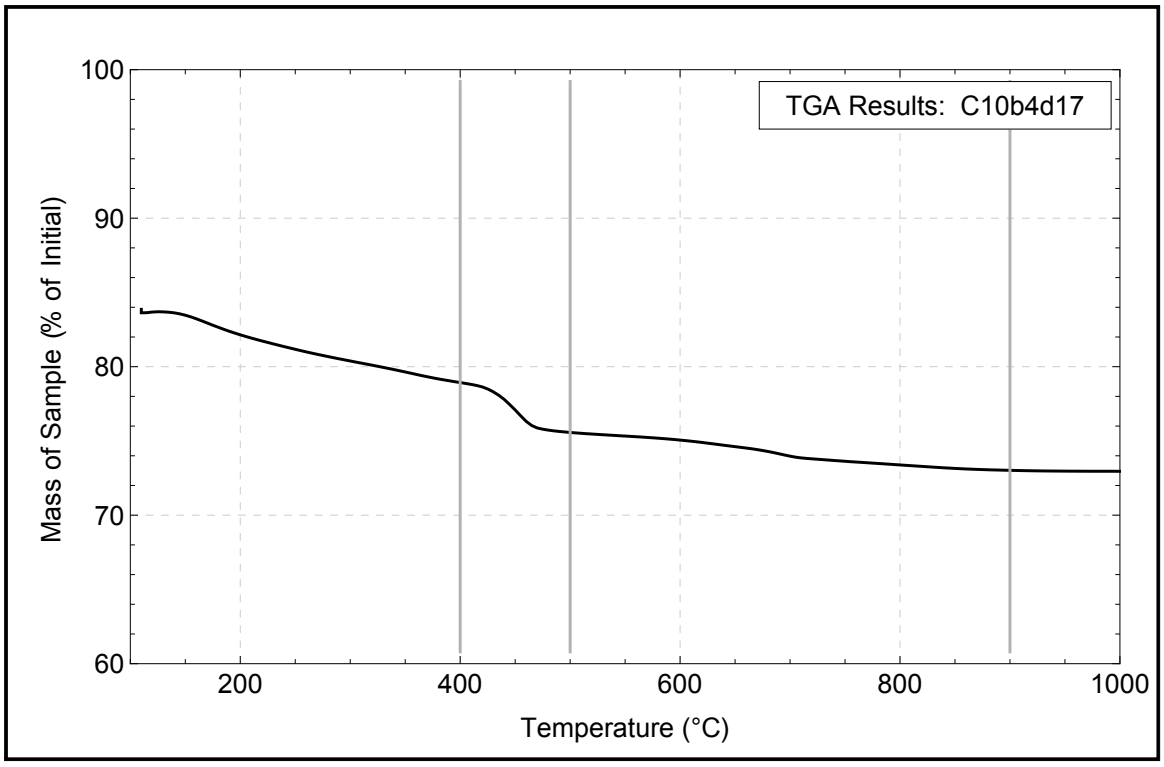
TGA Results: C10b4d17
Mass of Sample (% of Initial)
100
90
80
70
60
200
400
600
800
1000
Temperature (°C)

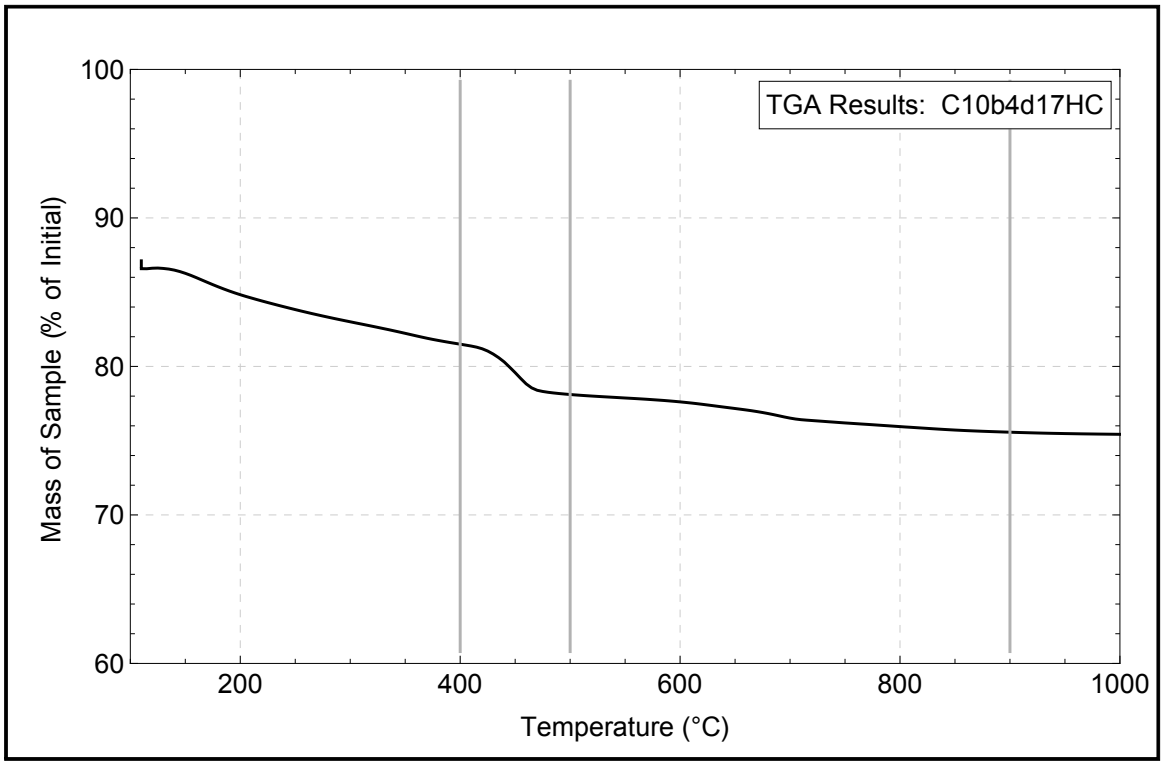
TGA Results: C10b4d17HC
Mass of Sample (% of Initial)
100
90
80
70
60
200
400
600
800
1000
Temperature (°C)

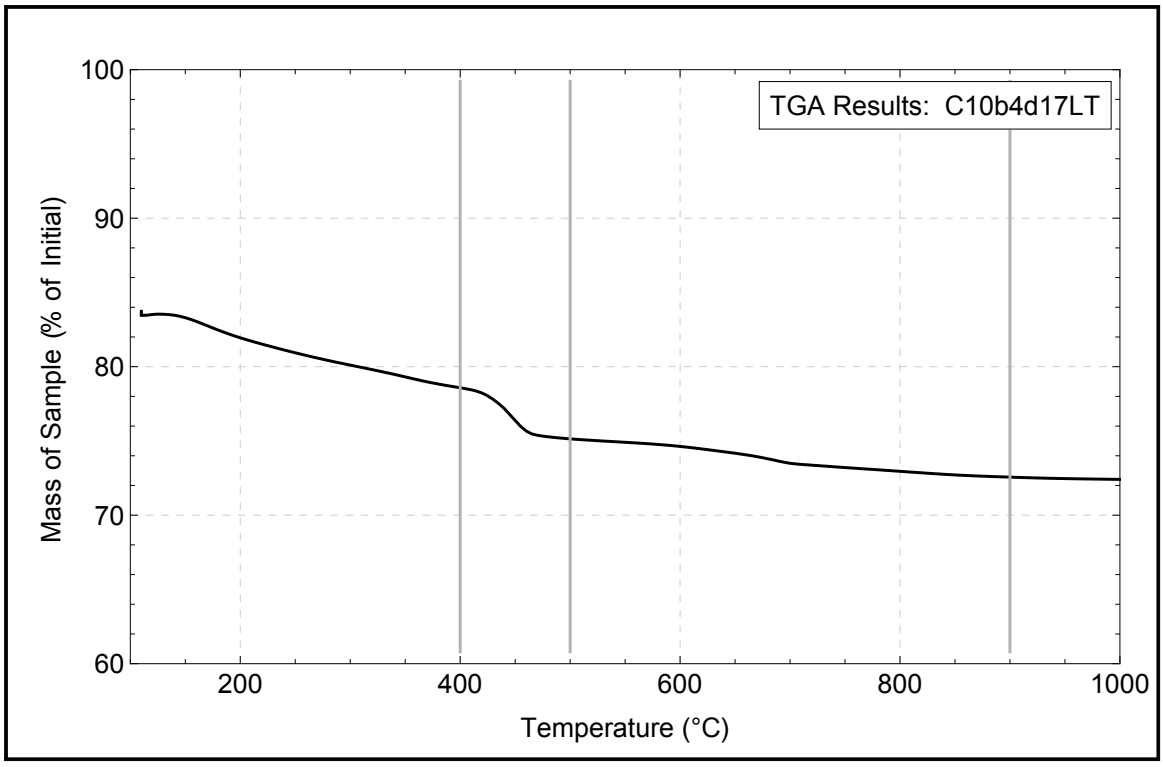
TGA Results: C10b4d17LT
Mass of Sample (% of Initial)
100
90
80
70
60
200
400
600
800
1000
Temperature (°C)

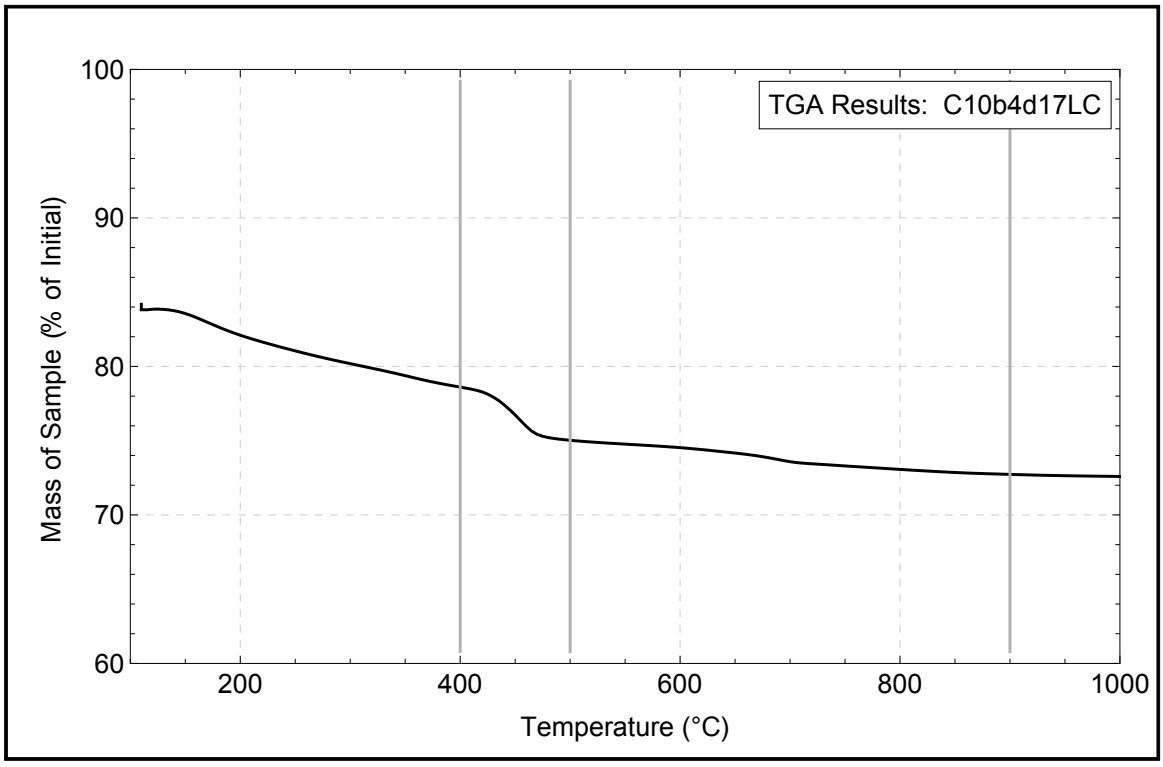
TGA Results: C10b4d17LC
Mass of Sample (% of Initial)
100
90
80
70
60
200
400
600
800
1000
Temperature (°C)

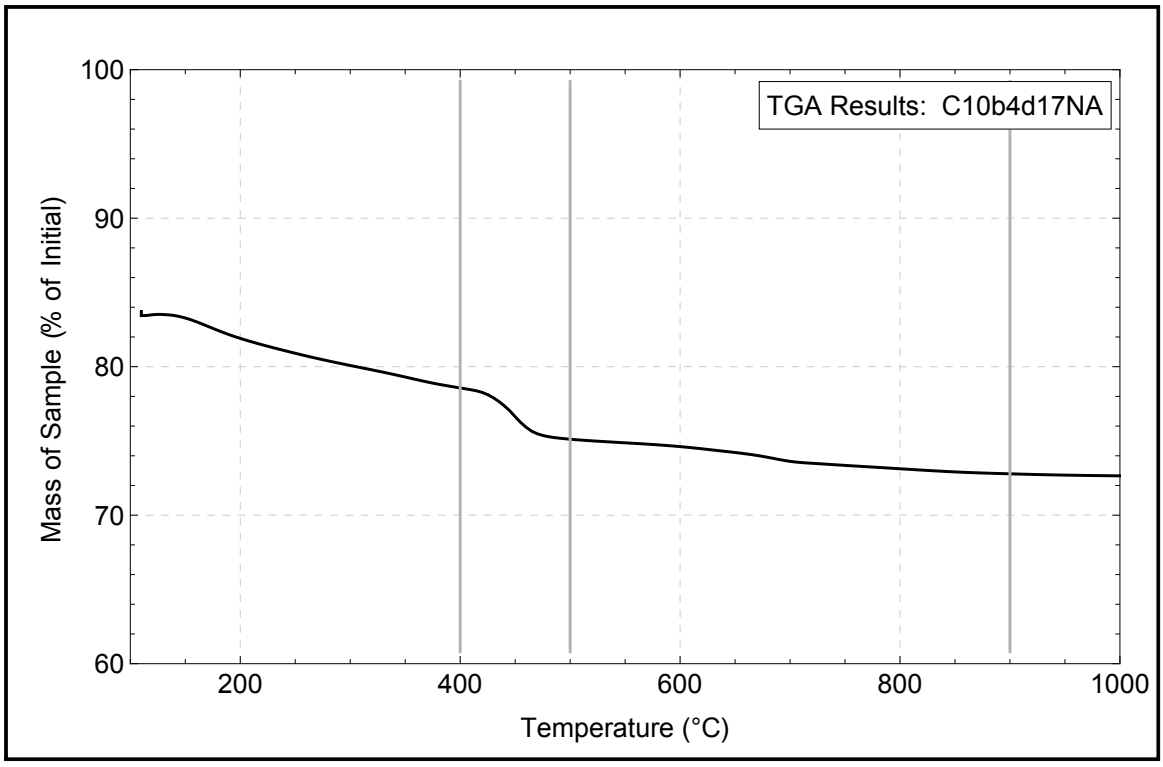
TGA Results: C10b4d17NA
Mass of Sample (% of Initial)
100
90
80
70
60
200
400
600
800
1000
Temperature (°C)

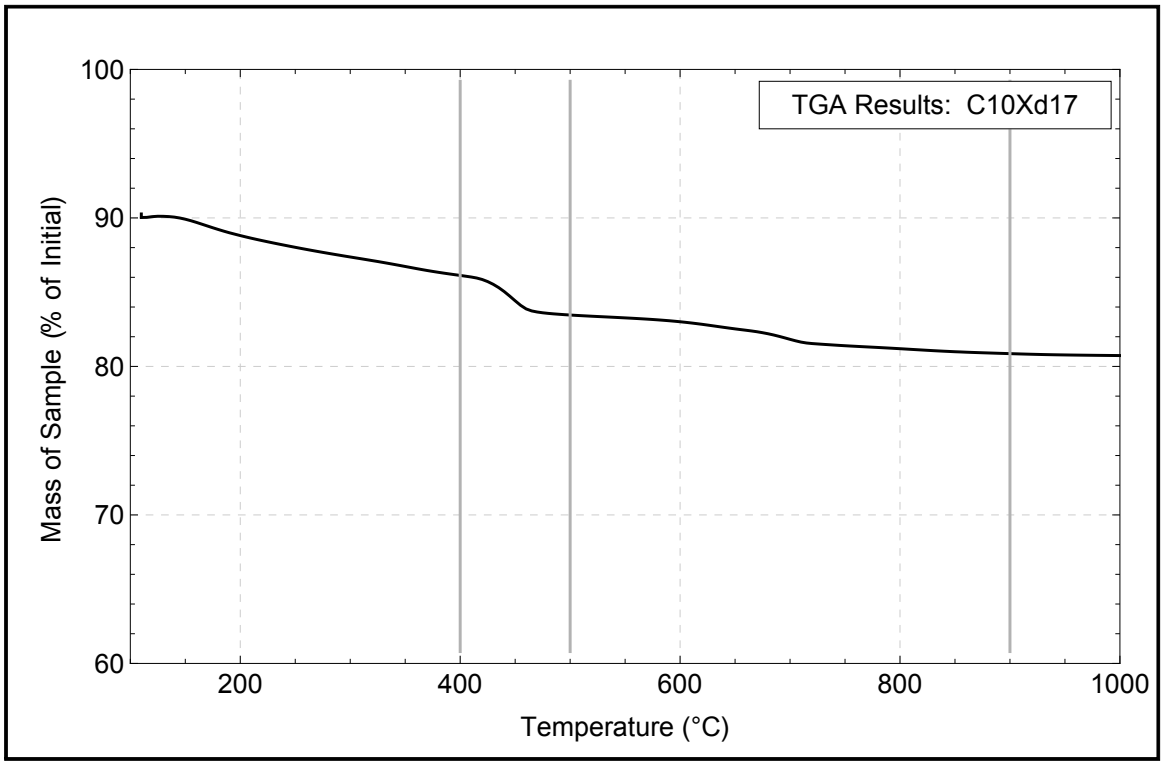
TGA Results: C10Xd17
Mass of Sample (% of Initial)
100
90
80
70
60
200
400
600
800
1000
Temperature (°C)

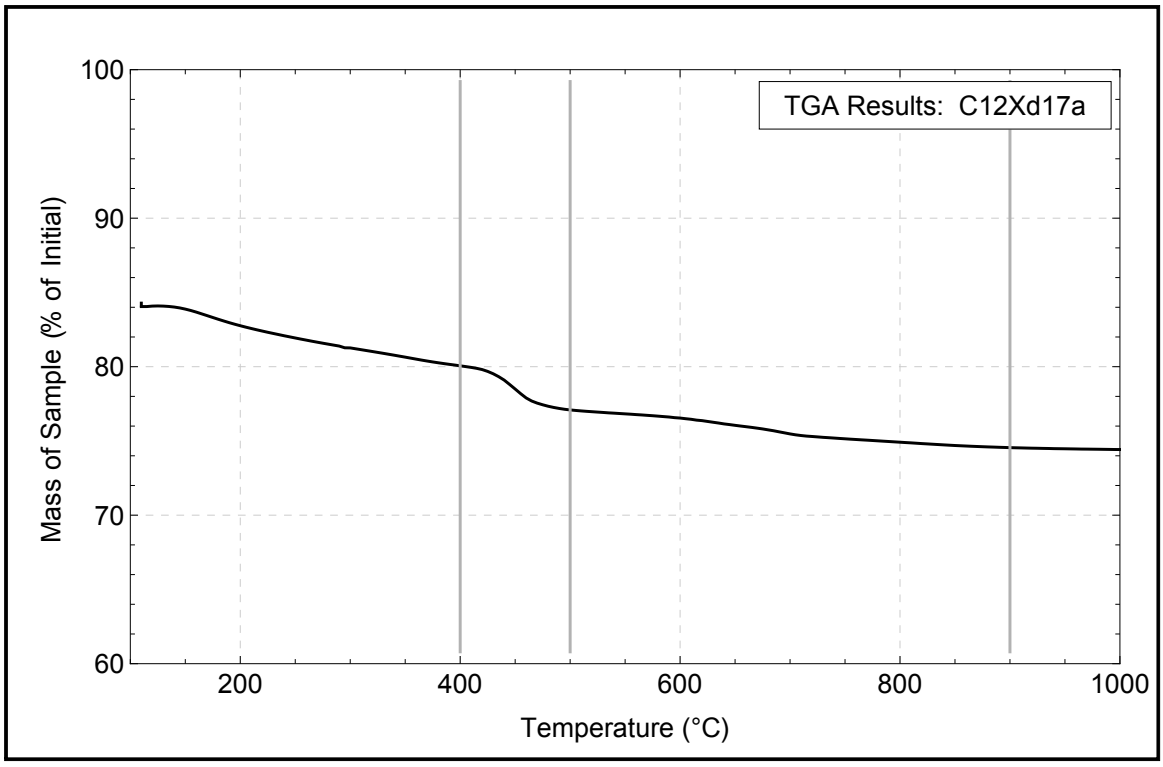
TGA Results: C12Xd17a
Mass of Sample (% of Initial)
100
90
80
70
60
200
400
600
800
1000
Temperature (°C)

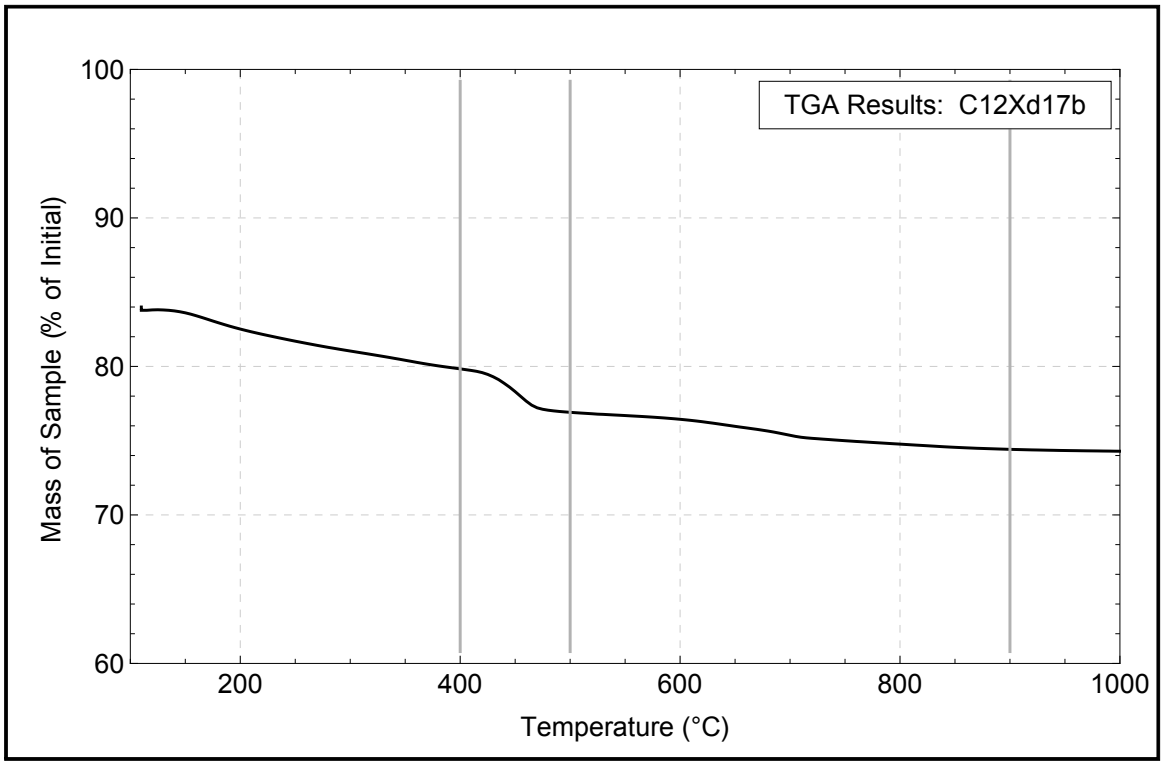
TGA Results: C12Xd17b
Mass of Sample (% of Initial)
100
90
80
70
60
200
400
600
800
1000
Temperature (°C)

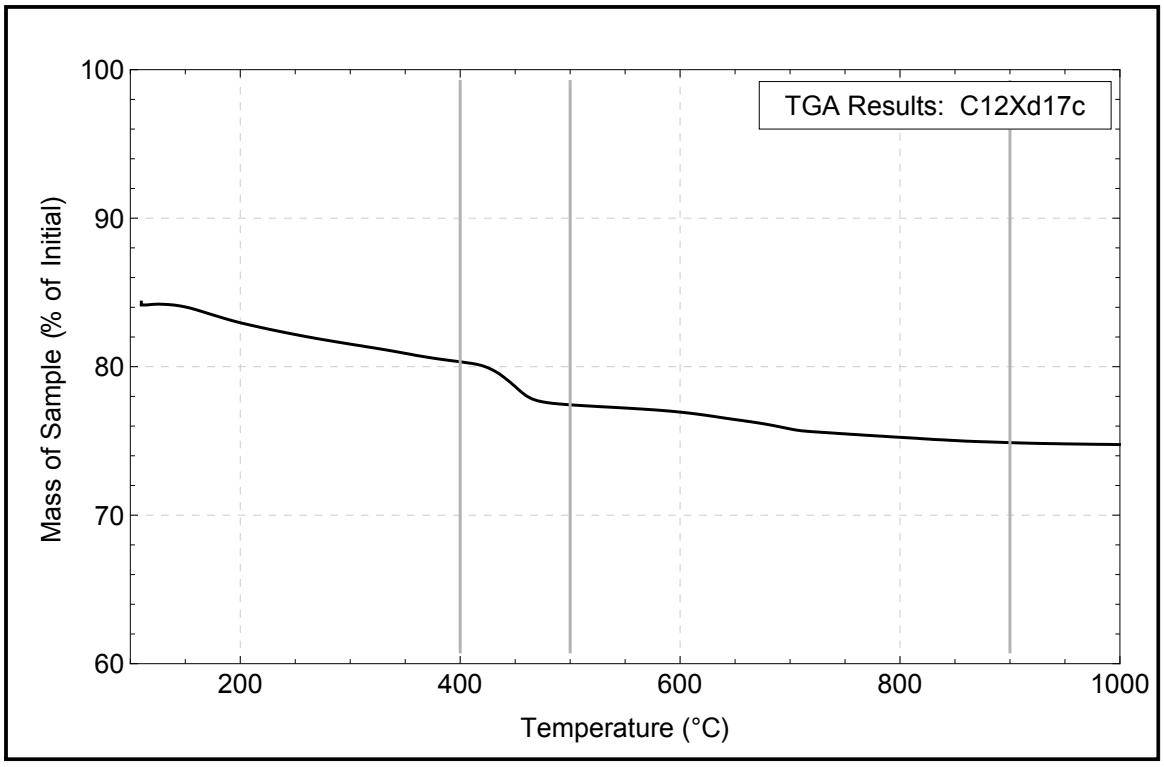
TGA Results: C12Xd17c
Mass of Sample (% of Initial)
100
90
80
70
60
200
400
600
800
1000
Temperature (°C)

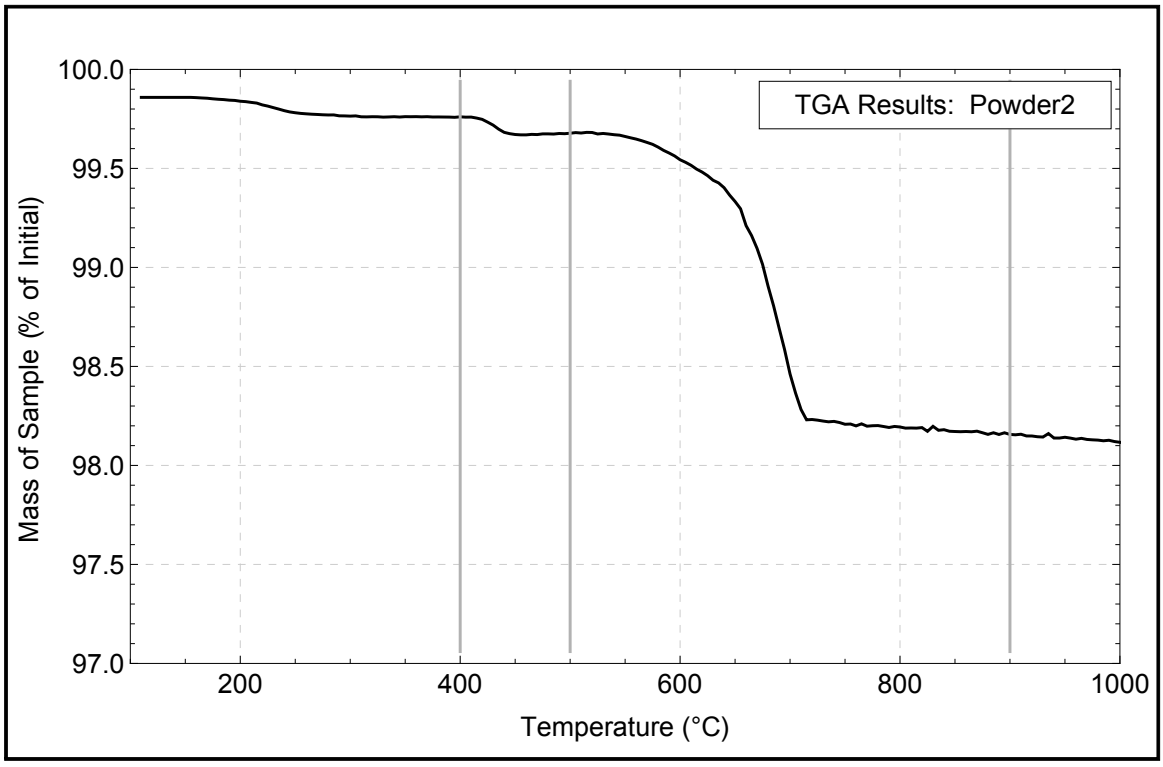
TGA Results: Powder2
Mass of Sample (% of Initial)
100.0
99.5
99.0
98.5
98.0
97.5
97.0
200
400
600
800
1000
Temperature (°C)

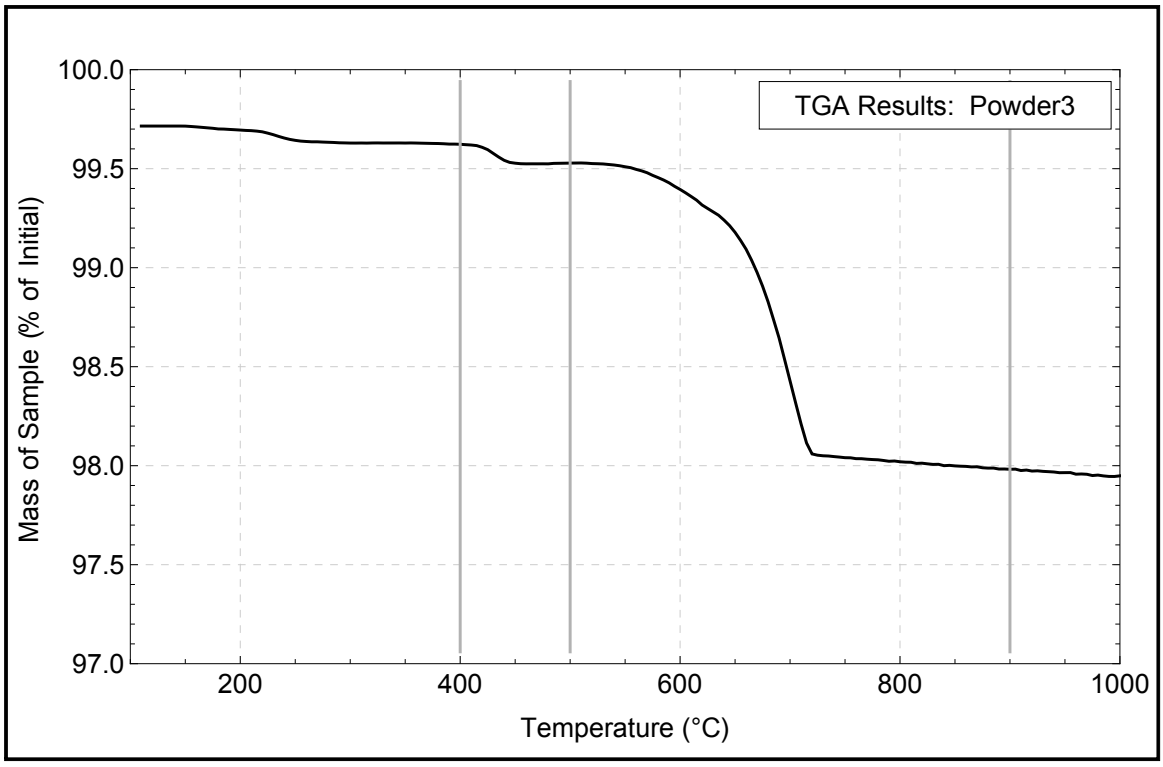
TGA Results: Powder3
Mass of Sample (% of Initial)
100.0
99.5
99.0
98.5
98.0
97.5
97.0
200
400
600
800
1000
Temperature (°C)

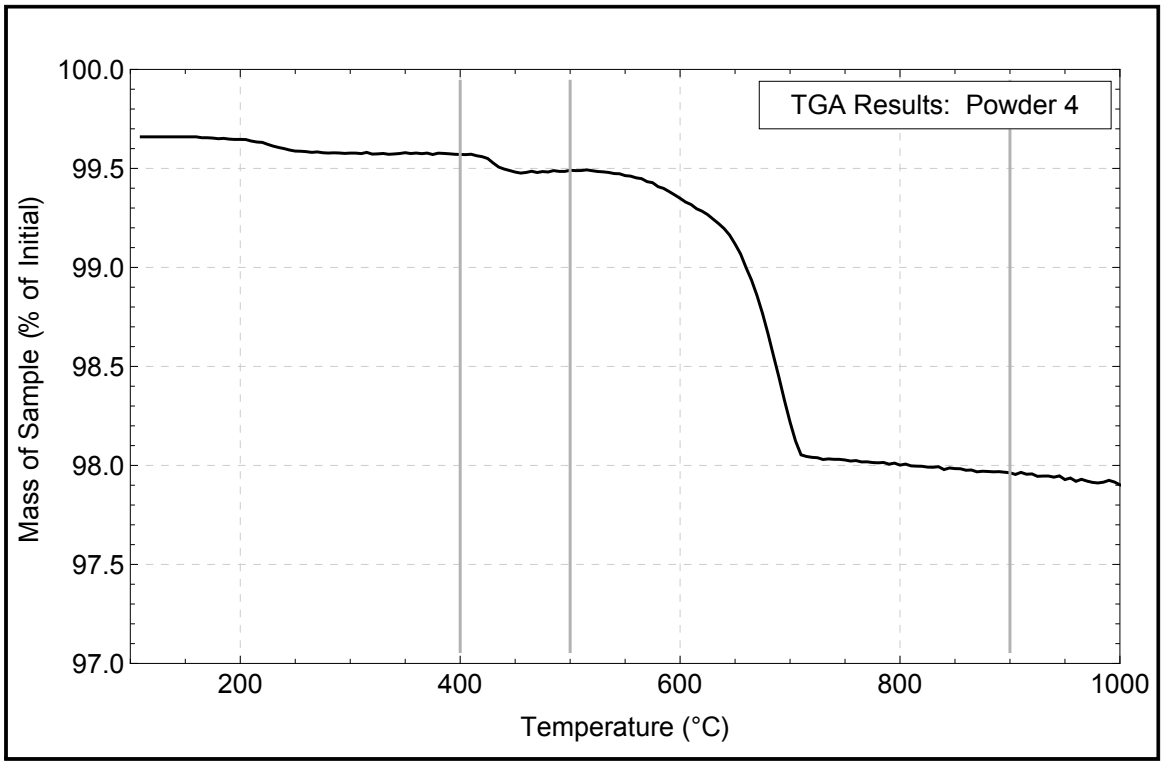
TGA Results: Powder 4
Mass of Sample (% of Initial)
100.0
99.5
99.0
98.5
98.0
97.5
97.0
200
400
600
800
1000
Temperature (°C)

Appendix B.2 – Hypothesis Testing using Welch's t-test

At various stages of the research presented herein, sets of data were collected from differing stress conditions. When comparing the two sets of data, the underlying question was whether the two sets were significantly different from one another. Answering this question could theoretically be accomplished in several ways with varying degrees of precision. Consider the three sets of data in Table B.2.1. The data points represent the ratio between the referenced stress condition and the baseline curve derived from unstressed controls. This data is plotted in Figure B.2.1. A cursory examination of the data reveals that for both stress conditions, ratios are significantly above the results for unstressed controls. However, this preliminary consideration cannot accurately distinguish between the samples taken from each stress condition when compared to one another.

Table B.2.1 – Mass loss ratios for TGA results in the 110 to 400 °C range

Stress Condition	High Tension	Neutral Axis	Unstressed Controls	
Data Points	1.268	1.117	0.940	1.235
	1.107	1.361	0.921	0.972
	1.125	1.239	0.950	0.930
	1.272	1.204	1.101	0.981
	1.124	1.293	1.060	1.035
	1.201	1.253	1.045	0.803
	1.326	1.371	0.964	0.947
	1.202	1.267	1.060	0.966
	1.221		1.068	1.014
			0.855	1.251
			1.084	0.937
			0.988	1.034
			0.992	1.027
			1.030	0.988
			0.817	
n	9	8	29	
Mean	1.205	1.263	1.000	
Std. Dev.	0.0757	0.0825	0.0991	

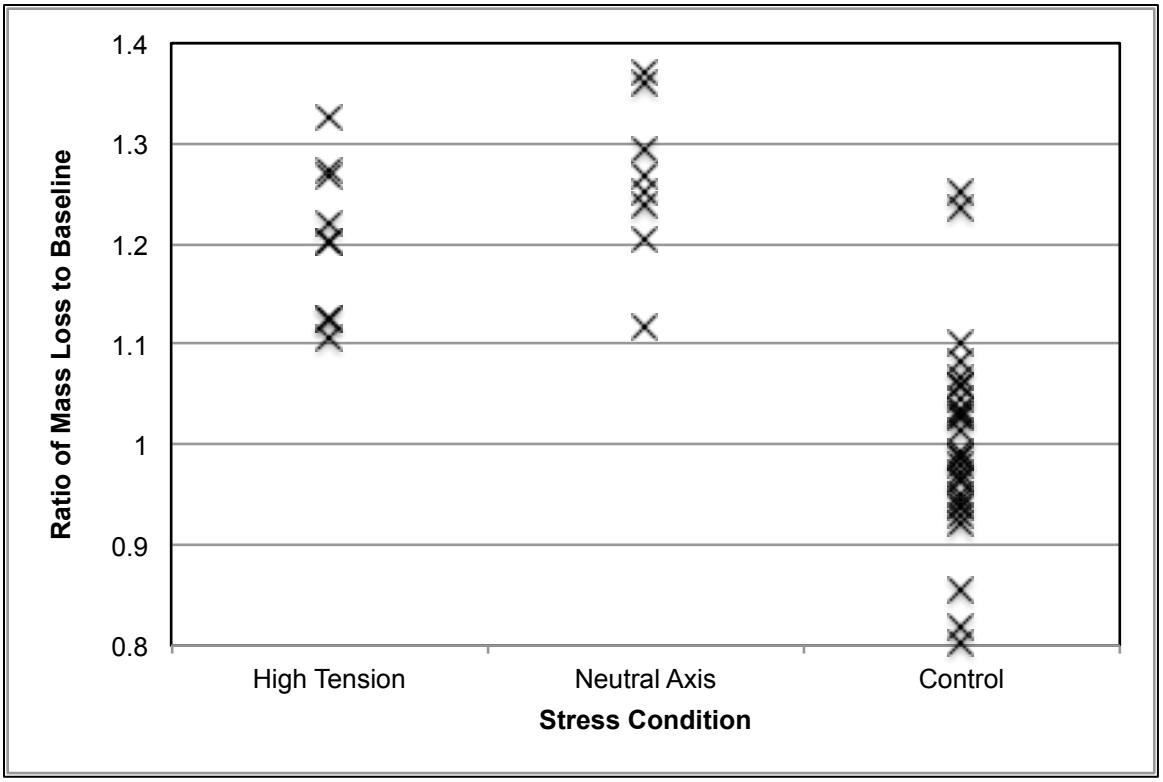

Figure B.2.1 – Sample data for ratio of mass loss to baseline used for hypothesis testing

Each of the data sets presented above represents a sampling of the underlying population corresponding to all possible samples within a particular stress condition. Therefore, it might be useful to consider the likely range of the mean of that population, μ, using confidence intervals,

$$\bar{x} - t_{\alpha/2}\frac{s}{\sqrt{n}} < \mu < \bar{x} + t_{\alpha/2}\frac{s}{\sqrt{n}}, \tag{B.2.1}$$

where $\bar{x}$ and s are the mean and standard deviation of the sample, n is the number of data points in the sample, and $t_{\alpha/2}$ represents the value for which t-distribution at a level of significance α and degrees of freedom of n-1 leaves an area to the right of the value equal to $\alpha/2$. This level of significance is used to determine the level of confidence, 1-α. Using this equation, the three series presented in Table B.2.1 show the confidence intervals for the underlying population means shown in Table B.2.2. Note that the use of Equation (B.2.1) assumes that the standard deviation of the population, σ, is unknown.

Table B.2.2 – Example confidence intervals for the population mean based on samples

Stress Condition		High Tension	Neutral Axis	Controls
95% Confidence	Lower Bound	1.136	1.180	0.956
	Upper Bound	1.275	1.346	1.043
90% Confidence	Lower Bound	1.147	1.194	0.962
	Upper Bound	1.263	1.332	1.037

Comparing the HT results to the NA results in Table B.2.2, it is seen the confidence intervals for the means of the two underlying populations overlap significantly at both the 90 per cent and 95 per cent level of confidence. Were no other analysis conducted, it might be stated that there is a high level of confidence that the samples come from populations with similar means. However, to get a more precise result, specifically, to determine with some degree of certainty that the two samples came from the same population, it is necessary to conduct hypothesis testing on the samples.

In any hypothesis testing, two hypotheses are formulated. The first, the null hypothesis, H_0, is used to determine a test statistic that is then compared to some threshold value at which the hypotheses must be rejected in favor of an alternate hypothesis H_1. When comparing two samples, such as with the current research, it is common for the null hypothesis to be the condition that the two population means are equal, corresponding to the condition that $\mu_1-\mu_2=0$. If the two populations are assumed to be Gaussian distributions, the resulting distribution for the difference between the population means is a t-distribution as depicted in Figure B.2.2. For hypothesis testing, it is necessary to calculate a t-statistic such that if it lies within the shaded region of the figure, the null hypothesis cannot be rejected and if it lies outside the shaded region, the null hypothesis is rejected in favor of the alternate hypothesis. In the case of a two-tailed test, such as is depicted, the null hypothesis includes the possibility that the difference between the means is either significantly higher or significantly lower than zero. In the case of the current research however, it is expected that stressed regions show results in only one of the two tails, e.g., it is hypothesized that stress causes acceleration and not retardation of hydration, and therefore all hypothesis testing herein was conducted using a one-tailed test.

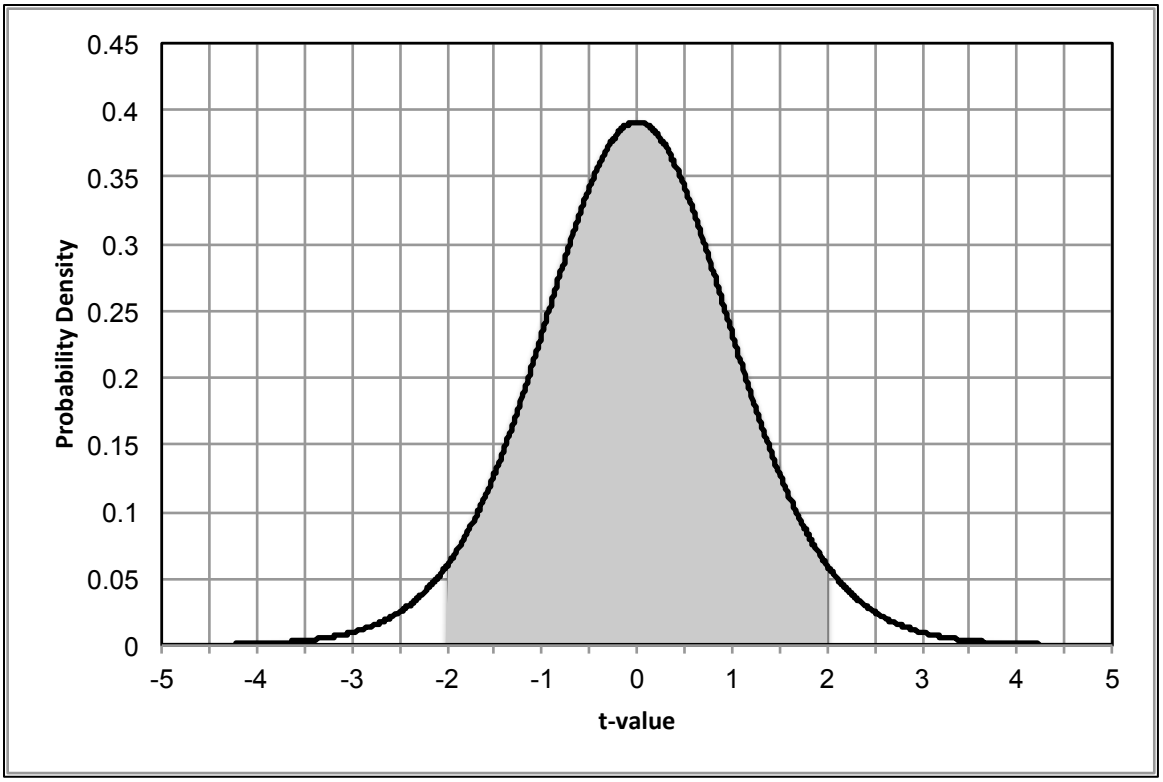

Figure B.2.2 – Example t-distribution showing region where the value of the t-statistic dictates that the null hypothesis cannot be rejected.

Given the general approach of hypothesis testing, the actual t-statistic to be used must be determined. For the data used for the current research, it is assumed that the samples compared come from two different populations with potentially two different standard deviations. Given that the data sets being compared do not correspond to matched pairs of information, the resulting t-statistic to be used is based on the pooled (also referred to as "unpaired" or "independent") two-sample t-test known as the Welch's t-test. The t-statistic is calculated by

$$t = \frac{\left|\overline{x}_1 - \overline{x}_2\right|}{\sqrt{\frac{{s_1}^2}{n_1} + \frac{{s_2}^2}{n_2}}}. \qquad \text{(B.2.2)}$$

The absolute value in the numerator of Equation (B.2.2) is used because only one of the unshaded tails in Figure B.2.2 is being considered for a particular comparison. Thus, H_1 can be written as $|\mu_1-\mu_2|>0$ and examination of the data would decide whether the test is concluding μ_1 is greater or less than μ_2. From examination of Equation B.2.2 it can be

seen that the smaller the difference between the sample means, the smaller the t-statistic and from Figure B.2.2, the more likely the null hypothesis will not be rejected. Also from the equation it is apparent that a very small value for the standard deviation of either sample would result in a very narrow distribution for that population and would result in a larger t-statistic, favoring rejection of the null hypothesis in all cases other than a very small difference in the means.

With the t-statistic calculated based on the samples, it is next necessary to compute the t-distribution of the difference between the means of the potential populations. Using the Welch's t-test, the t-distribution is dependent upon the degrees of freedom, v, of the combined samples, calculated using

$$v = \frac{\left(\frac{{s_1}^2}{n_1} + \frac{{s_2}^2}{n_2} \right)^2}{\frac{{s_1}^4}{{n_1}^2(n_1 - 1)} + \frac{{s_2}^4}{{n_2}^2(n_2 - 1)}}. \qquad \text{(B.2.3)}$$

The last step to apply the Welch's t-test is determining the limits of the shaded region from Figure B.2.2. The limit is determined similarly to the t-value used for confidence intervals in Equation (B.2.1) except that now the value is t_α for a one-tailed test. For the current research, two values of the level of significance, α, were considered. The first was set to 0.05 for all comparisons. Depending on the degrees of freedom, this corresponded to a t-value of approximately 2.20. This level of significance indicates that there would be a 95 per cent probability that the t-statistic calculated from two samples pulled from the same population would lie within the shaded region, including the one appropriate tail. Conversely, if the t-statistic falls within the unshaded tail, there would be less than a 5 per cent probability that the two samples came from the same population or, a greater than 95 per cent chance they came from different populations. The second value of α was calculated based on the determined t-statistic. Thus, this calculated level of significance would be the likelihood that the two samples came from the same population and subtracting from 1 would give the likelihood that the two samples came from different populations.

The calculations of the three comparisons made using the data from Table B.2.1 are given below in Table B.2.3.

Table B.2.3 – Results of example Welch's t-test comparison

Comparing	HT to X	NA to X	HT to NA
t-Statistic	6.577	7.639	1.505
Degrees of Freedom, ν	17.37	13.16	14.36
t-Value at α=0.05	2.110	2.160	2.145
α at t-Statistic	0.0000047	0.0000037	0.155

Based on the values in Table B.2.3, when either the high tension or neutral axis samples are compared to the unstressed control samples, there is a greater than 99.999 per cent chance that they are from different populations indicating that stressed samples show a different mass loss in the 110 to 400 °C range of the TGA testing than do the control specimens. This is in line with what would be expected from examination of the raw data. In comparing the high tension region of the beam to the region surrounding the neutral axis, the two sets of results cannot be considered different (the null hypothesis that they are the same holds) at a 0.05 level of significance. However, based on the calculated α value, there is only a 15.5 per cent likelihood that the two samples came from the same population meaning there is an 84.5 per cent chance that stress at the tensile region has a different effect on the mass loss than does the smaller stress at the neutral axis region. This conclusion is not readily apparent from consideration of Figure B.2.1 but is the result of the more rigorous Welch's t-test.

Appendix C.1 – XRD Raw Data

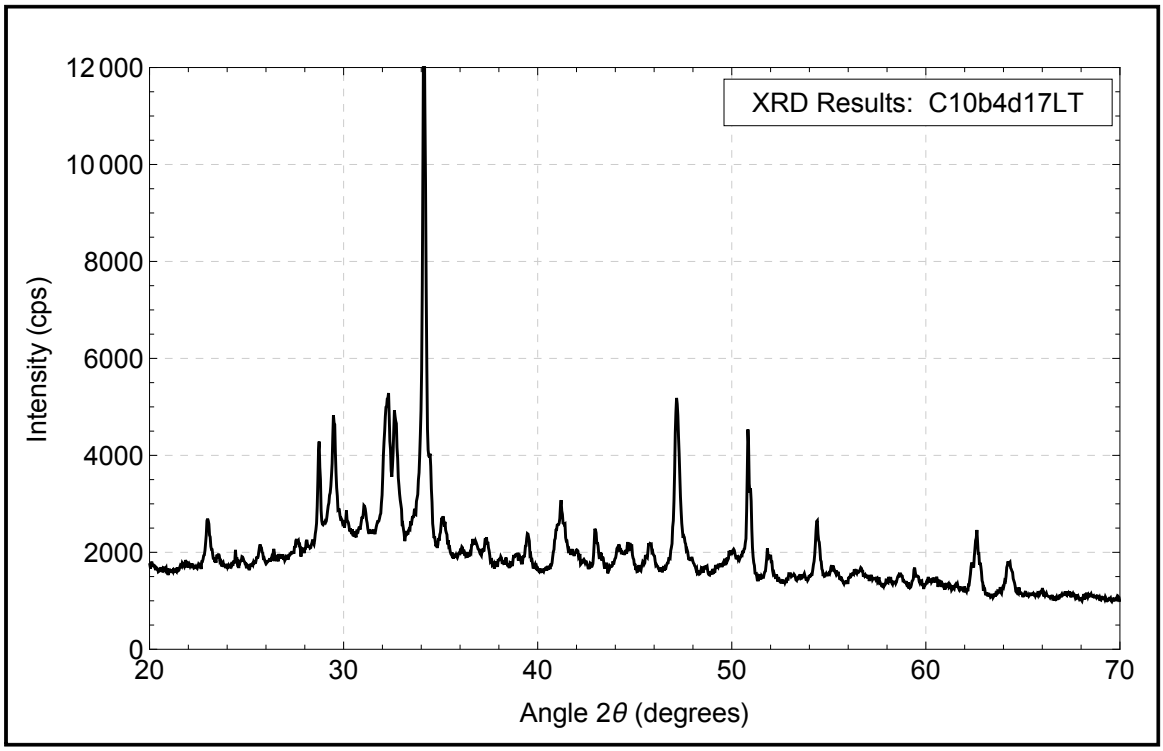
XRD Results: C10b4d17LT
Intensity (cps)
12 000
10 000
8000
6000
4000
2000
0
20
30
40
50
60
70
Angle 2θ (degrees)

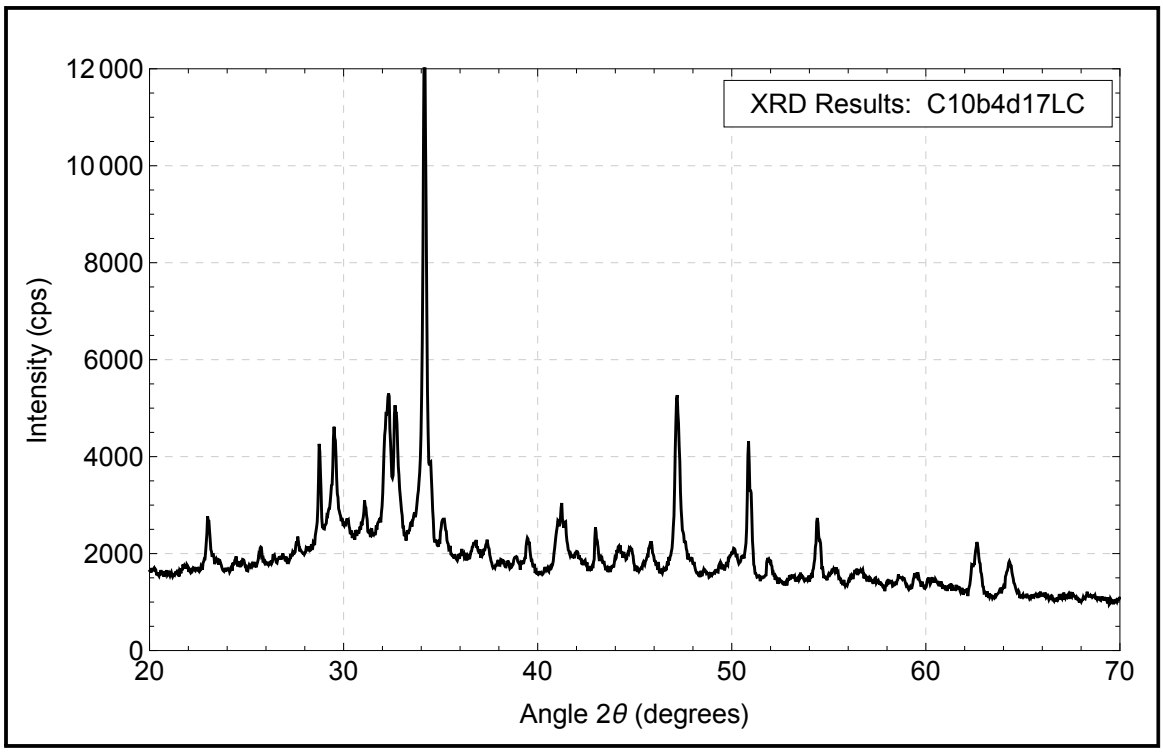
XRD Results: C10b4d17LC
Intensity (cps)
12 000
10 000
8000
6000
4000
2000
0
20
30
40
50
60
70
Angle 2θ (degrees)

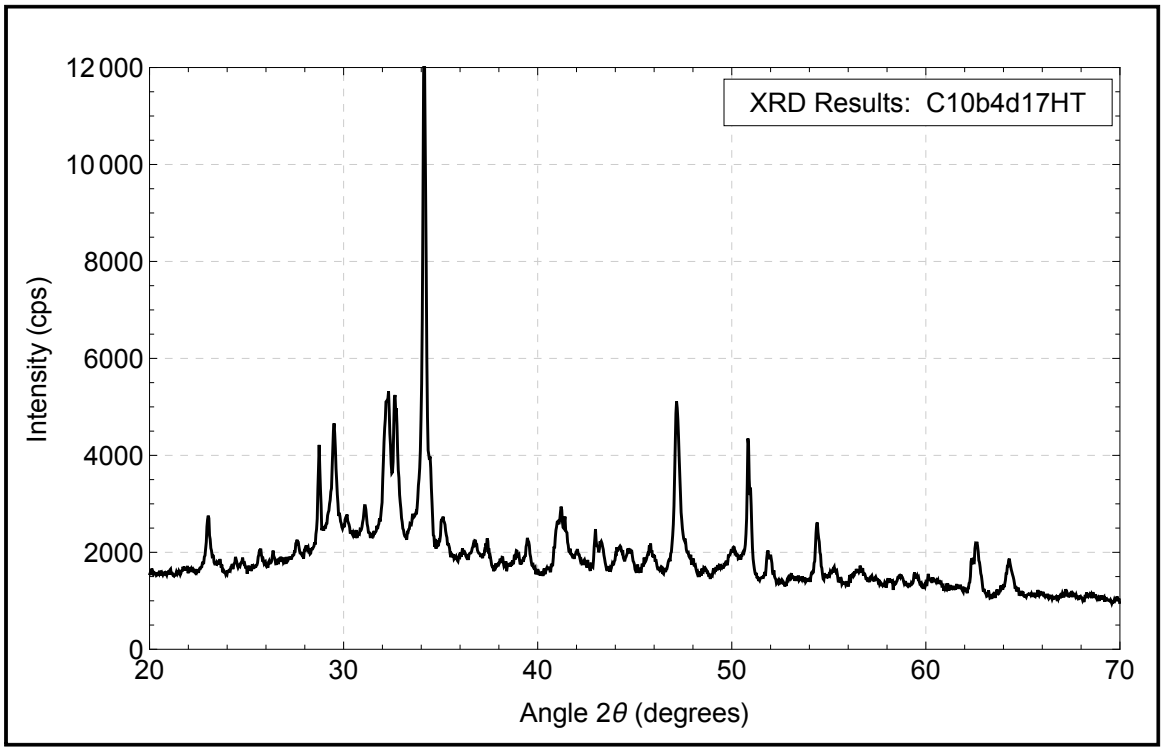
XRD Results: C10b4d17HT
Intensity (cps)
12 000
10 000
8000
6000
4000
2000
0
20
30
40
50
60
70
Angle 2θ (degrees)

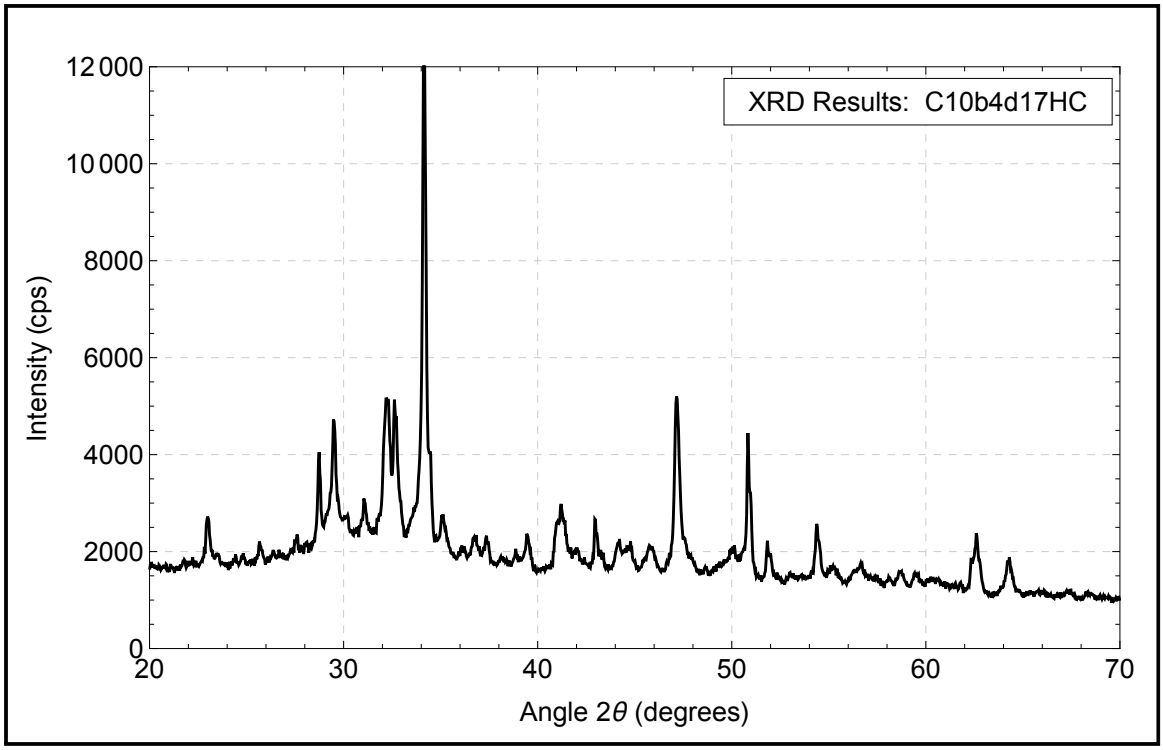
XRD Results: C10b4d17HC
Intensity (cps)
12 000
10 000
8000
6000
4000
2000
0
20
30
40
50
60
70
Angle 2θ (degrees)

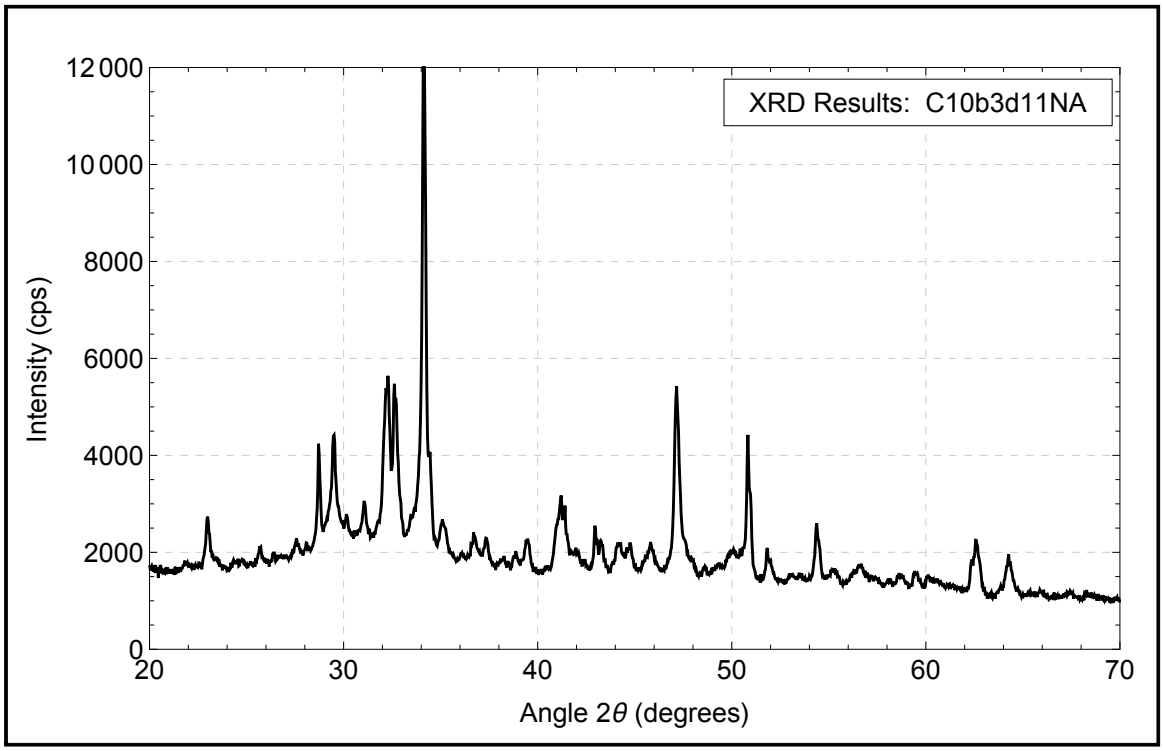
XRD Results: C10b3d11NA
Intensity (cps)
12 000
10 000
8000
6000
4000
2000
0
20
30
40
50
60
70
Angle 2θ (degrees)

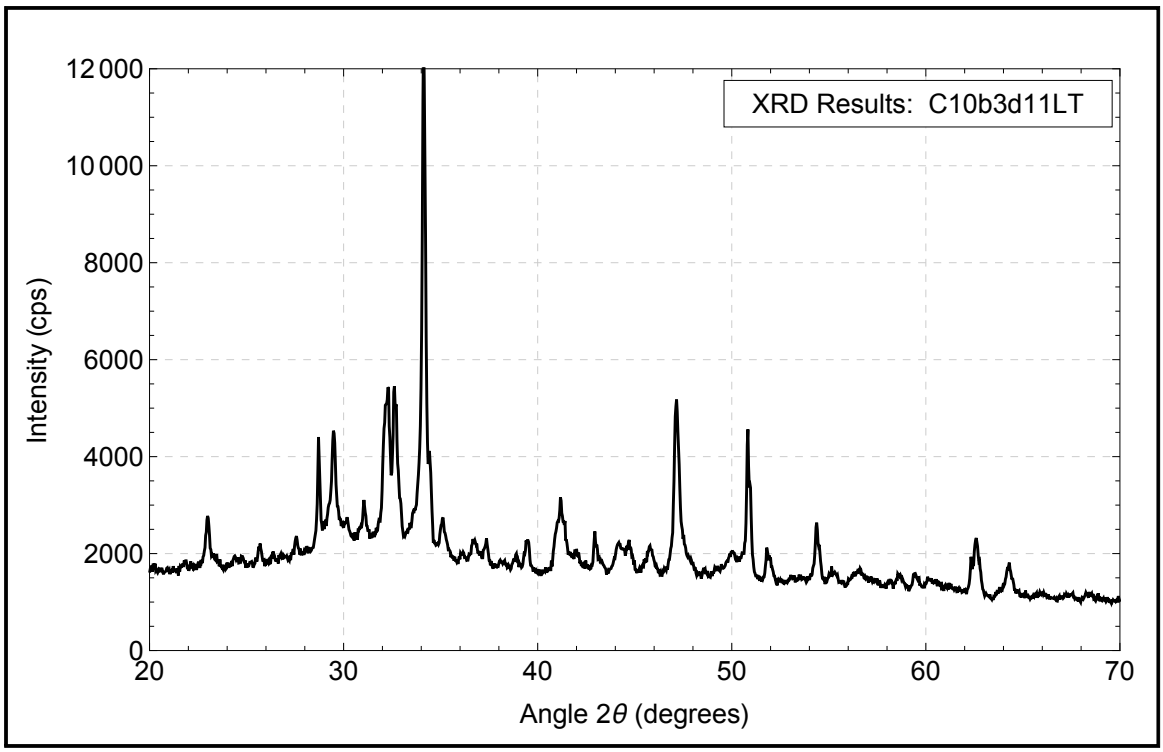
XRD Results: C10b3d11LT
Intensity (cps)
12 000
10 000
8000
6000
4000
2000
0
20
30
40
50
60
70
Angle 2θ (degrees)

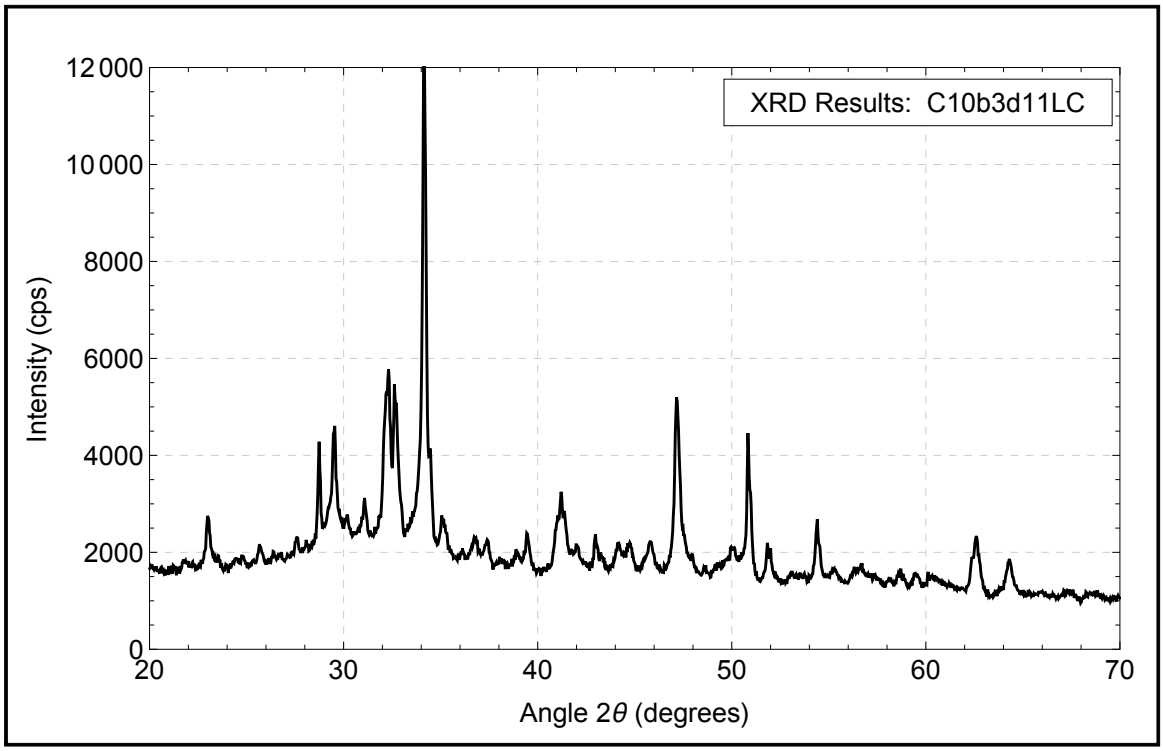
XRD Results: C10b3d11LC
Intensity (cps)
12 000
10 000
8000
6000
4000
2000
0
20
30
40
50
60
70
Angle 2θ (degrees)

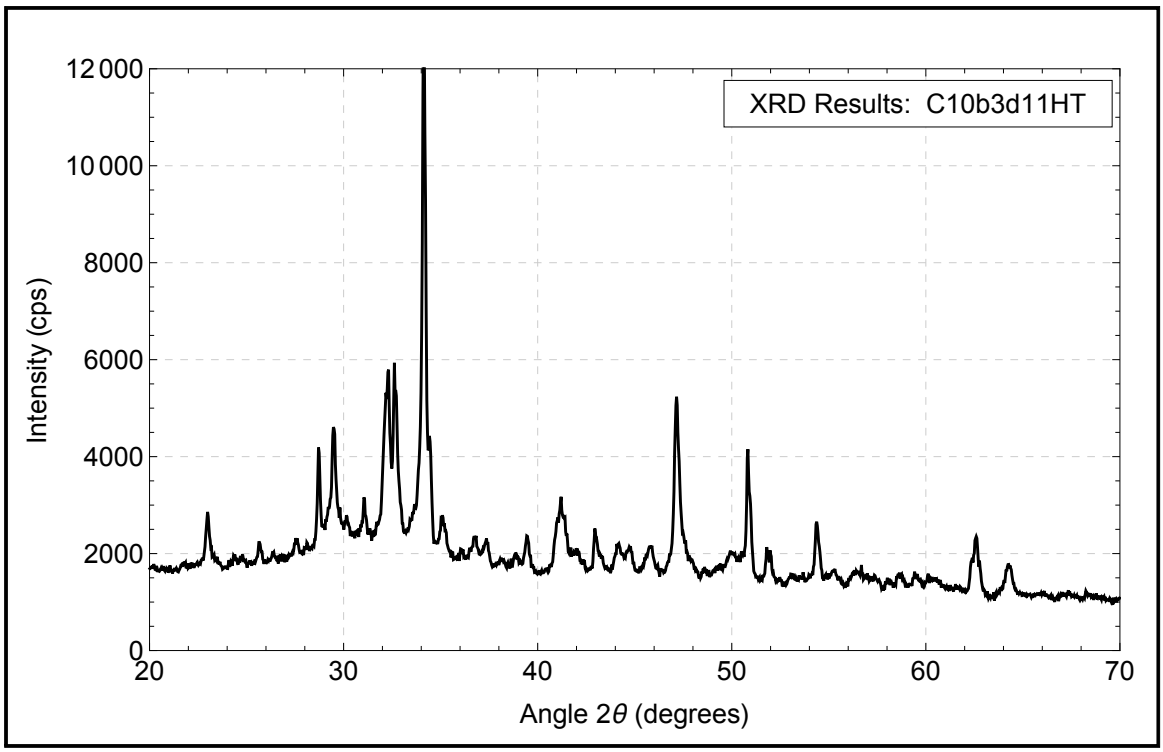
XRD Results: C10b3d11HT
Intensity (cps)
12 000
10 000
8000
6000
4000
2000
0
20
30
40
50
60
70
Angle 2θ (degrees)

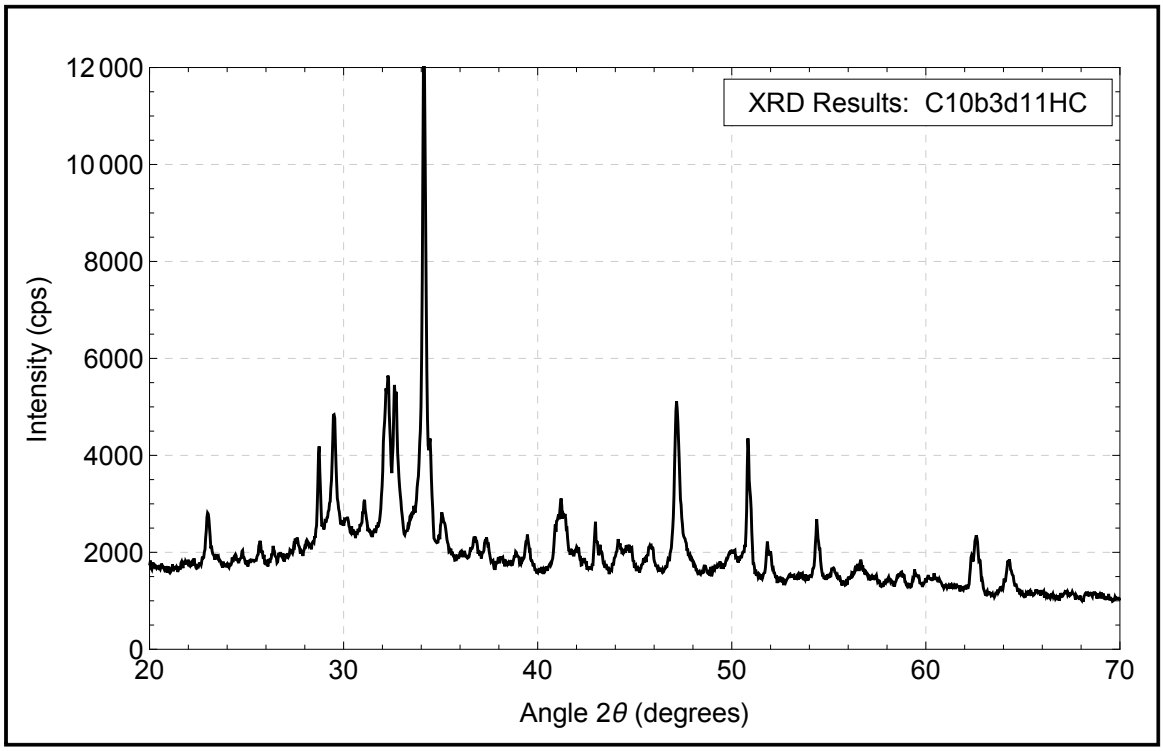
XRD Results: C10b3d11HC
Intensity (cps)
12 000
10 000
8000
6000
4000
2000
0
20
30
40
50
60
70
Angle 2θ (degrees)

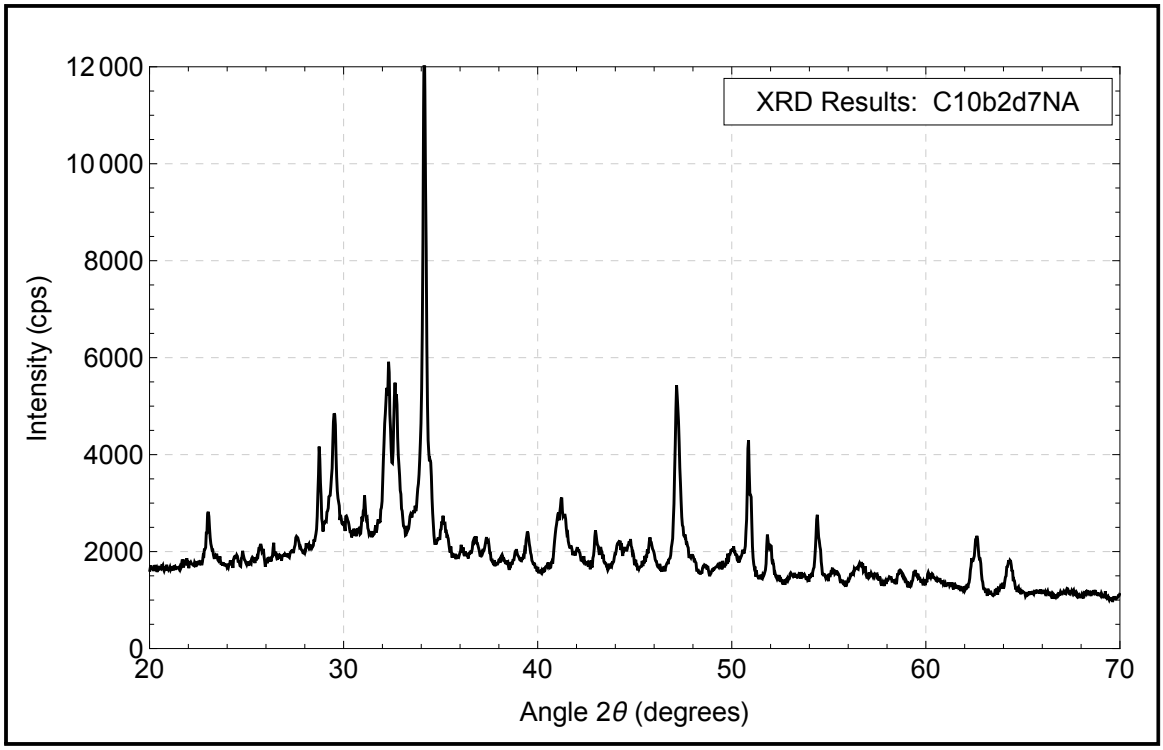
XRD Results: C10b2d7NA
Intensity (cps)
12 000
10 000
8000
6000
4000
2000
0
20
30
40
50
60
70
Angle 2θ (degrees)

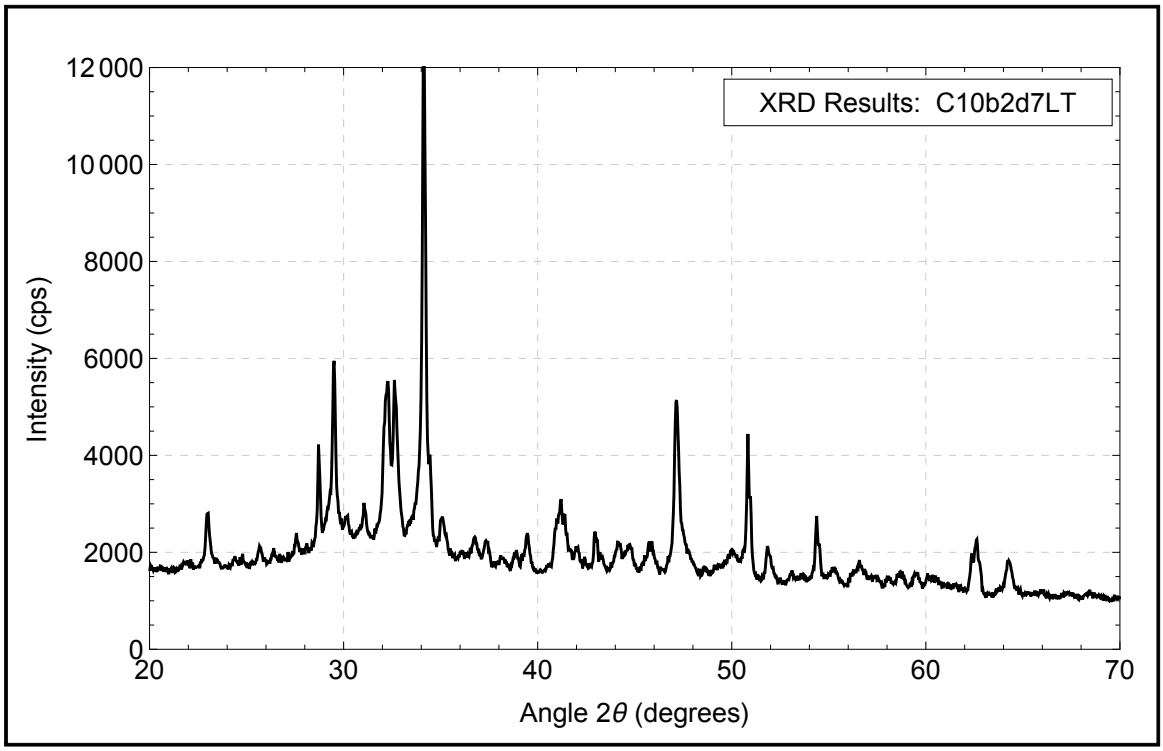
XRD Results: C10b2d7LT
Intensity (cps)
12 000
10 000
8000
6000
4000
2000
0
20
30
40
50
60
70
Angle 2θ (degrees)

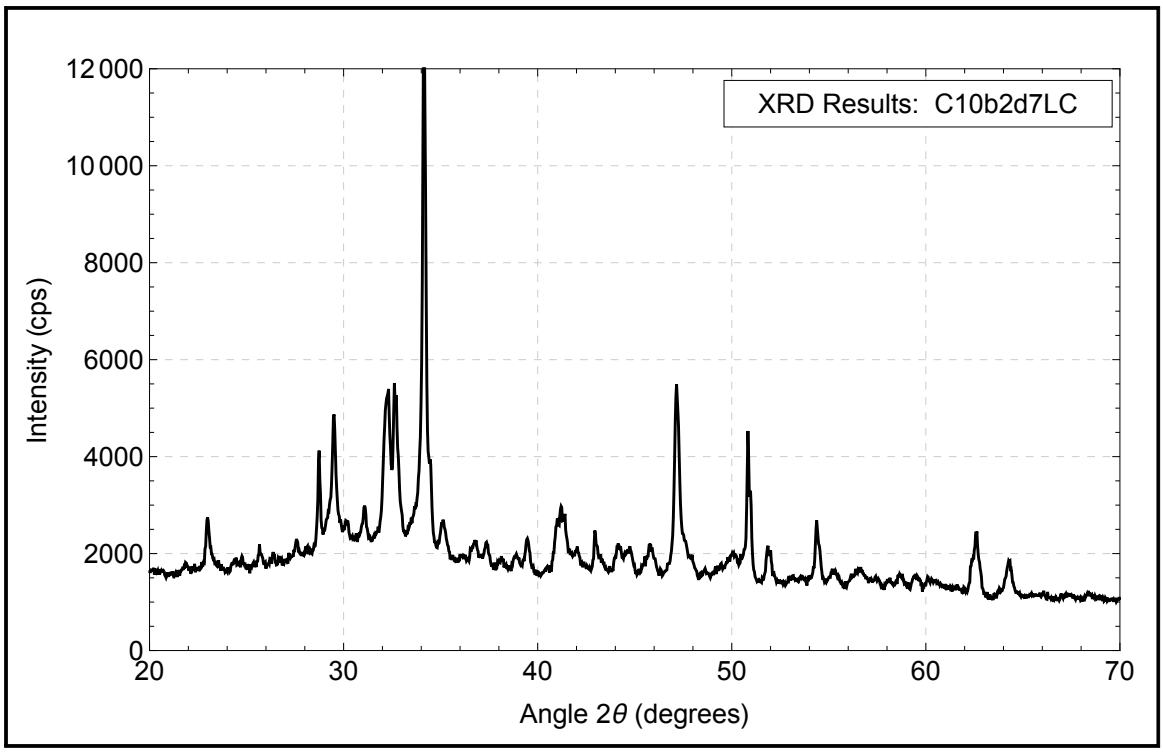
XRD Results: C10b2d7LC
Intensity (cps)
12 000
10 000
8000
6000
4000
2000
0
20
30
40
50
60
70
Angle 2θ (degrees)

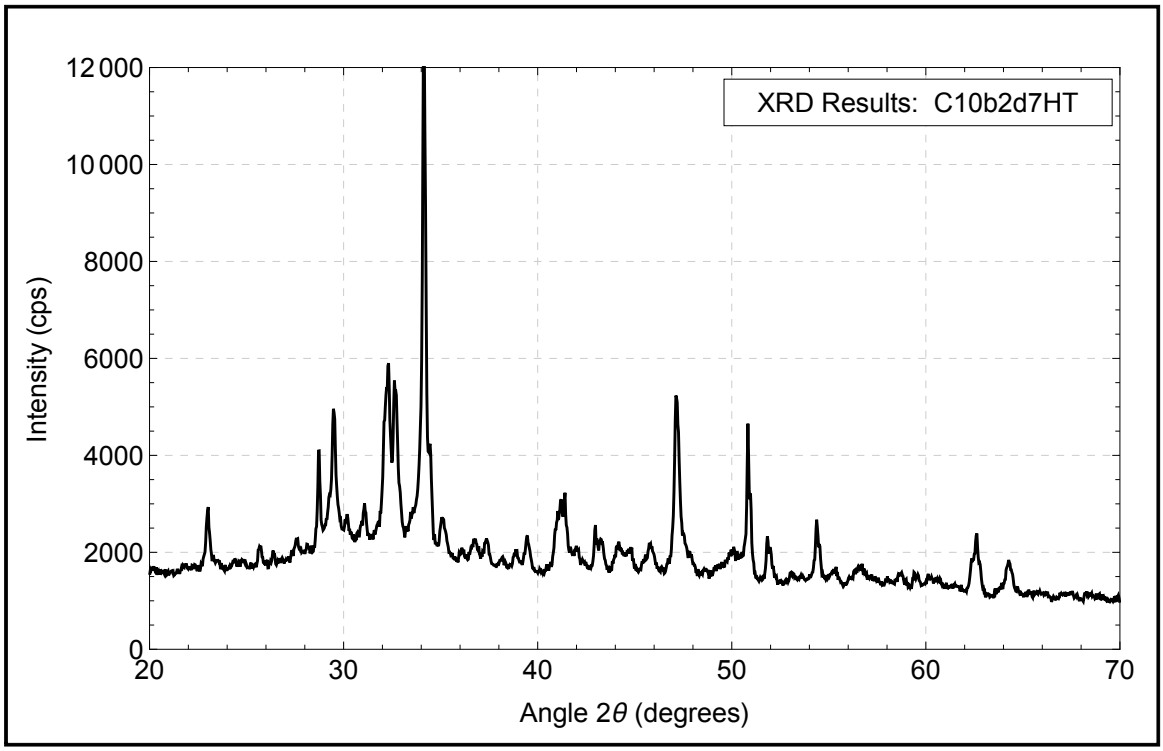
XRD Results: C10b2d7HT
Intensity (cps)
12 000
10 000
8000
6000
4000
2000
0
20
30
40
50
60
70
Angle 2θ (degrees)

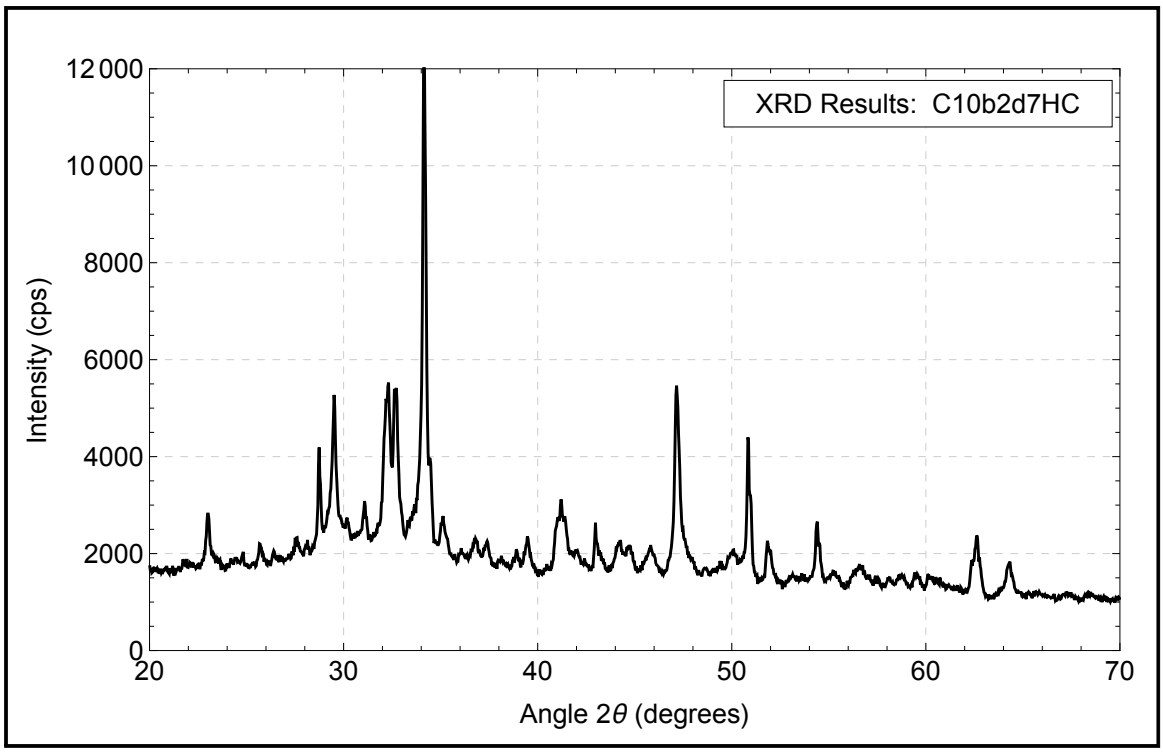
XRD Results: C10b2d7HC
Intensity (cps)
12 000
10 000
8000
6000
4000
2000
0
20
30
40
50
60
70
Angle 2θ (degrees)

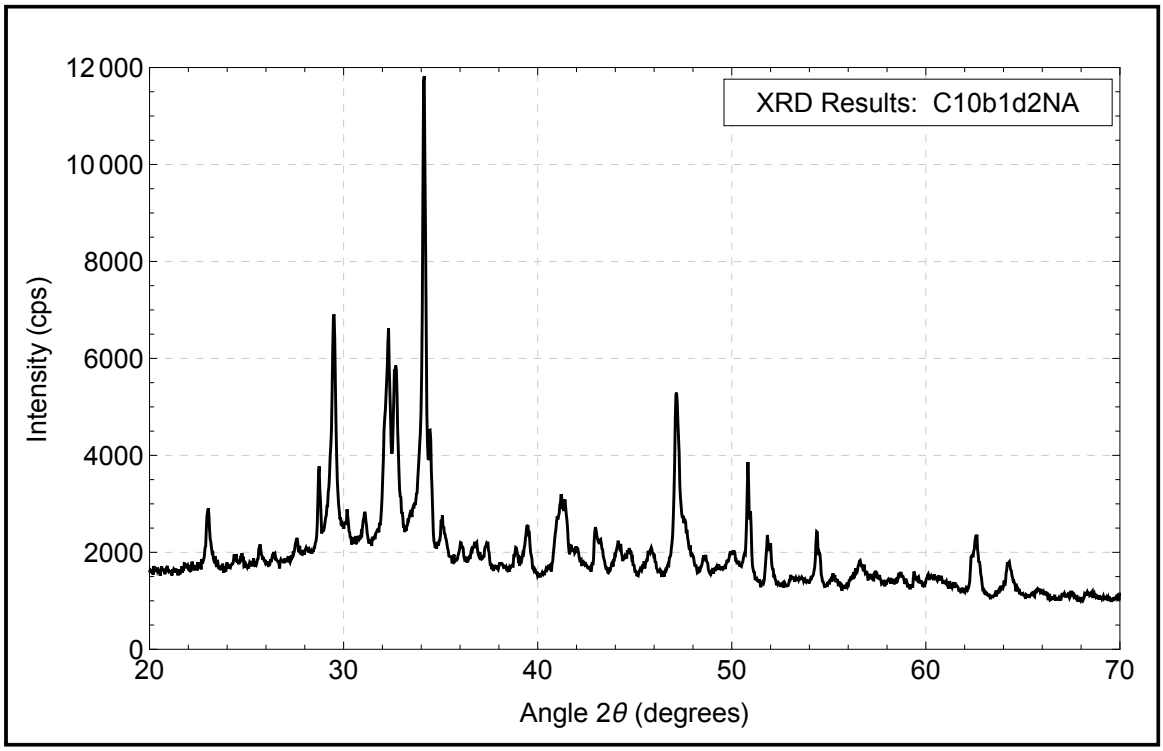
XRD Results: C10b1d2NA
Intensity (cps)
12 000
10 000
8000
6000
4000
2000
0
20
30
40
50
60
70
Angle 2θ (degrees)

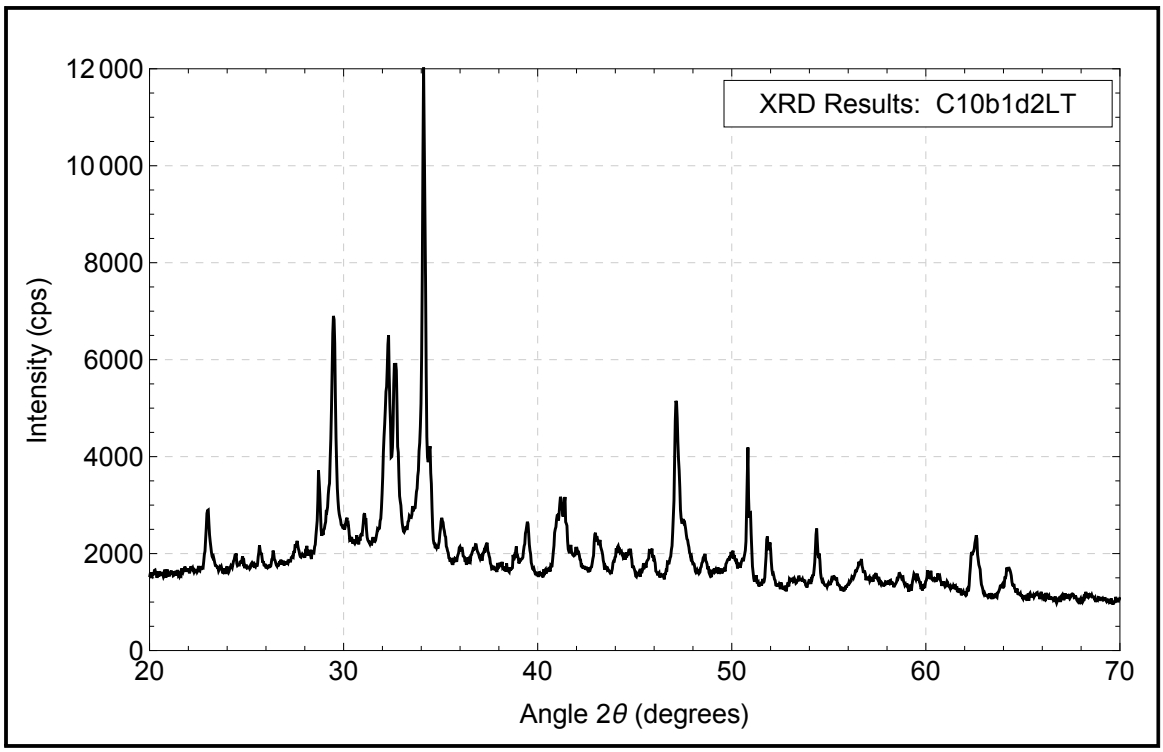
XRD Results: C10b1d2LT
Intensity (cps)
12 000
10 000
8000
6000
4000
2000
0
20
30
40
50
60
70
Angle 2θ (degrees)

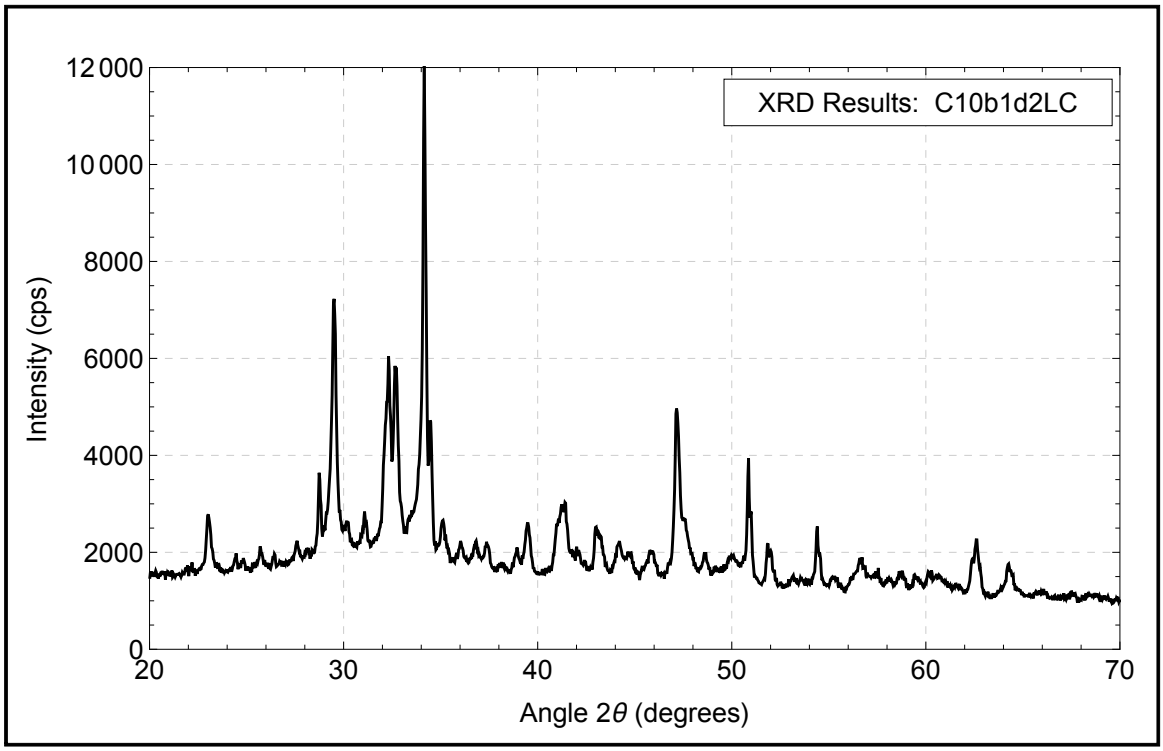
XRD Results: C10b1d2LC
Intensity (cps)
12 000
10 000
8000
6000
4000
2000
0
20
30
40
50
60
70
Angle 2θ (degrees)

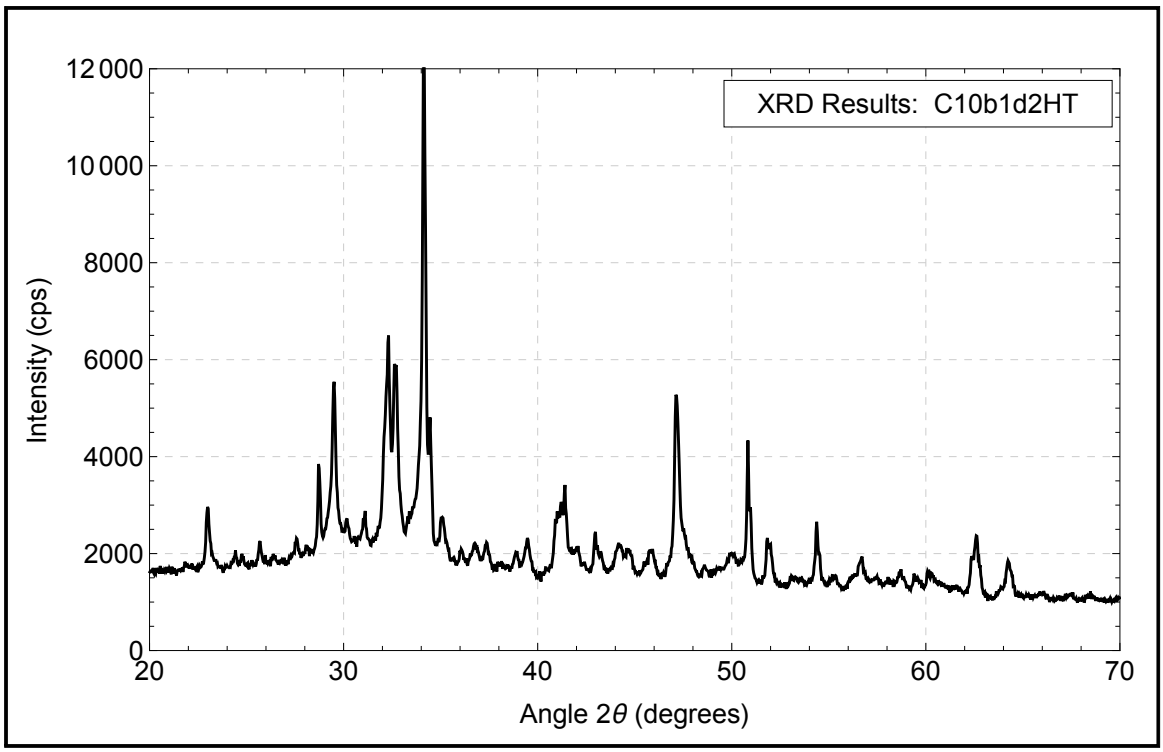
XRD Results: C10b1d2HT
Intensity (cps)
12 000
10 000
8000
6000
4000
2000
0
20
30
40
50
60
70
Angle 2θ (degrees)

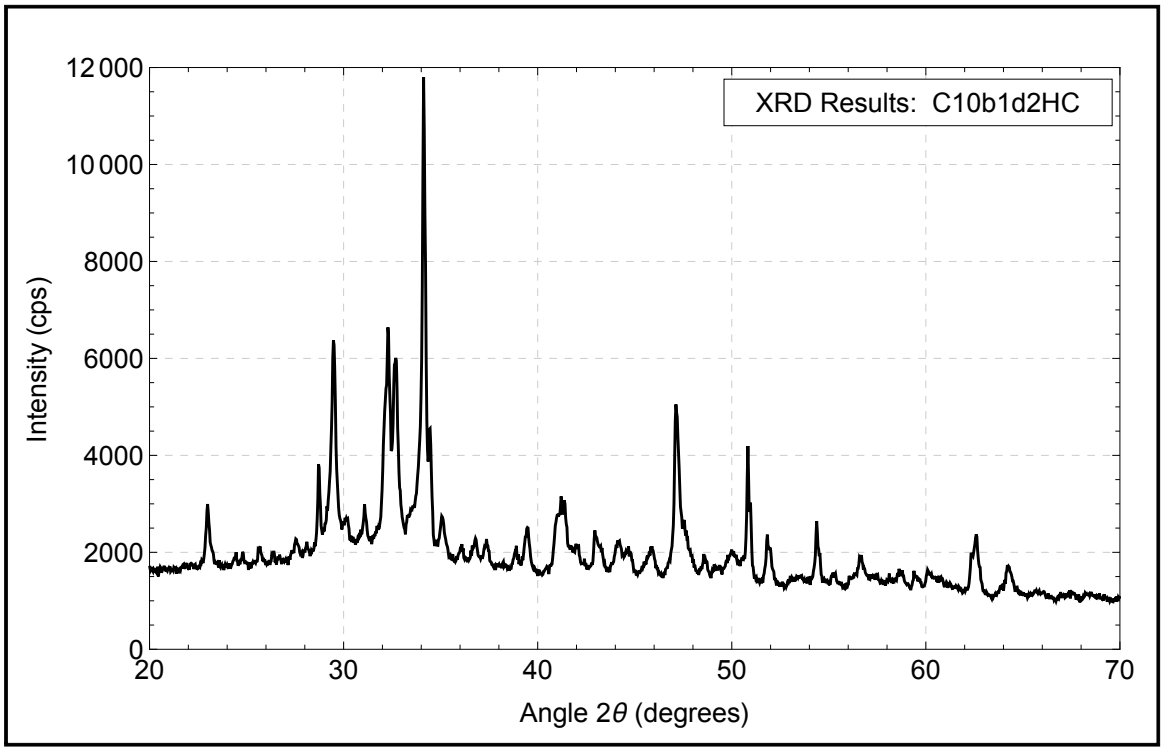
XRD Results: C10b1d2HC
Intensity (cps)
12 000
10 000
8000
6000
4000
2000
0
20
30
40
50
60
70
Angle 2θ (degrees)

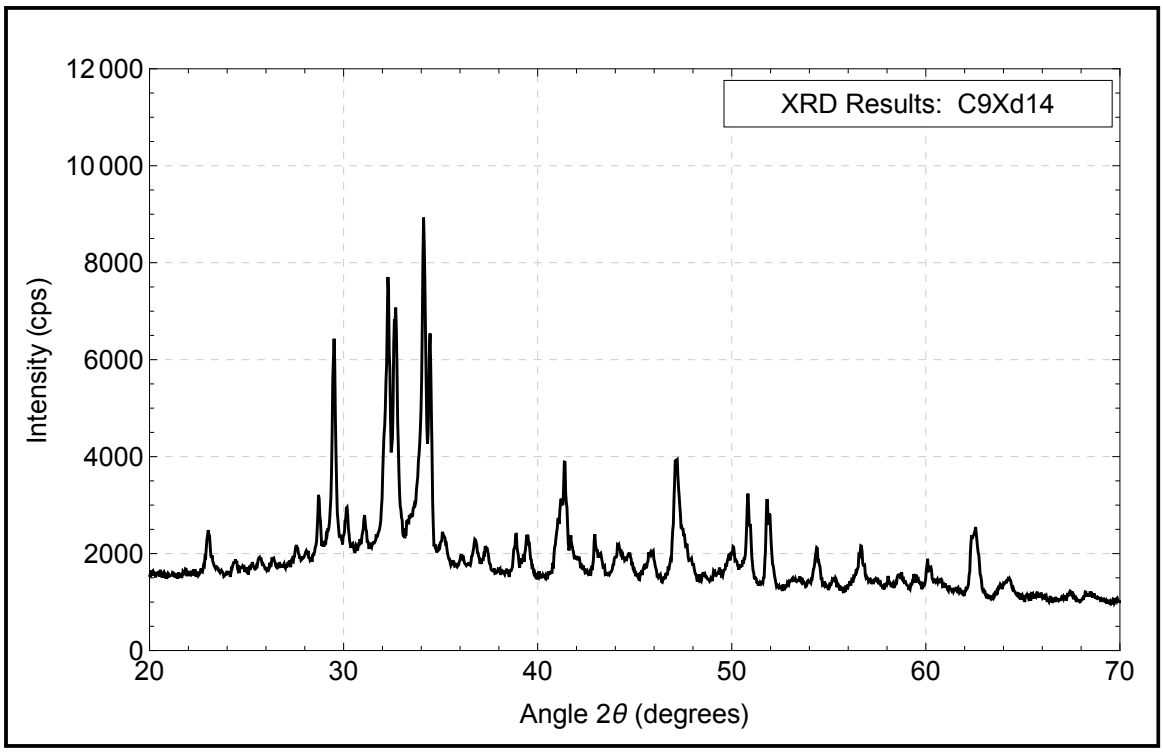
XRD Results: C9Xd14
Intensity (cps)
12 000
10 000
8000
6000
4000
2000
0
20
30
40
50
60
70
Angle 2θ (degrees)

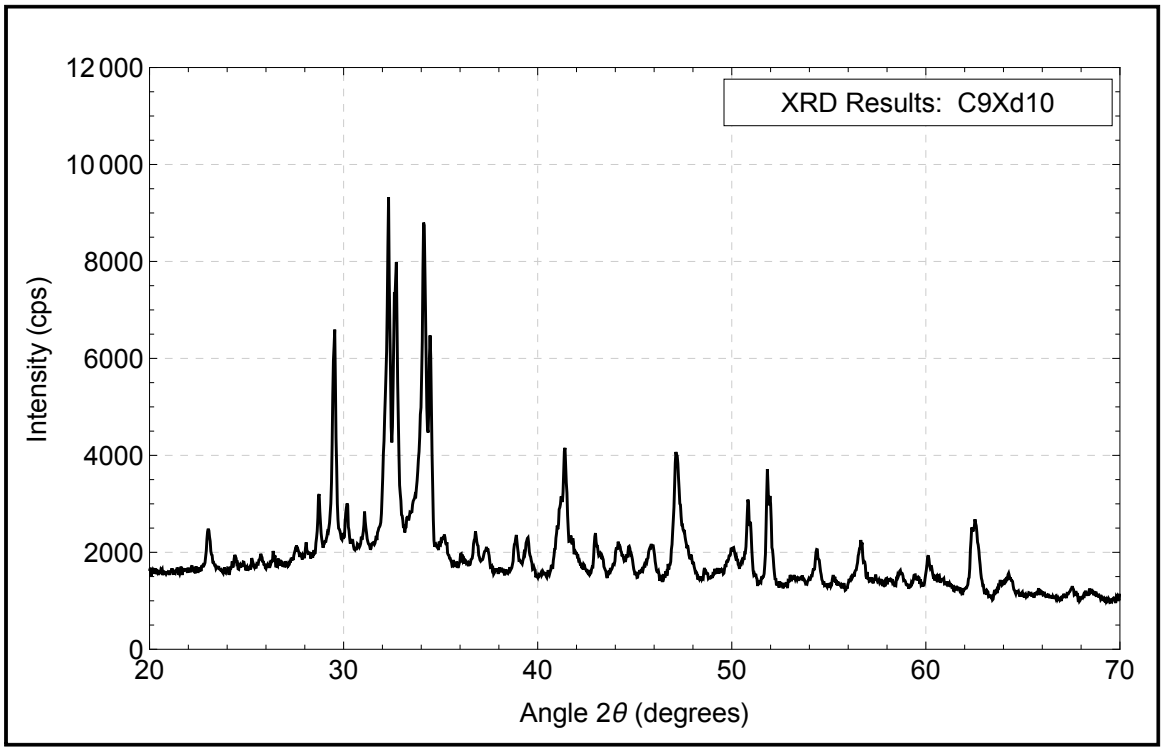
XRD Results: C9Xd10
Intensity (cps)
12 000
10 000
8000
6000
4000
2000
0
20
30
40
50
60
70
Angle 2θ (degrees)

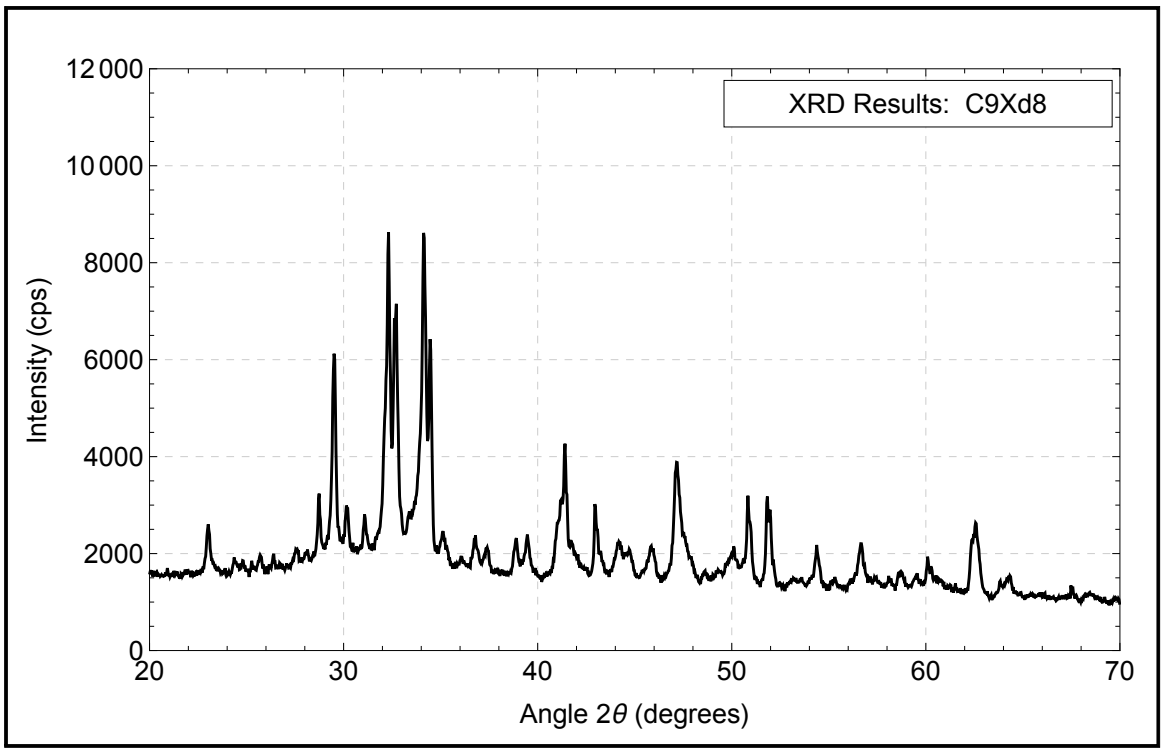
XRD Results: C9Xd8
Intensity (cps)
12 000
10 000
8000
6000
4000
2000
0
20
30
40
50
60
70
Angle 2θ (degrees)

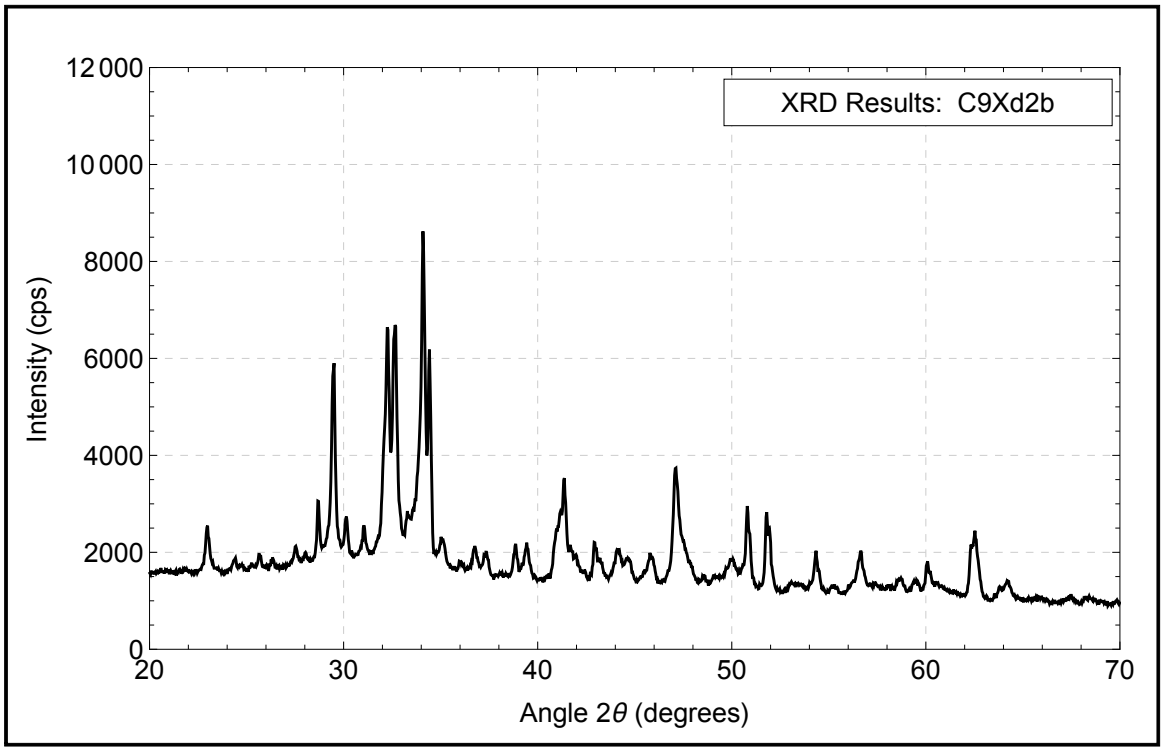
XRD Results: C9Xd2b
Intensity (cps)
12 000
10 000
8000
6000
4000
2000
0
20
30
40
50
60
70
Angle 2θ (degrees)

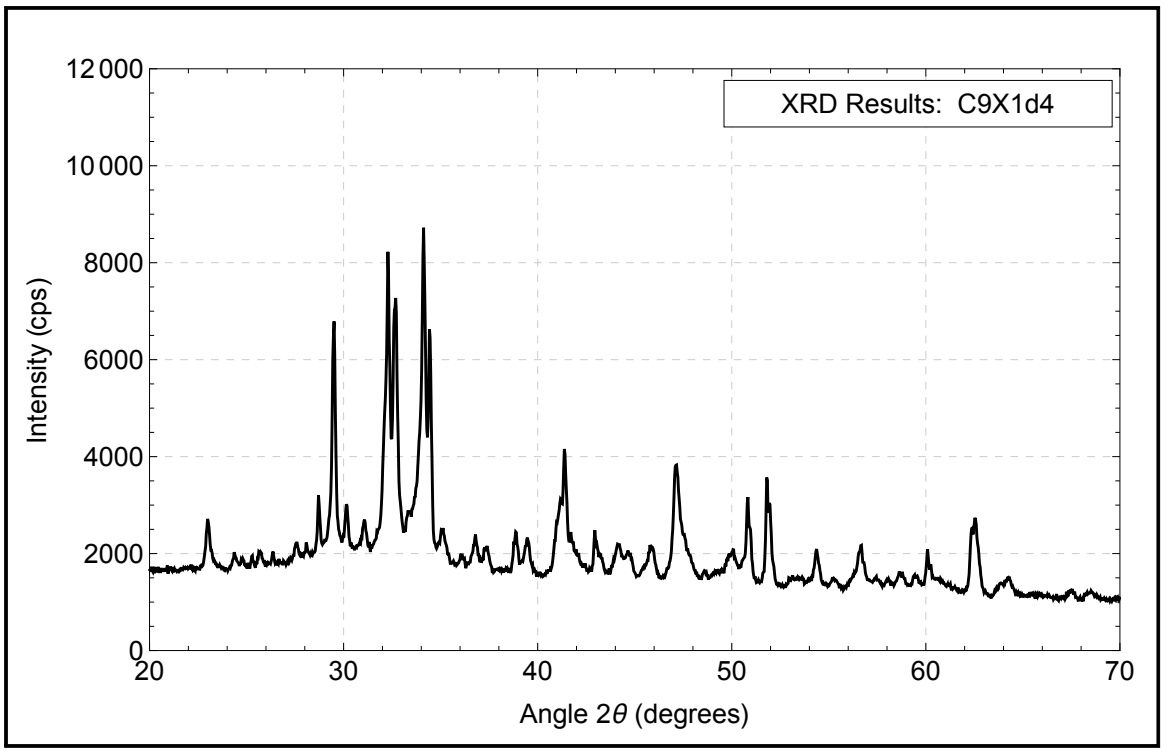
XRD Results: C9X1d4
Intensity (cps)
12 000
10 000
8000
6000
4000
2000
0
20
30
40
50
60
70
Angle 2θ (degrees)

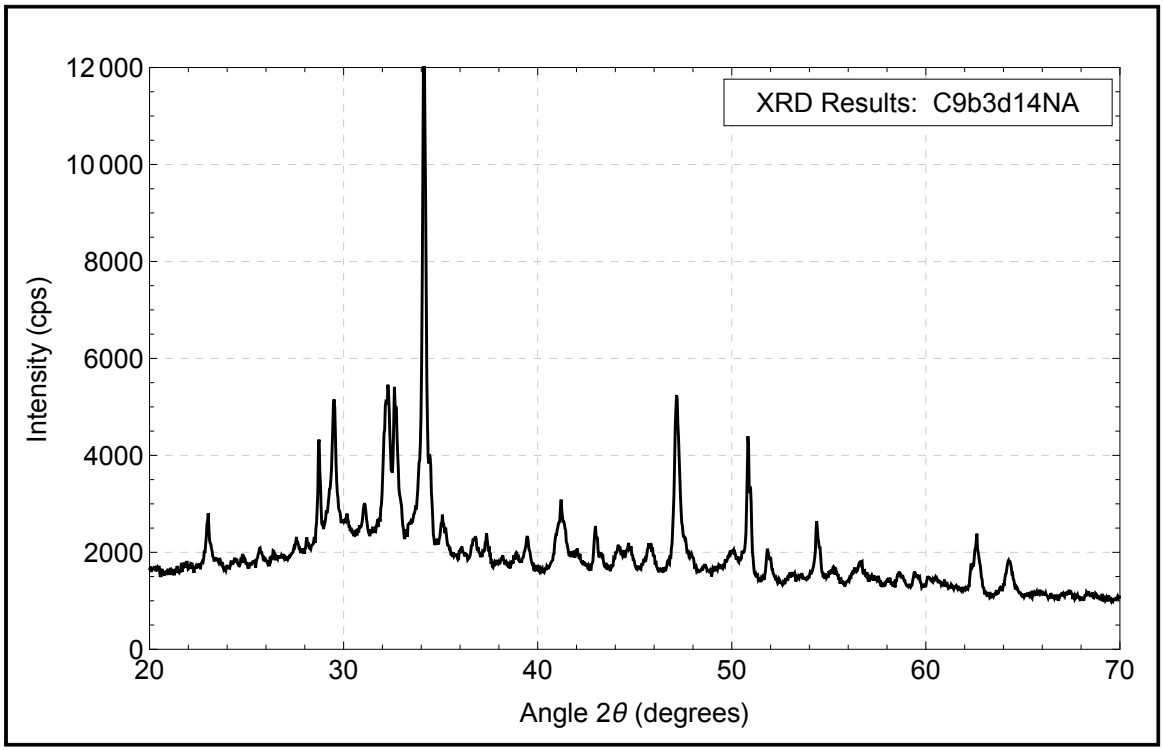
XRD Results: C9b3d14NA
Intensity (cps)
12 000
10 000
8000
6000
4000
2000
0
20
30
40
50
60
70
Angle 2θ (degrees)

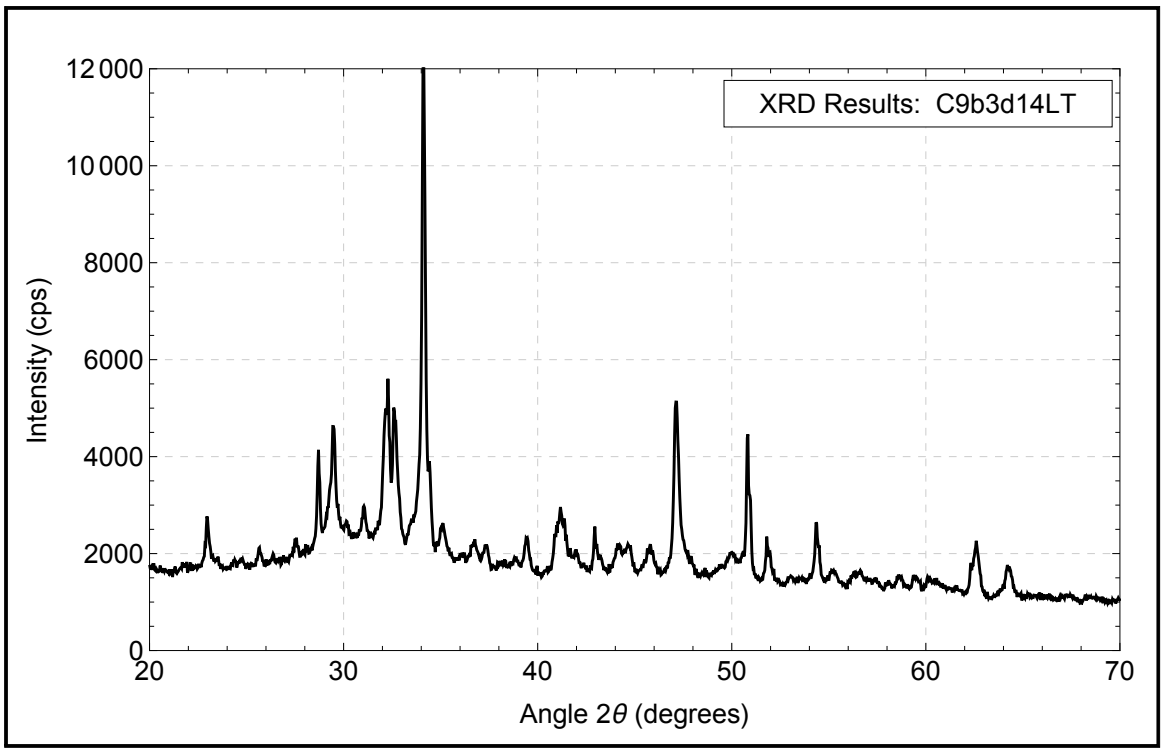
XRD Results: C9b3d14LT
Intensity (cps)
12 000
10 000
8000
6000
4000
2000
0
20
30
40
50
60
70
Angle 2θ (degrees)

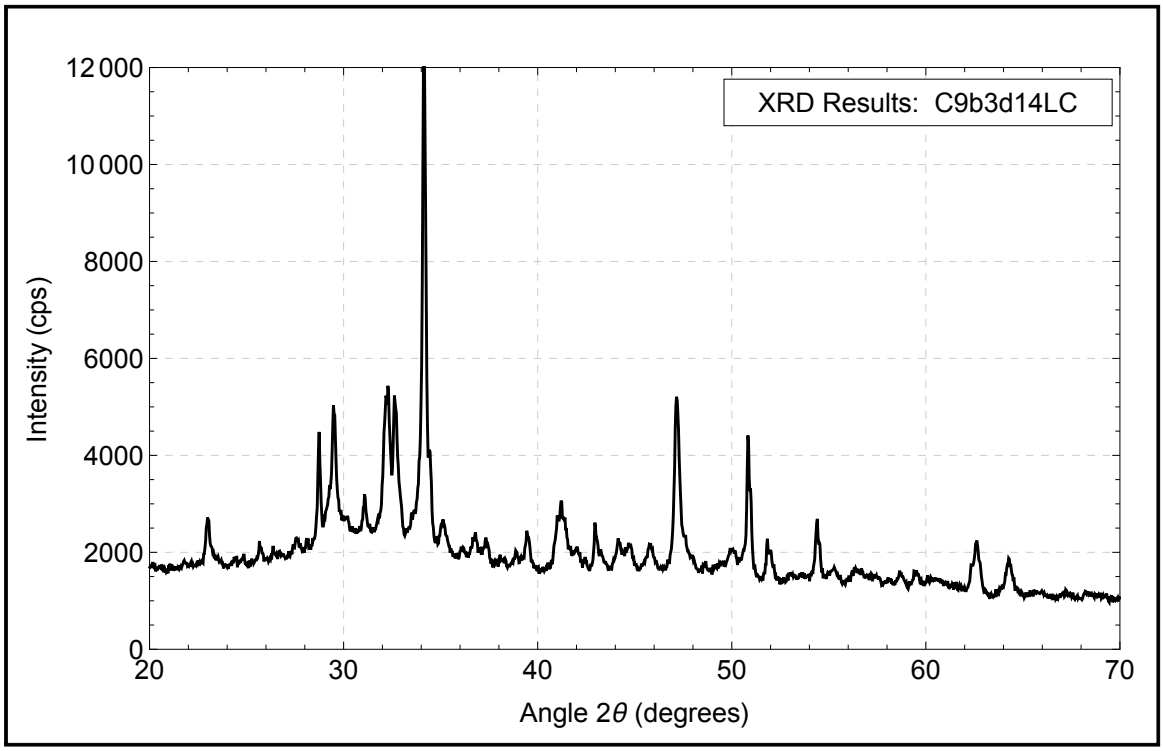
XRD Results: C9b3d14LC
Intensity (cps)
12 000
10 000
8000
6000
4000
2000
0
20
30
40
50
60
70
Angle 2θ (degrees)

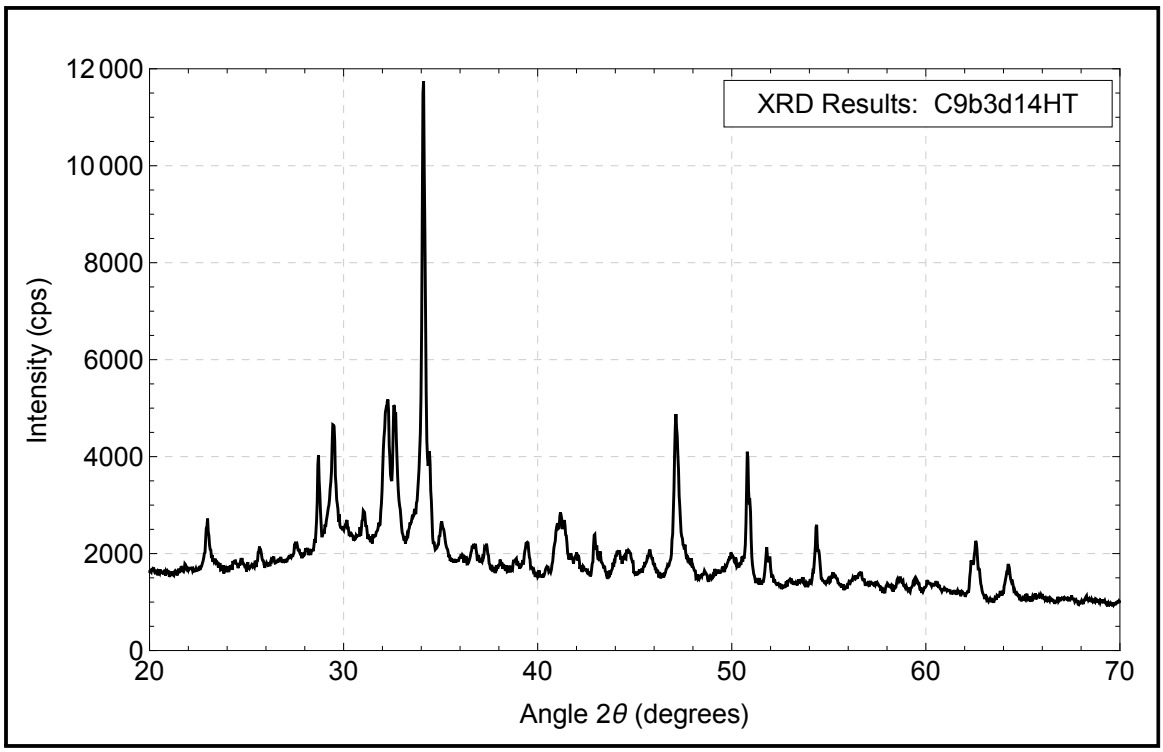
XRD Results: C9b3d14HT
Intensity (cps)
12 000
10 000
8000
6000
4000
2000
0
20
30
40
50
60
70
Angle 2θ (degrees)

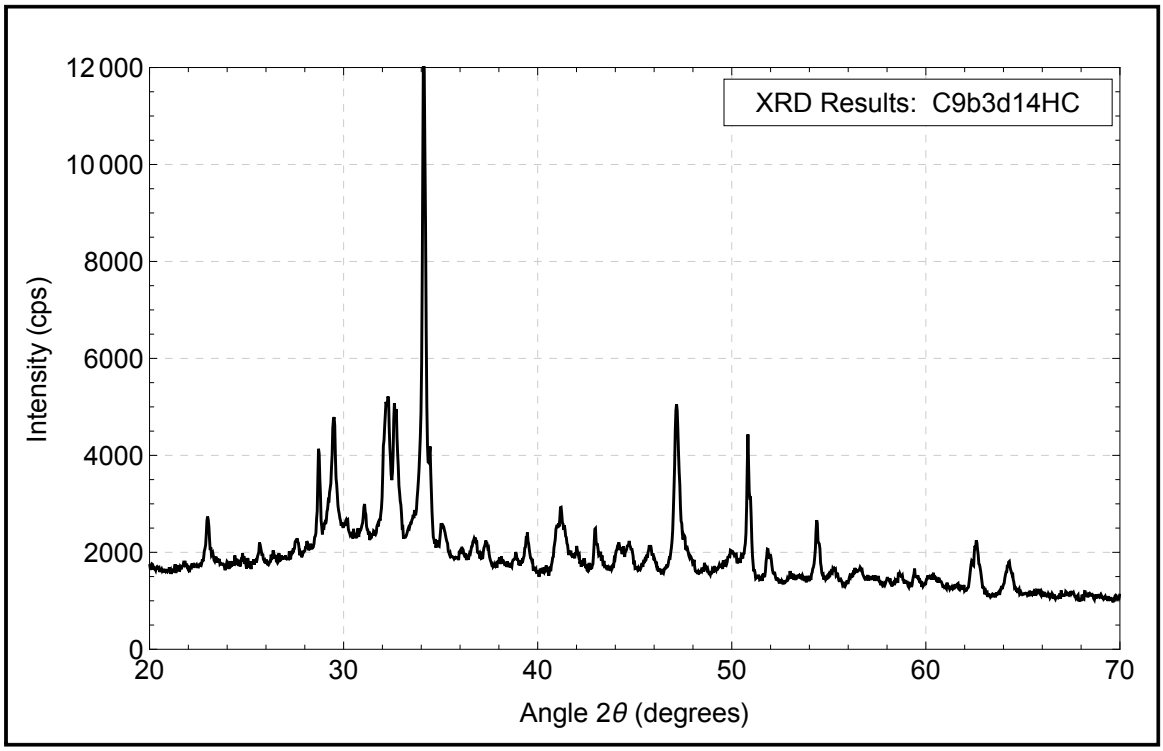
XRD Results: C9b3d14HC
Intensity (cps)
12 000
10 000
8000
6000
4000
2000
0
20
30
40
50
60
70
Angle 2θ (degrees)

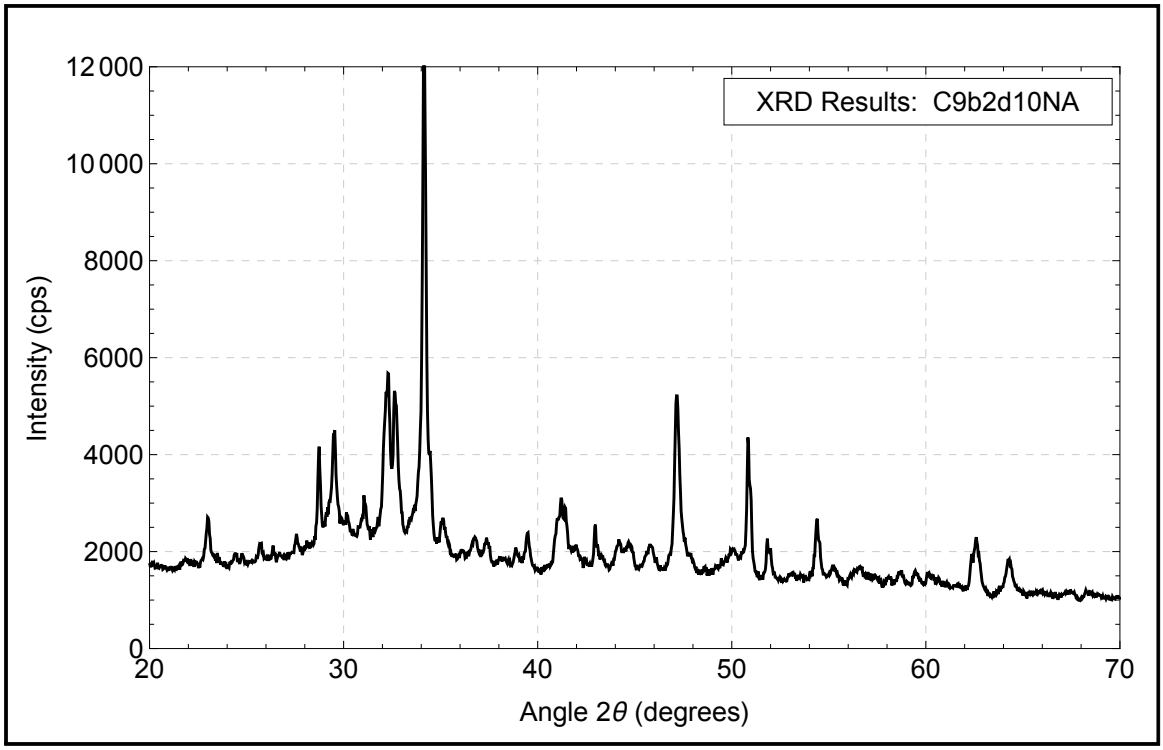
XRD Results: C9b2d10NA
Intensity (cps)
12 000
10 000
8000
6000
4000
2000
0
20
30
40
50
60
70
Angle 2θ (degrees)

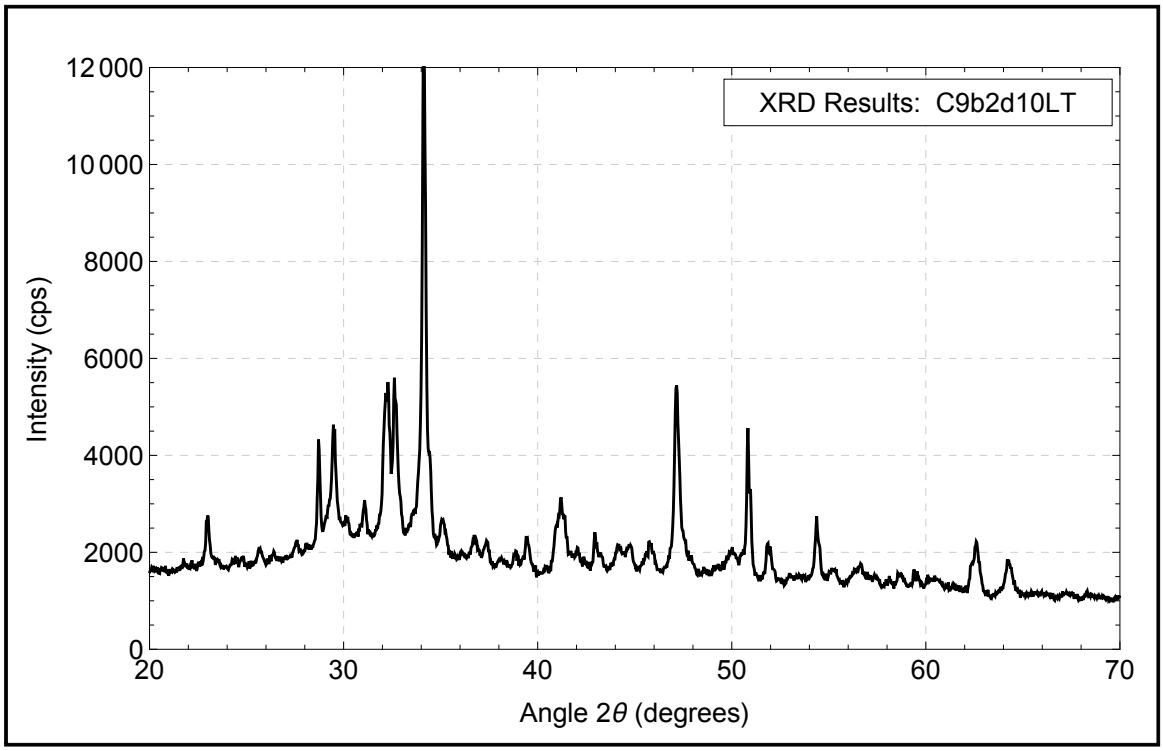
XRD Results: C9b2d10LT
Intensity (cps)
12 000
10 000
8000
6000
4000
2000
0
20
30
40
50
60
70
Angle 2θ (degrees)

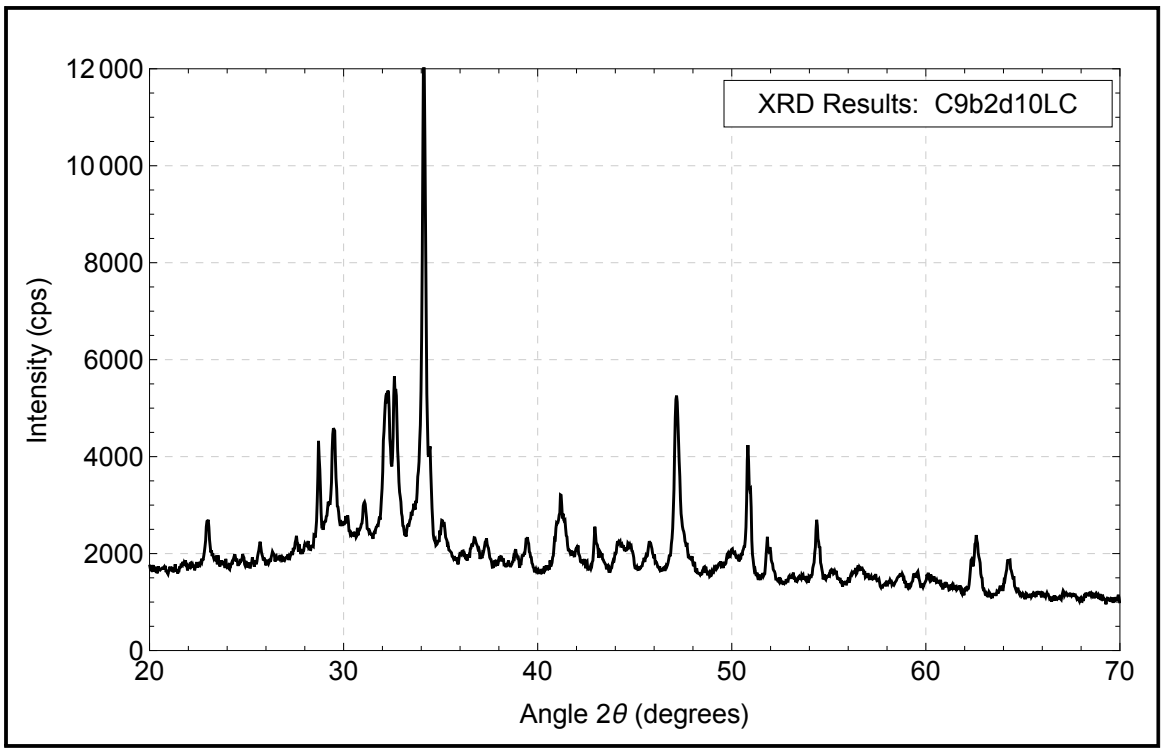
XRD Results: C9b2d10LC
Intensity (cps)
12 000
10 000
8000
6000
4000
2000
0
20
30
40
50
60
70
Angle 2θ (degrees)

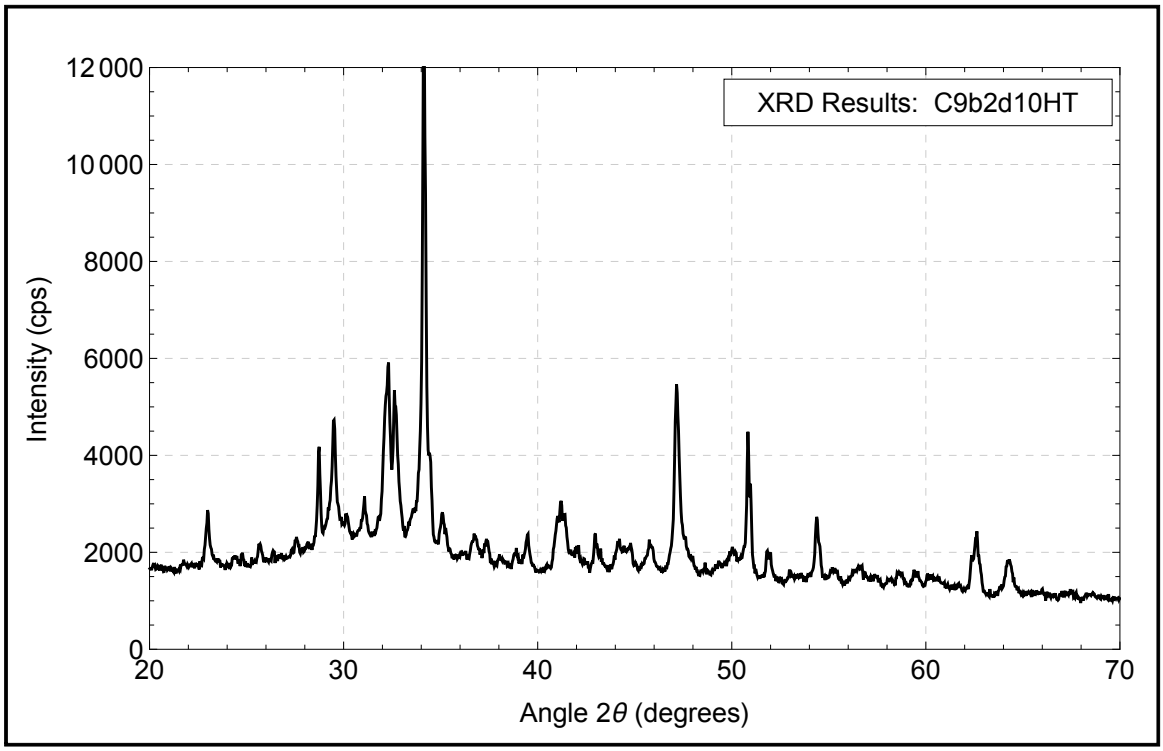
XRD Results: C9b2d10HT
Intensity (cps)
12 000
10 000
8000
6000
4000
2000
0
20
30
40
50
60
70
Angle 2θ (degrees)

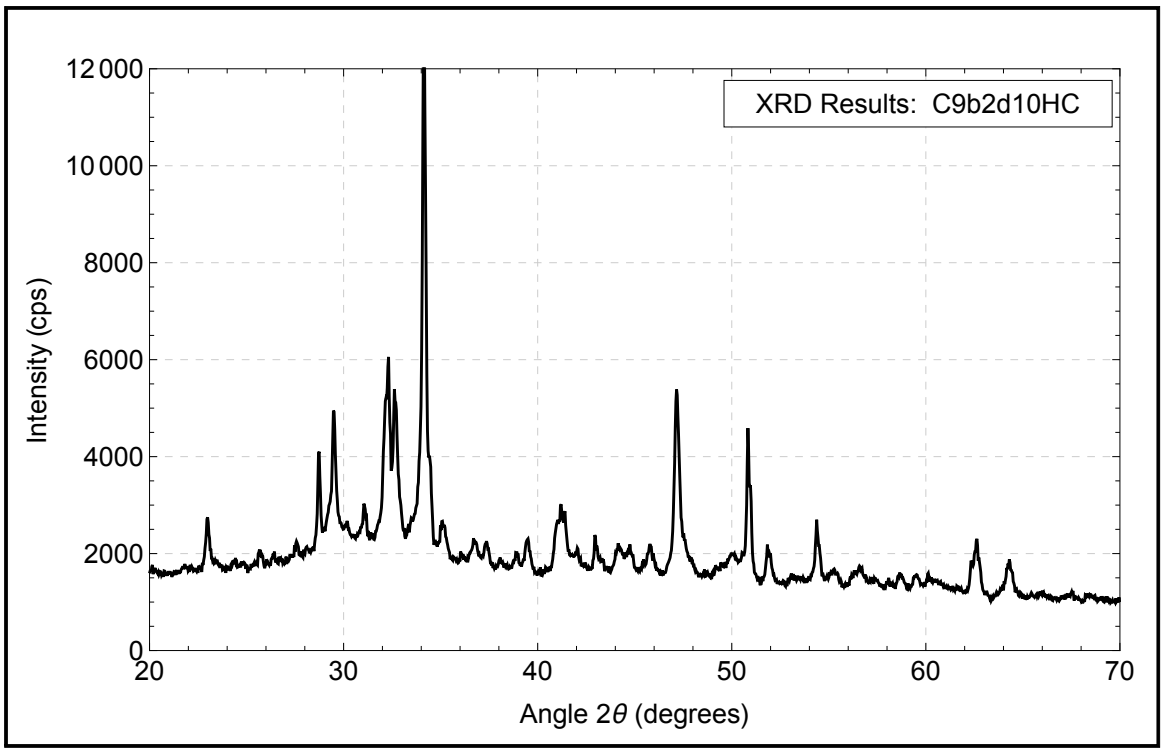
XRD Results: C9b2d10HC
Intensity (cps)
12 000
10 000
8000
6000
4000
2000
0
20
30
40
50
60
70
Angle 2θ (degrees)

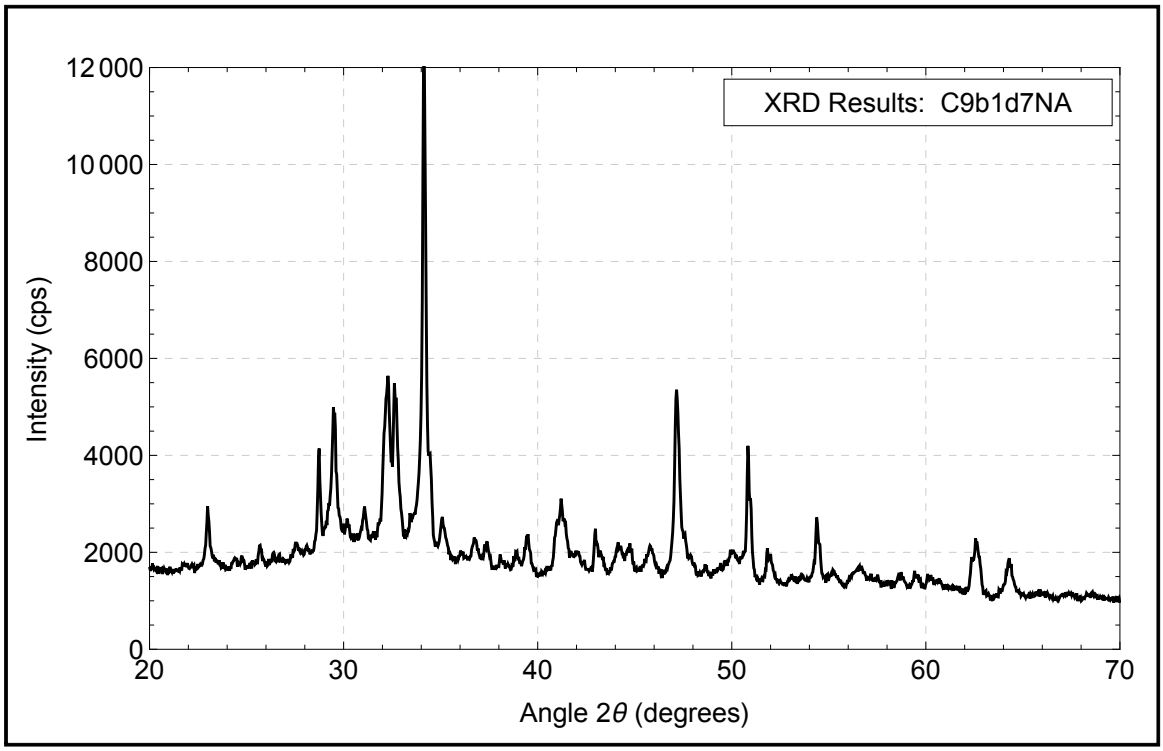
XRD Results: C9b1d7NA
Intensity (cps)
12 000
10 000
8000
6000
4000
2000
0
20
30
40
50
60
70
Angle 2θ (degrees)

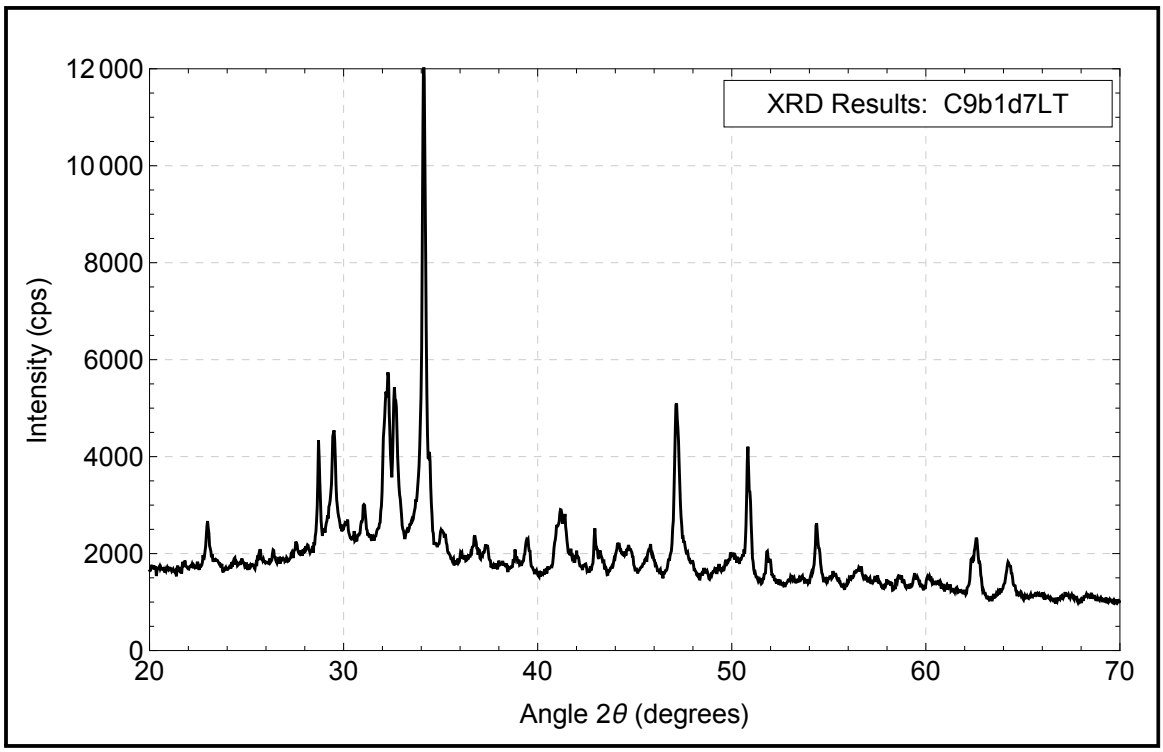
XRD Results: C9b1d7LT
Intensity (cps)
12 000
10 000
8000
6000
4000
2000
0
20
30
40
50
60
70
Angle 2θ (degrees)

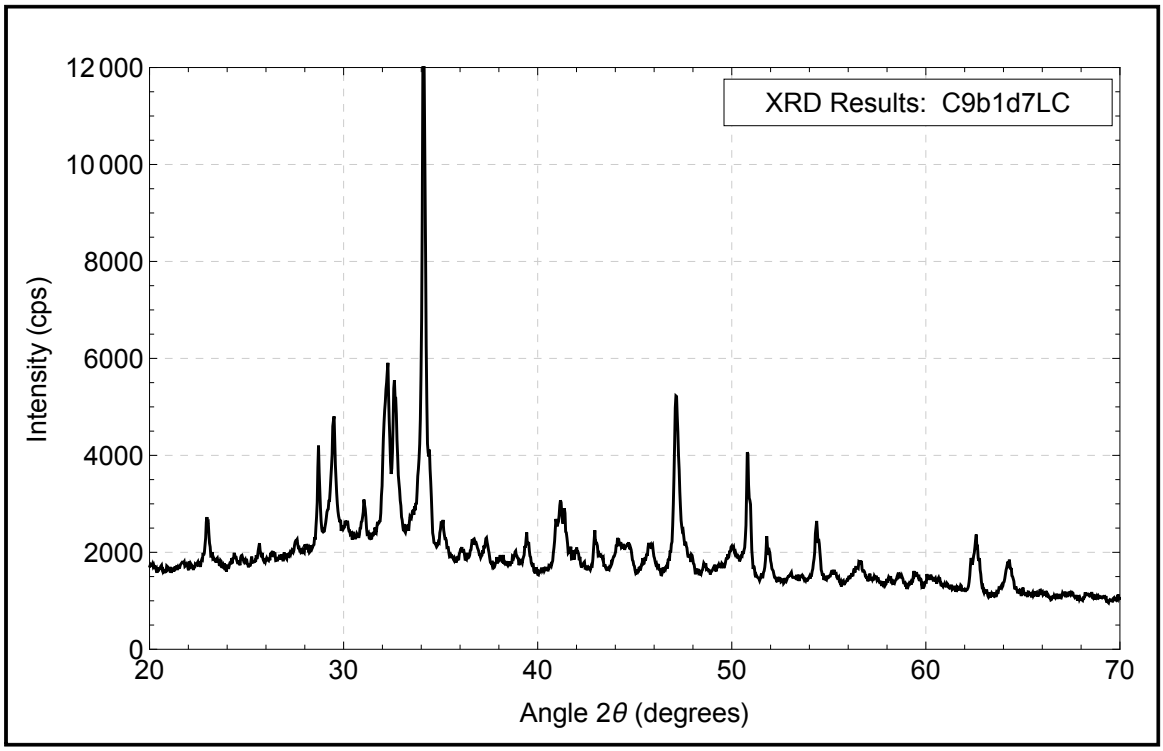
XRD Results: C9b1d7LC
Intensity (cps)
12 000
10 000
8000
6000
4000
2000
0
20
30
40
50
60
70
Angle 2θ (degrees)

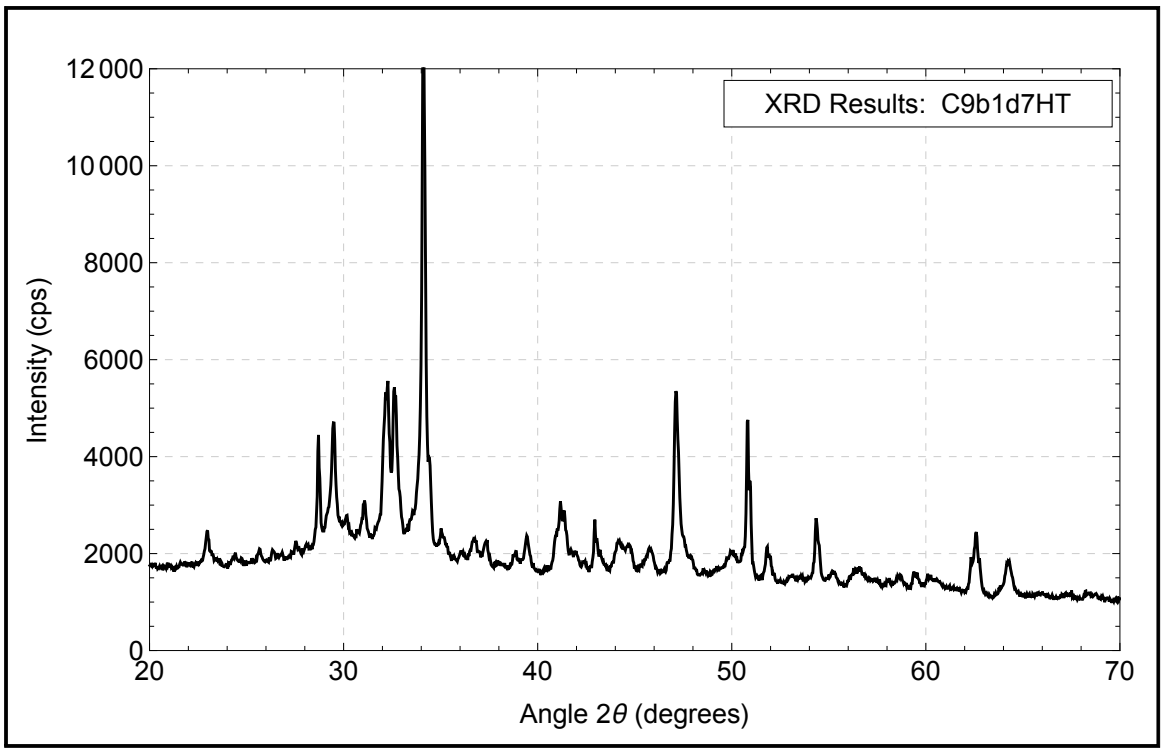
XRD Results: C9b1d7HT
Intensity (cps)
12 000
10 000
8000
6000
4000
2000
0
20
30
40
50
60
70
Angle 2θ (degrees)

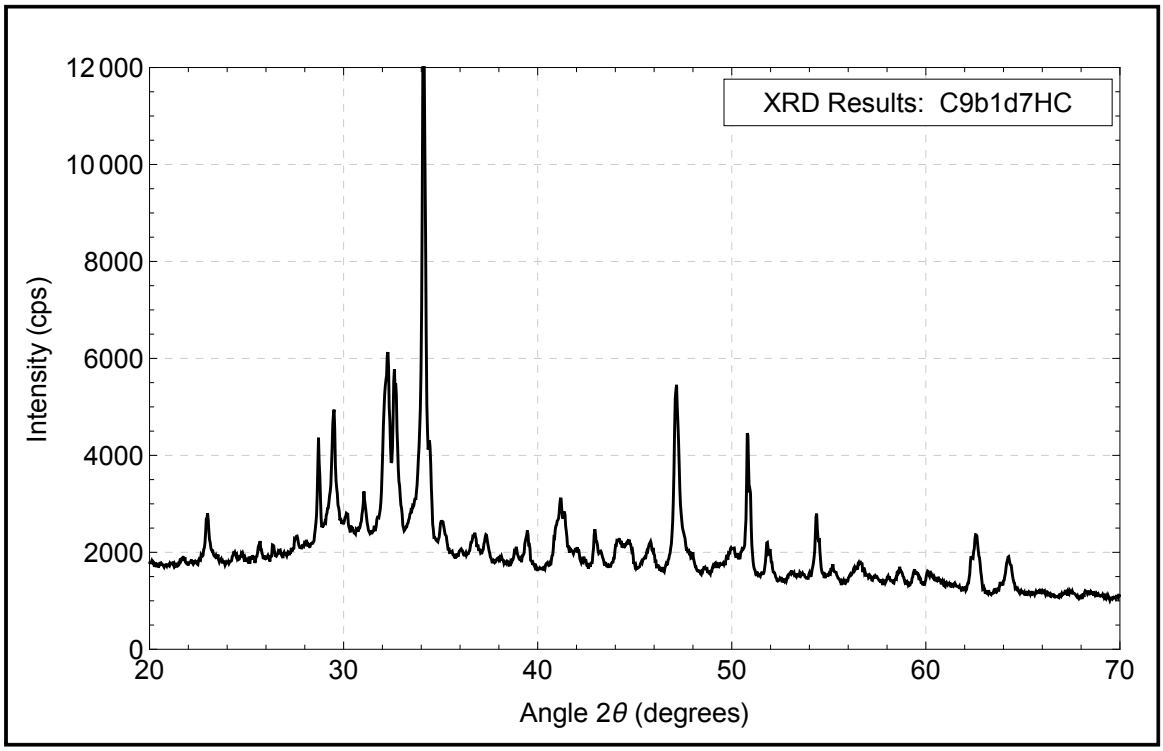
XRD Results: C9b1d7HC
Intensity (cps)
12 000
10 000
8000
6000
4000
2000
0
20
30
40
50
60
70
Angle 2θ (degrees)

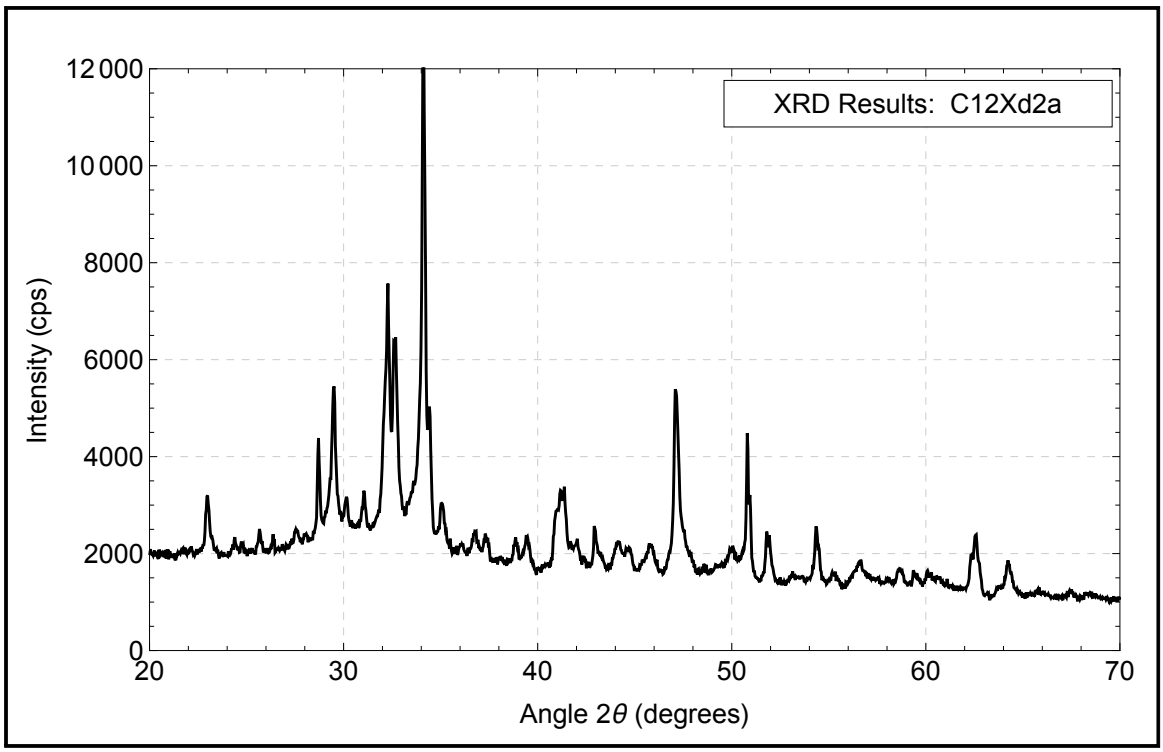
XRD Results: C12Xd2a
Intensity (cps)
12 000
10 000
8000
6000
4000
2000
0
20
30
40
50
60
70
Angle 2θ (degrees)

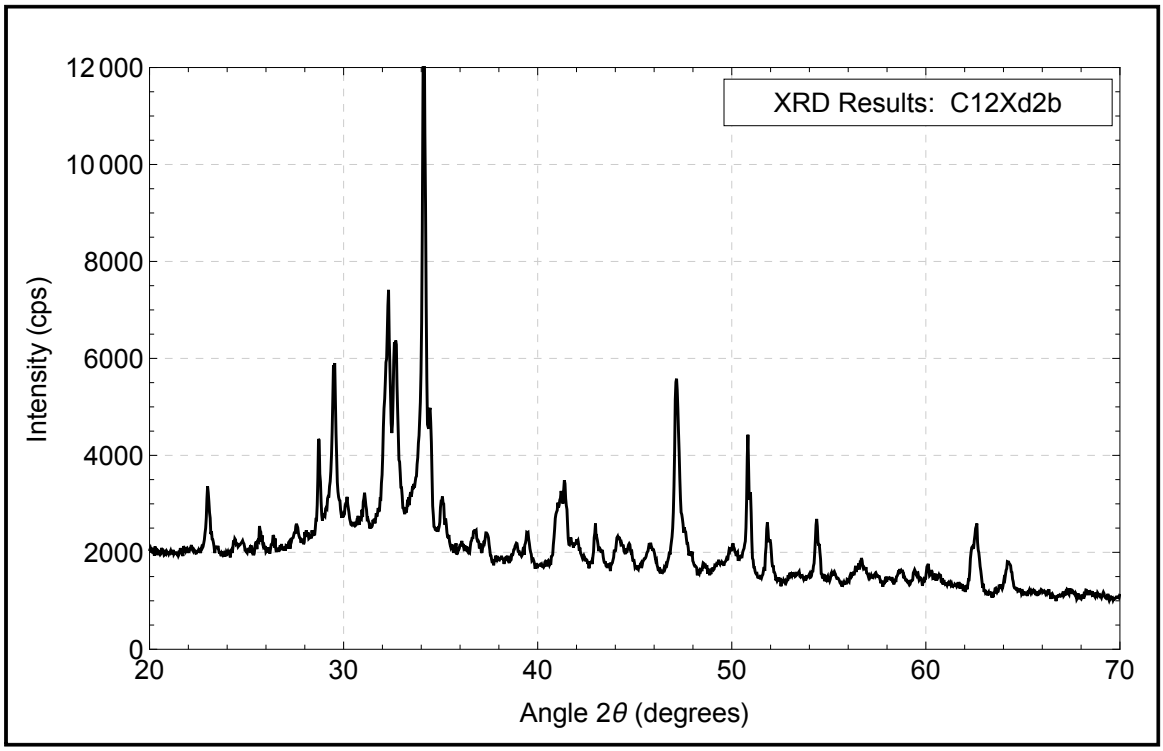
XRD Results: C12Xd2b
Intensity (cps)
12 000
10 000
8000
6000
4000
2000
0
20
30
40
50
60
70
Angle 2θ (degrees)

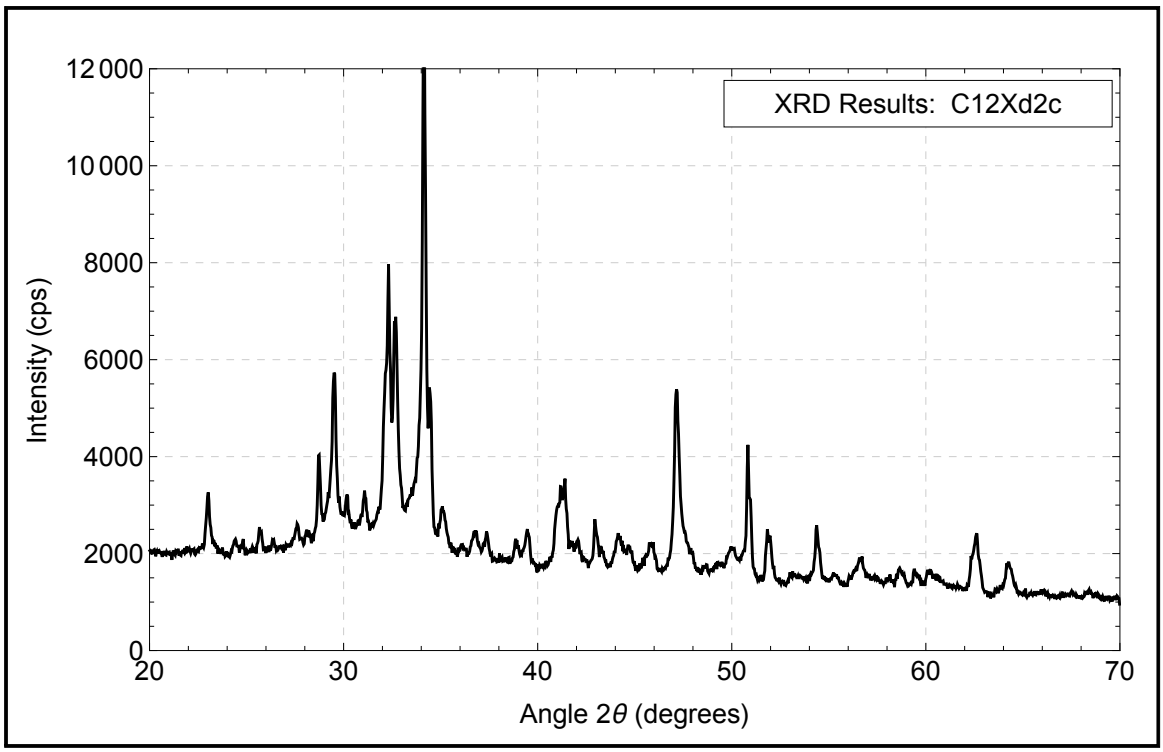
XRD Results: C12Xd2c
Intensity (cps)
12 000
10 000
8000
6000
4000
2000
0
20
30
40
50
60
70
Angle 2θ (degrees)

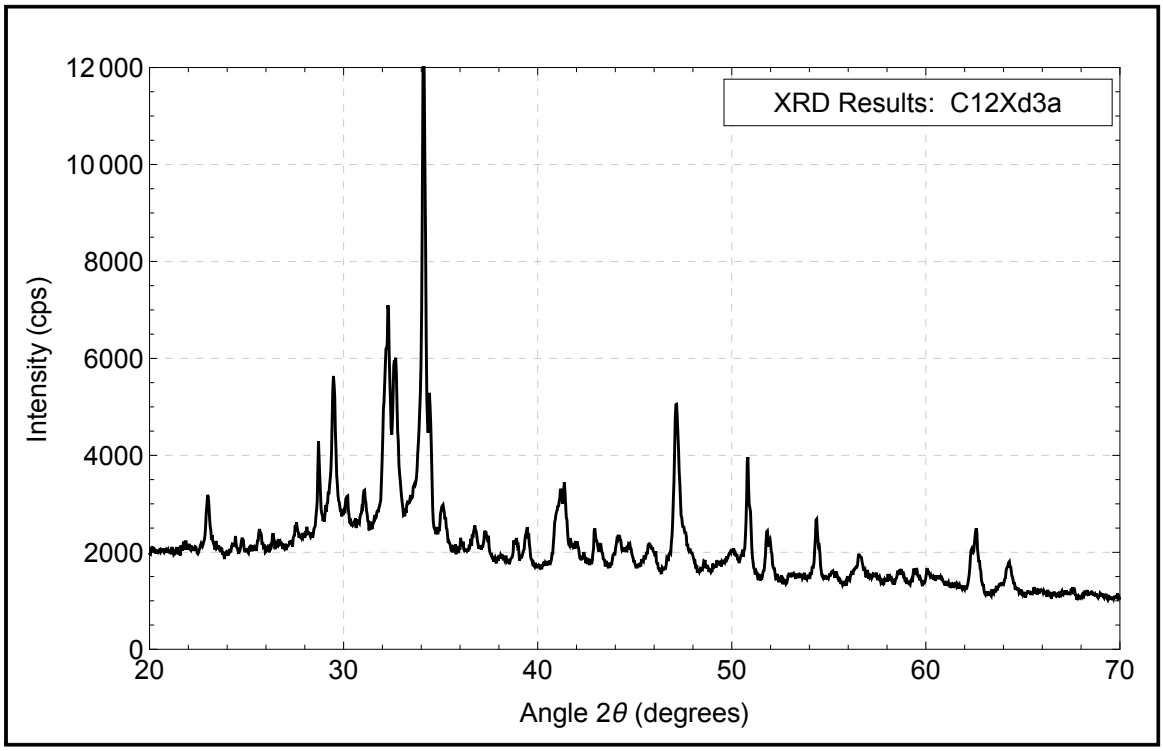
XRD Results: C12Xd3a
Intensity (cps)
12 000
10 000
8000
6000
4000
2000
0
20
30
40
50
60
70
Angle 2θ (degrees)

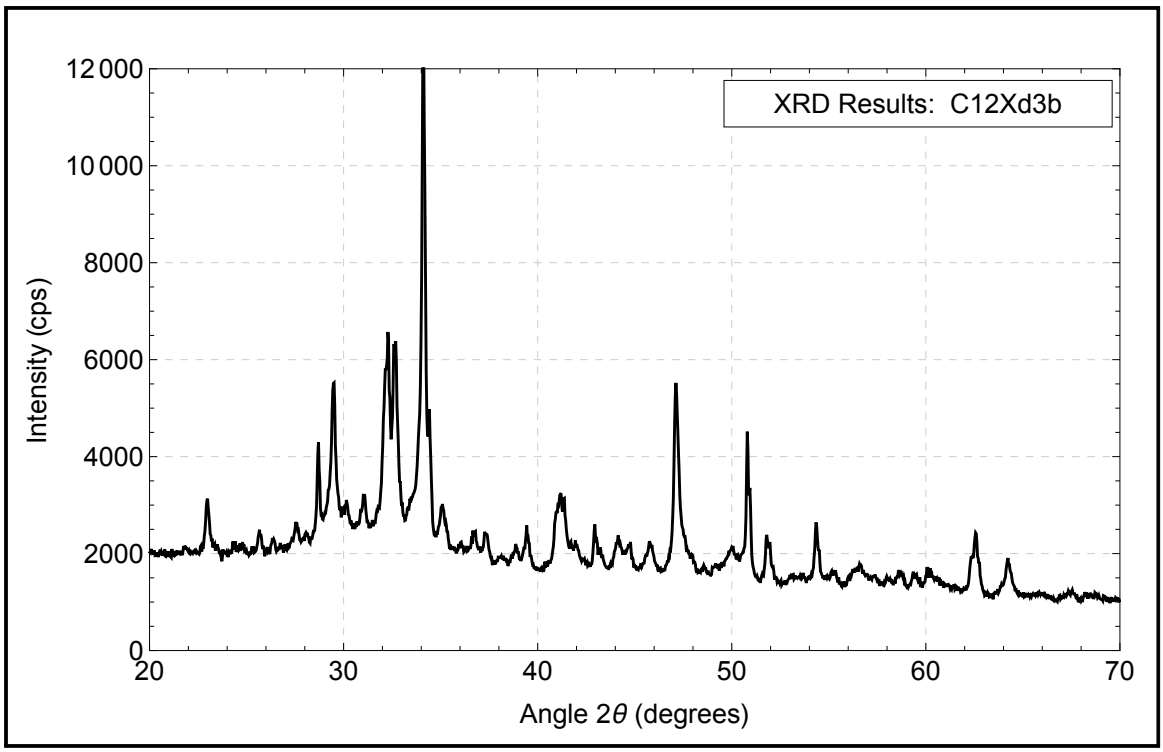
XRD Results: C12Xd3b
Intensity (cps)
12 000
10 000
8000
6000
4000
2000
0
20
30
40
50
60
70
Angle 2θ (degrees)

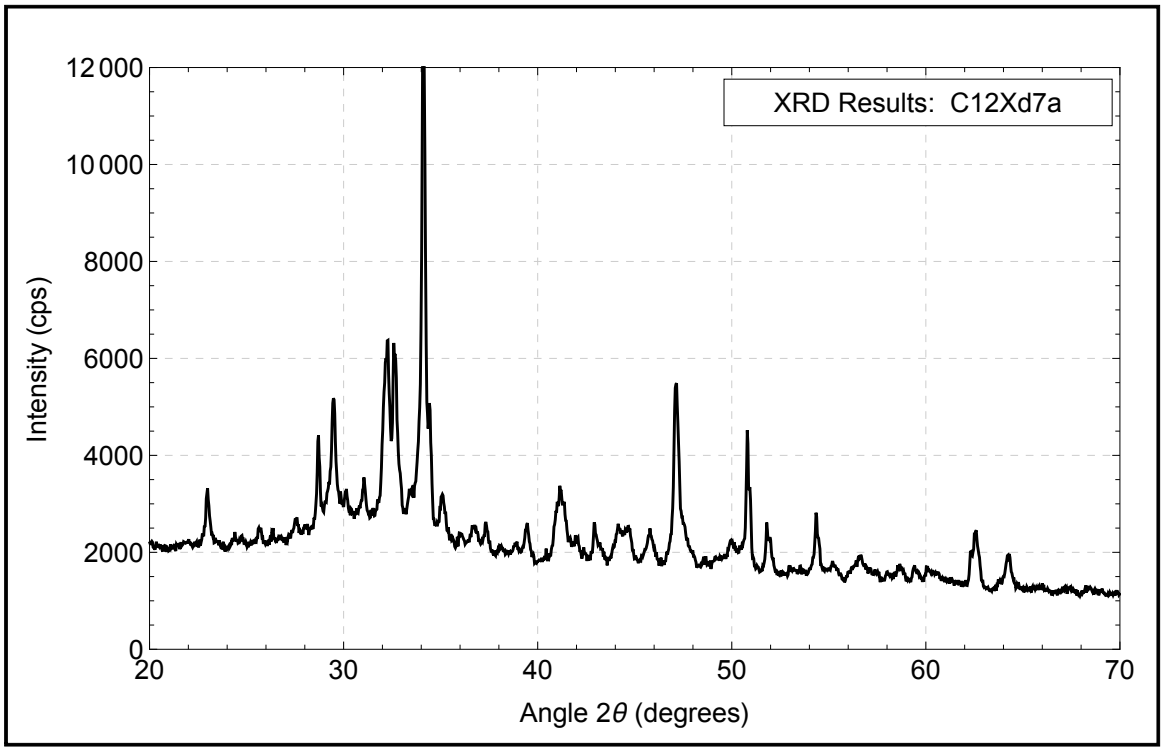
XRD Results: C12Xd7a
Intensity (cps)
12 000
10 000
8000
6000
4000
2000
0
20
30
40
50
60
70
Angle 2θ (degrees)

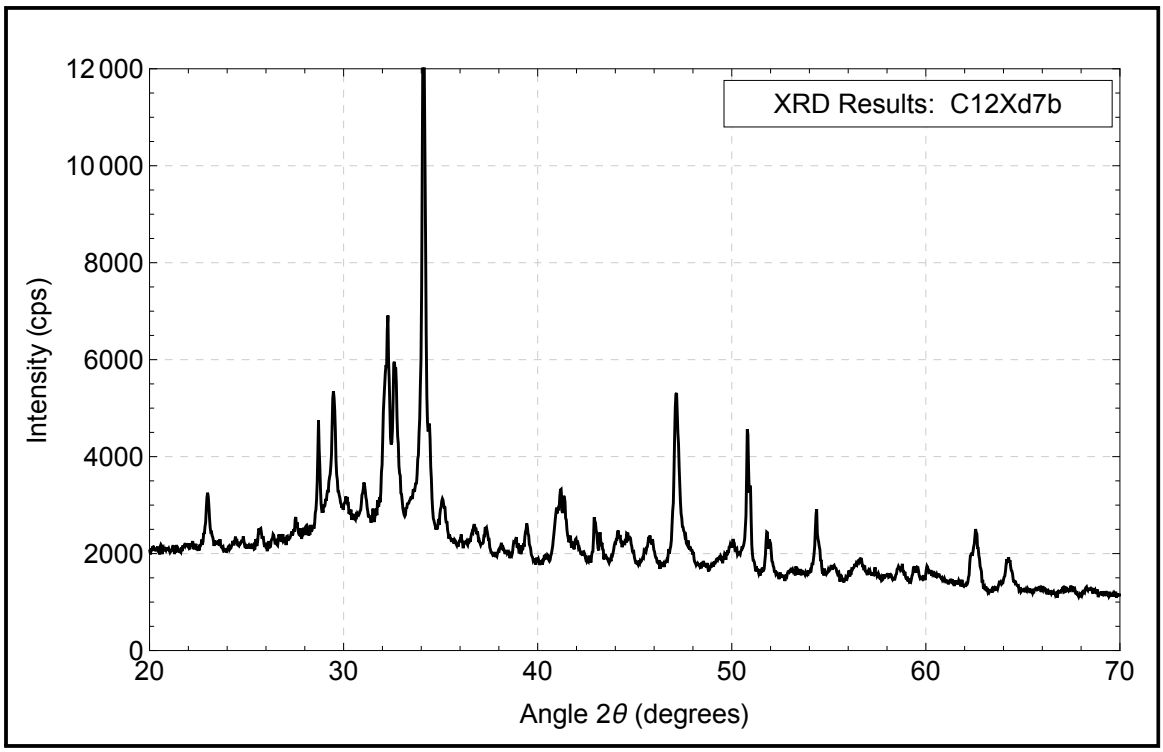
XRD Results: C12Xd7b
Intensity (cps)
12 000
10 000
8000
6000
4000
2000
0
20
30
40
50
60
70
Angle 2θ (degrees)

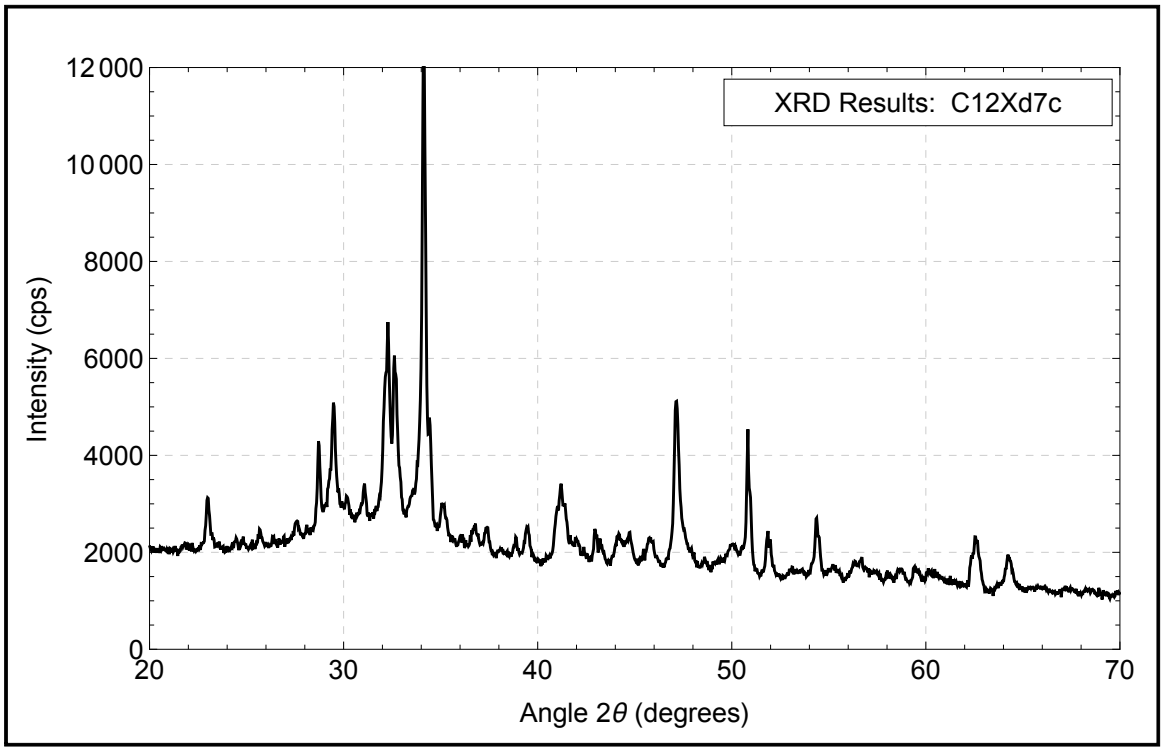
XRD Results: C12Xd7c
Intensity (cps)
12 000
10 000
8000
6000
4000
2000
0
20
30
40
50
60
70
Angle 2θ (degrees)

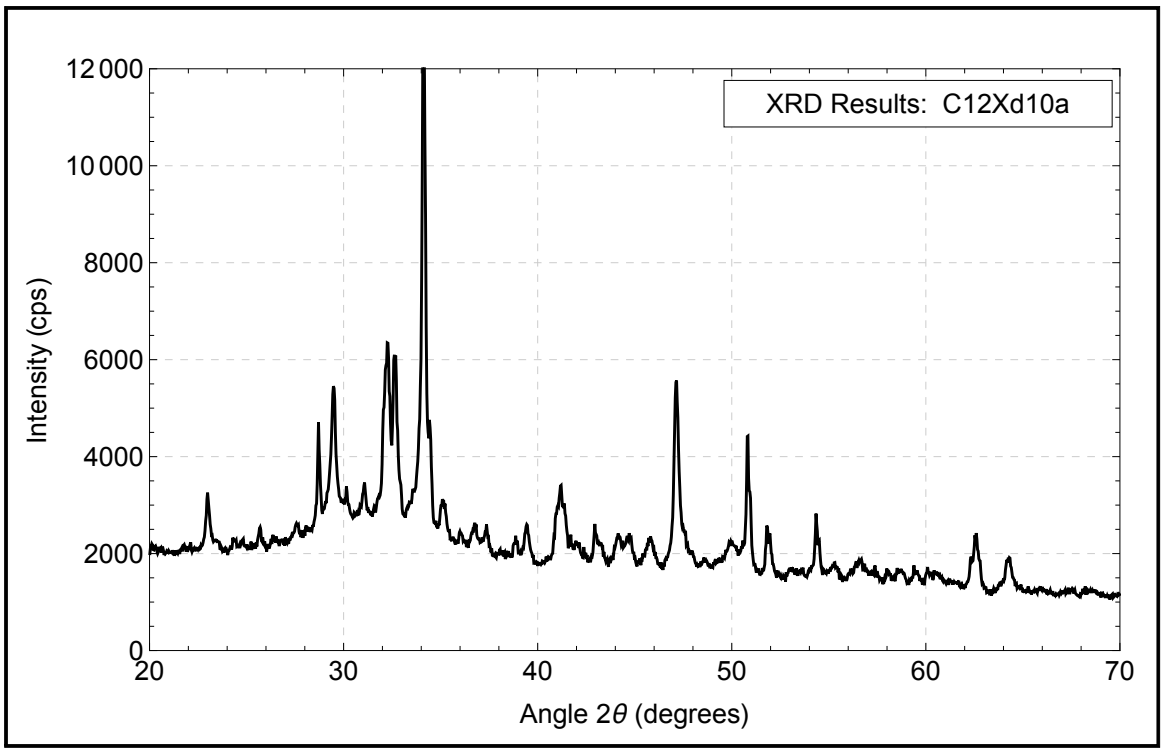
XRD Results: C12Xd10a
Intensity (cps)
12 000
10 000
8000
6000
4000
2000
0
20
30
40
50
60
70
Angle 2θ (degrees)

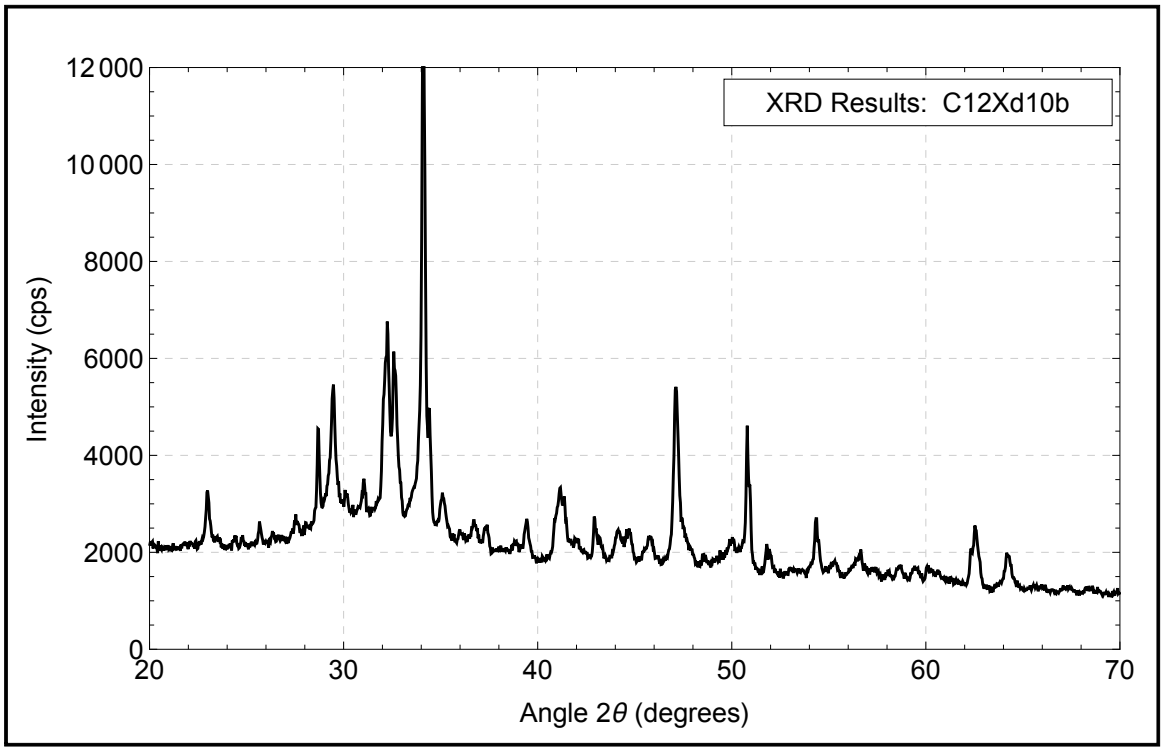
XRD Results: C12Xd10b
Intensity (cps)
12 000
10 000
8000
6000
4000
2000
0
20
30
40
50
60
70
Angle 2θ (degrees)

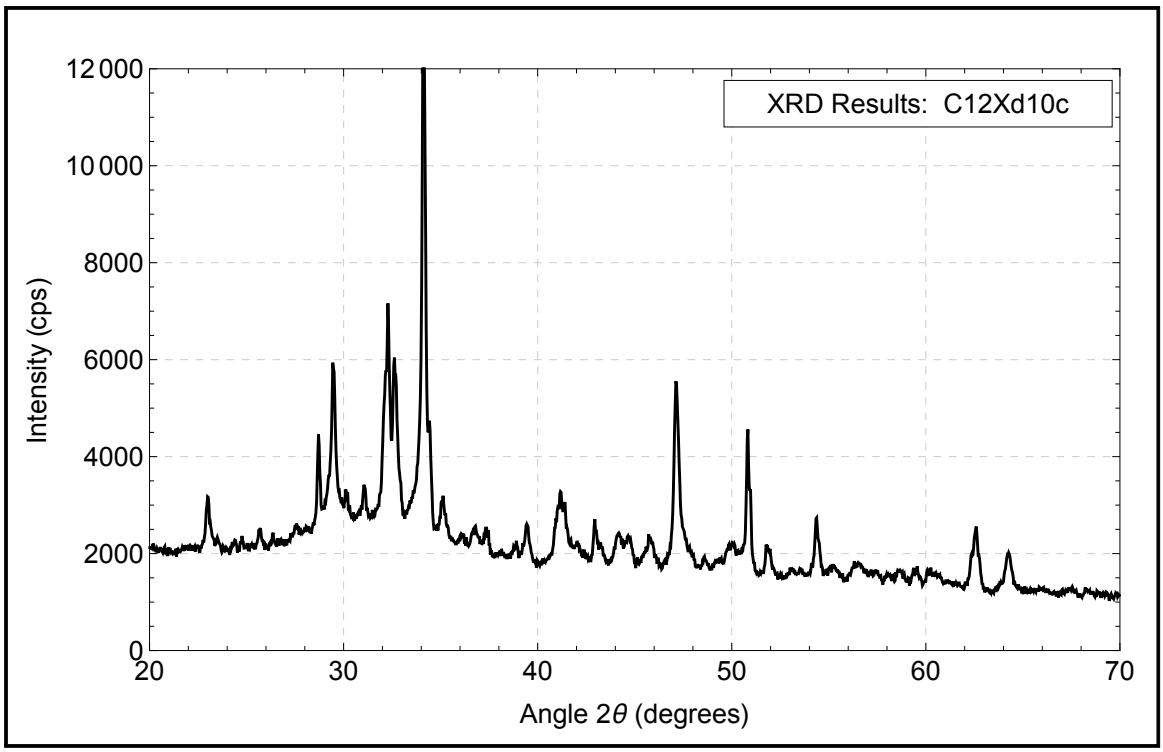
XRD Results: C12Xd10c
Intensity (cps)
12 000
10 000
8000
6000
4000
2000
0
20
30
40
50
60
70
Angle 2θ (degrees)

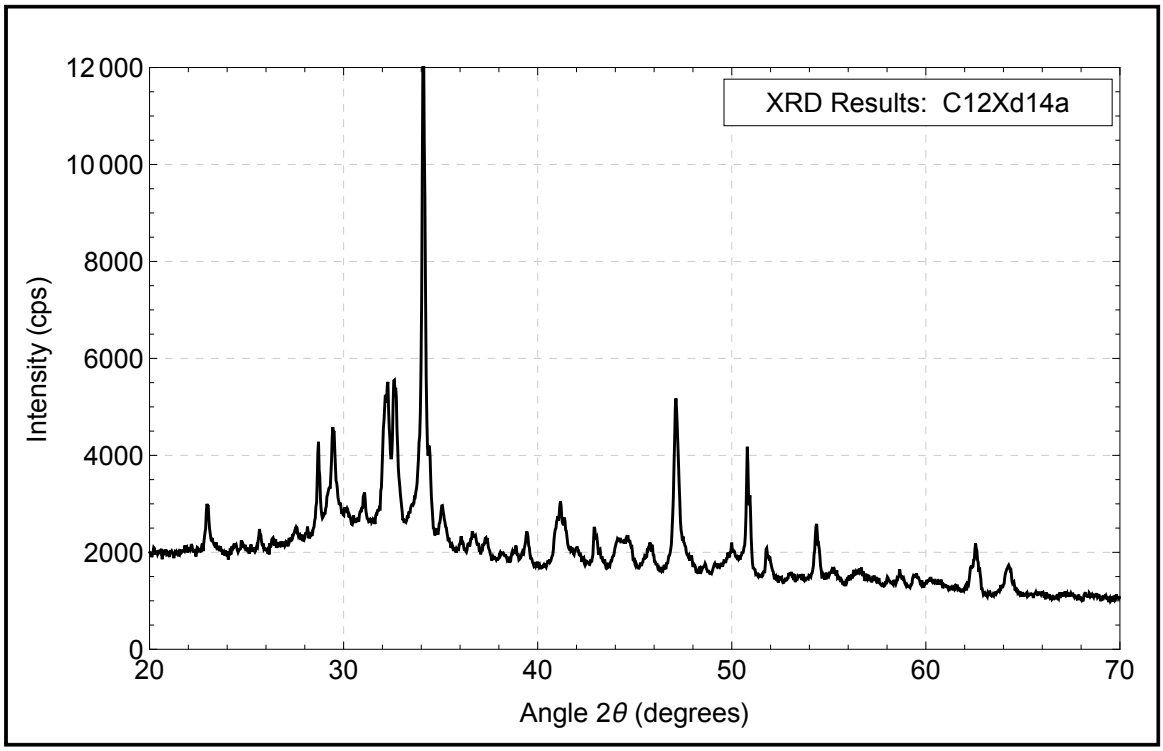
XRD Results: C12Xd14a
Intensity (cps)
12 000
10 000
8000
6000
4000
2000
0
20
30
40
50
60
70
Angle 2θ (degrees)

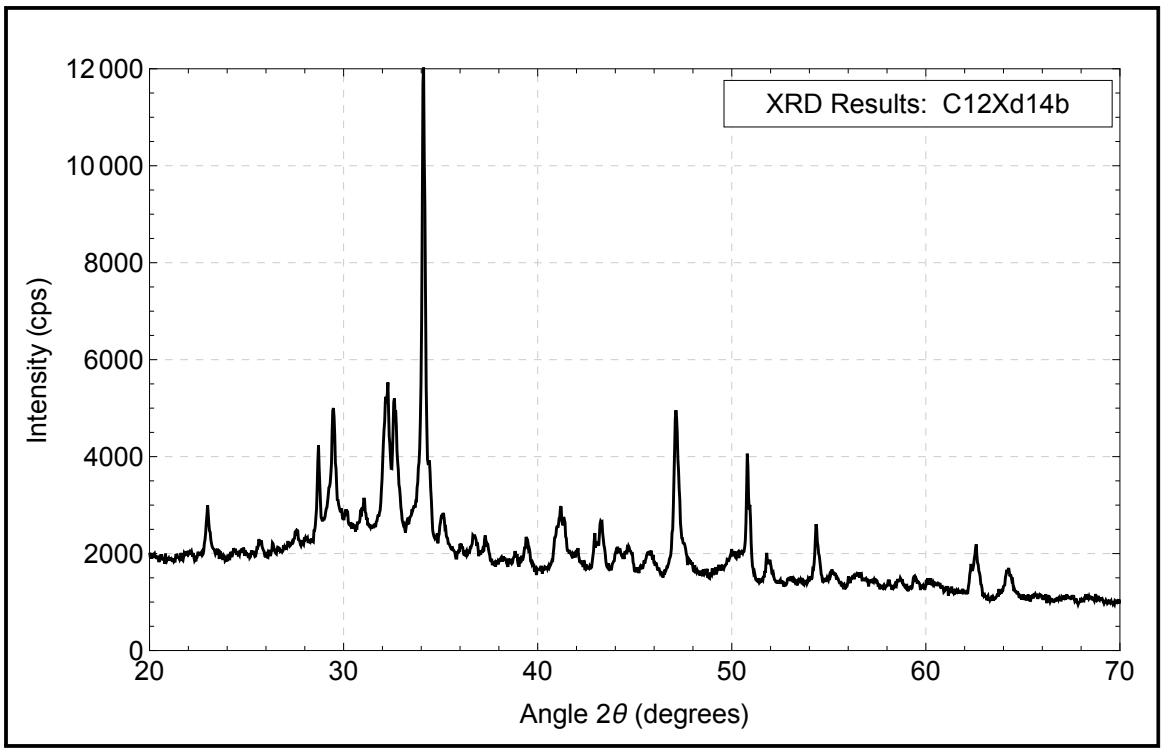
XRD Results: C12Xd14b
Intensity (cps)
12 000
10 000
8000
6000
4000
2000
0
20
30
40
50
60
70
Angle 2θ (degrees)

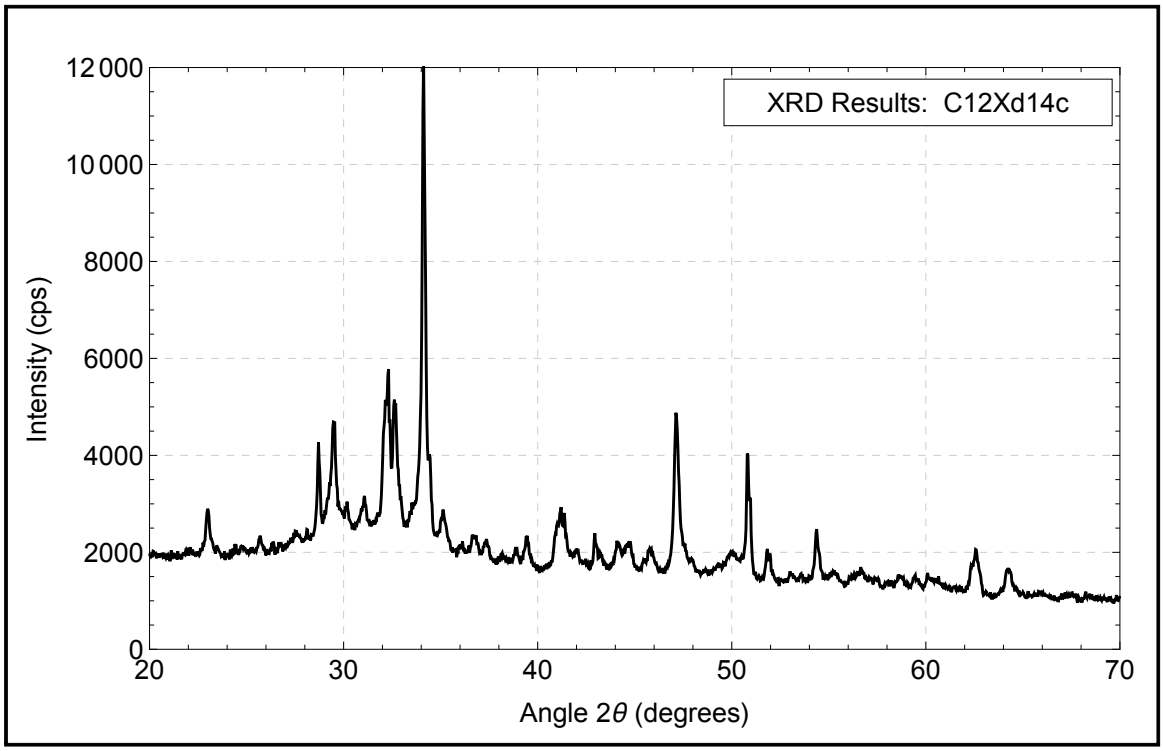
XRD Results: C12Xd14c
Intensity (cps)
12 000
10 000
8000
6000
4000
2000
0
20
30
40
50
60
70
Angle 2θ (degrees)

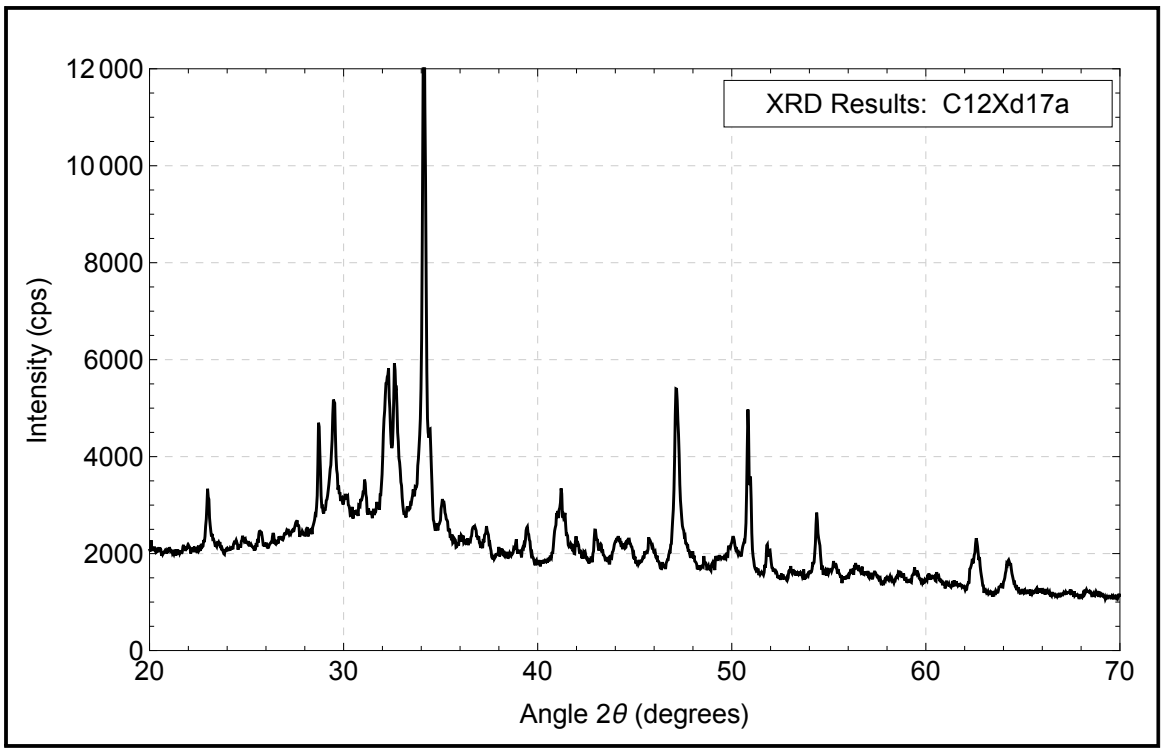
XRD Results: C12Xd17a
Intensity (cps)
12 000
10 000
8000
6000
4000
2000
0
20
30
40
50
60
70
Angle 2θ (degrees)

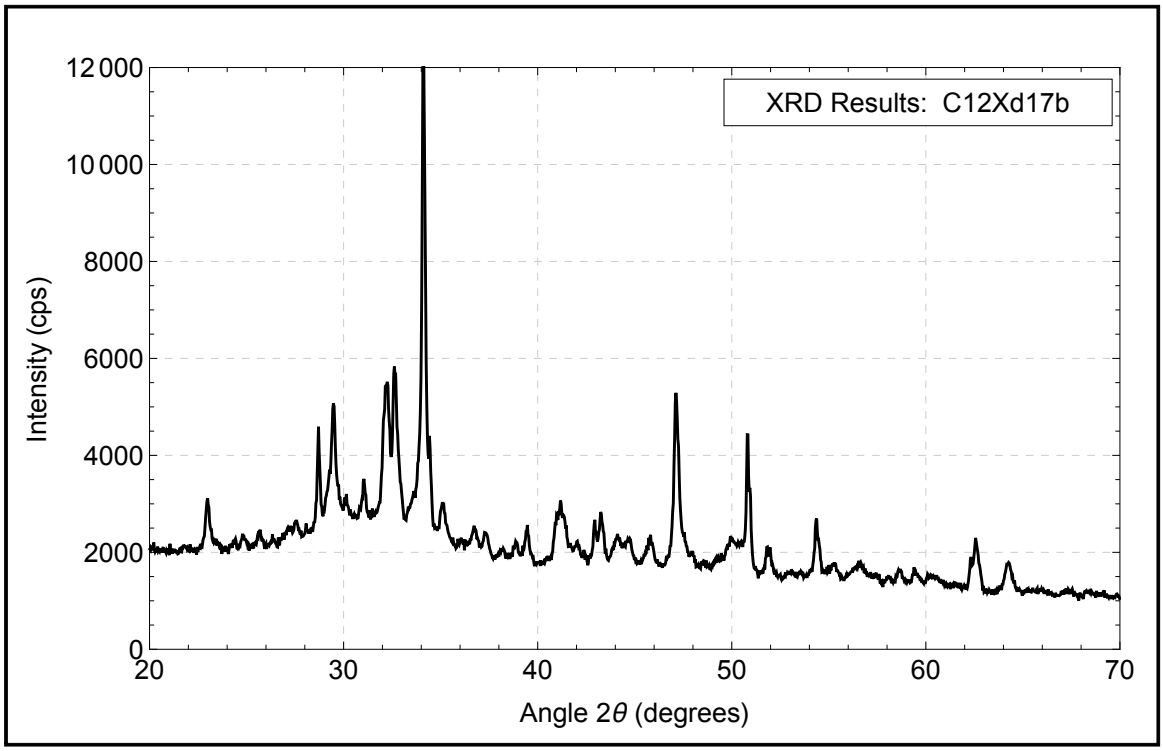
XRD Results: C12Xd17b
Intensity (cps)
12 000
10 000
8000
6000
4000
2000
0
20
30
40
50
60
70
Angle 2θ (degrees)

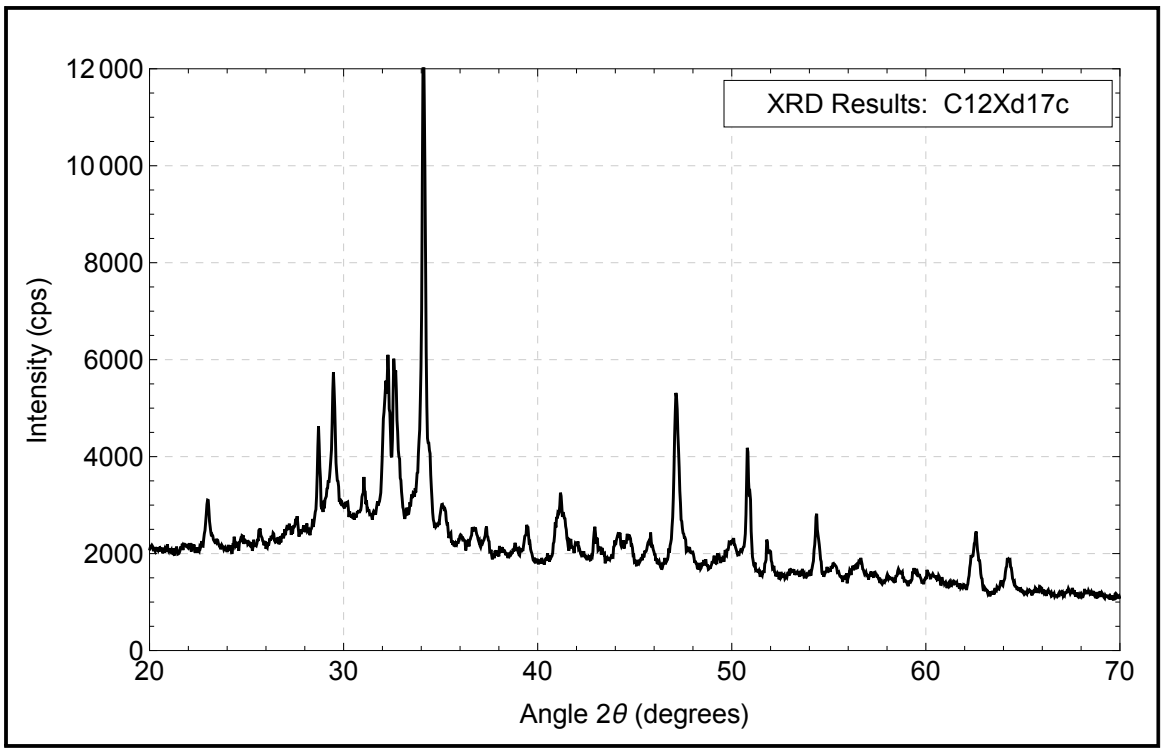
XRD Results: C12Xd17c
Intensity (cps)
12 000
10 000
8000
6000
4000
2000
0
20
30
40
50
60
70
Angle 2θ (degrees)

Appendix C.2 – XRD Fit Curves

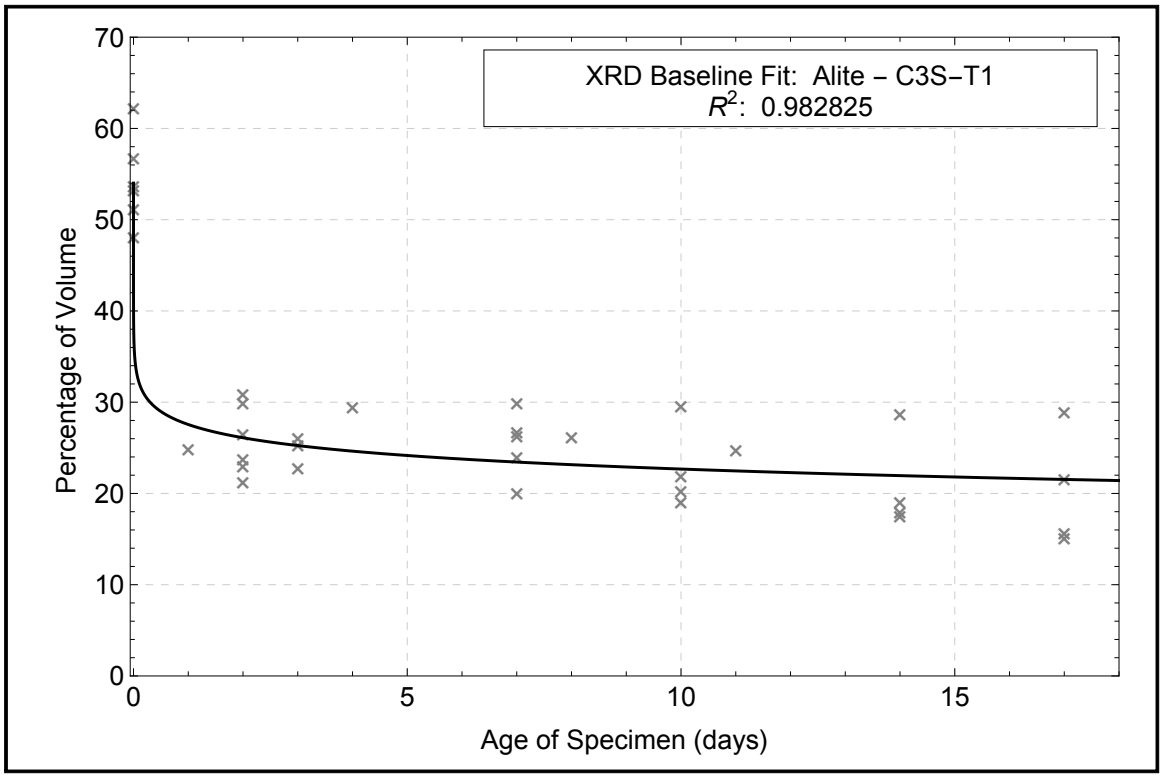
XRD Baseline Fit: Alite – C3S–T1
R^2: 0.982825
Percentage of Volume
Age of Specimen (days)
0
10
20
30
40
50
60
70
0
5
10
15

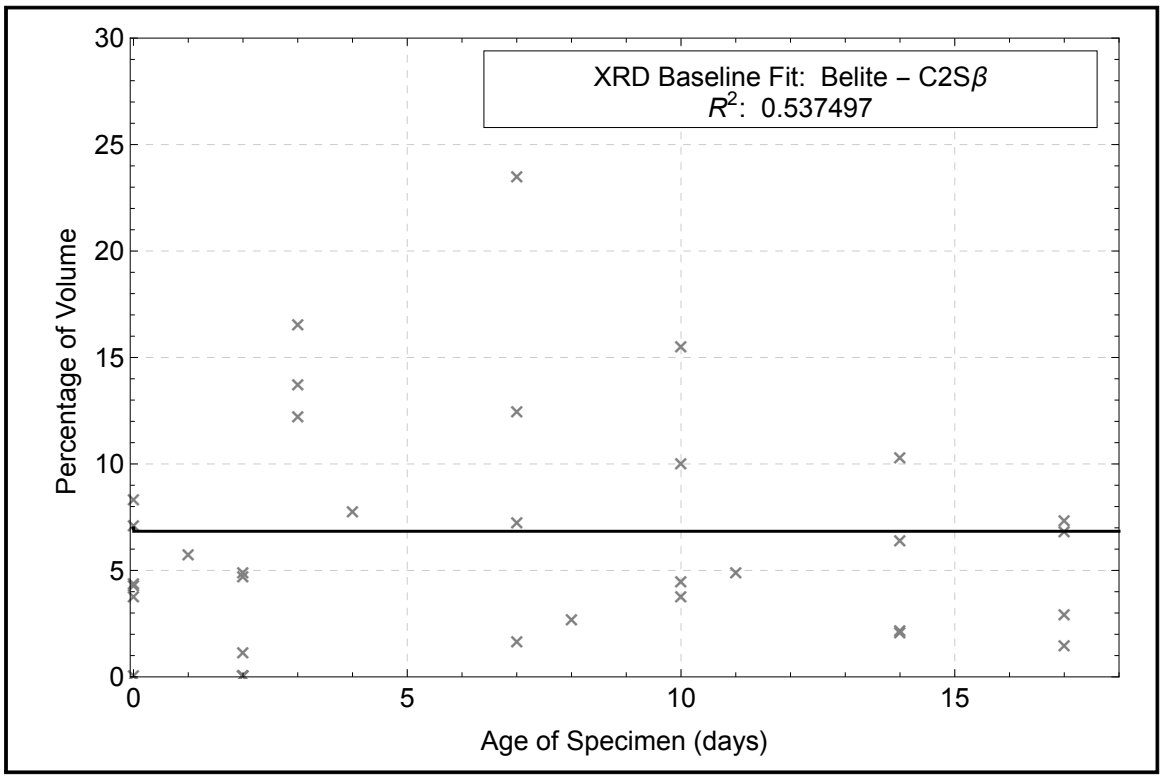
XRD Baseline Fit: Belite – C2Sβ
R^2: 0.537497
Percentage of Volume
Age of Specimen (days)
0
5
10
15
20
25
30
0
5
10
15

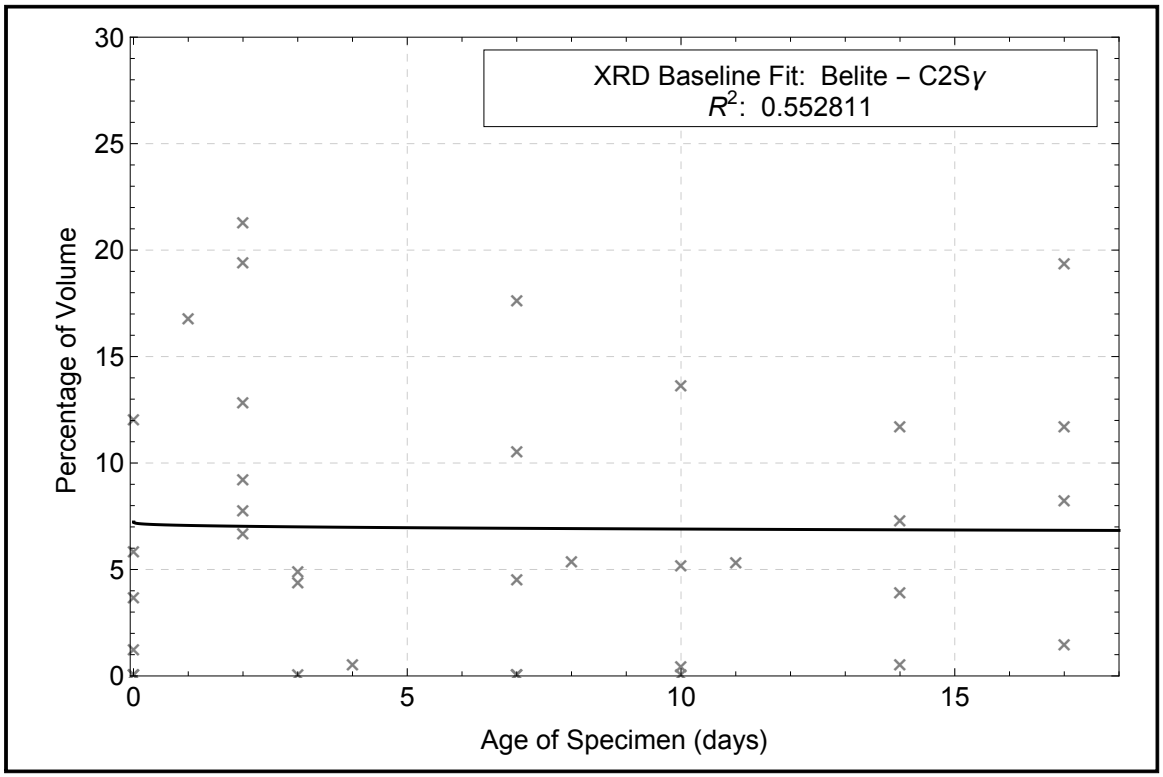
XRD Baseline Fit: Belite – C2Sγ
R^2: 0.552811
Percentage of Volume
Age of Specimen (days)
0
5
10
15
20
25
30

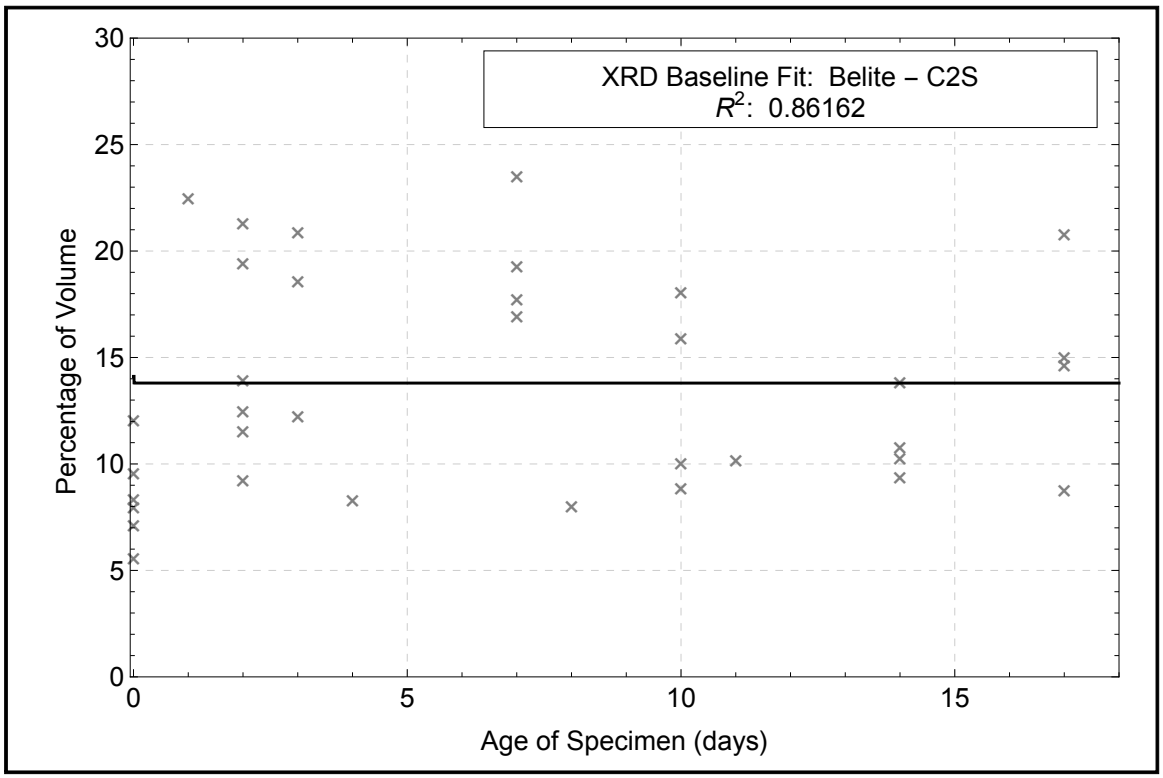
XRD Baseline Fit: Belite – C2S
R^2: 0.86162
Percentage of Volume
Age of Specimen (days)
0
5
10
15
20
25
30

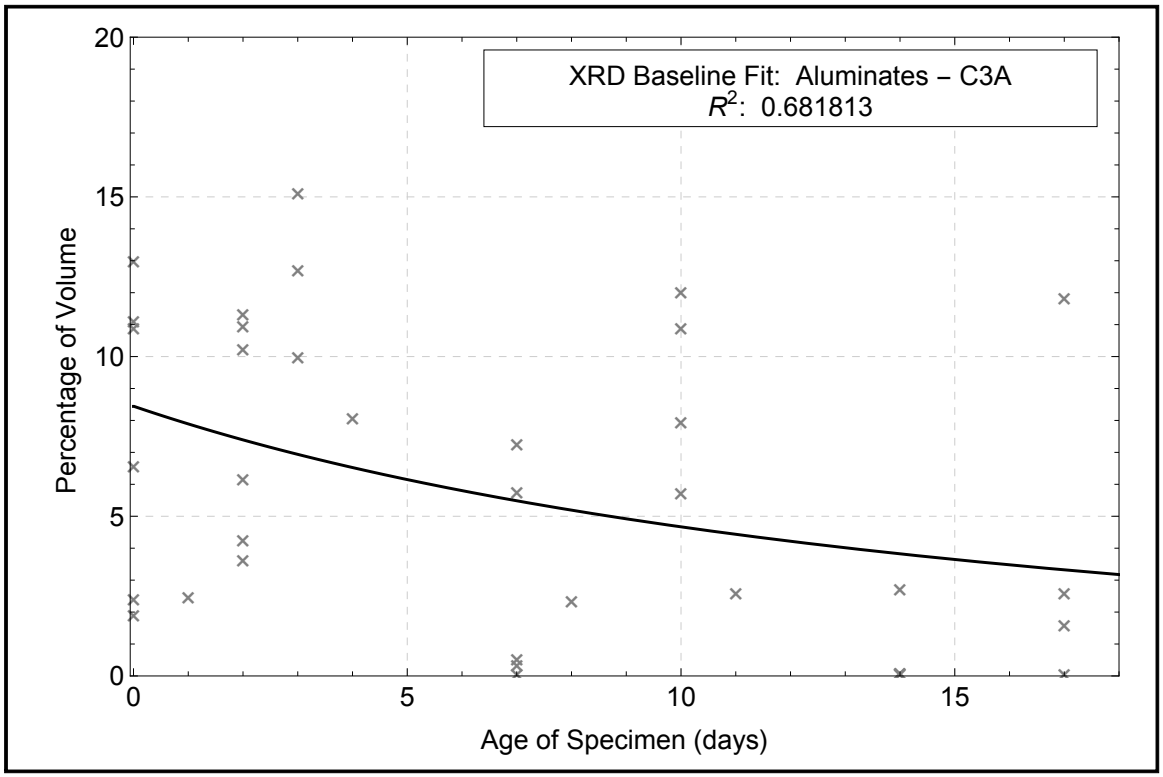
XRD Baseline Fit: Aluminates – C3A
R^2: 0.681813
Percentage of Volume
Age of Specimen (days)
0
5
10
15
20

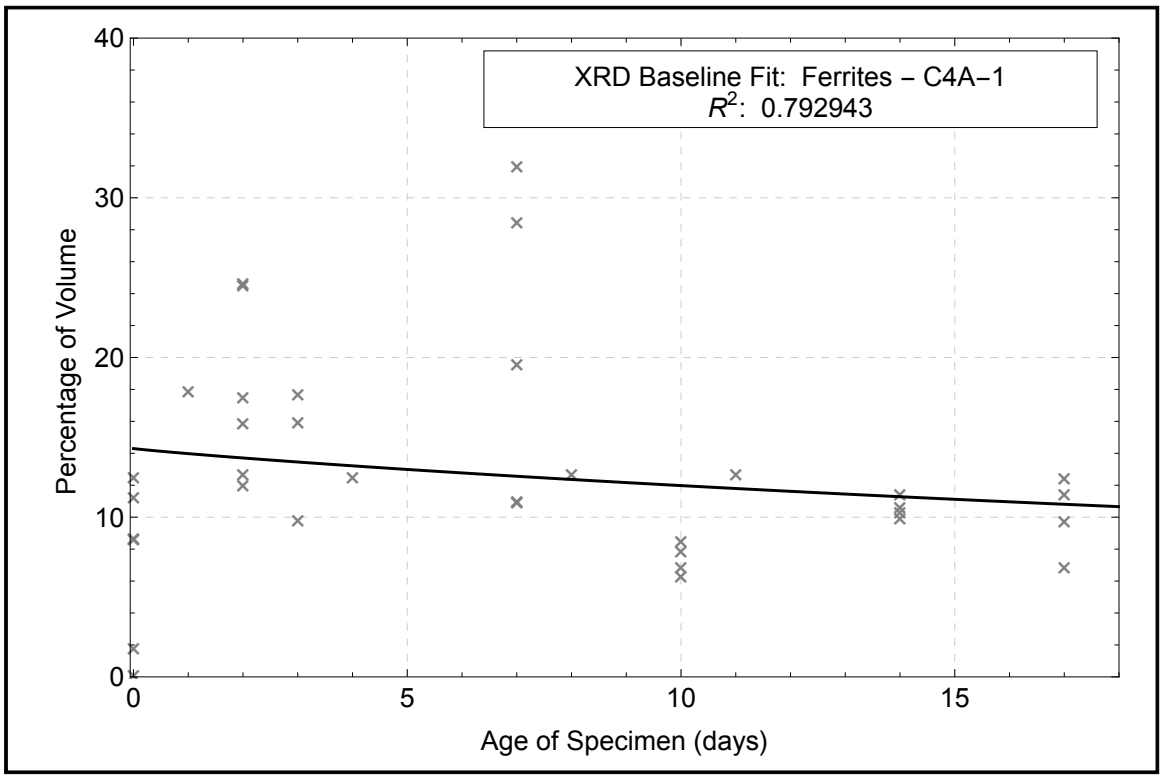
XRD Baseline Fit: Ferrites – C4A–1
R^2: 0.792943
Percentage of Volume
Age of Specimen (days)
0
10
20
30
40
5
15

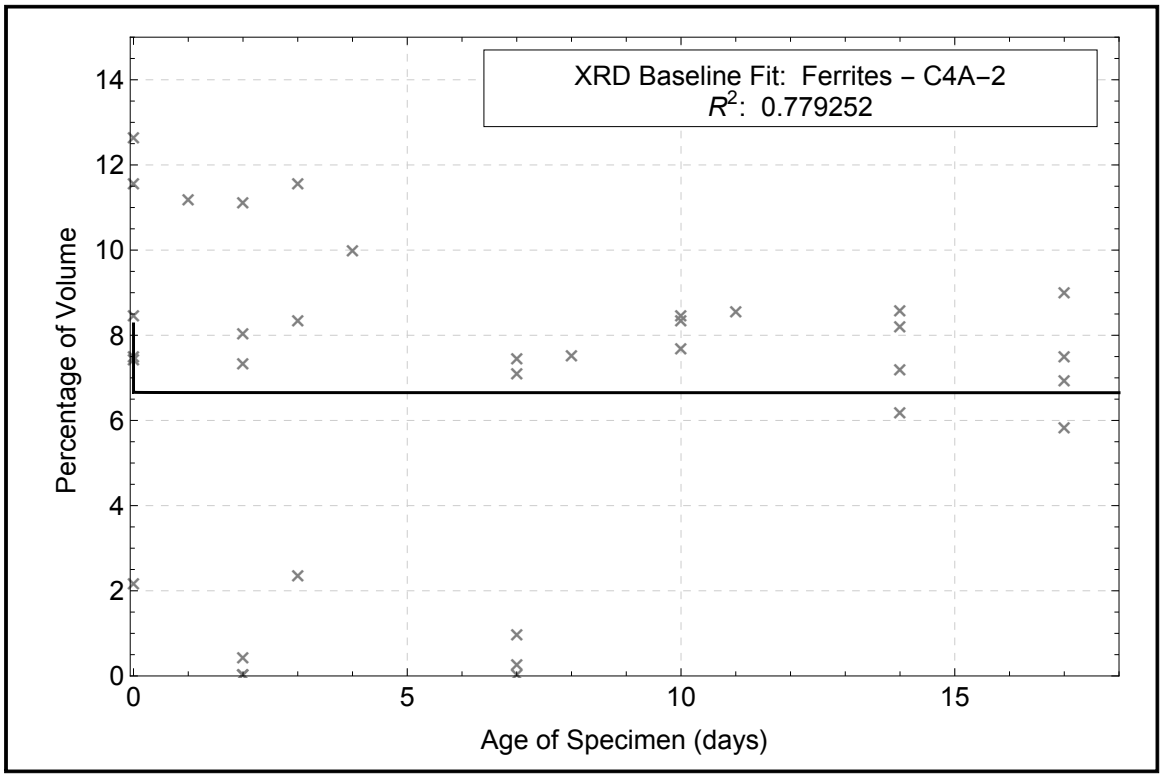
XRD Baseline Fit: Ferrites – C4A–2
R^2: 0.779252
Percentage of Volume
Age of Specimen (days)
0
2
4
6
8
10
12
14
0
5
10
15

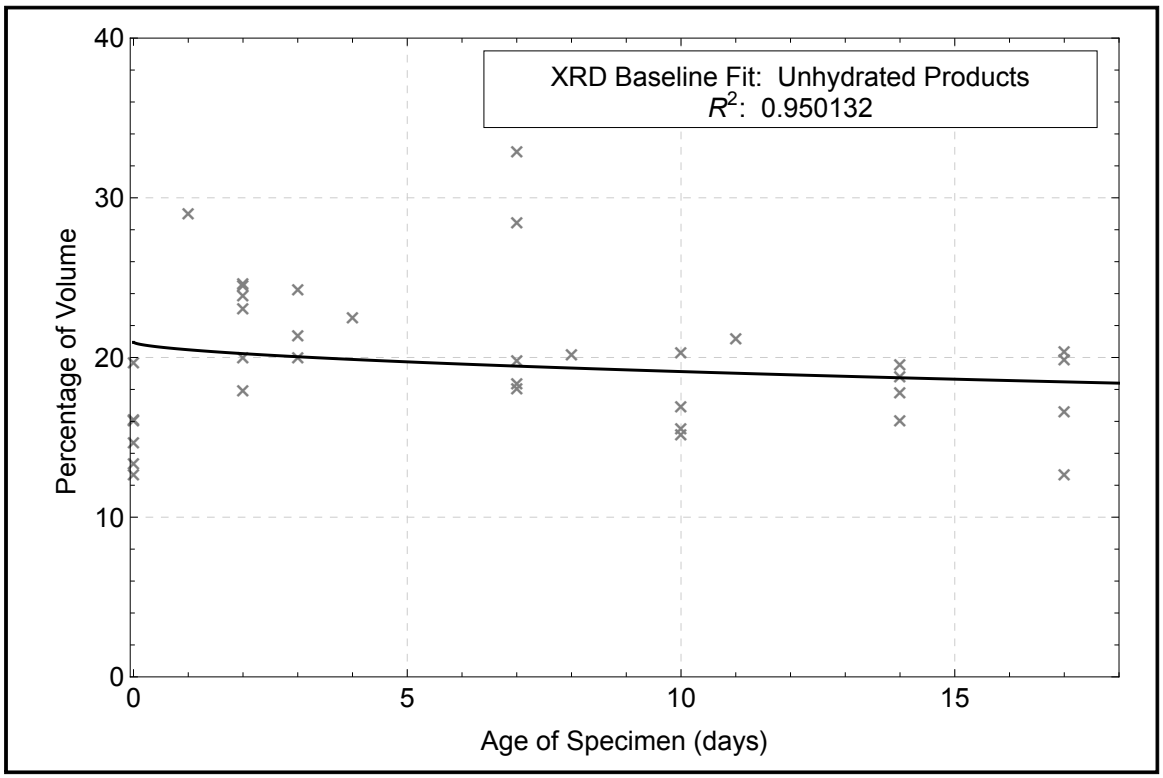
XRD Baseline Fit: Unhydrated Products
R^2: 0.950132
Percentage of Volume
Age of Specimen (days)
0
10
20
30
40
0
5
10
15

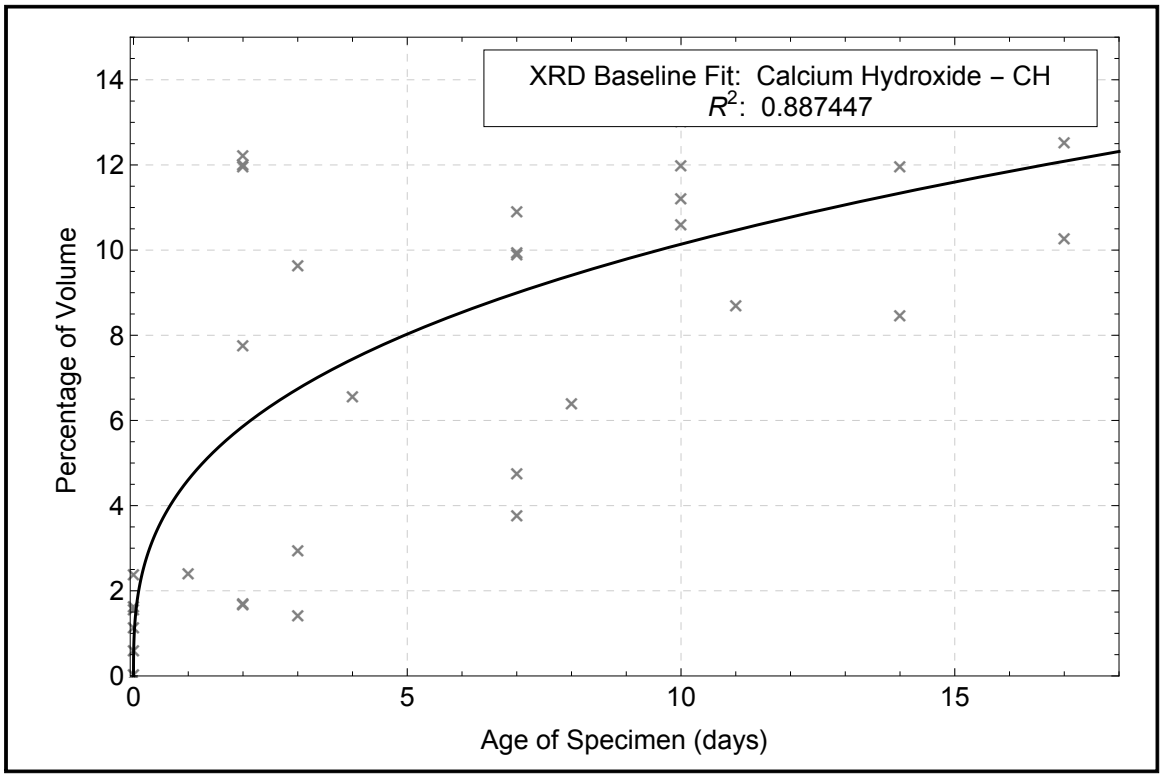
XRD Baseline Fit: Calcium Hydroxide – CH
R^2: 0.887447
Percentage of Volume
Age of Specimen (days)
0
2
4
6
8
10
12
14
0
5
10
15

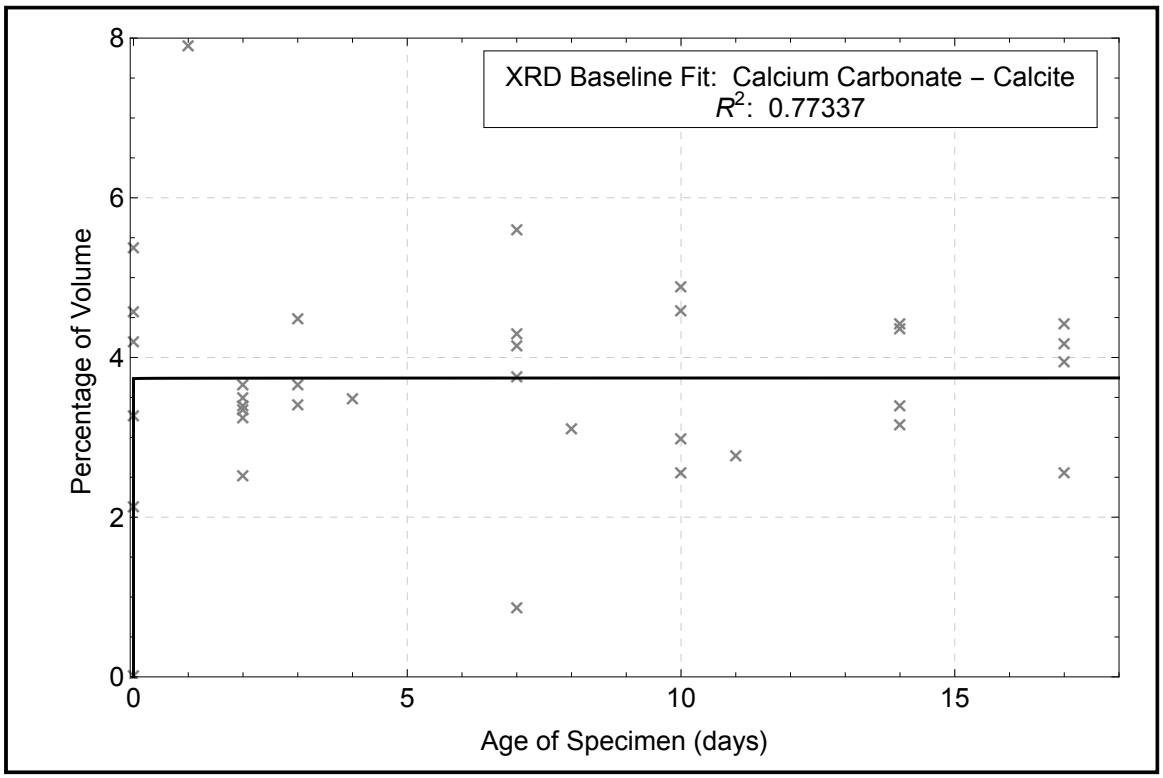
XRD Baseline Fit: Calcium Carbonate – Calcite
R^2: 0.77337
Percentage of Volume
Age of Specimen (days)
0
2
4
6
8
0
5
10
15

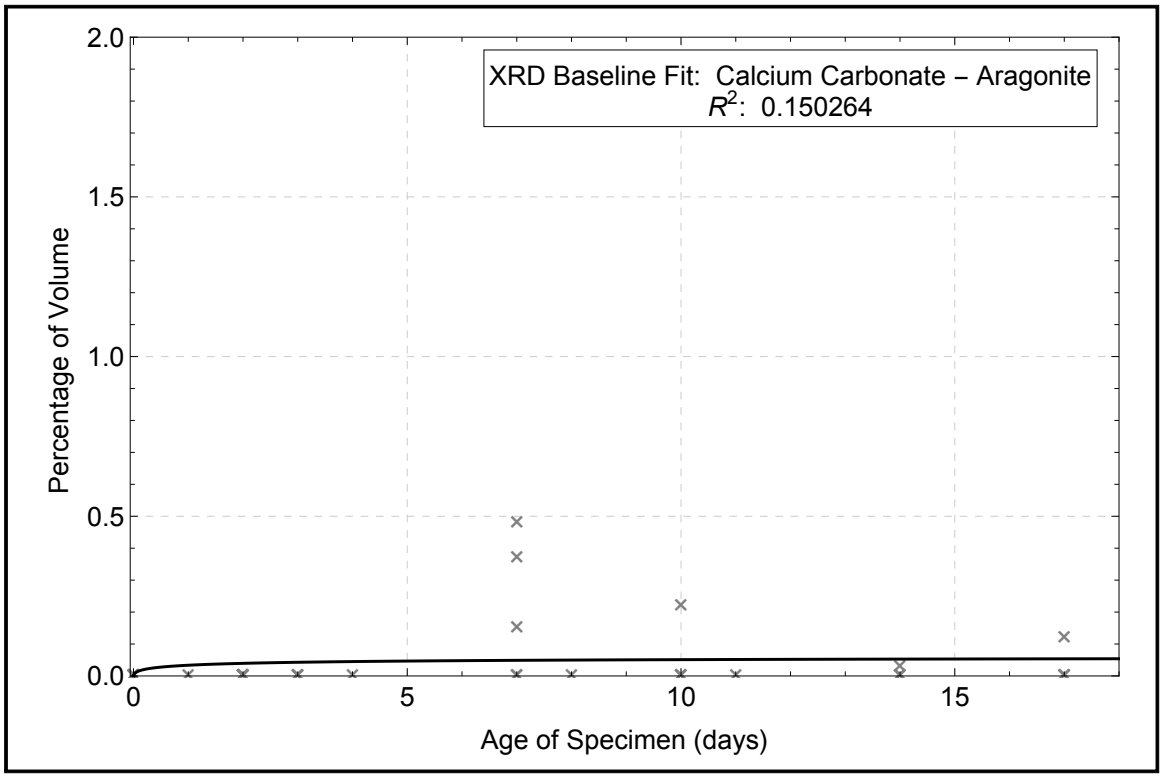
XRD Baseline Fit: Calcium Carbonate – Aragonite
R^2: 0.150264
Percentage of Volume
Age of Specimen (days)
2.0
1.5
1.0
0.5
0.0
0
5
10
15

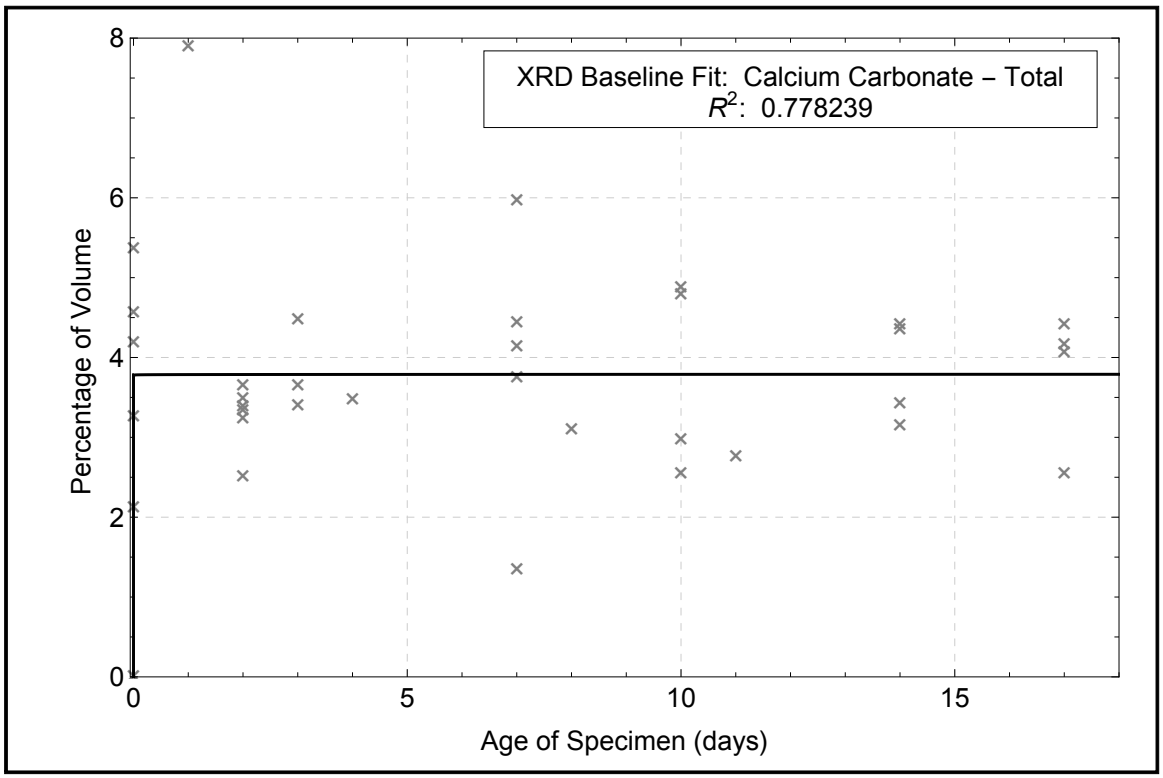
XRD Baseline Fit: Calcium Carbonate – Total
R^2: 0.778239
Percentage of Volume
Age of Specimen (days)
8
6
4
2
0
0
5
10
15

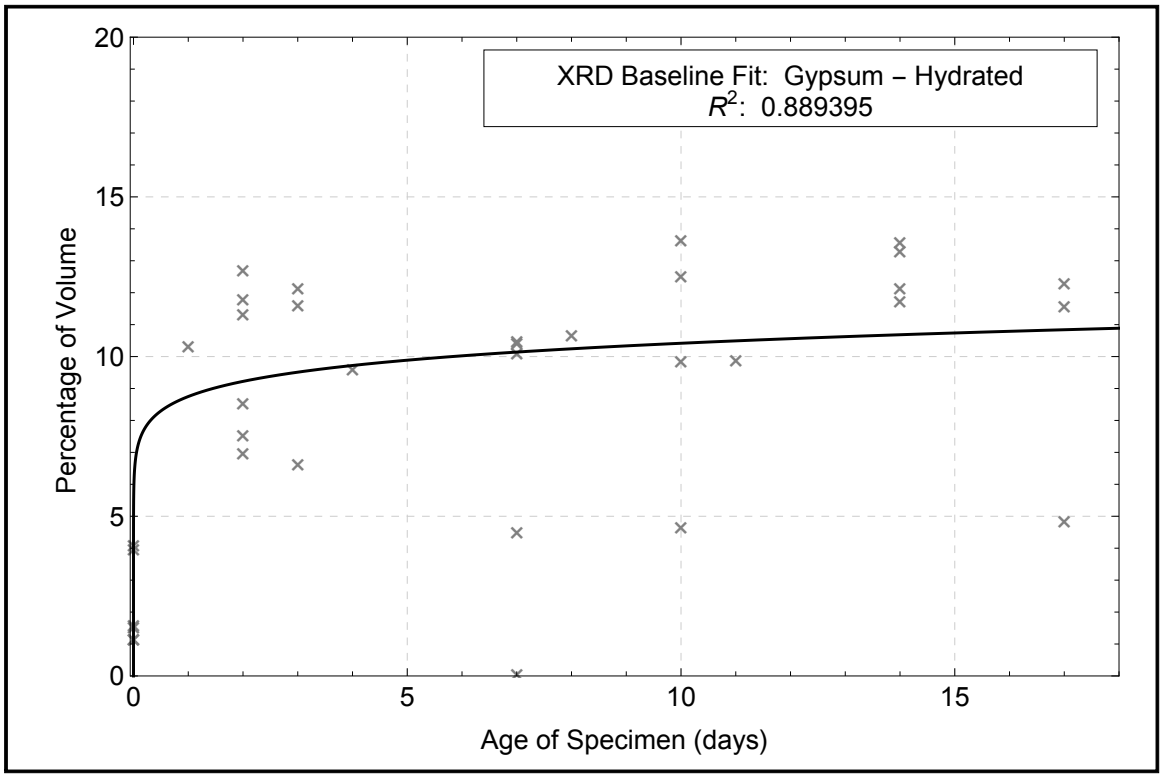
XRD Baseline Fit: Gypsum – Hydrated
R^2: 0.889395
Percentage of Volume
Age of Specimen (days)
0
5
10
15
20

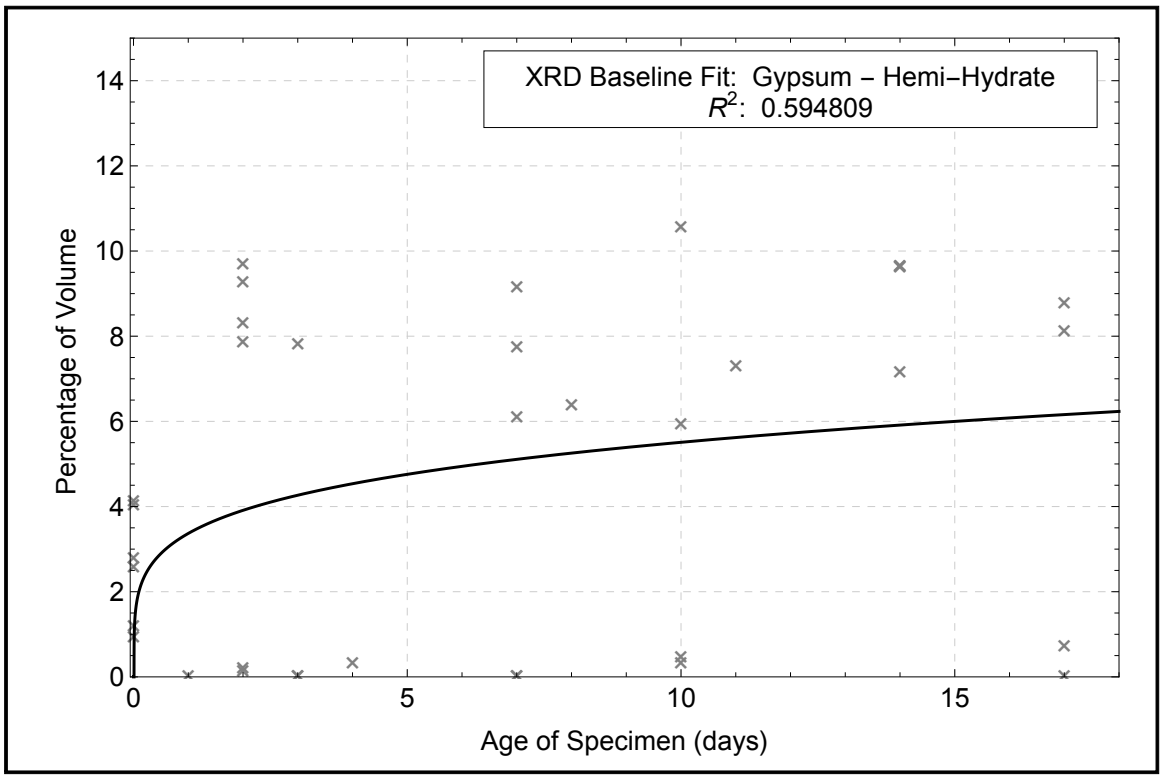
XRD Baseline Fit: Gypsum – Hemi–Hydrate
R^2: 0.594809
Percentage of Volume
Age of Specimen (days)
0
2
4
6
8
10
12
14
5
15

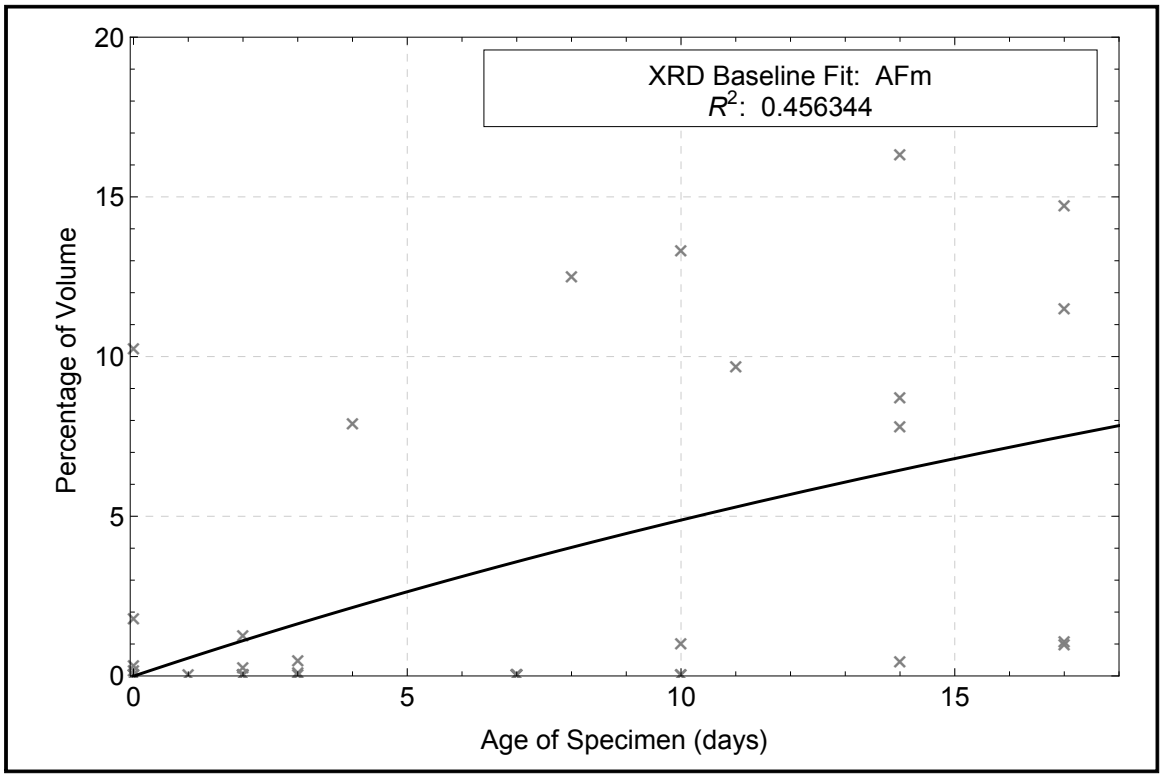
XRD Baseline Fit: AFm
R^2: 0.456344
Percentage of Volume
Age of Specimen (days)
0
5
10
15
20

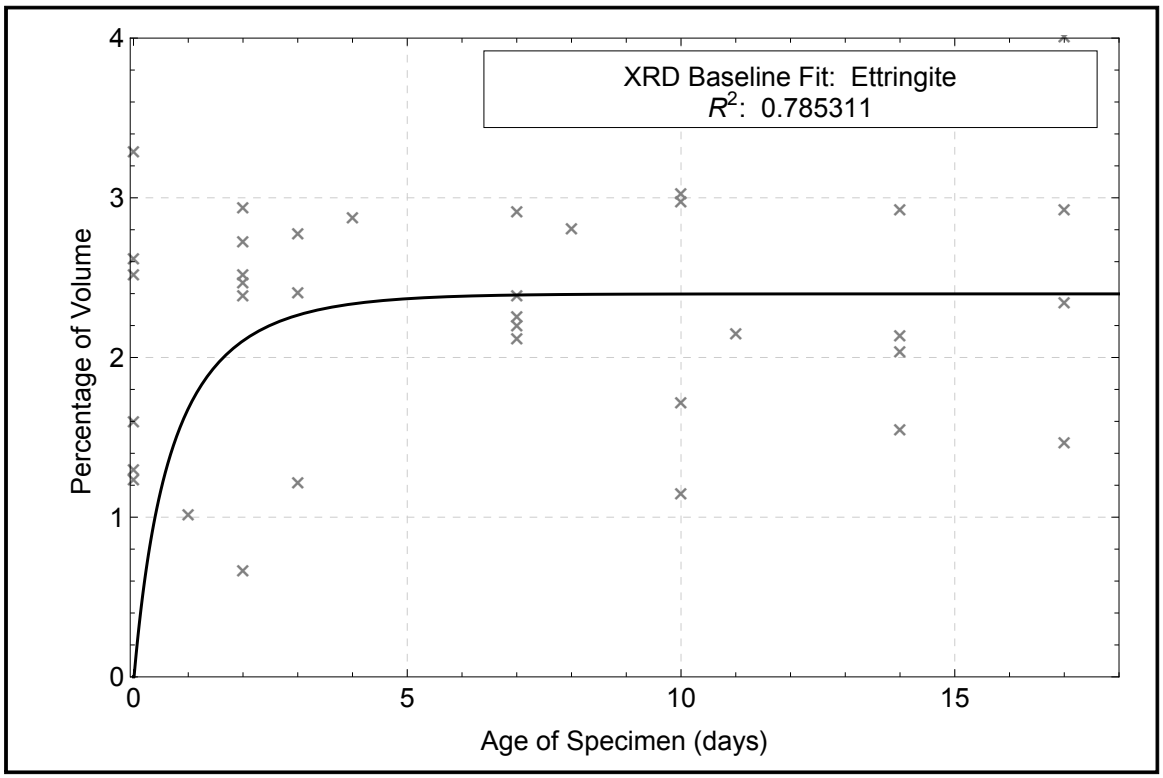
XRD Baseline Fit: Ettringite
R^2: 0.785311
Percentage of Volume
Age of Specimen (days)
0
1
2
3
4
5
10
15

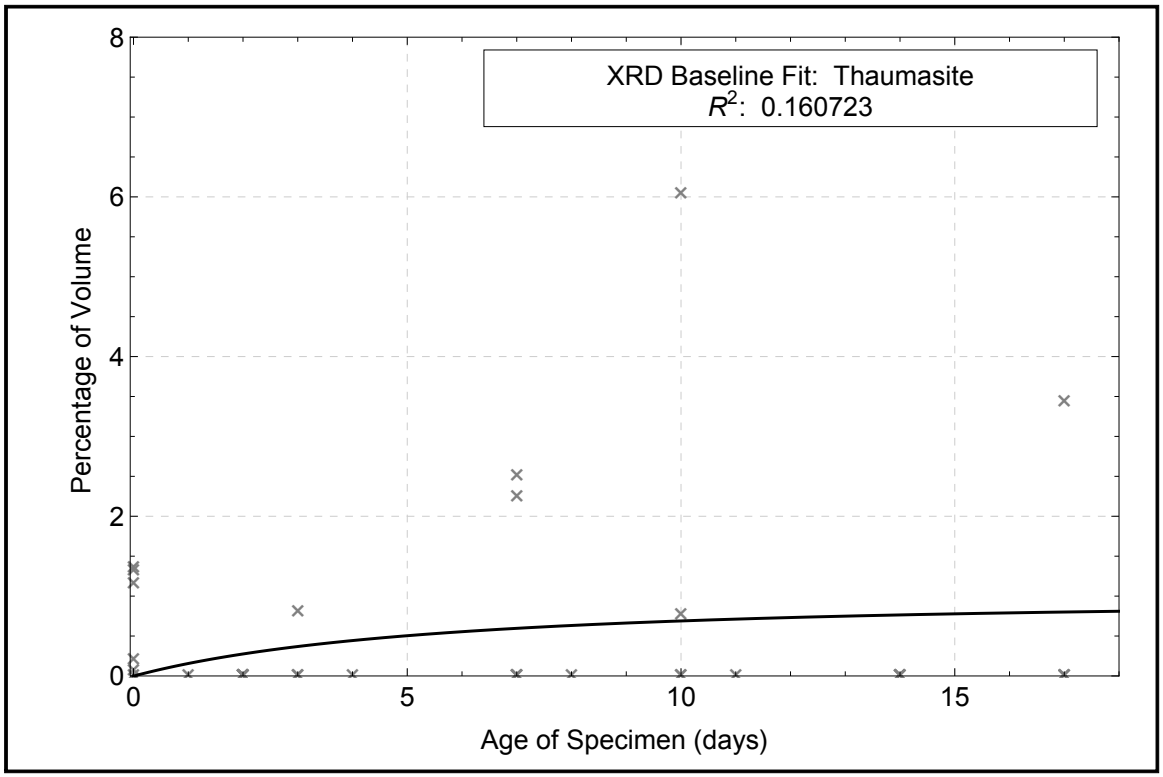
XRD Baseline Fit: Thaumasite
R^2: 0.160723
Percentage of Volume
Age of Specimen (days)
0
2
4
6
8
0
5
10
15

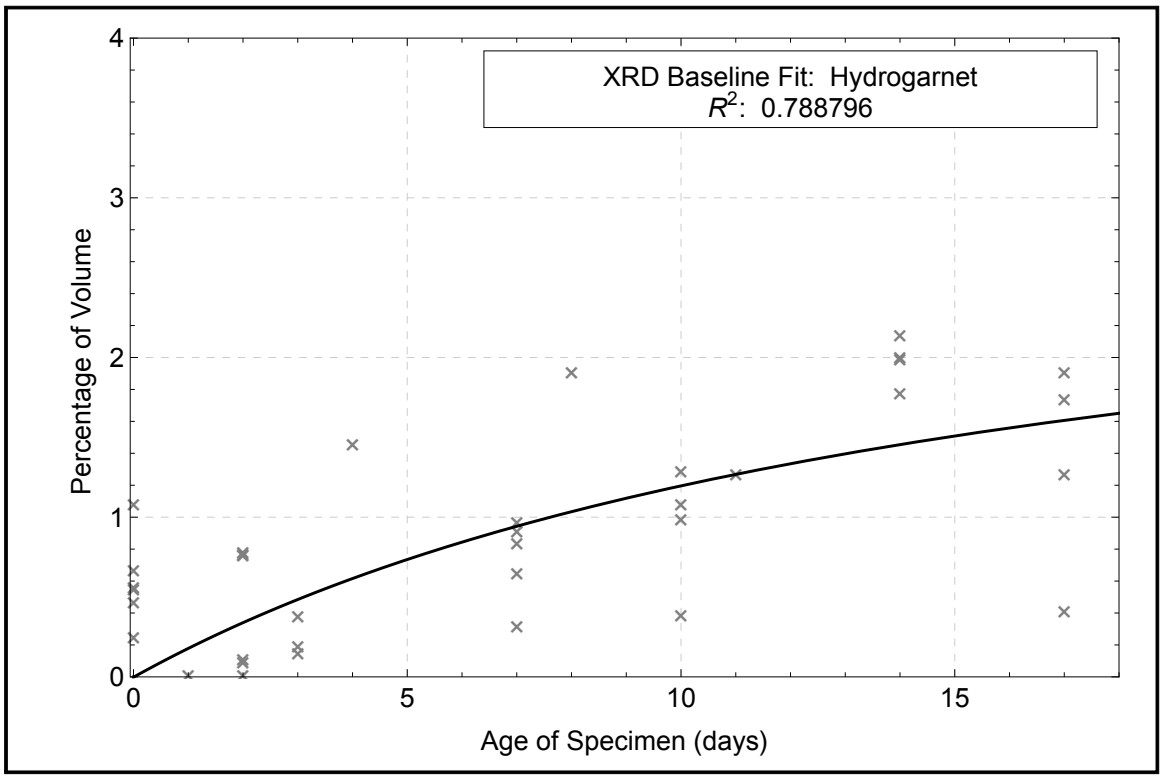
XRD Baseline Fit: Hydrogarnet
R^2: 0.788796
Percentage of Volume
Age of Specimen (days)
0
1
2
3
4
0
5
10
15

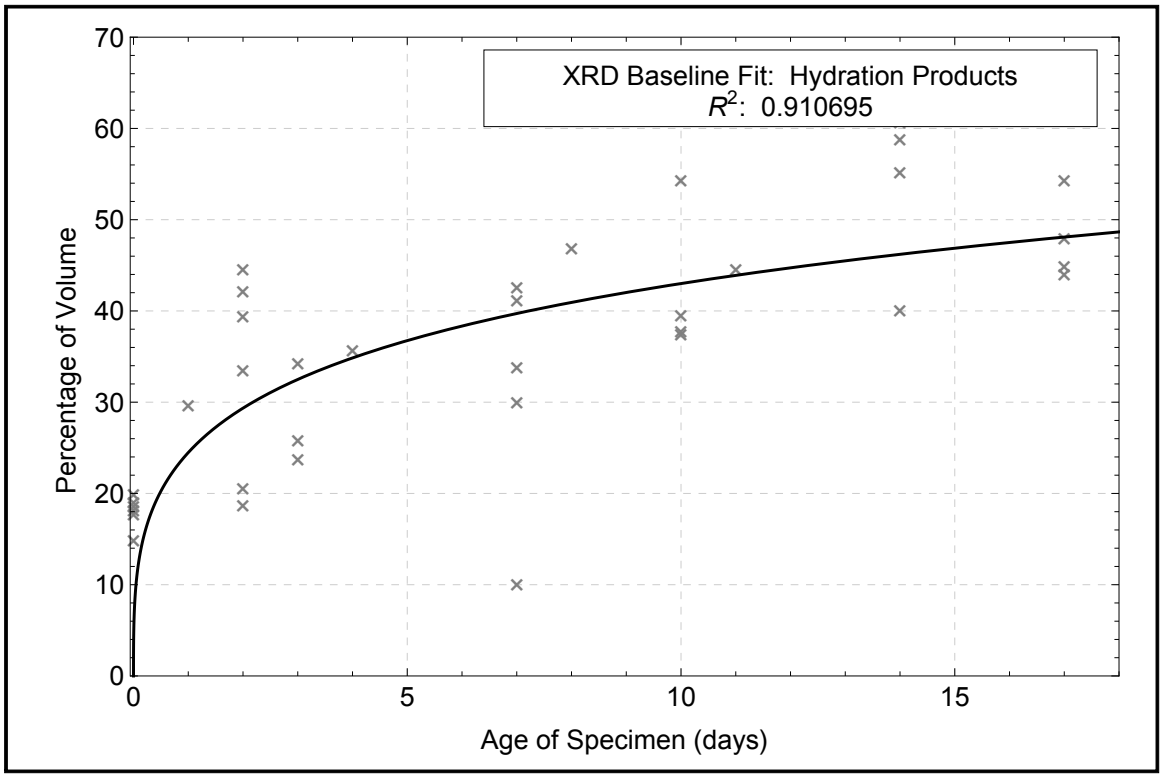
XRD Baseline Fit: Hydration Products
R^2: 0.910695
Percentage of Volume
Age of Specimen (days)
0
10
20
30
40
50
60
70
0
5
10
15

Appendix C.3 – XRD Ratios

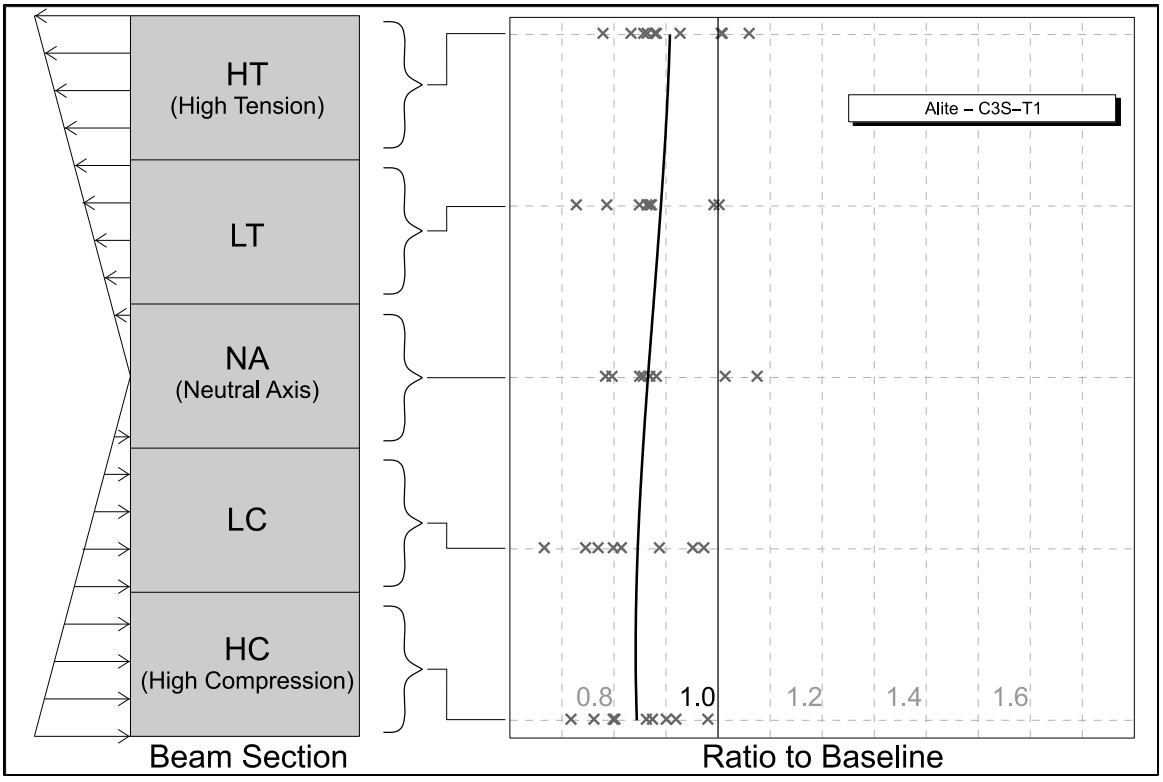
HT
(High Tension)
LT
NA
(Neutral Axis)
LC
HC
(High Compression)
Beam Section
Alite – C3S–T1
0.8
1.0
1.2
1.4
1.6
Ratio to Baseline

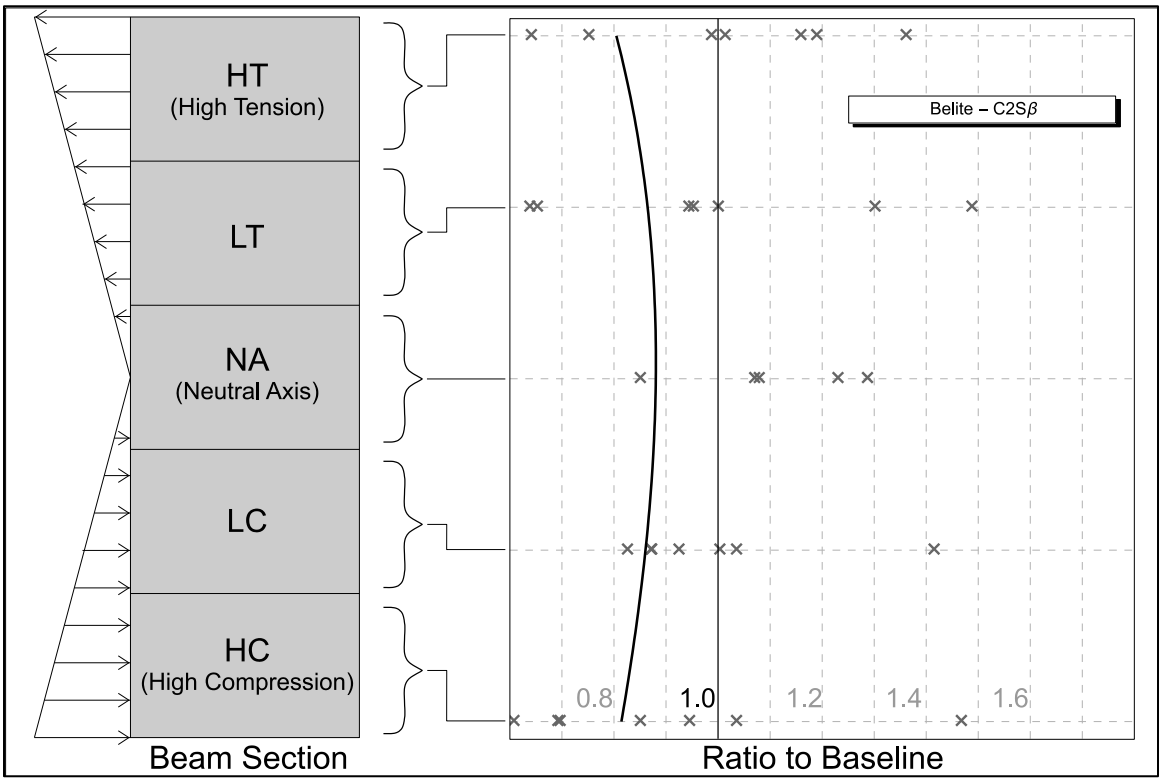
HT
(High Tension)
LT
NA
(Neutral Axis)
LC
HC
(High Compression)
Beam Section
Belite – C2Sβ
0.8
1.0
1.2
1.4
1.6
Ratio to Baseline

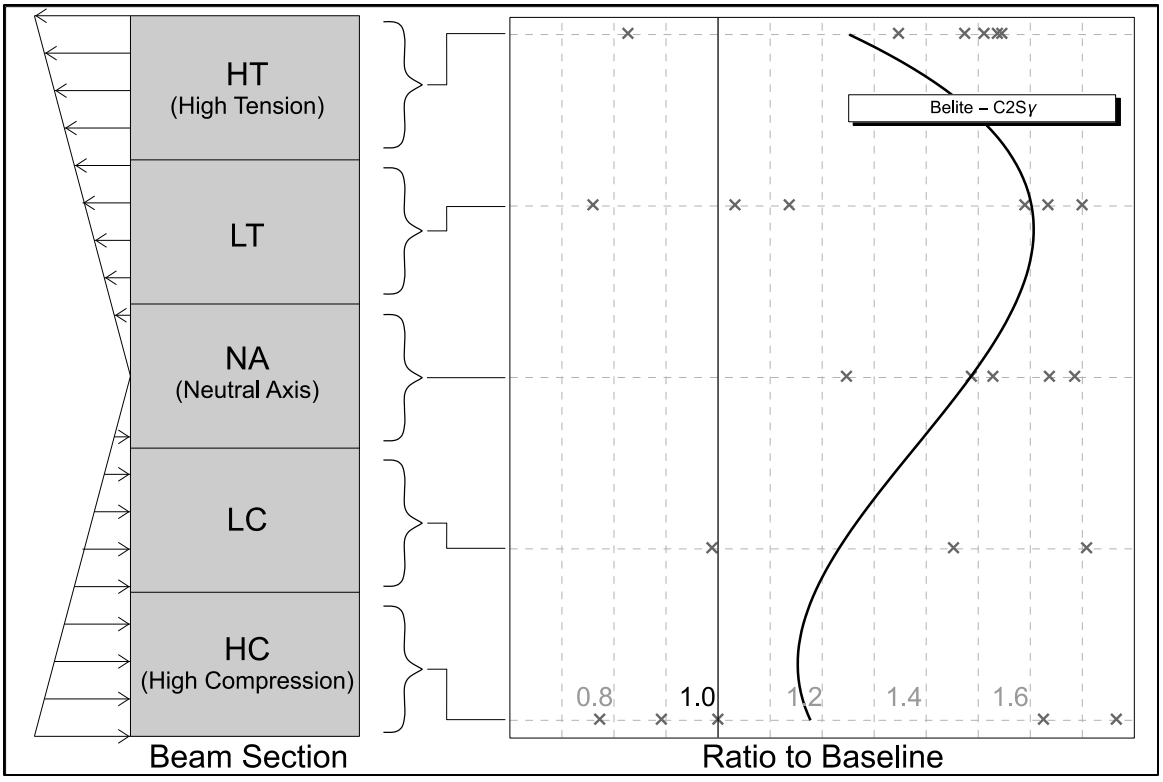
HT
(High Tension)
LT
NA
(Neutral Axis)
LC
HC
(High Compression)
Beam Section
Belite – C2Sγ
0.8
1.0
1.2
1.4
1.6
Ratio to Baseline

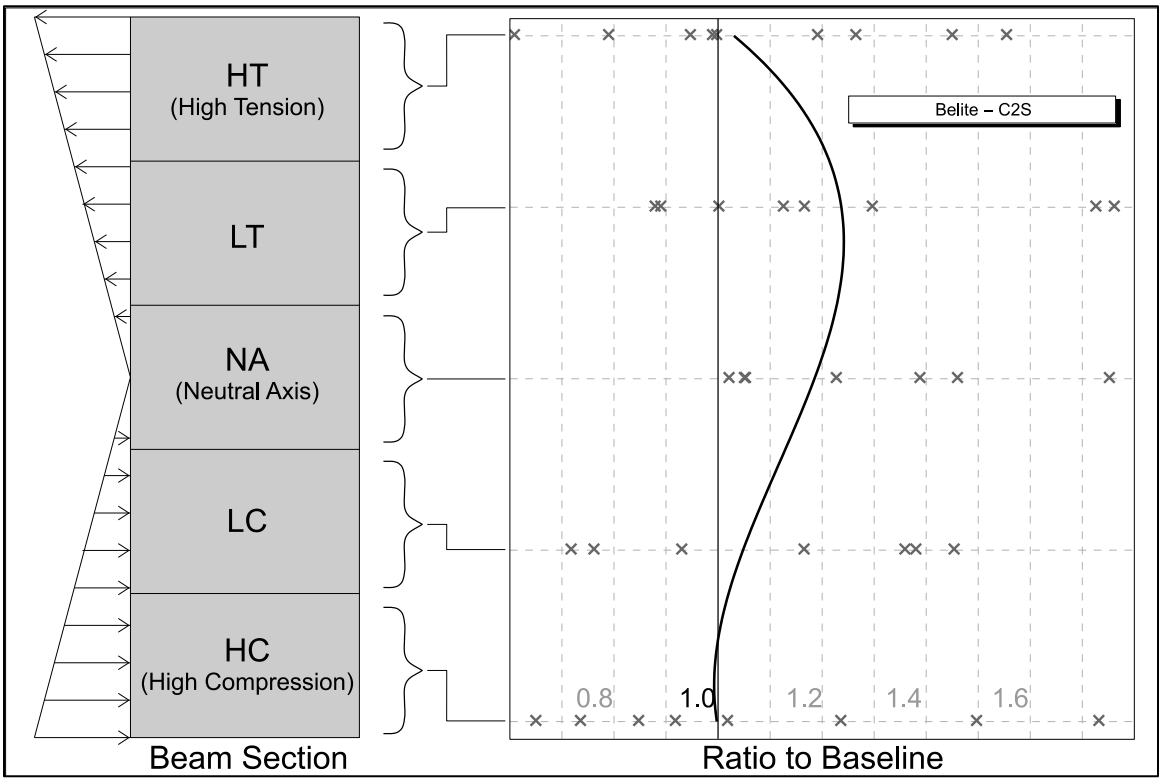
HT
(High Tension)
LT
NA
(Neutral Axis)
LC
HC
(High Compression)
Beam Section
Belite – C2S
0.8
1.0
1.2
1.4
1.6
Ratio to Baseline

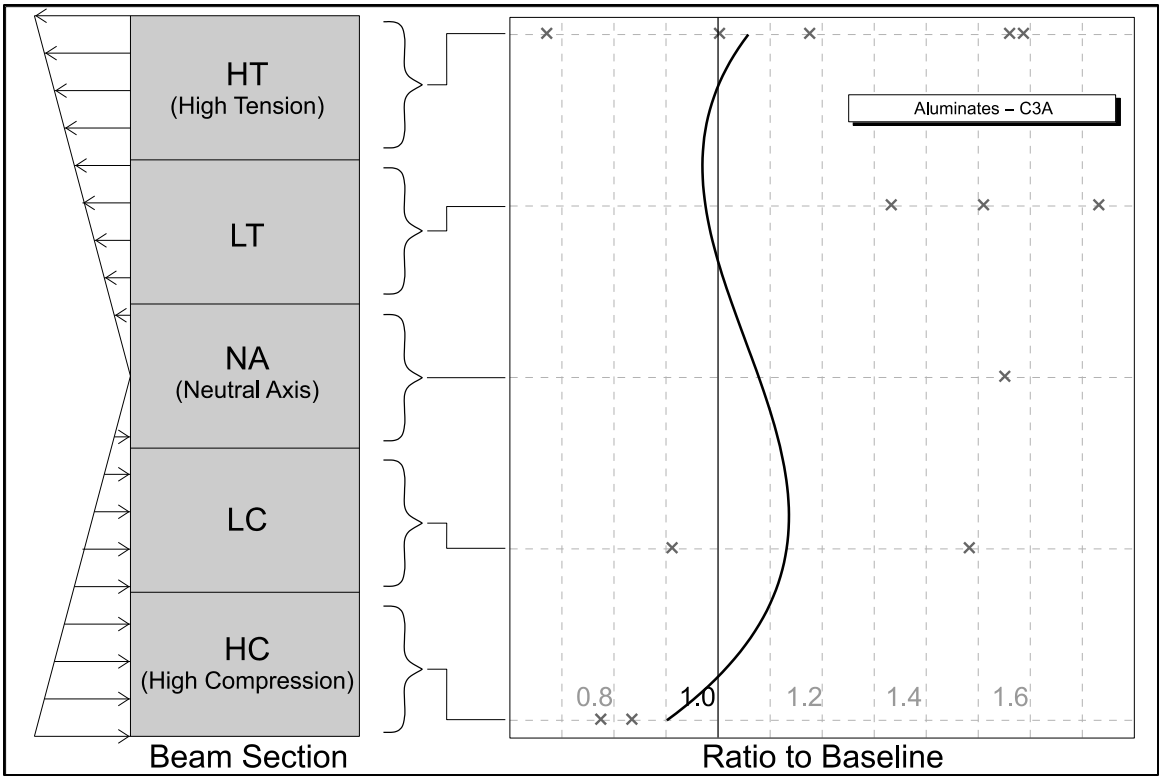
HT
(High Tension)
LT
NA
(Neutral Axis)
LC
HC
(High Compression)
Beam Section
Aluminates – C3A
0.8
1.0
1.2
1.4
1.6
Ratio to Baseline

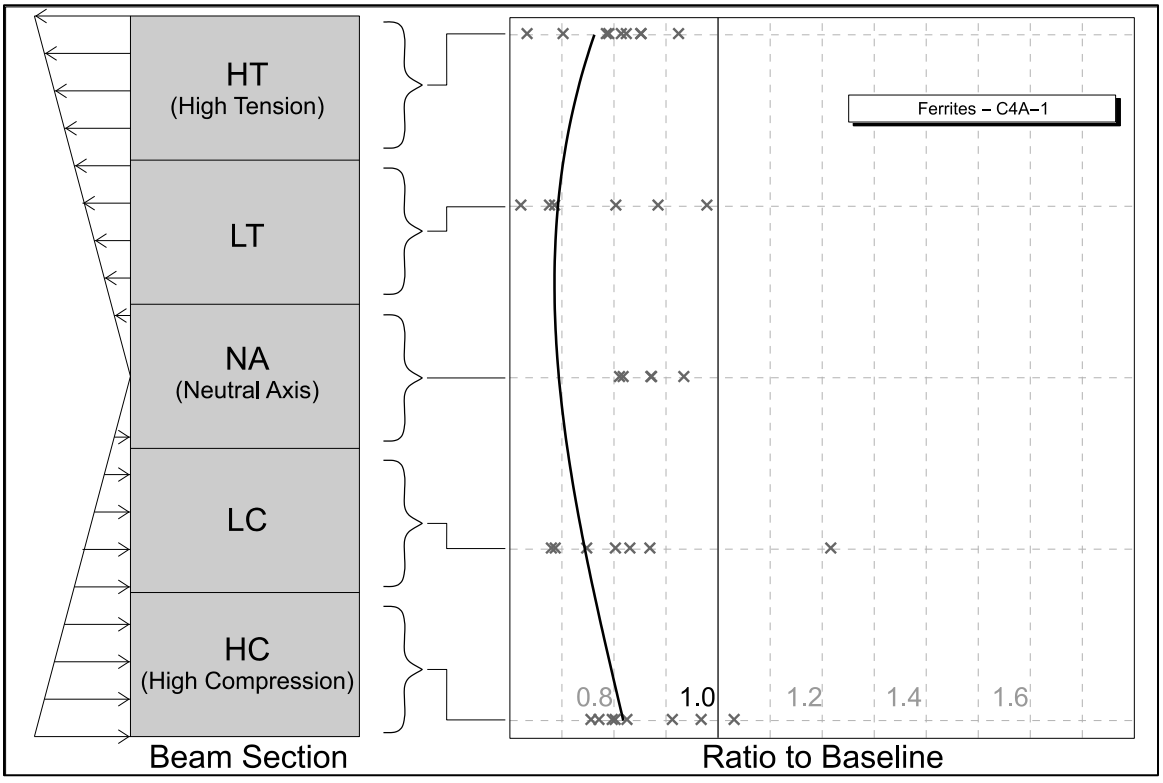
HT
(High Tension)
LT
NA
(Neutral Axis)
LC
HC
(High Compression)
Beam Section
Ferrites – C4A–1
0.8
1.0
1.2
1.4
1.6
Ratio to Baseline

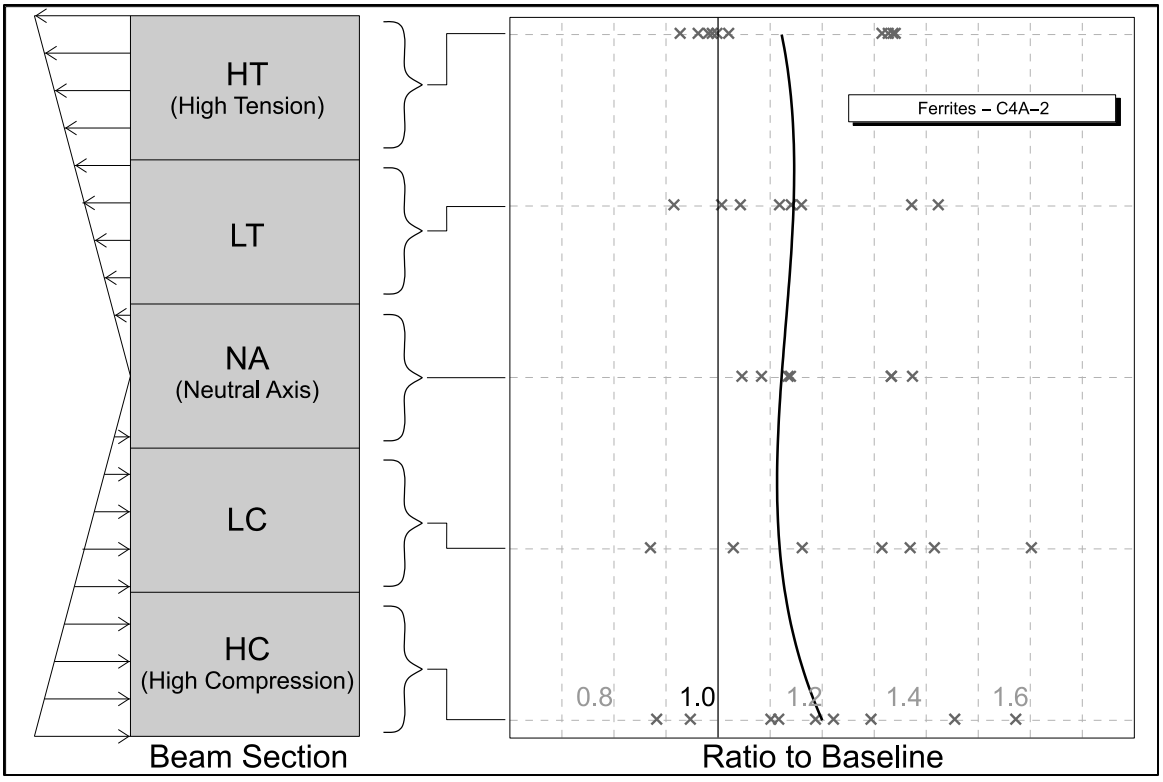
HT
(High Tension)
LT
NA
(Neutral Axis)
LC
HC
(High Compression)
Beam Section
Ferrites – C4A–2
0.8
1.0
1.2
1.4
1.6
Ratio to Baseline

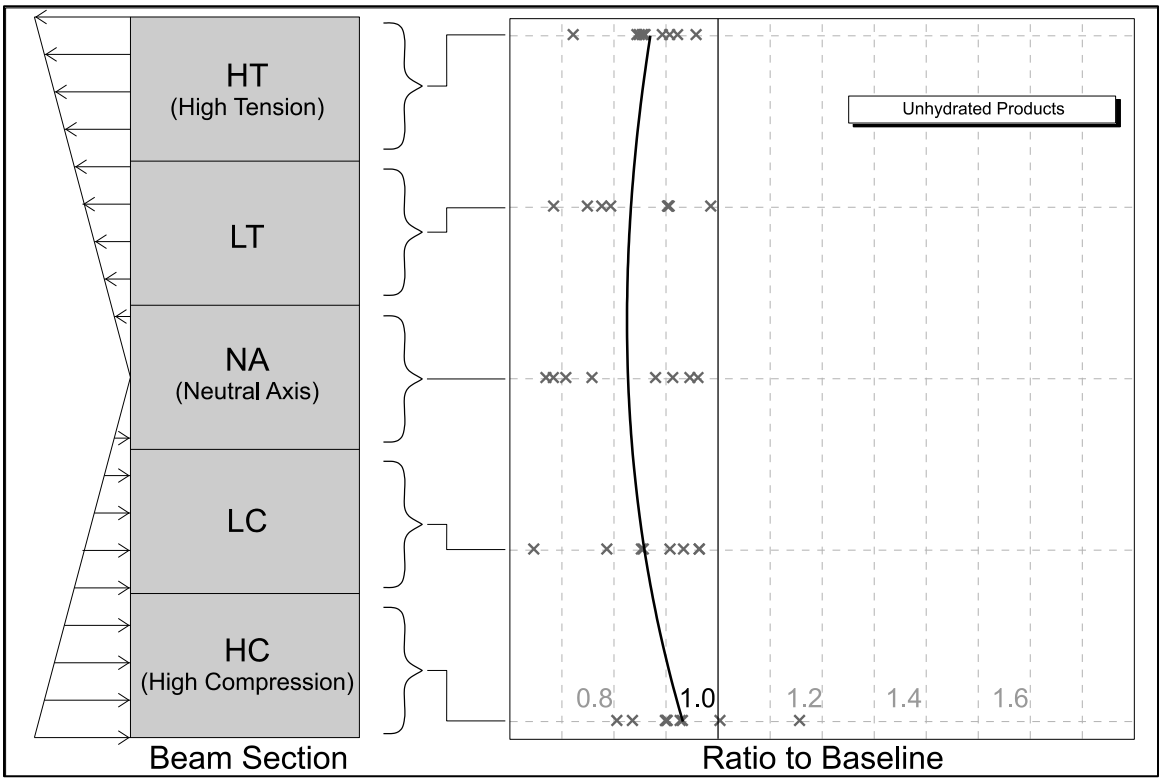
HT
(High Tension)
LT
NA
(Neutral Axis)
LC
HC
(High Compression)
Beam Section
Unhydrated Products
0.8
1.0
1.2
1.4
1.6
Ratio to Baseline

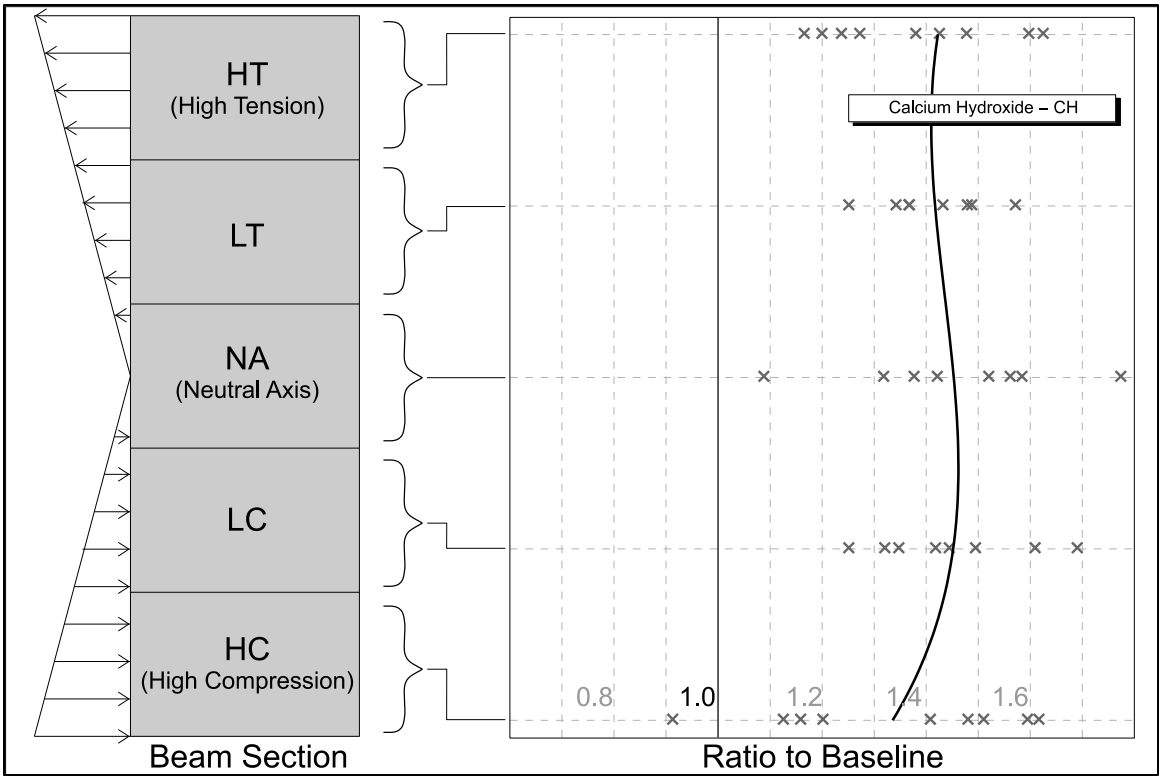
HT
(High Tension)
LT
NA
(Neutral Axis)
LC
HC
(High Compression)
Beam Section
Calcium Hydroxide – CH
0.8
1.0
1.2
1.4
1.6
Ratio to Baseline

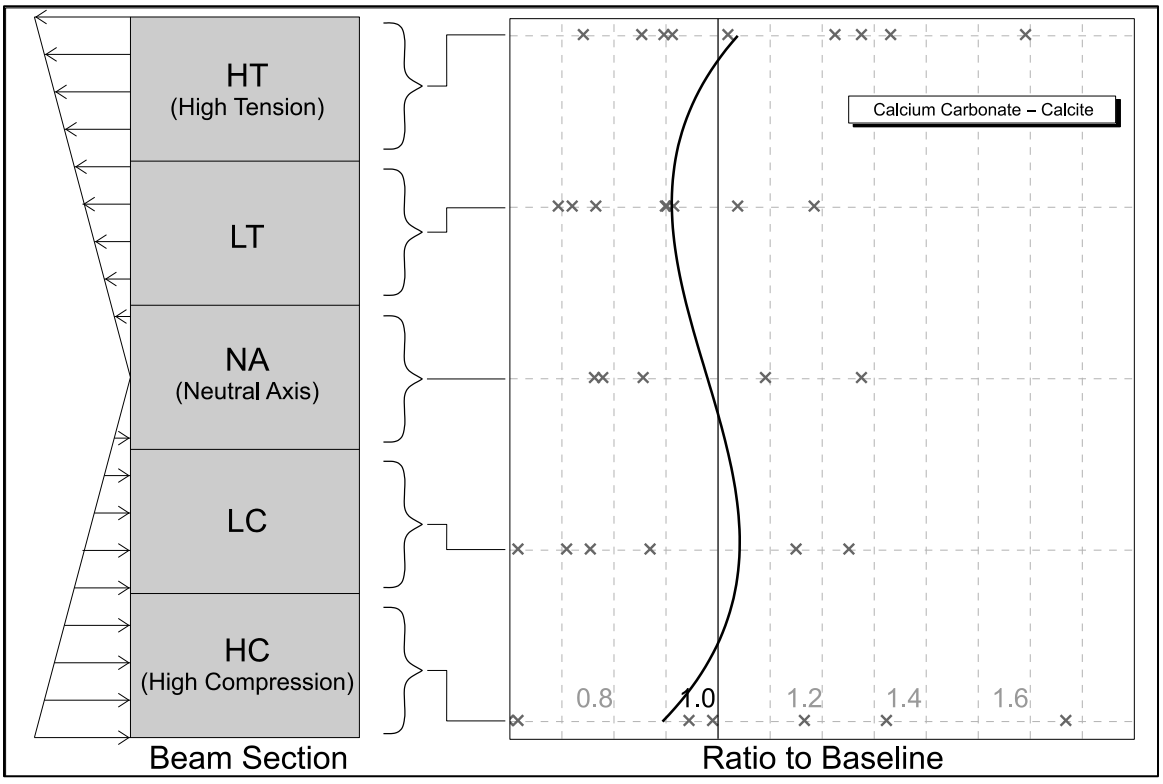
HT
(High Tension)
LT
NA
(Neutral Axis)
LC
HC
(High Compression)
Beam Section
Calcium Carbonate – Calcite
0.8
1.0
1.2
1.4
1.6
Ratio to Baseline

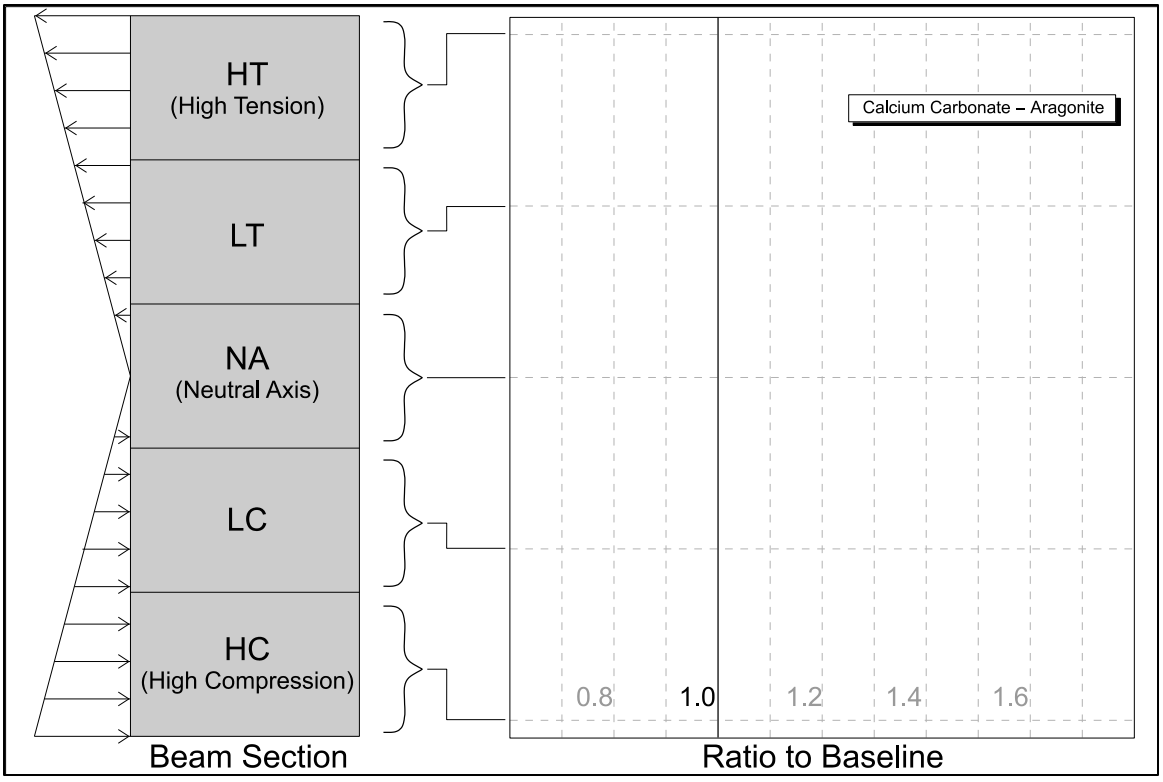
HT
(High Tension)
LT
NA
(Neutral Axis)
LC
HC
(High Compression)
Beam Section
Calcium Carbonate – Aragonite
0.8
1.0
1.2
1.4
1.6
Ratio to Baseline

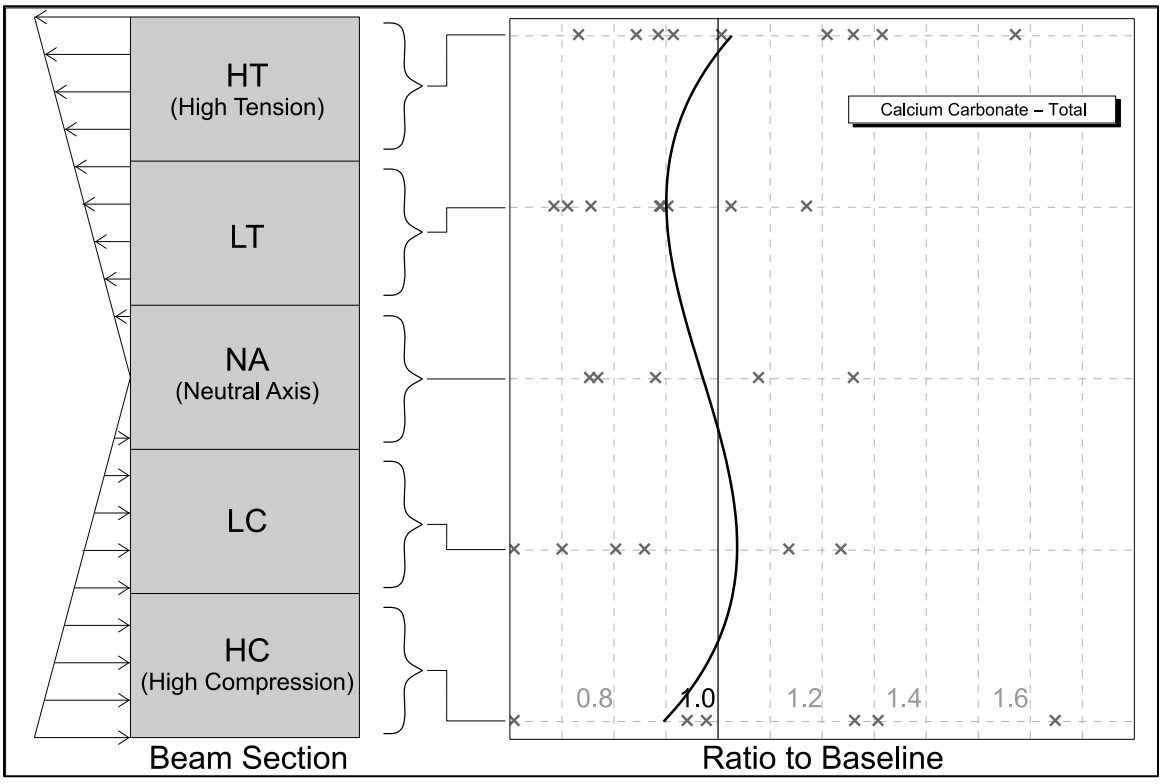
HT
(High Tension)
LT
NA
(Neutral Axis)
LC
HC
(High Compression)
Beam Section
Calcium Carbonate – Total
0.8
1.0
1.2
1.4
1.6
Ratio to Baseline

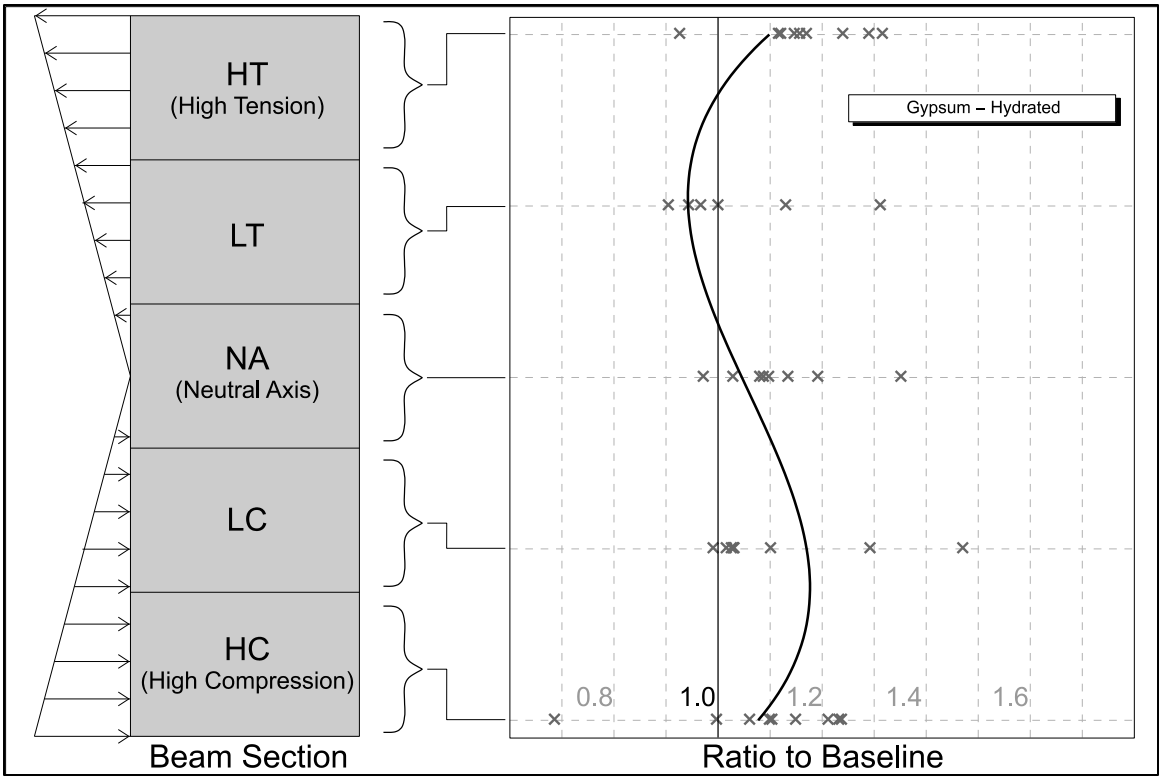
HT
(High Tension)
LT
NA
(Neutral Axis)
LC
HC
(High Compression)
Beam Section
Gypsum – Hydrated
0.8
1.0
1.2
1.4
1.6
Ratio to Baseline

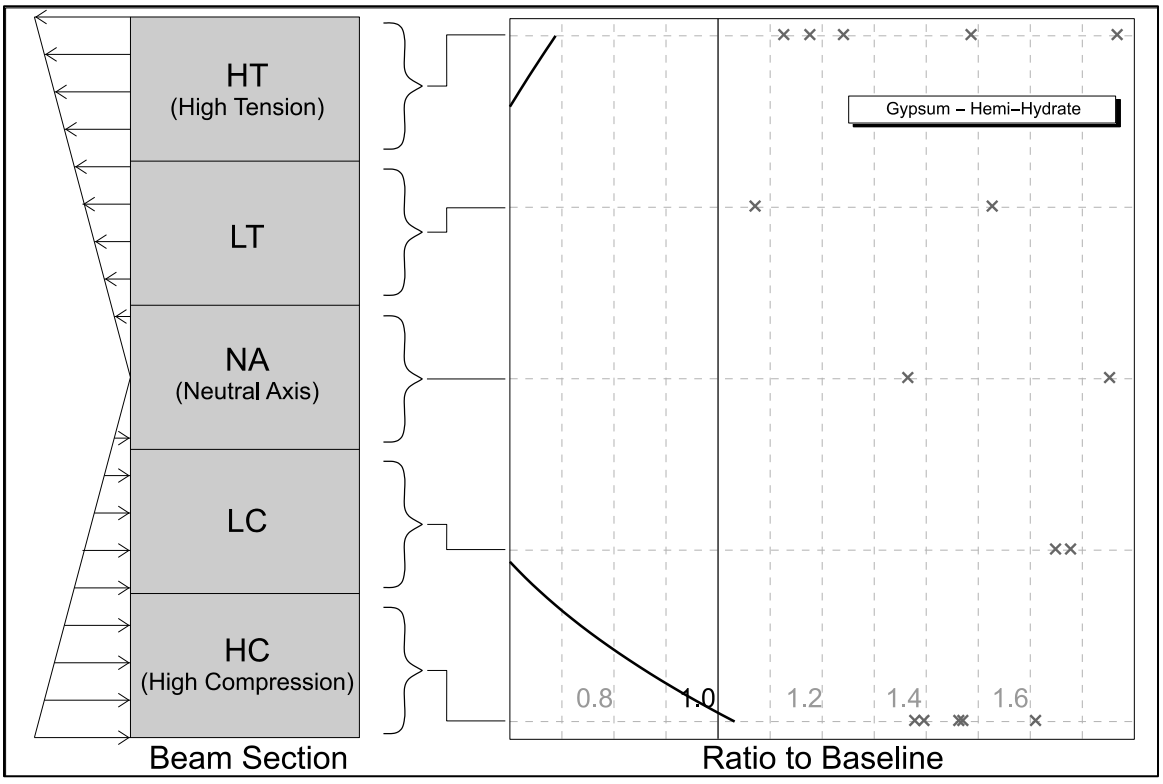
HT
(High Tension)
LT
NA
(Neutral Axis)
LC
HC
(High Compression)
Beam Section
Gypsum – Hemi–Hydrate
0.8
1.0
1.2
1.4
1.6
Ratio to Baseline

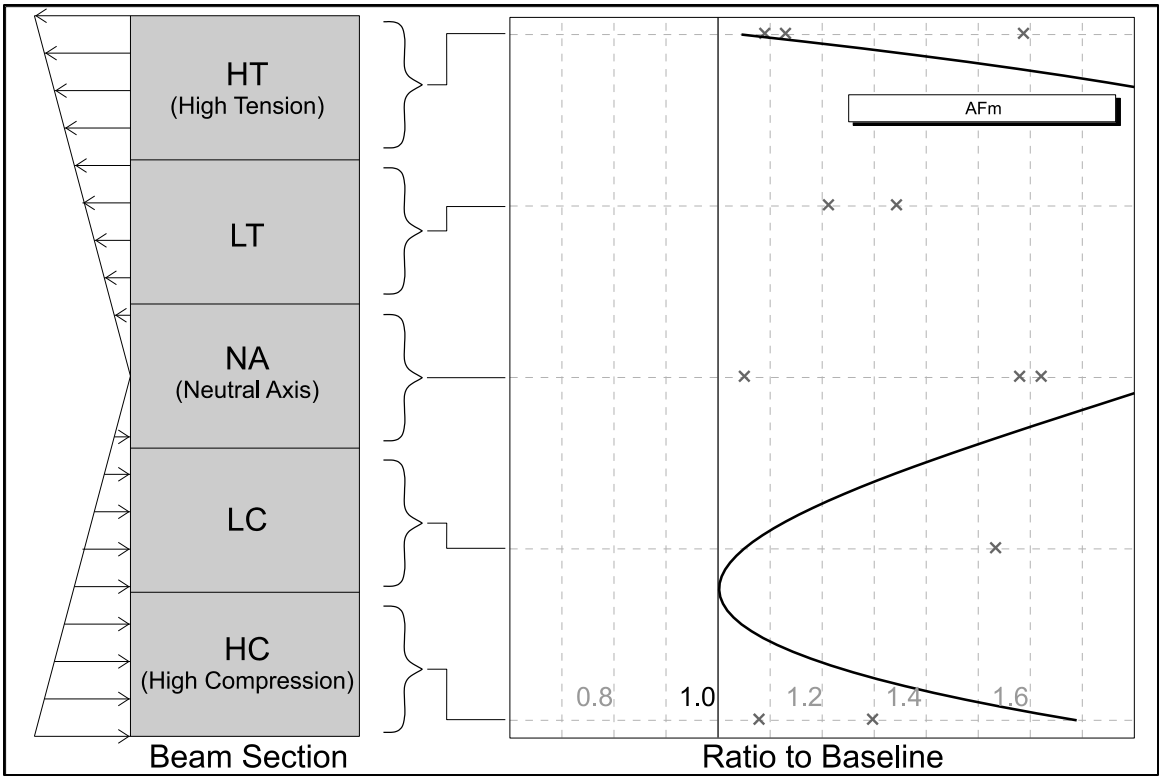
HT
(High Tension)
LT
NA
(Neutral Axis)
LC
HC
(High Compression)
Beam Section
AFm
0.8
1.0
1.2
1.4
1.6
Ratio to Baseline

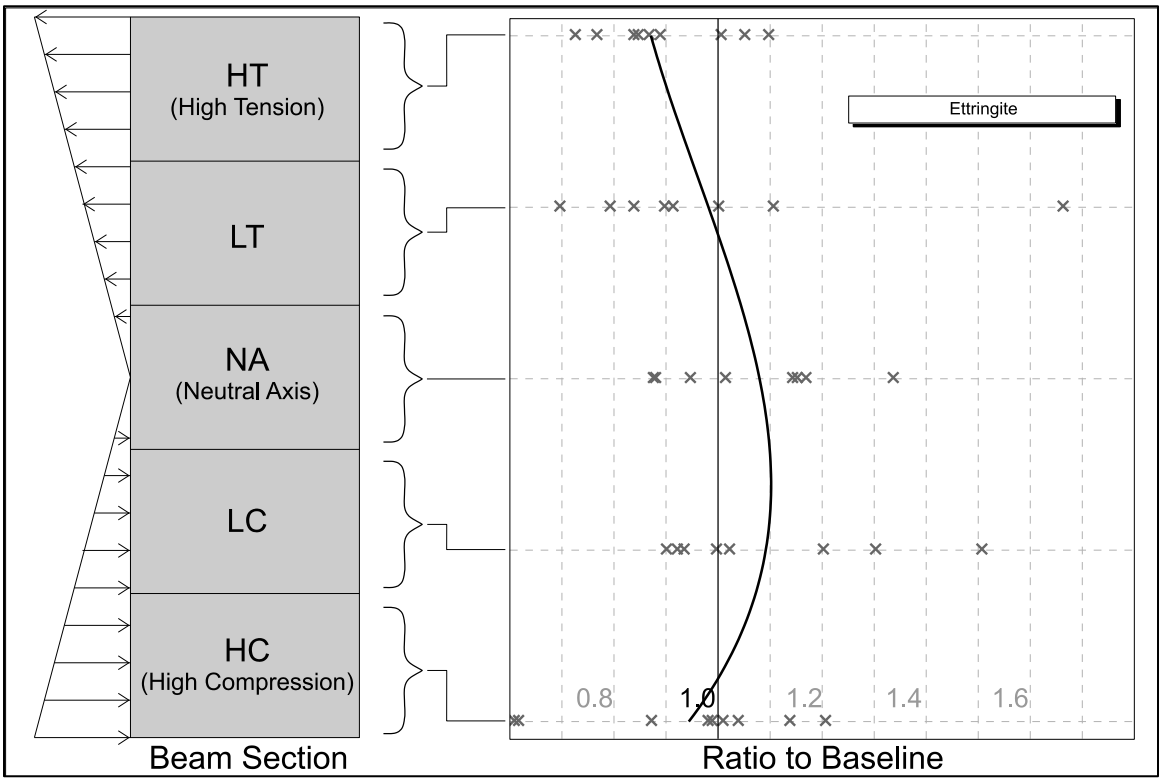
HT
(High Tension)
LT
NA
(Neutral Axis)
LC
HC
(High Compression)
Beam Section
Ettringite
0.8
1.0
1.2
1.4
1.6
Ratio to Baseline

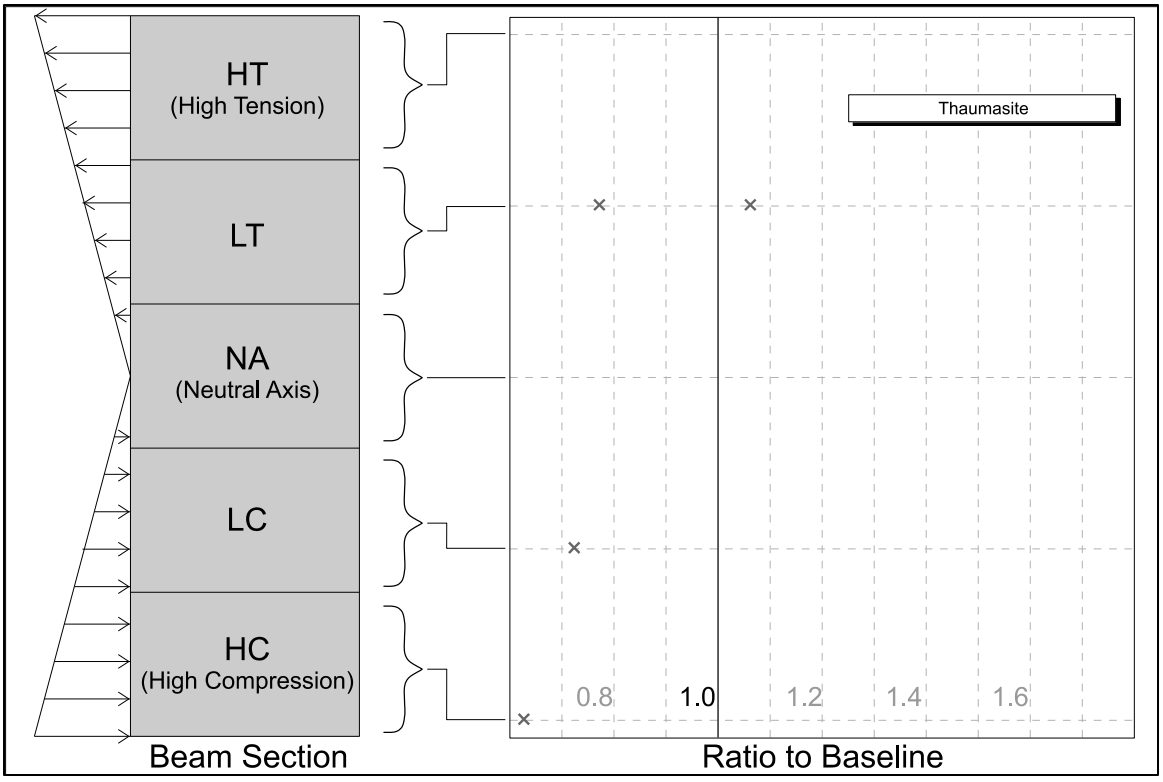
HT
(High Tension)
LT
NA
(Neutral Axis)
LC
HC
(High Compression)
Beam Section
Thaumasite
0.8
1.0
1.2
1.4
1.6
Ratio to Baseline

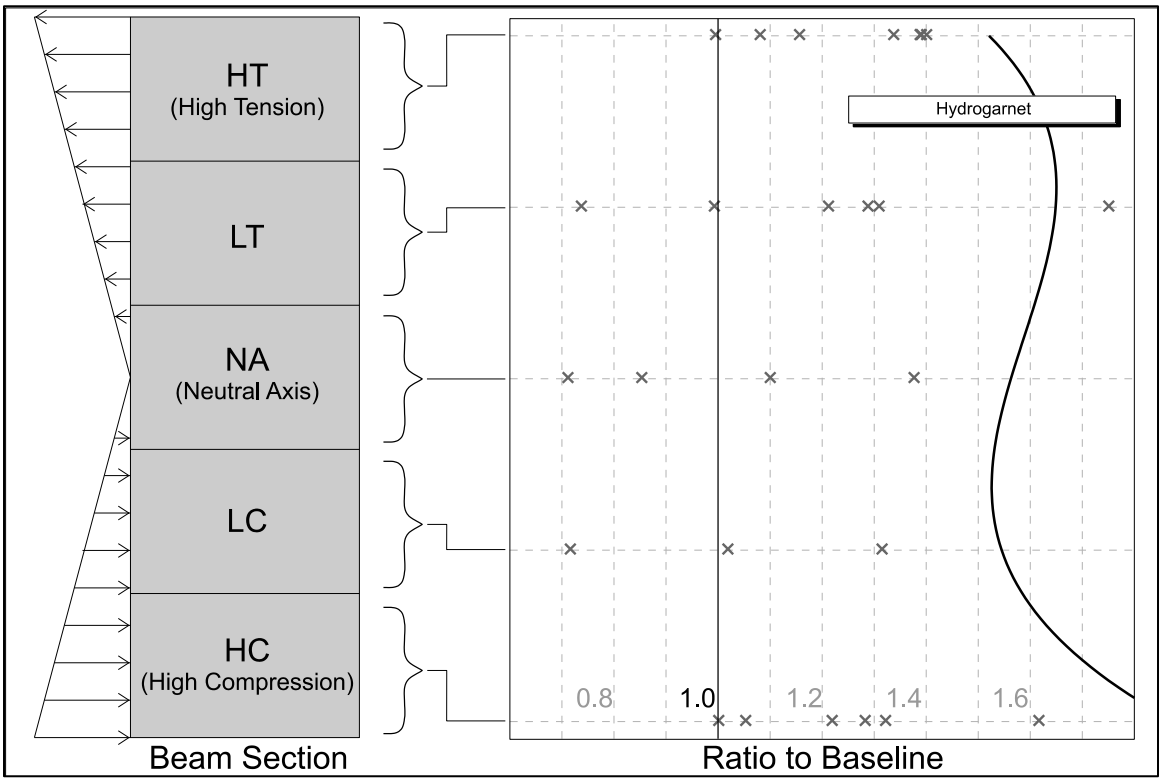
HT
(High Tension)
LT
NA
(Neutral Axis)
LC
HC
(High Compression)
Beam Section
Hydrogarnet
0.8
1.0
1.2
1.4
1.6
Ratio to Baseline

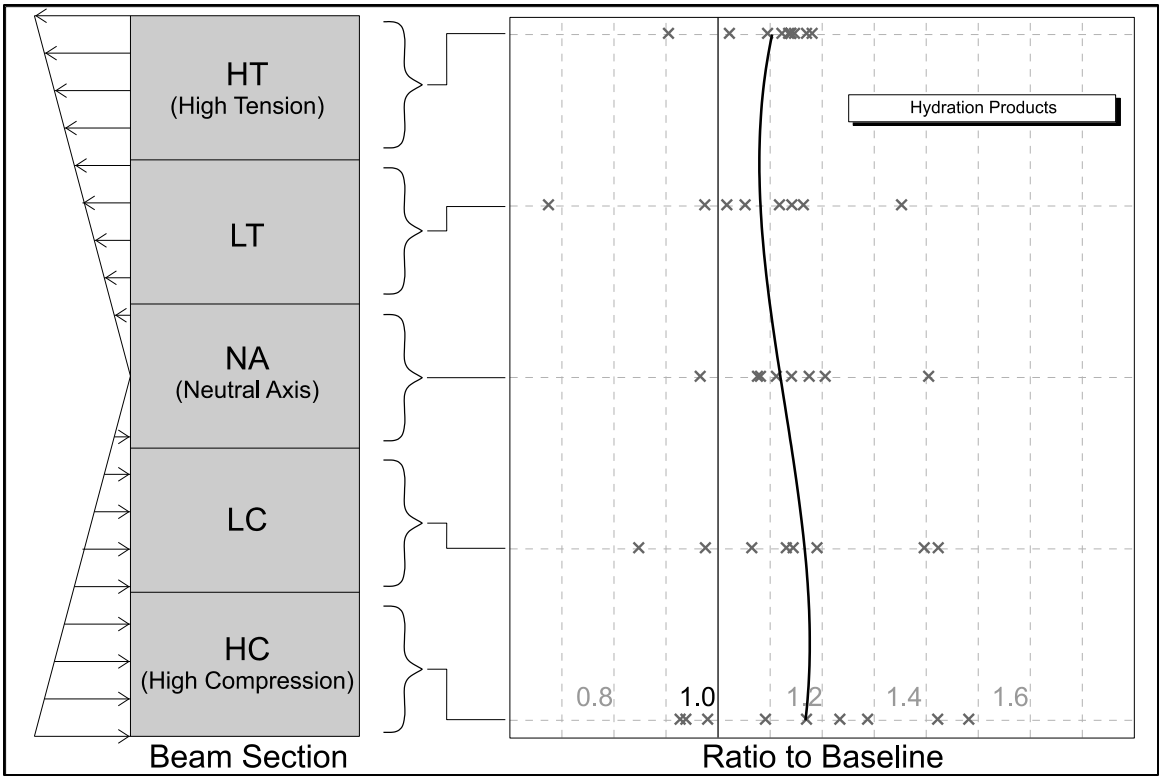
HT
(High Tension)
LT
NA
(Neutral Axis)
LC
HC
(High Compression)
Beam Section
Hydration Products
0.8
1.0
1.2
1.4
1.6
Ratio to Baseline

Appendix D.1 – Micro-CT Histogram Fit Curves

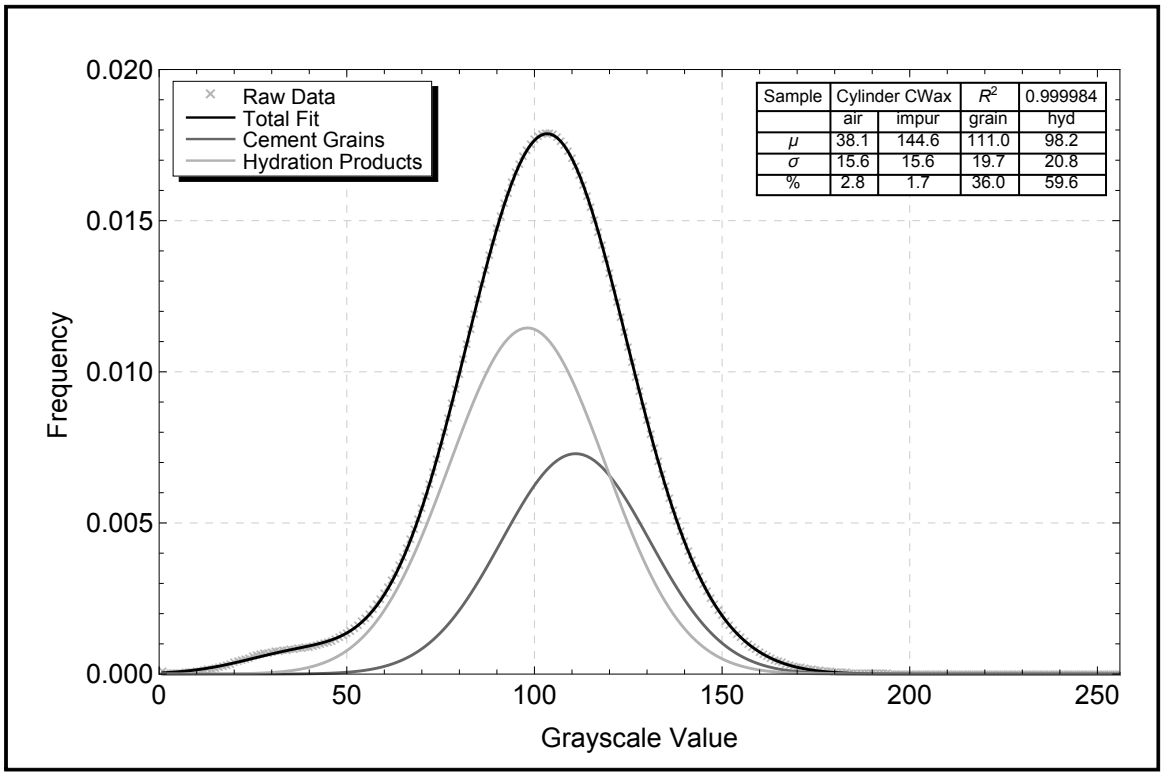

Sample	Cylinder CWax		R^2	0.999984
	air	impur	grain	hyd
μ	38.1	144.6	111.0	98.2
σ	15.6	15.6	19.7	20.8
%	2.8	1.7	36.0	59.6

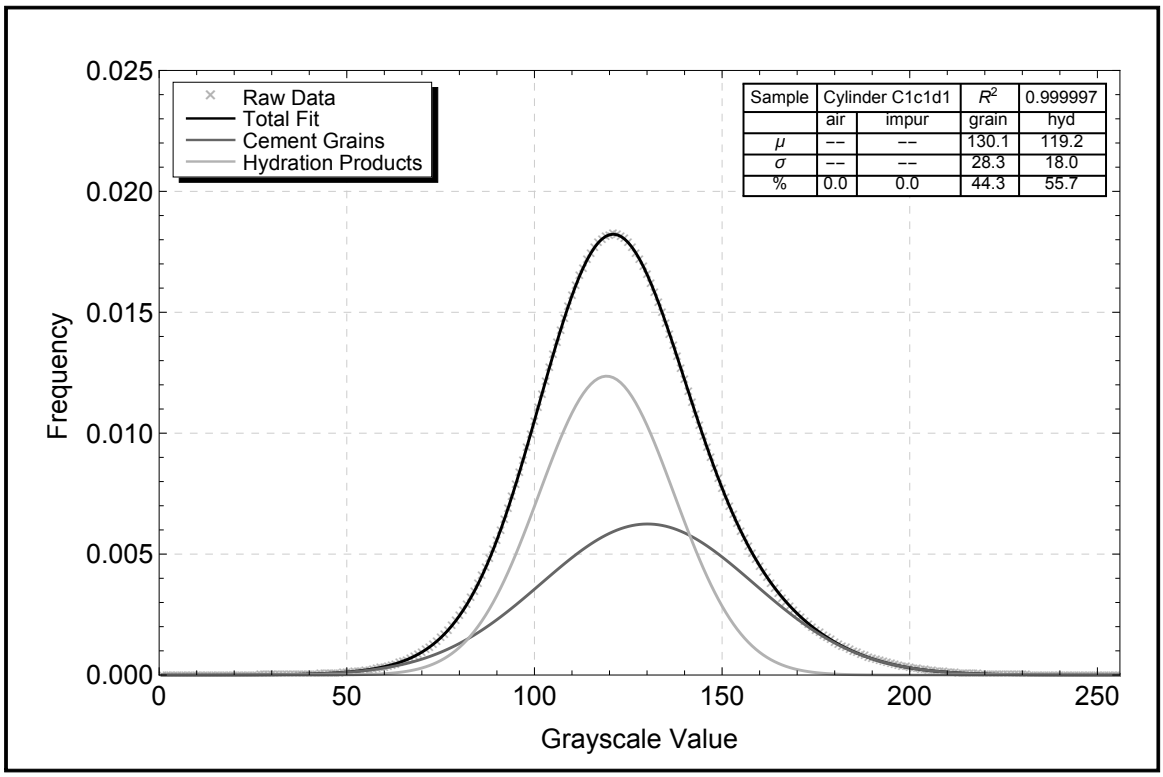

Sample	Cylinder C1c1d1		R^2	0.999997
	air	impur	grain	hyd
μ	--	--	130.1	119.2
σ	--	--	28.3	18.0
%	0.0	0.0	44.3	55.7

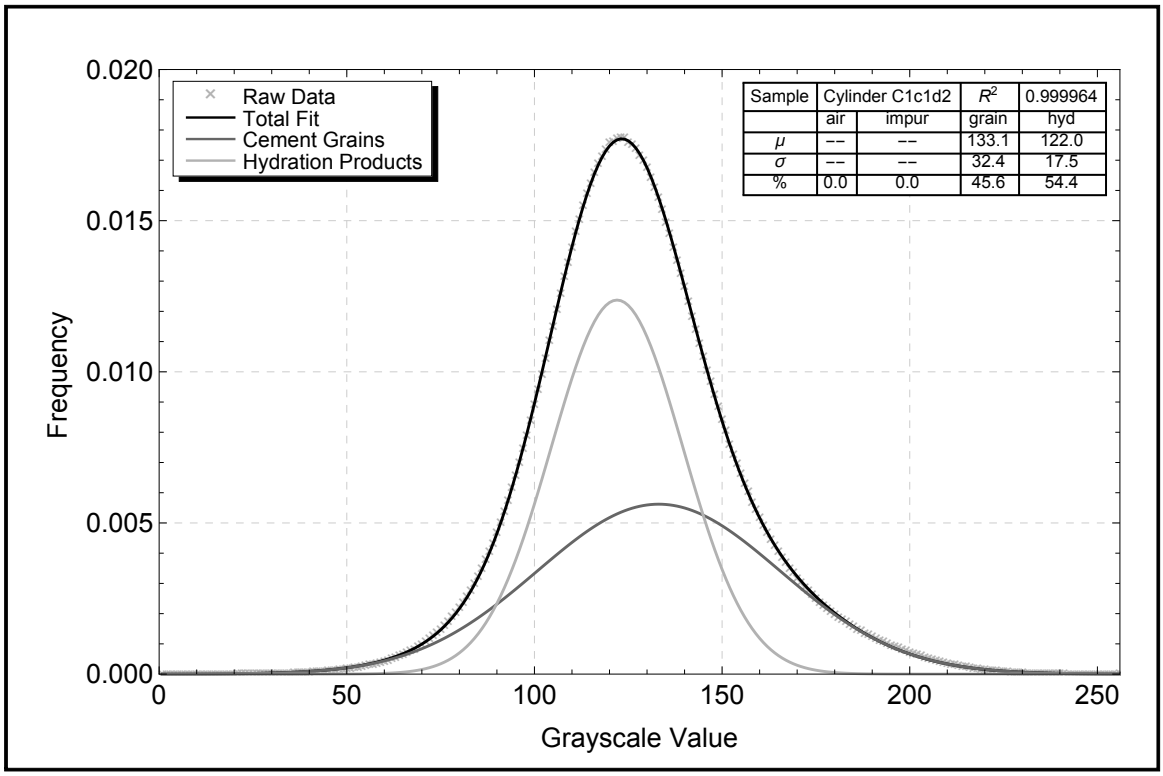

Sample	Cylinder C1c1d2		R^2	0.999964
	air	impur	grain	hyd
μ	--	--	133.1	122.0
σ	--	--	32.4	17.5
%	0.0	0.0	45.6	54.4

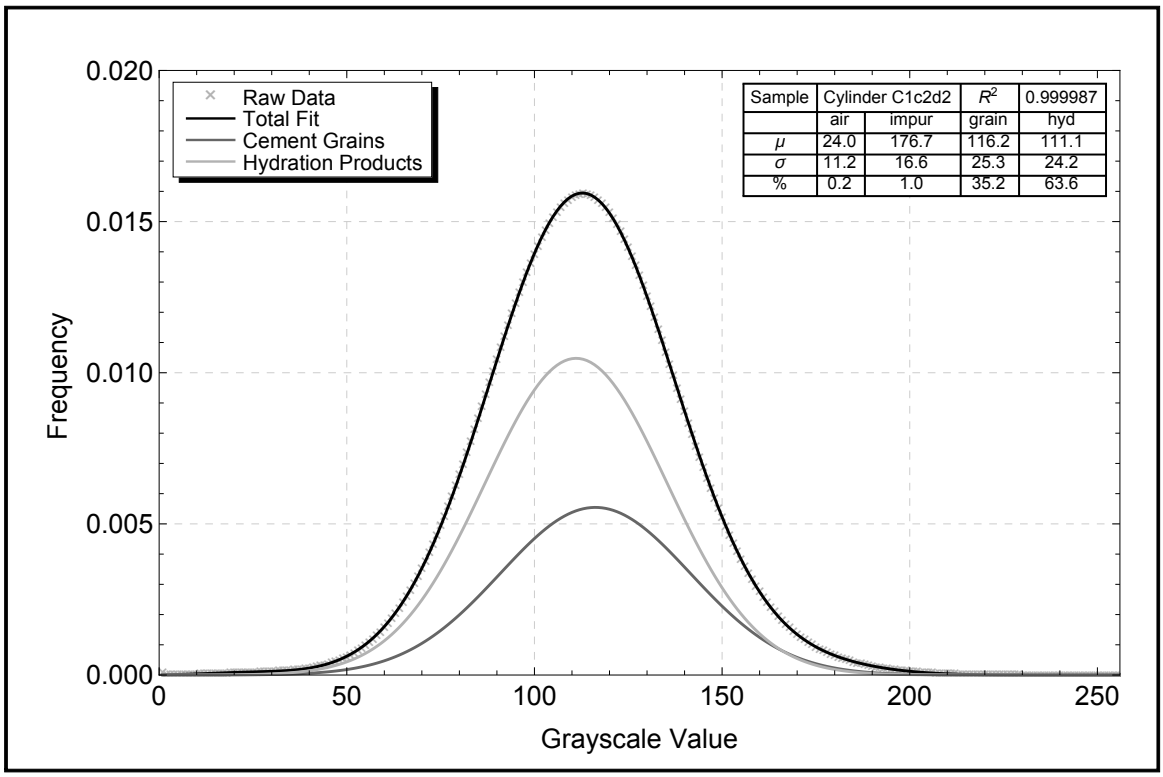

Sample	Cylinder C1c2d2		R^2	0.999987
	air	impur	grain	hyd
μ	24.0	176.7	116.2	111.1
σ	11.2	16.6	25.3	24.2
%	0.2	1.0	35.2	63.6

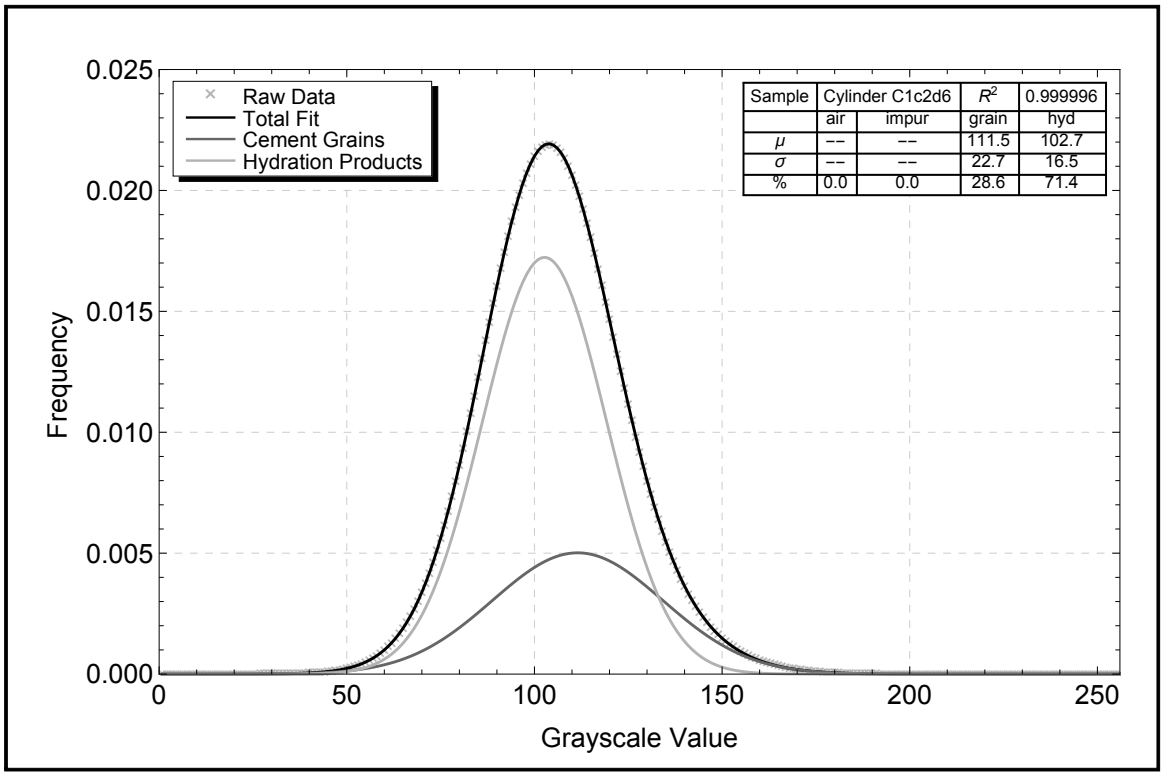

Sample	Cylinder C1c2d6		R^2	0.999996
	air	impur	grain	hyd
μ	--	--	111.5	102.7
σ	--	--	22.7	16.5
%	0.0	0.0	28.6	71.4

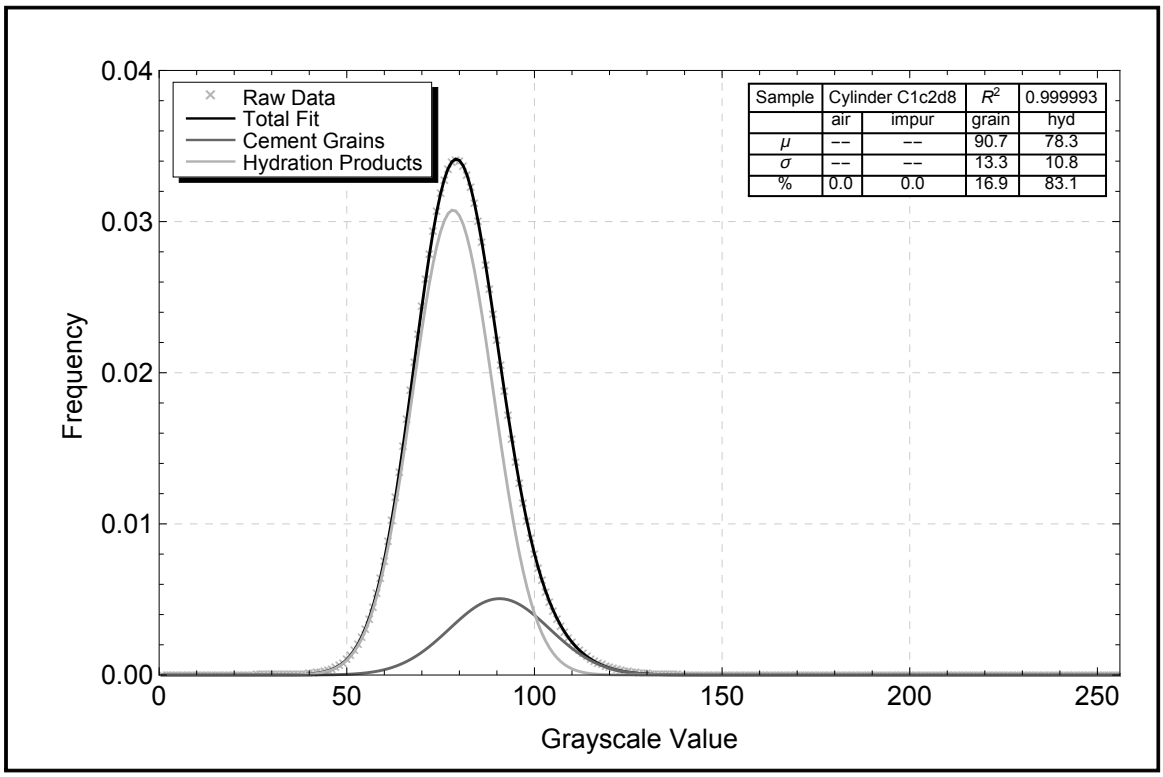

Sample	Cylinder C1c2d8		R^2	0.999993
	air	impur	grain	hyd
μ	--	--	90.7	78.3
σ	--	--	13.3	10.8
%	0.0	0.0	16.9	83.1

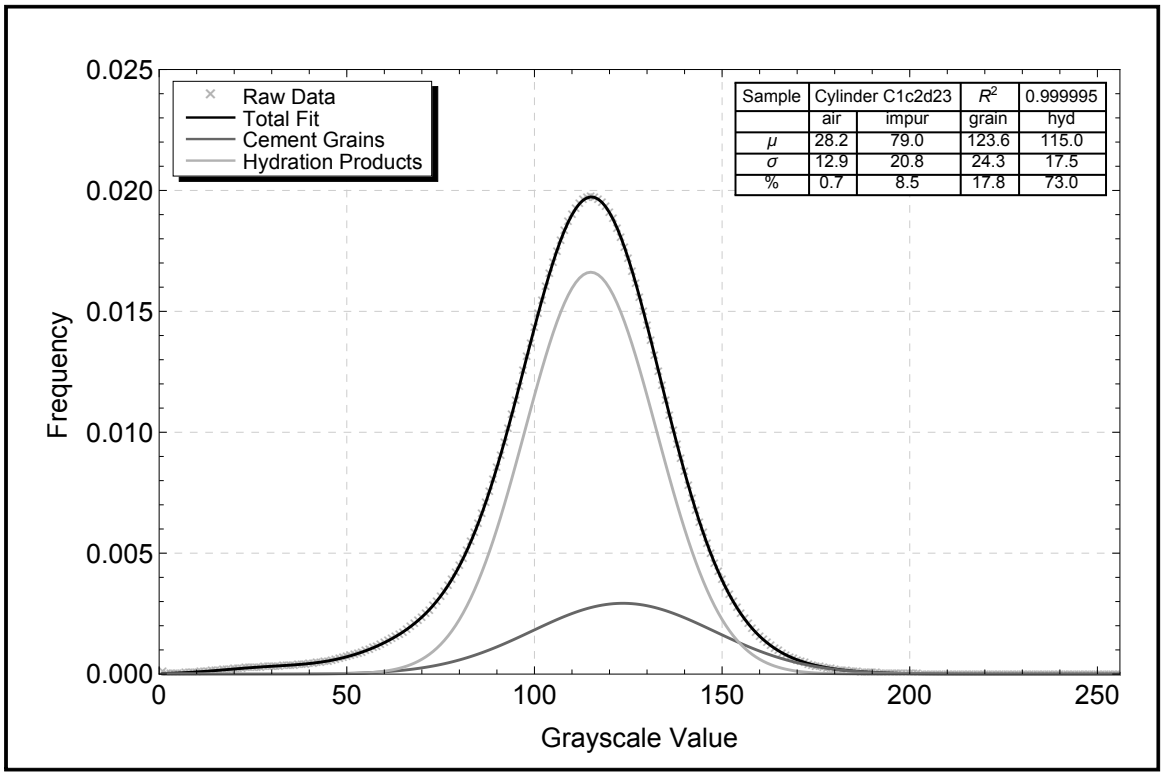

Sample	Cylinder C1c2d23		R^2	0.999995
	air	impur	grain	hyd
μ	28.2	79.0	123.6	115.0
σ	12.9	20.8	24.3	17.5
%	0.7	8.5	17.8	73.0

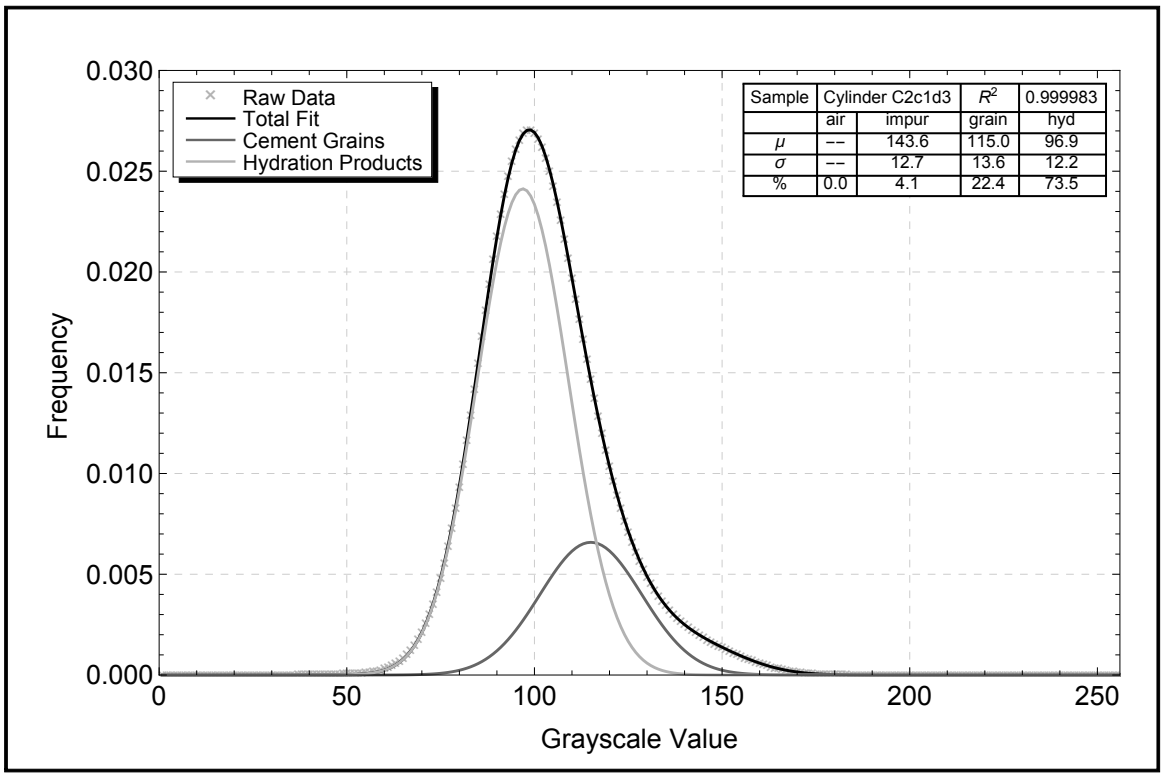

Sample	Cylinder C2c1d3		R^2	0.999983
	air	impur	grain	hyd
μ	--	143.6	115.0	96.9
σ	--	12.7	13.6	12.2
%	0.0	4.1	22.4	73.5

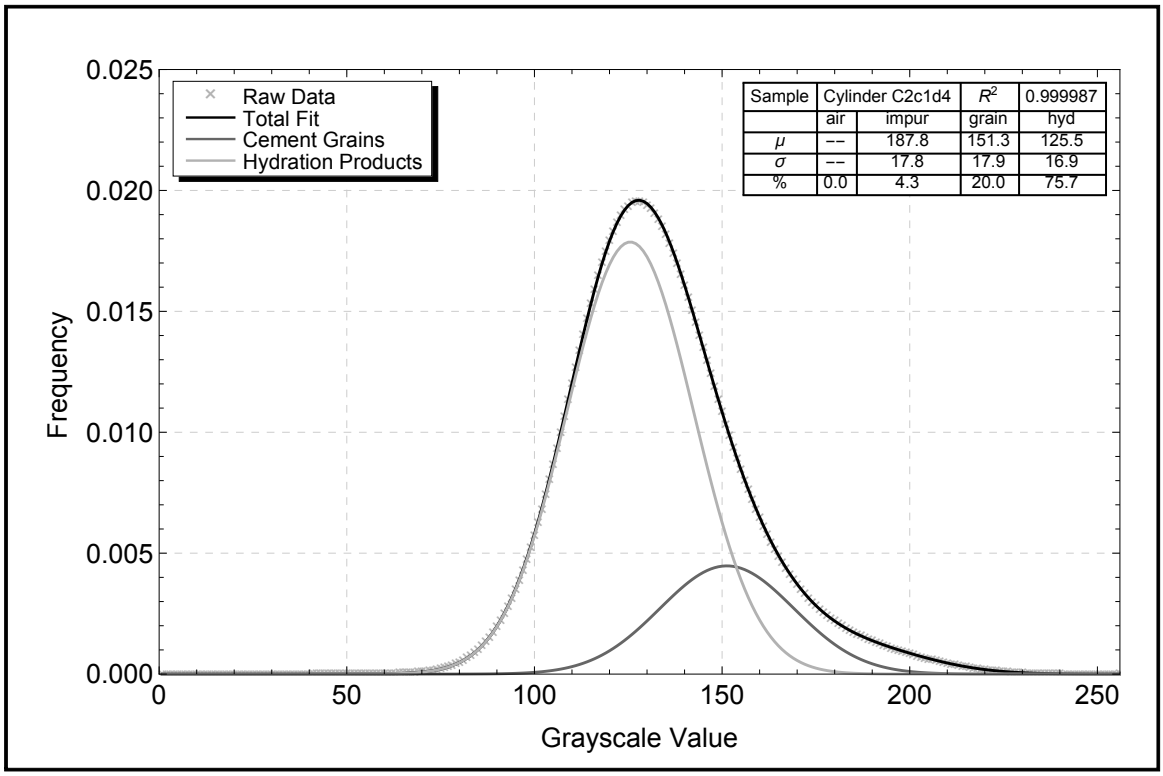

Sample	Cylinder C2c1d4		R^2	0.999987
	air	impur	grain	hyd
μ	--	187.8	151.3	125.5
σ	--	17.8	17.9	16.9
%	0.0	4.3	20.0	75.7

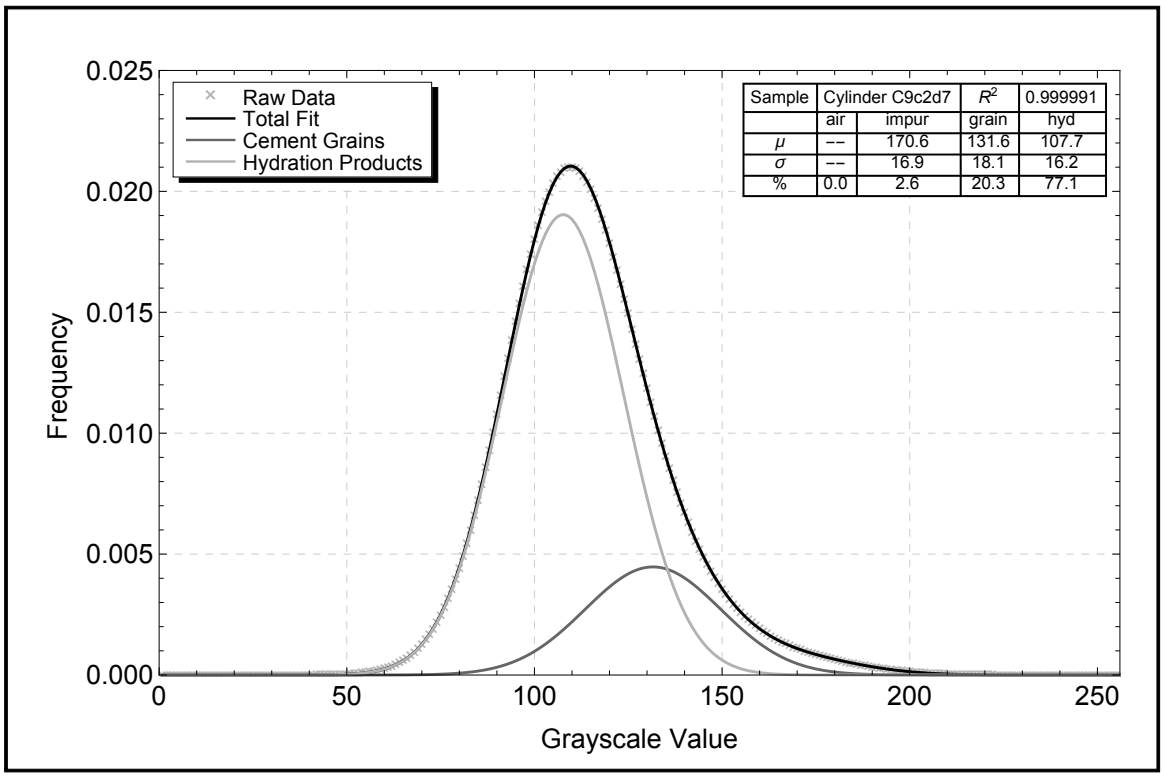

Sample	Cylinder C9c2d7		R^2	0.999991
	air	impur	grain	hyd
μ	--	170.6	131.6	107.7
σ	--	16.9	18.1	16.2
%	0.0	2.6	20.3	77.1

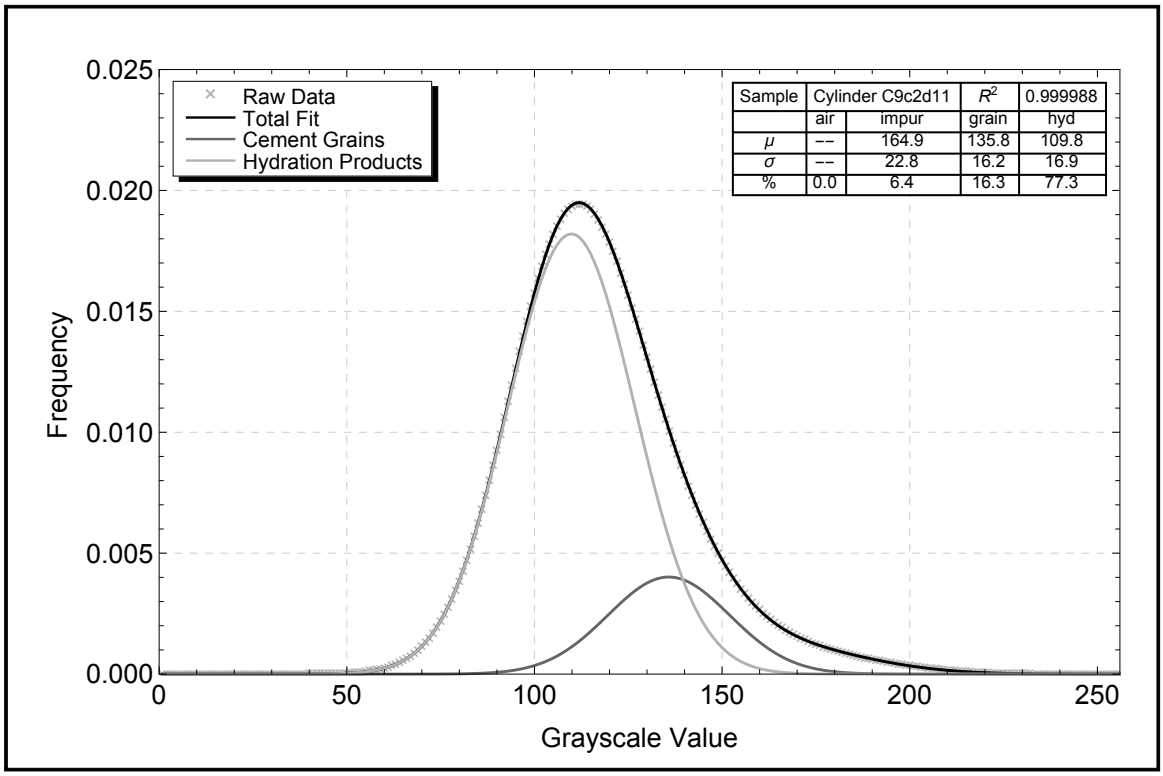
Raw Data
Total Fit
Cement Grains
Hydration Products
Sample | Cylinder C9c2d11 | R^2 | 0.999988
air | impur | grain | hyd
μ | -- | 164.9 | 135.8 | 109.8
σ | -- | 22.8 | 16.2 | 16.9
% | 0.0 | 6.4 | 16.3 | 77.3
Frequency
0.025
0.020
0.015
0.010
0.005
0.000
0
50
100
150
200
250
Grayscale Value

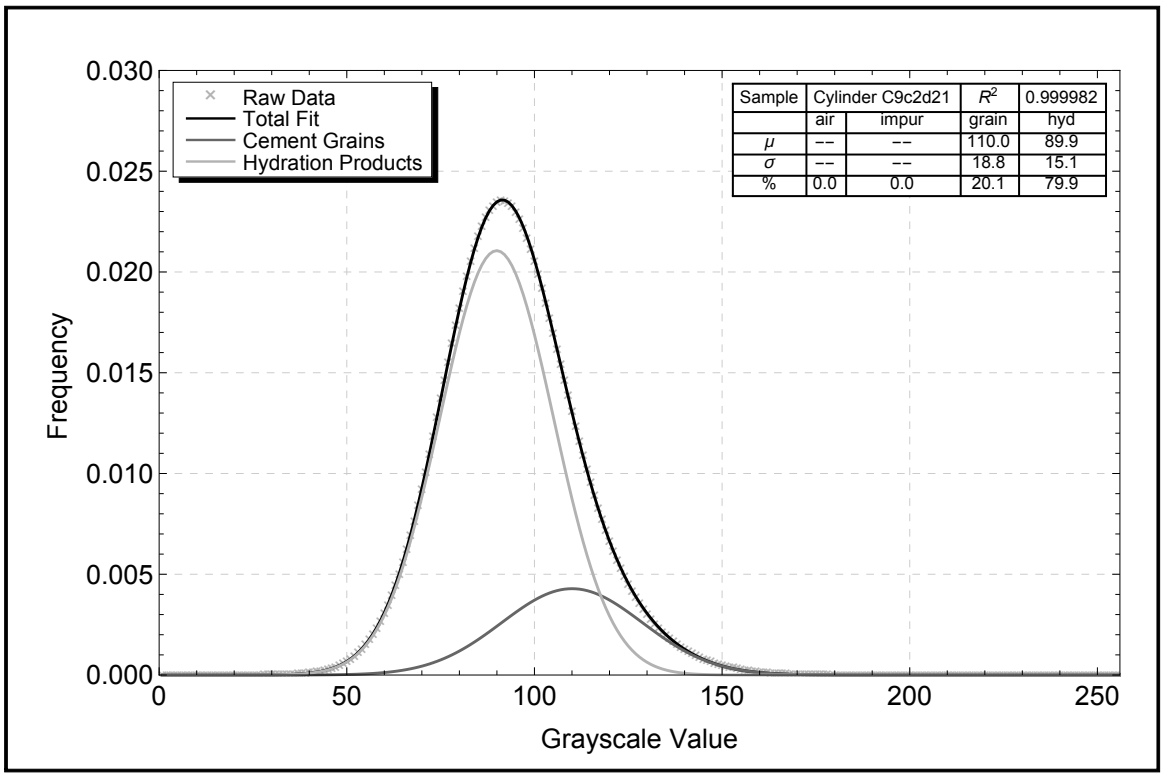
Raw Data
Total Fit
Cement Grains
Hydration Products
Sample | Cylinder C9c2d21 | R^2 | 0.999982
air | impur | grain | hyd
μ | -- | -- | 110.0 | 89.9
σ | -- | -- | 18.8 | 15.1
% | 0.0 | 0.0 | 20.1 | 79.9
Frequency
0.030
0.025
0.020
0.015
0.010
0.005
0.000
0
50
100
150
200
250
Grayscale Value

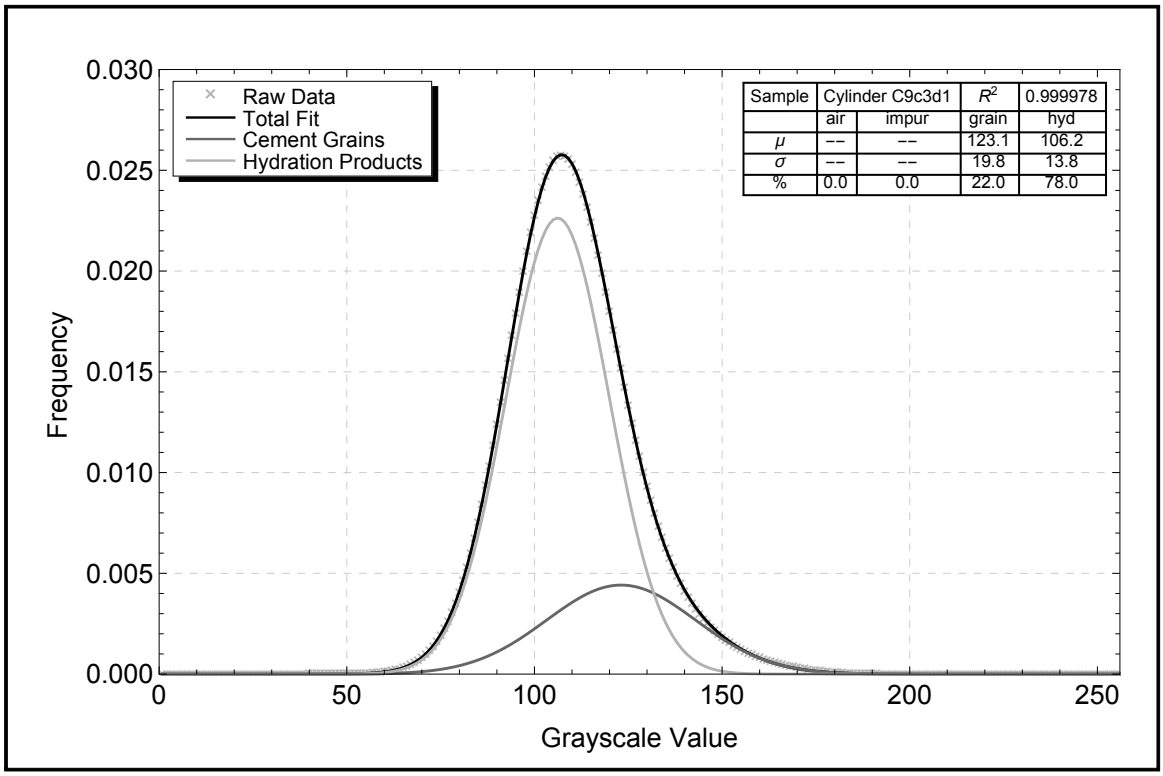

Sample	Cylinder C9c3d1		R^2	0.999978
	air	impur	grain	hyd
μ	--	--	123.1	106.2
σ	--	--	19.8	13.8
%	0.0	0.0	22.0	78.0

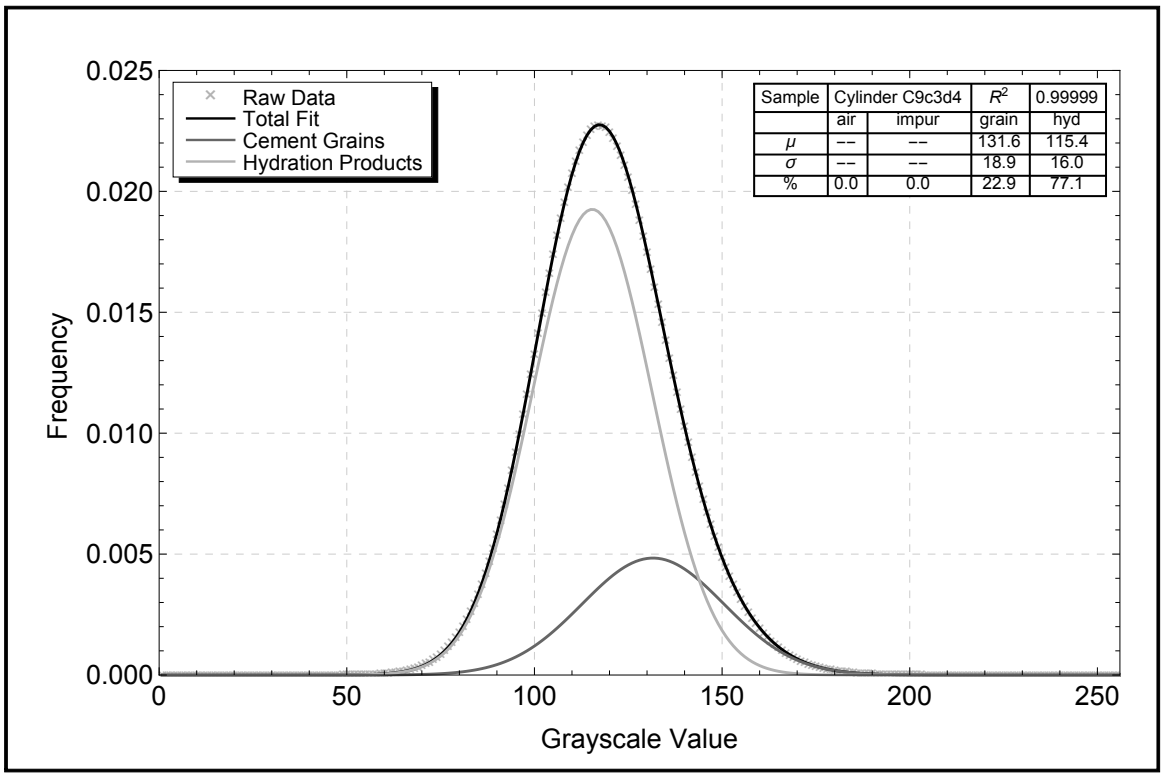

Sample	Cylinder C9c3d4		R^2	0.99999
	air	impur	grain	hyd
μ	--	--	131.6	115.4
σ	--	--	18.9	16.0
%	0.0	0.0	22.9	77.1

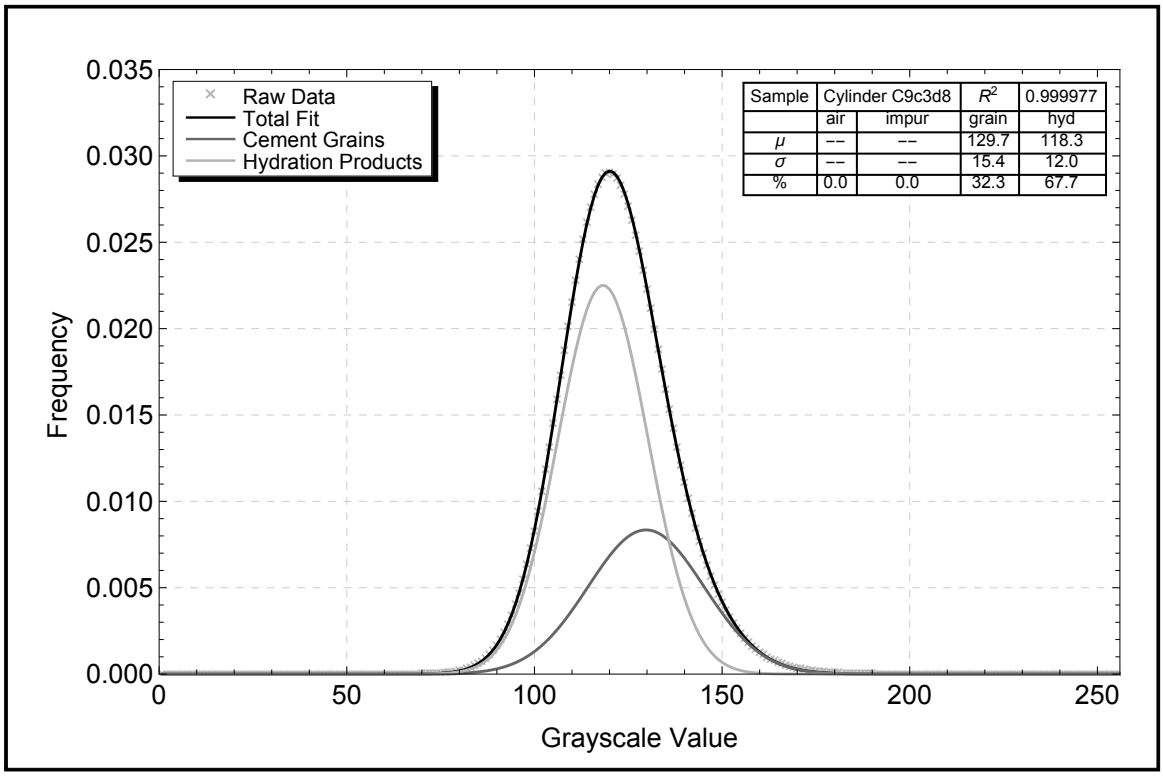

Sample	Cylinder C9c3d8		R^2	0.999977
	air	impur	grain	hyd
μ	--	--	129.7	118.3
σ	--	--	15.4	12.0
%	0.0	0.0	32.3	67.7

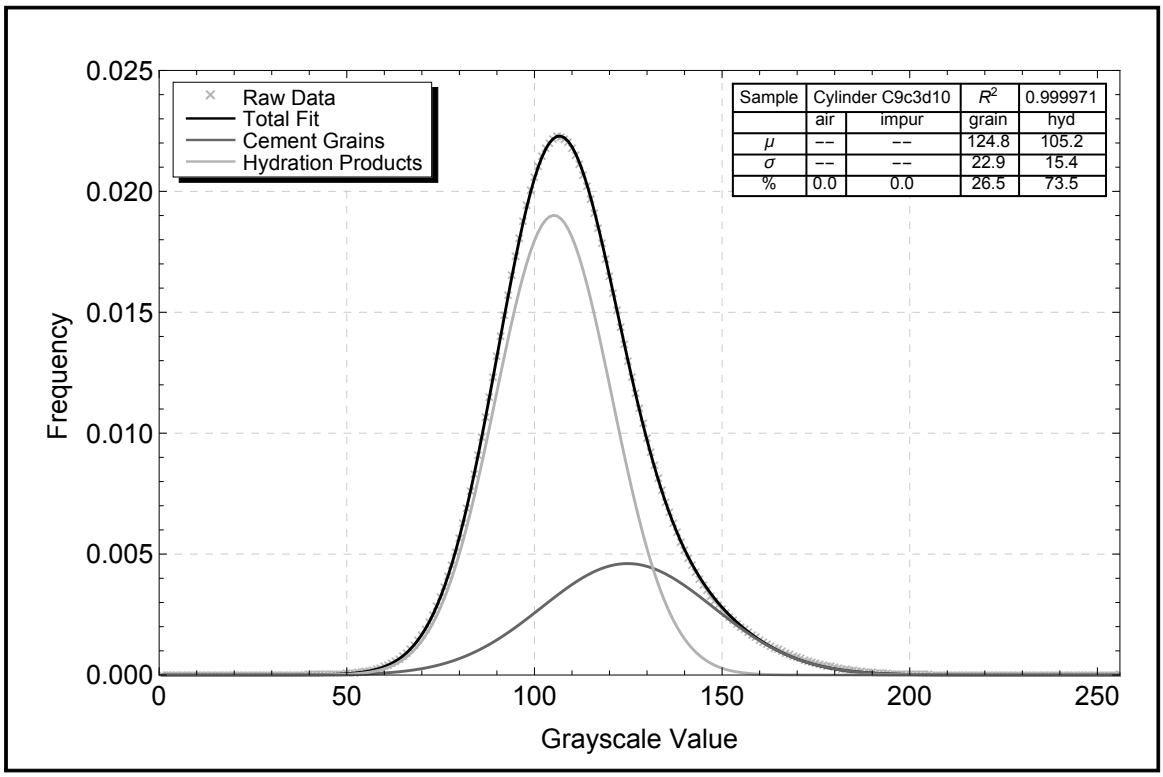

Sample	Cylinder C9c3d10		R^2	0.999971
	air	impur	grain	hyd
μ	--	--	124.8	105.2
σ	--	--	22.9	15.4
%	0.0	0.0	26.5	73.5

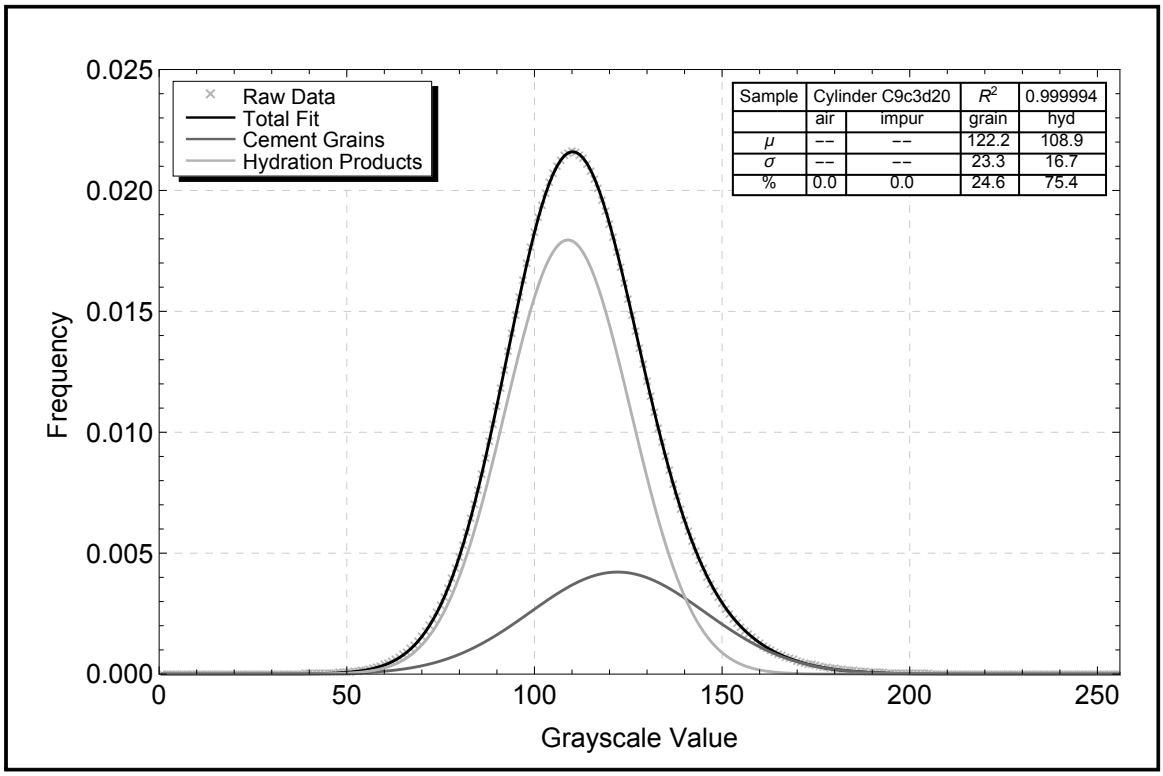

Sample	Cylinder C9c3d20		R^2	0.999994
	air	impur	grain	hyd
μ	--	--	122.2	108.9
σ	--	--	23.3	16.7
%	0.0	0.0	24.6	75.4

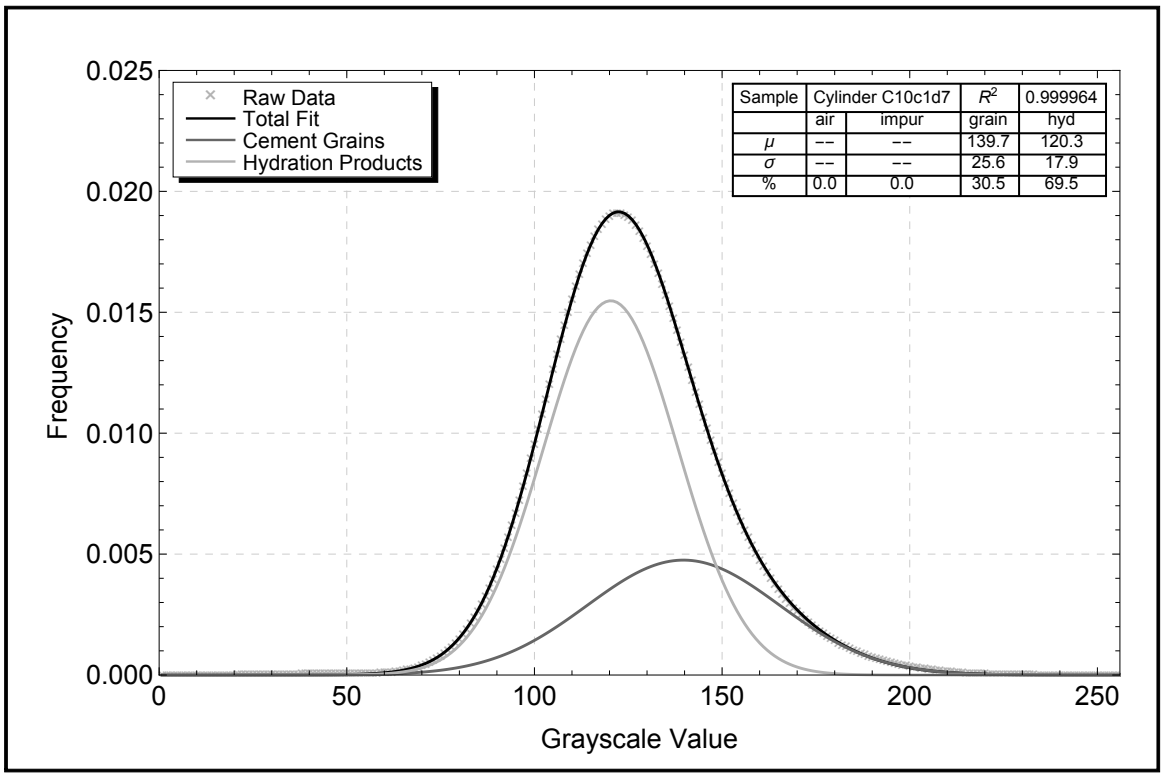

Sample	Cylinder C10c1d7		R^2	0.999964
	air	impur	grain	hyd
μ	--	--	139.7	120.3
σ	--	--	25.6	17.9
%	0.0	0.0	30.5	69.5

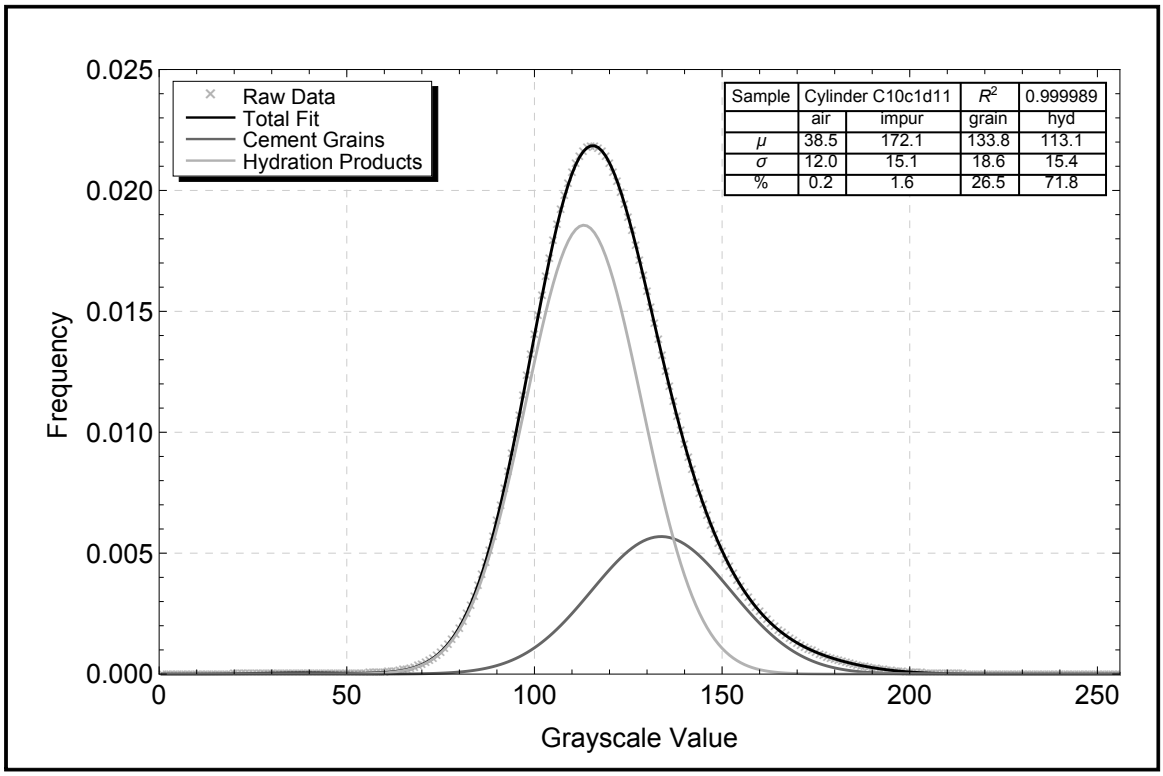
Raw Data
Total Fit
Cement Grains
Hydration Products
Sample | Cylinder C10c1d11 | R^2 | 0.999989
air | impur | grain | hyd
μ | 38.5 | 172.1 | 133.8 | 113.1
σ | 12.0 | 15.1 | 18.6 | 15.4
% | 0.2 | 1.6 | 26.5 | 71.8
Frequency
0.025
0.020
0.015
0.010
0.005
0.000
0
50
100
150
200
250
Grayscale Value

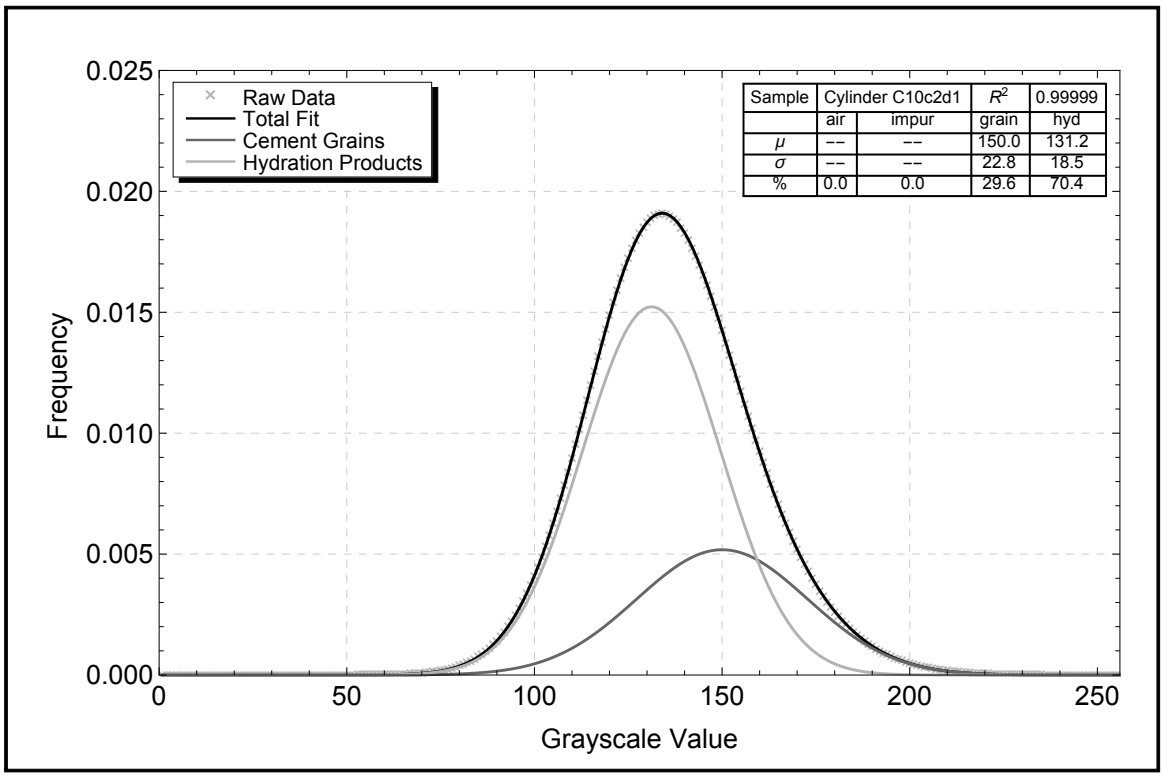
Raw Data
Total Fit
Cement Grains
Hydration Products
Sample | Cylinder C10c2d1 | R^2 | 0.99999
air | impur | grain | hyd
μ | -- | -- | 150.0 | 131.2
σ | -- | -- | 22.8 | 18.5
% | 0.0 | 0.0 | 29.6 | 70.4
Frequency
0.025
0.020
0.015
0.010
0.005
0.000
0
50
100
150
200
250
Grayscale Value

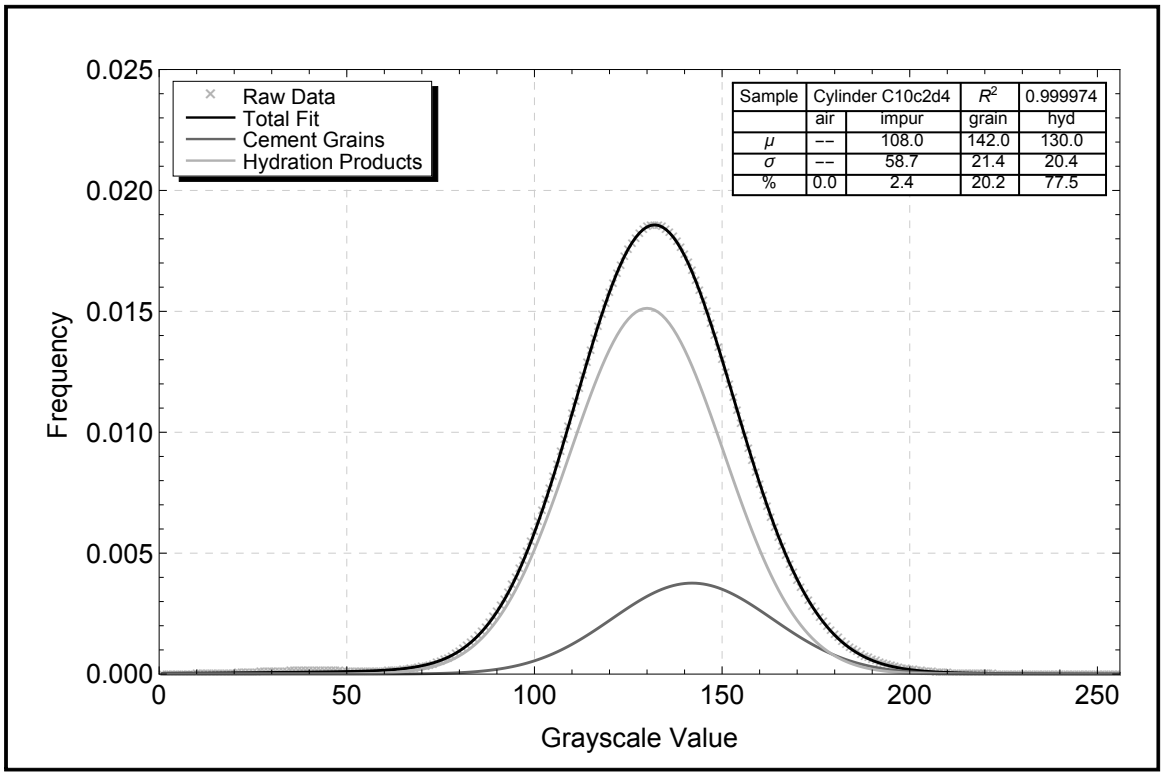
Raw Data
Total Fit
Cement Grains
Hydration Products
Sample | Cylinder C10c2d4 | R^2 | 0.999974
air | impur | grain | hyd
μ | -- | 108.0 | 142.0 | 130.0
σ | -- | 58.7 | 21.4 | 20.4
% | 0.0 | 2.4 | 20.2 | 77.5
Frequency
0.025
0.020
0.015
0.010
0.005
0.000
0
50
100
150
200
250
Grayscale Value

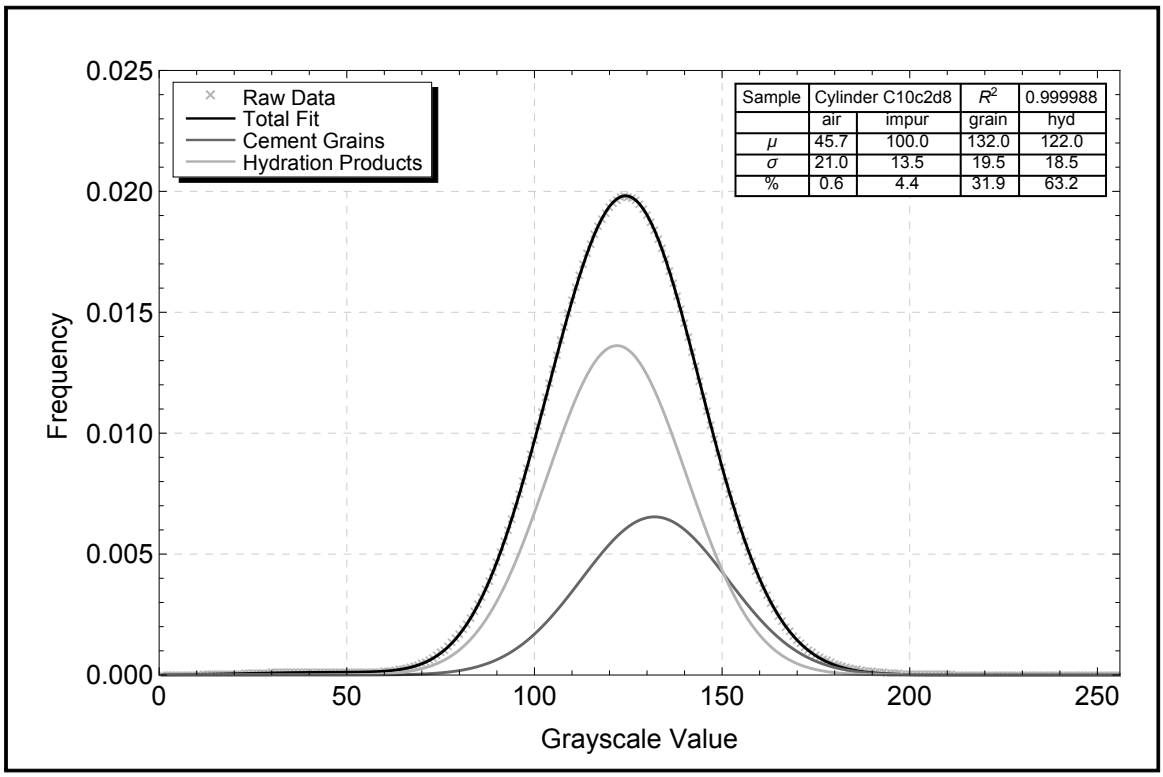
Raw Data
Total Fit
Cement Grains
Hydration Products
Sample | Cylinder C10c2d8 | R^2 | 0.999988
air | impur | grain | hyd
μ | 45.7 | 100.0 | 132.0 | 122.0
σ | 21.0 | 13.5 | 19.5 | 18.5
% | 0.6 | 4.4 | 31.9 | 63.2
Frequency
0.025
0.020
0.015
0.010
0.005
0.000
0
50
100
150
200
250
Grayscale Value

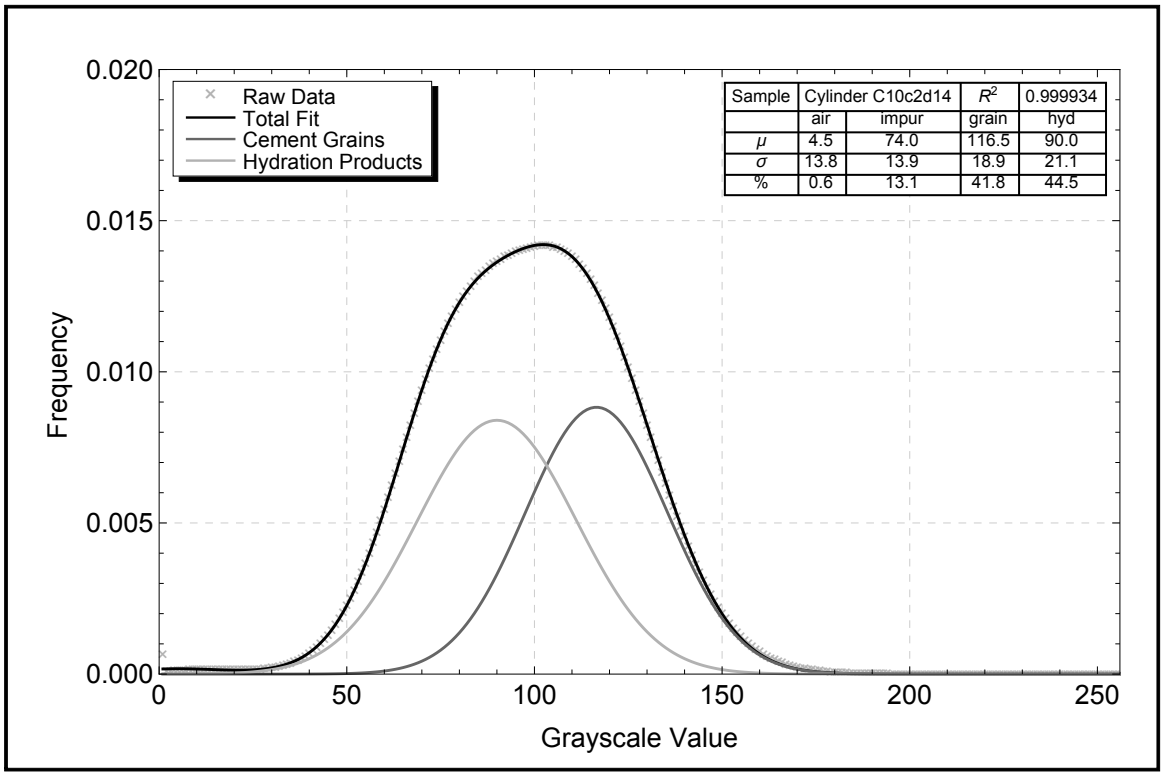
Raw Data
Total Fit
Cement Grains
Hydration Products
Sample | Cylinder C10c2d14 | R^2 | 0.999934
air | impur | grain | hyd
μ | 4.5 | 74.0 | 116.5 | 90.0
σ | 13.8 | 13.9 | 18.9 | 21.1
% | 0.6 | 13.1 | 41.8 | 44.5
Frequency
0.020
0.015
0.010
0.005
0.000
0
50
100
150
200
250
Grayscale Value

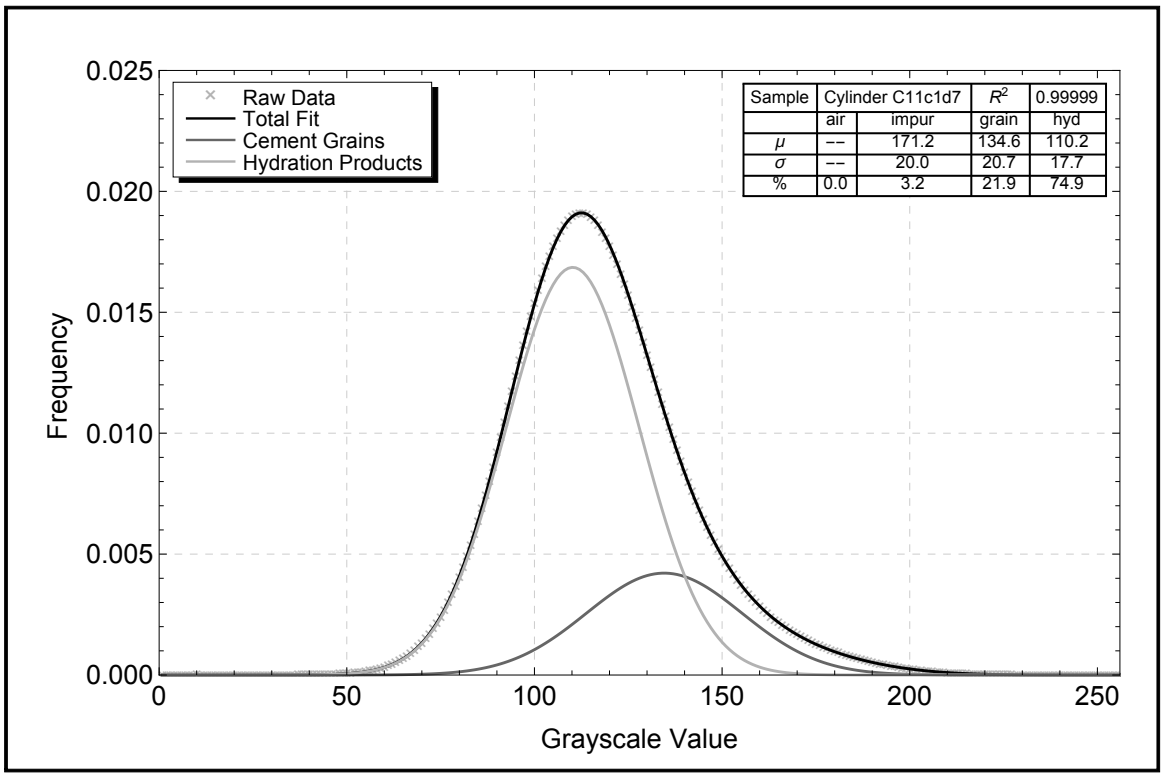
Raw Data
Total Fit
Cement Grains
Hydration Products
Sample | Cylinder C11c1d7 | R^2 | 0.99999
air | impur | grain | hyd
μ | -- | 171.2 | 134.6 | 110.2
σ | -- | 20.0 | 20.7 | 17.7
% | 0.0 | 3.2 | 21.9 | 74.9
Frequency
0.025
0.020
0.015
0.010
0.005
0.000
0
50
100
150
200
250
Grayscale Value

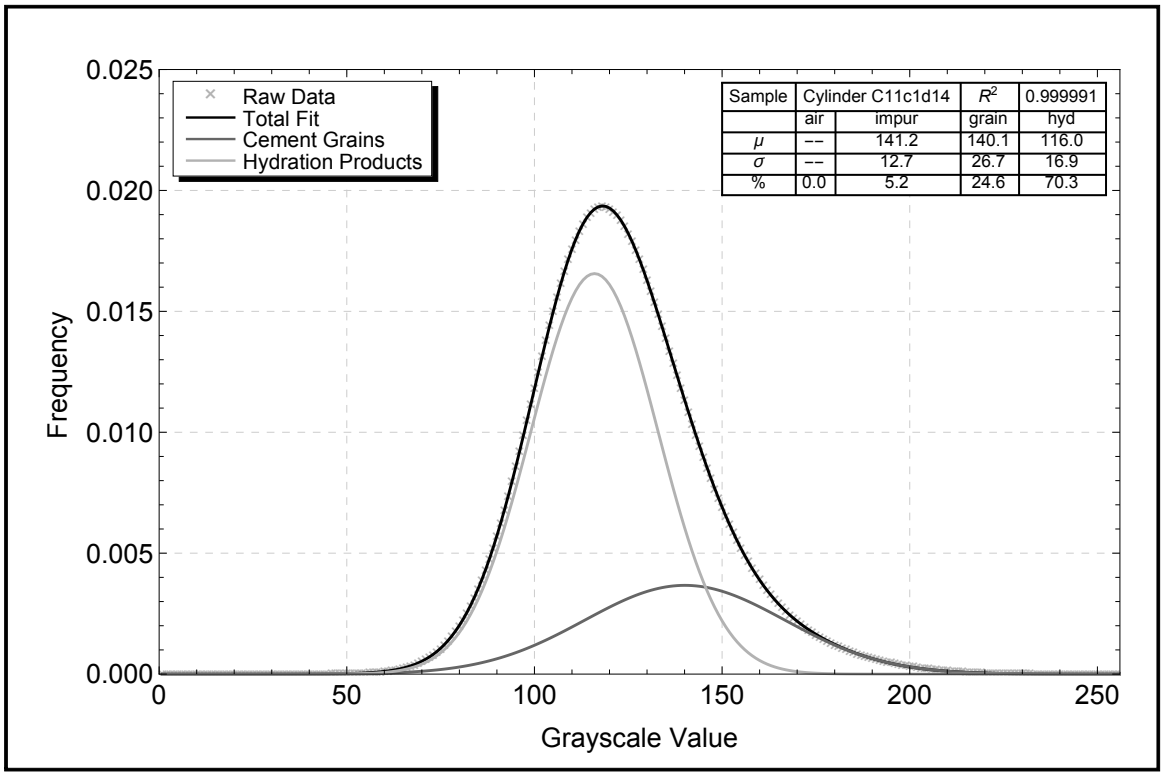
Raw Data
Total Fit
Cement Grains
Hydration Products
Sample | Cylinder C11c1d14 | R^2 | 0.999991
air | impur | grain | hyd
μ | -- | 141.2 | 140.1 | 116.0
σ | -- | 12.7 | 26.7 | 16.9
% | 0.0 | 5.2 | 24.6 | 70.3
Frequency
0.025
0.020
0.015
0.010
0.005
0.000
0
50
100
150
200
250
Grayscale Value

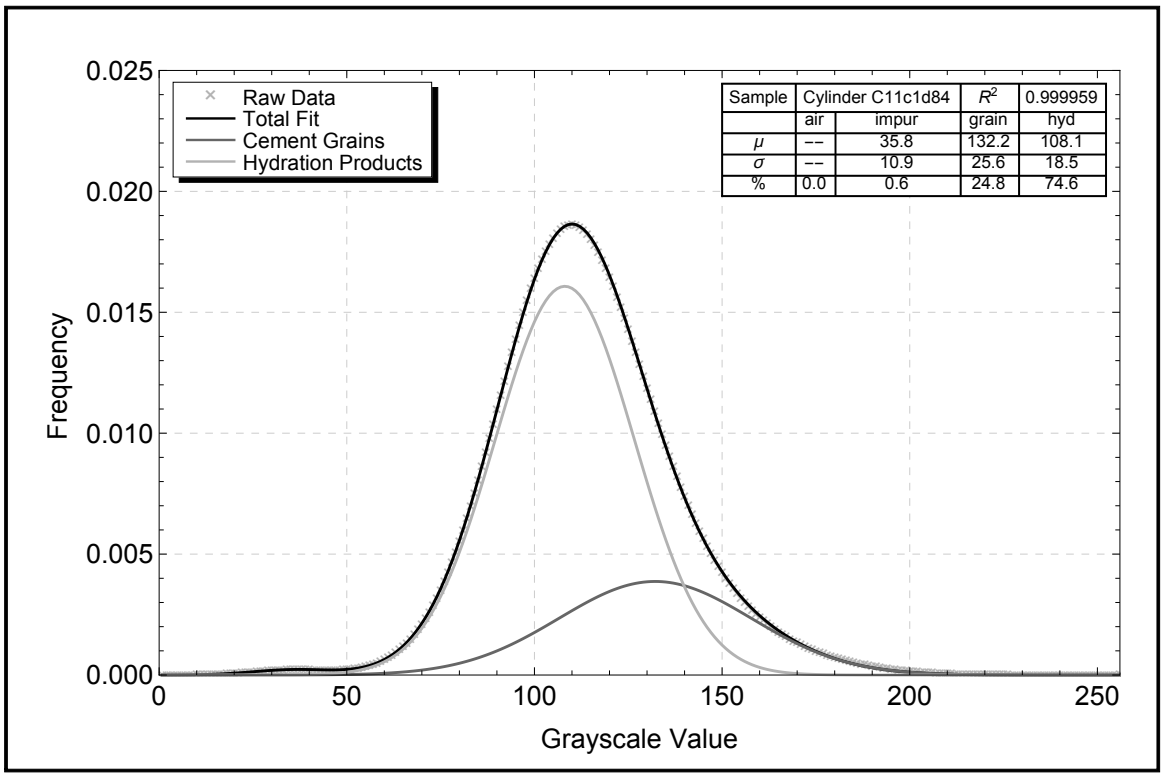
Raw Data
Total Fit
Cement Grains
Hydration Products
Sample | Cylinder C11c1d84 | R^2 | 0.999959
air | impur | grain | hyd
μ | -- | 35.8 | 132.2 | 108.1
σ | -- | 10.9 | 25.6 | 18.5
% | 0.0 | 0.6 | 24.8 | 74.6
Frequency
0.025
0.020
0.015
0.010
0.005
0.000
0
50
100
150
200
250
Grayscale Value

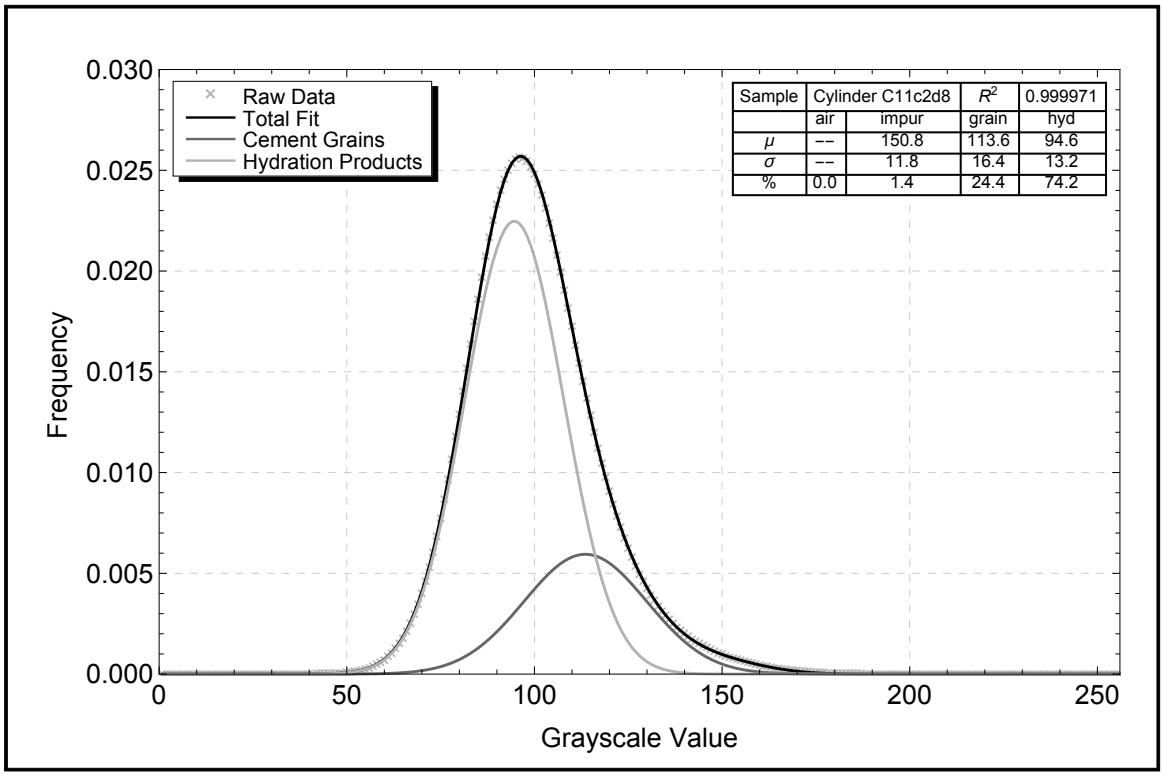
Raw Data
Total Fit
Cement Grains
Hydration Products
Sample | Cylinder C11c2d8 | R^2 | 0.999971
air | impur | grain | hyd
μ | -- | 150.8 | 113.6 | 94.6
σ | -- | 11.8 | 16.4 | 13.2
% | 0.0 | 1.4 | 24.4 | 74.2
Frequency
0.030
0.025
0.020
0.015
0.010
0.005
0.000
0
50
100
150
200
250
Grayscale Value

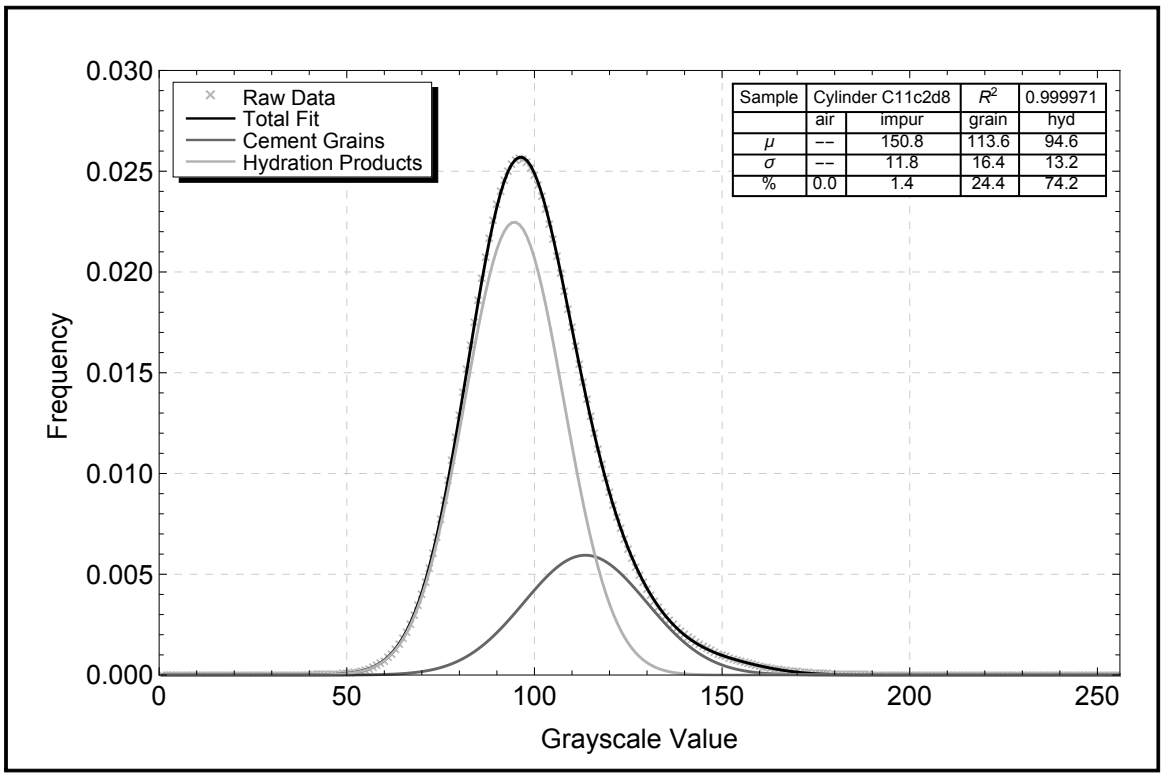
Raw Data
Total Fit
Cement Grains
Hydration Products
Sample | Cylinder C11c2d8 | R^2 | 0.999971
air | impur | grain | hyd
μ | -- | 150.8 | 113.6 | 94.6
σ | -- | 11.8 | 16.4 | 13.2
% | 0.0 | 1.4 | 24.4 | 74.2
Frequency
0.030
0.025
0.020
0.015
0.010
0.005
0.000
0
50
100
150
200
250
Grayscale Value

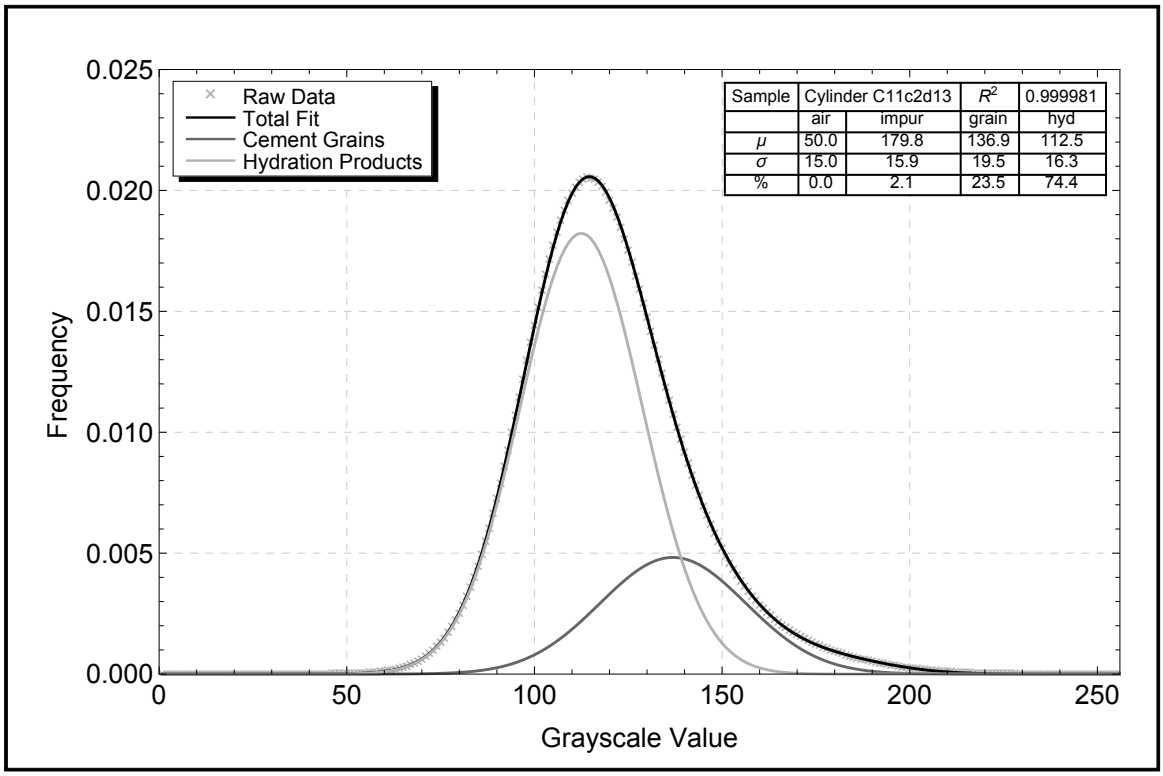
Raw Data
Total Fit
Cement Grains
Hydration Products
Sample | Cylinder C11c2d13 | R^2 | 0.999981
air | impur | grain | hyd
μ | 50.0 | 179.8 | 136.9 | 112.5
σ | 15.0 | 15.9 | 19.5 | 16.3
% | 0.0 | 2.1 | 23.5 | 74.4
Frequency
0.025
0.020
0.015
0.010
0.005
0.000
0
50
100
150
200
250
Grayscale Value

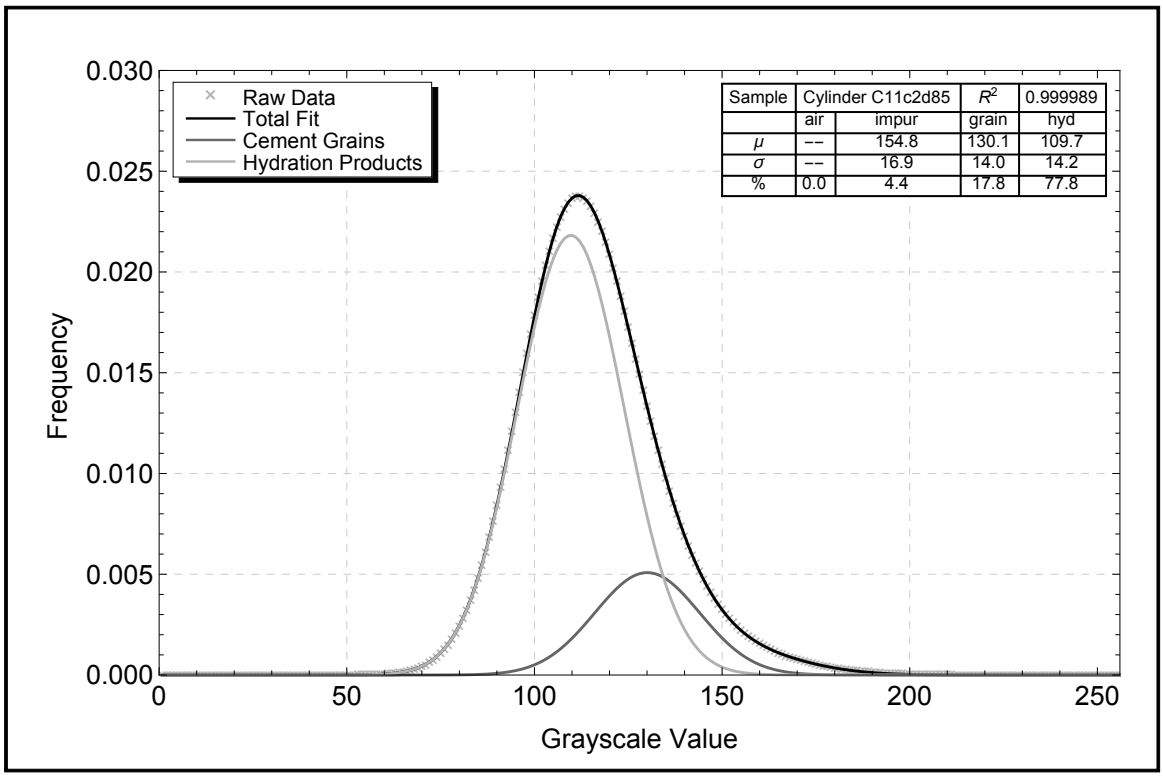
Raw Data
Total Fit
Cement Grains
Hydration Products
Sample | Cylinder C11c2d85 | R^2 | 0.999989
air | impur | grain | hyd
μ | -- | 154.8 | 130.1 | 109.7
σ | -- | 16.9 | 14.0 | 14.2
% | 0.0 | 4.4 | 17.8 | 77.8
Frequency
0.030
0.025
0.020
0.015
0.010
0.005
0.000
0
50
100
150
200
250
Grayscale Value

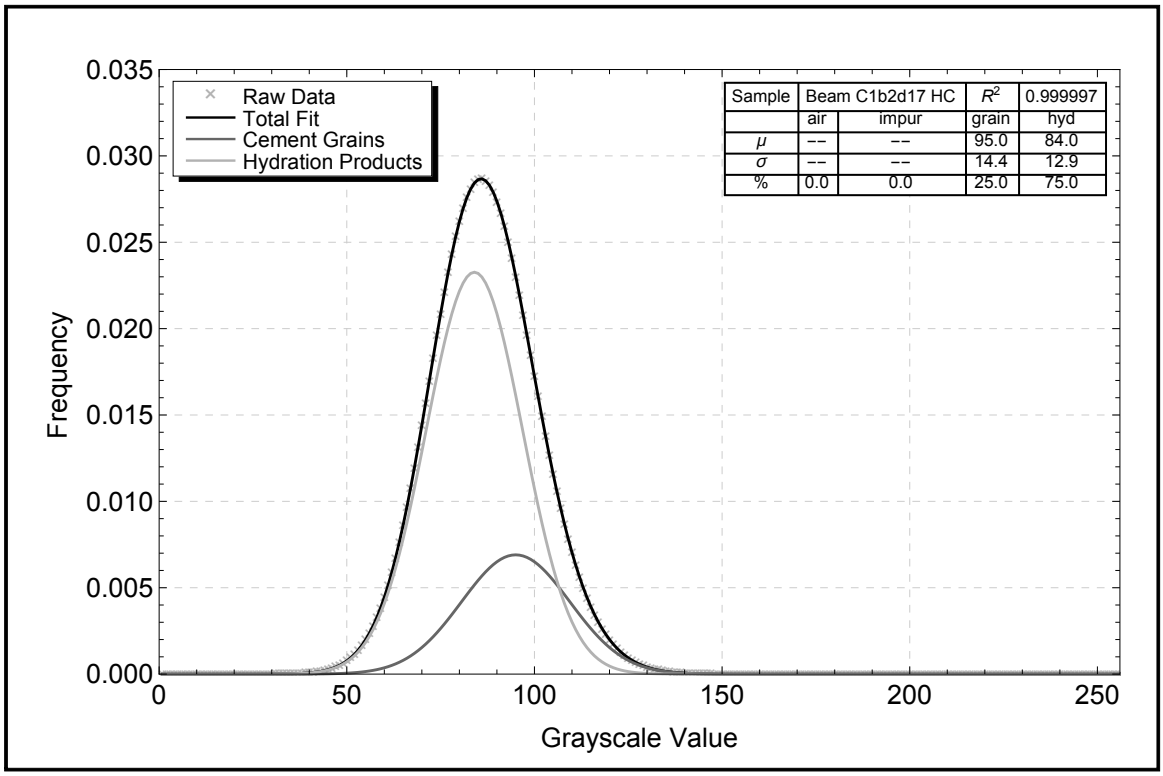

Sample	Beam C1b2d17 HC		R^2	0.999997
	air	impur	grain	hyd
μ	--	--	95.0	84.0
σ	--	--	14.4	12.9
%	0.0	0.0	25.0	75.0

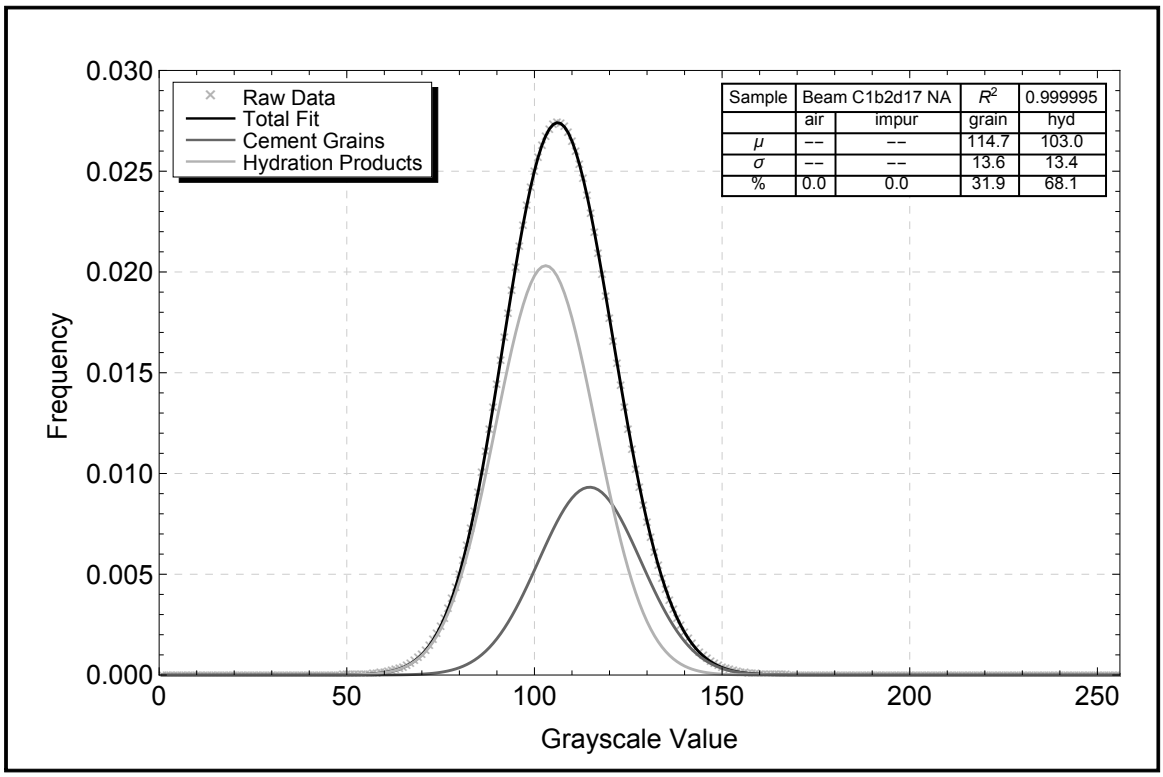

Sample	Beam C1b2d17 NA		R^2	0.999995
	air	impur	grain	hyd
μ	--	--	114.7	103.0
σ	--	--	13.6	13.4
%	0.0	0.0	31.9	68.1

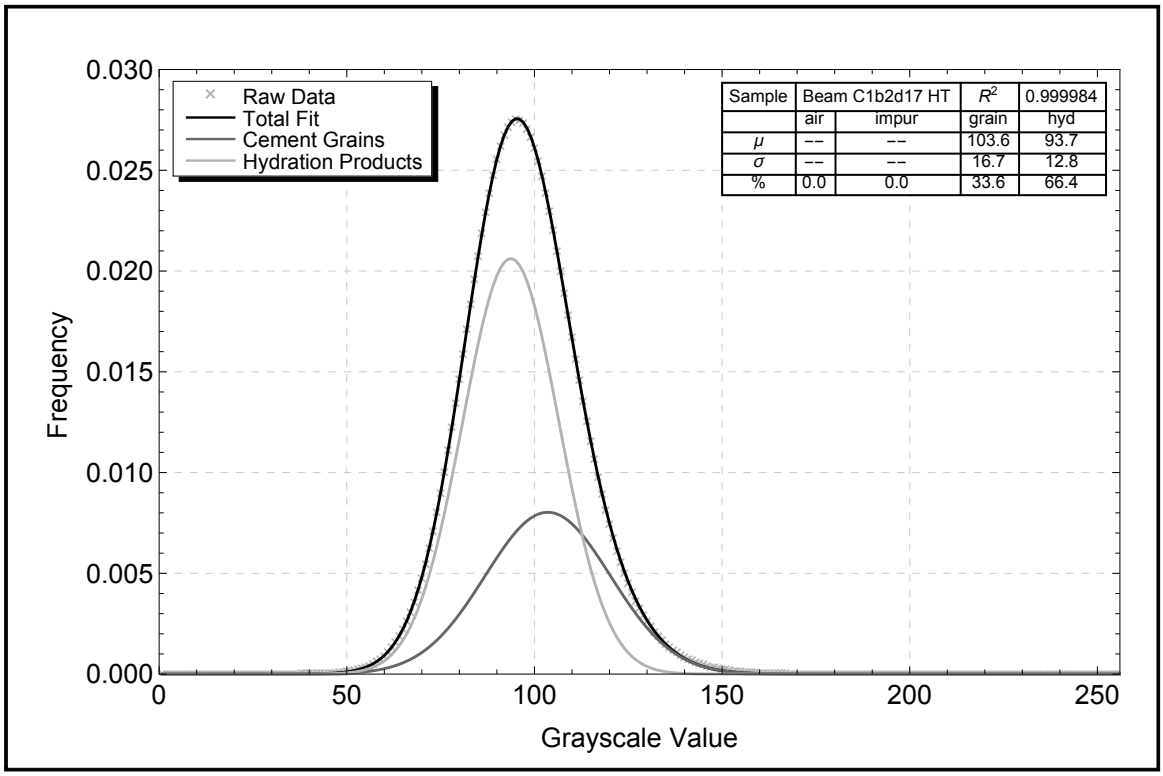

Sample	Beam C1b2d17 HT		R^2	0.999984
	air	impur	grain	hyd
μ	--	--	103.6	93.7
σ	--	--	16.7	12.8
%	0.0	0.0	33.6	66.4

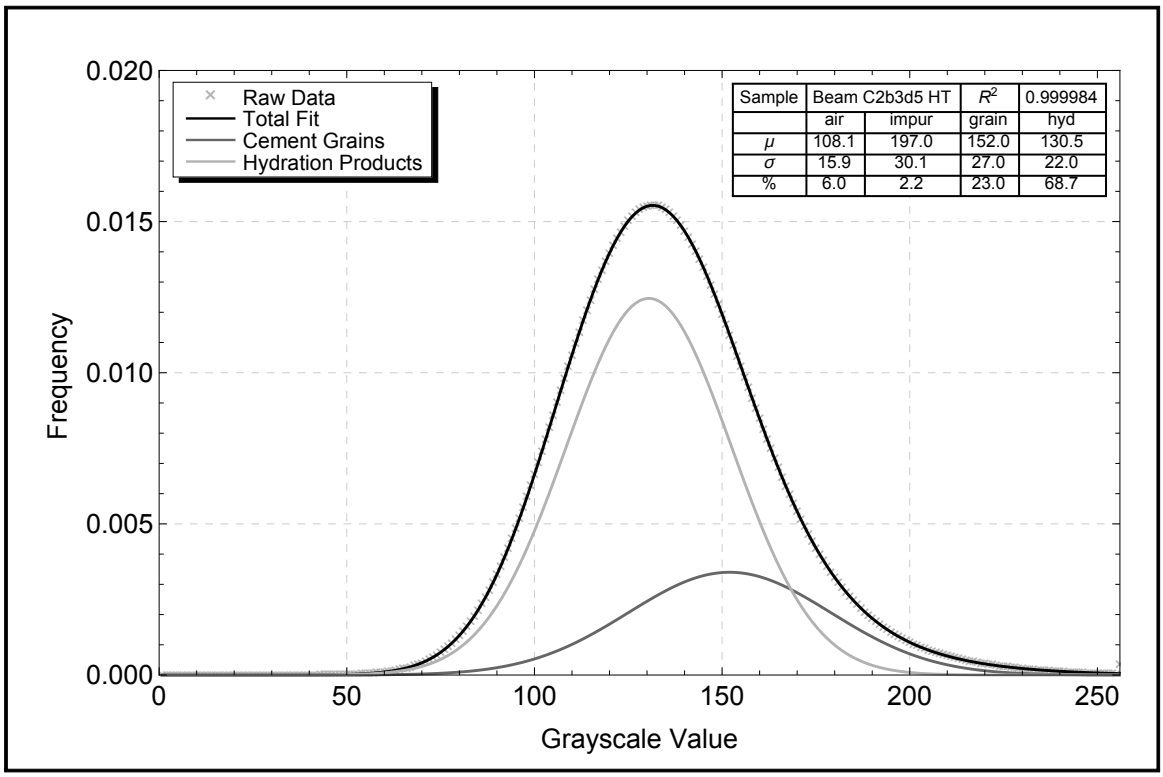

Sample	Beam C2b3d5 HT		R^2	0.999984
	air	impur	grain	hyd
μ	108.1	197.0	152.0	130.5
σ	15.9	30.1	27.0	22.0
%	6.0	2.2	23.0	68.7

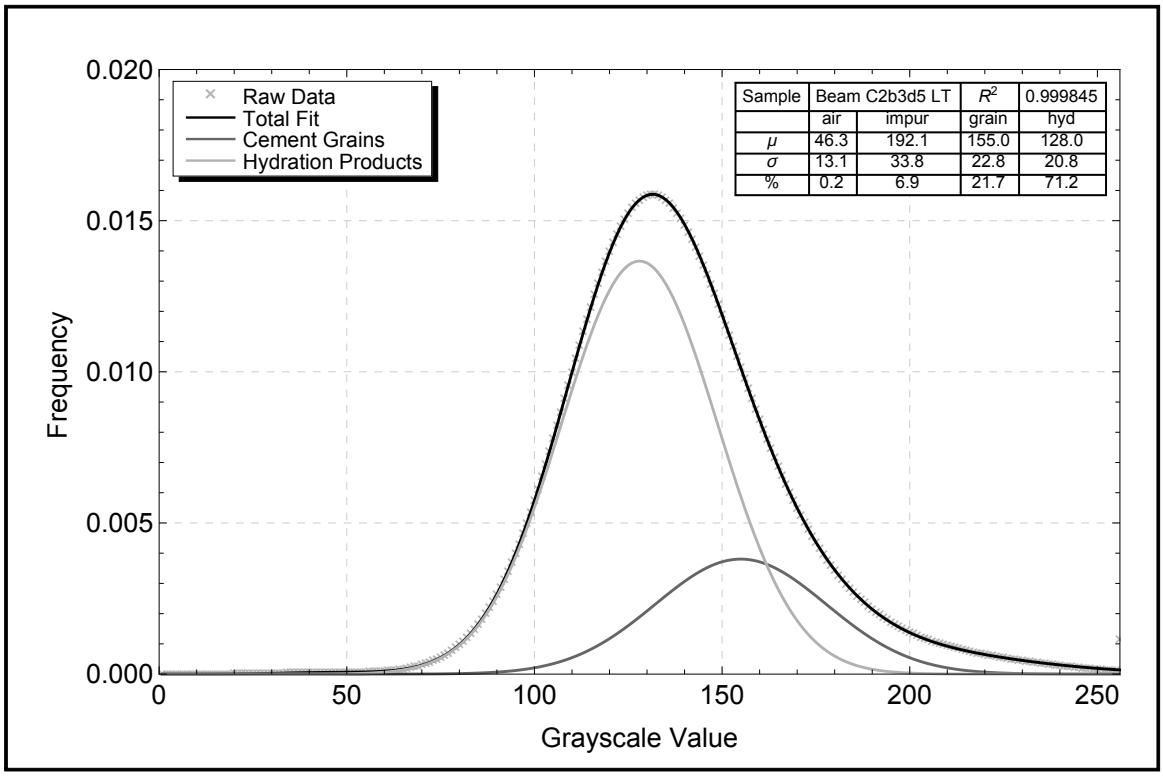

Sample	Beam C2b3d5 LT		R^2	0.999845
	air	impur	grain	hyd
μ	46.3	192.1	155.0	128.0
σ	13.1	33.8	22.8	20.8
%	0.2	6.9	21.7	71.2

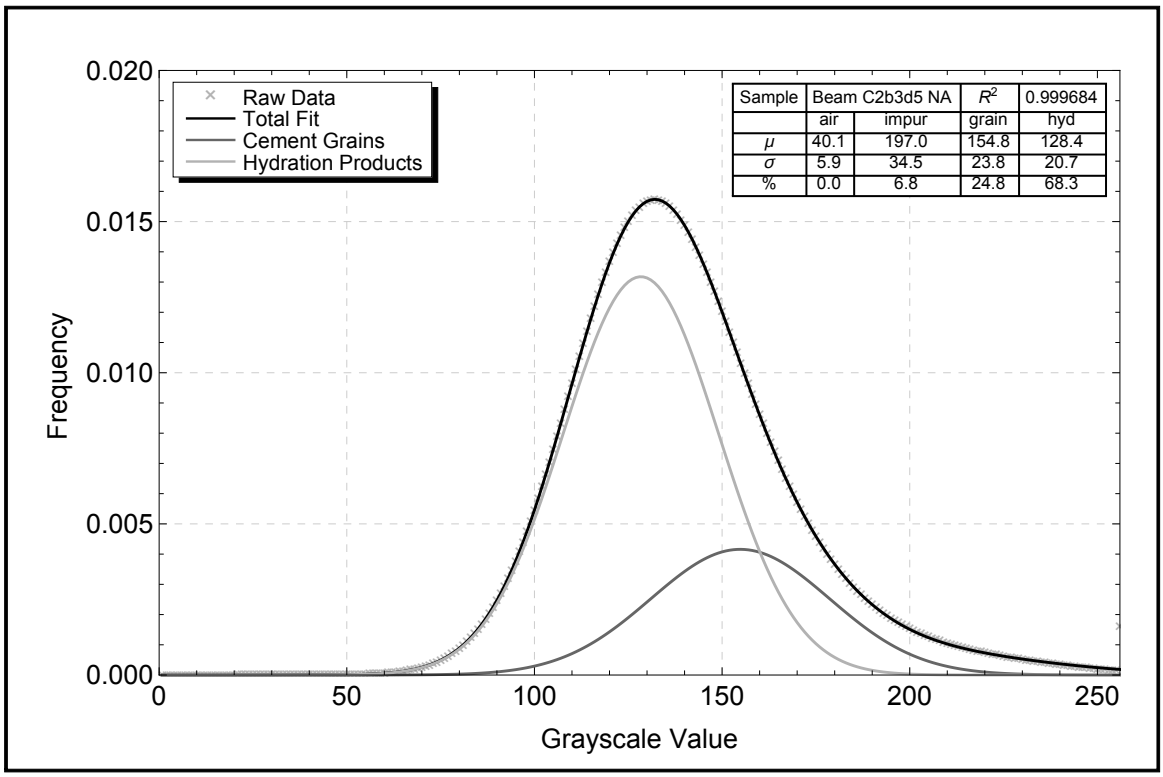

Sample	Beam C2b3d5 NA		R^2	0.999684
	air	impur	grain	hyd
μ	40.1	197.0	154.8	128.4
σ	5.9	34.5	23.8	20.7
%	0.0	6.8	24.8	68.3

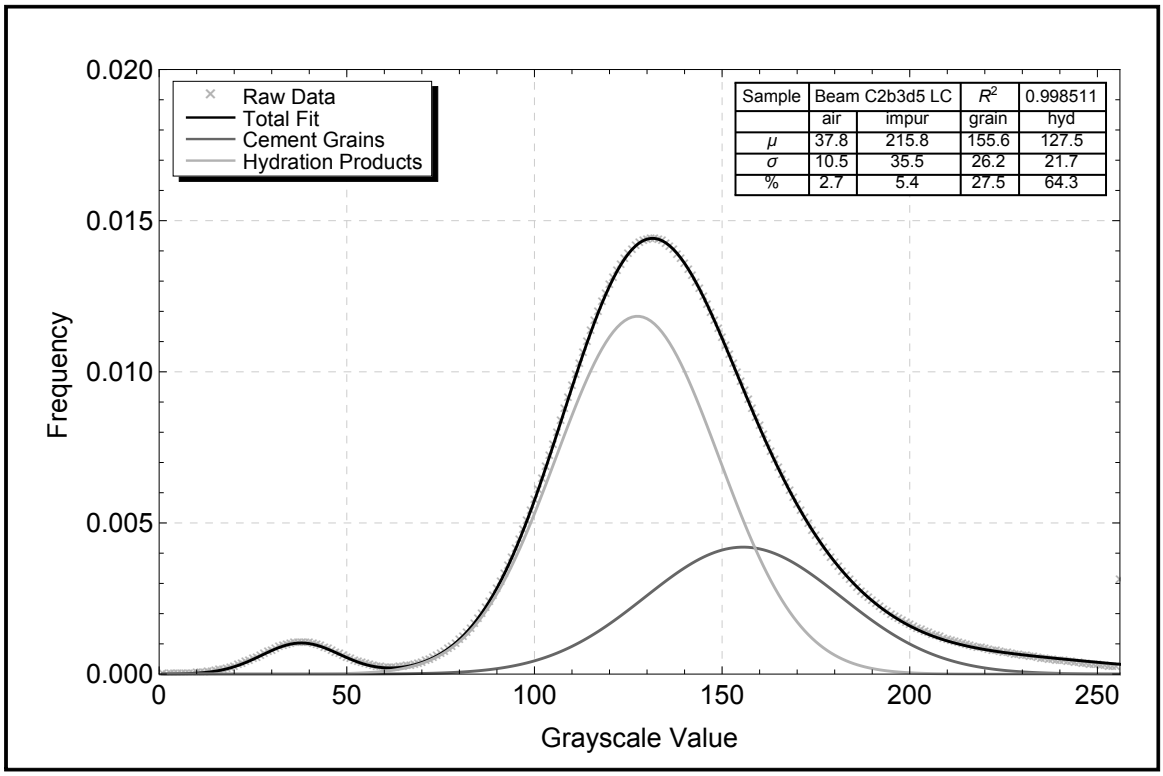
Raw Data
Total Fit
Cement Grains
Hydration Products
Sample | Beam C2b3d5 LC | R^2 | 0.998511
air | impur | grain | hyd
μ | 37.8 | 215.8 | 155.6 | 127.5
σ | 10.5 | 35.5 | 26.2 | 21.7
% | 2.7 | 5.4 | 27.5 | 64.3
Frequency
0.020
0.015
0.010
0.005
0.000
0
50
100
150
200
250
Grayscale Value

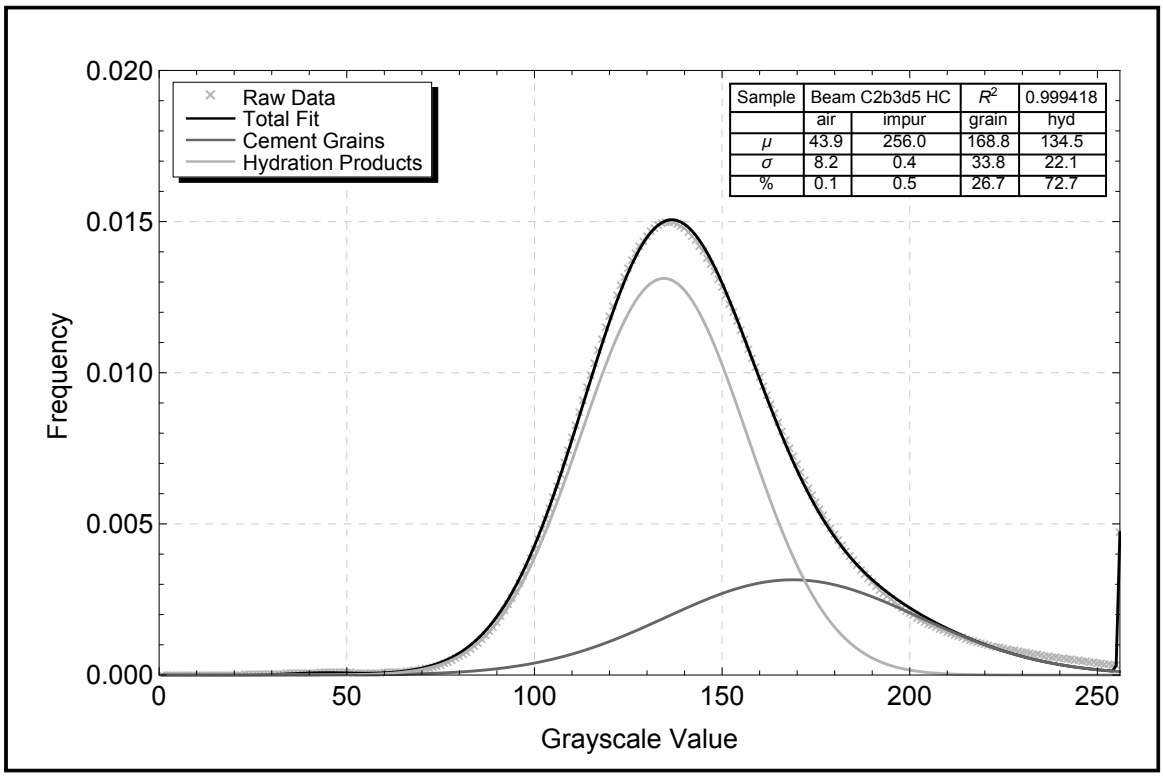
Raw Data
Total Fit
Cement Grains
Hydration Products
Sample | Beam C2b3d5 HC | R^2 | 0.999418
air | impur | grain | hyd
μ | 43.9 | 256.0 | 168.8 | 134.5
σ | 8.2 | 0.4 | 33.8 | 22.1
% | 0.1 | 0.5 | 26.7 | 72.7
Frequency
0.020
0.015
0.010
0.005
0.000
0
50
100
150
200
250
Grayscale Value

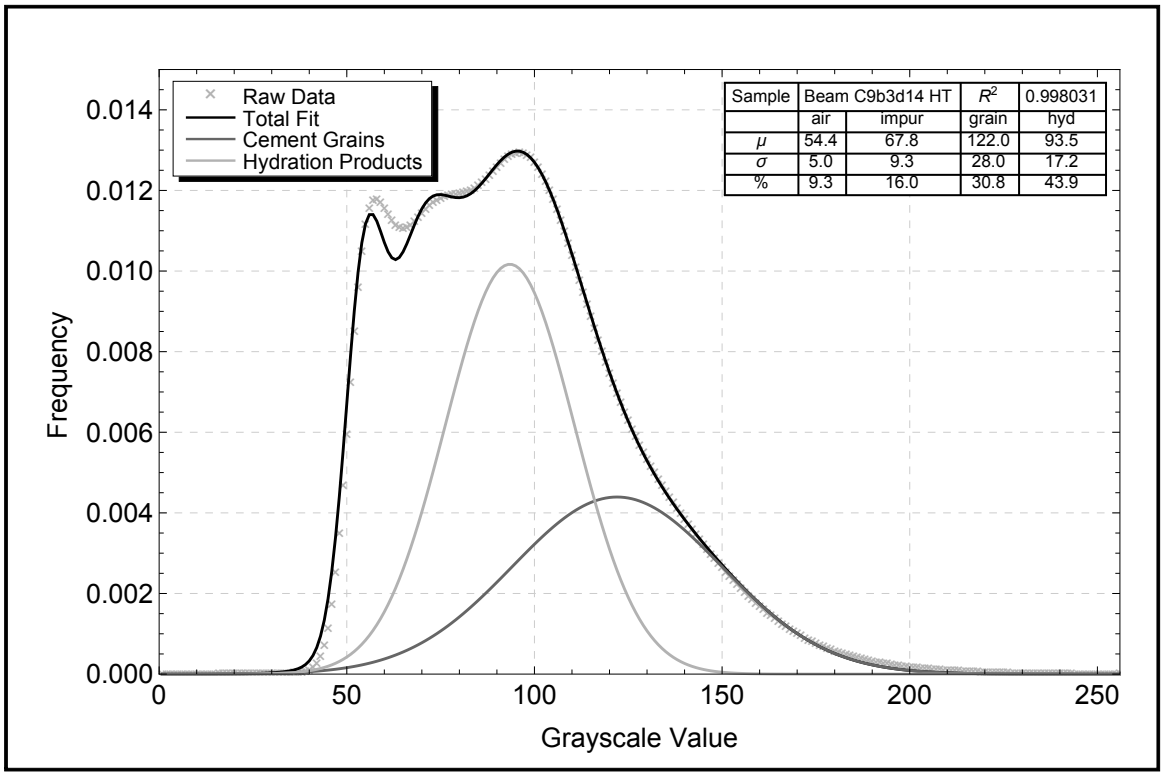

Sample	Beam C9b3d14 HT		R^2	0.998031
	air	impur	grain	hyd
μ	54.4	67.8	122.0	93.5
σ	5.0	9.3	28.0	17.2
%	9.3	16.0	30.8	43.9

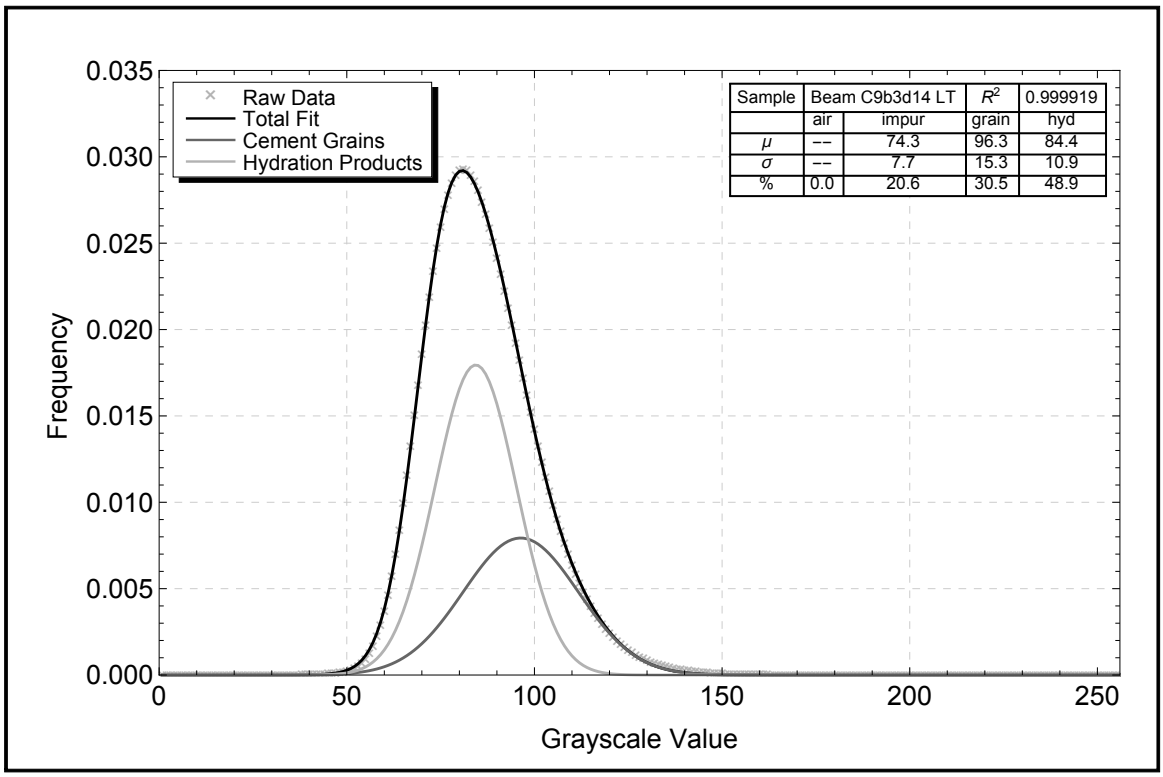

Sample	Beam C9b3d14 LT		R^2	0.999919
	air	impur	grain	hyd
μ	---	74.3	96.3	84.4
σ	---	7.7	15.3	10.9
%	0.0	20.6	30.5	48.9

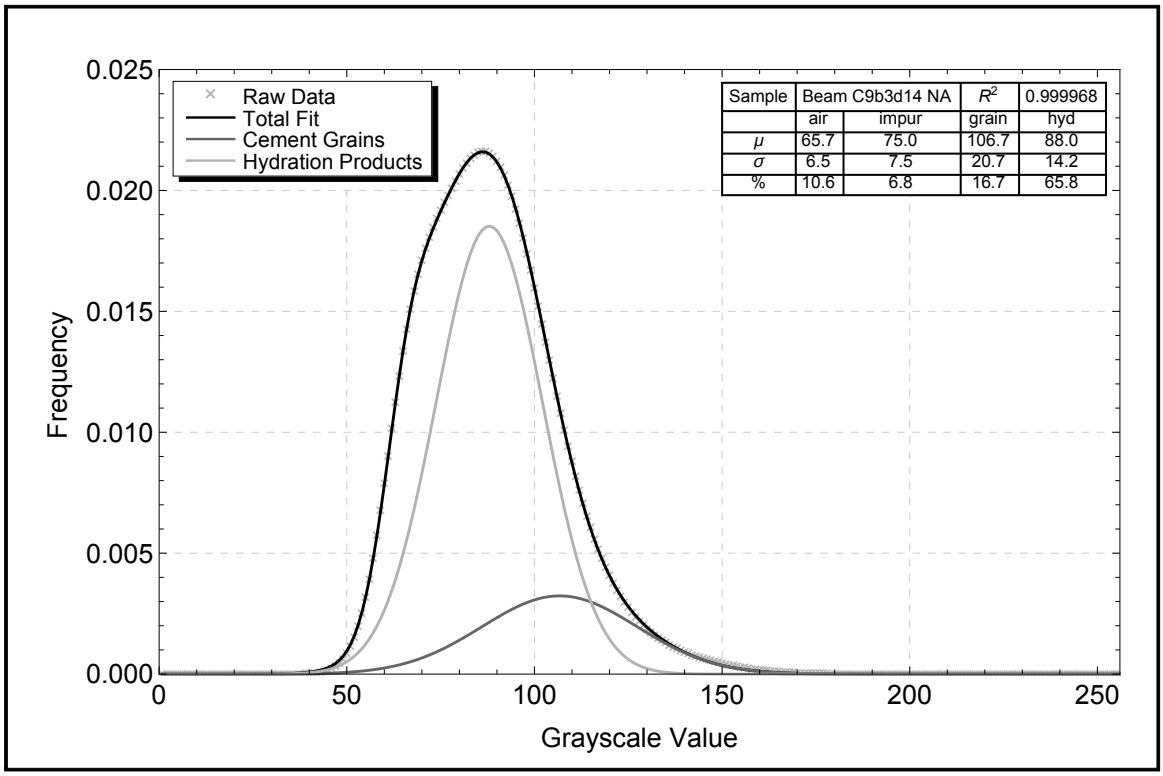

Sample	Beam C9b3d14 NA		R^2	0.999968
	air	impur	grain	hyd
μ	65.7	75.0	106.7	88.0
σ	6.5	7.5	20.7	14.2
%	10.6	6.8	16.7	65.8

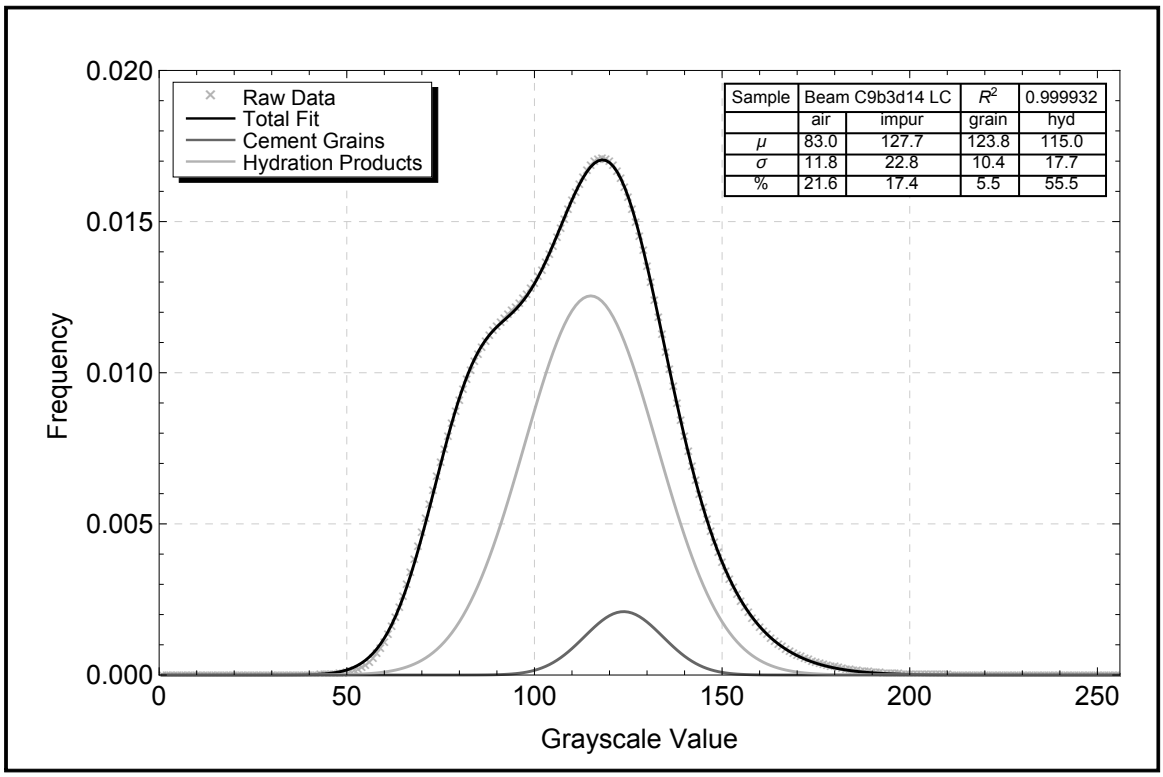

Sample	Beam C9b3d14 LC		R^2	0.999932
	air	impur	grain	hyd
μ	83.0	127.7	123.8	115.0
σ	11.8	22.8	10.4	17.7
%	21.6	17.4	5.5	55.5

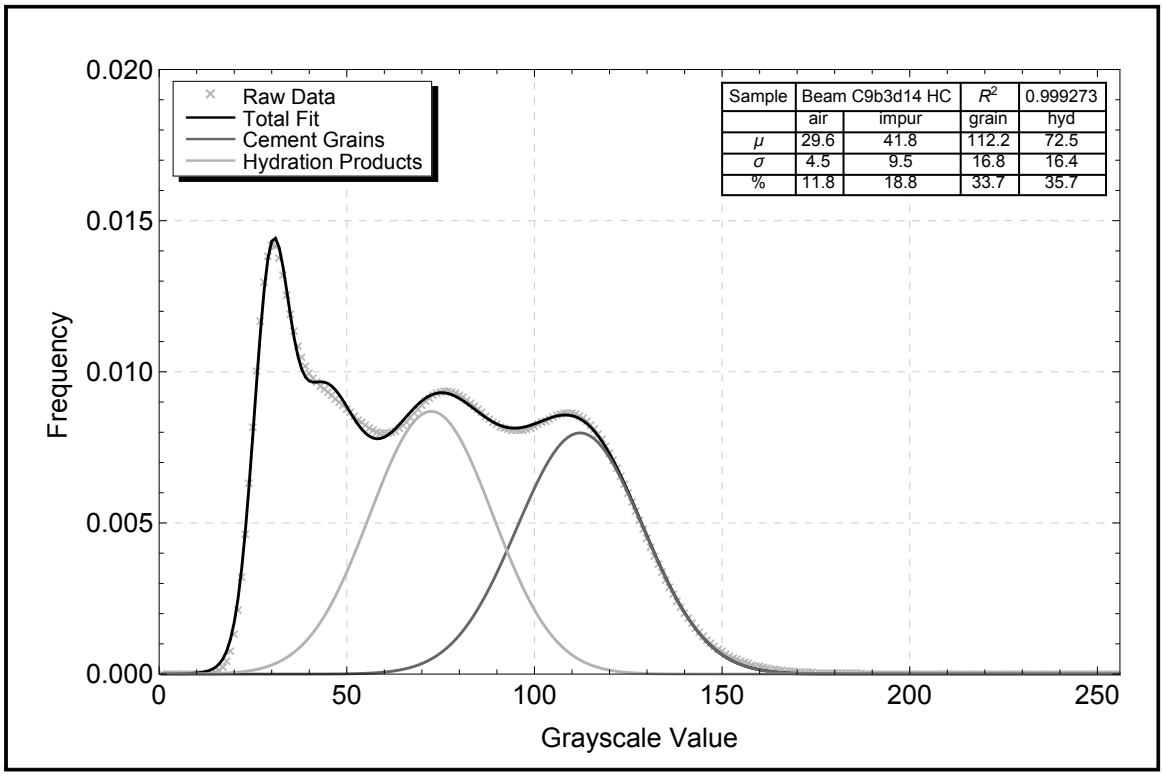

Sample	Beam C9b3d14 HC		R^2	0.999273
	air	impur	grain	hyd
μ	29.6	41.8	112.2	72.5
σ	4.5	9.5	16.8	16.4
%	11.8	18.8	33.7	35.7

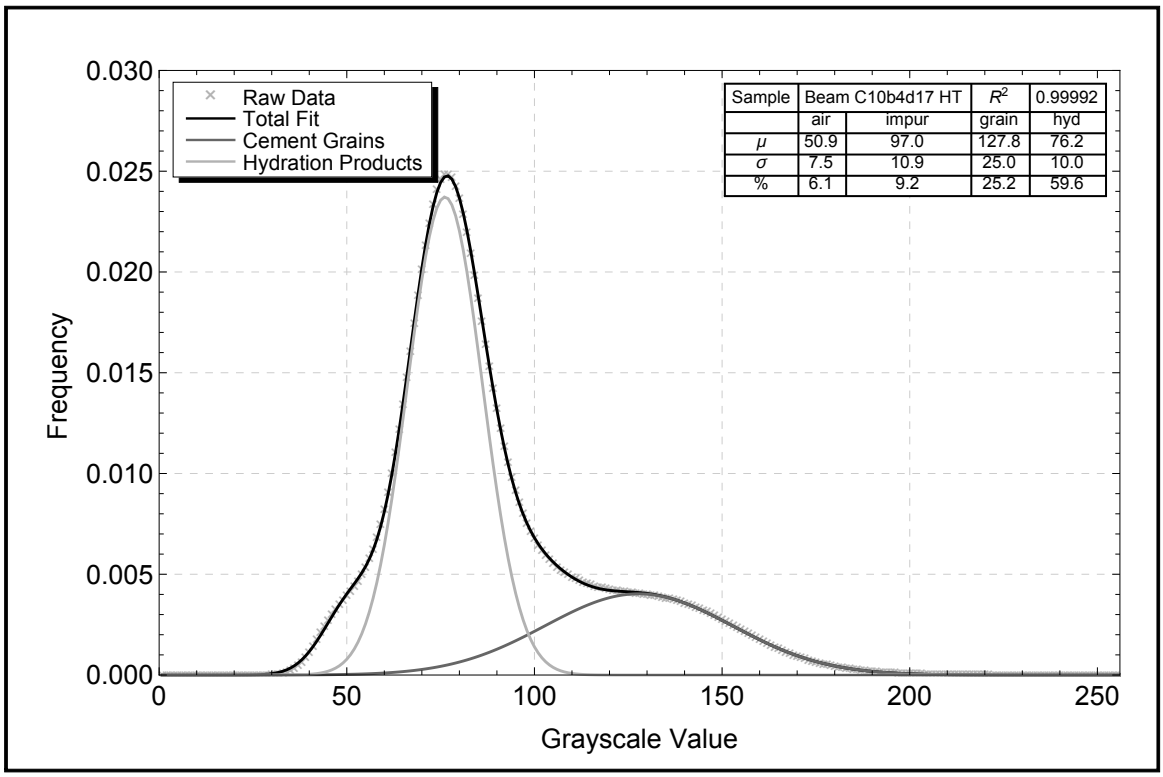

Sample	Beam C10b4d17 HT		R^2	0.99992
	air	impur	grain	hyd
μ	50.9	97.0	127.8	76.2
σ	7.5	10.9	25.0	10.0
%	6.1	9.2	25.2	59.6

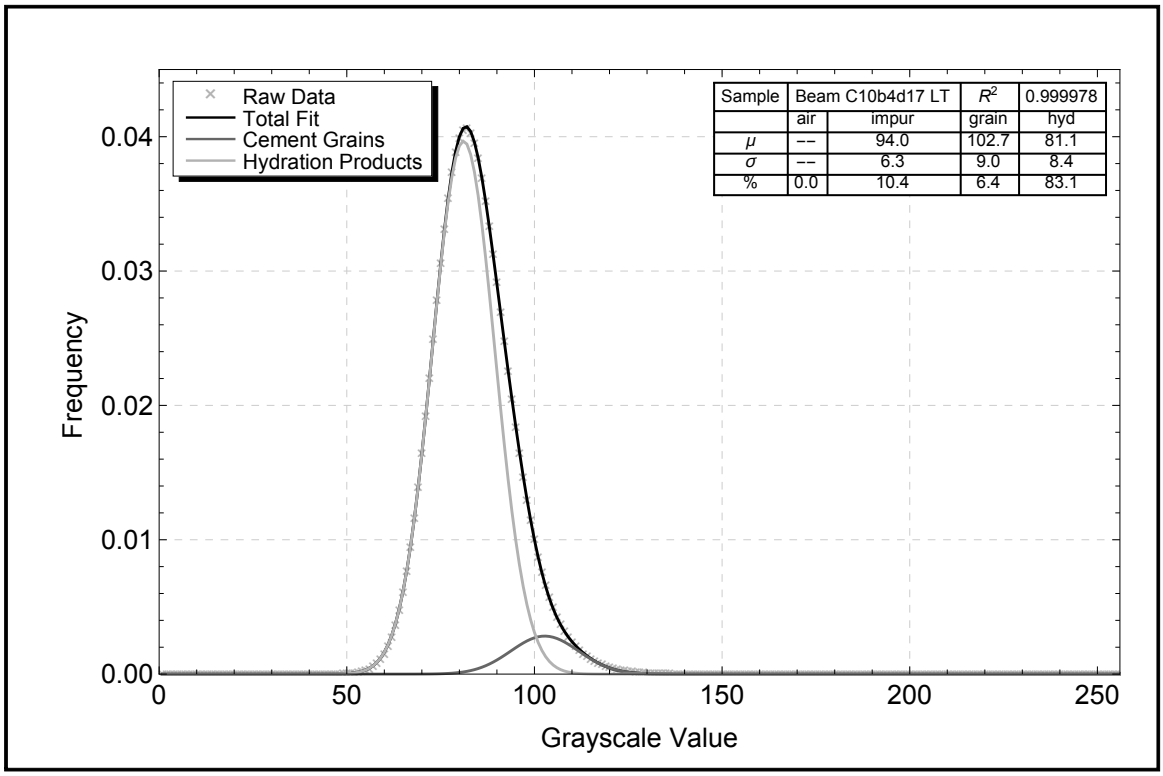
Raw Data
Total Fit
Cement Grains
Hydration Products
Sample | Beam C10b4d17 LT | R^2 | 0.999978
air | impur | grain | hyd
μ | -- | 94.0 | 102.7 | 81.1
σ | -- | 6.3 | 9.0 | 8.4
% | 0.0 | 10.4 | 6.4 | 83.1
Frequency
0.00
0.01
0.02
0.03
0.04
0
50
100
150
200
250
Grayscale Value

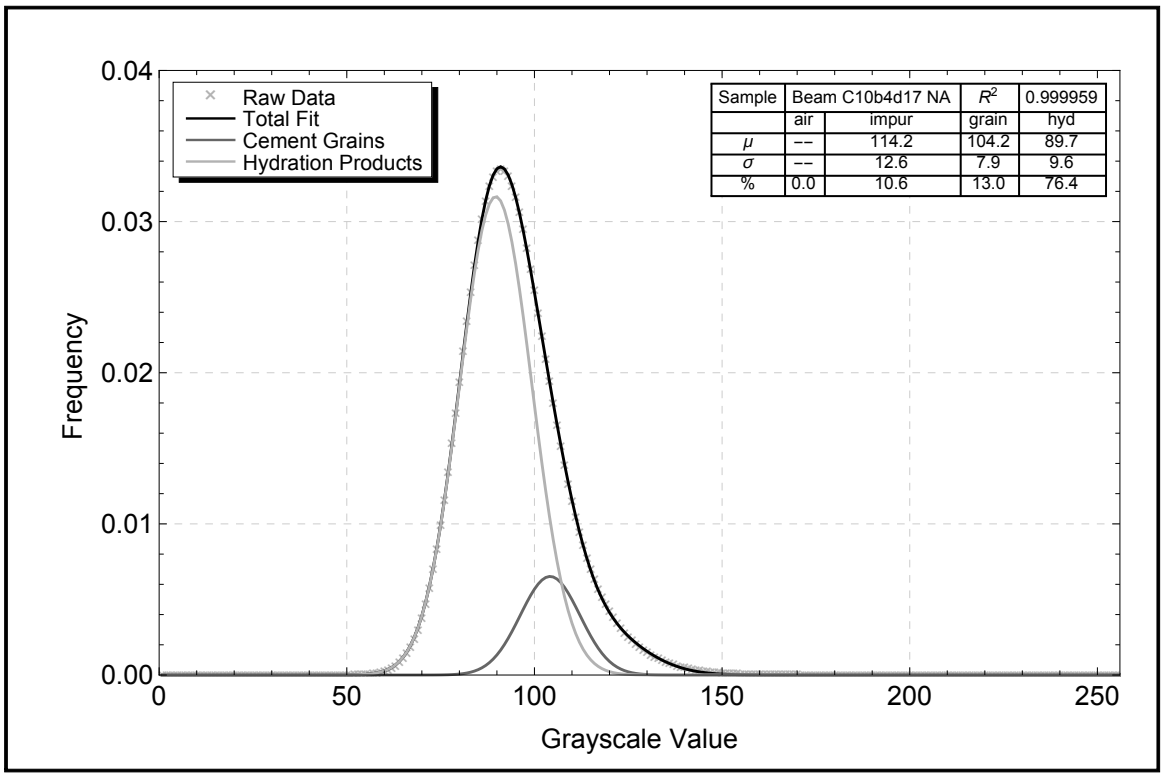
Raw Data
Total Fit
Cement Grains
Hydration Products
Sample | Beam C10b4d17 NA | R^2 | 0.999959
air | impur | grain | hyd
μ | -- | 114.2 | 104.2 | 89.7
σ | -- | 12.6 | 7.9 | 9.6
% | 0.0 | 10.6 | 13.0 | 76.4
Frequency
0.00
0.01
0.02
0.03
0.04
0
50
100
150
200
250
Grayscale Value

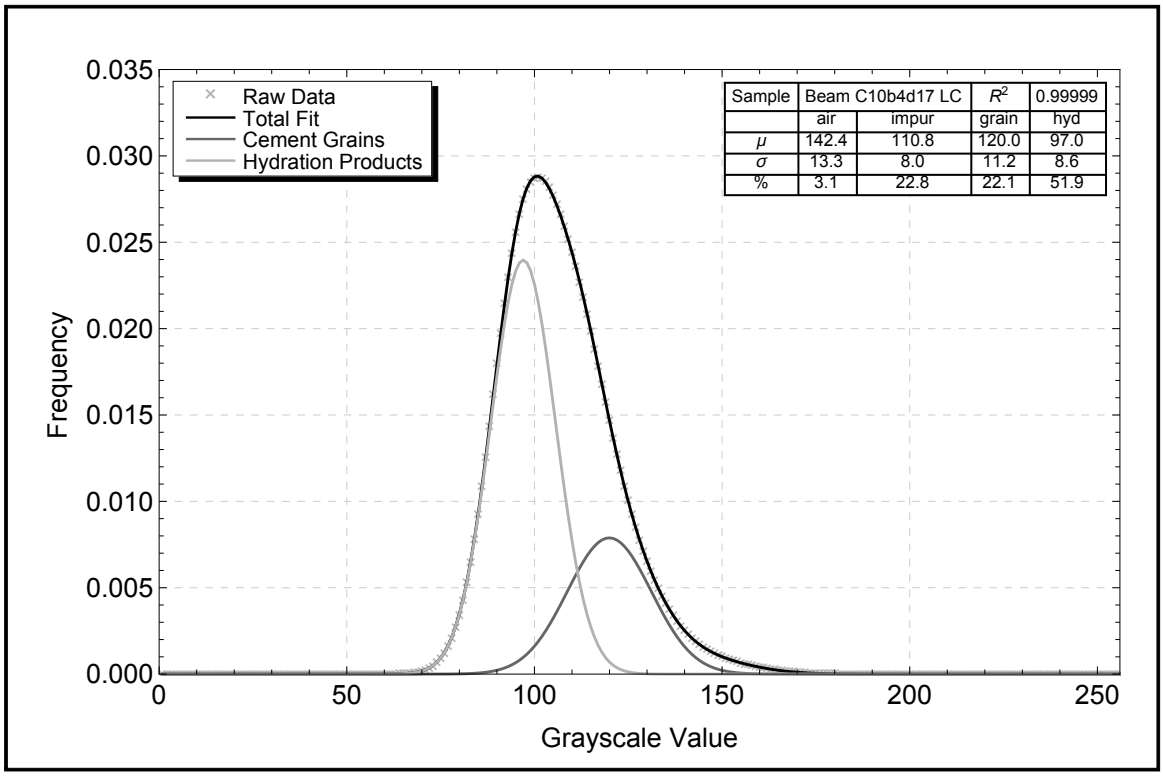

Sample	Beam C10b4d17 LC		R^2	0.99999
	air	impur	grain	hyd
μ	142.4	110.8	120.0	97.0
σ	13.3	8.0	11.2	8.6
%	3.1	22.8	22.1	51.9

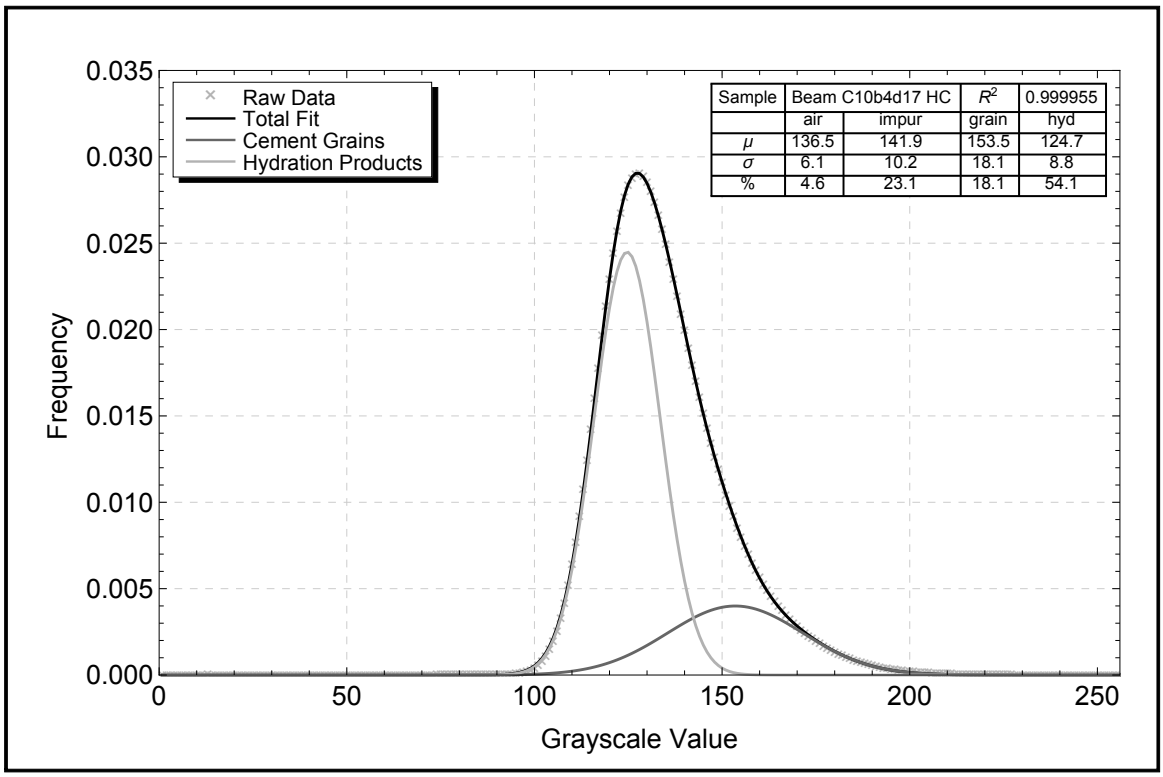

Sample	Beam C10b4d17 HC		R^2	0.999955
	air	impur	grain	hyd
μ	136.5	141.9	153.5	124.7
σ	6.1	10.2	18.1	8.8
%	4.6	23.1	18.1	54.1

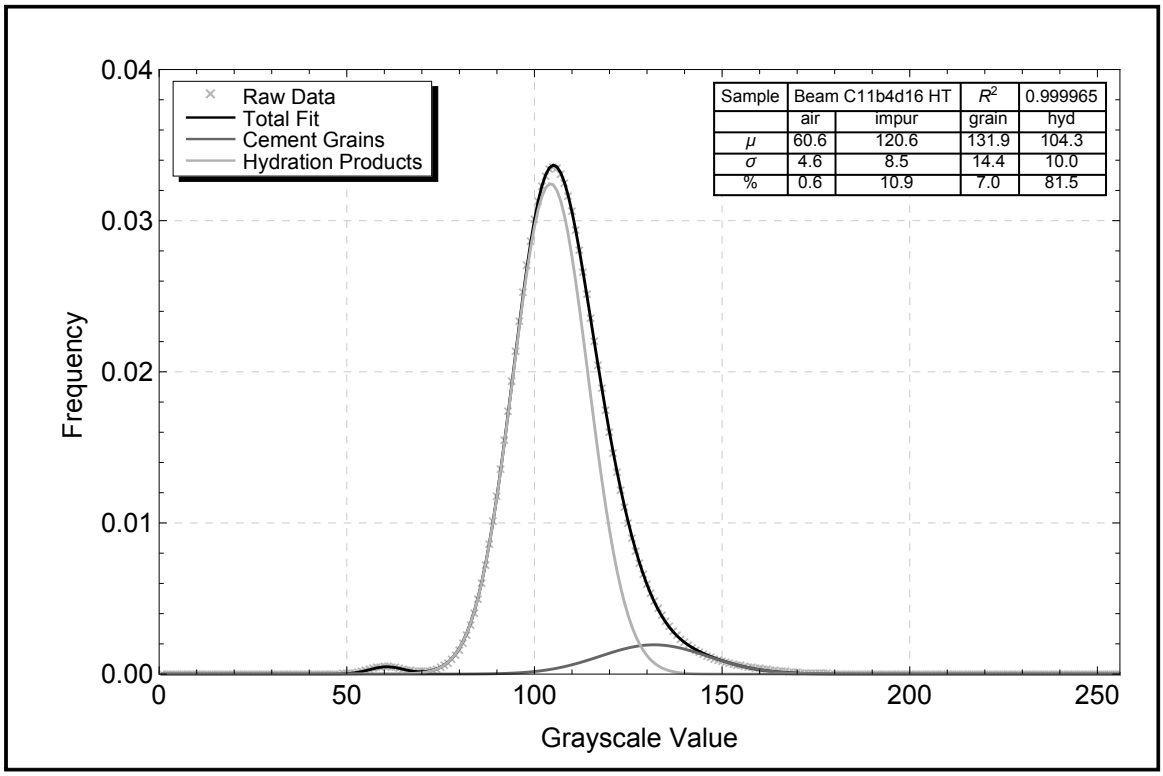

Sample	Beam C11b4d16 HT		R^2	0.999965
	air	impur	grain	hyd
μ	60.6	120.6	131.9	104.3
σ	4.6	8.5	14.4	10.0
%	0.6	10.9	7.0	81.5

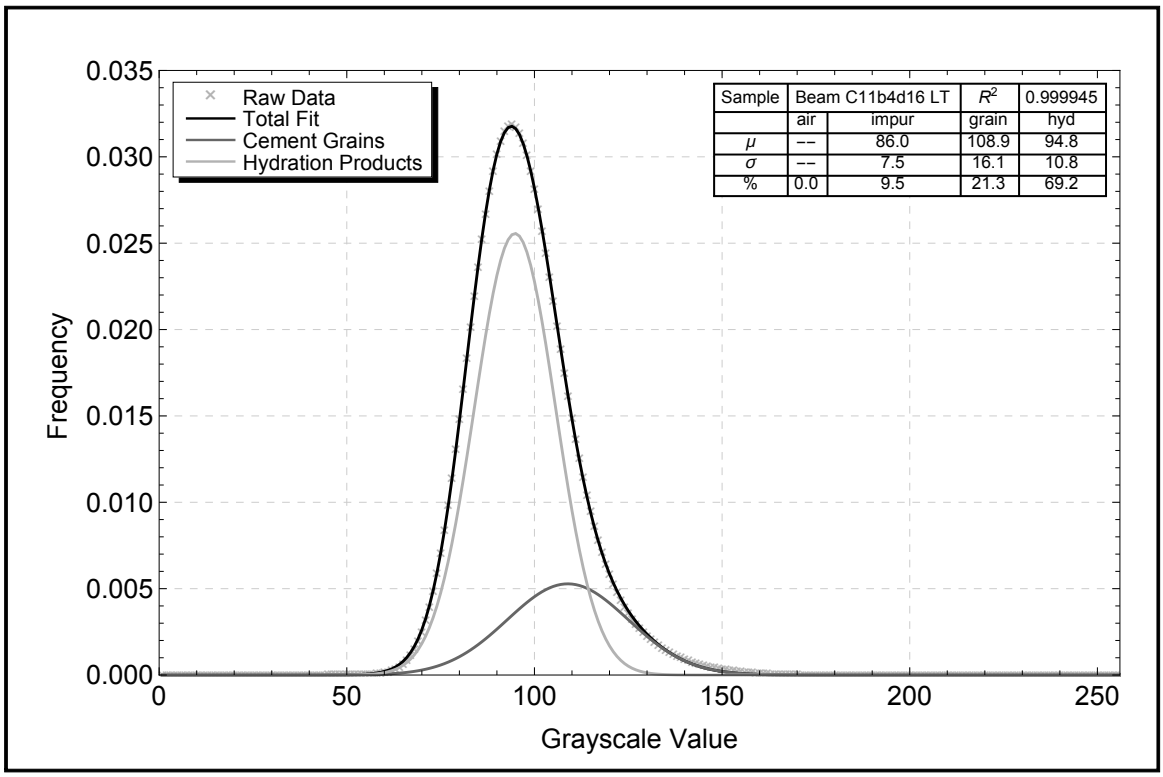

Sample	Beam C11b4d16 LT		R^2	0.999945
	air	impur	grain	hyd
μ	--	86.0	108.9	94.8
σ	--	7.5	16.1	10.8
%	0.0	9.5	21.3	69.2

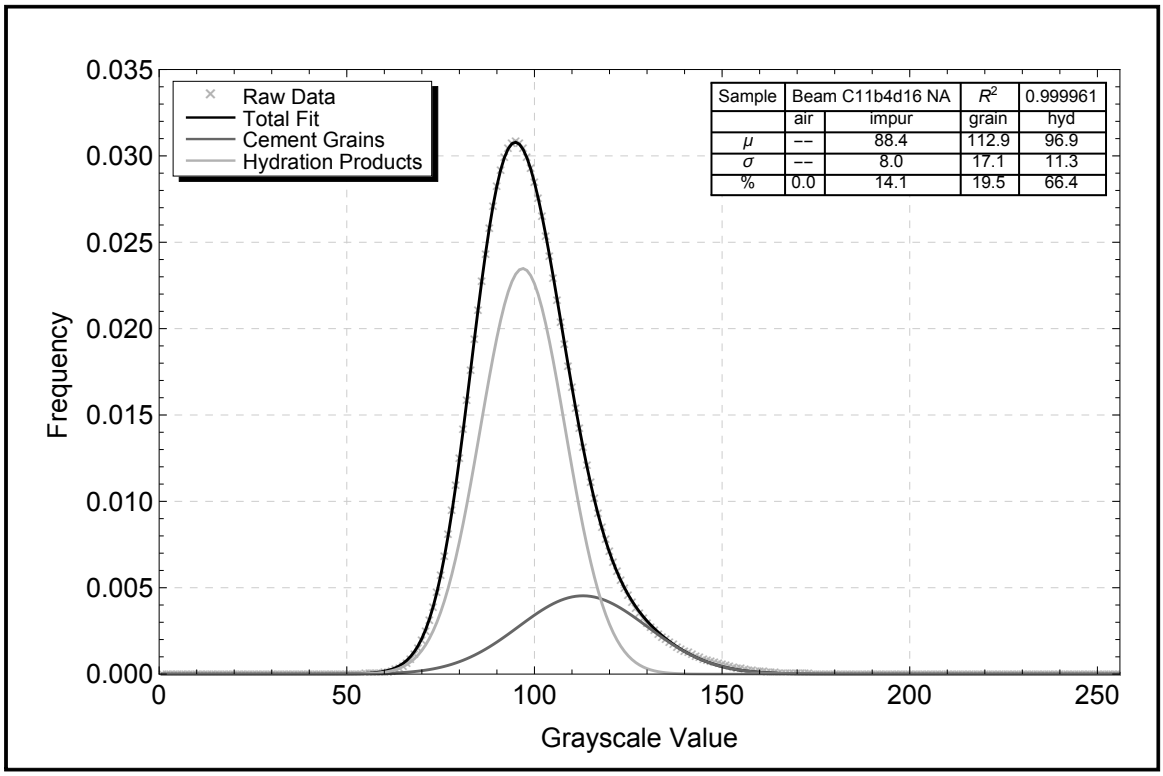

Sample	Beam C11b4d16 NA		R^2	0.999961
	air	impur	grain	hyd
μ	--	88.4	112.9	96.9
σ	--	8.0	17.1	11.3
%	0.0	14.1	19.5	66.4

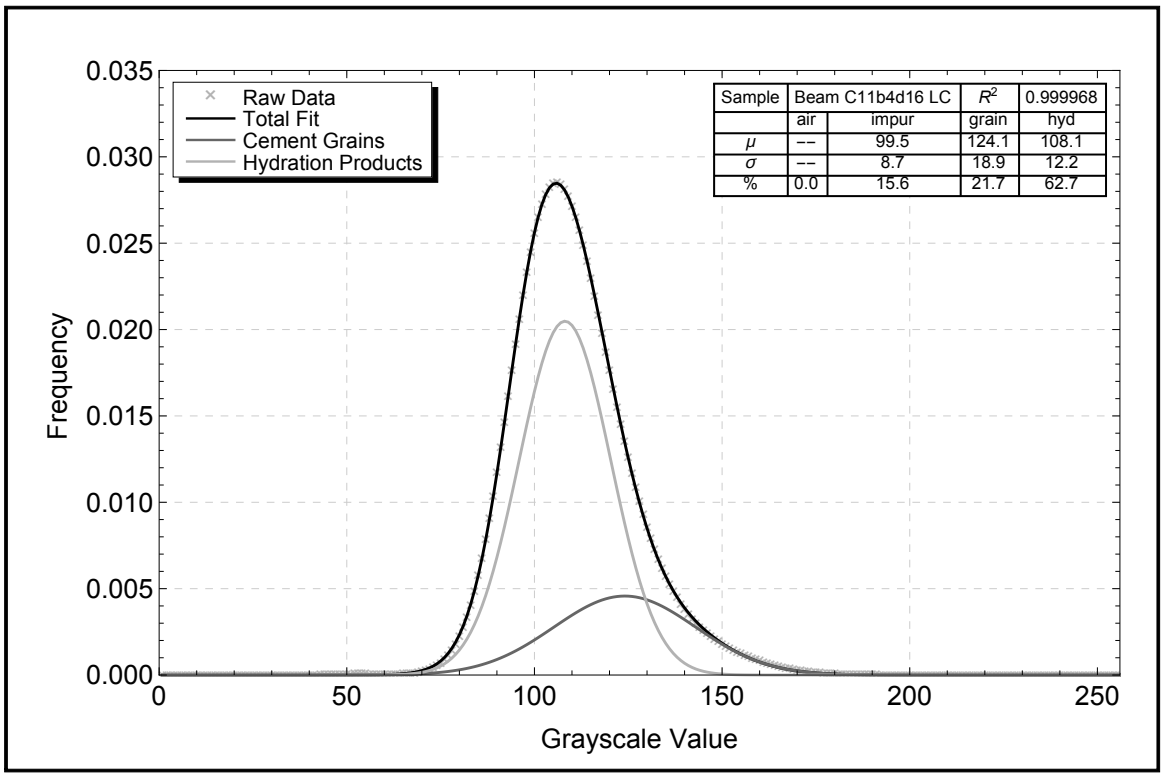

Sample	Beam C11b4d16 LC		R^2	0.999968
	air	impur	grain	hyd
μ	--	99.5	124.1	108.1
σ	--	8.7	18.9	12.2
%	0.0	15.6	21.7	62.7

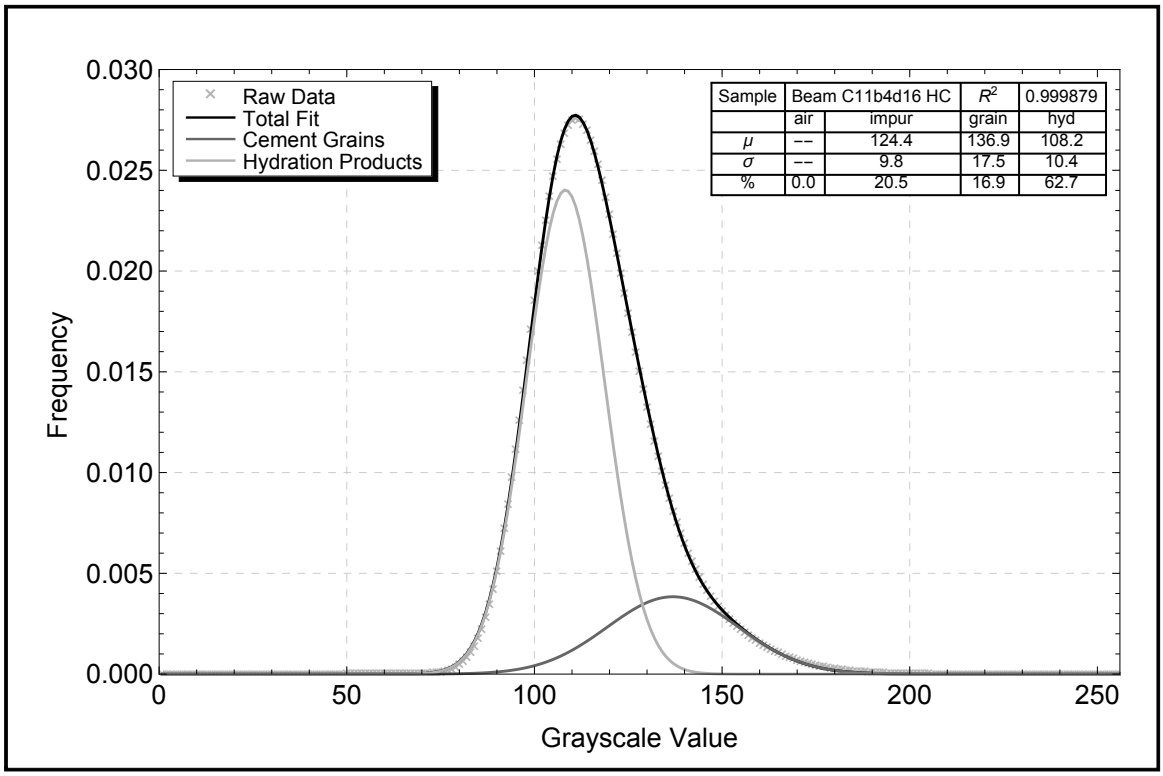
Raw Data
Total Fit
Cement Grains
Hydration Products
Sample | Beam C11b4d16 HC | R^2 | 0.999879
air | impur | grain | hyd
μ | -- | 124.4 | 136.9 | 108.2
σ | -- | 9.8 | 17.5 | 10.4
% | 0.0 | 20.5 | 16.9 | 62.7
Frequency
0.030
0.025
0.020
0.015
0.010
0.005
0.000
0
50
100
150
200
250
Grayscale Value